

Department of Chemical Engineering  
Technical University of Denmark

# Graduate Schools Yearbook 2006

Editors:  
Kim Dam-Johansen  
Martin Bøjer

Address: Department of Chemical Engineering  
Søltofts Plads, Building 229  
Technical University of Denmark  
DK-2800 Kgs. Lyngby  
Denmark

Telephone: +45 4525 2800  
Fax: +45 4588 2258  
E-mail: kt@kt.dtu.dk  
Internet: <http://www.kt.dtu.dk>

Print: Vester Kopi as  
Valby, Denmark  
Januar 2007

Cover: Anne Mette Dion

Cover photos: Klaus Holsting

ISBN-13: 978-87-91435-44-7  
ISBN-10: 87-91435-44-7

# Contents

PREFACE TO GRADUATE SCHOOLS YEARBOOK by Professor Kim Dam-Johansen .....	1
--	---

## **Contributions**

Andersen, Jimmy <i>CFD MODELING AND VALIDATION BY BENCH SCALE MEASUREMENTS</i> .....	3
Andersen, Sidsel Marie <i>MICROBIAL ACTIVITY IN OIL RESERVOIRS</i> .....	5
Andrić, Pavle <i>BIO-ETHANOL PROCESS DEVELOPMENT: APPLICATION OF ENZYMES DURING HYDROLYSIS OF THE PRE-TREATED WHEAT STRAW</i> .....	7
Arnous, Anis <i>WINE AND BERRY FRUIT JUICE WITH IMPROVED HEALTH POTENTIAL</i> .....	11
Bech, Niels <i>IN-SITU FLASH PYROLYSIS OF STRAW</i> .....	15
Beier, Søren Prip <i>MODULE DESIGN AND PERFORMANCE IN MICROFILTRATION, ULTRAFILTRATION, AND MEMBRANE CONTACTORS</i> .....	21
Castellino, Francesco <i>DEACTIVATION OF SCR CATALYSTS BY ADDITIVES</i> .....	23
Christensen, Henrik <i>SCALE UP OF PHARMACEUTICAL PRODUCTION OF ORGANIC CHEMICAL COMPOUNDS</i> .....	27
Christensen, Steen <i>MULTI-SCALE MODELING OF COMPLEX SYSTEMS</i> .....	31
Dall’Ora, Michelangelo <i>REACTIVITY AND BURNOUT OF WOOD FUELS</i> .....	35
Davidescu, Paul Florin <i>QUALITATIVE EXPERIMENTAL DESIGN FOR DYNAMIC MODELLING</i> .....	39
Drews, Joanna Maria <i>SURFACE POLYMERISATION METHODS FOR OPTIMIZED ADHESION</i> .....	43
Eenschooten, Corinne <i>DEVELOPMENT OF HYALURONIC ACID-BASED NANOPARTICLES FOR TOPICAL DELIVERY OF COSMETIC ACTIVES</i> .....	47
Egholm, Runi Ditlev <i>MODELLING AND SIMULATION OF TWO-PHASE FLUID SYSTEMS</i> .....	53
Elmøe, Tobias Dokkedal <i>PRODUCTION OF CERAMIC CATALYTIC MEMBRANES BY DEPOSITION OF NANO-PARTICLES</i> .....	57
Enevoldsen, Ann Dorrit <i>ENZYME RECOVERY BY CROSSFLOW ELECTRO-ULTRAFILTRATION</i> .....	61
Fosbøl, Philip Loldrup <i>CO<sub>2</sub> CORROSION IN NATURAL GAS PIPELINES – EXPERIMENTS AND MODELING</i> .....	65
Gabrielsen, Jostein <i>CO<sub>2</sub> CAPTURE FROM COAL FIRED POWER PLANTS</i> .....	71
Guo, Fengxiao <i>ANOPOROUS POLYMERS BY LIVING ANIONIC POLYMERIZATION AND ATOM TRANSFER RADICAL POLYMERIZATION</i> .....	75
Hansen, Brian Brun <i>GYPSUM CRYSTALLISATION AND FOAMING PREVENTION IN WET FLUE GAS DESULPHURISATION (FGD) PLANTS</i> .....	77

Hansen, Natanya Majbritt Louie <i>SYNTHESIS OF AMPHIPHILIC BLOCK COPOLYMERS BY ATOM TRANSFER RADICAL POLYMERIZATION</i> .....	81
Hansen, Thomas Steen <i>TESTING AND FABRICATION OF ALL POLYMER MICROPUMP</i> .....	87
Hede, Peter Dybdahl <i>FLUID BED AGGLOMERATION AND COATING</i> .....	93
Heiredal, Michael Lykke <i>PARTICLE DYNAMICS IN MONOLITH CATALYSTS</i> .....	99
Hu, Guilin <i>SO<sub>2</sub> EMISSION FROM CEMENT PRODUCTION</i> .....	101
Hua, Ling <i>UPGRADING OF MICROBIAL BIOMASS FOR RECOVERY OF VALUABLE PRODUCTS</i> .....	107
Huusom, Jacob Kjøbsted <i>MODEL IDENTIFICATION FOR CONTROL - UNDER CONTROL</i> .....	109
Jensen, Jacob Skibsted <i>PREDICTION OF WINE QUALITY FROM PHENOLIC PROFILES OF GRAPES</i> .....	113
Johansen, Kent <i>STATISTICAL METHODS FOR HISTORY MATCHING</i> .....	115
Kristensen, Morten Rode <i>NUMERICAL SIMULATION OF IN-SITU COMBUSTION</i> .....	121
Larsen, Thomas Ølholm <i>TRIBOLOGICAL PROPERTIES OF POLYMER-MATRIX COMPOSITES WHEN DRY-SLIDING AGAINST STEEL COUNTERFACES</i> .....	125
Laursen, Jens Lolle <i>PROCESSABILITY AND FRACTURE MECHANICAL PERFORMANCE OF TRIBOLOGICALLY MODIFIED PLASTICS</i> .....	131
Lin, Yi <i>MULTI COMPONENT EQUATIONS OF STATE FOR ELECTROLYTES AT A WIDE TEMPERATURE RANGE</i> .....	133
Mitkowski, Piotr Tomasz <i>COMPUTER AIDED DESIGN OF HYBRID PROCESSES CONSISTING OF REACTOR AND MEMBRANE-BASED SEPARATION UNIT</i> .....	139
Morales-Rodríguez, Ricardo <i>COMPUTER-AIDED MULTISCALE MODELLING FOR CHEMICAL PROCESS ENGINEERING</i> .....	145
Mortensen, Martin Nordvig <i>STABILISATION OF POLYETHYLENE GLYCOL IN ARCHAEOLOGICAL WOOD</i> .....	147
Nielsen, Hanne Hostrup <i>IN-SITU INVESTIGATIONS OF THE COMBUSTION IN LARGE, TWO-STROKE, DIESEL ENGINES</i> .....	151
Nielsen, Jens Kromann <i>RHEOLOGY, STRUCTURAL STUDIES, AND SYNTHESIS</i> .....	153
Nielsen, Rudi Pankratz <i>ANALYSIS OF THE PHYSICAL CHEMISTRY OF THE CATLIQ<sup>TM</sup> PROCESS</i> .....	159
Niu, Ben <i>CARBON DIOXIDE INJECTION IN THE CARBONATE RESERVOIR</i> .....	161
Olsen, Stefan Møller <i>CONTROLLED RELEASE OF ENVIRONMENTALLY FRIENDLY ANTIFOULING AGENTS FROM MARINE COATINGS</i> .....	163
Overgaard, Anne Kathrine Kattenhøj <i>COUPLING OF ACTIVE COMPONENTS TO SYNTHETIC POLYMERS</i> .....	165
Pauw, Brian Richard <i>ON THE MICROSTRUCTURE OF HIGH-PERFORMANCE POLYMER MATERIALS</i> .....	169

Pedersen, Kim Hougaard <i>APPLICATION OF FLY ASH FROM SOLID FUEL COMBUSTION IN CONCRETE</i> .....	171
Petersen, Nanna <i>DATA-DRIVEN MODELING FOR MONITORING AND CONTROL OF STREPTOMYCES CULTIVATIONS</i> .....	177
Petersen, Trine Lütken <i>AVOIDING PROTEOLYSIS IN FERMENTATION BROTHS THROUGH REMOVAL OF PROTEASES USING HIGH GRADIENT MAGNETIC FISHING (HGMF)</i> .....	179
Rashed, Jamal El Bashir Ali <i>MODEL-BASED RETROFIT DESIGN AND ANALYSIS OF PETROCHEMICAL PROCESSES</i> .....	181
Rasmussen, Christian Lund <i>DIRECT PARTIAL OXIDATION OF NATURAL GAS TO LIQUID CHEMICALS</i> .....	185
Rosgaard, Lisa <i>ENZYMATIC HYDROLYSIS OF LIGNOCELLULOSE</i> .....	191
Satyanarayana, Kavitha Shelakara <i>MOLECULAR MODELLING OF POLYMERS USING GRID TECHNOLOGY</i> .....	195
Schäpper, Daniel <i>CONTINUOUS CULTURE MICROBIOREACTORS</i> .....	197
Singh, Ravendra <i>MODEL-BASED COMPUTER AIDED FRAMEWORK FOR DESIGN OF PROCESS MONITORING AND ANALYSIS SYSTEMS</i> .....	199
Sloth, Jakob <i>FORMATION OF ENZYME CONTAINING PARTICLES BY SPRAY DRYING</i> .....	201
Soni, Vipasha <i>MODEL AND ANALYSIS OF VACUUM MEMBRANE DISTILLATION FOR THE RECOVERY OF VOLATILE AROMA COMPOUNDS FROM BLACK CURRANT JUICE</i> .....	205
Szewczykowski, Piotr <i>NANO-POROUS MATERIALS BASED ON BLOCK COPOLYMER SELF-ASSEMBLY AND THEIR POSSIBLE MEMBRANE APPLICATION</i> .....	211
Thomsen, Anders Daugaard <i>MICRO-SENSOR BASED ON CLICK CHEMISTRY</i> .....	215
Tihic, Amra <i>ADVANCED THERMODYNAMIC TOOLS FOR COMPUTER-AIDED PRODUCT DESIGN</i> .....	217
Villalba, Hugo Edson Gonzalez <i>DEVELOPMENT OF GROUP CONTRIBUTION<sup>PLUS</sup> MODELS FOR PROPERTIES OF ORGANIC CHEMICAL SYSTEMS</i> .....	221
Wang, Yanwei <i>MOLECULAR MODELING OF POLYMER PROPERTIES</i> .....	227
Yilmaz, Ayten <i>PARTICLE FORMATION DURING NATURAL GAS COMBUSTION AT DOMESTIC APPLIANCES</i> .....	231



## Preface

For the first time the chemical engineering department published in 2003 a Graduate Schools Yearbook. A new generation of graduate students has since then initiated their studies and the publications have become a tradition for the department.

In the yearbook our newly matriculated graduate students present the background and the aims that motivate their studies while the graduate students matriculated for longer time present the progress and the status of their research projects. Readers of the yearbooks may thereby follow the progress of the individual graduate students and their studies during the entire enrollment period and read about the numerous high quality research results from the department.



The present yearbook illustrates the broad spectrum of research activities performed by our graduate students within chemical and biochemical engineering disciplines: chemical kinetics and catalysis, process simulation and control, process integration and development, reaction engineering, thermodynamics and separation processes, oil and gas technology, combustion technology, enzyme technology polymers science, aerosols physics, mathematical modeling, and our newly established field of chemical, biochemical and pharmaceutical product design.

It is with great pleasure that I present to you:

### **The Chemical Engineering Graduate Schools Yearbook 2006**

Kim Dam-Johansen  
Professor, Head of Department





### **Jimmy Andersen**

Phone: +45 4525 28 38  
Fax: +45 4588 2258  
E-mail: [jia@kt.dtu.dk](mailto:jia@kt.dtu.dk)  
WWW: <http://www.chec.dtu.dk>  
Supervisors: Peter Glarborg  
Peter Arendt Jensen  
Søren Lovmand Hvid, DONG Energy

Ph.D. Study  
Started: April 2006  
To be completed: April 2009

## **CFD Modeling and Validation by Bench Scale Measurements**

### **Abstract**

The project concerns development and validation of CFD models that can predict mixing as well as chemical reactions in combustion processes. The primary focus of the project is on NO formation and destruction in the freeboard of grate fired boilers. Therefore a model reactor has been developed, that can reproduce the conditions present in the freeboard of grate fired boilers.

### **Introduction**

Computational Fluid Dynamics (CFD) is a powerful tool to predict mixing and fluid motion, and it have gained increasing popularity in design and trouble shooting industrial combustion installations. It is however challenging to include detailed kinetic models in CFD codes.

The focus of this project is to combine knowledge of detailed kinetic mechanisms with the prediction of mixing and local combustion stoichiometry that commercial CFD codes can provide.

In particular the project focuses on modeling the formation and destruction of NO in the freeboard section of grate fired boilers. For this purpose a bench scale freeboard combustion chamber has been designed and constructed, that will make it possible to provide well controlled and detailed measurements for verification of a CFD freeboard model. At present only limited well controlled measuring data on combustion in non swirled flames that can be applied to verification are available in the literature.

Validation of CFD models is essential if the modeling approach is to be the basis of research and design work. The initial objective of this project is therefore to supply reliable and relevant test data for modeling the mixing and gas phase reactions taking place in the freeboard section of grate fired boilers.

### **Specific objective**

The overall objectives of this PhD study are:

- To provide detailed verification data for CFD models.
- To develop and verify a CFD based model of freeboard processes in grate fired boilers.

- To implement and verify a chemical kinetic model of the formation and destruction of NO in a CFD model.

### **Experimental setup**

An experimental setup has been constructed to investigate the detailed chemical reactions taking place in the freeboard section of a grate fired power plant. The setup is designed so that the flue gas from a substoichiometric natural gas flame is mixed with additional natural gas. This gas mixture is supposed to simulate the pyrolysis and primary combustion gasses emerging from a straw layer at grate firing conditions.

The combustion gasses are led through a flow straightner, which can be thought of as the surface of the bed layer, and into the freeboard section, where secondary gas is added to complete the combustion process.

The setup is an almost 3 meter long cylindrical construction that consists of two major sections; a 1<sup>st</sup> stage and a freeboard section, the diameter in the freeboard section is 49 cm. (see figure 1).

Several ports give entrance to the reactor and thereby make it possible to to perform temperature measurements and gas sampling at many different positions, as well as visual access is possible for Laser measurements.

Ammonia addition to the reactor is done to simulate fuel nitrogen – a major precursor to NO<sub>x</sub> [1], since natural gas contains almost no nitrogen.

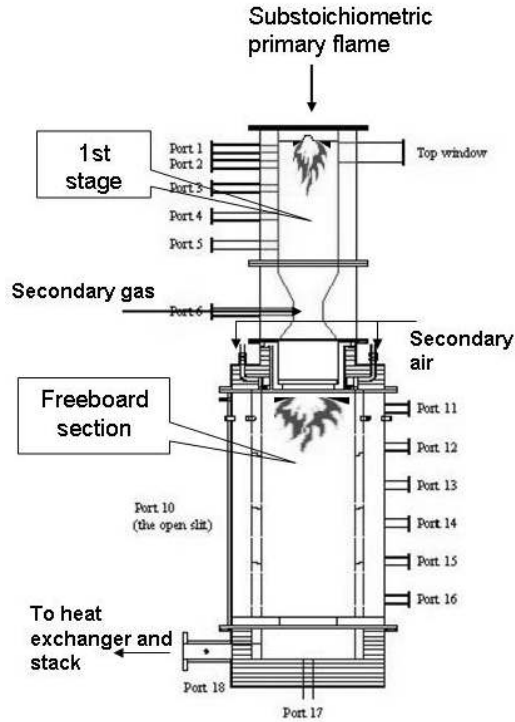


**Figure 1:** Sketch of the experimental setup – a natural gas fired freeboard simulator

Complete mapping of the freeboard combustion chamber is being done for important parameters:

- Temperature – Shielded thermocouples provide detailed temperature mapping in the freeboard chamber.
- Velocity – Laser Doppler Anemometry (LDA) measurements provide gas velocity measurements, using a non-intruding particle tracer technique



**Figure 2:** Picture from the LDA experiments.

- Gas species concentrations - Extractive gas analysis using water cooled probes makes it possible to detect and quantify numerous gas phase (for instance O<sub>2</sub>, CO, CO<sub>2</sub>, NO and NO<sub>x</sub> by means of standard analyzing techniques.

### CFD modeling approach

What a CFD model basically does is to predict the flow of fluid and heat in a computational domain. This is done by solving the governing transport equations, the equation of continuity, momentum and Energy respectively:

$$(1) \quad \frac{\partial \rho}{\partial t} + (\nabla \cdot \rho \vec{v}) = 0$$

$$(2) \quad \frac{\partial \rho}{\partial t} (\rho \vec{v}) = -\nabla \cdot (\rho \vec{v} \vec{v}) - \nabla p + \nabla \cdot \vec{\tau}$$

$$(3) \quad \frac{\partial}{\partial t} (\rho E) + \nabla \cdot (\vec{v} (\rho E + p)) = \nabla \cdot (k_{eff} \nabla T \sum_j h_j F_j + (\vec{\tau} \cdot \vec{v})) + S_h$$

The CFD code will then discretize, linearize and solve the governing transport equations including submodel input from radiation, turbulence and chemical reaction-turbulence interaction submodels.

For this project CFD modeling can be carried out in two steps, one that describes the general combustion based on a simplified reaction scheme – for instance the global reaction scheme from Jones and Lindstedt[3]:

- (4)  $H_2 + \frac{1}{2} O_2 \leftrightarrow H_2O$
- (5)  $CO + H_2O \leftrightarrow CO_2 + H_2$
- (6)  $CH_4 + H_2O \rightarrow CO + 3H_2$
- (7)  $CH_4 + O_2 \rightarrow CO + 2H_2$

The second step will take into consideration the advanced kinetic aspects of NO formation. These two steps can either be coupled directly (which will be computationally expensive), or post-processing the NO chemistry is possible, by assuming that the NO processes does not affect the global combustion or flow parameters significantly. This reasonable assumption makes post-process a detailed NO mechanism on an already verified general temperature and flow field a good option.

### Acknowledgements

The project is funded by the Danish PSO program and from STVF (Danish Technical Research Council), DONG Energy, Vattenfall, Babcock & Wilcox Vølund, and B&W Energy.

### References

1. P. Glarborg, A.D. Jensen, J.E. Johnsson, Progress in Energy and Combustion Science 29 (2003) 89-113.
2. Fluent inc. Fluent 6.2 users guide.
3. W.P. Jones, R.P. Lindstedt, Combustion and Flame 73 (1988) 233-249.



### **Sidsel Marie Andersen**

Phone: +45 4525 2982  
Fax: +45 4525 2258  
E-mail: sa@kt.dtu.dk  
WWW: <http://www.ivc-sep.dtu.dk>  
Supervisors: Erling H. Stenby  
Michael L. Michelsen  
Alexander Shapiro

Ph.D. Study  
Started: September 2006  
To be completed: September 2009

## **Microbial Activity in Oil Reservoirs**

### **Abstract**

A potential method for enhancing oil recovery is to utilize the activity of microorganisms which are either present in or injected into the oil reservoirs. Microbial enhanced oil recovery is an emerging method for further exploitation of existing but non-productive oil fields to mobilize more residual oil. Another interesting area is microbial treatment, where some microorganisms can be used to outcompete other microorganisms with an undesired activity by adding selected nutrients. Initially, this project is concerned with inclusion of a generic model for microbial activity in an existing simulator.

### **Introduction**

The principle source of fluid fuels is and will be the hydrocarbon resources. However, the finite nature of our hydrocarbon reserves has been discussed as discoveries of new oil reservoirs decrease. For the present techniques of oil recovery, a large amount of oil remains in the reservoir when the production fields are no longer economically feasible. Methods of enhanced oil recovery (EOR) have been developed, but often they are economically unattractive.

The biotechnology research has advanced and the oil industry has matured to consider microorganisms in the context of oil production. Often, the oil reservoirs contain indigenous microorganisms, where bacteria are the dominating organisms. Microbial enhanced oil recovery (MEOR) uses these indigenous bacteria or injects selected bacteria. For bacterial growth and metabolite production, the requirements are different nutrient, which are led to the reservoir. In some cases, the carbon source is residual oil.

The MEOR purpose is, like other EOR methods, to mobilize the residual oil and thus reduce its content and/or increase the volumetric efficiency. MEOR address the same physical parameters as chemical EOR, where they are subject to the same *in situ* technical difficulties. The essential difference between MEOR and chemical EOR resides in the method of introducing the recovery-enhancing chemicals into the reservoir. Enhancement of the oil recovery through microbial action can be performed through several mechanisms as follows:

- Reduction of oil-water interfacial tension and alteration of wettability by surfactant production and bacterial presence.
- Viscosity reduction by gas production or degradation of long-chain saturated hydrocarbons.
- Selective plugging by bacteria and their metabolites.
- Generation of acids that dissolve rock improving absolute permeability.

MEOR is considered a potential 'high risk, high reward' process, where the high risk originates from the many performance constraints of the process. The reward is that the implementation difficulties and the cost resemble those of water flooding than those of the chemical EOR.

An oil reservoir is a harsh environment, which can have high temperature, high salinity and low pH (3-7). In general, this extreme environment should be taken into account when selecting bacteria and nutrient media. As the reservoir conditions change from reservoir to reservoir, an extra effort has to be put on selecting and developing suitable bacteria and nutrient media for each reservoir, which has the potential to undermine microbial process economic viability.

In the oil reservoir, toxic H<sub>2</sub>S is produced by sulfate-reducing bacteria. H<sub>2</sub>S is corrosive, increases sulfur content in oil and gas, and may also lead to reservoir plugging. An approach to minimize bacterial H<sub>2</sub>S

production is the addition of nitrate to the injected water. This action stimulates nitrate-reducing bacteria which to some extent could outcompete the sulfate-reducing bacteria.

### **Specific objectives**

The specific objectives of this project consist of two parts. The first part is to include microbial activity in a simulator, which can be either MEOR or reduction of bacterial H<sub>2</sub>S production.

The second part of the project is currently to extend streamline simulator. The capillary force formulation should be extended from two to three phases and also the compositional feature should be developed further.

### **Future work**

A generic model for MEOR should be set up and included in a simulator. The modeling approach should be performed in order to understand the relationships between reservoir characteristics, operating conditions and microbial performance more thoroughly.

In the end these more or less predictive simulators could through cooperation with the advancing biotechnological research facilitate development of more reliable oil recovery strategies.

### **Acknowledgements**

The project is part of the Molecular Products and Product Technology (MP<sub>2</sub>T) in the graduate school in chemical engineering. The industrial cooperators are DONG A/S.

### **References**

1. S.L. Bryant, T.P. Lockhart, SPE 63229 presented at SPE Annual Technical Conference and Exhibition, Dallas, Texas, 2000
2. F.L. Dietrich, F.G. Brown, Z.H. Ahou, M.A. Maure, SPE 36746 presented at the SPE Annual Technical Conference and Exhibition, Denver, Colorado, 1996.
3. G. Hamer, N. Al-Awadhi, Acta Biotechnol. 20 (2000) 335-350.
4. J.D. van Hamme, A. Singh, O.P. Ward, Microbiology and Molecular Biology Reviews 67 (4) (2003) 503-549.
5. E. Kowalewski, I. Rueslåtten, K.H. Steen, G. Bødtker, O. Torsæter, Journal of Petroleum Science and Engineering 52 (2006) 275-286.
6. M. Magot, B. Ollivier, B.K.C. Patel, Antonie van Leeuwenhoek 77 (2000) 103-116.



**Pavle Andrić**

Phone: +45 4525 2842 / +45 2546 1832  
Fax: +45 4588 2258  
E-mail: pan@kt.dtu.dk  
WWW: <http://www.chec.kt.dtu.dk>  
Supervisors: Kim Dam-Johansen  
Peter Arendt Jensen  
Anne Meyer

**Ph.D. Study**

Started: October 2005  
To be completed: September 2008

## **Bio-Ethanol Process Development: Application of Enzymes during Hydrolysis of the Pre-Treated Wheat Straw**

**Abstract**

Large-scale application of enzymatic hydrolysis is limited by lack of an effective bio-reactor for the complex heterogeneous reaction and high cost of cellulases, due to their inefficient action on ligno-cellulose. The central problem related to reactor design is in inefficient stirring of highly viscous reaction mixture, which is needed to enable efficient contact of cellulases and biomass. This is pronounced in the initial part of the reaction and especially with the reaction mixtures containing high dry matter content (>10 %) that are desired due to the overall process economy. The main objective of this work is to investigate the enzymatic hydrolysis of the pre-treated wheat straw and develop an improved bio-reactor concept for efficient cellulose conversion utilizing enzymes.

**Introduction**

The limitation of the reserves of the fossil-based crude oil, uncertainty of its supplies and constantly rising price; the pronounced green-house-gas effect and increased governmental regulations in respect to the emissions, and growing fuel markets in developing countries, are some of the main factors that have led to the increased interest for the alternative sources of energy.

Ethanol produced from renewable sources such as biomass is emerging as a promising transportation fuel, which can be used as an alternative to the fossil gasoline. Ethanol produced from any kind of biomass is termed as bio-ethanol.

Bio-ethanol is today the world's most widely used transport bio-fuel, accounting for around 90% of total consumption [1], and has a central place in a new EU target for total share of bio-fuels (25%) by year 2030 [2]. Furthermore, in the USA the bio-ethanol is one of the main bio-fuels in research focus, which is going to be further intensified, as indicated several times in US President Bush speeches [3].

Production of ethanol from primary biomass, i.e. starch, which can be used as a food or feed, is a well established and known process [4]. However, this process is significantly limited by the high value of this kind of biomass.

An alternative way to produce ethanol is from secondary biomass. Secondary or ligno-cellulosic biomass has low or no value as food (Figure 1).

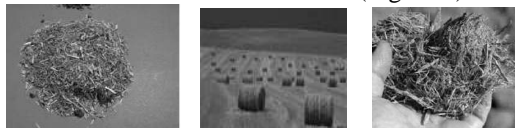


**Figure 1:** Ligno-cellulosic biomass includes various types of agricultural, forestry or industrial wastes

It includes a variety of a relatively cheap agricultural or forestry residues, dedicated crops and different kinds of waste, such as wheat straw, corn stover, wood chips, etc.

Use of bio-ethanol, produced from ligno-cellulose, as a renewable transportation fuel could potentially offer many benefits. Some believe that, in the near future, no other sustainable option for production of transportation fuels will be able to match ethanol made from ligno-cellulosic biomass with respect to its environmental, economic, strategic and infrastructural advantages [5]. Compared to fossil fuels, the bio-ethanol contribution to the net emission of CO<sub>2</sub> is low [6]. Blended with gasoline, combustion of ethanol in car engines lowers the emissions of many pollutants such as CO, volatile organic compounds and hydrocarbons [7]. Furthermore, ethanol increases the octane number of the fuel [8].

Ligno-cellulose is a generic term describing the main constituents in most of the plants, namely cellulose, hemi-cellulose and lignin. In the ligno-cellulose, cellulose chains are aggregated together into elementary fibrils of crystalline structure, as it is in the cell wall of different kind of biomass (Figure 2). In the biomass, bunches of elementary fibrils are embedded in a matrix of hemi-cellulose with a thickness of 7-30nm, while lignin is located primarily on the exterior of such formed micro-fibril [9].

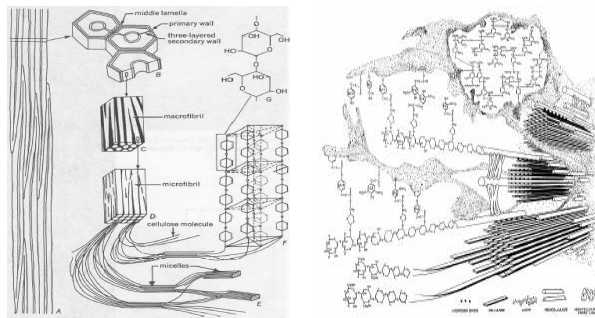


**Figure 2:** Two similar views of ligno-cellulose structure: cellulose micro- and macro-fibrils protected by lignin and hemi-cellulose [10], [11]

Cellulose, in naturally occurring materials, is closely associated with hemi-cellulose, while the carbohydrate-rich micro-fibrils are surrounded by a lignin seal. Hemi-cellulose is connected by hydrogen bonds to cellulose elementary fibrils, thus forming a network that provides the structural backbone to the plant cell wall [12]. The role of hemi-cellulose is to provide a linkage between lignin and cellulose. Lignin gives mechanical strength and structural rigidity to the plants, by stiffening and holding the fibers of polysaccharides together, but also chemical and resistance against pests and diseases. Of the three components presented, lignin is the most resistant to degradation [13]. Thus, the compounding of ligno-cellulose is almost perfect: linear cellulose chains contribute to tensile strength, while hydrophobic amorphous lignin brings chemical resistance and protection against water.

One of the possible process layouts for Bio-Ethanol production is shown on Figure 3.

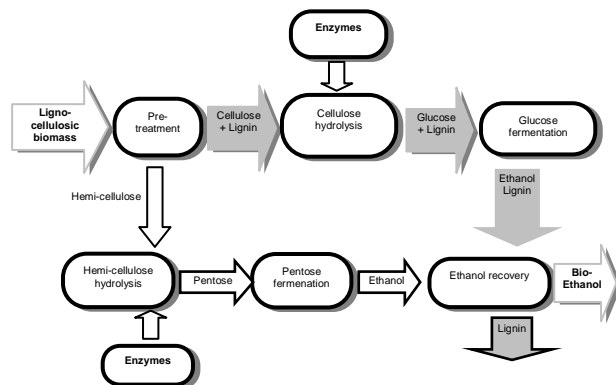


**Figure 3:** Bio-Ethanol production from ligno-cellulosic biomass-simplified scheme

The envisaged Bio-Ethanol production process from ligno-cellulosic biomass can be divided into several main steps: biomass transport and handling, biomass pre-treatment, cellulose and hemi-cellulose hydrolysis, fermentation of sugars and ethanol recovery.

Upon transport to the site of production, biomass is handled using various mechanical operations (separation from dirt and stones, cutting, shredding, milling, conveying, etc.) to facilitate satisfactory heat and mass transfer in the subsequent steps. In the pre-treatment, biomass is usually submitted to rapid conditions such as high temperature and/or use of chemical agents, in order to open the ligno-cellulosic structure and make cellulose and hemi-cellulose susceptible to the hydrolysis. In hydrolysis, cellulose and hemi-cellulose are converted to monosaccharide sugars using enzymes or different acids, while in fermentation these sugars are converted by microorganisms to ethanol. Ethanol can be further purified using stripping, distillation, pervaporation, etc., to obtain fuel grade. The process also yields a variety of co-products that can be used for electricity and heat generation and feed applications, such as lignin rich residues, proteins, vinasse, etc. which are obtained from different operations (screw-pressing, drying, centrifugation, evaporation, etc.).

#### Enzymatic hydrolysis of ligno-cellulosic biomass

Bio-ethanol can be produced from the ligno-cellulose by using concentrated acid, dilute acid or enzymes.

The enzymatic hydrolysis of ligno-cellulosic biomass is a most promising method for production of bio-ethanol. The use of enzymes to produce sugars from ligno-cellulosic biomass is a relatively recent concept [14]. Enzymatic hydrolysis is performed at mild conditions (usually 40-50°C and pH 4-5 [15]) and consequently the utility costs are lower than in acid hydrolysis. Furthermore, since the enzymes are catalysts that catalyze very specific reactions, minimum of the degradation products are formed as well as no corrosion problems are associated with this reaction [16]. It is stated that enzymes have advantage in that they are naturally occurring compounds which are biodegradable and environmentally benign [5].

However, bio-ethanol production from ligno-cellulose has not yet been demonstrated on a commercial scale, due to technical and economical obstacles. A key element underlying bio-ethanol processing cost reductions is improvement in the pre-treatment and enzymatic hydrolysis technology [17].

The use of enzymatic hydrolysis for the production of bio-ethanol from ligno-cellulose is a very difficult and challenging task. The large-scale application of enzymatic hydrolysis has in general been limited by lack of an effective bio-reactor for the complex heterogeneous catalysis, due to ligno-cellulose structure, and the high cost of cellulose degrading enzymes-cellulases, which arises from their inefficient action (application) on (ligno-)cellulose.

The pre-treated substrate, used for the enzymatic hydrolysis, is highly water retaining and thus viscous and not mixable with enzymes (Figure 4a and 4b). The central problem associated with the bio-reactor design is in inefficient stirring of highly viscous reaction mixture, which is needed to enable efficient contact of cellulases and pre-treated biomass substrate. This is pronounced in the initial part of the reaction and especially with the reaction mixtures containing high dry matter content (>5-10 %DM) that are desired due to the overall economy of the process. As a result, the use of continuously stirred batch reactor (CSBR) for enzymatic hydrolysis reaction is inadequate.

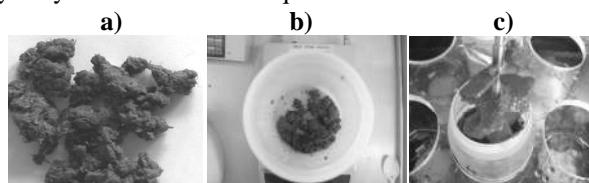


**Figure 4:** Pre-treated straw with 20% dry matter content (a, b) and its hydrolysis in CSBR (c) [18]

Furthermore, the most important reasons for the inefficient action of enzymes are in the crystalline structure of cellulose, which is resistant to enzymatic attack, and de-activation of cellulases due to: a) inhibition by intermediate and final products (cellobiose and glucose, respectively), b) un-productive adsorption to lignin and c) shear stress.

To summarize, due to the problems with resistant crystalline structure of cellulose, de-activation and mixing with biomass substrate, the application of cellulases in CSBR is considered as inefficient, which results in a high contribution of enzymes costs to the overall processing costs. Moreover, the slow reaction rate is the additional consequence that makes this process unsuitable for a continuous reactor system.

### Specific Objectives

The main objective of this work is to investigate the enzymatic hydrolysis of the pre-treated wheat straw and to develop an improved bio-reactor concept for a more efficient cellulose conversion utilizing enzymes. The general idea is to change bio-reactor's mechanical (type, mixing equipment) and operational design (loading strategies, stream recycles, integration with separation units), in order to improve mixing of enzyme and substrate, and reduce cellulase de-activation by product inhibition, un-productive adsorption to lignin and shear stress.

The first part of the work includes characterization of the enzymatic hydrolysis reaction, e.g. examination of the cellulose conversion with the time, determination of maximal conversion and quantification of cellulase de-activation rates, in an experimental reactor which can process high dry matter mixtures, since these data are missing in the literature and are relevant for the reactor design. This is accompanied by the examination of some the key pre-treated biomass structure characteristics (particle size and shape, surface,

assessable area), which are changing during the course of the reaction.

In the final part, obtained knowledge will be used to develop an improved bio-reactor concept for a more efficient conversion utilizing cellulases, where it is desired to maximize the glucose yield and productivity, and minimize glucose concentration in the reactor, reaction time and enzyme loading needed for the hydrolysis reaction. The emphasis will be on facilitating the enzyme contact with biomass, in order to improve the effectiveness of the cellulase application on the pre-treated ligno-cellulosic biomass. The mechanical design of the reactor will mainly be used for realization of the improved stirring, while operational design for further improving the contact of cellulases with the biomass and reducing the de-activation. The improved concept will be chosen from already available options, such as improved batch reactors, reactors with recycle of enzymes or coupled with membranes, fixed bed, improved SSF or will be a new type of bio-reactor.

### Experimental methods

The enzymatic hydrolysis experiments are done with the wheat straw, which is hydro-thermally pre-treated in 3 steps (60, 180, 195°C; 15, 10, 3 min, respectively) in a pilot plant operated by DONG A/S (previous Elsam). The cellulase activity measurement is done using standard FPU assay [19], while biomass compositional analysis is performed in accordance with the NREL procedure [20].

The reaction is performed at 50°C and pH = 5, using commercial enzyme preparations Celluclast® 1.5L and Novozym® 188, produced by Novozymes A/S, with the enzyme loading of 8 FPU/g<sub>substrate</sub> and 13 CBU/g<sub>substrate</sub>, respectively. The reaction mixture is analyzed for glucose and cellobiose concentration using Dionex HPLC system. In certain cases, additional experiments are performed with the model substrates, such as pure cellulose.

### Current work

Initial experiments done on pre-treated barley straw [18] have shown that experimental continuously stirred batch reactor (CSBR) is highly inefficient for reaction mixtures with dry matter contents higher than 10%. However, even if problematic in the first hours of hydrolysis, all samples become significantly hydrolyzed after 24hr of reaction [18].

The current work involves design of an experimental reactor that can process reaction mixtures with high dry matter content, which will be used for investigation of different factors limiting hydrolysis and, subsequently, investigation of different strategies for improved application of cellulases.



**Figure 5:**  $\alpha$ -cellulose with 30%, 40% and 50% dry matter, note embedded impellers

The preliminary experiments have shown that conventional stirring would not be possible to utilize with pure cellulose, especially for mixtures higher than 20% DM (Figure 5). From the other side, they have also shown that a certain degree of stirring is necessary for these mixtures, since the fixed bed systems do not yield significant conversions.

The future work is directed towards design of an experimental reactor for processing mixtures with dry matter content larger than 20% DM.

### Acknowledgements

This Ph.D. study is sponsored by the Technical University of Denmark.

### References

1. Pathways to Biofuels: A European Biofuels Technology Platform, Background paper, 2004
2. Biofuels in the EU, A vision for 2030 and beyond, Final draft of the Biofuels Research Advisory Council, 2006
3. President Bush Discusses Energy at Renewable Energy Conference, St. Louis Convention Center, <http://www.whitehouse.gov/news/releases/2006/10/20061012-4.html>, 2006
4. A. McAloon, F. Taylor, W. Yee, K. Ibsen, R. Wooley, Determining the Cost of Producing Ethanol from Starch and Lignocellulosic Feedstocks, Technical Report, U.S. Department of Agriculture and U.S. Department of Energy, NREL, 2000
5. C. E. Wyman, Biomass Ethanol: Technical Progress, Opportunities, and Commercial Challenges, *Annu. Rev. Energy Environ.* 24 (1999) 189-226.
6. M. Galbe, G. Zacchi, A review of the production of ethanol from softwood, *Appl. Microbiol. Biotechnol.* 59 (2002) 618-628.
7. H. L. MacLean, L. B. Lave, Evaluating automobile fuel/propulsion system technologies, *Progress in Energy and Combustion Science* 29 (2003) 1-69.
8. L.R. Lynd, Overview and evaluation of fuel ethanol from cellulosic biomass: Technology, Economics, the Environment, and Policy, *Annu. Rev. Energy Environ.* 21 (1996) 403-65.
9. Y. P. Zhang, L. R. Lynd, Toward an Aggregated Understanding of Enzymatic Hydrolysis of Cellulose: Noncomplexed Cellulase Systems, *Biotechnology and Bioengineering*, 88 (7) (2004) 797-824.
10. K. Esau, *Anatomy of Seed Plants*, 2<sup>nd</sup> Edition, John Wiley, 1977
11. J. Bidlack, M. Malone, R. Benson, Molecular Structure and Component Integration of Secondary Cell Walls in Plants, *Proc. Okla. Acad. Sci.*, 72 (1992) 51-56.
12. N. Mosier, C. Wyman, B. Dale, R. Elander, Y.Y. Lee, M. Holtzapfle, M. Ladisch, Features of promising technologies for pre-treatment of lignocellulosic biomass, *Bioresource Technology*, 96 (2005) 673-686.
13. R.L. Howard, E. Abotsi, E.L. Jansen van Rensburg, S. Howard, Lignocellulose biotechnology: issues of bioconversion and enzyme production, *African Journal of Biotechnology*, December, 2 (12) (2003) 602-619.
14. Y. Sun, J. Cheng, Hydrolysis of lignocellulosic materials for ethanol production: a review, *Bioresource Technology* 83 (2002) 1-11.
15. D. Gregg, J. N. Saddler, Bioconversion of lignocellulosic residue to ethanol: process flowsheet development, *Biomass and Bioenergy*, 9 (1-5) (1995) 287-302.
16. J. Sheehan, M. Himmel, Enzymes, Energy, and the Environment: A Strategic Perspective on the U.S. Department of Energy's Research and Development, *Activities for Bioethanol*, *Biotechnol. Prog.*, 15 (1999) 817-827.
17. D. Gregg, J. N. Saddler, A Techno-Economic Assessment of the Pretreatment and Fractionation Steps of a Biomass-to-Ethanol Process, *Applied Biochemistry and Biotechnology*, 57-58 (1996) 711-725.
18. P. Andric, Enzymatic Hydrolysis of Ligno-Cellulose, MSc project, KT, DTU, 2005
19. B. Adney, J. Baker, Chemical Analysis and Testing Task, Laboratory Analytical Procedure, Measurement of Cellulase Activities, NREL, 1996
20. R. Ruiz, T. Ehrman, Chemical Analysis and Testing Task, Laboratory Analytical Procedure, Determination of Carbohydrates in Biomass by High Performance Liquid Chromatography, NREL, 1996

### List of publications

L. Rosgaard, P. Andric, K. Dam-Johansen, S. Pedersen, A.S. Meyer, Effects of substrate loading on enzymatic hydrolysis and viscosity of pretreated barley straw, *Applied Biochemistry and Biotechnology*, 2006 (submitted for publication)

L. Rosgaard, P. Andric, K. Dam-Johansen, S. Pedersen, A.S. Meyer, Effect of Fed-Batch Loading of Substrate on Enzymatic Hydrolysis and Viscosity of Pretreated Barley Straw, Conference proceedings and oral presentation, AIChE Annual Meeting, San Francisco, 2006

P. Andric, K. Dam-Johansen, R. Gani, P. A. Jensen, Retrol vision: Preliminary Techno-Economical Analysis, Conference proceedings and oral presentation, AIChE Annual Meeting, San Francisco, 2006

P. Andric, K. Dam-Johansen, P. A. Jensen, A. S. Meyer, Bio-ethanol process development: Application of enzymes during hydrolysis of the pre-treated wheat straw, Bio-process Engineering Course, Book of abstracts, poster and oral presentation, Brac, Croatia, (2006)



**Anis Arnous**

Phone: +45 4525 2958  
Fax: +45 4593 2906  
e-mail: aar@kt.dtu.dk  
www: <http://www.bioeng.kt.dtu.dk>  
Supervisors: Prof. Anne S. Meyer

Ph.D. Study  
Started: March 2004  
To be completed: September 2008

## Wine and Berry Fruit Juice with Improved Health Potential

### Abstract

Fruits skins contribute a main part of produced fruits pomaces which are a rich source of phenolics phytochemicals compounds. Knowledge about fruits skins composition is needed to understand how phenolics phytochemicals are locked inside skin cell wall polysaccharides matrix. Such detailed compositional knowledge is a key issue to upgrade the press residues wine making or valorise the fruit skin for phenolics phytochemicals production as functional food additive. The overall objective is to provide more detailed knowledge on the use of enzymes in pre-press treatments of fruits used in juices and wines processing. This knowledge will be used to improve the release of the phenolics phytochemicals having potential health benefits.

### Introduction:

It has been amply documented that phenolic phytochemicals from fruits and berries, including mixed extracts, juice samples, different individual flavonoids and phenolic acids exert antioxidant activity towards human low-density lipoprotein (LDL) oxidation *in vitro* [1-4]. Since oxidation of LDL is a key step in the pathogenicity of atherosclerosis and thus inductive to coronary heart disease, compounds exerting antioxidant activity on LDL may exert protective, disease preventing effects in humans. Enzyme assisted plant cell wall breakdown of press residues, i.e. mainly skins and seeds, from red wine production and black currant juice pressing results in improved release of phenolics that inhibit *in vitro* oxidation of human LDL [5- 7], Fig. 1.

The antioxidant potency of the released phenols varies depending on the enzyme treatment [5, 6], Fig. 2. This suggests that it may be possible to optimize the enzyme treatments to increase concentrations of certain potent antioxidant phenols. Enzymatic pre-press treatments are already widely employed in the berry juice and wine industries. A better understanding of the plant cell wall degrading enzymes action on fruit skin materials for release of potentially health beneficial compounds appear transferable to juice and wine processing operations. The knowledge gained can therefore pave the ground for production of wines and fruit juices with improved health properties.

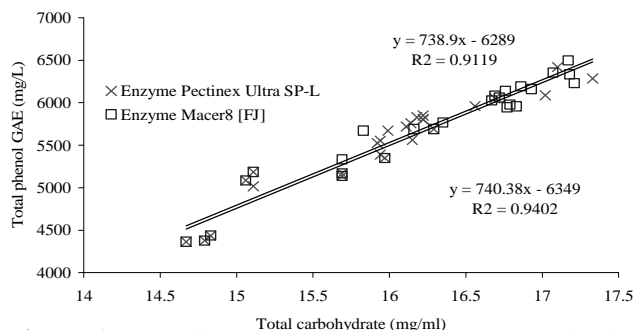


**Figure 1:** Phenolics determined as gallic acid equivalent (GAE) released when the polysaccharides in the cell wall, notably in the skin fraction, are degraded [7].

Human LDL, 37 °C, 5 μM CuSO<sub>4</sub>, Abs. 234 nm  
LDL: Low Density Lipoprotein "cholesterol"

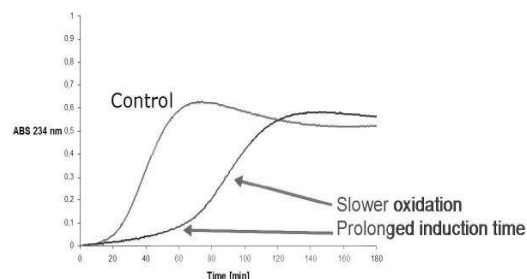
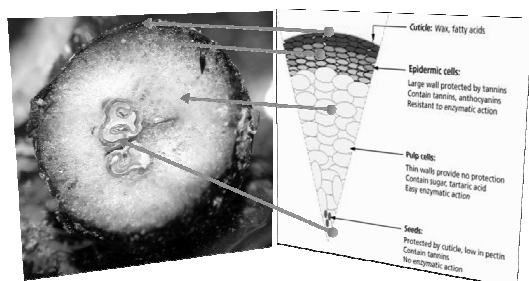


**Figure 2:** Enzyme gives different antioxidant activity.

## Specific Objectives

The aim of the proposed Ph.D. project is to explore in detail the enzyme assisted extraction of phenolics from different berry and grape press residues resulting from juice and wine processing. As a part of this, the project will also provide knowledge on how the phenols are bound in the skin polysaccharide-lignin matrix.



A separate aim is to expand the methods to evaluate possible health benefits to other effects than antioxidant activity on human LDL oxidation.

The main hypothesis to be tested during the PhD study are:

- Whether it is possible to selectively extract and retain the most potent antioxidants by novel physical and enzymatic treatments of the press residues.
- Whether it is possible to enzymatically modify the phenolics to optimize their health potential.

## Results and Discussion

Practically there is sparse knowledge about the phenolics detailed locations, and how they are bound into the fruit skin polysaccharides matrix. Knowledge about skins composition is needed. As first attempt we used grapes and apples skins as model to understand the relation between skin cell walls polysaccharides and phenolics compounds. Such detailed compositional knowledge is a key issue to upgrade the press residues wine making or valorise the fruit skin for phenolics phytochemicals production as functional food additive. Polysaccharide composition of cell walls fruits skins are usually determined by measuring the monosaccharides released after hydrolysis with acid, alkaline, or enzyme. Chemical hydrolysis is simple, standardised, and an easily repeatable technique. By acid chemical hydrolysis, chromatographic data are simplified and interferences from undesired substances could be minimized. Trifluoroacetic (TFA) and hydrochloric acid (HCl) are commonly used as hydrolysing agents. The difference in monosaccharides and phenolics profiles between grape and apple skins was expected. And it simply reflects the difference in polysaccharides cell structures between distant plants species [8].

During enzymatic extraction higher phenolics content was released from apples skin (Gold and Red delicious) relative to chemical extraction of phenolics by 60% methanol [8]. This supports the hypothesis: phenols are bound in the skin polysaccharide-lignin matrix and not only present in cell vacuoles. We also

found a strong relation between antioxidant capacity (lag-phase) and the content flavan-3-ols in the different extracts, Fig. 3 suggesting the possibility of selecting and extracting certain antioxidants using specific enzymes treatments.

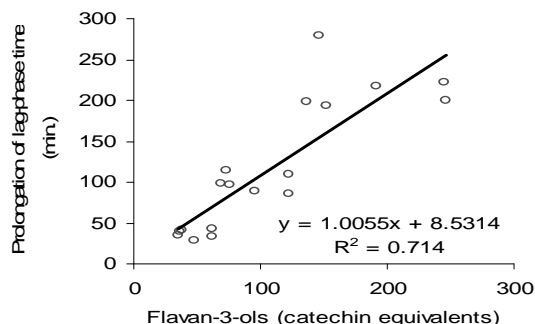


**Figure 3:** Correlation between antioxidant capacity to inhibit human LDL oxidation *in vitro* and flavan-3-ol content in Red delicious and Golden delicious peel extracts, [8].

## Conclusions

A better understanding of the cell walls in fruit skins is needed. We need to know more about how enzymes influence the antioxidant potency of the phenolics. Exploring more specific and mono-active enzymes will help in building the right tailored enzymatic matrix to fit different propose.

## References

- Meyer, A. S.; Heinonen, M.; Frankel, E. N. *Food Chemistry* 1998, 61 (1-2), 71-75.
- Meyer, A. S.; Donovan, J. L.; Pearson, D. A.; Waterhouse, A. L.; Frankel, E. N. *Journal of Agricultural and Food Chemistry* 1998, 46 (5), 1783-1787.
- Frankel, E. N.; Bosanek, C. A.; Meyer, A. S.; Silliman, K.; Kirk, L. L. *Journal of Agricultural and Food Chemistry* 1998, 46 (3), 834-838.
- Meyer, A. S.; Yi, O. S.; Pearson, D. A.; Waterhouse, A. L.; Frankel, E. N. *Journal of Agricultural and Food Chemistry* 1997, 45 (5), 1638-1643.
- Meyer, A. S.; Jepsen, S. M.; Sorensen, N. S. *Journal of Agricultural and Food Chemistry* 1998, 46 (7), 2439-2446.
- Landbo, A. K.; Meyer, A. S. *Journal of Agricultural and Food Chemistry* 2001, 49 (7), 3169-3177.
- Bagger-Jorgensen, R.; Meyer, A. S. *European Food Research and Technology* 2004, 219 (6), 620-629.
- Anis Arnous, Rikke A. Trinderup, Manuel Pinelo, and Anne S. Meyer. *Journal of Agriculture and Food Chemistry*; (in preparation).

**List of Publications:**

1. Pinelo, M.; Arnous, A.; Meyer, A. S. Trends in Food Science & Technology; 2006, 17 (11), 579-590.
2. Anis Arnous, Rikke A. Trinderup, Manuel Pinelo, and Anne S. Meyer. Journal of Agriculture and Food Chemistry; (in preparation).
3. Anis Arnous, and Anne S. Meyer. Journal of Agriculture and Food Chemistry; (in preparation).
4. Anis Arnous, and Anne S. Meyer. Bioresource technology, (in progress).



**Niels Bech**

Phone: +45 4525 2851 / +45 2178 4547  
Fax: +45 4588 2258  
E-mail: nsb@kt.dtu.dk  
WWW: <http://www.chec.kt.dtu.dk>  
Supervisors: Kim Dam-Johansen  
Peter A. Jensen

**Ph.D. Study**

Started: September 2004  
To be completed: August 2007

## In-Situ Flash Pyrolysis of Straw

**Abstract**

Energy derived from straw remains a largely untapped energy resource offering a significant potential in the cereal-growing parts of the world. The main barrier for introducing straw to the energy market competitively is its higher cost relative to fossil fuels. The thermochemical process Flash Pyrolysis is capable of converting straw to an attractive liquid fuel. This project focuses on developing an ablative flash pyrolysis process specifically targeted for the production of heavy fuel substitute Bio-oil from straw.

**Introduction**

Bioenergy in the form of straw represents a significant energy source on a world-wide scale but is today largely unutilized. According to FAO [1], the aggregate world production of cereals including barley, mixed grains, oats, rye sorghum, triticale and wheat amounted to 814 million tons in 2003 of which wheat constituted close to 70%. Geographically, the most significant wheat production areas were Western Europe (17%), North America (16%), India (12%) and the former USSR (12%). Assuming a straw/grain ratio equivalent to the Danish average for 1994-1996 of 40% [2] and straw availability for energy to be 50%, these areas potentially have a virtually untapped energy reserve equivalent to 40 mill. tons (approx. 215 mill. barrels) of heavy fuel originating from wheat. For 2003, this amount of energy corresponded to 8 days of OPEC crude oil production (27 mill. barrels/day) [3] or a market value close to \$13 bill. For the net energy importing areas (*i.e.* North America, Western Europe and India), utilization of straw for energy production is thus a CO<sub>2</sub> neutral prospect to gain more independence from the historically less stable oil exporting regions.

Unfortunately, straw does not possess the attractive properties that crude-oil products do such as a relatively high volumetric energy content, good transportability, standardized specifications and simplicity in use. The result is that utilization of straw is only practiced under primitive conditions where it is readily available or where massive public subsidies or regulation warrant it.

Apart from the unresolved problems in handling combustion of raw straw, the expense associated with logistics (*e.g.* baling, storage and transport) is the single largest barrier for utilizing straw efficiently in competition with fossil fuels under free market conditions. Access to an uninterrupted supply of fuel is also of importance to energy consumers and accordingly, expenses arising from long-distance transport of straw-derived energy need to be insignificant compared to the value of the fuel itself in order to market the product successfully.

**Specific Objectives**

Flash pyrolysis is a thermochemical process which under conditions of medium temperature and short residence time converts organic materials to char, tar and gas. Tar, a homogeneous mixture of organics and water commonly referred to as Bio-oil, is a highly compressed energy carrier and may be used in the existing combustors and distribution systems for fossil heavy fuel, while gas can be utilized for process heat.

For straw, the yields of Bio-oil, char and gas are approximately 50, 30 and 20% on dry weight basis [4]. Straw is a relatively inexpensive material provided baling and transportation are not needed. This implies that capital cost is of higher importance for in situ conversion and the development of a high capacity compact reactor system is a cardinal point. Accordingly, the main objective of the project is to identify a suitable reactor system and optimize its performance.

## Reactor System

Fluid bed and ablative reactors are the two principal technologies available for flash pyrolysis. In the former, biomaterial is introduced into a bed of hot fluidized inert material, usually sand. Although a well-known technology, fluid beds do have several disadvantages including the requirement for a large flow of inert gas for heat transport and fluidization, a relatively poor capacity/volume ratio and the need for small particle size feed. Therefore, the project focuses on developing and optimizing an ablative process for straw flash pyrolysis.

Figure 1 depicts the reactor which has been specifically developed for this project. Straw in the form of rolled and sieved straw pellets are introduced by a screw feeder into a horizontal heated tube. Here, a three-blade rotor with close clearance to the reactor wall provides rotation to the gas phase and the straw particles.

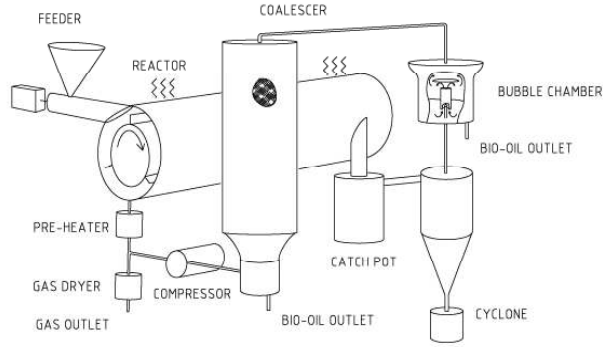


**Figure 1:** Schematic diagram of the developed ablative pyrolysis bench reactor system.

The residence time in the reactor for the evolved gasses is controlled by means of a recirculation compressor. Liquids are condensed by passing the gasses through a cool pool of tar/water mixture after char particles have been removed in the catch pot and cyclone. Aerosols are collected to large droplets in a coalescer and removed by gravity. Before the gas is metered, it is cooled to ambient temperature in order to remove water. Gas for recirculation is preheated in order to avoid condensation of liquid products within the reactor.

## Modelling

When a particle undergoes pyrolysis in the ablative regime the degradation will take place as a pseudo surface reaction. Under these conditions the energy transported to the surface will balance the requirement for heating the material to the reaction temperature. This phenomenon has been modelled in order to describe the reaction temperature of the particle as a function of reactor parameters (*e.g.* reactor temperature and rotor speed), material properties and particle conversion.

Degradation of the particle is treated as a pseudo-surface reaction even though, strictly speaking, the reaction does not proceed on the surface. For ablative pyrolysis, the steep temperature gradient observed experimentally (*e.g.* [5]) combined with a reaction rate

which is strongly dependent on temperature suggest, that reaction is concentrated in a relatively thin shell near the surface. This approach is inspired by the study of L  d   [6] for slab geometry.

An expression for the movement of the surface is obtained by setting up a shell balance for the particle to obtain the differential equation:

$$\frac{d}{dr}(r^s v) + r^s r_p = 0 \quad (1)$$

Here  $v$  is the velocity of the retracting surface and  $r_p$  is the rate of reaction. Integration within limits and substituting  $r_p$  with the Arrhenius first order expression gives:

$$\frac{dR_{surf}(t)}{dt} = -\frac{1}{R_{surf}} \int_0^{R_{surf}} r^s A \exp\left(\frac{-E}{RT(r)}\right) dr \quad (2)$$

The transient temperature distribution in the solid is described with the following partial differential equation [7]:

$$\rho \cdot c_p \frac{\partial T}{\partial t} = \frac{1}{r^s} \frac{\partial}{\partial r} \left( k \cdot r^s \frac{\partial T}{\partial r} \right) \quad (3)$$

where  $s$  is the shape factor ( $s=0$  for plate,  $s=1$  for cylinder and  $s=2$  for sphere),  $\rho$  is the density,  $c_p$  is the specific solid heat capacity and  $k$  is the thermal conductivity and since these are considered constant, (3) is rewritten as:

$$\frac{\partial T}{\partial t} = \alpha \frac{1}{r^s} \frac{\partial}{\partial r} \left( r^s \frac{\partial T}{\partial r} \right) \quad (4)$$

where  $\alpha$  is the thermal diffusivity ( $=k/\rho c_p$ ). The initial and boundary conditions for the system of differential equations (1) and (4) are:

$$\text{IC1} : R_{surf}(t=0) = R_0 \quad (5)$$

$$\text{IC2} : T(t=0, r) = T_0 \quad (6)$$

$$\text{BC1} : k \frac{\partial T}{\partial r} \Big|_{r=R_{surf}} = h(T^\infty - T_{R_{surf}}) \quad (7)$$

$$\text{BC2} : \frac{\partial T}{\partial r} \Big|_{r=0} = 0 \quad (8)$$

IC1 states the initial size of the particle considered, IC2 states that the initial spatial temperature profile is uniform, BC1 states that heat transferred to the external surface by convection is transported into the material by conduction and finally BC2 states that that the particle is symmetric around the particle centre.

The model is made dimensionless by introducing a number of variables selected to fit the system in the best possible way. The dimensionless temperature  $\theta$ :

$$\theta = \frac{T - T_0}{T_0^\infty - T_0} \quad (9)$$

The dimensionless time  $\tau$  and location  $x$  within the particle:

$$\tau = \frac{\alpha t}{R_0^2} \quad (10)$$

$$x = \frac{r}{R_{surf}(t)} \quad (11)$$

To satisfy the symmetry boundary condition at the center, (8), the variable substitution is used:

$$u = x^2 \quad (12)$$

To track the position of the surface in time, a dimensionless position,  $\eta$ , is introduced:

$$\eta = \frac{R_{surf}(t)}{R_0} \quad (13)$$

A dimensionless activation energy,  $\gamma$ , is also introduced based on the initial temperature:

$$\gamma = \frac{E}{R_G T_0} \quad (14)$$

The dimensionless variables are introduced into the original equations (2) to (8). The conservation of energy in the solid particle becomes:

$$\frac{\partial \theta}{\partial \tau} \eta^2 = 2 \left( s + 1 + u \eta \frac{\partial \eta}{\partial \tau} \right) \frac{\partial \theta}{\partial u} + 4u \frac{\partial^2 \theta}{\partial u^2} \quad (15)$$

with corresponding initial and boundary conditions:

$$\left. \frac{\partial \theta}{\partial u} \right|_{u=1} = \frac{1}{2} \frac{h R_{surf}}{k} (\theta^\infty - \theta|_{u=1}) = \frac{Bi(R_{surf})}{2} (\theta^\infty - \theta|_{u=1})$$

Or

$$\left. \frac{\partial \theta}{\partial u} \right|_{u=1} = \frac{1}{2} \frac{h R_{surf}}{k} (\theta^\infty - \theta|_{u=1}) = \frac{Bi(R_0)}{2} \eta (\theta^\infty - \theta|_{u=1}) \quad (16)$$

$$\theta(t=0, u) = 0 \quad (17)$$

It is noted that the Biot number, a characteristic dimensionless group in transient heat conduction problems, is introduced. Generally, for non-moving boundaries and for  $Bi > 10$  particle heating can be assumed to be controlled by internal heat transfer and for  $Bi < 0.1$  heating is assumed to be controlled by external transfer. However, for moving boundaries caution must be taken when applying this empiricism, as the hot surface of the particle is consumed continuously. Finally, the movement of the surface is made dimensionless yielding:

$$\frac{d\eta}{d\tau} = -\frac{R_0^2 A}{2\alpha} \eta \int_0^1 u^{\frac{s-1}{2}} \exp \left( -\frac{\gamma}{\left( \frac{T_0^\infty}{T_0} - 1 \right) \theta(u) + 1} \right) du \quad (18)$$

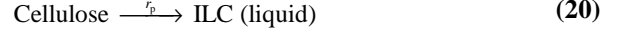
with the initial condition:

$$\eta(\tau=0) = 1 \quad (19)$$

Discretization by orthogonal collocation is used to approximate the transient temperature profile inside the particle. Integration of the coupled differential equations is performed using the semi-implicit Runge-Kuta

integration routine SIRUKE [8]. Equation (18) is solved by Gauss integration.

Due to heating the particle is decomposed into a short lifetime Intermediate Liquid Compound (ILC) which forms a film on the cylinder wall [9]. The reaction proceeds according to an irreversible first order reaction [10, 11]:



In subsequent steps, competing reactions lead to the formation of fine char particles and vapours by evaporation and thermal cracking. Following the idea of Diebold and Power [12], heat transfer to the particle is assumed to originate from wall-particle contact (i.e. solid convection) only.

For a rod of cellulose in contact with a rotating disk, the heat transfer coefficient has been experimentally established to be proportional to the contact pressure between rod and disk, provided the relative velocity is above 1.0 to 1.5 m/s [5]. It is assumed that particles of slab cylindrical geometry are indefinite and during conversion slabs are only submitted to wall contact on one side, whereas cylinders and spheres are evenly exposed to the hot surface due to rotation. Also, it is assumed that for cylinders and spheres, the contact pressure between particle and wall can be calculated using the area constituted by the part of the particle submerged in TLC as basis. For slabs, all the surface area of the exposed side is considered to be in intimate contact with the wall. Under these conditions, it can be shown that  $h$  is given by:

$$h = \frac{1}{59(s+1)} r \rho g G \quad (21)$$

where the usual notation is used. Table 1 contains information regarding the kinetic and physical properties used for the subsequent calculations with the exception of heat of reaction which has been ignored due to the insignificance in relation to the latent heat [12]. Particles are assumed to be converted when the characteristic size is reduced to 50  $\mu\text{m}$  which is comparable to the size of the char formed in the later degradation step of ILC.

**Table 1** – Physical and chemical parameters used in the simulation.

Parameter	Value	Unit	Ref.
$\rho$	700	kg/m <sup>3</sup>	[13]
$A$	$2.8 \cdot 10^{19}$	1/s	[11]
$E$	242	kJ/mol	[11]
$c_p$	2446	J/kg/K	[13]
$k$	0.21	W/m/K	[13]
$\Delta H$	$\sim 0$	kJ/kg	[12], [14]
$\varepsilon$	0.70	-	[13]
$\sigma$	$5.76 \cdot 10^{-8}$	W/m <sup>2</sup> /K <sup>4</sup>	-
$\gamma$	97.67	-	-
$R_0$	317	$\mu\text{m}$	-
$R_x$	50	$\mu\text{m}$	-

Figure 2 depicts modeling results for the surface temperature of a spherical particle undergoing ablative pyrolysis at levels of centrifugal force and reactor wall temperature obtainable in the experimental bench reactor system, see below. Generally, the surface temperature of the reacting particle will increase both by applying a higher reactor temperature and force against the wall of the reactor but remains almost constant for the main part of the conversion. This effect has earlier been demonstrated experimentally for wood by Lédé and co-workers [5]. They found the process to be well described as a melting phenomenon and assigned the “melting temperature” of wood to 466 °C. Due to a higher temperature of their rotating disc and a higher pressure applied to the wood cylinder, the results of the simulation presented here will naturally be lower.

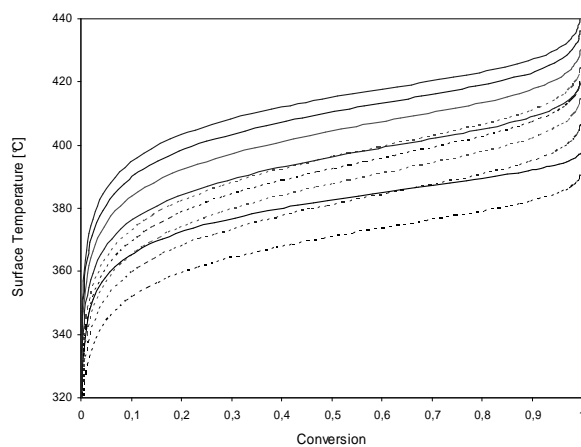


**Figure 2:** Surface temperature of a spherical particle ( $R_0 = 317 \mu\text{m}$ ) with an initial temperature of 20°C undergoing ablative pyrolysis at 4,917 (broken lines) and 17,004 G's (solid lines). Results for reactor wall temperatures of 400, 450, 500, 550 and 600°C.

The conditions necessary to obtain ablative pyrolysis have by Lédé [6] and Di Blasi [10] suggestively been defined by means of the Biot number,  $Bi$  and the thermal Thiele modulus,  $Th$ :

$$\begin{aligned} Bi &\geq 1 \\ Th &\gg 1 \end{aligned} \quad (22)$$

The physical interpretation of  $Th$  is that it gives the ratio between a characteristic time of solid heating and a characteristic time of solid degradation. The ablative envelope is thus characterized by internal control of particle heating and that solid degradation proceeds faster than the inward solid heating rate. As can be seen from Figure 3 the conditions studied in the simulation presented here can by this definition not stringently be characterized as ablative. Therefore, even though the characteristic constant particle surface temperature for ablative pyrolysis is approached, care must be taken when interpreting the experimental results in relation to the model.

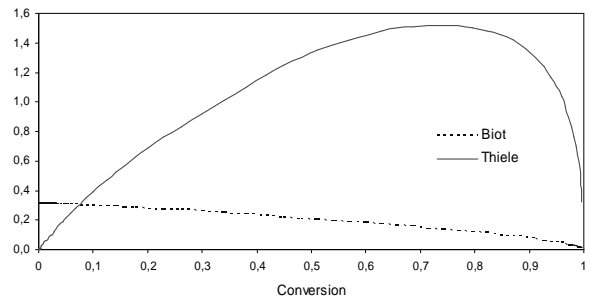


**Figure 3:** Biot number and Thiele modulus for a spherical particle undergoing pyrolysis (reactor wall temperature 600 C and centrifugal force 17,004 G's).

### Experimental

Crushed wheat straw pellets were treated in the reactor system depicted on figure 1. Table 2 displays the main properties of the feed material and the static conditions employed throughout the runs. Reactor wall temperature and centrifugal force was varied between runs and the influence on the yield of principal products recorded as reported in Figure 4. During the runs, the axial temperature profile on the reactor pipe followed the profile reported on figure 5, where the center temperature is the one referred to on figure 4. From figure 4 it is observed, that the yields reach a plateau for reactor temperatures above approximately 450 °C. Varying rotor speed and thus centrifugal force does not seem to influence the yield distribution in the temperature range from 480 to 620 °C. At 550 °C the yields of liquid, gas and char were 53, 21, and 23 pct. on dry ash free (daf.) basis, respectively.

**Table 2 – Experimental conditions.**

Parameter	Value	Unit
Particle size (MMD)	633	micron
Ash	6.8	% db.
Moisture	5.8	% wt.
Volatile matter	75	% db.
Solid feed rate	24	g/min
Feed Time	14	min
Gas recycle temperature	400	°C
Gas residence time	1.8- 3.3	S

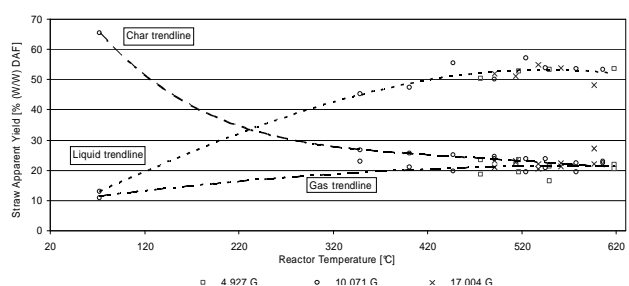


**Figure 4:** Experimentally determined yield distribution for wheat straw with reactor wall temperature and nominally centrifugal force.

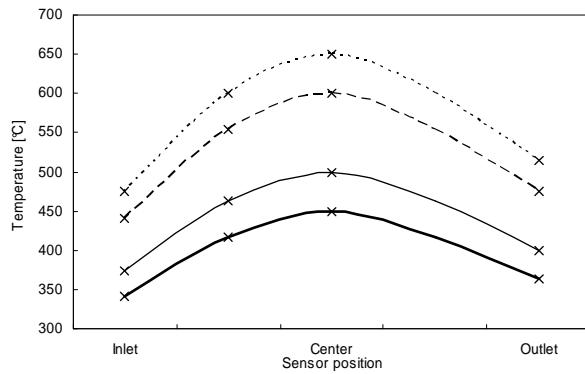


**Figure 5:** Axial temperature distribution on reactor wall.

### Discussion

In order to predict the distribution of reaction products, the surface temperature of the reacting particle may be combined with an appropriate kinetic model. Figure 6 displays a common kinetic model employed in flash pyrolysis, a modified version of the Broido-Shafizadeh model [15-17], where the products have been lumped according to their physical properties at standard conditions.

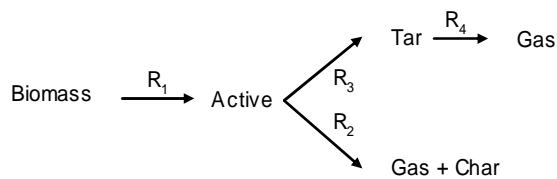


**Figure 6:** Broido-Shafizadeh model for prediction of yield distribution.

However, in order to extend the model in this direction, a requirement is that the particles in the experimental runs were in fact degraded by an ablative mechanism. According to Eq. (22) and figure 3 this was not the case, even for the most severe conditions employed. Study of the char resulting from the runs (figure 7) seems to confirm that the biomass did not go through a liquid phase (“active”) before being left on

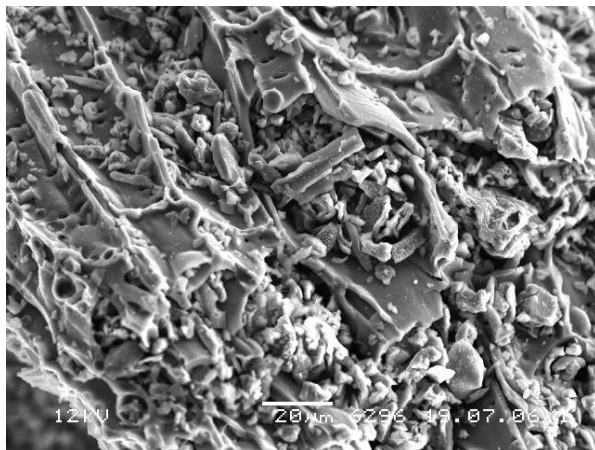


**Figure 7:** SEM photograph of a large wheat straw char particle treated at 596 °C and 10,071 G.

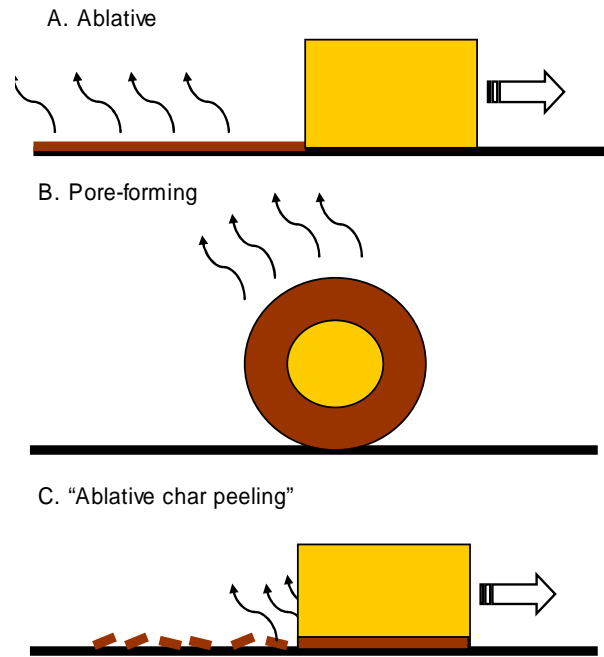


**Figure 8:** Mechanisms for pyrolytic degradation of biomass particle.

the hot surface by vapor evaporation. The char appears to be made up of pieces of cellular wall material broken of the reacting particle.

The ablative mechanism constitutes an extreme case of pyrolytic degradation. At the other extreme is the mechanism by which slow pyrolysis takes place. Here, the particle will retain its shape and material will be removed by the forming of pores. This is obviously not descriptive of the process discussed here. Therefore, neither the ablative nor the pore-forming mechanisms describe the pyrolytic degradation well. A mechanism where the tiny char particles are continuously peeled of the biomass particle as the reaction proceeds as illustrated in figure 8 appears more reasonable.

### Conclusions

A bench reactor system to study the ablative pyrolysis of straw has been constructed and a model to predict the fate of a particle submitted to the environment of the reactor has been developed. Simulation of the pyrolytic degradation of a spherical wheat straw particle reveals that the conditions previously identified in the literature as descriptive of the ablative mechanism are not fulfilled. SEM photographs of char particles obtained in experimental runs confirm this. It appears reasonable to characterize the mechanism by which degradation proceeds in the reactor as one where the continuously produced char are peeled away from the particle surface.

### Acknowledgements

CHEC is financially supported by the Technical University of Denmark, DONG Energy A/S, Energinet.dk, the Danish Research Council for Technology and Production Sciences, the Danish

Energy Research Program, Nordic Energy Research Program, EU and many industrial partners. This particular project is financed by the DTU Innovation Pro-gram and the Nordic Energy Research Program.

### References

1. FAOSTAT data, last accessed December 2004.
2. Handbook for Farm Management (in Danish), Landbrugsforlaget, Aarhus, 2003.
3. OPEC Annual Statistical Bulletin 2003, OPEC, Vienna, 2004.
4. Bech, N. In-Situ Flash Pyrolysis of Straw. In: Dam-Johansen, K., Skjøth-Rasmussen (eds.), M.S. Graduate Schools Yearbook 2004, Dept. of Chemical Engineering, DTU, Kgs. Lyngby, 2004, 13-14.
5. Lédé, J., Panagopoulos, J. Li, H.Z., Villermaux, J. Fuel, 64, 1985, 1514-1520.
6. Lédé, J. Biomass Bioenerg., 7, 1994, 49-60.
7. Bird, R.B., Stewart, W.E., Lightfoot, E.N. Transport Phenomena, 2nd edition, Wiley, New York, 2002.
8. Villadsen, J., Michelsen, M.L. Solution of Differential Equation Models by Polynomial Approximation, Prentice-Hall, New Jersey, 1978.
9. Lédé, J. J. Anal. Appl. Pyrol., 70, 2003, 601-618.
10. Di Blasi, C. Chem. Eng. Sci., 51, 1996, 2211-2220.
11. Boutin, O., Ferrer, M., Lédé, J. Chem. Eng. Sci., 57, 2002, 15-25.
12. Diebold, J.P., Power, A. Engineering aspects of the vortex pyrolysis reactor to produce primary pyrolysis oil vapors for use in resins and adhesives. In: Bridgwater, A.V. (ed.) Research in thermochemical biomass conversion, Elsevier, London, 1988, 609-628.
13. Jensen, P.A., Sander, B., Dam-Johansen, K. Biomass Bioenerg., 20, 2001, 431-446.
14. Stenseng, M., Jensen, A., Dam-Johansen, K. J. Anal. Appl. Pyrol., 58-59, 2001, 767-783.
15. Bradbury, A.G.W., Sakai, Y., Shafizadeh, F. J. Appl. Polym. Sci., 23, 1979, 3271-3280.
16. Di Blasi, C. Biomass Bioenerg., 7, 1994, 87-98.
17. Lédé, J. Ind. Eng. Chem. Res., 39, 2000, 893-903.

**Søren Prip Beier**

Phone: +45 4525 2955  
Fax: +45 4588 2258  
E-mail: spb@kt.dtu.dk  
WWW: <http://www.kt.dtu.dk>  
Supervisor: Gunnar Jonsson

**Ph.D. Study**

Started: September 2005  
To be completed: August 2008

## **Module Design and Performance in Microfiltration, Ultrafiltration, and Membrane Contactors**

**Abstract**

When using membranes for separation purposes the flux often decreases to a level much below the clean water flux due to concentration polarization and membrane fouling. Different ways of dealing with this is investigated in this Ph.D. project in order to design and test filtration modules with better separation performances. A novel dynamic microfiltration system has been investigated and presented. The decoupling of high feed cross-flow velocity and high surface shear rate by vibrations of the membrane module leads to the possibility of filtrating at very low cross-flow velocity and very low transmembrane pressure which reduces the pumping costs and fouling problems. At the same time high transmission of macromolecules is possible.

**Introduction**

Today membrane processes are mainly used as one or more downstream processes after batch fermentation. However, combining a membrane process directly with a fermentation process, the system can be operated either as a fully continuous fermentation process or as a fed batch process, where the products and eventual inhibitants formed during the fermentation can be continuously removed. Thereby the overall productivity of the fermentation can be increased and the formation of byproducts might be reduced as well. Such a set-up can be regarded as a membrane bio reactor (MBR). One of the main limitations by using membrane processes directly on fermentation broths is the possible clogging of the membrane channels by yeast cells and bacteria and the fouling of the membrane surfaces by proteins and other macromolecules. Possible solutions to such problems are to be found and investigated in this Ph.D. project.

**Objectives**

The possibility of decoupling the driving force of the membrane process and the necessary cross-flow velocity in the membrane feed channels has been and will be investigated. The decoupling is done in order to get a high mass transfer of solutes away from the membrane surface. Different ways of achieving the decoupling is given here:

- Vibrations and rotations of the membranes or the feed solutions.
- Very frequent pressure pulsation and back flushing.
- Electrical and/or acoustic fields.
- Using spacers and inserts with optimized performance.

**Results**

Decoupling of the feed flow velocity and the surface shear rate has been done for a microfiltration system by letting the membrane module vibrate vertically up and down at frequencies up to ~ 40 Hz and amplitudes up to ~ 1 mm. The membrane module consists of hollow fibers placed vertically in a bundle. Critical fluxes at different vibration degrees have been measured for the filtration of Bakers yeast suspensions [1]. The system was also able to handle solutions containing different types of macromolecules. When separating yeast cells from alpha-amylase enzymes the critical flux could be used as a guideline flux for the constant flux filtration. Below the critical flux fouling problems were reduced very much and macromolecular transmission above 90 % was observed. Above the critical flux membrane fouling increased leading to a severe increase in fouling resistance and a severe decrease in macromolecular transmission [2]. The critical flux is identified by stepwise increasing the flux and monitoring the transmembrane pressure. From the pressure-time data

the fouling resistance can be calculated according to Darcy's law [3]. The critical flux is identified as the flux below which the fouling resistance is kept constant which is sketched in figure 1.

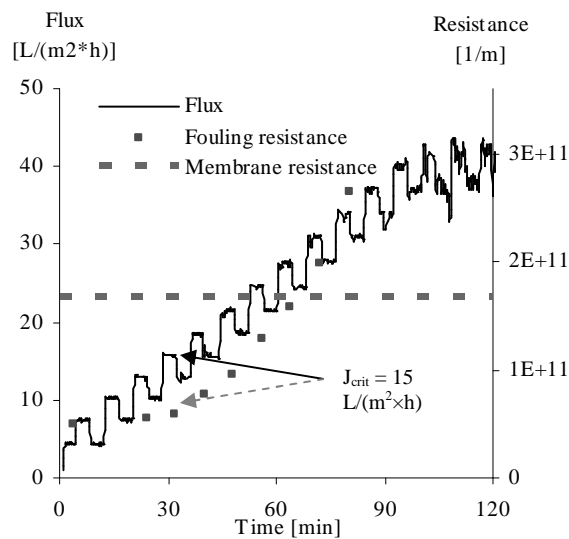


**Figure 1:** Identification of the critical flux [4]. The stepwise increased flux and the fouling resistance as function of the time. The constant membrane resistance is shown as well. Feed: 1 % alpha-amylase + 5 g/L yeast. Vibration frequency = 25 Hz, vibration amplitude = 0.7 mm. Feed flow velocity = 0.91 cm/s.

The critical flux is increased when the vibration frequency is increased and the critical flux varies with the average surface shear rate as a power function [1,2,4]. The feed flow velocity is kept *very* low resulting in very low pumping costs.

### Conclusion and Future Work

The decoupling of the driving force and cross-flow velocity has been investigated in a novel dynamic microfiltration system by use of vibrations of the membrane module. The critical flux depends on the surface shear rate and the feed flow composition described by a power function expression. It was possible to filtrate at low feed flow velocity and low transmembrane pressure resulting in low and constant membrane fouling. At the same time high macromolecular transmission was possible which often is very difficult to achieve in microfiltration due to gel-layer formation and pore blocking. In the future filtrations of solutions containing other macromolecules will be investigated as well as the performance of other microfiltration and ultrafiltration configurations will be investigated. At the moment new membrane materials are tested in the vibration microfiltration system as well as in a back flushing cross-flow set-up. The aim is to reach a better understanding of the membrane fouling in order to reduce the problem and to improve the separation performance in general.

### References/List of Publications

1. S.P. Beier, G. Jonsson, M. Guerra, A. Garde, Dynamic Microfiltration with a Vibrating Hollow Fiber Membrane Module; Filtration of Yeast Suspensions, *J. Membr. Sci.* 281 (2006) 281-287.
2. S.P. Beier, G. Jonsson, Separation of Enzymes and Yeast Cells with a Vibrating Hollow Fiber Membrane Module, *Sep. Purif. Technol.* 53 (2007) 111-118.
3. M. Mulder, Basic principles of membrane technology, 2<sup>nd</sup> edition, Kluwer Academic Publishers, 1996.
4. S.P. Beier, G. Jonsson, Dynamic Microfiltration with a Vibrating Hollow Fiber Membrane Module, *Desalination* 199 (2006) 499-500, Presented at EUROMEMBRANE 2006, 24-28 September 2006, Giardini Naxos, Italy.



## Francesco Castellino

Phone: +45 4525 2829  
Fax: +45 4588 2258  
E-mail: frc@kt.dtu.dk  
WWW: <http://www.kt.dtu.dk>  
Supervisors: Anker Degn Jensen  
Jan Erik Johnsson  
Rasmus Fehrmann

### Ph.D. Study

Started: December, 2004  
To be completed: November, 2007

## Deactivation of SCR Catalysts by Additives

### Abstract

The Danish power companies are obliged to burn biomass at the central power stations. The alkali fraction introduced by biomass into the combustion system is responsible for high rates of deposition and corrosion at the surface of the super-heat exchangers. To minimize these undesired effects, the power companies are planning to mix the biomass burned in their plants some additives, which are able to fix the alkali fraction in harmless compounds. The objective of this Ph.D. project is to evaluate the effect of the selected additives on the commercial catalysts employed in the SCR process.

### Introduction

Nitrogen oxides ( $\text{NO}_x$ ) emitted from stationary sources can be effectively reduced by using the so-called Selective Catalytic Reduction (SCR) process. Ammonia is injected into the flue gas and reacts with the NO fraction according to the following reaction:



The reactor operates at atmospheric pressure and temperature ranging between 300 and 400°C. The catalysts employed are vanadia-based catalysts. This technology was first developed in Japan during the 1970s and is still nowadays the best-developed and worldwide used for fossil fuel combustion processes [1].

However, the application of this technology to the treatment of flue gas from (co)-combustion of biomass or secondary fuels such as sewage sludge or meat and bone meal (MBM) is problematic. This is mainly due to the high rates of catalyst deactivation observed and related to different compounds (*e.g.* alkali and alkaline earth metals, chlorides, etc.) introduced into the system by these alternative fuels [4]. The alkali fraction of the biomass is also responsible for a higher deposition rate on the superheater surfaces in the boiler. In fact, the fly ash produced during biomass combustion, due to the high content of alkali, has relative low melting point temperatures. At the temperatures of the superheaters, they thus present a melted fraction which makes them particularly sticky.

Deposition on the heat exchanger surfaces is a highly undesired process since it decreases the heat transport through the heat exchangers and causes corrosion, thus affecting the overall efficiency in steam production. The use of additives to the fuel is considered by the Danish power companies as a way to minimize this undesired effect, rendering the combustion of biomass more efficient. Preliminary tests have mainly involved compounds rich in phosphorus like phosphoric acid, mono- and di-calcium phosphate [2]. Due to the presence of the phosphorus during combustion, ashes mainly constituted by K, P and Ca with higher melting point temperatures (>1300°C) were formed. Accordingly, the deposition rate measured during addition of P-compounds was found to decrease up to 90%.

However phosphorus is known to be by itself a moderate poison for the vanadia-based catalysts normally employed in the SCR process. Studies about poisoning by phosphorus have been conducted in the laboratory mainly by wet impregnation with phosphoric acid solutions [5],[7]. The activity of the powdered doped catalysts still showed up to 80-85% of the original activity at P/V ratio greater than 2. Commercial vanadia-based catalysts exposed at full-scale during (co)-combustion of sewage sludge and MBM has shown enrichment in phosphorus on the surface and the bulk of the catalysts [8]. The samples presented a decreased total pore volume and a shift of the average pore diameter towards smaller values. Formation of surface layers and pore condensation by phosphorus was thus indicated as

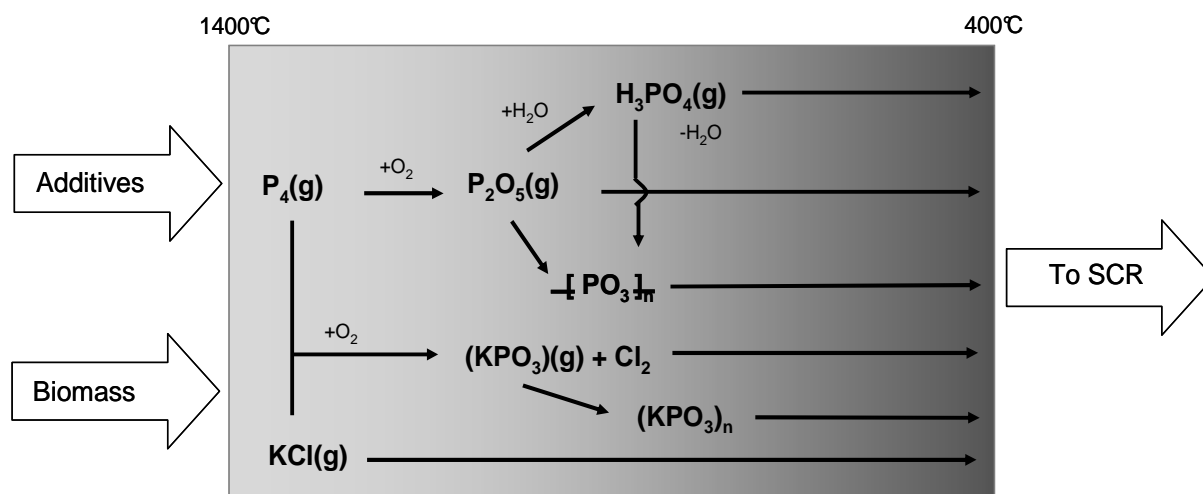


**Figure 1:** Examples of reactions given by gaseous molecular phosphorus, introduced into the system by the additives, and the KCl released during biomass combustion. Both the products of combustion of the additives, and the reaction between the additives and the alkali fraction of the flue gas could reach the SCR reactor and deactivate it. The different mechanisms of deactivation due to each of these species will be studied in this project.

the main mechanism of deactivation by phosphorus. However, since the catalysts were enriched also by other known poisons like potassium and arsenic, it was not possible to directly correlate the influence of the phosphorus alone on the overall deactivation.

The purpose of this project is to investigate whether the P-additives may cause accelerated deactivation, what the mechanisms of the deactivation are and whether the deactivation can be inhibited or slowed down to an acceptable rate. Investigations will include both tests involving the additives, and the possible products of the addition process as shown in Figure 1.

In the present contribution the main results about deactivation by phosphoric acid  $H_3PO_4$  at a pilot plant are presented.

### Experimental

The catalysts employed were commercial Haldor Topsøe A/S DNX 3%  $V_2O_5$ - $WO_3$ - $TiO_2$  full-length monoliths. The pilot-scale setup mainly consists of a 50 kW natural gas burner, a lance for injection of solutions into the flue gas, ammonia storage and addition line, and a reactor hosting the SCR monolith. The activity measurements have been performed at 350°C, in the presence of about 500 ppmv NO and 600 ppmv of  $NH_3$  in the pilot scale reactor. Three different monoliths have been exposed during addition of 10, 100 and 1000 ppm of  $H_3PO_4$  respectively by spraying directly into the hot flue gas ( $T > 700^\circ C$ ) different aqueous solutions of  $H_3PO_4$ .

Both the aerosol particle sizes and concentrations in the flue gas have been measured by a TSI<sup>®</sup> SMPS. Particle measurements have been performed for  $H_3PO_4$  addition in the range 0.044-1.76 g/Nm<sup>3</sup> corresponding to  $H_3PO_4$  concentrations in the range 10-400 ppm on a molar basis.

The fresh and the spent catalysts have been characterized by Hg-porosimetry, SEM analysis and chemical composition.

### Results and Discussion

Particle measurements were necessary in order to verify the formation of poly-phosphoric acids, which has been reported to constitute one of the possible deactivating agents by phosphorus [8]. These acids are formed by condensation reactions between the phosphoric acid molecules and have boiling temperatures higher than 800°C. The SMPS measurements confirmed the formation of particles during the addition of phosphoric acid even at very low concentrations. The mean particle diameter measured at the catalyst inlet by the SMPS was found equal to 25.4 nm when adding 10 ppm of  $H_3PO_4$ . This then increased according to the acid concentration in the flue gas, reaching 66.9 nm when adding 400 ppm of acid. The small sizes of the particles clearly indicate condensation of gaseous species, whereas the increased value at higher acid concentrations can be explained by agglomeration of small particles or condensation of gas-phase P-species on previously formed particles. The particle mass concentration was calculated assuming a particle density equal to 1.864 g/cc, which is the value of  $H_3PO_4$ . This was found to linearly increase with the acid concentration: up to 50% of the added acid was found at the reactor inlet. Considering both the relative high amount of deposits found in the setup and the formation of particles already at 10 ppm of  $H_3PO_4$ , it is believed that almost all the acid present in the gas phase had condensed already before the SCR reactor. Deactivation by nano-particle of polyphosphoric acid is then the only mechanism of deactivation experienced during this investigation.

The activity of the monolith exposed to flue gas containing 10 ppm of  $H_3PO_4$  was periodically measured

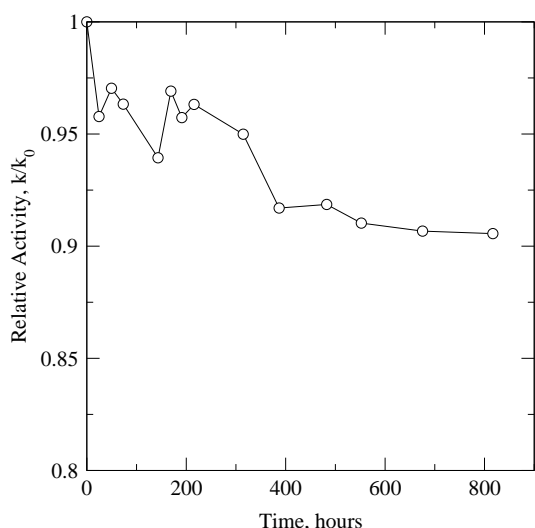


**Figure 2:** Relative activity of a SCR monolith exposed to 10 ppm of  $H_3PO_4$ . Activity measurement data: flow=40 Nm<sup>3</sup>/h, NO=500 ppmv, NH<sub>3</sub>=600 ppmv, O<sub>2</sub>>5% v, H<sub>2</sub>O>10% v.

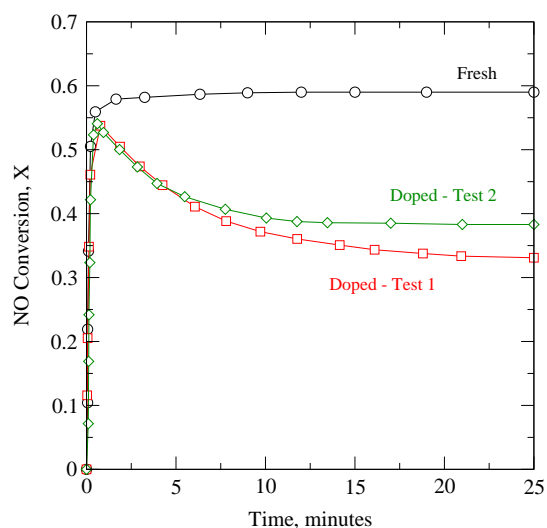


**Figure 3:** Activity measurements of a SCR monolith before (Fresh) and after (Doped – Test 1) the addition of 0.44 g/Nm<sup>3</sup> for 38 hours. Activity measurement data: flow=50 Nm<sup>3</sup>/h, NO=500 ppmv, NH<sub>3</sub>=600 ppmv, O<sub>2</sub>>5% v, H<sub>2</sub>O>10% v. Doped –Test 2 was performed 13 days after Doped – Test 1.

during 819 hours of exposure. In total 0.8 kg of acid were added to the flue gas. The decrease in relative activity is shown in Figure 2: after 800 hours, the catalyst lost around 10% of its original activity.

The addition of 100 ppmv of  $H_3PO_4$  was carried out for only 38 hours: already at this point the catalyst lost around 60% of its original activity. Interestingly in this case the activity measurements showed an influence of ammonia on the catalyst activity itself as shown in Figure 2. During the first activity measurements carried out after 38 hours of acid injection ('Doped – Test 1' in Figure 3), right after the addition of ammonia the catalyst was still able to convert NO to a value corresponding to 90% of its original activity. However

the NO conversion then started to decrease with time reaching a steady value only after around 25 minutes of ammonia injection. The corresponding value of relative activity ( $k/k_0$ ) in this case dropped to 42%. Based on this result, it is assumed that: i) the polyphosphates partially deactivate the catalyst by pore blocking and condensation; ii) ammonia and the polyphosphates deposited on the catalyst surface react together, further deactivating the catalyst. The same transient NO response was obtained when the test was repeated after closing the NH<sub>3</sub> flow for at least 1 hour. Moreover, repeating the test in the following days without adding any acid or NH<sub>3</sub> in the meantime showed a regain in activity ('Doped – Test 2' in Figure 3): the steady NO

**Table 1:** SEM pictures and Hg-porosimetry results of the fresh and some of the doped catalysts.

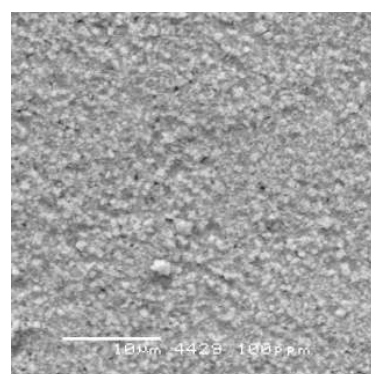
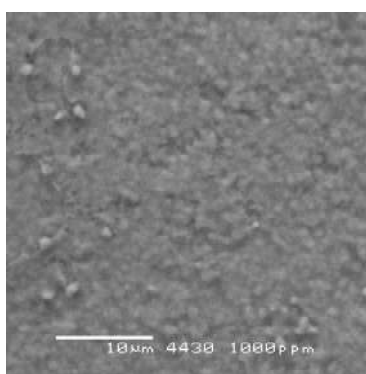
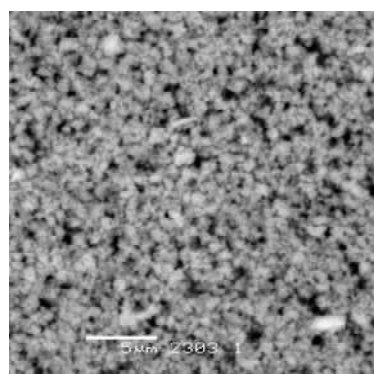
**Sample**

Fresh Haldor Topsøe A/S monolith

Exposed to 1000 ppm of  $H_3PO_4$  for 91 h.

Exposed to 100 ppm of  $H_3PO_4$  for 38 h.

**SEM Analysis**



**Hg Porosimetry**

Intrusion. Vol. (ml/g): 0.744  
Pore Area (m<sup>2</sup>/g): 54.937

Intrusion. Vol. (ml/g): 0.076  
Pore Area (m<sup>2</sup>/g): 21.450

Intrusion. Vol. (ml/g): 0.551  
Pore Area (m<sup>2</sup>/g): 48.962

conversion was reached faster and at higher values. All these facts thus indicate that: i) the products of the reaction between the deposited poly-phosphates and ammonia are in equilibrium with the  $\text{NH}_3$  partial pressure in the gas phase; ii) part of the polyphosphates leave the surface when exposed to a *clean* flue gas.

The catalyst exposed to 1000 ppmv of  $\text{H}_3\text{PO}_4$  was massively covered by the polyphosphates and lost 80% of its original activity after only 25 hours of exposure.

The pore volumes of the three different monoliths exposed to  $\text{H}_3\text{PO}_4$  were measured by Hg-porosimetry and compared to the value of a fresh monolith. The relative total intrusion volume (TIV) was found equal to 0.81, 0.74 and 0.10 for the monoliths exposed to 10, 100 and 1000 ppm of  $\text{H}_3\text{PO}_4$  respectively. Moreover, a shift toward smaller pore diameters resulted from the pore size distribution for the different monoliths, pointing out the occurrence of pore blocking and condensation due to deposition of polyphosphates. This fact is further shown by the SEM pictures taken of the different catalyst surfaces and shown in Table 1.

### Conclusions

The main objective of this Ph.D. project is to study the effects of the proposed “anti-deposition” additives on the SCR catalysts. Phosphorus is the main constituent of the additives.

Due to inefficiency in the addition process or to addition of too much additives, “free-phosphorus” could be released in the gas phase during combustion. This phosphorus can then react with oxygen and water present in the flue gas forming polyphosphate acids which will then reach the SCR reactor. In the SCR pilot plant the effect of the polyphosphate acids on a commercial SCR monolith have been tested. By spraying a phosphoric acid solution into a hot flue gas,

nano-particles of polyphosphoric acid have been formed. These particles easily penetrated the catalyst walls and deposited on the surface physically deactivating the catalyst by pore blocking and condensation. Moreover, ammonia used in the SCR reaction was also found to react with the deposited polyphosphates, and further deactivating the catalyst.

The results show that P can potentially be a very harmful poison, much more than previously shown by wet impregnation tests.

### Acknowledgements

This project is supported by the PSO system. Supply of the catalyst samples by Haldor Topsøe A/S is gratefully acknowledged.

### References

- [1] V.I. Parvulescu, P. Grange, B. Delmon, *Catalysis Today* 46 (1998) 233-316.
- [2] P. A. Jensen, L.H. Sørensen, G. Hu, J.K. Holm, F. Frandsen and U.B. Henriksen. Technical University of Denmark (2005). KT-Report No. 0504.
- [3] Y. Zheng, A.D. Jensen, J.E. Johnsson, *Ind. Eng. Chem. Res.* 43 (2004) 941-947.
- [4] R. Khodayari, C.U.I. Odenbrand, *Applied Catalysis B: Environmental* 30 (2001) 87-99.
- [5] J.P. Chen, M.A. Buzanowski, R.T. Yang, *J. Air Waste Manage. Assoc.* 40, (1990) 1403-1409.
- [6] J. Beck, R. Muller, J. Brandenstein, B. Matschenko, J. Matschke, S. Unterberger, K.R.G. Hein, *Fuel* 84 (2005) 1911-1919.
- [7] H. Kamata, K. Takahashi, C.U.I. Odenbrand, *Catalysis Letters* 53, (1998) 65-71.
- [8] J. Beck, J. Brandenstein, S. Unterberger, K.R.G. Hein, *Applied Catalysis B: Environmental* 49, (2004) 15-25.



## Henrik Christensen

Phone: +45 4525 2853  
Fax: +45 4588 2258  
E-mail: hc@kt.dtu.dk  
WWW: <http://www.chec.kt.dtu.dk>  
Supervisors: Søren Kiil  
Kim Dam-Johansen  
Ole Nielsen & Michael Bech Sommer, H. Lundbeck A/S

### Ph.D. Study

Started: September 2004  
To be completed: September 2007

## Scale Up of Pharmaceutical Production of Organic Chemical Compounds

### Abstract

The design of an efficient reactor system for a chemical reaction requires knowledge on the kinetic data related to the reaction. Kinetics makes it possible to simulate how the reaction is affected by different reaction conditions. This is a discipline, which has not yet been widely used in the pharmaceutical industry. However, due to environmental, economical and quality considerations an increasing interest in this field has appeared. This gives the opportunity for investigating the possibilities for the implementation of new reactor configurations and analysis techniques, which provides a more detailed understanding of the chemical process.

### Introduction

The production of Active Pharmaceutical Ingredients (API) is a special area compared to other chemical productions. Typically, the amounts of products produced are rather small, but on the other side the trade prices on the products are high [1]. This has resulted in little focus on process development and optimization from an engineering point of view.

Reactions traditionally take place in batch reactors. These reactors can be used for a range of reactions and in terms of documentation it is convenient to trace errors back to the source. From a scale up point of view batch reactors give rise to a number of challenges: Loss of selectivity and formation of hot spots due to slow mixing and problems with exothermic reactions due to a high volume to surface ratio [2]. This has the consequence that a reaction, which performs satisfying in gram-scale, may fail when it is performed in kg-scale. Until now the typical way of solving these upscale problems has been to change the critical reaction steps in the synthesis rather than finding a convenient solution by changing from batch reactors to other reactor configurations. This has the drawback that it is time consuming to develop a new synthesis route and it may result in additional synthesis steps or use of an excess of chemicals, which all-together means that the turnover may decrease.

However, a number of changes in the pharmaceutical market have made it relevant to investigate the possibility of optimizing or changing some of the existing production methods. Example given: The competition has increased, due to generic

production and more attention on the environmental impact is paid.

An aspect, which until now has also prevented the pharmaceutical industry in process development and implementation of new techniques, is the commitments to the US Food and Drug Administration (FDA). The FDA is responsible for the guidelines that ensure the quality of the pharmaceuticals [3].

Until August 2003 the accepted way of ensuring a product with a given quality was to describe the production method in every detail and finally receive an approval from FDA. From that stage no changes on the approved method are allowed without preapproval from the FDA. This means that even if the production method is inefficient, it is not possible to optimize the process without using precious time on new approvals.

Meanwhile FDA has realized that the lack of optimization has resulted in excessive manufacturing costs. Therefore the FDA has encouraged the pharmaceutical industry to implement new technologies. The new technologies shall ensure a more effective, safe, and affordable production of pharmaceuticals and by that help the consumer to get the pharmaceuticals; they need to improve their health.

These requirements may be met by the implementation of Process Analytical Technology (PAT) [4]. The aim of this technique is to provide a more elaborate understanding of the chemical process. By using modern analysis equipment real time concentration profiles can be recorded for a chemical process. Based on these profiles operating conditions

may be changed during the process and the final quality may be improved [5].

To investigate these new possibilities for the manufacturing of pharmaceuticals the Department of Chemical Engineering at the Technical University of Denmark and the pharmaceutical company H. Lundbeck A/S has agreed on a partnership with the main title: "Active Pharmaceutical Ingredients".

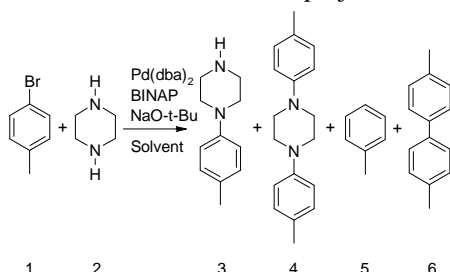
### Specific Objective

The purpose of this project is to investigate the possibilities for developing a more efficient method for up scaling organic synthesis in pharmaceutical production. This will require:

- Methods to increase the understanding of chemical reaction mechanisms and kinetics, this will also include the efficiency of the analytical methods and apparatus.
- Efficient methods for application of mechanism and kinetic to optimize and scale up organic synthesis to industrial pharmaceutical production.
- Formulate guidelines for future synthesis and scale up problems, which may be met in the pharmaceutical industry.

### Chemical Reaction

Mono-substituted aryl piperazines are of great importance in the pharmaceutical production [6], and they can be produced by the Buchwald-Hartwig amination reaction. The reaction in Scheme 1 has been chosen as a model reaction for this project.



**Scheme 1:** Formation of aryl piperazine by the Buchwald-Hartwig amination reaction.

The Buchwald-Hartwig amination reaction is the coupling reaction between an aryl halogen (**1**) and a primary or a secondary amine (**2**) in the presence of a homogeneous palladium catalyst and a base. The identified products are: Mono-substituted aryl piperazine (**3**), bi-substituted aryl piperazine (**4**), reduced aryl halogen (**5**) and homo-coupled aryl halogen (**6**). However, it is only **3**, which is desired. **4**, **5** and **6** are unwanted side products.

So far the reaction has been carried out in batch reactors, and the two following strategies have been used in order to avoid formation of **4**: One strategy has been to introduce a protection group, which protects one of the two nitrogen atoms in **2** [7]. Another strategy has been to change the ratio between **1** and **2** [8]. However, from an economic point of view, it will be favorable if the reaction can be carried out without the introduction

of protection groups and with equivalent amounts of **1** and **2**, or even better with an excess of **A**. The products given in Scheme 1 have no connection to the an actual pharmaceutical, however, the coupling reaction of the aryl halide and the amine is a very important class of reactions.

### Chemical Reaction Mechanism

The Buchwald-Hartwig amination reaction is a homogeneously catalyzed reaction, which takes place in the presence of a palladium complex. In the literature it is reported that the formation of the *N*-aryl amine occurs according to the mechanism given in Figure 1 [9 and 10]. Figure 1 is divided into two different areas. The pathway outside the box describes the formation of **3** and **4** and the pathway inside the box describes the formation of **5**.

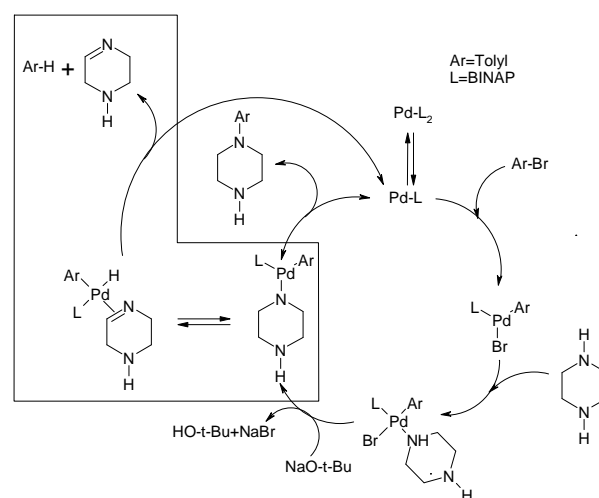


**Figure 1:** Reaction mechanism for the formation of *N*-aryl amine and the reduction of the aryl halide.

The formation of **3** and **4** can be divided into five intermediate reaction steps:

- Dissociation of the ligand from the palladium complex.
- Oxidative addition of the aryl halide to the palladium complex.
- Coordination of the amine.
- Neutralization of the amine.
- Dissociation of the *N*-arylated amine from the palladium complex.

The formation of the undesired reduced aryl halide adds two additional intermediate reaction steps:

- $\beta$ -hydride elimination.
- Dissociation of the reduced aryl halide and the oxidized amine.

It has not been possible to find a reaction mechanism, which accounts for the formation of **6**.

### Prior considerations

In the initial phase of the project it was desired to investigate the possibilities for creating a continuously

operated reactor configuration for the reaction given in Scheme 1. To obtain a simple reaction system it was attempted to create a homogenous system, where both the reactants and the catalyst were dissolved. The classic solvents employed in the Buchwald-Hartwig amination reaction are non-polar aprotic solvents such as *m*-xylene and 1,4-dioxane. However, due to the low polarity of these solvents, it is not possible to dissolve the base NaO-*t*-Bu. Therefore it was decided to change the class of solvent from non-polar aprotic solvents to polar aprotic solvents, because they had a better ability for creating a homogeneous system. Meanwhile, as later described the change of the class of solvent had a significant impact on the product distribution.

### Method of Analysis

One of the challenging parts of the project was to develop a method of analysis, which allowed the reactants and products to be detected and quantified. A HPLC method was developed and this gave the possibility for quantification of the following compounds: **1**, **3**, **4**, **5** and **6**. The primary drawback of this method is that it was not able to detect **2**, which is due to the lack of a chromophore group. Time has also been devoted to evaluate the possibility for the implementation of online Near-Infrared spectrometry (NIR) as a method of analysis. This method has the advantage that it is able to detect **2**. However, it was found that the properties of the reaction mixture were not appropriate for NIR measurements.

### Experimental Results

The following ration between the reactants and catalyst has been used: 1.0 eq of **1**, 1.1 eq of **2**, 0.05 eq of Pd(dba)<sub>2</sub>, 0.075 eq of BINAP and 1.5 eq of NaO-*t*-Bu dissolved in a fixed amount of solvent. In the initial phase of the experiments the reaction was done in the polar and aprotic solvent 1-methyl-2-pyrrolidone (NMP). However, the data obtained for the product distribution revealed that the selectivity towards the desired product **3** was low. This was due to a high production of the undesired product **5** (Figure 2). The same tendencies were observed for another polar aprotic solvent: *N,N*-dimethylacetamide.

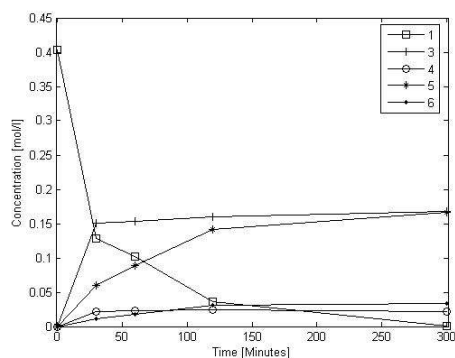


**Figure 2:** Concentration versus time for the reaction carried out in NMP.

To investigate whether this unexpected high production of **5** was due to the change of solvent (from a nonpolar aprotic to a polar aprotic solvent) the reaction was done in some of the classic solvents for the Buchwald-Hartwig amination reaction i.e. a nonpolar aprotic solvent. The results for the reaction done in 1,4-dioxane is displayed in Figure 3. Figure 3 shows that the formation of **5** is strongly suppressed for reactions performed in 1,4-dioxane compared to the reaction done in NMP. This means that the product distribution is affected by the type of solvent.

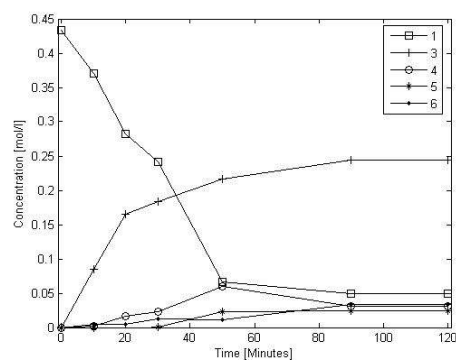


**Figure 3:** Concentration versus time for the reaction carried out in 1,4-dioxane.

Another observation from figure 3 is that reaction terminates even though there are still unreacted starting material left in the reaction mixture. It was experienced that by applying 2.2 eq of **2** instead of 1.1 of **2**, which are used in Figure 2 and 3, it is possible to obtain full conversion of **1** (Figure 4).

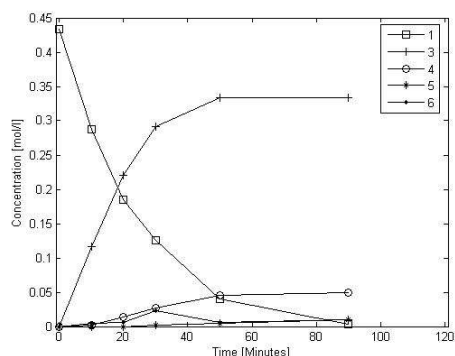


**Figure 4: Concentration versus time for the reaction carried out in 1,4-dioxane. 2.2 eq. of 2 were employed.**

#### Future Work

- A study of the effect of the different parameters in the reaction (i.e. concentrations and temperature) will be performed.
- Based on available reaction mechanisms in the literature a model, which predicts the product distribution for the reaction in Scheme 1 will be developed.
- New methods of analysis will be evaluated for the reaction. It is also the intention to develop a method, which allows 2 to be detected and quantified.

#### Conclusion

Regarding the model reaction it has been found that the product distribution is strongly dependent on the choice of solvent.

During the experimental work with the reaction, it has been found that the bottleneck in obtaining information about the kinetics of a reaction is related to the method of analysis.

#### Acknowledgements

This project is performed in close collaboration with H. Lundbeck A/S. H. Lundbeck A/S provides the laboratory facilities and their expertise on organic synthesis.

#### References

1. Jensen K.F., Chemical Engineering Science, 2001, 56, 293-303.
2. Anderson N.G., Organic Process Research & Development 2001, 5, 621.
3. <http://www.fda.gov/opacom/morechoices/mission.html>
4. <http://www.fda.gov/cder/ops/pat.htm>
5. <http://www.ptemag.com/pharmtecheurope/article/articleDetail.jsp?id=129539&pageID=1>
6. De Prins, L., Psychotropics 2000/2001, 2002, Herman & Fischer A/S, Denmark.

7. Hepperle, M.; Eckert, J.; Gala, D.; Shen, L.; Evans, A.; Goodman, A., Tetrahedron Letters, 2002, 43, 3359-3363.
8. Zhao, S.; Miller, A.; Berger, J.; Flippin, L., Tetrahedron Letters, 1996, 37, 4463-4466.
9. Urgaonkar, S.; Xu, J.; Verkade, J., Journal of Organic Chemistry, 2003, 68, 8416-8423.
10. Wagaw, S.; Rennels, R.A.; Buchwald, S.L., Journal of American Chemical Society, 1997, 119, 8451-8458.



### **Steen Christensen**

Phone: +45 4525 2912  
Fax: +45 4593 2906  
E-mail: sch@kt.dtu.dk  
WWW: <http://www.capec.kt.dtu.dk>  
Supervisor: Jens Abildskov

#### **Ph.D. Study**

Started: August 2004  
To be completed: July 2007

## **Multi-Scale Modeling of Complex Systems**

### **Abstract**

Most chemical systems can only be fully understood based on physical and chemical property data. Property data can not be calculated in a fully rigorous fashion. Normally semi-empirical property prediction models (SEPPs) have been used but they are all limited by insufficient reliable data available for development. In a highly competitive climate, chemical engineers are forced to rely increasingly on predicted data. The purpose of this project is to develop a methodology for extracting maximum information from available experimental results and provide extra data. The project combines SQPP models with molecular modeling to give qualified prediction of pure and mixture behavior of novel compound groups to minimize extensive experimental data generation. The method of predicting derivative properties and integrating to obtain integral properties is surprisingly accurate.

### **Introduction**

Traditionally, process systems engineering (PSE) is concerned with the computer-aided design of products and processes, and the operation and control of these processes throughout their lifecycle. The overwhelming majority of all chemical systems can only be fully understood based on accurate physical and chemical property data. Such property data can not be calculated in a fully rigorous fashion, so chemical engineers have for decades developed numerous semi-empirical property prediction models. Great emphasis has been on models of residual properties of pure components and mixtures and excess property models for liquid mixtures. As the materials of interest to the modern chemical industry become ever more complex, PSE relies on increasingly sophisticated molecular modeling (MM) techniques for the characterization of their properties and behavior. The use of advanced equations of state within mathematical process models is now well established, as is the use of molecular modeling for the derivation of parameters used in these equations, e.g. by generation of "pseudo-experimental" data points to complement real experimental data that are available. During the past fifteen years, theoretical and algorithmic advances along with the revolution in computing technology have made it possible for design questions of practical importance to be addressed by MM. The advances offered by these methods will continue to make inroads in the chemical and related industries in the coming decade.

### **Methodology**

The main objective of this work is to develop a methodology for using molecular modeling results to expand the predictive capabilities of existing SEPP models to new chemical systems with insufficient experimental data available. The MM simulations are too extensive to use directly in for example a design phase of a purification unit. The SEPP models are preferred in the design phase because of the computational simplicity resulting from their current analytical form. A general approach for handling a new class of chemicals includes five steps:

1. Search literature for all relevant physical property data (liquid densities, vapor pressure data, PVT data, phase diagram data, mixture equilibrium data vapor-liquid-equilibrium (VLE), liquid-liquid-equilibrium (LLE), solid-liquid-equilibrium (SLE), activity coefficients at infinite dilution, excess volumes etc.).
2. Test existing property prediction methods (if available) both for pure compounds and mixtures. Test if it is possible extend the SEPP models (for example UNIFAC) to improve predictions by regression of parameters using experimental data collected.
3. Evaluate if predictive capability for the new class is acceptable.

- Identify areas with insufficient data. Obtain relevant pseudo-experimental data from molecular modeling. For developing molecular models use known data to establish suitable potentials.
- Combine experimental and pseudo-experimental data for regression of parameters for SEPP models.

Steps 3 to 5 are repeated until the predictive capability of the SEPP models have reached an acceptable level of precision and an acceptable range of applicability.

Steps 1 to 2 are the traditional steps taken by engineering researchers when trying to model a new compound group. The first evaluation of the predictive capability is a “stop or go” point because extensive experimental work might be needed. With the above procedure we now propose to proceed to the design phase of a project before any “stop or go” decision has to be made. That makes it possible to explore many options qualitatively, before experimental work is required.

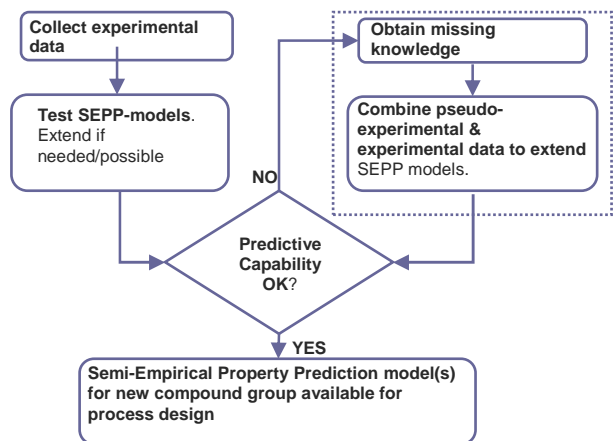


**Figure 1: Overview of methodology**

### Fluctuation Solution Theory

Fluctuation solution theory (FST) describes the connection between the local composition at microscopic level and the macroscopic properties of a fluid [1]. The key quantity is the total correlation function integral (TCFI),  $H_{ij}$ , given by [2]:

$$H_{ij} = 4\pi\rho \int_0^{\infty} r^2 \left( g_{ij}^{\mu VT}(r) - 1 \right) dr$$

### Equation 1

where  $\rho$  is the density of the system.  $r$  is the center-of-mass to center-of-mass distance between molecules of type  $i$  and  $j$ .  $g_{ij}(r)$  is the radial distribution function (RDF) in the grand canonical ensemble. The RDF describes the fluctuation in the macroscopic density at a microscopic level. The macroscopic activity coefficient derivatives,  $(\partial \ln \gamma_i / \partial x_i)_{T,P}$  are related to the TCFIs

$$\left( \frac{\partial \ln \gamma_i}{\partial x_i} \right)_{T,P} = \frac{-x_2 (H_{11} + H_{22} - 2H_{12})}{1 + x_1 x_2 (H_{11} + H_{22} - 2H_{12})}$$

### Equation 2

The partial molar volumes and isothermal compressibility can be determined through similar equations. Thus, FST provides a direct relationship between RDFs obtained from simulations and macroscopic measurable thermodynamic properties. FST has been used by numerous researchers to investigate the properties of liquid mixtures. Some studies extract the appropriate FST integrals from experimental data. Fewer studies have determined FST integrals from computer simulations. An example follows.

### Simulations Details

Previous simulations suggest that FST analysis of simulation results can provide quantitative information concerning the thermodynamics of solutions. We employed the isobaric-isothermal ensemble (NPT) for different mixing ratios. The TCFIs can be determined from the quantity:

$$H_{ij} = 4\pi\rho \int_0^{r_{\max}} r^2 \left( g_{ij}^{NPT}(r) - 1 \right) dr$$

### Equation 3

which can be extracted from MD simulation results. We used the software package NAMD [12]. Using periodic boundary conditions, and integration time steps of 1fs, the simulation box is initialized using a template which contains the equilibrium positions of each atom in the molecule. In two cases studies the system sizes were set to 512 molecules for simulating ethanol/benzene and 1000 for methyl acetate/benzene. The simulation box is divided into a simple grid and the molecule templates are inserted at the grid points in accordance with the composition. Two steps are used for equilibrating the system. Firstly, the system is relaxed by a steepest descent method to eliminate atomic overlaps in the initial setup of the system. The process is ended when the potential energy has leveled out to a nearly constant value. Secondly, the NPT conditions (pressure of 1 atm and a temperature equal to the experimental value) are imposed and the simulations run for 500ps to ensure that equilibrium has been obtained. The criterion is that there is no drift in the radial pair distribution functions with respect to time. The length of the production period varies depending on the composition. In most cases periods of nearly 50ns were used. The production period increases for small mole fractions.

The all-atom CHARMM27 force field has been applied in the simulations. The force field is characterized by flexible bonds, a Urey-Bradley (UB) term for 1-3 interactions and a Lennard/Jones term for 1-4 interactions and non-bonded interactions in general.

In special cases a modified parameter set is used for 1-4 interactions. Coulombic forces are included using charges positioned at the center of mass of the atoms where interactions are included for atoms separated by three or more bonds. The general form of the potential is given by:

$$U(R) = \sum_{bonds} K_b (b - b_0)^2 + \sum_{angles} K_\theta (\theta - \theta_0)^2 + \sum_{UB} K_{UB} (S - S_0)^2 + \sum_{dihedrals} K_\chi (1 + \cos(n\chi - \delta)) + \sum_{impropers} K_\phi (\phi - \phi_0)^2 + \sum_{nonbond} \left( \epsilon_{ij} \left[ \left( \frac{R_{min,ij}}{r_{ij}} \right)^{12} - 2 \left( \frac{R_{min,ij}}{r_{ij}} \right)^6 \right] + \frac{q_i q_j}{\epsilon_1 r_{ij}} \right) \quad (4)$$

#### Equation 4

where  $K_b$ ,  $K_{UB}$ ,  $K_\theta$ ,  $K_\chi$ , and  $K_\phi$  are the bond, Urey-Bradley, angle, dihedral angle, and improper dihedral angle force constants, respectively;  $b$ ,  $S$ ,  $\theta$ ,  $\chi$ , and  $\phi$  are the bond length, Urey-Bradley 1,3-distance, bond angle, dihedral angle, and improper torsion angle, respectively, and the subscript zero represents the equilibrium values for the individual terms.  $\epsilon$  is the Lennard/Jones well depth and  $R_{min,ij}$  is the distance at the minimum of the Lennard/Jones potential. The unlike interactions are calculated with Lorentz-Berthelot combining rules.  $q_i$  is the atomic partial charge,  $\epsilon_1$  is the effective dielectric constant and  $r_{ij}$  is the distance between atoms  $i$  and  $j$ .

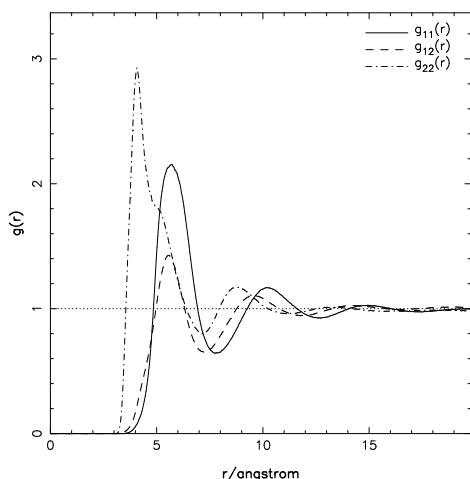


Figure 2: Example of radial pair distribution functions for benzene –ethanol system.

#### Application of FST

The following recipe is applied to every binary system where VLE data is needed:

1. Run MD simulations for series of compositions at fixed T and P (NPT)
2. Sample state every 0.5ps
3. Generate  $g_{ij}(r)$ 's and  $\rho$
4. Calculate  $H_{ij}$ 's and  $d \ln \gamma_j / dx_1$
5. Fit  $d \ln \gamma_j / dx_1$  data using a simple model
6. Generate xP and xy diagram

In step 5 the derivatives of the activity coefficient generated from the FST analysis of the MD simulation results are applied to determine the Modified Margules parameters of the binary set. In the 6<sup>th</sup> and final step the modified Margules model is used together with pure

component vapor pressures to calculate the bubble point pressure curve (xP) and the vapor phase composition (xy) at the temperature from the MD simulations. The error propagation law can then be applied to determine the variances of the calculated pressures and vapor phase compositions.

#### Results of test systems

The methodology was applied to two test system: The first is benzene + methyl-acetate at 303.15K (Figure 3) which is almost ideal, the second system is benzene + ethanol at 298.15K (Figure 4).

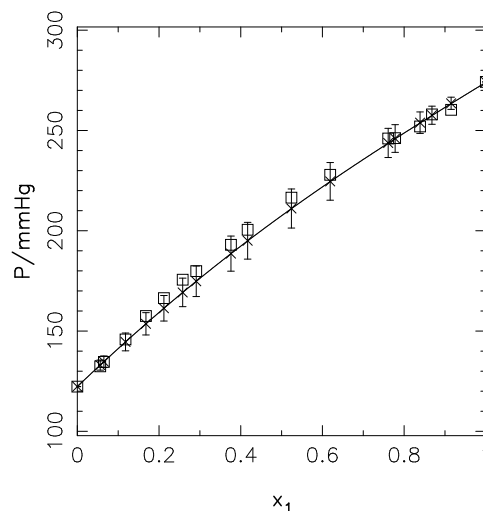


Figure 3: Isothermal bubble point pressure vs. composition for benzene – methyl acetate at 303.15K.  $\square$  are experimental points and full line and  $\times$  are predicted by method.

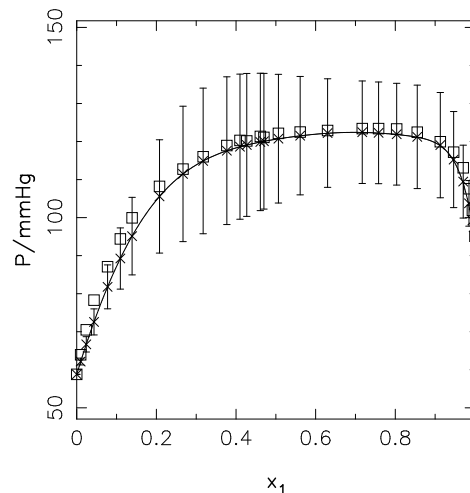
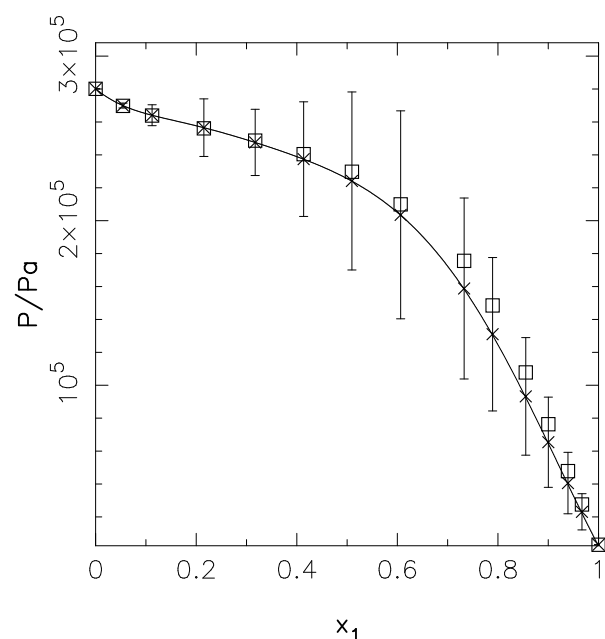


Figure 4: Isothermal bubble point pressure vs. composition for benzene – ethanol at 298.15K.  $\square$  are experimental points and full line and  $\times$  are predicted.

#### 3rd Industrial Fluid Phase Simulation Challenge

The method based on predicting derivative properties using molecular simulations and integrating to obtain integral properties has proven to be surprisingly accurate. The IFPSC (<http://fluidproperties.org>) is now a

biennial program for driving improvements in the practice of molecular simulation, formalizing methods for the evaluation and validation of simulation results with experimental data, and ensuring relevance of simulation activities to industrial requirements. The main activity in the project is arranging the Industrial Fluid Phase Simulation Challenge (IFPSC). The third challenge contain among other categories the 'State Conditions Transferability' challenge testing the ability of computer modeling (any method) to predict the change in bubble point pressure of a binary mixture when temperature is changed. The ability to predict properties for state points that are challenging, inaccessible to experiment, difficult to predict with existing engineering methods or simply missing is often used as a justification for development of computer modeling. The purpose of the challenge is to test/promote/validate this capability. The challenge system was binary mixture of ethanol and 1,1,1,2,3,3,3-heptafluoropropane. The contestants were allowed to use all pure component data and already published force field parameters together with a data set for the mixture at 283.17K. The challenge was then to predict the bubble point pressure curve at 343.13K.



**Figure 5: Isothermal bubble point pressure vs. composition for ethanol - 1,1,1,2,3,3,3-heptafluoropropane at 283.17K.  $\square$  are experimental points and full line and  $\times$  are predicted by method.**

Our (Christensen S., Peters G.H., Hansen F.Y., O'Connell J.P., Abildskov J.) entry, based on the above steps, used only pure component densities of 1,1,1,2,3,3,3-heptafluoropropane to optimize a force field description of that compound. Together with an existing description of ethanol, MD simulations were made at different mixing ratios, where a set of simulations were made at both the temperature of the training data set (283.17K) and the challenge temperature (343.13 K). The FST analysis was applied to both systems. The

results for the training system at 283.17K are given in Figure 5 and the results of the challenge system are given in Figure 6.

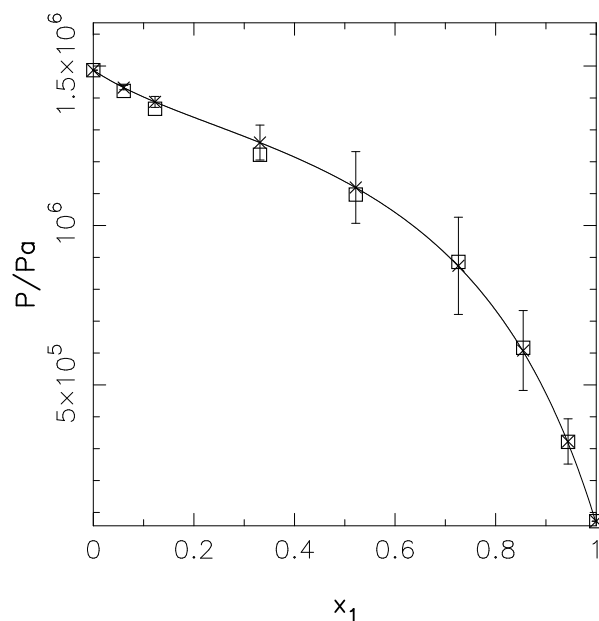


**Figure 6: Isothermal bubble point pressure vs. composition for ethanol - 1,1,1,2,3,3,3-heptafluoropropane at 343.13K.  $\square$  are experimental points and full line and  $\times$  are predicted by method.**

The average relative error of the predicted bubble point pressures at 343.13K was 1.52 % which was the best result of all submissions.



#### References

1. J.G. Kirkwood, F. Buff, J. Chem. Phys. 19 (1951) 774-777.
2. J.P. O'Connell, Molecular Physics, 20 (1971), 27-33.



### Michelangelo Dall'Ora

Phone: +45 4525 2839  
Fax: +45 4588 2258  
E-mail: mid@kt.dtu.dk  
WWW: <http://www.chec.kt.dtu.dk>  
Supervisors: Anker Degn Jensen  
Peter Arendt Jensen

### Ph.D. Study

Started: December 2004  
To be completed: November 2007

## Reactivity and Burnout of Wood Fuels

### Abstract

Wood is increasingly used as a CO<sub>2</sub>-neutral and renewable fuel for the production of heat and power in highly efficient suspension fired power plant boilers. Compared to coal, the most often used solid fuel, knowledge on wood combustion is limited. In suspension fired boilers wood char oxidation is the slowest step and determines the degree of burnout of the fuel, thus affecting the efficiency of the plant. In order to enable prediction of the burnout and main heat release profile, wood char needs to be characterized, its reactivity to oxygen has to be assessed and kinetic data must be coupled with suitable models accounting for transport processes and char transformation during combustion. This project addresses these issues by means of experimental work at laboratory, pilot and full scale as well as modeling.

### Introduction

The large availability of wood, neutrality with respect to CO<sub>2</sub> emissions and the fact that it is a renewable source make it a very attractive solid fuel for combined heat and power plants. A variety of wood species are burned nowadays in power plants, depending on the location of the plant, the wood-related activities in the area (pulp and paper industry, sawmills, etc.) and other economical reasons; wood from conventional forestry, residues from manufacturing of wood based products such as bark, sawdust and off-cuts from sawmills are some of the sources of wood fuel.

The most common techniques for the combustion of wood in combined heat and power plants are grate and suspension firing; this project deals with the latter. Suspension firing has been used for decades to burn pulverized coal; environmental concern and legislation have contributed to the conversion of some of those plants to wood combustion and to the building of new pulverized wood power plants. Today, the world's largest pulverized wood fired power plant in operation is in Denmark.

Wood is usually delivered to the plant as wood pellets (see Figure 1) that are opened by milling prior to entering the boiler; what is fed to the boiler is thus pulverized wood, as is seen in Fig.1.

As they enter the furnace, the wood particles are heated up very quickly to high temperatures and thereby release volatiles (this process is known as pyrolysis), leaving a solid residue called char. The subsequent

oxidation of the char is the slowest step in the conversion of wood and thus determines the degree of burnout of the fuel as well as the heat release profile in the boiler, affecting the operation and efficiency of the plant.

It is well known that pyrolysis conditions influence both the yield of char and its properties, including size, morphology, composition and reactivity. On the other hand, few works are available in literature about characterization of char produced at boiler-like conditions [1-3].

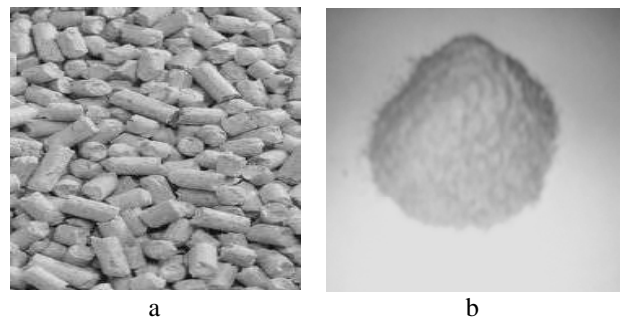


**Figure 1:** a) wood pellets, b) pulverized wood.

In suspension boilers wood pyrolysis occurs in a time interval of the order of ms, whereas the subsequent oxidation of the char takes up to several seconds [4]. It is therefore evident that the process of char oxidation is the most relevant when the degree of burnout

(conversion) of the fuel is to be calculated. In this perspective, it is vital to assess the reactivity of the char to oxygen.

There is a well established awareness that the reactivity of chars from wood is far higher than the reactivity of chars from coal [5]; nevertheless, the dependence of char properties on pyrolysis conditions together with the heterogeneity of wood, result in a relatively poor agreement among published kinetic data for the oxidation of wood char.

### Specific Objectives

The overall objective of the project is to develop tools that can be applied to predict wood fuel burnout in suspension fired boilers.

This goal is approached by:

- ✓ Investigation of the relation between wood char properties and pyrolysis conditions;
- ✓ Assessment of wood char oxidation reactivity;
- ✓ Modeling of wood char particle combustion.

### Experimental

Experimental work was carried out to investigate the influence of high temperature pyrolysis on wood char properties. Chars from different wood fuels (bark and pine) were produced at different conditions in a pilot-scale entrained flow reactor (EFR). With this reactor the wood particles experienced rapid heating and high reactor temperatures, which reproduces the conditions in a real suspension boiler and differs substantially from the much lower temperatures and heating rates often applied in pyrolysis studies. For comparison, char was also produced in a thermogravimetric apparatus (TGA). The produced chars were analyzed by SEM microscopy and their oxidation reactivity derived by thermogravimetry.

### Results and Discussion

Figure 2 shows a SEM picture of a pine particle in which the typical fibrous structure of wood is easily recognized. Figure 3 to Figure 5 show chars from pine wood produced at different conditions. Pine pyrolysis at 1373K and heating rate 10K/min in the TGA yielded a char that retained completely the fibrous structure, as seen in Figure 3.

The influence of pyrolysis conditions on char morphology is evident when char in Figure 3 is compared to the one in Figure 4 and Figure 5, produced in the EFR at close-to-boiler conditions: during pyrolysis in EFR wood particles went most likely through a molten phase and completely lost the typical fiber-like structure of wood. The char appears as porous spheres. These observations agree with results of previous works by Cetin et al. [1] and Zolin [2], whose studies on straw showed that straw char produced at high temperatures and high heating rate appears as a spherical shell that has undergone plastic deformation.



Figure 2: SEM picture of a pine particle.

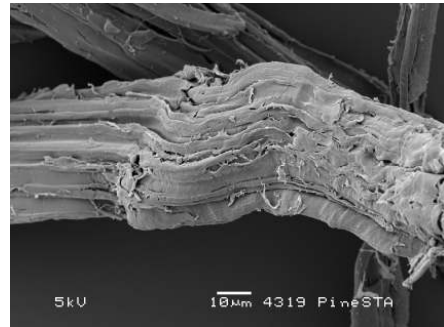


Figure 3: SEM picture of a pine char particle produced in a TGA. The original pine was heated in  $N_2$  at 10K/min to 1373K and was held at this temperature for 30 minutes.

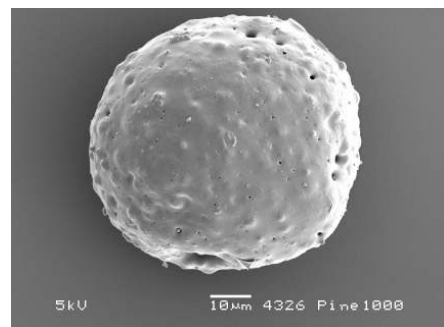


Figure 4: SEM picture of a char particle produced by fast pyrolysis of pine wood in the EFR. Pyrolysis temperature 1273K.

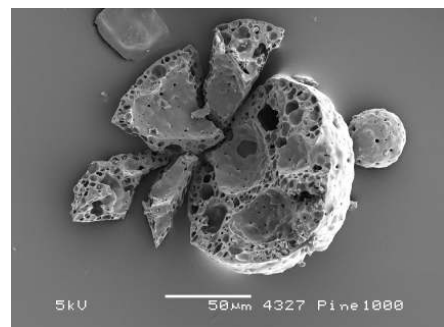


Figure 5: SEM picture of char produced by fast pyrolysis of pine wood in the EFR. Pyrolysis temperature 1273K.

EDX analyses of the chars produced in EFR showed a very uniform composition of the char. Indeed, it seems realistic that combustion models for pulverized wood power plant describe wood char as spherical particles of uniform properties.

As far as char particle size is concerned, wood particles exposed to higher temperatures resulted in smaller char particles.

The oxidation reactivity of the produced wood chars was derived by thermogravimetry. Chars have been oxidized in 4% O<sub>2</sub> – 96% N<sub>2</sub> atmosphere, during non-isothermal runs; the applied heating rate was as low as 2 K/min, so that transport limitations could be avoided.

A volumetric reaction model was used to analyze the mass loss curves from TGA experiments to determine the oxidation kinetics. The model assumes a single first order reaction (SFOR). Initially both activation energy E<sub>a</sub> and pre-exponential factor were derived from the experimental curves. In order to make comparison of char reactivity easier E<sub>a</sub> was then fixed at 166,28 kJ/mol and the pre exponential factor was thus the only parameter to be derived.

As shown in Figure 6, good agreement was generally found between experimental data and DTG curves generated with the derived SFOR kinetic parameters. This confirms that char oxidation in TGA occurred without any transport limitation and the obtained kinetics is the true oxidation reactivity of the wood chars.

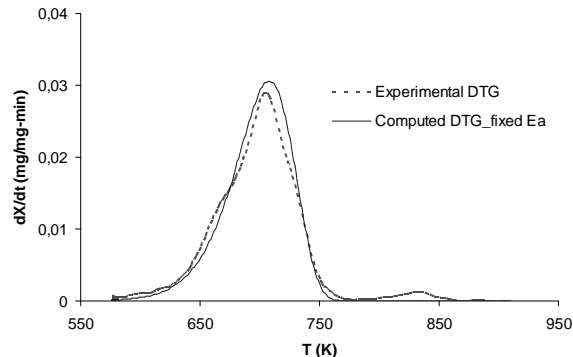


**Figure 6:** DTG curves of oxidation of bark char produced in EFR reactor at 1573K in 4% O<sub>2</sub>. Oxidation in TGA at 2K/min in 4% O<sub>2</sub>.

Figure 7 shows the reactivity (pre exponential factor) of different chars, as calculated assuming a common activation energy. Some of the chars of Figure 7 were produced in TGA by heating pine wood in nitrogen atmosphere at 20 K/min up to the final pyrolysis temperature and holding the sample at this temperature for 20 min. The other chars included in the figure are produced in the EFR reactor.

Char produced in inert atmosphere showed a tendency to deactivate when the pyrolysis temperature increased. For the chars produced in TGA, there exists a pyrolysis temperature interval (1273K – 1373K) where char reactivity does not vary; a similar behavior was observed for straw char by Zolin [2].

As can be seen, all the chars produced in EFR under boiler-like conditions had higher reactivity than those produced at much milder conditions in the TGA. This could be due to the major transformation of the particle structure during fast pyrolysis. Re-arrangement of the mineral matter during pyrolysis may also contribute to some extent to the differences in char reactivity, although we do not, at present, have clear evidence to support this hypothesis.

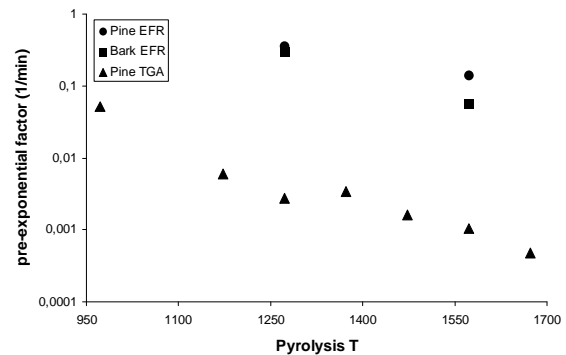


**Figure 7:** Summary of SFOR reactivity (pre-exponential factor) of pine wood chars and bark chars derived from TGA experiments. All chars produced in 100% N<sub>2</sub>.

## Conclusions

Pyrolysis experiments were carried out in an Entrained Flow Reactor (EFR) and in a thermogravimetric balance (TGA), to investigate how char properties depend on pyrolysis conditions. The produced char was analyzed by SEM microscopy and its reactivity to oxygen was assessed by thermogravimetry, assuming single first order reaction.

So far, results have shown that:

- ✓ wood particles subjected to rapid heating to high temperatures do not retain the typical wood fibrous structure;
- ✓ char particles from fast pyrolysis are spherical and highly porous; it is thus realistic to model them as spheres in combustion models;
- ✓ chars produced under boiler-like conditions have higher reactivity than those produced at milder conditions.

## Future work

Further investigation of char reactivity in relation to pyrolysis conditions and original fuel characteristics is ongoing; apart from pyrolysis temperature and heating rate, the effect of the presence of oxygen during pyrolysis will be investigated.

The obtained kinetic parameters will allow a more accurate simulation of char particle combustion in pulverized wood power plants and accordingly a better prediction of fuel burnout.

## Acknowledgements

The project is funded by Energinet.dk and is carried out at CHEC (Combustion and Harmful Emissions Control)

Research Center in cooperation with DONG Energy A/S.

### References

1. E. Cetin et al., Fuel 83 (2004) 2139-2150
2. A. Zolin, Reactivity of solid fuels, Ph.D. Thesis, 2001, DTU
3. E. Biagini, C. Fantozzi and L. Tognotti, Combust.Sci. and Tech. 176 (2004) 685-703
4. T. F. Wall in: C.J. Lawn (Ed), Principles of Combustion Engineering for Boilers, Academic Press, UK, 1987
5. M.J. Wornat et al., 26th Symp. on Comb., The Comb. Inst., 1996, 3075-3083



## Florin Paul Davidescu

Phone: +45 4525 2811  
Fax: +45 4593 2906  
E-mail: fpd@kt.dtu.dk  
WWW: <http://www.capec.kt.dtu.dk>  
Supervisors: Sten Bay Jørgensen  
Henrik Madsen

Ph.D. Study  
Started: January 2005  
To be completed: December 2007

## Qualitative Experimental Design for Dynamic Modelling

### Abstract

Parameter identifiability constitutes an important issue for development of quantitative dynamic process models from experimental data. The focus of this paper is on the presentation of a methodology for parameter identifiability, which can be applied systematically for qualitative experimental design. An enzymatic reaction network is used as a case study to illustrate the methodological aspects.

### Introduction

There is an increasing interest in producing complex intermediates and expensive fine chemicals in the pharmaceutical industry using biochemical synthesis. Up to now, only one or a few biotransformation steps are involved in complex synthesis problems in industry, although enzymes are widely known as being specific, fast and working under mild conditions. To develop a purely enzymatic synthesis for complex molecules from completely different substrates, large reaction networks are necessary. One way to construct such a functional network is the System of Biotransformations (SBT). The SBT is based on a micro-organism's metabolic network containing the synthesis path including cofactor regeneration reactions down to the desired product which most often is an intermediate in the metabolic network. Hence expression of the enzymes catalyzing reactions from this intermediate are turned off prior to the extraction i.e the genes are knocked-out.

The SBT is used as cell free extract in the production phase, combining the easy handling of a viable culture with the advantages of *in vitro* biotransformations [1].

The general goal of this PhD study is to identify the bottlenecks of the SBT, to describe them evenly and thereby to optimize the productivity of the selected reaction network.

The workhorse of the de-bottlenecking and optimization process is a model describing the biochemical reaction network with good long-term prediction properties.

Thereby, the SBT contains the relevant reactions of the glycolysis, leading to a system of high dynamics and complexity. Therefore, it is not realistic to develop a

"perfect model" from first principle engineering methods. For this reason, in this work a grey-box stochastic model development framework [2] is used to develop a stochastic state space model.

Once an acceptable stochastic state space model has been developed using the framework described above it is necessary to further calibrate and validate it over a wider range of states space. In this process it is necessary to assess the parameters identifiability. This operation is usually done prior to the parameter estimation step. In this work a method based on generating series and Lie algebra was employed. By performing qualitative and quantitative experimental design it is possible to further assess and improve the parameters identifiability.

After introduction and demonstration of the identifiability method, a systematic quantitative experimental design methodology is introduced based upon application of the identifiability analysis.

### Specific Objectives

After describing the scope of the project the main objectives of the project are defined as follows:

-to further develop the grey-box stochastic grey-box methodology further developed by Kristensen [2].

-to develop a grey-box stochastic model for the enzymatic reaction network (system of biotransformation)

-to expand both the methodology and the associated software tools for performing experimental design.

### Background

Once a model has been formulated it is necessary to assess the identifiability of the parameters and to

determine which should be the inputs and the outputs of the experiments in order to be able to make all the model parameters identifiable [3]. Concerning identifiability analysis then a parameter set can be globally identifiable, which means that there is only one unique solution; or locally identifiable, which means that there are more than one solution; or simply unidentifiable, in which case there is no solution for this parameter set. For nonlinear models, there are only very few methods for assessing parameter identifiability. The first tool to be mentioned is the local or global (multi local) sensitivity analysis together with the co-linearity indexes [6], which is one of the widely used, methods; the second method is an optimization-based approach, proposed recently by [4]. The theoretical-based methods are applicable only to some classes of models. The first methods listed are based on differential algebra and Grobner basis; the second methods are based on Taylor or generating series [1,5]. The advantages of the theoretical methods, are, first that they constitute a definitive test and, second, are unaffected by scaling. However they are limited to some classes of models and, they can only be applied for relatively small problems. The method used in this contribution is the last method described above, based on generating series. The application of the method is limited however to the deterministic part of the model and assuming the data are error free. Model parameter identifiability is investigated first, and then qualitative experimental design is applied.

### Method

This section describes briefly, the theoretical identifiability method based on generating series and Lie algebra [5]. For batch models the method is similar to the Taylor based method, but for fed-batch models the generating series-based method is simpler. In the given model structure  $M(\theta)$  in equation 1,

$$\begin{cases} \frac{dx(t)}{dt} = f_0(x(t), \theta) + \sum_{i=1}^m u_i(t) \cdot f_i(x(t), \theta), & x(0) = x_0(\theta) \\ y(t, \theta) = h(x(t), \theta) \end{cases} \quad (1)$$

the  $f_0$  functions are represented by the part of the right hand-side of the equations which is not affected by the feed flow-rate; while the part affected by the flow-rate are represented by the  $f_i$  functions. For a given model as in equation 1 a series expansion can be written based on the Lie derivatives so that the model output can be expanded in series with respect to inputs and time [5] around an initial time denoted by sub index  $_0$ . The index  $m$  represents the number of inputs and  $d$  is the maximum order of derivation. In the equation above  $_0$  indicates evaluation at  $t=0$  in  $h|_0 = h(x(t), \theta)|_0$  and the terms  $L_{f_i} L_{f_j} \dots L_{f_m} L_{f_0} h(x(t), \theta)|_0$ .

$$\begin{aligned} y(t, \theta)|_0 &= h|_0 + L_{f_0} h|_0 + L_{f_0} L_{f_0} h|_0 + \dots + \underbrace{L_{f_0} \dots L_{f_0} h|_0}_{n \text{ times derivation}} + \\ &\sum_{i=1}^m u_i(t) \cdot L_{f_i} L_{f_0} h|_0 + \sum_{i=1}^m u_i(t) \cdot \sum_{j=0}^d L_{f_i} L_{f_j} L_{f_0} h|_0 + \\ &\sum_{i=1}^m u_i(t) \cdot \sum_{j=0}^d \sum_{k=0}^d L_{f_i} L_{f_j} L_{f_k} L_{f_0} h|_0 + \\ &\sum_{i=1}^m u_i(t) \cdot \sum_{j=0}^d \sum_{k=0}^d \dots \sum_{l=0}^d L_{f_i} \underbrace{L_{f_j} L_{f_k} \dots L_{f_l}}_{n-1 \text{ times derivation}} L_{f_0} h|_0 \end{aligned} \quad (2)$$

Note that  $L_{f_i} h$  is the Lie derivative of  $h$  along the vector field  $f_i$  given by equation 3.

$$L_{f_i} h(x(t), \theta) = \sum_{j=1}^n f_{i,j}(x(t), \theta) \cdot \frac{\partial}{\partial x_j} h(x(t), \theta) \quad (3)$$

In equation 3,  $n$  is the number of states and the index  $j$  is the  $j^{\text{th}}$  element of the  $f_i$  function vector. Let  $s(\theta)$  be the coefficients of the expansion given in equation 2, which are in fact combinations of Lie derivatives. The identity  $M(\hat{\theta}) \equiv M(\tilde{\theta})$  translates into  $s(\hat{\theta}) \equiv s(\tilde{\theta})$ . One can therefore test the identifiability of  $M(*)$  by calculating the number of solutions for  $\hat{\theta}$  of the set of equations  $s(\hat{\theta}) \equiv s(\tilde{\theta})$  [5]. The uniqueness of the solution is determined by solving  $s(\hat{\theta}) = 0$ . If the underlying system of equations has one solution then the parameter set is theoretically globally identifiable; if there are more solutions then the parameters at best may be only locally identifiable and if the system has no solution the parameters are unidentifiable. Once the Lie brackets have been computed e.g., the  $s(\hat{\theta})$  then a system of algebraic equations is obtained. The elements in the parameter vector  $\theta$  are the initial model parameters and the initial values of the states. It should be mentioned that if two parameters e.g.  $a$  and  $b$  are unidentifiable then a combination of the two, e.g. the sum or the ratio could be identifiable. As discussed in the introductory section, the model under investigation is an ode representation of an enzymatic reaction network [2]. given below, in equation 4. Initially two species are measured, thus there are two  $h$  equations. The analysis will first focus on the batch model i.e. the  $f_0$  functions. Since there are only two states, which are measured, only some of the parameters may be identifiable. The model investigated is given in the next section.

### Model description and identifiability analysis

This section described the model under investigation. As discussed above the model is a representation of an enzymatic reaction network and it has been obtained and improved using the grey-box stochastic methodology mentioned in the introductory section. The model equations are given below:

$$\begin{aligned}
\frac{dc_{GL}}{dt} &= -r_{1max} \cdot \frac{c_{GL}}{c_{GL}+K_{11}} \\
\frac{dc_{F16B}}{dt} &= r_{1max} \cdot \frac{c_{GL}}{c_{GL}+K_{11}} - r_{2max} \cdot \frac{c_{F16B}}{c_{F16B}+K_{21}+\frac{c_{DHAP} \cdot c_{G3P}}{K_{22}}} \\
\frac{dc_{DHAP}}{dt} &= r_{2max} \cdot \frac{c_{F16B}}{c_{F16B}+K_{21}+\frac{c_{DHAP} \cdot c_{G3P}}{K_{22}}} - r_{6max} \cdot c_{DHAP} \\
\frac{dc_{G3P}}{dt} &= r_{2max} \cdot \frac{c_{F16B}}{c_{F16B}+K_{21}+\frac{c_{DHAP} \cdot c_{G3P}}{K_{22}}} - r_{3max} \cdot c_{G3P} \cdot c_{NAD} \\
\frac{dc_{PYR}}{dt} &= r_{3max} \cdot c_{G3P} \cdot c_{NAD} - r_{4max} \cdot c_{PYR} \\
\frac{dc_{LAC}}{dt} &= r_{4max} \cdot c_{PYR} \\
\frac{dc_{ATP}}{dt} &= -2 \cdot r_{1max} \cdot \frac{c_{GL}}{c_{GL}+K_{11}} + 2 \cdot r_{3max} \cdot c_{G3P} \cdot c_{NAD} - r_{5max} \cdot c_{ATP} \\
\frac{dc_{NAD}}{dt} &= -r_{3max} \cdot c_{G3P} \cdot c_{NAD} + r_{4max} \cdot c_{PYR} \\
\frac{dc_{PO4}}{dt} &= -r_{3max} \cdot c_{G3P} \cdot c_{NAD} + r_{5max} \cdot c_{ATP}
\end{aligned} \tag{4}$$

They are two species measured, thus there are two h equations:

$$\begin{aligned}
h_1 &= c_{GL} \\
h_2 &= c_{DHAP}
\end{aligned} \tag{5}$$

The  $f_0$  functions are represented by the right hand-side of the equations 3. Since there are only two states, which are measured, only some of the parameters should be identifiable. The first Lie derivatives are given below:

$$\begin{aligned}
L_{f_0}(h_1) &= f_{01} \frac{\partial h_1}{\partial c_{GL}} = \frac{-r_{1max} \cdot c_{GL}}{c_{GL}+K_{11}} \\
L_{f_0}(h_2) &= f_{03} \frac{\partial h_2}{\partial c_{DHAP}} = \frac{r_{2max} \cdot c_{F16B}}{c_{F16B}+K_{21}+\frac{c_{DHAP} \cdot c_{G3P}}{K_{22}}} - r_{6max} \cdot c_{DHAP}
\end{aligned} \tag{6}$$

They are 6 parameters occurring in equations 5. In order to have a determined system of equations it is necessary to compute two more of the higher order derivatives. Once the derivatives have been computed, two more parameters appeared in the higher order terms and therefore two more Lie derivatives have to be computed, thus the Lie derivatives up to the fourth order have been used for this analysis. The method has a drawback in the sense that there is no way to know a-priori how many Lie derivatives need to be computed in order to obtain a determined system of equations. The following eight parameters  $r_{1max}$ ,  $K_{21}$ ,  $K_{22}$ ,  $r_{6max}$ ,  $r_{2max}$ ,  $K_{11}$ ,  $r_{3max}$ ,  $r_{4max}$ , occurred in the equations. The system of equations has been solved for the parameters and more solutions were found meaning that the parameter set is only locally identifiable. In the next step, all the reduced set of 7 parameters formed from the full parameter set. The analysis led to the same conclusion that the parameters set is only locally identifiable since more the equations system had multiple solutions. When further reducing to 6, the parameters set, the analysis have been repeated for all the possible combinations of 6 parameters obtained from the original full parameter set and all the combinations proved to be only locally identifiable. Analyzing the first Lie brackets for the first measurement, it can be observed that there are dependent only on  $c_{GL}$ ,  $r_{1max}$  and  $K_{11}$ . The Lie brackets for the first measurement depends only on  $c_{GL}$ ,  $r_{1max}$ , and  $K_{11}$  and thus including extra terms will be redundant, therefore only one Lie bracket corresponding to the first measurement, will be included. This observation led to an even more simplified set of only 5 equations. The

system of equations has been solved for all the combinations of 5 parameters obtained from the full parameter set. The analysis led to the same conclusions as before. Finally, only 4 parameter subsets were considered for investigation. This time, for several parameters subsets a unique solution was found, thus the particular combination of parameters is globally identifiable. The equations used for the last step of the analysis are  $L_{f_0}h_1$ ,  $L_{f_0}h_2$ ,  $L_{f_0}L_{f_0}h_2$ ,  $L_{f_0}L_{f_0}L_{f_0}h_2$ .

**Table 1: Globally identifiable parameters subsets**

Parameter subset			
$r_{1max}$	$K_{21}$	$K_{22}$	$r_{6max}$
$r_{1max}$	$K_{21}$	$K_{22}$	$r_{4max}$
$r_{1max}$	$K_{21}$	$r_{2max}$	$r_{4max}$
$r_{1max}$	$K_{21}$	$r_{3max}$	$r_{4max}$
$r_{1max}$	$K_{21}$	$r_{6max}$	$r_{4max}$
$r_{1max}$	$K_{22}$	$r_{2max}$	$r_{4max}$
$r_{1max}$	$K_{22}$	$r_{3max}$	$r_{4max}$
$r_{1max}$	$r_{3max}$	$r_{2max}$	$r_{4max}$
$r_{1max}$	$r_{3max}$	$r_{6max}$	$r_{4max}$

The combinations of parameters that were found to be globally identifiable are given in the table 4. It can be concluded that for the model given in equations 4 and for the model output in equations 2 only four parameters could be identified globally. The results of the analysis are definitive, however if the model will change only slightly, all the analysis has to be repeated.

### Qualitative experimental design

The generating series and Lie algebra introduced above can also be used in a systematic manner to determine which inputs should be perturbed and which outputs should be measured in order to be able to identify more if not all the model parameters.

In this report a single input was considered, that is, a feed flow-rate of the main reactant, thus the operation mode moved from batch to fed-batch.

$$\begin{aligned}
\frac{dc_{GL}}{dt} &= -r_{1max} \cdot \frac{c_{GL}}{c_{GL}+K_{11}} + \frac{F}{V} \cdot (c_{GLf} - c_{GL}) \\
\frac{dc_{F16B}}{dt} &= r_{1max} \cdot \frac{c_{GL}}{c_{GL}+K_{11}} - r_{2max} \cdot \frac{c_{F16B}}{c_{F16B}+K_{21}+\frac{c_{DHAP} \cdot c_{G3P}}{K_{22}}} - \frac{F}{V} \cdot c_{F16B} \\
\frac{dc_{DHAP}}{dt} &= r_{2max} \cdot \frac{c_{F16B}}{c_{F16B}+K_{21}+\frac{c_{DHAP} \cdot c_{G3P}}{K_{22}}} - r_{6max} \cdot c_{DHAP} - \frac{F}{V} \cdot c_{DHAP} \\
\frac{dc_{G3P}}{dt} &= r_{2max} \cdot \frac{c_{F16B}}{c_{F16B}+K_{21}+\frac{c_{DHAP} \cdot c_{G3P}}{K_{22}}} - r_{3max} \cdot c_{G3P} \cdot c_{NAD} - \frac{F}{V} \cdot c_{G3P} \\
\frac{dc_{PYR}}{dt} &= r_{3max} \cdot c_{G3P} \cdot c_{NAD} - r_{4max} \cdot c_{PYR} - \frac{F}{V} \cdot c_{PYR} \\
\frac{dc_{LAC}}{dt} &= r_{4max} \cdot c_{PYR} - \frac{F}{V} \cdot c_{LAC} \\
\frac{dc_{ATP}}{dt} &= -2 \cdot r_{1max} \cdot \frac{c_{GL}}{c_{GL}+K_{11}} + 2 \cdot r_{3max} \cdot c_{G3P} \cdot c_{NAD} - r_{5max} \cdot c_{ATP} - \frac{F}{V} \cdot c_{ATP} \\
\frac{dc_{NAD}}{dt} &= -r_{3max} \cdot c_{G3P} \cdot c_{NAD} + r_{4max} \cdot c_{PYR} - \frac{F}{V} \cdot c_{NAD} \\
\frac{dc_{PO4}}{dt} &= -r_{3max} \cdot c_{G3P} \cdot c_{NAD} + r_{5max} \cdot c_{ATP} - \frac{F}{V} \cdot c_{PO4}
\end{aligned} \tag{7}$$

The model equations will change slightly and are given in equation 7. It is considered that the same compounds are being measured, thus the measurements equations are the same as in equation 5. For this case it is possible to compute mixed terms of the Lie derivatives in order to include the influence of the input to the process. The following Lie derivatives have been computed for this analysis:  $L_{f_1}L_{f_1}L_{f_0}L_{f_0}(h_2)$ ,  $L_{f_1}L_{f_1}L_{f_0}(h_1)$ ,

$L_{j0}L_{j0}(h_2)$ ,  $L_{j1}L_{j1}L_{j0}(h_2)$ ,  $L_{j1}L_{j0}(h_2)$ ,  $L_{j1}L_{j0}L_{j0}(h_2)$ ,  $L_{j1}L_{j0}(h_1)$ ,  $L_{j0}(h_1)$ ,  $L_{j0}(h_2)$  where  $i$  indicate the measurement equations  $h_i$ . The derivatives obtained only from the first term have been discarded for analysis as well as the first mixed term for the first measurement and the reason explained for the model without inputs applies here as well. The system of equations formed by the remaining six equations has been solved for the possible combinations of 6 parameters. Among the parameters to be investigated the initial concentration of glucose  $c_{GL}$  has been included as well since the input to the process is glucose. The glucose feed concentration  $c_{G\text{feed}}$  is a known parameter and the feed flow-rate  $F$  is the process input. The results of the investigation showed that combinations of 6 parameters were globally identifiable. By considering an input to the process, that is, by switching from batch to fed-batch operation, some of the parameters which were only locally identifiable they became globally identifiable. In order to render more parameters identifiable more measurements needs to be included in the analysis. Since ATP is involved in many of the balances it was decided to include it first. After ATP has been included among the  $h$  functions the same Lie brackets were computed as for the other measurements. In the search for a system of equations that would make more parameters identifiable, four combinations each with seven parameters were found to be identifiable. It has been noticed that, in particular  $r_{4\text{max}}$  and  $r_{5\text{max}}$  could not be identified simultaneously. The balance for Lactate is related only to the  $r_{4\text{max}}$  parameter and thus indicating that a measurement for Lactate could help improving identifiability. Hence a measurement of Lactate was included in the analysis, two combinations of eight parameters can be uniquely identified, and furthermore this time the two parameters  $r_{4\text{max}}$  and  $r_{5\text{max}}$  can be identifiable together with other parameters. As an alternative for the Lactate measurement the Pyruvate measurement can be considered, and the same information can be obtained. Out of the total number of 10 parameters there are two parameters, which could not be identified, i.e.  $r_{6\text{max}}$  and  $K_{22}$ . The two parameters are related to the balances for DHAP and F16B and G3P. A measurement for DHAP is already included in the original measurement set; therefore in the next step a measurement for F16B is included as an extra measurement. Subsequently, the parameter  $K_{22}$  became identifiable. All the attempts to find a system of equations formed with the various equations to obtain a unique solution for all the ten parameters was unfruitful since  $r_{6\text{max}}$  remains unidentifiable. Since  $r_{6\text{max}}$  does not influence the balances for the rest of the compounds, the last remaining option is to consider simultaneously the measurements for F16B and for G3P. In the last step of the analysis therefore the two measurements were included simultaneously. The search for a combination of equations that would give a unique solution for all the parameters still was unfruitful. The parameter  $r_{6\text{max}}$  still remained unidentifiable even using all the possible measurements. Five output measurements, which

qualitative are: GL, DHAP, ATP, LAC, F16B or GL, DHAP, ATP, PYR, G3P would give the optimum information in terms of minimum measured outputs and maximum number of identifiable parameters. Thus, in order to also identify  $r_{6\text{max}}$  then measurement of the product of DHAP conversion may be considered.

### Discussion

With respect to the general economy of the project, more information became available in terms of measured concentrations and more complicated models with much more parameters were developed using the grey-box stochastic methodology. For this large models and if it is to consider the grey box terms that are stochastic terms, the method illustrated above is already impractical. Some of the other methods mentioned above, like the local sensitivity analysis, has been applied. In the next step if necessary the optimization based approach [4] will be applied in order to assess the identifiability of the model parameters and to determine the inputs outputs.

Once it has been determined which inputs and outputs to the process should be considered, the Fisher information matrix for the grey-box stochastic models will form the basis for qualitative experimental design.

### Conclusions

Enzymatic reaction network models have been investigated for theoretical identifiability using a general method based upon generating series. The theoretical identifiability analysis is subsequently used as a basis for quantitative experimental design. It is demonstrated that additional parameters can be identified by changing the operation mode to fed-batch. Furthermore the effect of the inclusion of additional measurements upon parameter identifiability is clearly demonstrated.

### References

1. Michael Schümperli, Matthias Heinemann, Anne Kümmel and Sven Panke, in preparation 2006
2. Niels Rode Kristensen, Henrik Madsen and Sten Bay Jørgensen, *Comp. and Chem. Eng.*, 28 (2004), 1431-1449
3. Walter Eric, Pronzato Luc, *Automatica*, 26, No 2, (1990), 195-213
4. Asprey S.P., Macchietto, *Comp. and Chem Eng.*, 24 (2000), 1261-1267
5. Wlater Eric, Pronzato Luc, *Mathematics and Computers in Simulation*, 42, (1996)

### List of publications

1. Marquardt, Pantelides, 16<sup>th</sup> European symposium on computer aided process engineering and 9<sup>th</sup> International Symposium on process systems engineering, ELSEVIER, Germany 2006
2. F.P. Davidescu, Henrik Madsen, Sten Bay Jørgensen, submitted for the 17<sup>th</sup> European symposium on computer aided process engineering



## Joanna Maria Drews

Phone: +45 4677 5490  
Fax: +45 4677 4791  
E-mail: [jmd@polymers.dk](mailto:jmd@polymers.dk)  
WWW: <http://www.polymers.dk>  
<http://www.risoe.dk/pol>  
<http://www.risoe.dk/interface>  
Supervisors: Søren Hvilsted  
Keld West, Risø National Laboratory  
Peter Kingshott, iNANO, Aarhus  
University  
Ph.D. Study  
Started: February 2005  
To be completed: January 2008

## Surface Polymerisation Methods for Optimized Adhesion

### Abstract

The focus of my Ph.D. studies is on surface modification as well as surface characterization. The aim is to understand and optimise the adhesion between carbon or glass fibres and a polymer matrix. The approach is to modify planar models of fibres using soft plasma polymerisation with controlled surface chemistry, e.g. specific monomers. The surface characterisation facilitates our understanding of the physical and chemical processes taking place, e.g. during mechanical stress.

### Introduction

The Ph.D. study is part of the project "Interface Design of Composite Materials". The project is placed at the Materials Research Department, Risø National Laboratory, and collaborates with DPC/DTU, Risø National Laboratory, Aalborg University and Danish industries. The main focus of the project is to improve the mechanical properties of composite materials for wind turbine blades, i.e. by better understanding the chemical and physical processes between the fibres and the matrix.

The Ph.D. study contributes to the project by concentrating on surface modification and surface characterization of planar substrates. Glassy carbon substrates were chosen as a planar model of carbon fibres. The surfaces are modified with an AC pulsed plasma system [1], where monomers are introduced in the gas phase. The advantage of using this technique is that the polymerisation process runs very close to conventional polymerisation of monomers. Using plasma polymerization it is easy to test different monomers including some which are not very easy to polymerise using conventional techniques. Moreover, it is easy to handle the monomers, since one do not need the purified forms. The disadvantage of the plasma process is that it is very difficult to interpret the results. In addition one is in general not able to show the exact structure of the polymer.

For surface characterization the following techniques are used: X-ray Photoelectron Spectroscopy (XPS), Attenuated Total Reflectance Fourier Transform

Infrared Spectrometry (ATR-FTIR; for chemical characterisation of the surface), and Atomic Force Microscopy (AFM; for measuring the thickness and roughness of the film). The toluidine blue staining method is used to derive the amount of carboxylic acid groups on the surface.

### Methods

The present studies are soon running to the end of their second year. The last year has focused on surface modification and surface analysis techniques. Maleic anhydride and 1,2-(methylenedioxy) benzene were used for pulsed plasma surface modification, and the homo-polymer coatings (ppMAH and ppMDOB) and co-polymer coatings (ppMDOB/MAH) were obtained. Surfaces were modified as a function of the plasma polymerisation power and a variation in the amount of carboxylic acid groups on the surface was expected [2]. Since maleic anhydride has the tendency of taking up water from the environment, i.e. hydrolysing the anhydride groups to carboxylic acid groups, the work concentrated on surface analysis of ppMAH. Some samples were also sent to the Materials Research Department for fracture toughness measurements. For most of the modified surfaces we observed an improvement in the fracture toughness. Some results from these mechanical tests were presented during a conference at Risø National Laboratory in September 2006 by S. Goutianos. Detailed information about the mechanical tests can be found in the conference proceedings [3].

## Results and discussion

As mentioned above and reported previously, I have modified glassy carbon substrates with soft plasma. Different changes in the surface layers were observed according to the applied monomer or monomer mixture. The surfaces were modified at varying plasma polymerisation power. From AFM measurements we found that the thickness of the modified layers changed with the power for constant polymerisation time (10 min). XPS and ATR-FTIR, however, did not show any indication of changes in the surface chemistry as a function of the power. Likewise, measurements of the roughness after water treatment were also quite similar [4].

On the other hand, the preliminary results of the fracture toughness tests as well as from the toluidine blue staining method [5] did indicate changes in the structure of ppMAH as function of the plasma polymerisation power. The plasma modified layer has therefore been studied more carefully, starting with the hydrolysis of the polymerised layer under controlled conditions and the checking of the stability of the film on the substrate. This analysis was believed to help to explain the high scatter in the data from the mechanical tests.

All the tests of the hydrolysis and stability were performed on polyethylene (PE) substrates (20x20 mm<sup>2</sup>). PE is cleaned with acetone (5 minutes), methanol (5 minutes) and water (5 minutes) in an ultrasonic bath. The residuals of the solvents are then removed with an argon gun.

After plasma modification the surfaces were measured with XPS and ATR-FTIR. Only insignificant changes were observed. Afterwards the samples were placed into water and according to the ATR-FTIR data, six hours proved sufficient to hydrolyse the plasma polymerised films of maleic anhydride. The samples were then stored in air for varying amounts of time.

From the toluidine blue staining method the number of carboxylic acid groups was found to increase with the storage time. Considerable effort was therefore put into setting up optimal conditions for the hydrolysis of anhydride groups, e.g. temperature and environment. The following parameters were probed: the acidity of the environment, the water at room temperature and reflux, weak and strong base at room temperature and reflux.

From staining with dye I found that neither water nor acid is an optimal environment for hydrolysis of anhydride groups in the plasma polymerised films. Temperature changes did also not influence the speed of the hydrolysis. According to measurements of the dye concentration, the concentration of carboxylic acid groups increases linearly with the exposure time to water (measurements not shown here).

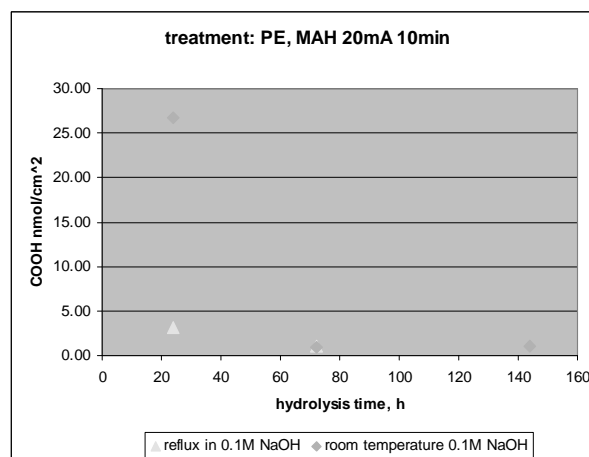


**Figure 1.** Concentration of carboxylic acid groups in the surface layers of plasma modified polyethylene with maleic anhydride as function of the hydrolysis of film.

The environment used was an alkaline solution where samples were placed at room temperature and reflux (Figure 1). Changing to an alkaline solution caused the reaction to progress faster, while changing temperature to reflux caused complete delamination of the plasma polymerised coating layer. Even at room temperature in alkaline solution delamination was observed albeit at a considerably longer time scale.

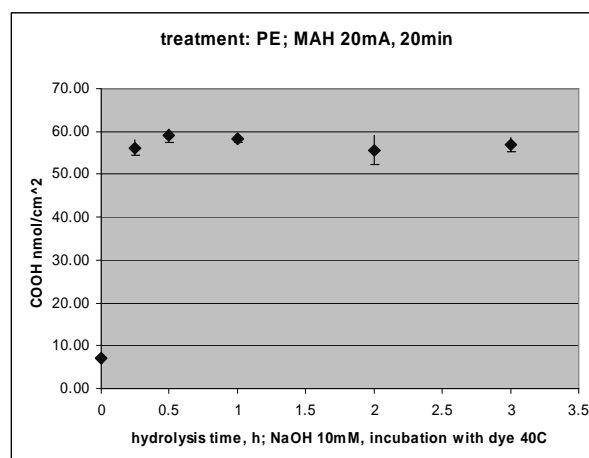


**Figure 2.** Concentrations of carboxylic acid groups in the surface plasma modified layer on polyethylene with MAH as function of hydrolysis time (10mM NaOH) in room temperature.

In the further studies 3 hours hydrolysis of anhydride groups in solution of 10 mM sodium hydroxide was used. We would like to know if the kinetics of hydrolysis depends on the thickness of polymerised film or the plasma power. Figure 2 shows time dependents of hydrolysis of anhydride groups in plasma modified layer of maleic anhydride for 20 minutes. As one can observe the hydrolysis is rather rapid and takes less than 15 minutes. This is the case for films polymerised with 20 mA (0.7 W/L). Films which are polymerised for longer time but with the same plasma power e.g. 30 minutes are not stable in NaOH –

delamination occurs almost immediately after contact with sodium hydroxide (visible flakes).

Some samples were also analysed with ATR-FTIR and XPS before and after the staining process. ATR-FTIR recorded hydrolysis of anhydride groups after staining treatment. XPS recorded only insignificant changes in the high resolution spectra and atom percentage.

### Conclusions and further work

Hydrolysis of ppMAH was depended on solvent where the extensive treatment with sodium hydroxide leads to delamination. The delamination of plasma polymerised films depended also on the time of polymerisation. One possible explanation is that hydrolysis introduces internal stresses in the coatings due to uptake of water (swelling). In the thicker films these internal stresses overcome the relatively weak bonding between the coating and the substrate, and delamination occurs.

The future work on the subject would be to carry out experiments of polymerisation with different plasma power in time intervals chosen so they would lead to the same coating layer thickness. I believe that it should be possible to see changes in the film. I would expect that with the higher power, I have obtained films with higher cross-linking/ materials with different bulk properties. The changes could be responsible for different behaviour during the mechanical tests.

### Acknowledgements

The Graduate School of Polymer Science and The Technical University of Denmark, and "Interface Design of Composites Materials" (STVF fund no. 26-03-0160) are thanked for financial assistance.

I would like to thank Senior Scientist Bent Sørensen and post.doc. Stergios Goutianos from the Materials Research Department, Risø National Laboratory for discussions and for measuring the fracture toughness of the modified surfaces; post.doc. Helen Launay from Danish Polymer Centre, Risø National Laboratory; my supervisors Professor Søren Hvilsted, senior scientist Keld West and Senior Scientist Peter Kingshott; and finally the staff of the Danish Polymer Centres at DTU and Risø National Laboratory.

### References

1. B. Winther-Jensen, K. Glejboel, US patent No. 6,628,084 B1 (30 Sep 2003); B. Winther-Jensen, S.F. Christensen, S.G. Petersen, US patent No. 0086660 A1 (6 May 2004)
2. B. Winther-Jensen, K. Norrman, P. Kingshott, K. West, *Plasma Process. Polym.* 2 (2005) 319; E. Ryan, A.M. Hynes, J.P.S. Badyal, *Chem. Mater.* 8 (1996) 37.
3. S. Goutianos, J. Drews, S.F. Nielsen, P. Kingshott, S. Hvilsted, B.F. Sørensen, *Proceedings of the 27th Risø Inter. Symposium on Mat. Sci.*, Eds: H. Lillholt, B. Madsen, T.L. Andersen, L.P. Mikkelsen, A., Thygesen, 2006, 173.

4. J. Drews, S. Goutianos, P. Kingshott, S. Hvilsted, N. Rozlosnik, K. Almdal, B.F. Sørensen, submitted to *Journal of Vacuum Science and Technology A*.
5. S. Sano, K. Kato, Y. Ikada, *Biomaterials* 14 (1993) 817





### Corinne Eenschooten

Phone: +45 4525 2978  
Fax: +45 4588 2258  
E-mail: cre@kt.dtu.dk  
WWW: <http://ivc-sep.kt.dtu.dk/>  
Supervisors: E. H. Stenby  
G. M. Kontogeorgis  
Novozymes Biopolymer A/S:  
K. Schwach-Abdellaoui, F. Guillaumie-Longin  
Third party: R. Gurny

### Industrial Ph.D. Study

Started: May 2005  
To be completed: May 2008

## Development of Hyaluronic Acid-Based Nanoparticles for Topical Delivery of Cosmetic Actives

### Abstract

The objective of this PhD project is the development of hyaluronic acid (HA)-based nanoparticles for topical delivery of cosmetic actives. So far a proof of concept that HA can be used as a building block for the design of nanoparticles to encapsulate hydrophobic ingredients was obtained. The chemical structure of HA was adjusted to impart this macromolecule new physico-chemical properties by grafting hydrophobic pendant groups onto HA backbone. The associative properties of the resulting amphiphilic HA (AmphiHA) in aqueous media were investigated and revealed that it could spontaneously form polymeric micelles in which core the hydrophobic model compound Nile Red was encapsulated. Further characterization of AmphiHA polymeric micelles showed that these were spherical, with a negatively charged surface (-25 mV) and submicronic dimensions (typically between 30 and 150 nm). Departing from this latest knowledge we are currently screening various strategies to formulate AmphiHA-based nanoparticles. Percutaneous penetration and release profile of an encapsulated ingredient in AmphiHA nanoparticles will be assessed later.

### Introduction

Hyaluronic acid (HA) is a natural linear polymer consisting of repeated disaccharide units of  $\alpha$ -D-glucuronic acid- $\beta$ -1,3-D-N-acetyl glucosamine- $\beta$ -1,4- (Figure 1).

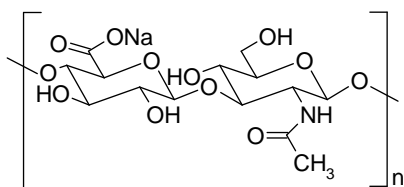


Figure 1: Repeating unit of hyaluronic acid

HA is found in most animal and human tissues. Particularly abundant in the vitreous humor of human eye and synovial joint fluid it is found in its largest amount in skin tissues [1].

As this biopolymer serves numerous important biological functions in connective tissues it has found applications in the prevention and treatment of symptoms related to disorders such as: fractures,

hernias, glaucoma, keratoconus, detached retinas, osteoarthritis, prevention of scarring, vocal cord repair, cartilage damage, wound and ligament healing [2]. HA is also involved in nutritional supplements and cosmetic care where it is considered as an efficient skin moisturization, anti-ageing and radical-scavenging agent.

Most cosmetic active ingredients are highly unstable compounds that need specific formulation strategies to act efficiently on or within skin tissues. Traditional approaches involve protection of these by means of encapsulation in micro/nano/multiple emulsions or liposomes.

Polymeric nanoparticles have recently been proposed as an advantageous alternative to these systems [3]. Indeed their "rigid" nature seems to offer better stability of the formulations made thereof and to improve skin uptake of their encapsulated ingredients compared to traditional "soft" carriers. In addition polymeric nanoparticles can provide a better controlled and sustained release over time to targeted organs.

### Specific objectives

Due to its biocompatibility and biodegradability hyaluronic acid (HA) has become an interesting building block for medical, pharmaceutical and cosmetic applications.

The main objective of this PhD project is to develop HA-based nanoparticles for topical cosmetic delivery. Whereas HA microparticles have already been devised for drug delivery (hydrocortisone [4], nerve growth factor [5], calcitonin [6]), very little has been reported on HA nanoparticles and even less about their potential use as delivery devices. It is our second aim to provide an innovative technology to produce completely tolerated and resorbable nanoparticles conveying all HA cosmetic properties in addition to the encapsulated compound activity.

This project has required the chemical modification of HA into more processable forms towards the design of nanoparticles. It is currently involving the screening of various strategies to formulate HA nanoparticles. It will finally call for the testing of their ability to encapsulate and release cosmetic ingredients both *in vitro* and *in vivo*.

### Methods

Hyaluronic acid (HA) was chemically modified by the covalent grafting of hydrophobic pendant groups onto HA backbone using a proprietary technology by Novozymes Biopolymer A/S.

The structure of the resulting amphiphilic hyaluronic acid (AmphiHA) was characterized by Proton Nuclear Magnetic Resonance ( $^1\text{H}$  NMR) (Mercury VX, Varian).

The critical micelle concentration (cmc) of AmphiHA was determined by fluorescence spectroscopy using a thermostated spectrofluorometer (FluoroMax, Spex) and Nile Red as the fluorophore.

The morphology of AmphiHA polymeric micelles was studied by transmission electron microscopy (EM 410, Philips).

The mean size and size distribution of AmphiHA polymeric micelles were determined by multi-angle dynamic light scattering (AVL-CGS-8, AVL).

The zeta potential of AmphiHA polymeric micelles was measured by electrophoretic mobility (Zetasizer 3000HS, Malvern).

### Results and Discussion

#### *Hydrophobization of hyaluronic acid*

The high hydrophilicity of native hyaluronic acid (HA) represents an obstacle for the fabrication of colloidal carriers such as micro/nanoparticles. Indeed HA does not form spontaneous individualized structures in aqueous media. In consequence it was our first priority to render HA amphiphilic. We envisioned that the introduction of hydrophobic groups onto HA would at least bring two major advantages:

- ease the preparation of HA colloidal carriers by altering HA physico-chemical properties

- allow the encapsulation by HA of highly hydrophobic moieties.

We modified HA by the covalent grafting of hydrophobic pendant groups onto HA backbone. The structure of the resulting amphiphilic HA (AmphiHA) was a comb type copolymer (Figure 2).

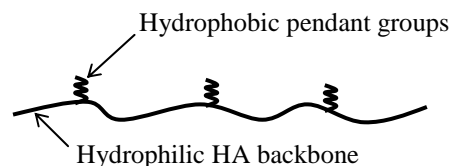


**Figure 2:** Schematic structure of amphiphilic hyaluronic acid

Surprisingly, the range of covalent grafting was not highly dependent on the reaction conditions. In addition the extent of grafting was limited by competitive reactions. In order to synthesize AmphiHA with higher degree of substitution (DS) we studied the influence of four reaction parameters on the DS of AmphiHA by implementing an experimental plan. We managed to uncover the most influential reaction parameters and this allowed the synthesis of AmphiHA with DS up to 44 % per disaccharide unit according to  $^1\text{H}$  NMR.

#### *Formulation and characterization of amphiphilic hyaluronic acid polymeric micelles*

As a step towards the formulation of nanoparticle-based encapsulating systems we studied the ability of AmphiHA to form polymeric micelles and encapsulate hydrophobic moieties in such simple molecular assemblies.

AmphiHA was mixed with the highly hydrophobic compound Nile Red. Besides being very hydrophobic Nile Red is also a potent and extensively used fluorophore for biological and physico-chemical purposes [7] (Figure 3).

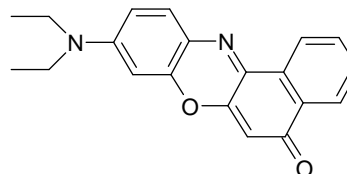


**Figure 3:** Molecular structure of Nile Red

Nile Red can indeed absorb light energy and restore it through a process called fluorescence (Figure 4).

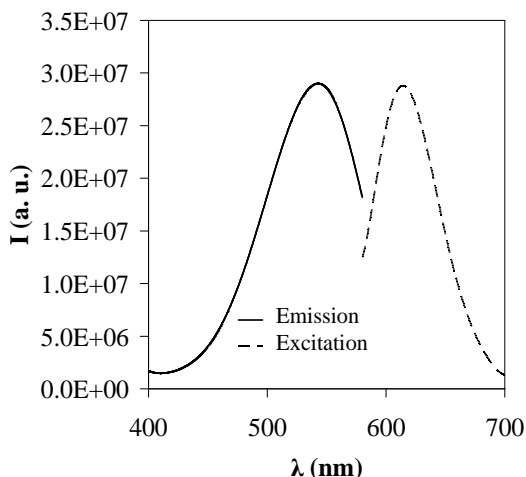


**Figure 4:** Emission and excitation spectra of Nile Red in a concentrated micellar solution of AmphiHA

The fluorescence behaviour of Nile Red is dependent of the polarity of its immediate environment. When the latter changes from polar to non-polar the intensity of maximum fluorescence emission of Nile Red ( $I_{\max}$ ) increases and the wavelength corresponding to the maximum emission ( $\lambda_{\max}$ ) drops significantly [8]. Figure 5 shows the fluorescence behaviour of Nile Red as a function of AmphiHA concentration.

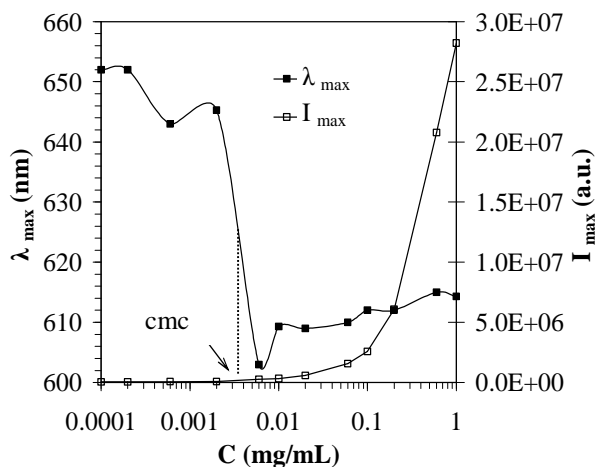


**Figure 5:** Fluorescence behaviour of Nile Red as a function of amphiphilic hyaluronic acid concentration

A positive value for  $I_{\max}$  was detected when  $C$  ranged between 0.002 and 0.006 mg/mL. At the same time  $\lambda_{\max}$  dropped from 652 to 602 nm (blue shift).  $I_{\max}$  then increased exponentially with increasing  $C$ . This meant that from  $C = 0.002$  mg/mL the immediate environment of Nile Red changed from a completely polar environment (zero fluorescence, high  $\lambda_{\max}$ ) to a more and more non-polar environment (increasing fluorescence lower  $\lambda_{\max}$ ). The only mechanism that could accommodate these observations was the transfer of Nile Red from the aqueous medium into the core of AmphiHA polymeric micelles upon their formation

between 0.002 and 0.006 mg/mL. Indeed the hydrophobic core of AmphiHA polymeric micelles presented a more favourable environment for Nile Red than the aqueous medium. We derived the critical micelle concentration (cmc) of AmphiHA at the inflection point of the  $\lambda_{\max}$  plot as shown by Coutinho et al. [9]. The cmc of AmphiHA was found at 0.0035 mg/mL.

We therefore demonstrated that not only AmphiHA exhibited some affinity for hydrophobic moieties but that it could also form spontaneous micellar structures and solubilize such compounds.

AmphiHA polymeric micelles were further characterized for their morphology, surface charge, mean size and size distribution.

Transmission electron microscopy snapshots of a concentrated micellar solution (Figure 6) showed that AmphiHA polymeric micelles had a spherical shape and were rather polydisperse.

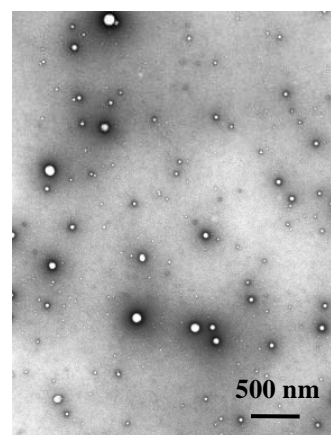


**Figure 6:** Morphology of amphiphilic hyaluronic acid polymeric micelles

Two main micelle populations with mean diameters of approximately 30 and 100 nm were identified by comparison of several different snapshots.

However the exact molecular structure of AmphiHA polymeric micelles could not be ascertained by this technique. Due to the affinity of hyaluronic acid for aqueous systems there is some probability that AmphiHA self-associates in the form of a ball of thread in which the hydrophobic pendant groups are localized inside the core of the ball. Such a structure is created due to the low affinity of the pendant groups for the aqueous bulk (Figure 7).



**Figure 7:** Schematic representation of a potential molecular structure for AmphiHA polymeric micelles

In Figure 7 the light-weighted lines represent HA backbone whereas the heavy-weighted lines represent hydrophobic pendant groups. Such polymeric micelles could be formed by one or more polymeric chains.

The surface charge of AmphiHA polymeric micelles in a concentrated micellar solution was negative with a zeta potential ( $\zeta$ ) value of approximately -25 mV. This was in good agreement with what could have been expected from a polyanion such as AmphiHA as native HA exhibits one carboxylate group per disaccharide unit at neutral pH (Figure 8).

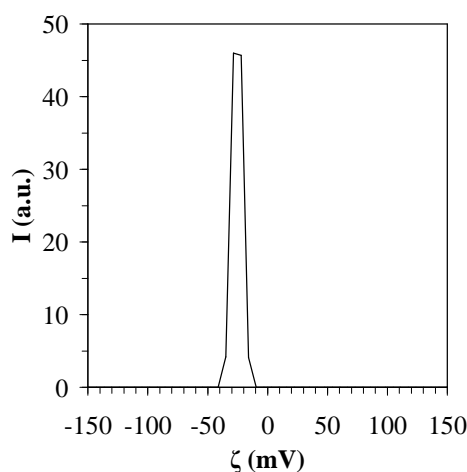


**Figure 8:** Zeta potential of amphiphilic hyaluronic acid polymeric micelles

Light scattering experiments were performed to ascertain the mean size and size distribution of AmphiHA polymeric micelles. In Figure 9 the diffusion coefficient of AmphiHA polymeric micelles ( $D$ ) was followed as a function of the scattering vector modulus ( $q$ ). Because  $q$  and the scattering angle ( $\theta$ ) are related to each other by the simple relation  $q = 4\pi/\lambda_0 \sin(\theta/2)$  ( $\lambda_0$  being the wavelength of light in vacuum) the experiment practically consisted in varying  $\theta$  and noting down corresponding  $D$  values.  $D$  remained a function of  $q$  ( $\theta$ ) over the whole range of  $q$  ( $\theta$ ) tested. In particular  $D$  decreased with decreasing  $q$  ( $\theta$ ). In other words no quantitative size distribution of AmphiHA polymeric micelles could be derived due to the instability of  $D$ .

We nevertheless computed a size distribution using data from the autocorrelation function at the smallest  $q$  ( $\theta$ ) available (i.e.  $19^\circ$ ). This value represents the condition for which the size distribution is representative of the broadest range of sizes detectable by the set-up used (Figure 10).

In Figure 10  $D_H$  and  $I$  represent the hydrodynamic diameter of AmphiHA polymeric micelles and the weighed intensity of light scattered by the micelles respectively. The size distribution clearly showed the coexistence of two micelle populations as confirmed by transmission electron microscopy (Figure 6). However their relative abundance and exact position on the  $D_H$  scale could not be ascertained. In brief our results most likely show that there exist two micelle populations

which exact size could not be determined and that a light scattering analysis using scattering angles below  $19^\circ$  was needed to quantitatively describe AmphiHA micellar systems.

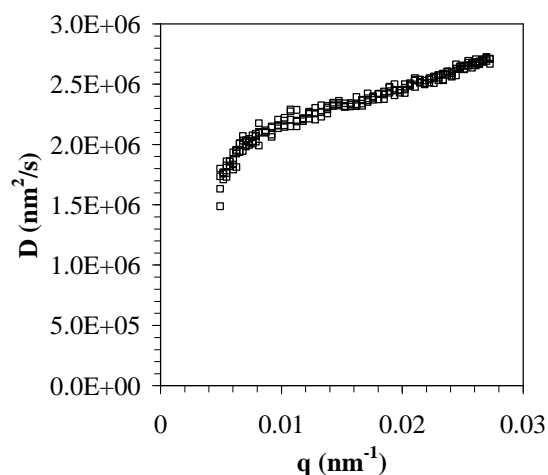


**Figure 9:** Diffusion coefficient as a function of the scattering vector modulus of amphiphilic hyaluronic acid polymeric micelles

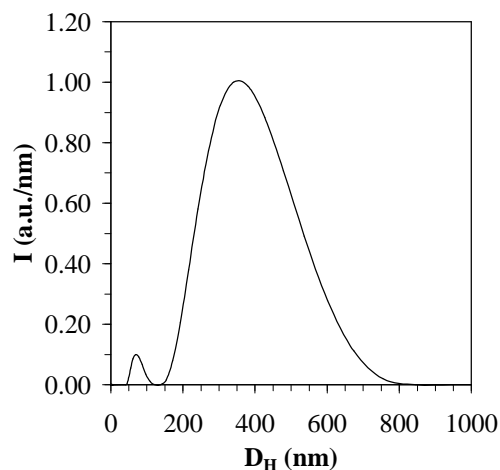


**Figure 10:** Size distribution of amphiphilic hyaluronic acid polymeric micelles

## Conclusions

Since the beginning of this PhD project in May 2005 we have extended the use of a proprietary technology to prepare amphiphilic hyaluronic acid (AmphiHA) with high degrees of substitution. We have shown that AmphiHA could spontaneously form polymeric micelles and solubilize hydrophobic moieties such as Nile Red into the core of its own nanoassemblies.

Whereas traditional methods for designing polymeric nanoparticles rely on random collisions in the medium, we are currently investigating innovative molecular techniques that could allow the design of novel AmphiHA nanoparticles with controlled features without using any organic solvents or surfactants.

In a later stage we will study skin penetration and release of ingredient-loaded AmphiHA nanoparticles.

We foresee that this will involve the use of standard robust skin models such as excised pig ear skin mounted on diffusion cells or modern synthetic skin substitutes developed to mimic skin tissues. The detection of percutaneous penetration will call for analytical techniques such as tape stripping combined with high pressure liquid chromatography and laser scanning confocal microscopy.

### Acknowledgements

This research programme is co-funded by Novozymes Biopolymer A/S and the Danish Ministry of Science, Technology and Innovation.

We express our gratitude to the Laboratory of Pharmaceutics and Biopharmaceutics, School of Pharmaceutical Sciences, University of Geneva (Professor R. Gurny and Assistant Professor F. Delie) for hosting Corinne Eenschooten in the period July-August 2006. During this period most of the experimental work on the formulation and characterization of HA-based polymeric micelles was performed.

We are finally obliged to the Bioimaging Platform (Doctor C. Bauer) and the Department of Inorganic, Analytical, and Applied Chemistry (Doctor A. Vaccaro), University of Geneva for the excellent transmission electron microscopy and multi-angle dynamic light scattering analysis respectively.

### References

1. R. Tammi, M. Tammi, <http://www.glycoforum.gr.jp/science/hyaluronan/HA04/HA04E.html>
2. <http://ezinearticles.com/?Popular-Applications-of-Hyaluronic-Acid&id=64214>
3. R. Alvarez-Román, A. Naik, Y.H. Kalia, R.H. Guy, H. Fessi, J. Controlled Release 99 (2004) 53-62
4. L.M. Benedetti, E.M. Topp, V.J. Stella, J. Controlled Release 13 (1990) 33-41
5. E. Ghezzi, L.M. Benedetti, M. Rochira, F. Biviano, L. Callegaro, Int. J. Pharm. 87 (1992) 21-29
6. M. Rochira, M.R. Miglietta, J.L. Richardson, L. Ferrari, M. Beccaro, L.M. Benedetti, Int. J. Pharm. 144 (1996) 19-26
7. N.C. Maiti, M.M.G. Krishna, P.J. Britto, N. Periasamy, J. Phys. Chem. B 101 (1997) 11051-11060
8. G.B. Dutt, S. Doriswami, J. Chem. Phys. 96 (4) (1992) 2475-2491
9. P.J.G. Coutinho, E.M.S. Castanheira, C. Rei, E.C.D. Real Oliveira, J. Phys. Chem. B 106 (2002) 12841-12846
2. C. Eenschooten, R. Alvarez Roman, F. Guillaumie-Longin, R. Guy, K. Schwach-Abdellaoui, E. Sublet, Towards an understanding of the Percutaneous Penetration of Hyaluronic Acid, a poster presented at the conference Perspectives in Percutaneous Penetration 2006, La Grande Motte, France, 2006
3. C. Eenschooten, F. Guillaumie-Longin, R. Gurny, G.M. Kontogeorgis, K. Schwach-Abdellaoui, E.H. Stenby, Development and Formulation of Hyaluronic Acid-based Nanoparticles for Cosmetic Applications, poster presented at the Nano•DTU and Nano-Science Centre Kick-off meeting, Hoersholm, Denmark, 2006

### List of Publications

1. C. Eenschooten, F. Delie, F. Guillaumie-Longin, R. Gurny, G.M. Kontogeorgis, K. Schwach-Abdellaoui, E.H. Stenby, Development of Colloidal Carrier from Modified Hyaluronic Acid, a poster presented at the Skin and Formulation Second Symposium, Versailles, France, 2006





## Runi Ditlev Egholm

Phone: +45 4525 6825  
Fax: +45 4588 2161  
E-mail: rde@kt.dtu.dk  
WWW: <http://www.dtu.dk/Centre/DPC>  
Supervisor: Peter Szabo

Ph.D. Study  
Started: July 2004  
To be completed: July 2007

## Modelling and Simulation of Two-Phase Fluid Systems

### Abstract

In order to investigate the mechanisms behind drop deformation and break-up in simple and complicated flow fields a model which combines the methods of Finite Elements (FEM) and Volume of Fluid (VOF) has been developed and implemented. Single drop simulations carried out in simple flow fields are used as benchmark problems in order to validate the model. Although rigorous simulations have not yet been carried out preliminary results indicate correct behaviour of interface deformation and break-up at least on a qualitative level.

### Introduction

Emulsions are dispersed two-phase systems which typically enter as process intermediates or as the final product in a number of industries. Examples of such products are foods, pharmaceuticals, cosmetics and various polymeric materials. The properties of emulsion based products are highly dependent on the microscopic morphology, i.e. mean drop size and drop size distribution. Understanding the dispersion process is therefore a key step in order to be able to control the intermediate and final properties of an emulsion based product. Typical theoretical and experimental studies on emulsion behaviour when subjected to shear and elongational stresses have been carried out using flow cells with simple and very well defined flow fields. In experimental investigations drop deformation and break-up is normally analyzed by monitoring a single drop using a still or video camera. Investigations of this type were first carried out in the pioneering work of Taylor in the 30's [1,2]. Taylor carried out experimental studies on drop deformation in flow cells with either pure shear flow (parallel band apparatus) or pure elongational flow (four roll mill). Taylor was also able to predict the steady state deformation in a given flow field when the surface tension (constant) and the viscosity of the dispersed and continuous phases were known. However, his analysis is only valid in the small deformation region. Since the work of Taylor improvements in imaging technology (e.g. digital cameras) and controller systems has led to great improvements in the experimental techniques as demonstrated in [3] where a fully computer controlled

shear flow cell is described. Various methods for obtaining narrow drop size distributions can be found in the literature – e.g. in ref. [4] very close to mono-disperse drops are obtained using a double capillary setup. For general treatments on experimental and theoretical work carried out on drop deformation and break-up in various flow fields reviews are given e.g. by Rallison [5] and recently by Windhab et al. [6].

In order to investigate the deformation of single drops on a theoretical level at large deformations and beyond the point of break-up large scale numerical simulations are necessary. The numerical methods used to simulate the drop behaviour need to be able to handle flows with deforming interfaces and should also be able to handle merging and break-up of the interfaces. The most popular methods are the Boundary Integral Method (BIM) and Volume of Fluid (VOF) method. In the BIM method the flow field is calculated using a flow solver, e.g. a finite difference, finite volume or finite element solver and then the information from the solver is passed along to the BIM part of the code which handles the interface. This method has been used with success by several authors, e.g. [7,8]. The VOF method is an interface tracking method, where different phases are identified by a colour function. The deformation of the two phases relative to each other is carried out by advecting the colour function in the flow field. As was the case for the BIM method the flow field is calculated using a flow solver. However in this case the VOF algorithm is coupled to the flow solver through the interfacial tension and the densities and viscosities of

the disperse and continuous phase respectively. This method is well suited for handling break-up and merging of drops and has been applied with success in e.g. [9,10].

The main objective of this ph.d. project is to implement a micro-mechanical model in order to make it possible to simulate drop break-up and merging in complicated flow fields and geometries. For this purpose we have chosen to base the model on the VOF method coupled with a Finite Element method.

### The VOF method

In order to track the interface of a two-fluid system the VOF method utilizes a so-called colour function  $F$ . At a given point in space the value of the colour function corresponds to the volume fraction of the disperse phase at that point. The interface itself is assumed to have a finite thickness such that  $F$  varies from 1 to 0 over a distance comparable with some characteristic discretization length. The function  $F$  is thus defined as

$$F = \begin{cases} 1, & \text{inside disperse phase} \\ 0, & \text{outside disperse phase} \end{cases}$$

$0 < F < 1, \text{inside interface}$

The orientation of the interface is characterized by the surface normal which can be estimated as the gradient of the colour function, i.e.

$$\mathbf{n} = \nabla F \quad (1)$$

where  $\nabla F$  is calculated using a discrete  $\nabla$  operator. On the discrete level the domain is divided into a number of rectangular grid cells in which the volume fraction of the disperse phase determines the value of  $F$ .

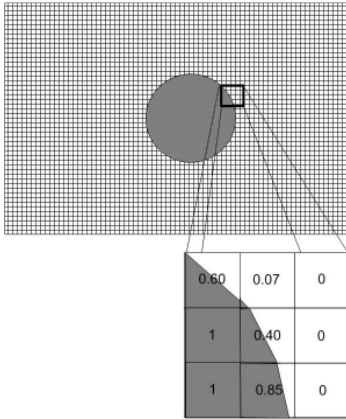


**Figure 1:** Sketch of a 2D colour field showing how the interface can be approximated as line segments.

The interface can be approximately reconstructed in each interface cell using planes (lines in 2D). The orientation of the planes is given by  $\mathbf{n}$  and the position by the value of  $F$ , cf. Figure 1. It is also necessary to be able to transport the colour function in a given velocity field. This is done by solving the convection equation:

$$\frac{\partial F}{\partial t} + \nabla F \cdot \mathbf{v} = 0 \quad (2)$$

In order to avoid numerical diffusion when solving Eq. 2 the piecewise linear reconstruction of the interface is utilized using the so-called Piecewise Linear Interface Calculation (PLIC) method, e.g. [11].

### The model

The flow solver is based on a finite element discretization of the momentum balance and the continuity equation. We assume pure Stokes flow thus the momentum balance is given by

$$\nabla \cdot \boldsymbol{\pi} + \rho \mathbf{g} = \mathbf{0} \quad (3)$$

where  $\rho$  is the density,  $\mathbf{g}$  is the gravitational acceleration and  $\boldsymbol{\pi}$  is the total stress tensor given by

$$\boldsymbol{\pi} = \mu \dot{\boldsymbol{\gamma}} - p \mathbf{I}$$

Here  $\mu$  is the viscosity,  $\dot{\boldsymbol{\gamma}}$  is the rate of strain tensor,  $p$  is the pressure and  $\mathbf{I}$  is the unit tensor.

Since we are dealing with a two-phase system it is necessary to include interfacial tension in the model. However, as described above the interface is not sharply defined, i.e. the interface has a finite thickness. In order to overcome this problem the interfacial tension is incorporated as a body force  $\mathbf{F}_s$  rather than directly onto the interface. Two models are available for this purpose the Continuous Surface Force (CSF) model [12]:

$$\mathbf{F}_s = \sigma \kappa \mathbf{n} \delta_s \quad (4)$$

and the Continuous Surface Stress (CSS) model [13]:

$$\mathbf{F}_s = -\nabla \cdot \mathbf{T} = \nabla \cdot (\sigma (\mathbf{I} - \mathbf{nn})) \delta_s \quad (5)$$

In Eq. 4 and 5  $\sigma$  is the interfacial tension coefficient (assumed constant),  $\kappa$  is the interface curvature,  $\mathbf{n}$  is the interface unit normal and  $\delta_s$  is a delta function defined on the interface. Due to its conservative form we have chosen to use the CSS model which, as will be evident, results in a nice finite element formulation. Mass conservation is applied by requiring continuity, i.e.

$$\nabla \cdot \mathbf{v} = 0 \quad (6)$$

here  $\mathbf{v}$  is the velocity field.

### The finite element formulation

The finite element formulation is obtained by multiplying the momentum balance (Eq. 3) with a trial function  $\varphi$  and integrating over the domain of interest  $\Omega$ :

$$\int_{\Omega} \varphi (\nabla \cdot \boldsymbol{\pi} + \rho \mathbf{g}) d\Omega = \mathbf{0} \quad (7)$$

Rewriting Equation 7 using partial integration and the Gauss-Ostrogradskii divergence theorem leads to

$$\int_S \varphi(\boldsymbol{\pi}_1 - \boldsymbol{\pi}_2) \cdot \mathbf{n} dS - \int_{\Omega} \nabla \varphi \cdot \boldsymbol{\pi} d\Omega + \int_{\Omega} \rho \mathbf{g} d\Omega = \mathbf{0} \quad (8)$$

In Equation 8 the stress jump  $\mathbf{n} \cdot (\boldsymbol{\pi}_1 - \boldsymbol{\pi}_2)$  across the interface can be written as

$$(\boldsymbol{\pi}_1 - \boldsymbol{\pi}_2) \cdot \mathbf{n} = \sigma \boldsymbol{\kappa} \mathbf{n}$$

which leads to

$$\begin{aligned} \int_S \varphi(\boldsymbol{\pi}_1 - \boldsymbol{\pi}_2) \cdot \mathbf{n} dS &= \int_{\Omega} \varphi(\boldsymbol{\pi}_1 - \boldsymbol{\pi}_2) \cdot \mathbf{n} \delta_s d\Omega = \\ \int_{\Omega} \varphi \sigma \boldsymbol{\kappa} \delta_s d\Omega &= - \int_{\Omega} \varphi \nabla \cdot \mathbf{T} d\Omega \end{aligned} \quad (9)$$

It can be shown that the last term in Equation 9 can be rewritten into

$$- \int_{\Omega} \varphi \nabla \cdot \mathbf{T} d\Omega = - \int_{\Omega} \nabla \varphi \cdot \mathbf{T} d\Omega \quad (10)$$

The final model is then obtained by substituting the surface integral in Equation 8 with Equation 10. Furthermore the continuity equation is rewritten into its finite element form.

Momentum:

$$\int_{\Omega} \nabla \varphi \cdot (\boldsymbol{\pi} - \mathbf{T}) d\Omega + \int_{\Omega} \rho \mathbf{g} d\Omega = \mathbf{0} \quad (11)$$

Continuity:

$$\int_{\Omega} \varphi^p \nabla \cdot \mathbf{v} d\Omega = 0 \quad (12)$$

In Eq. 12  $\varphi^p$  is a trial function associated with the pressure field.

### Discretization

The finite element discretization of Equation 11 and 12 is based on

- Isoparametric hexahedral elements
- Quadratic velocities
- Discontinuous constant pressures

Using constant pressures ensures that the continuity equation is fulfilled on the element level which is an advantage when advecting the colour function. Since we want to be able to handle arbitrary domain geometries the VOF calculations are carried out on the rectangular parent finite elements using finite element shape functions.

### Results and discussion

Due to the vast amount of available experimental and theoretical work carried out on single drop deformation

in pure shear flow fields we use the shear flow cell as a test problem for our model. A measure of the strength of the shear flow field relative to forces arising from the interfacial tension is the capillary number  $Ca$  defined as

$$Ca = \frac{r_0 |\dot{\gamma}| \mu_c}{\sigma}$$

where  $r_0$  is the initial radius of the drop,  $|\dot{\gamma}|$  is the shear rate,  $\mu_c$  is the viscosity of the continuous phase and  $\sigma$  is the interfacial tension.

Simulations of drop deformation and break-up are shown in Figure 2 and 3. The simulation in Figure 2 is carried out using parameters corresponding to a capillary number of 0.38 while the simulation in Figure 3 corresponds to  $Ca=0.5$ . All simulations are carried out using rectangular finite elements with side length  $h=0.05$ . Due to symmetry in the  $z$ -direction only half of the domain needs to be considered in the simulations. From Figure 2 it is seen that as time proceeds the drop breaks up into two almost equally sized drops with a small droplet in the centre. In Figure 3 the drop is severely elongated before it breaks up into four equally sized drops with droplets in between.

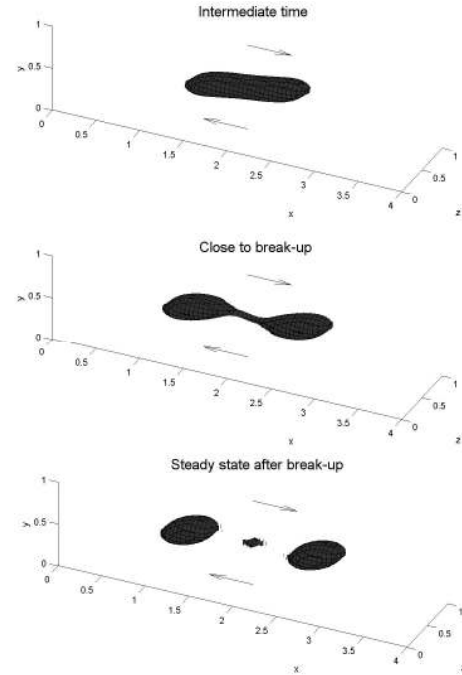


**Figure 2:** Simulation of a shear experiment with  $Ca=0.38$ . Mesh with  $60 \times 20 \times 10$  finite elements was used (~150000 unknowns).

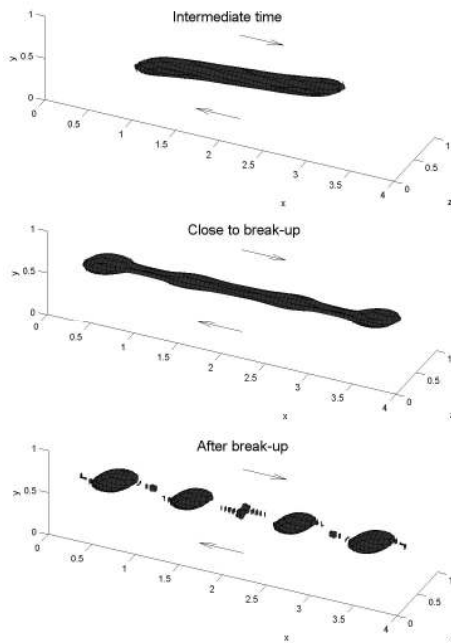


**Figure 3:** Simulation of a shear experiment with  $Ca=0.50$ . Mesh with  $80 \times 20 \times 10$  finite elements was used ( $\sim 190000$  unknowns).

This behaviour is in agreement with the  $Ca$  number used since a larger  $Ca$  corresponds to larger shear stresses relative to interfacial tension and thus a larger drop deformation. Figure 4 shows the drops after break-up for  $Ca$  ranging from 0.38 to 0.50. Here it is seen how the final drop size distribution is determined by the  $Ca$  number. The figure also indicates how such simulations can be useful in determining drop size distributions in a given flow field.

In the simulations shown the width and height ( $z$ - and  $y$ -direction) of the domain are small compared to the drop radius ( $L_z=L_y=1$  and  $r_0=0.25$ ) which means that wall effects are present. The results are therefore not very applicable for comparison between simulations and experiments because in experiments wall effects are usually negligible. In order to carry out more systematic numerical tests of the model, simulations carried out in a domain with  $L_z$  and  $L_y$  much larger than  $r_0$  are necessary. Furthermore the simulations shown above were carried out using a relatively coarse mesh which means that the interface is not very smooth. In order to overcome these problems a non-structured finite element mesh will be applied in order to concentrate elements in the vicinity of the drop. Furthermore the colour function can be defined on a different and finer mesh than the finite element mesh. However, this requires interpolation of the velocity field from the finite element mesh onto the VOF mesh which results in loss of element level mass conservation. This gives rise to some difficulties when solving Equation 2. We are addressing this problem at the moment.

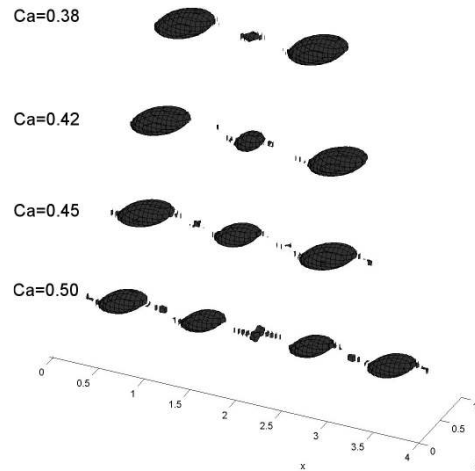


**Figure 4:** Drop size distributions from 4 different shear flow cell simulations.

### Conclusions

The 3D simulations carried out indicate that the implemented model can be used for simulating the morphological changes associated with interface deformation and break-up in two-phase flows. However, in order to verify the model on a quantitative level simulations using a domain where wall effects can be neglected are necessary. This requires a non-structured mesh and/or more computational effort. In order to get a better description of the interface a mesh different from the finite element mesh will be used for the colour function.

### Acknowledgements

This project is financed by the Danish Technical Research council (grant. no. 26-03-0282).

### References

1. G. I. Taylor, Proc. R. Soc. A 138 (1932) 41-48
2. G. I. Taylor, Proc. R. Soc. A 146 (1934) 501-523
3. B. H. Birkhofer, J. -C. Eischen, D. Megias-Alguacil, P. Fischer and E. J. Windhab, I&EC Research, 44 (2005) 6999-7009
4. B. Walther, C. Cramer, A. Tiemeyer, L. Hamberg, P. Fischer, E. J. Windhab, A. M. Hermansson, J. Colloid and Interface Science 286 (2005) 378-386
5. J. M. Rallison, Annu. rev. Fluid. Mech. 16 (1984) 45
6. E. J. Windhab, M. Dressler, K. Feigl, P. Fischer, D. Megias-Alguacil, Chemical Engineering Science 60 (2005) 2101-2113
7. M. Loewenberg, E. J. Hinc, J. Fluid. Mech. 321 (1996) 395
8. C. Pozrikidis, J. Eng. Math. 41 (2001) 237
9. Y. Renardy, M. Renardy, J. Comp. Phys. 183 (2002) 400
10. I Ginzburg, G. Wittum, J. Comp. Phys. 166 (2001) 302
11. W. J. Rider, D. B. Kothe, J. Comp. Phys. 141 (1998) 112-152
12. J. U. Brackbill, D. B. Kothe, C. Zemach, J. Comp. Phys. 100 (1992) 335-354
13. B. Lafaurie, C. Nardone, R. Scardovelli, S. Zaleski, G. Zanetti, J. Comp. Phys. 113 (1994) 134-147



## **Tobias Dokkedal Elmø**

Phone: +45 4525 2936  
Fax: +45 4525 2399  
E-mail: tde@kt.dtu.dk  
WWW: <http://www.aerosol.kt.dtu.dk>  
Supervisors: Hans Livbjerg  
Tue Johannessen

### **Ph.D. Study**

Started: March 2005  
To be completed: February 2008

## **Production of Ceramic Catalytic Membranes by Deposition of Nano-Particles**

### **Abstract**

The deposition of nano-particles (catalytic or non-catalytic) on top of a porous substrate tube is a technique developed by the Aerosol Laboratory [1,2] and offers a simple one-step method for preparation of membranes, compared to the more complex traditional sol-gel technique. During deposition (which is done at constant pressure) the flow through the membrane is measured and the accumulated flow is used in the calculation of the deposited mass.

The topic of enhancing the stability and adherence of the membranes the particle deposition is still under investigation, however methods of deep bed filtration by particle growth seems to help by trapping the particles irreversibly. As a new way of characterizing the generated membrane a permporometry apparatus has been constructed and allows for the determination of the pore-size/volume distribution. Modelling work has been applied successfully to describe the various mechanisms during the nano-particle filtration.

### **Introduction**

Porous ceramic membranes can be used for several purposes which includes particle filtration, liquid-gas/liquid separation or gas-separation. The ceramic material assures that the membranes are resistant to high temperatures whereas porous membranes based on polymeric materials are not. Futhermore, ceramic membranes also have higher chemical and mechanical stability than the polymeric membranes [3].

Apart from acting as a separating layer, where the difference in mass-transfer flux results in the separation of e.g. two gasses, the ceramic membranes can also be produced to include a supported catalyst. There are two types of such composite membranes: the porous catalytic membrane and the dense catalytic membrane. In the porous catalytic membrane, the membrane works as both a mass-transfer resistance and as a contactor between the reactant and the catalyst. This type of configuration can for instance be used to allow, what would otherwise be an explosive reaction to occur safely as the reactants are brought to the reaction-zone, due to the mass-transfer hindrance in the membrane. Another clear benefit is when the products have a higher permeation flux through the membrane, which can make equilibrium controlled reactions run at an even higher rate, due to Le Chatelier's principle [4].

In the dense catalytic membrane a thin layer of usually metallic coating (e.g. Ag and Pd) is applied on

top of a porous substrate, but also solid-oxide ionic conducting species such as modified zirconia or perovskites can be used. The dense layer is extremely selective in that it only allows for the permeation of a single species. The advantage of this is extremely selective membranes, but with a low permeation flux because solid-state diffusion is much lower than the Knudsen-type diffusion, which is usually the predominant type of mass-transfer in a the porous membrane [5].

### **Project goals**

The scopes of this PhD project are mentioned here:

1. Produce and characterize stabile (temperature, chemical and mechanically resistant) membranes with a well-defined thichkness and controllable pore-structure using the existing flame-pyrolysis equipment developed at the Aerosol Laboratory
2. Generate porous and dense catalytically active membranes by using suitable methods (electroless deposition of Pd, co-combustion of precious metal-precursors and Mg/Al-precursors etc.)
3. Test and compare these membranes against those mentioned in the litterature

### **Generation of nano-particles using flame-pyrolysis**

Using the flame-pyrolysis equipment developed at the Aerosol Laboratory it has previously been shown that

metal-oxide and precious metal-oxide particles, with a controllable size-distribution, can be produced [6]. Lately also composite oxides with an accurate stoichiometry such as  $MgAl_2O_4$  spinel has been produced [2]. The equipment is shown schematically in Figure 1

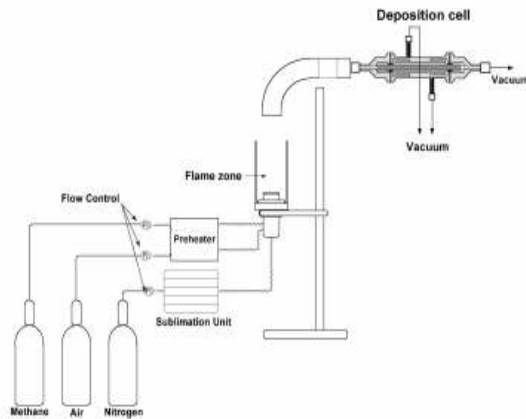


**Figure 1:** Nano-particle formation and deposition apparatus

A gas-stream of inert nitrogen is led through a heated saturator unit, where a metal-organic compound, in our case Metal-acetylacetonate (MeAcAc) is sublimated until the gas is saturated. The carrier gas is then led to a mixing chamber, where it is mixed with the fuel for the flame (air and methane/hydrogen). A flame arrester accelerates the gas and assures that the flame-front is stable. In the flame the organic component (AcAc) is burned off and the metal part is oxidized. The extreme super-saturation results in the nucleation metal-oxide monomers and the formation particles. By adjusting the flame-temperature, saturator temperature and the carrier gas flow, one can control the particle size-distribution. The filtration experiments can now be carried out under constant pressure and the flow through the membrane is measured on-line during the entire filtration, which allows for the calculation of the deposited mass (since the weight increase is too low to measure directly).

### Membrane formation

The Aerosol Laboratory has developed a simple method, where the particles generated in the flame are filtered off onto a porous substrate tube [1]. The particles form an extremely porous "filter-cake" ( $\approx 98\%$  porosity) which constitutes a new membrane layer, with a much smaller pore size (nm) than the initial substrate pore-size ( $\mu m$ ).

The deposition mechanism, which is responsible for the highly porous deposits, is by brownian motions. One of the major concerns with this method is the adhesion of the deposited particles on the substrate tube. Several tests have been carried out at high temperatures in order to improve adhesion, however the high porosity seems to induce some thermal mismatch which prevents

complete adhesion as the layer flakes or delaminates completely when exposed liquids in particular.

Tests have also shown that deposition of an internal filter-cake (by deep bed filtration) provides much more stable composites. To do this one must first change the mechanism of deposition, which is loosely done by increasing the particle size several orders of magnitude (however without sacrificing the primary particle size).

### Membrane characterization

Because the deposited layer is very thin, the deposited pore-volume is very low. This means that traditional methods of characterization (Hg-porometry, BET measurement etc.) can in principle not be used. We have constructed an apparatus based on a method known as permoporometry. The flux of oxygen is measured as a function of the open pore-size, which is controlled by a condensing a vapour such as cyclohexane. The relative pressure of cyclohexane ( $S$ ) therefore determines the maximum size of the open pores. This size is directly expressed through the Kelvin-equation:

$$\ln S = - \frac{2\sigma}{r_k \rho_m RT}$$

where  $\sigma$  is the surface tension [N/m],  $\rho_m$  is the molar density [mole/m<sup>3</sup>] and  $RT$  is the product of the temperature and the gas-constant [J/mole]. This apparatus is still under development.

The permoporometry apparatus has been tested and verified on membranes with a known pore-size distribution. Figure 2 shows the comparison between an  $N_2$  adsorption/desorption measurement (here made possible because of the amount of membrane material was sufficient) and the home-built permoporometry apparatus.

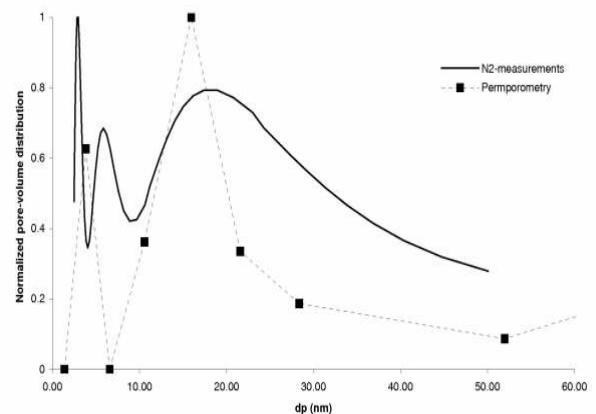


**Figure 2:** Permoporometry vs.  $N_2$  adsorption/desorption determined pore-volume distribution (normalized for easier comparison)

One should also note that as the industry-built  $N_2$  apparatus takes several hours to complete its measurements, the home-built permoporometry apparatus only takes approximately 10 minutes per measurement point, which yields a much smaller total measurement time.

### Mathematical modelling

The deposition of particles starts off by clogging the substrate pores then proceeds into the building of a filter-cake. Models have been tested out in which the deposition only occurs by filter-cake formation excluding the clogging, however these have not been able to account for the rapid decrease in relative flow, that occurs right after the onset of deposition. The two models that have been proposed are the "equilibrium pressure-drop model" (Eqpdm) [7] and the "shrinking-pore model". In the equilibrium pressure-drop model, the clogging is assumed to take place randomly and only on non-clogged pores. The flow ( $Q_t$ ) is assumed to consist of two separate contributions: the flow through the non-clogged structure ( $Q_{open}$ ) and the flow through the clogged structure ( $Q_c$ ).

The governing equations are:

$$\underbrace{\Delta P_f}_{\text{Total pressure drop}} = \underbrace{\Delta P_s}_{\text{Non clogged pores}} + \underbrace{\Delta P_c}_{\text{Clogged pores}} \quad (1)$$

$$\underbrace{A_c}_{\text{Area of clogged pores}} = \frac{C_0 v_{part} \int_{t=0}^t Q_{open} dt'}{\varepsilon_s (1 - \varepsilon_c) \delta_c} \quad (2)$$

where  $C_0 v_{part}$  is the particle volume fraction contained in the gas,  $\varepsilon_s$  is the substrate porosity,  $\varepsilon_c$  is the porosity of the deposit in the clogged pores and  $\delta_c$  is the depth of clogging.

$$\Delta P_c = \frac{P_0 \delta_c}{\varepsilon_s A_c D_{Kn,c}} Q_c \quad (3)$$

where  $D_{Kn,c}$  is the Knudsen diffusion coefficient through the clogged pores and  $P_0$  is the inlet pressure.

$$\Delta P_s = \Delta P_f - P_0 \phi_s - P_0 \sqrt{\left( \phi_s - \frac{\Delta P_f}{P_0} \right)^2 - \frac{X_s}{A_c} Q_c} \quad (4)$$

where  $\phi_s$  and  $X_s$  are constants relating to the properties of the substrate (see [7]). The last equation required to solve the 5 unknowns ( $\Delta P_s$ ,  $\Delta P_c$ ,  $A_c$ ,  $Q_c$ ,  $Q_{open}$ ) is:

$$\Delta P_f = P_0 \phi_s - P_0 \sqrt{\phi_s^2 + \frac{X_s}{A_t - A_c} Q_{open}} \quad (5)$$

where  $A_t$  is the total substrate surface area. Figure 3 shows a fit using the Eqpdm model to a real deposition experiment.

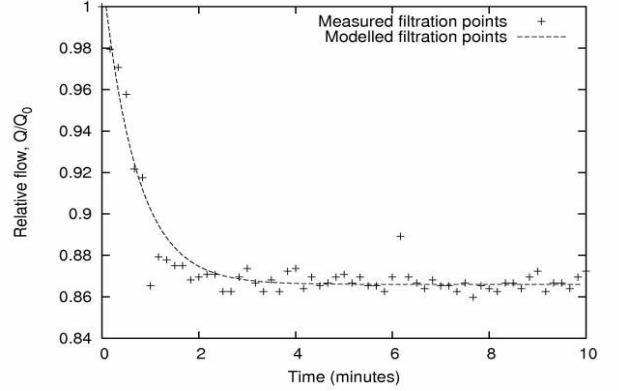


**Figure 3:** Results of the Eqpdm fit. Experiment carried out at 363°C with a particle production rate of 18.7 mg/h ( $\text{MgAl}_2\text{O}_4$  spinel). Fitting parameters are:  $d_p = 16$  nm (pore-diameter of the clogged structure),  $\varepsilon_c = 0.9$  and  $\delta_c = 0.65$   $\mu\text{m}$

### Future work

Future work still includes improving membrane/deposit stability toward liquids, deposition of catalytically active nano-particles and testing of the entire system in an membrane-reactor-separator unit. Emphasis is, however on improving adhesion of the particles. In January to April next year a visit to ETH in Zürich will hopefully provide some much needed results and answers on this issue.

### Acknowledgements

The PhD study is completely sponsored by the Technical University of Denmark

### References

1. S.K. Andersen *et al.*, Journal of nano-particle research, 4:405-416, 2002
2. M. Mosleh, *Preparation of Micro Porous Ceramic Membranes by Flame generated Aerosol Nano-Particles*, PhD thesis, Technical University of Denmark, 2003
3. M. Mulder, *Basic principles of membrane technology*, Kluwer Academic Publishers, 2<sup>nd</sup> edition, 1996
4. J. Coronas *et al.*, Catalysis Today, 51:377-389, 1999
5. J.G.S. Marcano and T.T. Tsotsis, *Catalytic membranes and Membrane reactors*, Wiley-VCH, 1<sup>st</sup> edition, 2002
6. T. Johannessen, *Synthesis of Nano-particles in Flames*, PhD thesis, Technical University of Denmark, 1999
7. J. Johansen, *Synthesis of ceramic membranes by deposition of aerosol particles*, PhD thesis, Technical University of Denmark, 2006





**Ann Dorrit Enevoldsen**

Phone: +45 4525 2955  
Fax: +45 4593 2906  
E-mail: ade@kt.dtu.dk  
WWW: <http://www.capec.kt.dtu.dk>  
Supervisors: Gunnar Jonsson  
Ernst B. Hansen, Novozymes A/S

**Industrial Ph.D.**

Started: April 2004  
To be completed: March 2007

## Enzyme Recovery by Crossflow Electro-Ultrafiltration

### Abstract

To reduce the problems with fouling and concentration polarization during crossflow ultrafiltration of industrial enzyme solutions an electric field is applied across the membrane. A 3-7 times flux increase is observed at an electric field strength of 1600 V/m. The influence of crossflow velocity and transmembrane pressure are also studied together with the conductivity of the enzyme solutions.

### Introduction

Membrane processes are widely used in the biochemical industry for separation and concentration of proteins. Flux decline due to fouling and concentration polarization are however major problems in both micro and ultrafiltration. Usually the flux has declined a factor of 10 from its initial value. Large membrane areas are therefore needed to get the required production capacity. During production it is also necessary to use a high crossflow to enhance the shear rate at the membrane surface and thereby reduce concentration polarization. To maintain a high crossflow large pumping capacities are required; which uses a large amount of energy. Application of an external dc electric force field across the membrane is another promising method to reduce fouling and concentration polarization. A schematic drawing of a crossflow electro-ultrafiltration (EUF) module is shown on Figure 1. The electric field imposes an electrophoretic effect on the charged molecules dragging them away from the membrane surface. This reduces the thickness of the concentration polarization layer and the flux increases. The solvent flow through the membrane is also increased by the electroosmotic effect, but is considered secondary.

The technique has many applications. It has been successfully used on biomolecules [1], proteins [2], cleaning of wastewater [3], inorganic metallic compounds [4] and water soluble polymers [5].

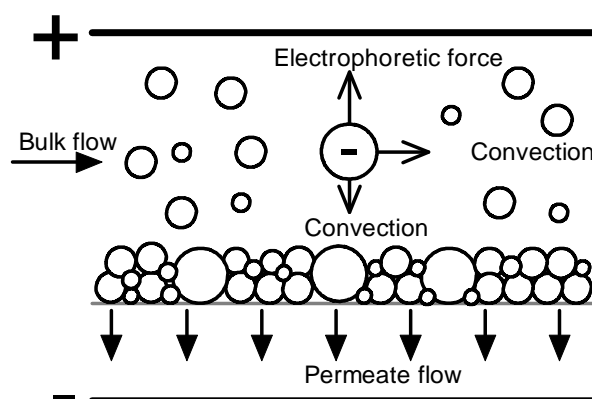


**Figure 1:** Schematic drawing of crossflow EUF. Inspired by reference [4].

### Specific Objectives

In this work crossflow electro-ultrafiltration (EUF) is carried out with industrial enzyme solutions from Novozymes A/S, Denmark. The aim is to investigate the use of EUF in industrial production. Especially if it is possible to replace the need for a high crossflow with an electric field.

## Theory

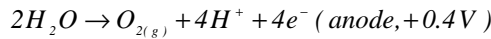
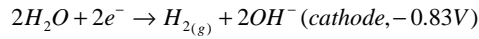
The flux improvement depends on the electrophoretic velocity  $v_e$ :

$$v_e = v_e E \quad 1$$

where  $E$  is the electric field strength and  $v_e$  the electrophoretic mobility of the enzyme, which depends on the  $\zeta$ -potential of the enzyme and the viscosity of the solution  $\eta$ :

$$v_e = \frac{2\varepsilon_0\varepsilon\zeta}{3\eta} \quad 2$$

where  $\varepsilon_0$  and  $\varepsilon$  are the permittivity in vacuum and the dielectric constant of the solution respectively. One of the side effects in EUF is the electrochemical reactions occurring at the electrodes. A typical reaction is splitting of water, where hydrogen gas together with hydroxide ions are formed at the cathode; and oxygen gas and hydrogen ions are formed at the anode.



the rate of the electrochemical reactions depend on the current intensity [6].

## Electro-ultrafiltration

The crossflow EUF rig is based on a commercial electro-dialysis module. To prevent direct contact between the enzymes and the electrodes the EUF cell is configured according to Figure 2.

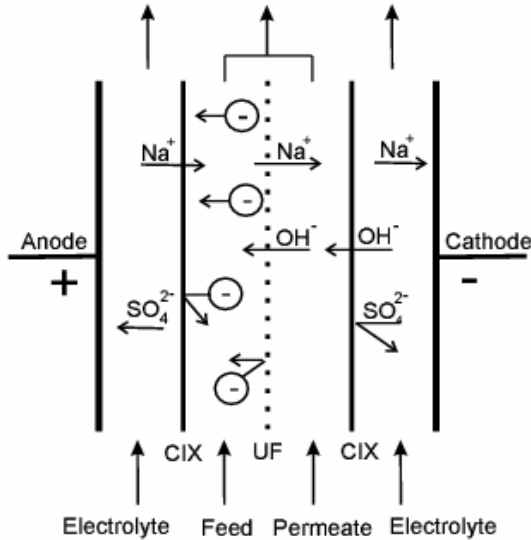


**Figure 2:** Electro-ultrafiltration cell.

The cell consists of four chambers separated by an UF membrane surrounded by two cation exchange membranes. The cation exchange membranes separate the electrolyte solutions from the feed and permeate solutions. Flow spacers are used to enable the different streams. The experiments are operated by full recycle

by returning the concentrate back to the feed container. The electrolyte consists of 0.1 M  $Na_2SO_4$ . The UF membrane is a 10 kDa surface-modified PVDF ETNA10PP membrane from Alfa Laval; and the cation exchange membrane is a RELAX-CMH membrane from Mega (Czech Republic). The membrane area is  $10 \times 10$  cm<sup>2</sup>. The enzymes used are two amylases: Amylase-F and amylase-S. The isoelectric point is 3.5 for both. The solutions were diafiltrated before use. The pH in the experiments is adjusted with NaOH to 5.5 for the amylase-S, and 7.0 for the amylase-F.

The experiments are carried out by increasing the voltage stepwise from 0 V to 50 V when steady state is reached as shown on Figure 3. After reaching 50 V the voltage is decreased in two steps back to 0 V. Figure 3 also shows that the system is reversible, since the flux returns to the same level when the electric field is decreased. However the flux is at a lower level when returning to 40 V; this is due to a small increase in the conductivity during the experiment.

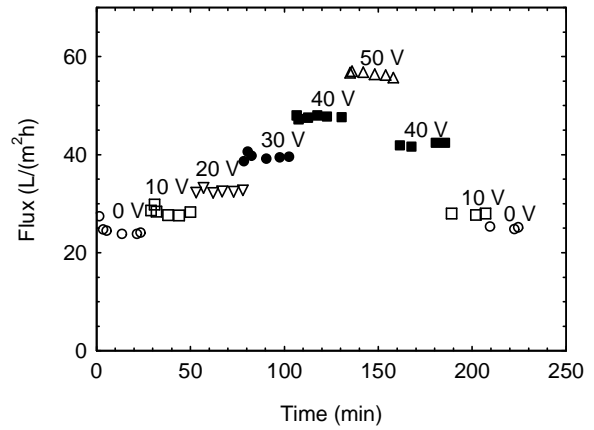


**Figure 3:** Stepwise increase in the electric field for a 24 g/L amylase-S solution.

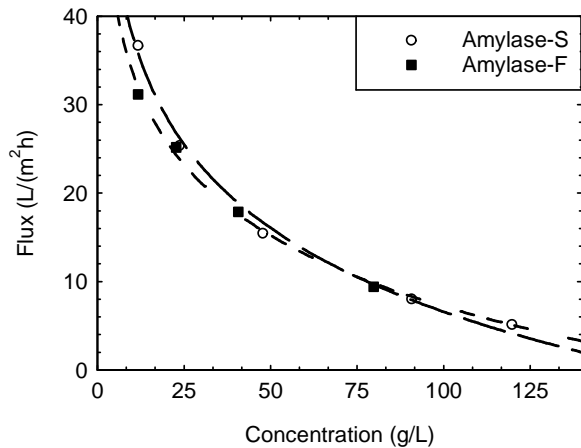
In the following section the results will be shown as a function of the  $E$ , which is defined as voltage  $U$  per distance (channel height  $h$ ). Since the module contains several chambers with different conductivities it is not possible to use the applied voltage directly. It is therefore necessary to calculate  $E$ , which is done by:

$$E = \frac{I}{\kappa_{feed} A} \quad 3$$

where  $\kappa_{feed}$  is the conductivity of the feed,  $I$  the current and  $A$  the electrode area.

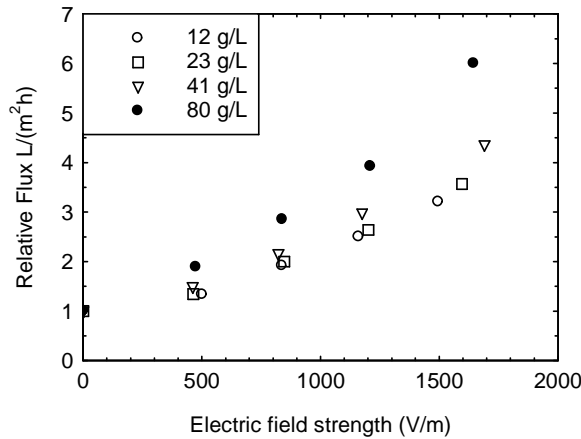
## Results and discussion

The flux data at 0 V is collected in Figure 4 for both the amylase-F and amylase-S. The experiments are carried out at a low crossflow of 0.07 m/s and a TMP of 1.5 bar. The flux decreases when the concentration increases as expected, and the levels are almost the same for both enzymes.



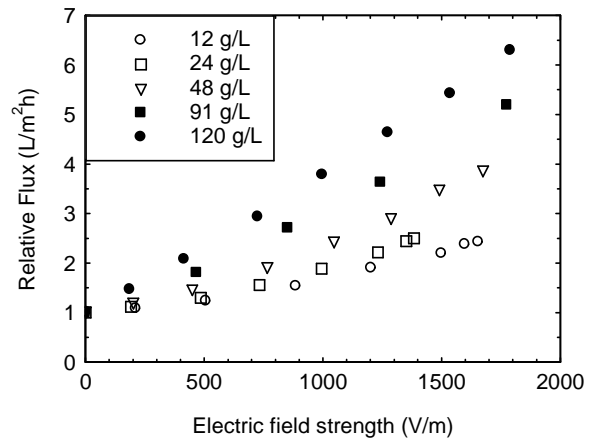
**Figure 4:** Flux levels at 0 V for both the amylases. Crossflow 0.07 m/s and TMP = 1.5 bar.

Figure 5 and Figure 6 shows the relative flux improvement when applying an electric field to the amylase-F and amylase-S solutions respectively.



**Figure 5:** Flux improvement for amylase-F solutions. Crossflow 0.07 m/s and TMP = 1.5 bar.

The flux improves a factor 3-7 at 1600 V/m for both enzymes. The electric field is more effective for amylase-F compared to amylase-S, probably because this enzyme is the smallest. There is also a concentration effect for both enzymes. At high concentration the flux improves relatively more compared to the lower concentrations. This is especially clear when the concentration is above 40 g/L. EUF will therefore be very effective for filtering high concentrated solution.



**Figure 6:** Flux improvements for amylase-S solution. Crossflow 0.07 m/s and TMP = 1.5 bar.

Figure 7 shows the effect of increasing the crossflow from 0.07 m/s to 0.13 m/s at a TMP of 1.5 bar and 2.4 bar when filtering a 48 g/L amylase-S solution. The flux is given in absolute values.

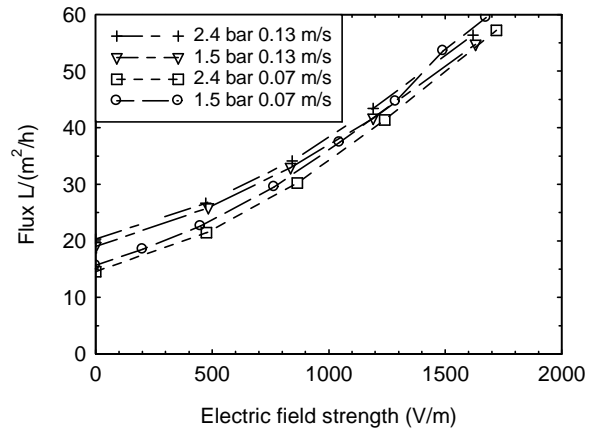


**Figure 7:** Effect of an increased pressure and crossflow for a 48 g/L amylase-S.

Clearly the effect of increasing the TMP is negligible, probably since the limiting pressure is already reached at this concentration. The effect of increasing the crossflow is more pronounced, especially at 0V. Here the flux increases from around 15 to 20 L/(m²h). However as the electric field strength increases the difference between the two crossflows becomes smaller; and at around 900 V/m it is no longer possible to distinguish the curves. The same effect is seen for amylase-F. It is therefore not necessary to use a high crossflow during EUF, since the effect of the electric field is the dominating force. This is in agreement with results reported by Lazarova et al. [7], they even observed a decrease in the flux if the crossflow was too high during electro-microfiltration of silicium oxide particles.

A low conductivity is preferred in EUF, since a higher conductivity requires a higher current intensity to reach the same electric field strength (see eq. 3). This does not only increase the energy used to maintain the electric field, but it also increases the amount of heat

and electrolyte gasses produced at the electrodes. If too much salt is present in the feed solution it could also decrease the zeta-potential of the enzymes, because the ions shield the enzymes. In the experiments carried out so far the main contribution to the conductivity of the feed solutions came from the enzymes themselves, since the solutions have been diafiltrated. It is however important to know the influence of the conductivity in EUF, since diafiltration may not be an option in industrial production.

In Figure 8 the effect of conductivity for a 48 g/L amylase-S solution is shown. Here 0.5, 1.0 and 2.5 g/L of CaCl<sub>2</sub> is added to the feed solution to gain conductivities of 1.1, 1.8 and 2.9 mS/cm compared to 0.7 mS/cm for the diafiltrated solution.

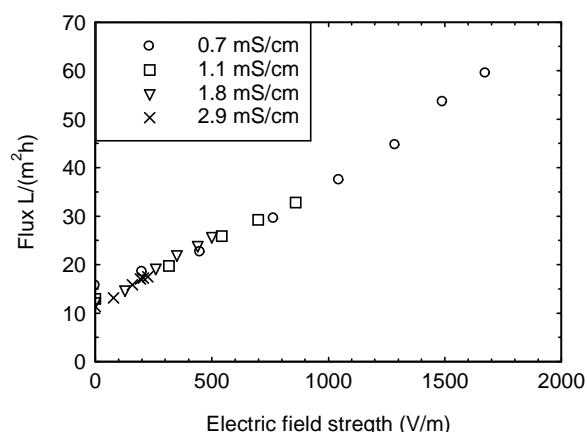


**Figure 8:** Effect of the added CaCl<sub>2</sub> to a 48 g/L amylase-S solution.

At 0V the flux decreases with an increasing concentration of CaCl<sub>2</sub>, probably due to a denser fouling layer. When the electric field is applied the flux improvement is the same, which indicates that the zeta-potential has not been affected by the calcium or chloride ions up to 2.9 mS/cm. As can be seen on Figure 8 the experiments at high conductivities are stopped at a lower electric field compared to the ones at lower conductivities. The reason is that the maximum voltage which can be obtained with the current design is reached at a lower  $E$  when salt is present. It is however promising that it is possible to carry out EUF at higher conductivities, if a better design of the cell is made.

### Conclusions

A 3-7 times flux increase was obtained by crossflow EUF compared to conventional crossflow UF for two industrial enzyme solutions. The highest improvement was achieved at high concentration. Increasing the crossflow and TMP did not improve the flux any further. This means that it is possible to filter high concentrated enzyme solutions at a low crossflow velocity when applying an electric field across the membrane. Addition of calcium chloride did not affect the flux improvement; however a low amount of salt is desired. Since the current consumption and heat developed at the electrodes increases with increasing conductivity.

### References

1. W. R. BOWEN, *AICHe journal*, 43 (1997) 959-970.
2. R. J. Wakeman, *Food and bioproducts processing*, 76 (1998) 53-59.
3. G. C. C. Yang, *Journal of membrane science*, 233 (2004) 151-159.
4. T. Weigert, J. Altmann, S. Ripperger, *Journal of Membrane Science*, 159 (1999) 253.
5. G. Akay, *Journal of membrane science*, 131 (1997) 229-236.
6. H.M. Huotari, G. Trägårdh and I.H. Huisman, *Trans IChemE*, 77 (A) (1999) 461.
7. Z. Lazarova and W. Serro, *Separation Science and Technology*, 37 (3) (2002) 515.

### List of publications

A.D. Enevoldsen, E. Hansen and G. Jonsson  
*Desalination*, 199 (2006) 55.



**Philip Loldrup Fosbøl**

Phone: +45 4525 2868  
Fax: +45 4588 2258  
E-mail: plf@kt.dtu.dk  
WWW: <http://www.ivc-sep.kt.dtu.dk>  
Supervisors: Kaj Thomsen  
Professor Erling H. Stenby  
Kim Rasmussen, Mærsk Oil and Gas A/S

**Ph.D. Study**

Started: February 2004  
To be completed: March 2007

## CO<sub>2</sub> Corrosion in Natural Gas Pipelines – Experiments and Modeling

**Abstract**

Small amount of CO<sub>2</sub> is often found in natural gas and it is corrosive like O<sub>2</sub>. Produced natural gas is saturated with water (wet gas) and it condenses at the cold pipe wall during transportation. NaOH and glycol (MEG) or methanol is injected to prevent gas hydrates and corrosion. CO<sub>2</sub> dissolves in the water-MEG-NaOH liquid phase and the electrolytes will corrode the lower peripheral part of the pipeline. Various protective corrosion products are produced, depending on the chemical environment. An equilibrium model of the corrosion products is being built using the extended UNIQUAC model. The model shows the stability of the products and the concentrations at which diffusion control may prevent pipe corrosion.

**Introduction**

The focus of this Ph.D. project is the natural gas transportation lines between platforms in the North Sea. A crude separation of oil, gas, and water is carried out close to the wellhead and the produced natural gas is transported 10-20 km in 16” pipelines downstream for processing, see figure 1.

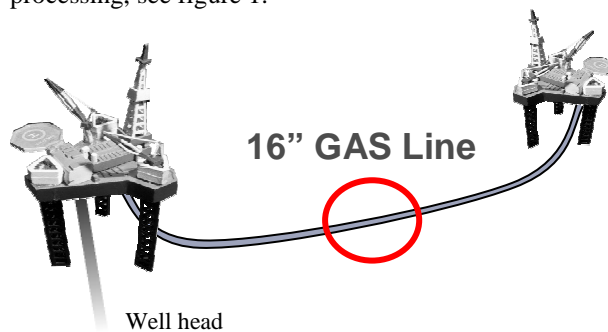


**Figure 1:** Shows an overview of the gas transportation systems.

Process equipment is exposed to Corrosion on a daily basis and maintenance and repair cost make up a significant part of the economy. CorrosionCost.com estimates that \$276 billion dollars/year is lost and spend in relation to corrosion only in the US which is 2.5% of the gross national product. 12 \$billion dollars/year are related directly to the transportation lines of the oil and gas industry [1].

The pipelines which are in focus of this study transport on average 4 million m<sup>3</sup> natural gas/day it is clear that a breakdown quickly ruins any business.

Off-shore corrosion is observed both on rigs and sub-sea. Problems are unfortunately dealt with as they arise, and not prevented beforehand using know-how and understanding of the problems.

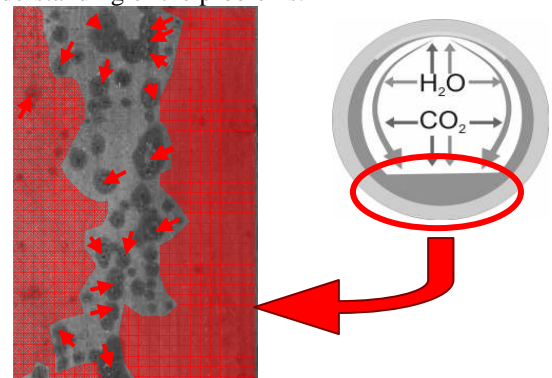


**Figure 2:** Shows inner part of the bottom of the pipeline. The dots marked by arrows are corrosion due to pitting. The remaining area is under general corrosion.

Studies of CO<sub>2</sub> corrosion have appeared in the literature since before the beginning of oil production [2]. In recent years significant advances have been made in describing the actual mechanism, [3-5].

Two types of corrosion are typically seen: Pitting and general corrosion. Figure 2 illustrates the two types of corrosion.

General corrosion is caused by an electrochemical dissolution of iron where  $\text{CO}_2$  is reduced to bicarbonate and iron is dissolved. The mechanism is dependent on the concentration of chemicals in the liquid phase. Corrosion can be diffusion controlled or kinetically controlled.

Pitting are small holes typically created by high flow conditions or local acidification. Pitting is a stochastic process and depends on additional properties compared to general corrosion. Pitting is generally seen as a track of spots in the pipe bottom.

### Process facts

Natural gas pipelines contain mainly gas, but they also contain a smaller liquid phase. The liquid originates from two sources. Some is injected by the operator of the platform and the rest is water condensed from the gas. There is a controlled MEG and NaOH injection and NaOH needs to be diluted using water. MEG is injected to maintain flow assurance preventing gas hydrates. NaOH is injected to lower corrosion.

There is a level difference from the pipe inlet to outlet of approximately 10 meters which causes liquid holdup.

Pipe	T(°C)	P(barg)	L(m <sup>3</sup> /day)
Inlet	45	Approx. 65	2.3
Outlet	23	Inlet P minus 5bar	6.5

The table shows temperature, pressure and liquid phase flow from pipe inlet to the outlet. The pipe is buried in the seabed and temperature is almost constant. Column L shows the liquid phase flow. It is not zero in the inlet due to MEG and NaOH injection. The build up arise from water condensation from the gas.

The amount of water in the inlet gas phase is very small, only 0,1bar of the total pressure. Still it is one of the significant factors for controlling  $\text{CO}_2$  corrosion.

$\text{CO}_2(\text{g})$  is injected at a partial pressure of approximately 1 bar and the  $\text{CO}_2(\text{g})$  flow is much higher than the liquid flow, up to 130 times greater. The gas phase acts as a storage of  $\text{CO}_2(\text{g})$  to be dissolved in the liquid phase.

High corrosion is observed in the first part of the pipelines falling towards the outlet.

### Specific objectives

$\text{CO}_2$  corrosion products are the focus of this study. The reason is that the products build a diffusion barrier of the corrosive components and prevents iron from dissolving. It has been determined through x-ray analysis [6] that  $\text{FeCO}_3(\text{s})$  is formed as a corrosion product and is the main component of the diffusion barrier.

In this work we seek to get a better understanding of the  $\text{CO}_2$  corrosion through experimental work and modeling.

The experimental work focuses on the corrosion products in the complicated  $\text{CO}_2$ -NaOH- $\text{H}_2\text{O}$ -MEG-Fe system. SLE experiments are carried out in the mixed solvent electrolyte subsystem  $\text{NaHCO}_3$ - $\text{Na}_2\text{CO}_3$ - $\text{H}_2\text{O}$ -MEG.

The modeling is done through correlation of the experimental VLE and SLE data using the electrolytic extended UNIQUAC activity coefficient model.

The aim of this study is to describe phase equilibria of the  $\text{CO}_2$ -NaOH- $\text{H}_2\text{O}$ -Inhibitor system. The activity coefficient model will be used for modeling the dissolution of corrosion products and corrosion under diffusion control.

At the moment UNIQUAC parameters are being regressed to 6 types of data for the system  $\text{Na}^+$ -MEG- $\text{H}_2\text{O}$ - $\text{CO}_2$ :

- Binary and ternary Solubility data
- PTx data
- Freezing point depression
- Heat of solution
- Heat excess
- Heat capacity

It will be shown which chemical factors control the dissolution of  $\text{FeCO}_3(\text{s})$ . Further goals are to link the model into an extended model of electrochemistry and diffusion which takes care of diffusion of  $\text{CO}_2(\text{aq})$  to the steel surface and surface reaction at the steel.

## Results and discussion

### Experimental

Through these studies an experimental setup were assembled. It consists of two parts, equilibrium chambers, A, and determination of the concentrations in the saturated solution, B, see figure 3.

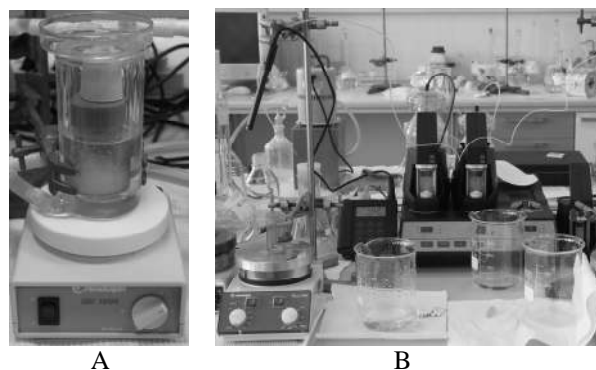


**Figure 3:** Shows the experimental equipment. A: The thermostated equilibrium chamber. B: The titration setup for determining solution concentrations.

The solutions were mixed and thermostated while rotated for approximately 24h, figure 3.A. Samples were acquired through filters and automatically potentiometrically titrated using standardized 0.1M HCl over 20 to 30minutes, figure 3.B. The titration results reveal the amount of  $\text{Na}^+$  ions in the liquid phase. It is important to emphasize that the results may *not* give the amount of carbonate and bicarbonate. This is due to the significant dilution while titrating which changes pH but also changes the temperature compared to equilibrium. Schreinemakers method, [7], was applied to calculate the actual solubility in the liquid phase.

### Ideal solubility of $FeCO_3$

pH-stabilization is one of the main acts taken against corrosion, figure 4 shows why. Choosing the right pH is directly correlated to the solubility of  $FeCO_3$  and thereby to the diffusion control of corrosion.

When no pH-stabilization (NaOH) is added, the pH is 5 and a high solubility of  $FeCO_3(s)$  is seen.

When small amounts of NaOH is added the pH increases fast and at an addition of approximately 25g NaOH/kg  $H_2O$  the pH is 7,5.

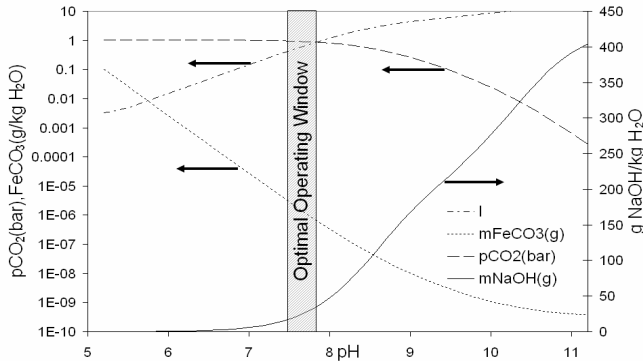


**Figure 4:** Ideal calculation of chemical environment in the pipes.

The solubility of  $FeCO_3(s)$  decreases rapidly in the pH interval 5 to 7,5 from 0.1g/kg $H_2O$  to  $10^{-6}$ g/kg $H_2O$ . It is key to notice that the partial pressure of  $CO_2$  stays almost constant in the interval pH=5 to 7,5 while above pH=8 significant amounts of  $CO_2(g)$  is dissolved in the liquid phase, neutralizing the NaOH and not effectively using it for pH-stabilization. The operating window, shown in figure 4 tells the engineer the correct amount of NaOH to inject with this amount of  $CO_2(g)$  to prevent iron dissolution and to keep the use of NaOH down to an economical level but also to prevent dissolution of  $CO_2(g)$  in the liquid phase.

The ionic strength (I) is also shown in figure 4. It rises from approximately .005 up to 10 in the pH interval. It tells that the solution becomes quickly non-ideal with the amount of NaOH. An advanced electrolytic model is required at  $I > 0.1$  and most existing models will not go higher then  $I = 6$ . The extended UNIQUAC has proven to be able to do this [9].

### Mixed solvent electrolyte system

Data of mixed solvent electrolyte systems are generally very sparse and often inaccurate. Luckily the glycol system has been partly studied by Gärtner, [8]. Figure 5 shows the important fluid layers next to the pipe wall. The bulk phase contains the aqueous phase of NaOH and dissolved  $CO_2(aq)$  and inhibitor (MEG).

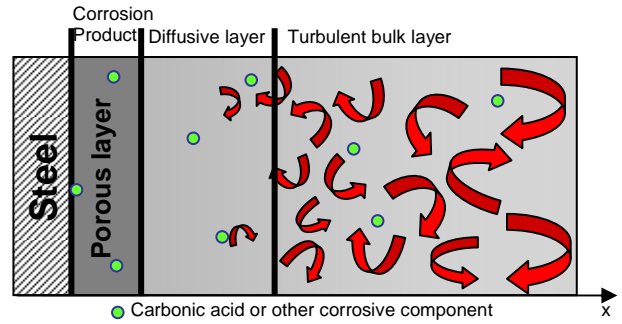
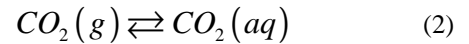
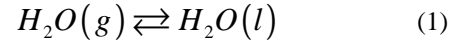


**Figure 5:** The figure shows the bulk phase containing corrosive species. They diffuse to the steel through a porous corrosion product layer, where they are reduced to corrosion products.

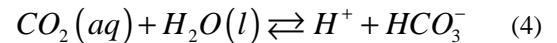
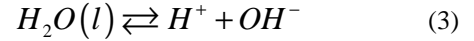
The bulk phase is very non-ideal. The activities of the species in the liquid phase are found through the extended UNIQUAC model. Parameters for the model are fitted to heat of solution, VLE and SLE data. Model details may be found in [9]. How well data are reproduced is shown in the following figures.

The reaction scheme of the electrolytic phase is given by:

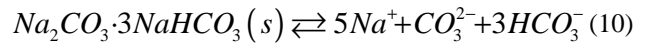
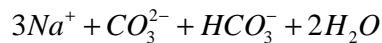
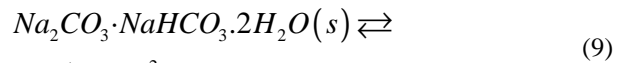
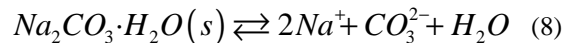
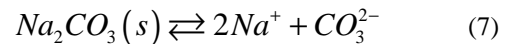
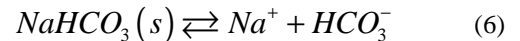
Vapour-Liquid Equilibria (VLE):



Liquid phase dissociation:



Solid-Liquid Equilibria (SLE):



The scheme is very complicated because  $CO_2$ ,  $HCO_3^-$  and  $CO_3^{2-}$  are linked through the equilibrium of carbonic acid. It includes both the heterogeneous equilibrium of VLE ((1)-(2)) and SLE ((6)-(10)) and homogeneous reactions in the liquid phase ((3)-(5)). In the system of  $NaHCO_3$ - $Na_2CO_3$ - $H_2O$ -MEG several different phases may possibly precipitate.

The solubility of  $NaHCO_3(s)$  in the mixed solvent of MEG- $H_2O$  is shown in figure 6.

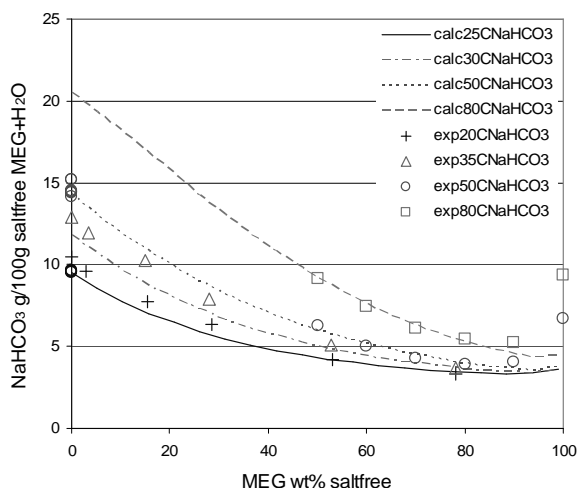


**Figure 6:** shows solubility in the system of  $\text{NaHCO}_3\text{-H}_2\text{O-MEG}$ . SLE is modeled using the extended UNIQUAC.

The experimental data are partly from this work and partly from the work by Gärtner, [8]. It is observed how the solubility decreases by a typical salting out effect with increasing glycol concentration. A steep increase is observed close to pure MEG. It is at the moment not fully described by the model and may be related to a complex formed between  $\text{NaHCO}_3$  and MEG.

A similar graph is shown in figure 7 for the solubility of  $\text{Na}_2\text{CO}_3$  in the system with mixed solvent of MEG- $\text{H}_2\text{O}$ . Data were taken from [8,10]. This system is much more complicated than the corresponding diagram for the solubility of  $\text{NaHCO}_3$ . The dotted lines near pure MEG signify that pure, anhydrous  $\text{Na}_2\text{CO}_3$  precipitates. At lower concentrations mono hydrate,  $\text{Na}_2\text{CO}_3\cdot\text{H}_2\text{O}$ , precipitates. A small offset is observed. This may be due to the way the authors interpreted their data. When  $\text{Na}_2\text{CO}_3\cdot\text{H}_2\text{O}$  precipitates the solvent composition changes because some solvent precipitates as part of the mono hydrate. The data is currently being reinterpreted and the model is probably the most correct in this situation.

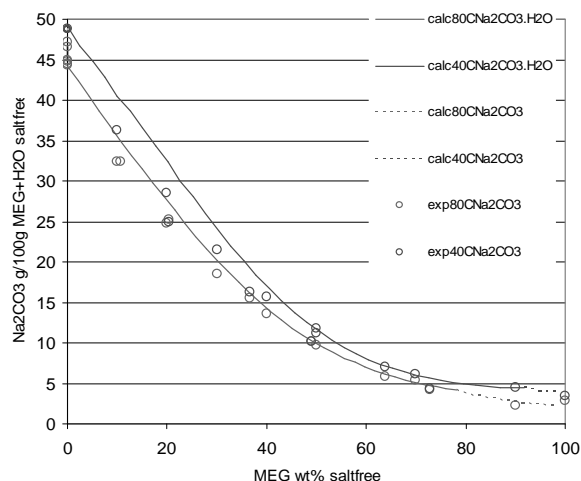


**Figure 7:** shows solubility in the system of  $\text{Na}_2\text{CO}_3\text{-H}_2\text{O-MEG}$ . SLE is modeled using the extended UNIQUAC and gives precipitation of  $\text{Na}_2\text{CO}_3\cdot\text{H}_2\text{O}$ . Dotted lines signify precipitation of pure, anhydrous  $\text{Na}_2\text{CO}_3$ .

The quaternary system  $\text{NaHCO}_3\text{-Na}_2\text{CO}_3\text{-H}_2\text{O-MEG}$  is shown in figure 8. The rings are experimental literature data of the pure water case, while crosses are the system of 3 wt% glycol. The pure water system shows only the existence of  $\text{NaHCO}_3$  and  $\text{Na}_2\text{CO}_3\cdot 10\text{H}_2\text{O}$ , but the 3 wt% MEG system reveals also trona,  $\text{NaHCO}_3\cdot\text{Na}_2\text{CO}_3\cdot 2\text{H}_2\text{O}$ . Usually a salting out effect is observed when adding a solvent, MEG, of lower relative permittivity (dielectric constant) but figure 8 shows that adding the 3 wt% increases the solubility in the region of  $< 0.5$  molal  $\text{NaHCO}_3$ . This can be explained by trona becoming more stable than the deca-hydrate due to the influence MEG has on the water activity.

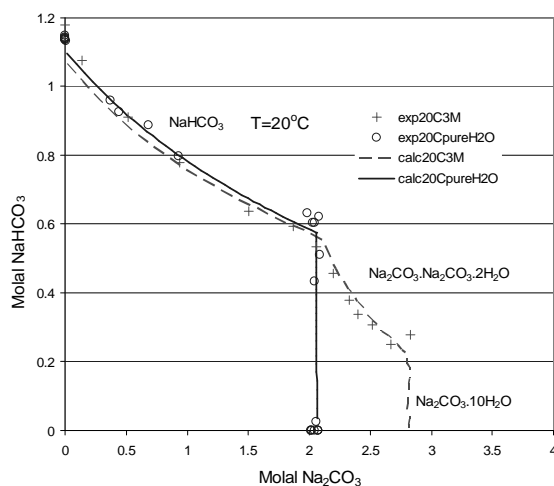
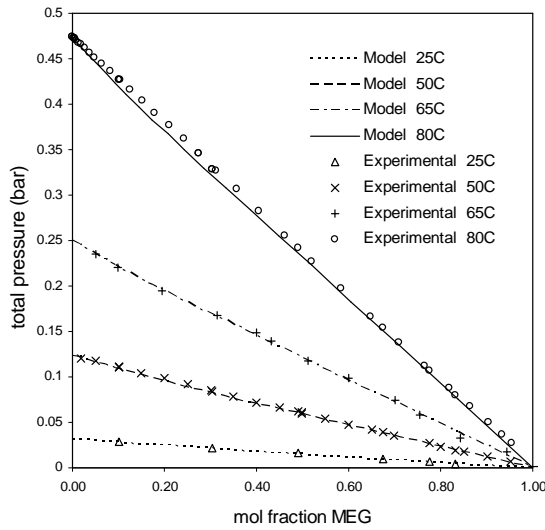


**Figure 8:** shows solubility in the system of  $\text{NaHCO}_3\text{-Na}_2\text{CO}_3\text{-H}_2\text{O-MEG}$ . Two MEG concentrations are given at significantly different outcome.

The phenomenon is not straight forward and probably more work is needed to elucidate this.

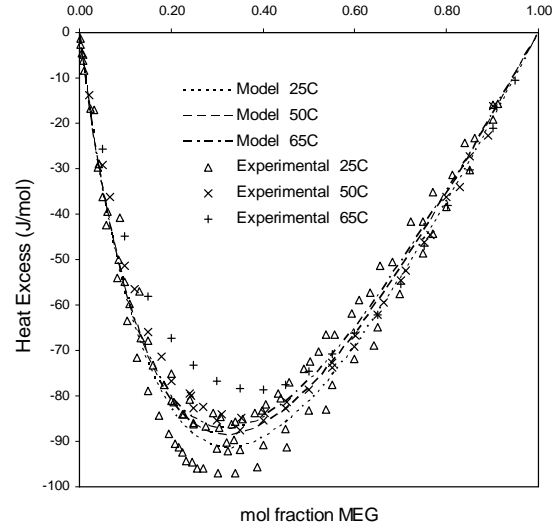
It is assumed that the vapor-phase consists only of water vapor. MEG is considered to be a solute equivalent to  $\text{CO}_2(\text{aq})$  and  $\text{Na}^+$ .

Figure 9 shows the bubble point pressure of the binary system of water-MEG calculated with the model and data obtained from the literature, [11-14]. The linear relationship indicates that data are almost ideal and follows Raoult's law. This also tells us, comparing figure 6, 7 and 9, that the non-ideality is purely related to the addition of electrolytes. The figure shows that the regressed parameters are consistent and that the model may also be used for describing both SLE and VLE.



**Figure 9:** PTx phase diagram of the system MEG-H<sub>2</sub>O modeled using the extended UNIQUAC model.

To obtain the most reliable and consistent model it is necessary to include data of many types as possible. This not only enhances the model but also stabilizes the fitting process. Figure 10 shows that the model will even reproduce excess enthalpy data to an acceptable degree of accuracy at least within the extreme scatter of the data.



**Figure 10:**  $\Delta H^E$  of the system MEG-H<sub>2</sub>O modeled using the extended UNIQUAC model. Data taken from [15-20]

#### *Applying the activity coefficient model*

The newer corrosion models describe corrosion by a full setup of Partial Differential Equations (PDEs). It is basically a description of the corrosive  $\text{CO}_2(\text{aq})$  which diffuses from the bulk phase to the surface by transportation through a thin stagnant liquid film followed by diffusion through a porous corrosion product layer, see figure 5. A similar steady state diffusion model follows Ficks law:

$$0 = D_{\text{eff},i} \frac{d^2 c_i}{dx^2} \quad (11)$$

Many of the newer corrosion models utilize this principle, [3-5]. It is unfortunately assumed in all cases that the liquid phase is ideal even though our result shows the opposite.

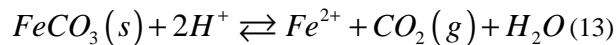
The activity can be used for obtaining a more accurate description of the diffusion process. The effective diffusion coefficient is related to the friction coefficient,  $D_i$ , by

$$D_{\text{eff},i} = D_i \left( 1 + \frac{d\gamma_i}{dm_i} \right) \quad (12)$$

through an activity coefficient model like the extended UNIQUAC model. It is important to stress that the diffusion coefficients are normally not dependent on the concentrations. But at ionic strengths of 1 and higher this becomes significant [21].

The ideality of the species in the liquid phase may also influence the corrosion modeling. Huge difficulties are often observed in modeling the  $\text{FeCO}_3$  corrosion product and especially its solubility. In many cases a correlation for super saturation is applied which could be explained by non-ideality of the liquid phase. The

dissolution process of  $\text{FeCO}_3$  is typically described by, [22]:



And the mass action law is:

$$K_{\text{FeCO}_3} = \frac{a_{\text{Fe}^{2+}} f_{\text{CO}_2} a_{\text{H}_2\text{O}}}{a_{\text{H}^+}^2} \quad (14)$$

It shows how the water activity plays an important role in the dissolution process. Rewriting the above equation it is even clearer how the water activity affects the iron solubility:

$$a_{\text{Fe}^{2+}} = \frac{K_{\text{FeCO}_3} a_{\text{H}^+}^2}{f_{\text{CO}_2} a_{\text{H}_2\text{O}}} \quad (15)$$

MEG would typically lower the water activity and thereby increase iron solubility. This contradicts to some extent the observations from the literature, [23]. It may be explained by the MEG effect on the  $\text{CO}_3^{2-}$  activity which is shown in the near future.

### Conclusion

Corrosion can be avoided by planning and being alert at the production site. It is important always to have an understanding of the chemicals. This project will expand the understanding of  $\text{CO}_2$  corrosion. The work shows the phase equilibria of the observed systems and the produced models will be used for making an extended  $\text{CO}_2$  corrosion model.

### Acknowledgement

I would like to thank Kaj Thomsen for his support in my studies and to Kim Rasmussen, Mærsk, for providing production data.

### References

1. CorrosionCost.com:  
<http://www.corrosioncost.com/infrastructure/gasliquid/index.htm>
2. Tillmans, J.; Klarmann, B., *Angewandte Chemie* 36, p. 94-7 103-4 113-5, 1924
3. Nordsveen M, Nestic S, Nyborg R, et al., *Corrosion* 59 (5): 443-456, 2003
4. Nestic S, Nordsveen M, Nyborg R, et al., *Corrosion* 59 (6): 489-497, 2003
5. Nestic S, Lee KLJ, *Corrosion* 59 (7): 616-628, 2003
6. Xia, Z.; Chou, K. C.; Szklarska-Smialowska, Z. *Corrosion* 45(8), p. 636-42, 1989
7. Schreinemakers, F.A.H. *Z. Physik. Chem.* 11, p. 75-109, 1893
8. Gärtner RS, Seckler MM, Witkamp GJ, *Journal Of Chemical And Engineering Data* 49(1): 116-125, 2004

9. M.Iliuta, K.Thomsen, P.Rasmussen, *Chemical Engineering Science* 55: 2673-2686, 2000
10. Oosterhof H, Witkamp GJ, van Rosmalen GM. *Fluid Phase Equilibria* 155(2): 219-227, 1999
11. Gonzalez, C.; Van Ness, H. C. *Journal Of Chemical And Engineering Data* 28: 410, 1983
12. Horstmann, Sven; Gardeler, Hergen; et al., *Journal of Chemical and Engineering Data* 49(6): 1508-1511, 2004.
13. Nath A, Bender E., *Journal Of Chemical And Engineering Data* 28 (4): 370-375 1983.
14. Mokbel, I.; Porcedda, S.; Guetachew, T.; Marongiu, B.; Jose, J., *The International Electronic Journal of Physico-Chemical Data*, *Eldata* 5(2): 79-84. 1999
15. Miguel A. Villamanan, Carlos Gonzalez, Hendrick C. Van Ness, *Journal of Chemical and Engineering Data* 29(4): 427-429, 1984.
16. Kracht C, Ulbig P, Schulz S, *Journal Of Chemical Thermodynamics* 31 (9): 1113-1127, 1999
17. Matsumoto, Y.; Touhara, H.; Nakanishi, K.; Watanabe, N., *Journal of Chemical Thermodynamics* 9(8): 801-5, 1977
18. Dohnal, Vladimir; Roux, Alain H.; Hynek, Vladimir., *Journal of Solution Chemistry* 23(8): 889-900, 1994
19. Arroyo Gallego, A., *Anales de Quimica, Serie A: Quimica Fisica e Ingenieria Quimica* 84(2): 179-82, 1988.
20. Biros, Jan; Pouchly, Julius; Zivny, Antonin., *Makromolekulare Chemie* 188(2): 379-94, 1987
21. J. Newman: "Electrochemical systems", John Wiley & Sons, 2004
22. Reiterer, F., Johannes, W., Gamjäger, H.v.. *Mikrochimica Acta* 1, p. 63-72, 1981
23. L. van Bodegom, K.V. Gelder, M.K.F. Paksa, L.V. Raam, *CORROSION/87* paper no. 55, NACE, 1987



### Jostein Gabrielsen

Phone: +45 4525 2869  
Fax: +45 4588 2258  
E-mail: jog@kt.dtu.dk  
WWW: <http://www.ivc-sep.dtu.dk>  
Supervisors: Georgios M. Kontogeorgis  
Michael L. Michelsen  
Erling H. Stenby

#### Ph.D. Study

Started: November 2003  
To be completed: October 2006

## CO<sub>2</sub> Capture from Coal Fired Power Plants

### Abstract

Carbon dioxide (CO<sub>2</sub>) solubility in aqueous solutions of monoethanolamine (MEA) has been correlated using a simple approach where only one chemical equilibrium reaction is taken into account, and assuming ideal gas and ideal liquid properties. The approach combines the Henry's law constant and the chemical reaction equilibrium constant for the formation of carbamate for primary alkanolamines, resulting in an explicit expression for calculating the partial pressure of CO<sub>2</sub> over an aqueous MEA solution. Accurate values for the solubility of CO<sub>2</sub> are obtained for a limited loading-, temperature-, and pressure range which is useful in modelling CO<sub>2</sub> capture from coal fired power plants. A rate-based steady-state model for CO<sub>2</sub> absorption into an MEA solution has been proposed, utilizing both the proposed expression for the CO<sub>2</sub> solubility and the calculated values of the heat of absorption along with an expression for the enhancement factor and physicochemical data from the literature. The proposed model has successfully been applied to absorption of CO<sub>2</sub> into an MEA solution in a packed tower, validated against pilot plant data from the literature.

### Introduction

Approximately one third of all CO<sub>2</sub> emissions from human activity come from generating electricity. Therefore CO<sub>2</sub> capture and storage from fossil fuel power plants present an opportunity to achieve large reductions in greenhouse gas emissions without having to change the energy supply infrastructure and without having to make large changes to the basic process of producing electricity.

CO<sub>2</sub> capture from process streams is an established concept which has achieved industrial practice. There are different process schemes for integrating CO<sub>2</sub> capture with combustion available including pre-, post-, and oxyfuel-combustion. The focus of our work is on post-combustion capture which means that CO<sub>2</sub> is removed from the flue gas; therefore the combustion process is not directly affected. However, energy for the CO<sub>2</sub> removal is taken from the power process, thus lowering the net efficiency of the power production.

There are several techniques for CO<sub>2</sub> capture from process gas streams, of which chemical absorption using alkanolamines in a packed absorption tower is the most commonly used. The technology is currently widely used, though for applications of a scale much smaller than power plant flue gas cleaning. A bottleneck in the process of capturing CO<sub>2</sub> from flue gases with aqueous

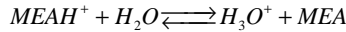
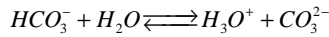
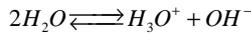
alkanolamines is the large amount of energy needed to regenerate the absorption liquid which in turn decreases the efficiency of the power plant dramatically. Efficiency reduction for coal fired power plants lies in the range of 7 to 12 %, depending on the alkanolamine and the packing of the absorption tower, which gives a relative decrease in efficiency in the range from 15 to 22 % (Lyngfelt et al.) [1]. The largest contribution to the efficiency decrease originates in the energy needed in the desorption of CO<sub>2</sub>.

The focus of our work is to contribute to the modeling and simulation of both the absorption and desorption of CO<sub>2</sub> in aqueous alkanolamines in order to develop reliable tools for the design and optimization of the process. The system is very complex due to the fact that it contains weak electrolytes. Among the key parameters in the design process are the thermodynamics associated with the phase equilibria of systems containing CO<sub>2</sub>-water-alkanolamines, the kinetics of the chemical reactions involved and the mass transfer in the system.

### A simple thermodynamic model for MEA

To be able to develop more efficient processes for the separation of acid gases from flue gases, thermodynamic modeling of the vapor-liquid phase

equilibrium is the first step. Most thermodynamic models used to represent the vapor-liquid equilibria of CO<sub>2</sub> in an aqueous solution of alkanolamines are very complex and require a large amount of adjustable parameters. This is due to the fact that the alkanolamines are weak electrolytes and chemical reactions between alkanolamine and CO<sub>2</sub> occur in the liquid phase. Another problem concerning the representation of the vapor-liquid equilibria is that the experimental data existing are not always plentiful and reliable. There is a large scattering particularly at low partial pressures and loadings. In this work a very simple model has been developed for representing the VLE of aqueous alkanolamine solutions. The chemical equilibrium taking place in the liquid phase when CO<sub>2</sub> is absorbed in an aqueous solution of MEA (monoethanolamine) can be written with the following equilibrium equations:



The reaction of CO<sub>2</sub> with aqueous MEA can, given that the loading (moles of dissolved CO<sub>2</sub>/moles of alkanolamine) is in the region between 0.02 and 0.48, be approximated by a single chemical equilibrium reaction (1) Astarita [2].



Equation (1) neglects the presence of bicarbonate (HCO<sub>3</sub><sup>-</sup>), hydroxide (OH<sup>-</sup>), and carbonate (CO<sub>3</sub><sup>2-</sup>) ions since the concentration of these ions will be very small in the region of loading which of interest to describe in CO<sub>2</sub> capture from power plants fired with fossil fuels. The concentration of the species involved in the chemical reaction can be written in the following manner:

$$[MEA] = (1 - 2\theta)a_0$$

$$[MEA H^+] = [MEACOO^-] = \theta a_0$$

$$[CO_3^{2-}] \cong [HCO_3^-] \cong 0$$

The expression for the partial pressure of CO<sub>2</sub> can now be written as shown in equation (2).

$$p_{CO_2}^* = K_{CO_2} X_{CO_2} \frac{a_0 \theta}{(a_0 (1 - 2\theta))^2} \quad (2)$$

Where the combined equilibrium – and Henry's law constant is given by equation (3):

$$\ln K_{CO_2} = A + \frac{B}{T} + C a_0 \theta \quad (3)$$

A, B and C are all parameters that have to be regressed from experimental data. Some calculations are shown in figure 1.

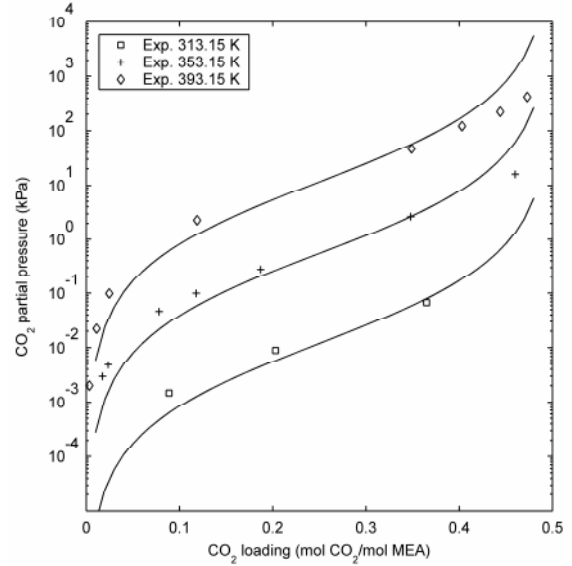


**Figure 1** Comparison of model correlation results (solid lines) with experimental data for CO<sub>2</sub> equilibrium partial pressures over an aqueous 30 wt % MEA solution.

Furthermore by using the Gibbs-Helmholtz equation the heat of absorption of CO<sub>2</sub> in the MEA solution ( $\Delta H_{CO_2}$ ) is found to be -87990 J/mol CO<sub>2</sub>.

### Packed Column Model

Due to the nature of the process a rate based model is chosen, and since it is a packed column differential mass and energy balances are set up. The model in this work is based on the model developed by Pandya [3] where the process is described by the two film theory and utilization of the assumptions 1-7:

1. The reaction is fast enough to take place in the liquid film and the bulk of the liquid is in equilibrium.
2. Liquid side heat transfer resistance is small compared to the gas phase, thus the interface temperature is the same as the bulk temperature.
3. The liquid side mass transfer resistance for the volatile solvent is negligible.
4. The interfacial surface area is the same for heat and mass transfer.
5. Axial dispersion is not accounted for.
6. The absorption tower is considered to be adiabatic.
7. Both the liquid phase and the gas phase are assumed to be ideal.

The following system of differential equations can be set up for the packed column based on mole and energy balances on a differential section, solving for eight variables including mole flow, mole fraction of water and CO<sub>2</sub>, and temperature in both phases.

$$\frac{dG}{dz} = -(N_{CO_2} + N_{H_2O})aA_c$$

$$\frac{dy_{CO_2}}{dz} = \frac{N_{CO_2}aA_c(y_{CO_2} - 1) + N_{H_2O}y_{CO_2}aA_c}{G}$$

$$\frac{dy_{H_2O}}{dz} = \frac{N_{H_2O}aA_c(y_{H_2O} - 1) + N_{CO_2}y_{H_2O}aA_c}{G}$$

$$\frac{dL}{dz} = -N_{H_2O}aA_c$$

$$\frac{dX_{CO_2}}{dz} = \frac{(N_{H_2O}X_{CO_2} - N_{CO_2})aA_c}{L}$$

$$\frac{dx_{H_2O}}{dz} = \frac{N_{H_2O}(x_{H_2O} - 1)aA_c}{L}$$

$$\frac{dT_G}{dz} = -\frac{qaA_c}{Gc_{p,G}}$$

$$\frac{dT_L}{dz} = \frac{(N_{CO_2}c_{p,CO_2} + N_{H_2O}c_{p,H_2O})aA_c(T_L - T_G) - qaA_c}{Lc_{p,L}}$$

The resulting boundary value problem is solved in Matlab 7.0 using a built in routine called *bvp4c* which implements a collocation method for the solution of boundary value problems. The boundary values needed are given by the conditions of the gas and liquid entering the column. All physicochemical data needed in the model is found in the literature. To verify the model it is compared with published pilot plant data. In figures 2 and 3 experimental data from Tontiwachwuthikul et al. [4], are compared with the proposed model.

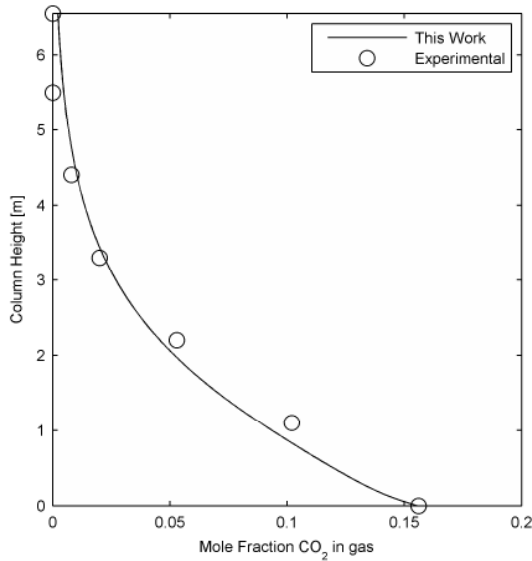


**Figure 2** Concentration profiles for CO<sub>2</sub> in the gas phase in the MEA-CO<sub>2</sub> system. Modeled (line) results and experimental data (circles)

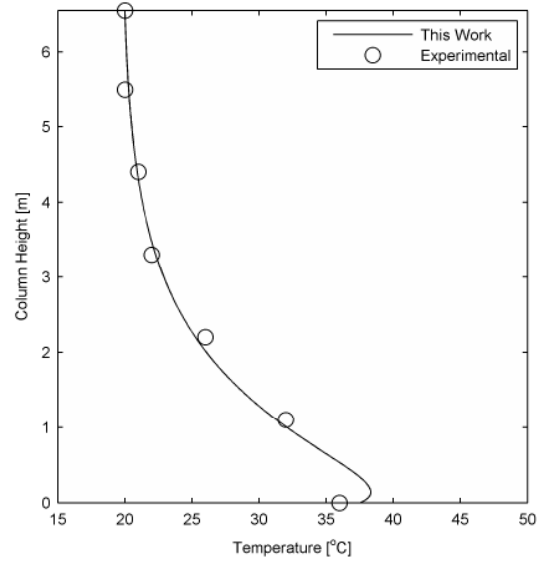


**Figure 3** Temperature profiles for the liquid phase in the MEA-CO<sub>2</sub> system. Modeled (line) results and experimental data (circles)

As it can be seen the proposed model gives a better representation of both the CO<sub>2</sub> concentration in the gas phase and temperature in the liquid phase along the column.

### Acknowledgements

The author gratefully acknowledges Nordic Energy Research for the financial support of this work.

### List of symbols

- $a$  = specific wetted area for mass transfer, m<sup>2</sup>/m<sup>3</sup>
- $a_0$  = initial concentration of amine =  $\frac{\text{amine}}{\text{amine} + \text{H}_2\text{O}}$
- $A_c$  = cross sectional area of the column, m<sup>2</sup>
- $c_{p,i}$  = molar heat capacity of component  $i$  in the gas phase, J/mol·K
- $c_{p,L}$  = molar heat capacity of the liquid, J/mol·K
- $G$  = molar gas flow, mol/s
- $h$  = heat transfer coefficient in gas, J/s·K·m<sup>2</sup>
- $H_{CO_2}$  = Henry's Law Constant for CO<sub>2</sub>, Pa·m<sup>3</sup>/mol
- $\Delta H_{H_2O}$  = heat of condensation of H<sub>2</sub>O, J/mol
- $\Delta H_{CO_2}$  = heat of absorption of CO<sub>2</sub>, J/mol CO<sub>2</sub>
- $K_{CO_2}$  = combined Henry's law and chemical equilibrium constant for CO<sub>2</sub> partial pressure, Pa
- $L$  = molar liquid flow, mol/s
- $N_i$  = Molar flux of component  $i$ , mol/m<sup>2</sup>·s
- $p_i$  = partial pressure of component  $i$  in the bulk gas phase, Pa
- $p_i^*$  = partial pressure of component  $i$  gas phase if it were in equilibrium with the liquid phase, Pa
- $q$  = heat flux, J/m<sup>2</sup>·s
- $T_L$  = liquid phase temperature, K
- $T_G$  = gas phase temperature, K
- $x_i$  = liquid phase mole fraction of component  $i$ , mol/mol
- $X_{CO_2}$  = liquid phase mole fraction of CO<sub>2</sub> in both reacted and unreacted form, mol/mol
- $y_i$  = gas phase mole fraction of component  $i$ , mol/mol
- $z$  = height of packing, m
- $\theta$  = loading =  $\frac{\text{mole CO}_2}{\text{mole amine}}$

### References

1. Lyngfelt, A., & Leckner, B. Technologies for CO<sub>2</sub> separation, Second Nordic Minisynposium on Carbon Dioxide Capture and Storage. Göteborg, 2001

2. Astarita G., Mass transfer with chemical reactions, Elsevier Publishing Company, Amsterdam/London/New York, 1967
3. Pandya, JD. Adiabatic Gas Absorption and Stripping with Chemical Reaction in Packed Towers. Chem. Eng. Comm. 19 (1983) 343-361.
4. Tontiwachwuthikul P, Meisen A, Lim CJ. CO<sub>2</sub> Absorption by NaOH, Monoethanolamine and 2-Amino-2-Methyl-1-Propanol Solutions in a Packed Column. Chem Eng Sci. 47 (1992) 381-390.

#### **List of Publications**

1. J. Gabrielsen, M.L. Michelsen, E.H. Stenby, G.M. Kontogeorgis, A Model for Estimating CO<sub>2</sub> Solubility in Aqueous Alkanolamines Ind. Eng. Chem. Res. 44 (2005) 3348-3354.
2. G.K. Folas, J. Gabrielsen, M.L. Michelsen, E.H. Stenby, G.M. Kontogeorgis, Application of the Cubic-Plus-Association (CPA) Equation of State to Cross-Associating Systems Ind. Eng. Chem. Res. 44 (2005) 3823-3833.
3. J. Gabrielsen, M.L. Michelsen, E.H. Stenby, G.M. Kontogeorgis, Modelling of CO<sub>2</sub> Absorber Using an AMP Solution AIChE Journal 52 (2006) 3443-3451.
4. J. Gabrielsen, H.F. Svendsen, E.H. Stenby, G.M. Kontogeorgis, Experimental Validation of a Rate-Based Model for CO<sub>2</sub> Capture using an AMP Solution. (Submitted for Publication)



**Fengxiao Guo**  
Phone: +45 4525 6821  
Fax: +45 4588 2161  
E-mail: feg@kt.dtu.dk  
WWW: <http://www.dtu.dk/Centre/DPC>  
Supervisors: Martin E. Vigild  
Sokol Ndoni, Risø  
Katja Jankova

Ph.D. Study  
Started: November 2006  
To be completed: October 2009

## Nanoporous Polymers by Living Anionic Polymerization and Atom Transfer Radical Polymerization

### Abstract

Self-assembly of block copolymers is a novel and versatile route to prepare nanostructured polymers. Block copolymers for nanoporous materials will be synthesized by a combination of living anionic polymerisation and atom transfer radical polymerisation. The synthesized block copolymers and finally rendered nanoporous polymers will be characterized by a variety of chromatographic, spectroscopic and radiation scattering techniques. This PhD study will aim at applications where these self-assembly polymers can serve as templates for the synthesis of other novel materials.

### Introduction

Figure 1 shows the micrograph of a nanoporous polymer which displays hexagonal features on the nanoscale [1]. It is a result of recent research studying the versatile and predictable structures displayed by the self-assembly block copolymers. [2-4].

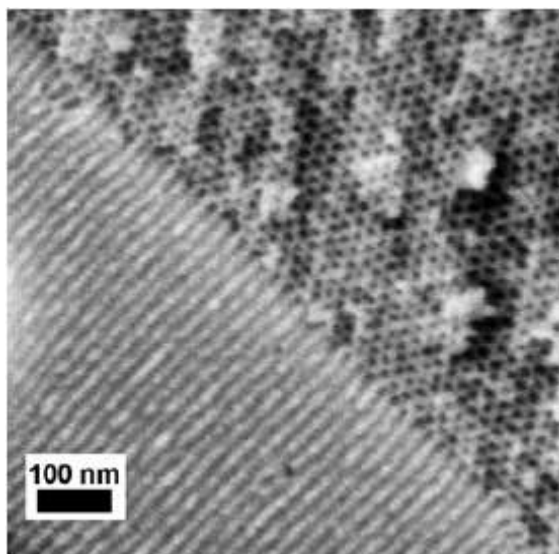


**Figure 1:** Scanning electron microscopy image of nanoporous 1,2-polybutadiene with hexagonal cavities [1].

This development opens for a wide range of technical applications which primarily depend on the

nanoscopic characteristics. However, future applications could also benefit on the potential control of morphology and functionality which is within reach for nanoporous polymers based on these block copolymers. Nanoporous polymers can serve as templates for the synthesis of other nanoscopic novel materials [3], give the basis for highly selective separation membranes [5], be utilized as high surface-area supports for catalysts [6], or be employed as carriers for drug delivery. Such a diverse set of application fields obviously demand various methodologies of preparation of the nanoporous polymer in order to target the proper chemical functionality and morphology for a given use. To this end there are many significant challenges on nanoporous materials covering a range of issues starting with the initial stage of the chemical synthesis and ending at the final stage of application in the daily life.

### Specific Objectives

Block copolymers are traditionally synthesised by living polymerization, mainly anionic polymerisation. The newly developed atom transfer radical polymerisation offer new approaches for the design of functional block copolymer materials with controlled structures. This PhD project will combine these two techniques and synergize their individual advantages, while eliminating existing limitations on the selection of chemical monomers for the polymer blocks. Furthermore, the project will extend the present options for polymeric architecture and monomer combinations. It will become

possible to design amphiphilic multiblock copolymers more freely and directly target the functionality and morphology at specific technical applications.

Advanced analysis and characterisation of the produced polymeric material on the molecular level and higher hierarchical structural levels are a fundamental parts of this project. Material properties and morphologies will be examined by techniques such as Small Angle X-ray Scattering (SAXS), Small Angle Neutron Scattering (SANS), Size Exclusion Chromatography (SEC), Nuclear Magnetic Resonance (NMR), Nitrogen Adsorption Isotherms, Transmission Electron Microscopy (TEM), Scanning Electron Microscopy (SEM) and Dynamic Mechanical Analysis (rheology).

The nanoporous block copolymer-based materials which we intend to develop in this PhD project are especially interesting in the light of precursors for novel materials. The nanocavities can be used for templating or moulding materials of unprecedented mechanical, structural and dielectrical properties which hold high expectations for use in diagnostics, catalysis and electronics.

## References

1. L. Schulte, P.P. Szewczykowski, F. Guo, K. Andersen, M.E. Vigild, R.H. Berg, S. Ndoni, Submitted.
2. J.-S. Lee, A. Hirao, S. Nakahama, *Macromolecules* 21 (1988) 274-276.
3. T. Thurn-Albrecht, J. Schotter, G.A. Kastle, N. Emley, T. Shibauchi, L. Krusin-Elbaum, K. Guarini, C.T. Black, M.T. Tuominen, T.P. Russell, *Science* 290 (2000) 2126-2129.
4. S. Ndoni, M.E. Vigild, R.H. Berg, *J. Am. Chem. Soc.* 125 (2003) 13366-13367.
5. Y. Ding, J. Erlebacher, *J. Am. Chem. Soc.* 125 (2003) 7772-7773.
6. Q. Zhang, T. Xu, D. Butterfield, M. Misner, D.Y. Ryu, T. Emrick, T.P. Russell, *Nano Lett.* 5 (2005) 357-361.



**Brian Brun Hansen**

Phone: +45 4525 2829  
 Fax: +45 4588 2258  
 E-mail: bbh@kt.dtu.dk  
 WWW: http://www.chec.dtu.dk  
 Supervisors: Søren Kiil  
 Jan E. Johnsson

Ph.D. Study  
 Started: March 2005  
 To be completed: April 2008

**Gypsum Crystallisation and Foaming in Wet Flue Gas Desulphurisation (FGD) Plants**

**Abstract**

This study consists of experimental as well as theoretical investigations of gypsum crystallisation and the unexpected occurrence of foaming in wet flue gas desulphurisation (FGD) plants. The observed nucleation, growth and breakage of gypsum crystals in a wet FGD pilot plant will be used to validate models describing the particle size distribution (PSD). A survey of the gypsum quality at Danish full-scale wet FGD plants will furthermore be performed. The origin of the unexpected occurrence of foaming in wet FGD plants will be investigated. The obtained knowledge will be used to point towards methods to optimize the operation of wet FGD plants.

**Introduction**

A substantial part of the worlds present energy demand is based on the combustion of fossil fuels, such as coal, oil and gas. Despite an increasing interest in alternative fuel sources, the combustion of fossil fuels is expected to continue to yield a significant part of the world's energy demand in the coming years (figure 1).

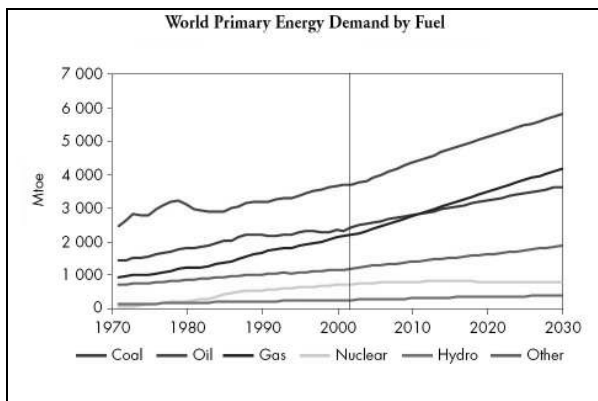


**Figure 1:** Projected development of the world's primary energy demand (Mtoe = Million ton oil equivalents) [1].

Due to the sulphur content of coals and oils, sulphur dioxide (SO<sub>2</sub>), and to a lesser extent sulphur trioxide (SO<sub>3</sub>), will be released by the combustion of these fuels. If emitted to the atmosphere the SO<sub>2</sub> can form sulphuric acid according to equation 1.

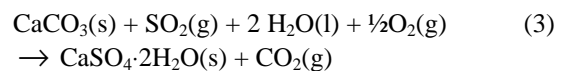
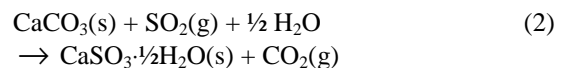


The acidification of the environment caused by the formation of sulphuric acid in the atmosphere has been associated with a number of detrimental effects, such as

- A reduction of biodiversity.
- Reduced crop and forest growth.
- Damage to buildings and architectural heritage.

Emitted SO<sub>2</sub> can furthermore contribute to the formation of aerosols in the atmosphere, affecting human health through respiratory and cardiovascular diseases.

In order to reduce these detrimental effects a range of FGD technologies have been developed and installed at power plants all over the world. The vast majority of the installed FGD capacity consists of the wet scrubber FGD technology [2] that either produces CaSO<sub>3</sub> sludge (equation 2) or CaSO<sub>4</sub>·2H<sub>2</sub>O/gypsum (equation 3) depending on the operating conditions.



Most European power plants use the gypsum-producing forced oxidation process (equation 3),

because of the sales potential of the gypsum for either wallboard or cement production. The sales potential of the produced gypsum depends on parameters such as the particle size distribution (PSD), the moisture content and the impurity content.

A better understanding of the gypsum crystallisation kinetics could facilitate a more consistent gypsum quality and point to ways of manipulating the gypsum properties. The incorporation of crystallisation kinetics predicting the gypsum PSD into mathematical process models is one way to obtain an increased control and understanding of the FGD process.

Non-wanted and unexpected foaming in wet FGD plants has been observed at several Danish power plants. This has caused a range of problems like scaling at the demister and FGD unit shut down, due to foam overflow from the reactor. The origin of this phenomenon is unknown and will be investigated with the aim of controlling foaming in wet FGD plants.

### Specific Objectives

The overall objectives of this PhD project are:

- Derivation of crystallisation and degradation kinetics for the prediction of gypsum PSD.
- Investigation of the origin of foaming and the development of methods to control it in wet FGD plants.
- The use of the obtained results to optimize the operation of wet FGD plants

### Crystallisation

The crystallisation process describes the formation and growth of solid crystals from a solution. Crystallisation can be encountered in nature or it can be used industrially as a solid liquid separation technique.

Before crystallisation can take place the solution must be supersaturated with respect to the crystal forming species. Super saturation can be obtained by either changing the solubility of the solution or by the formation of a product with a lower solubility than the reactants. The following different techniques may be used:

- Solution cooling.
- Solvent evaporation.
- Chemical reaction.
- The addition of an additional solvent (drowning out).
- Change of the pH.

The first step in the crystallisation process is the gathering of solute molecules into clusters (nuclei). Depending on whether the clusters are below or above a certain size (the critical cluster size) they may either redissolve or grow. The critical cluster size is a function of parameters such as super saturation and temperature. The process described above is known as homogenous nucleation, however new crystal may also be formed by heterogeneous or secondary nucleation. Heterogeneous

nucleation is the formation of “new” particles by precipitation on particles of other species. Secondary nucleation is the formation of new crystals by particle attrition caused by particle/particle, particle/wall or particle/stirrer collisions.

The next step of the crystallisation process is the subsequent growth of the formed nuclei. The crystal growth process consists of transport of the solute molecule to the surface, surface diffusion and incorporation into the crystal structure. The transport of solute molecules to the crystal surface depends on the concentration gradient and thereby the super saturation. The topography of the surface offers a range of different binding sites, the most favourable ones constitute only a small fraction of the total number of binding sites. Because of this even a small amount of a species preferably absorbed on these sites may have a significant effect on the rate of molecule incorporation (crystal growth) and the resulting crystal morphology. An example of the gypsum crystal morphology seen at full-scale wet FGD plants is shown in figure 2.

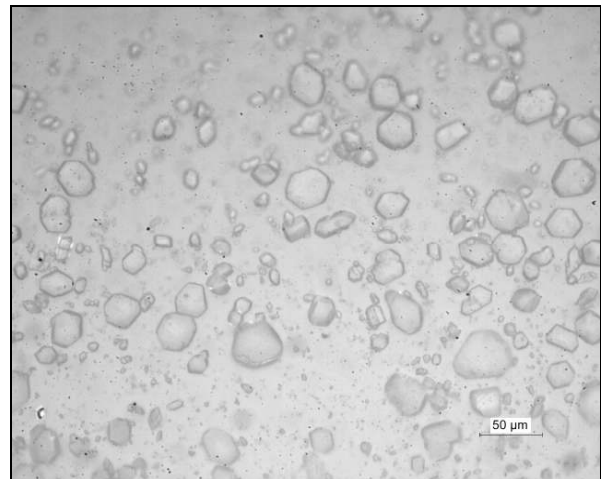


**Figure 2:** Morphology of gypsum crystals from a full scale wet FGD plant.

Apart from crystal nucleation and crystal growth the following other processes may take place within a crystalliser.

- Crystal breakage.
- Crystal agglomeration.
- Dissolution of small crystals and growth of large crystals (Ostwalds ripening)

### Experimental setup

The wet FGD pilot plant simulates a single vertical channel of the packing zone in a full-scale wet FGD plant (250 MW<sub>e</sub> coal fired power plant unit). The basic outline of the pilot plant is illustrated by figure 3. A 110 kW natural gas boiler and subsequent SO<sub>2</sub> addition generates the SO<sub>2</sub> containing flue gas. The flue gas is then brought into contact with the slurry in the absorber (a 7 m pipe with multiple sampling sites). The slurry leaving the absorber is collected in a hold-up tank where air injection and reactant addition take place. The pH of the holding tank is kept constant by an on/off control of the feed stream. A timer-controlled pump removes the slurry that exceeds a given level, ensuring a constant slurry level in the holding tank. The time to reach steady state operation is roughly a week.

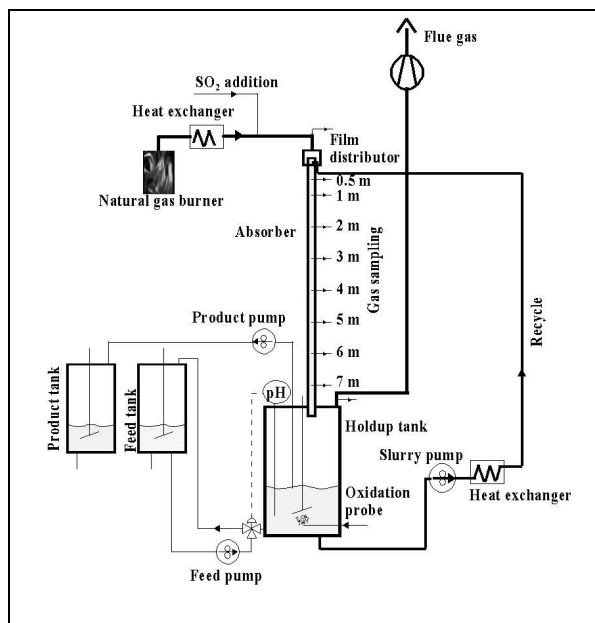


Figure 3: Principal diagram of the wet FGD pilot plant.

### Pilot plant experiments

Initial experiments have been focused on the extent of the mechanical crystal degradation taking place in the wet FGD pilot plant. Samples of gypsum slurry have been subjected to the mechanical stresses caused by stirring, recirculation and air injection for up to 600 hrs. The development in PSD as a function of time was monitored by analysing slurry samples with a Malvern Mastersizer S (laser diffraction measurements). No significant degree of degradation took place at short exposure times, but longer exposure times caused a decrease in the volume fraction of particles above approximately 25 μm and a corresponding increase in the volume fraction of particles below this size. The increased fraction of small particles may cause a reduced dewatering potential of the gypsum. Various breakage models are being tested against the experimental data.

Subsequently the effect of parameters such as the presence of additives and slurry saturation on the rate of nucleation and crystal growth will be investigated.

### Full scale experiments

A survey of the gypsum quality at a range of Danish full-scale wet FGD plants will be performed. It is the aim of this survey to collect and compare gypsum quality parameters and operational parameters of the selected wet FGD plants. A selected FGD unit is furthermore to be monitored during a couple of weeks operation, in order to obtain knowledge on the effect of operational variations on the slurry composition and ultimately the gypsum quality.

The quality and operational parameters include:

- PSD.
- Morphology.
- Slurry saturation and composition.
- Crystal residence time.
- Density.

The campaign has been initiated by a 3 weeks measurement series at a 250 MW<sub>e</sub> Danish wet FGD plant. The processing and interpretation of the obtained measurements is still ongoing.

### Acknowledgements

This work is part of the MP<sub>2</sub>T Graduate School within the CHEC (Combustion and Harmful Emission Control) Research Center funded a.o. by the Technical University of Denmark, the Danish Technical Research Council, the European Union, the Nordic Energy Research, Dong Energy A/S, Vattenfall A.B., F L Smidth A/S, and Public Service Obligation funds from Energinet.dk and the Danish Energy Research program.

### References

1. World energy outlook, International Energy Agency (IEA) & Organisation for Economic Co-operation and Development (OECD), Paris, France, 2004, p. 570.
2. H.N. Soud, Developments in FGD, IEA Coal Research, London, U.K., 2000, p. 138.





**Natanya Majbritt Louie Hansen**

Phone: +45 4525 6819  
Fax: +45 4588 2161  
E-mail: nha@polymers.dk  
WWW: <http://www.student.dtu.dk/~s960919>

Supervisors: Søren Hvilsted  
Michael Gerstenberg, Novo Nordisk A/S

Ph.D. Study  
Started: January 2004  
To be completed: March 2007

## Synthesis of Amphiphilic Block Copolymers by Atom Transfer Radical Polymerization

### Abstract

Fluorinated copolymers have been targeted, as these have a number of desirable properties including chemical inertness and low surface energy. Block copolymers of methyl methacrylate (MMA) and three fluorinated methacrylates have been polymerized by controlled radical polymerization (ATRP). Copolymerizations proceeded in a controlled fashion and polydispersities were low. Kinetic experiments evidenced that the length of the fluorinated pendant chain did not influence the reactivity in ATRP. Controlled polymerizations of MMA were undertaken using a fluorinated macroinitiator, hereby incorporating fluorine in the final product by an approach complementary to copolymerization.

### Introduction

Fluorinated polymers are highly hydrophobic and have recently received increased interest due to a number of unique properties including high biocompatibility and low surface energy, as well as high chemical and thermal resistance.

Controlled radical polymerization methods have been used to synthesize fluorinated block copolymers used to prepare low energy surfaces including water- and oil-repellent materials[1,2]. Several fluorinated surface active compounds have been synthesized by controlled radical polymerizations and successfully used to assist polymerizations of non-fluorinated polymers in supercritical carbon dioxide[3,4]. Biomimicking and potentially biocompatible copolymers have been introduced by combining inert fluoropolymers with biopolymers or polymers known to circumvent immunological rejection[5,6,7,8,9]. The chemical inertness of fluorine has been exploited for synthesizing fluorinated copolymers for coatings on metals that form a corrosion-protective layer on the surface[10]. Surface-initiated polymerizations of (co)polymer brushes on various surfaces have produced hydrophobic surfaces [11,12] as well as materials that are tunable in hydrophobicity and permeability dependant on treatment in terms of change in pH, temperature, or solvent[13,14,15,16]. A range of porous membranes with three-dimensionally ordered structures have been prepared and some have shown great potential as

proton-conducting materials for applications such as solid-state electrolytes in batteries[17].

Fluorinated compounds including commercially available polymers have been used as macroinitiators for non-fluorinated monomers to incorporate a fluorinated species in this way[18,19,20]. Focus in the area has especially been on tethering brushes of non-fluorinated polymers onto the fluoropolymer in this way benefiting from the inertness of the parent polymer and enhancing performance with respect to antifouling, conduction and/or permeability[21,22,23].

### Objective

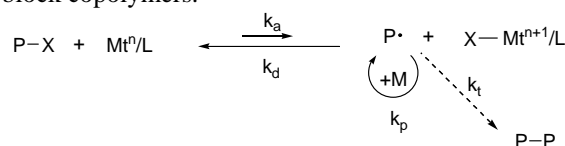
In our work fluorinated polymers were synthesized by the two different synthetic routes. **1.** Fluorinated monomers were copolymerized with non-fluorinated monomers yielding block copolymers. **2.** A commercially available fluorinated surfactant was utilized as a macroinitiator for the polymerization of a non-fluorinated monomer. For both approaches atom transfer radical polymerization (ATRP)[24,25] was chosen as the polymerization method.

### Synthesis method

The strategy chosen for the synthesis of the copolymers, ATRP, is a technique of controlled/"living" radical polymerization. The method involves the use of a transition metal catalyst (Mt), a multidentate ligand (L) and a halogenated initiator, which all interact with the active polymer chain (see Scheme 1). There exists

equilibrium between an activated (P·) and a dormant (P-X) polymer species with the deactivation reaction being kinetically favoured. Ideally, this eliminates the possibility of two activated polymer chain ends encountering to give termination, while in practice termination does occur to a small extent.

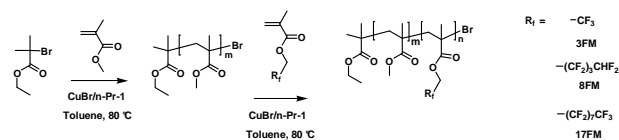
Using the ATRP method polymer products with well-defined structures and narrow molecular weight distributions can be obtained and the potential polymer structures are numerous. The product of an ATRP reaction is a potential initiator for yet another reaction, as it still has the halogen moiety in the growing chain end. This allows reactivation of the chain end and makes ATRP especially suited for synthesizing tailored block copolymers.



**Scheme 1.** Mechanism of ATRP. Mt=metal catalyst, P=polymer chain, X=halogen, M=monomer, L=ligand.  $k_a$ ,  $k_d$ ,  $k_p$  and  $k_t$  are the rates of activation, deactivation, propagation and termination, respectively.

### Copolymerization of fluorinated monomers and methyl methacrylate.

Three different fluorinated monomers were studied in copolymerization with methyl methacrylate (MMA) (Scheme 2). Polymerizations took place in toluene (50 vol-% solution) utilizing Cu(I)Br as catalyst and *N*-(*n*-propyl)-2-pyridylmethanimine (n-Pr-1) as ligand. Ethyl-2-bromoisobutyrate (EBB) was used as initiator.



**Scheme 2.** Copolymerization of MMA with fluorinated methacrylates 3FM, 8FM and 17FM.

### Homopolymerization of 3FM

To study the kinetics of the reaction homopolymerizations of the smallest fluorinated monomer 3FM was undertaken. Reactions were run at 4 different temperatures; 80, 90, 100 and 110 °C. The polymerization proceeded in a controlled fashion at all temperatures with linear first-order plots, molecular weights ( $M_n$ ) increasing with conversion and low polydispersities (PDI) throughout reaction. The first-order kinetic plots for all the homopolymerizations are shown in figure 1, while an example of molecular weight evolution is given in figure 2. The results of all the homopolymerizations are given in table 1. The indicated molecular weights are, however, probably lower than the actual values due to the difference in molecular weight of the 3FM-unit and the MMA-standards used for the size exclusion chromatography analysis (SEC). It was not possible to use  $^1\text{H-NMR}$  for end-group analysis to estimate molecular weights, as the

signal from the initiator and the signals from the polymer backbone overlap.

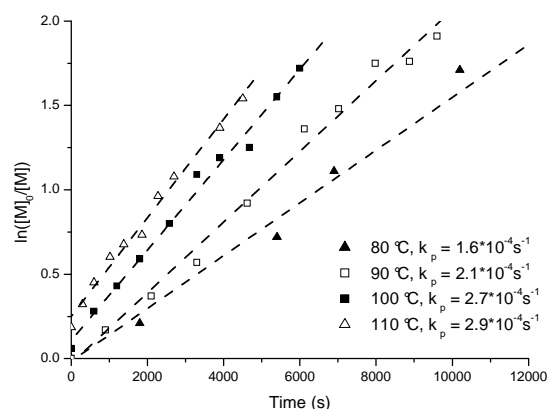


**Figure 1.** First-order plot of homopolymerizations of 3FM at 80 °C (▲), 90 °C (□), 100 °C (■) and 110 °C (△).  $[\text{I}]:[\text{Cu(I)Br}]:[\text{n-Pr-1}] = 1:1:2$ .

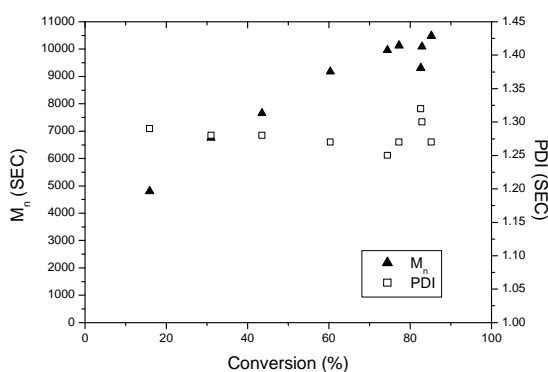


**Figure 2.** Evolution of  $M_n$  (▲) and PDI (□) for the synthesis of P3FM at 90 °C (entry II, table 1).  $[\text{I}]:[\text{Cu(I)Br}]:[\text{n-Pr-1}] = 1:1:2$

**Table 1.** Data for the homopolymerization of 3FM

	Temperature (°C)	Time (min)	Conversion (%)	$M_n$ SEC	PDI
I	80 °C	320	94	9,900	1.35
II	90 °C	160	85	8,800	1.38
III	100 °C	100	82	7,900	1.34
IV	110 °C	75	79	6,200	1.28

$$[\text{I}]:[\text{Cu(I)Br}]:[\text{n-Pr-1}] = 1:1:2.$$

The kinetic study exhibited a clear temperature dependency demonstrated by the acceleration of the polymerization reaction with increasing temperature. Apparent rate constants of reactivity,  $k_p^{\text{app}}$  ranging from  $1.6 \cdot 10^{-4} \text{ s}^{-1}$  to  $2.9 \cdot 10^{-4} \text{ s}^{-1}$  were found, which is in good agreement with the value of  $1.2 \cdot 10^{-4} \text{ s}^{-1}$  previously found for MMA at 90 °C in an identical reaction system[26]. The polymerization rate of 3FM was seen to be faster than for MMA, which has also been the observation for a number of fluoro-substituted styrenes compared to styrene in ATRP[27,28,29].

The polymerization proceeded in a controlled fashion at all temperatures with molecular weights increasing with conversion and relatively low

polydispersities (<1.4). The activation energy of the reaction can be found from the Arrhenius plot shown in figure 3, where the slope is equivalent to  $E_a/RT$ . From this  $E_a$ , the activation energy, of the polymerization is found to be 24 kJ/mol. This is a significantly lower than the one found by Haddleton et al. in the homopolymerization of MMA in toluene (25 % solution); 61 kJ/mol[30].

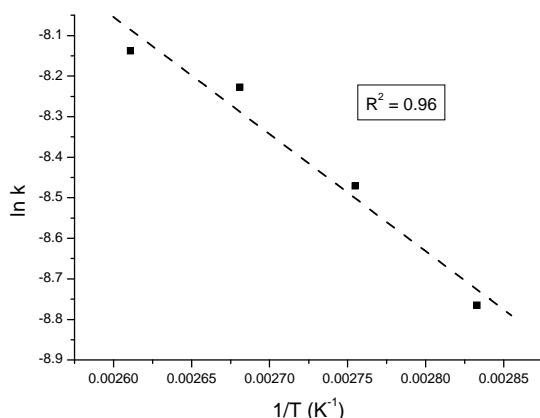


**Figure 3.** Arrhenius plot of the rate constants of reactivity for the homopolymerization of 3FM at 80, 90, 100 and 110 °C.  $[I]:[Cu(I)Br]:[n-Pr-1] = 1:1:2$ .

#### Synthesis of copolymers of 3FM and MMA

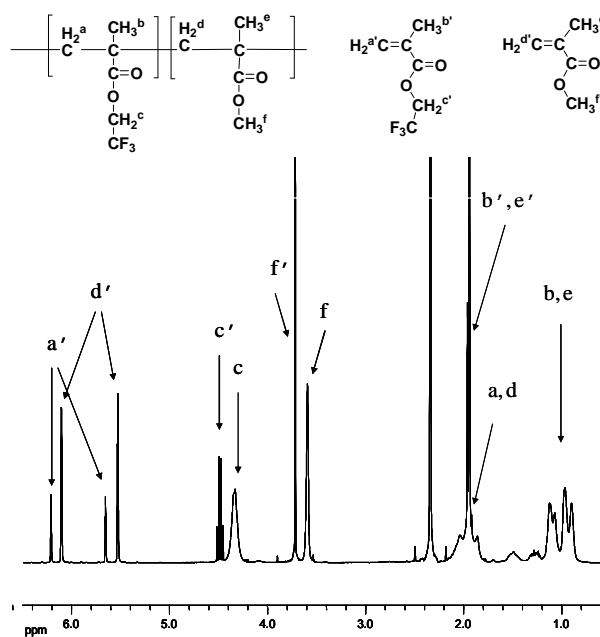


**Figure 4.**  $^1H$ -NMR-spectrum of a sample taken during the polymerization of P3FM-*b*-PMMA in toluene (only  $\phi-CH_3$   $\delta$  2.34 (s) from the solvent shown). Assignments according to the structures above are indicated by the arrows.

The monomer with the lowest amount of fluorine, 3FM, is the most soluble and therefore studies were initially undertaken with this monomer in copolymerization with MMA. Conversions were estimated from  $^1H$ -NMR-analysis using the peak for

$CH_2-CF_3$  in the fluorinated methacrylate:  $\delta_H$  4.49 (q) (monomer) and  $\delta_H$  4.33 (polymer) as shown in figure 4. Similarly the conversion of MMA was determined from the shift of the  $CH_3$ -group from  $\delta_H$  3.72 (s) in the monomer to  $\delta_H$  3.59 in the polymer.

The synthesis of the block copolymers were run as sequential polymerizations where the second monomer was added at relatively high conversions of the first monomer, with both monomers continuing to polymerize after addition, as observed by  $^1H$ -NMR to give a gradient copolymer.

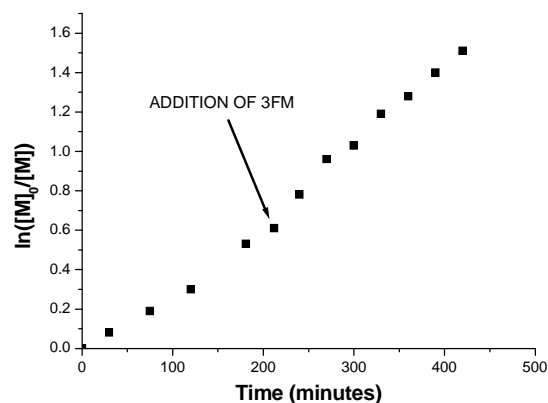


**Figure 5.** First-order kinetic plot of the synthesis of PMMA-*b*-P3FM (entry IV, table 2).

The first-order kinetic plot of the synthesis of PMMA-*b*-P3FM (fig. 5) was linear indicating a low amount of termination. Evolution of molecular weight was linear with conversion as seen in figure 6 and PDI's were low evidencing a controlled reaction mechanism.

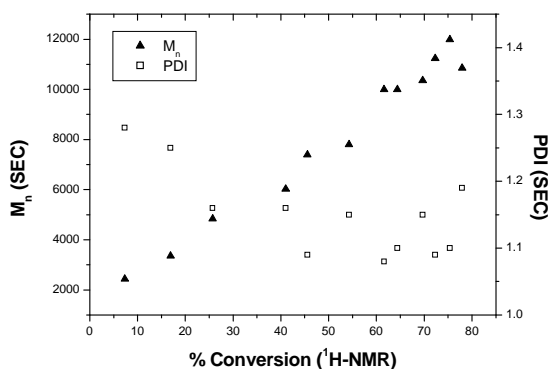


**Figure 6.** Evolution of  $M_n$  and PDI for the synthesis of PMMA-*b*-P3FM (entry IV, table 2).

For the polymerization of MMA from P3FM a small induction period was observed for the initiation of the second monomer. Narrower molecular weight distributions were obtained for the polymerization of 3FM from PMMA than for the converse approach, as can be seen in table 2. This may be due to the low solubility of P3FM in the solvent impeding further reaction. SEC-analysis showed a bimodal distribution for the synthesis of P3FM-*b*-PMMA (fig 7) indicating that some termination took place with the addition of the second monomer, whereas this was not the case for PMMA-*b*-P3FM (fig 8). All the distributions obtained

are, however, comparable with those found for the homopolymerization of 3FM, which indicates that these are the optimal results achievable with the given system. The values are also comparable with those found by Perrier et al.[31] in a very similar system.

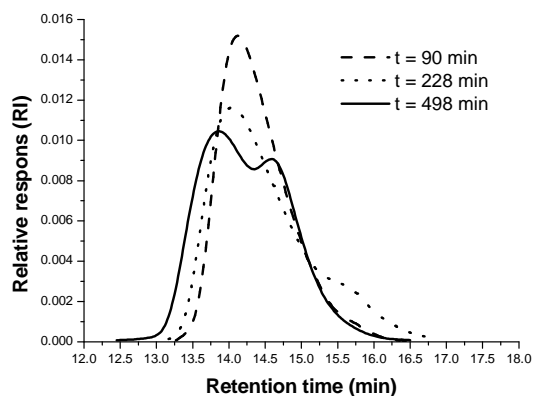


**Figure 7.** SEC-curves for the synthesis of P3FM-*b*-PMMA (entry I, table 2).

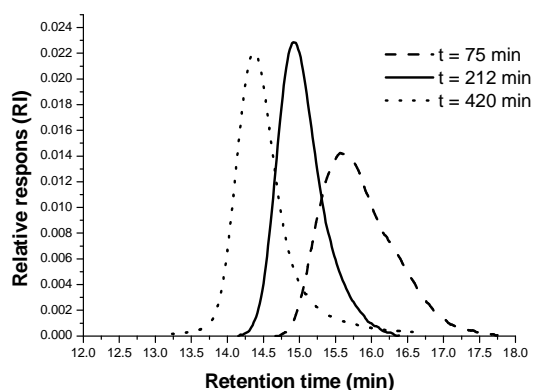


**Figure 8.** SEC-curves for the synthesis of PMMA-*b*-P3FM (entry IV, table 2).

**Table 2.** Copolymers of MMA and fluorinated monomers, 3FM, 8FM and 17FM

	Copolymer	[M <sub>1</sub> ]:[M <sub>2</sub> ]	M <sub>n</sub> ,	PDI
			SEC	
I	P3FM- <i>b</i> -PMMA	1 : 1	10,300	1.33
II	P3FM- <i>b</i> -PMMA	1 : 1	7,900	1.30
III	P3FM- <i>b</i> -PMMA <sup>a</sup>	1 : 1	9,200	1.50
IV	PMMA- <i>b</i> -P3FM	1.6 : 1	9,600	1.09
V	PMMA- <i>b</i> -P8FM	2.4 : 1	9,300	1.18
VI	PMMA- <i>b</i> -P17FM <sup>a</sup>	4.6 : 1	10,300	1.24

[I]:[Cu(I)Br]:[*n*-Pr-1] = 1:1:2, Reaction temperature: 80 °C. <sup>a</sup>Polymerized at 90 °C.

#### Synthesis of block copolymers with 8FM and 17FM

While the homopolymerization of 3FM could be monitored by <sup>1</sup>H-NMR (in CDCl<sub>3</sub>), it was not possible to use this technique for the homopolymerization of 8FM and 17FM due to low solubility of the polymers in the solvent. As we wished to obtain products that could be solubilized in non-fluorinated solvents, the approach synthesizing the fluorinated segment first was

abandoned for said monomers and only block copolymers generated from PMMA were synthesized i.e. PMMA-*b*-P8FM and PMMA-*b*-P17FM. Conversions were estimated from <sup>1</sup>H-NMR-analysis as before and the first-order kinetic plots were similar to those acquired for the synthesis of PMMA-*b*-P3FM and were linear for both polymerizations. Evolution of molecular weight of the copolymeric products was observed to be linear with conversion and SEC-analysis showed monomodal traces with low PDI's evidencing a controlled reaction mechanism.

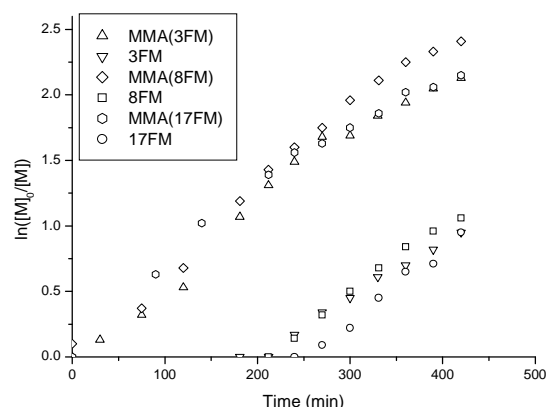
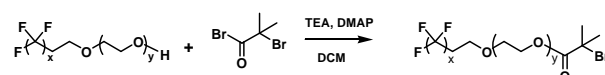


**Figure 9.** Individual conversions of MMA and fluorinated monomers in the synthesis of PMMA-*b*-P<sub>x</sub>FM copolymers.

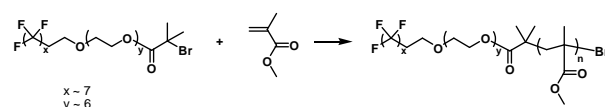
Comparison of the kinetics of the 3 fluoromonomers indicates that the fluorinated pendant chain does not influence the rate of polymerization as long as the product is soluble under reaction conditions. In figure 9 the conversions of both MMA and fluorinated monomers in the synthesis of PMMA-*b*-P<sub>x</sub>FM copolymers are shown. There are no significant differences between the curves evidencing similar reactivity of the monomers, thereby proving the influence of the fluorinated segment only to be important in terms of solubility.

#### Synthesis of the fluorinated macroinitiator

The surfactant Zonyl FSO-100® used previously by Perrier et al.[18,31] and Shemper et al.[19] was converted to a macroinitiator species by transesterification according to the method by Jankova et al[32] (Scheme 3).



**Scheme 3.** Synthesis of fluorinated macroinitiator, FMI from Zonyl FSO-100® by transesterification with 2-bromoisobutyryl bromide.



**Scheme 4.** Polymerization of MMA using the fluorinated macroinitiator, FMI.

Polymerizations of MMA (Scheme 4) were carried out with different initiator to monomer ratios, and reaction kinetics were compared to the conventional ATRP initiator EBB.

### Polymerization of MMA

Three different molecular weights were targeted in the polymerization of MMA with the fluorinated macroinitiator, FMI: 5,000; 10,000 and 20,000 g/mol. The kinetic plots can be seen in figure 10, which shows that the polymerization proceeds as a pseudo first-order reaction in all cases indicating a controlled mechanism. Rates of polymerization also increased with decreasing monomer to initiator ratio as expected. Evolution of molecular weights were linear with conversion in all cases (Fig. 11) and PDIs were low (<1.25) evidencing the “living” nature of the reactions.

**Table 3.** Polymerization of MMA by ATRP using a fluorinated macroinitiator.

Sample	[I]:[M]	$M_n$	$M_n$	$M_n$	PDI
		theory	SEC	NMR	
1	1 : 50	5,000	11,100	5,100	1.17
2	1 : 100	10,000	11,600	8,000	1.21
3	1 : 200	20,000	29,900	14,200	1.24

[I]:[Cu(I)Br]:[n-Pr-1] = 1:1:2, Reaction temperature: 90 °C.

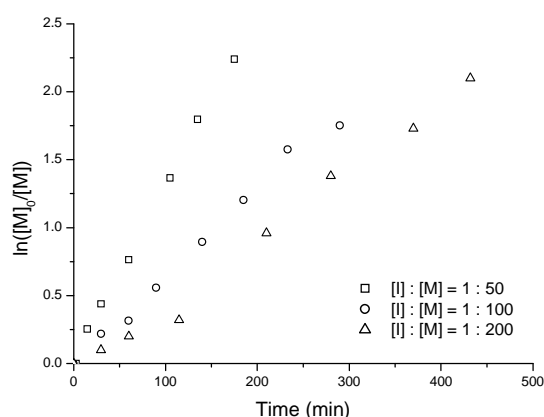


**Figure 10.** First-order kinetic plots of the polymerization of MMA from FMI. [I]:[Cu(I)Br]:[n-Pr-1] = 1:1:2, Reaction temperature: 90 °C.

The molecular weights of the FMI-PMMA polymers were further estimated by <sup>1</sup>H-NMR using the signal from the polyethylene glycol functionality in the macroinitiator  $\delta$  3.62 and comparing with the signal from the monomer at  $\delta$  3.58 (OCH<sub>3</sub>). Due to the adjacency of the signals the molecular weights obtained in this fashion are only rough estimates. The results obtained by <sup>1</sup>H-NMR were lower than those found by SEC-analysis in all cases, but showed the same tendencies i.e. lower molecular weight at relatively higher concentration of initiator, which is as expected.

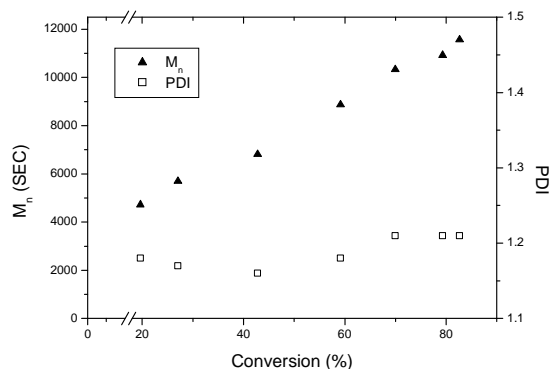


**Figure 11.** Evolution of  $M_n$  (▲) and PDI (□) for the polymerization of MMA from FMI. [M]:[I]:[Cu(I)Br]:[n-Pr-1] = 100:1:1:2.

SEC-analysis showed monomodal curves (figure 12), however a high molecular weight shoulder was seen for all reactions at high conversion, which could possibly be due to the surfactant nature of the initiator resulting in aggregation of the polymer.

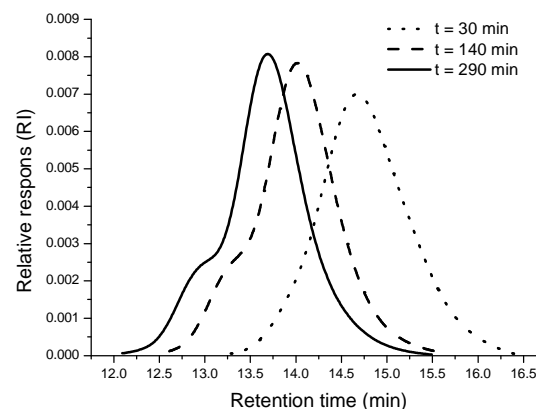


**Figure 12.** SEC-curves of the synthesis of FMI-PMMA [M]:[I]:[Cu(I)Br]:[n-Pr-1] = 100:1:1:2

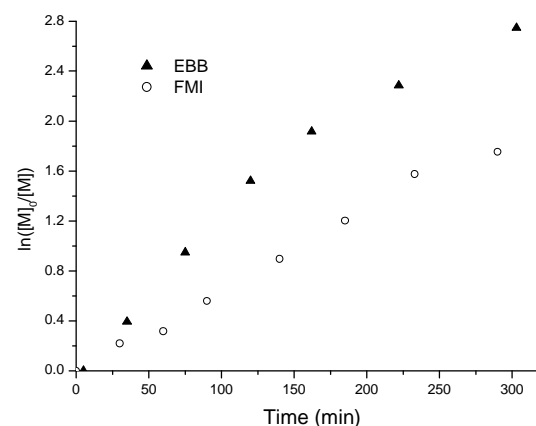


**Figure 13.** First-order kinetic plots of the polymerization of MMA from FMI (O) and EBB (▲). Reaction temperature: 90 °C. [M]:[I]:[CuBr]:[n-Pr-1] = 100:1:1:2.

Polymerization of MMA (target 10,000 g/mol) using EBB showed that the reactivity of FMI was comparable with EBB (figure 13). Almost identical polymerization rates for these two initiators were found by Perrier et al[18] when using the same type of system with a slightly different ligand (pentyl vs. propylfunctionalized methanimine). In that case, however an increase of the reaction rate was seen at higher conversions for the fluorinated macroinitiator, which we did not observe.

### Conclusions

Block copolymers of MMA and fluorinated methacrylates were polymerized by controlled radical polymerization (ATRP). It was possible to synthesize block copolymers starting from 3FM, although the converse approach yielded better results. Well-defined block copolymers of MMA and 8FM and 17FM, respectively were synthesized. Kinetic experiments evidenced that the length of the fluorinated pendant chain does not influence the reactivity in ATRP. Controlled polymerizations of MMA were undertaken using a fluorinated macroinitiator based on a commercially available fluorinated surfactant. Although the macroinitiator resulted in slower reaction kinetics than the conventional ethyl-2-bromoisobutyrate the obtained results were comparable in terms of molecular weight distributions.

### Acknowledgements

I would like to thank Novo Nordisk A/S for supporting my project. Professor D.M. Haddleton, University of Warwick is thanked for co-supervision on the work reported in this paper.

### Reference List

- Li, K., Wu, P. P., and Han, Z. W. *Polymer* 43(14) (2002) 4079-4086
- Wang, F., Li, H., Zhang, Z. B., Hu, C. P., and Wu, S. S. *J. Polym. Sci. Part A:Polym. Chem.* 42(19) (2004) 4809-4819
- Yang, Y. J., Wang, Z., Gao, Y., Liu, T., Hu, C. P., and Dong, Q. *Z. J. Appl. Polym. Sci.* 102(2) (2006) 1146-1151
- Woods, H. M., Nouvel, C., Licence, P., Irvine, D. J., and Howdle, S. M. *Macromolecules* 38(8) (2005) 3271-3282
- Villarroya, S., Zhou, J. X., Duxbury, C. J., Heise, A., and Howdle, S. M. *Macromolecules* 39(2) (2006) 633-640
- Eberhardt, M. and Theato, P. *Macromol. Rapid Commun.* 26(18) (2005) 1488-1493
- Lim, K. T., Lee, M. Y., Moon, M. J., Lee, G. D., Hong, S. S., Dickson, J. L., and Johnston, K. P. *Polymer* 43(25) (2002) 7043-7049
- Hussain, H., Budde, H., Horing, S., and Kressler, J. *Macromol. Chem. Phys.* 203(14) (2002) 2103-2112
- Inoue, Y., Watanabe, J., Takai, M., Yusa, S., and Ishihara, K. *J. Polym. Sci. Part A:Polym. Chem.* 43(23) (2005) 6073-6083
- Roche, V., Vacandio, F., Bertin, D., and Massiani, Y. *J. Electroceram.* 16(1) (2006) 41-47
- Plackett, D., Jankova, K., Eggsgaard, H., and Hvilsted, S. *Biomacromolecules* 6(5) (2005) 2474-2484
- Andruzzi, L., Hexemer, A., Li, X. F., Ober, C. K., Kramer, E. J., Galli, G., Chiellini, E., and Fischer, D. A. *Langmuir* 20(24) (2004) 10498-10506
- Granville, A. M. and Brittain, W. J. *Macromol. Rapid Commun.* 25(14) (2004) 1298-1302
- Granville, A. M., Boyes, S. G., Akgun, B., Foster, M. D., and Brittain, W. J. *Macromolecules* 37(8) (2004) 2790-2796
- Chen, R. X., Feng, C., Zhu, S. P., Botton, G., Ong, B., and Wu, Y. L. *J. Polym. Sci. Part A:Polym. Chem.* 44(3) (2006) 1252-1262
- Ying, L., Yu, W. H., Kang, E. T., and Neoh, K. G. *Langmuir* 20(14) (2004) 6032-6040
- Fu, G. D., Yuan, Z. L., Kang, E. T., Neoh, K. G., Lai, D. M., and Huan, A. C. H. *Adv. Funct. Mater.* 15(2) (2005) 315-322
- Perrier, S., Jackson, S. G., Haddleton, D. M., Ameduri, B., and Boutevin, B. *Tetrahedron* 58(20) (2002) 4053-4059
- Shemper, B. S. and Mathias, L. J. *Eur. Polym. J.* 40(4) (2004) 651-665
- Lu, G. L., Zhang, S., and Huang, X. Y. *J. Polym. Sci. Part A:Polym. Chem.* 44(18) (2006) 5438-5444
- Zhai, G. Q., Shi, Z. L., Kang, E. T., and Neoh, K. G. *Macromol. Biosci.* 5(10) (2005) 974-982
- Shi, Z. Q. and Holdcroft, S. *Macromolecules* 38(10) (2005) 4193-4201
- Chen, Y. W., Liu, D. M., Deng, Q. L., He, X. H., and Wang, X. F. *J. Polym. Sci. Part A:Polym. Chem.* 44(11) (2006) 3434-3443
- Kato, M., Kamigaito, M., Sawamoto, M., and Higashimura, T. *Macromolecules* 28(5) (1995) 1721-1723
- Wang, J. S. and Matyjaszewski, K. *J. Am. Chem. Soc.* 117(20) (1995) 5614-5615
- Haddleton, D. M., Crossman, M. C., Dana, B. H., Duncalf, D. J., Heming, A. M., Kukulj, D., and Shooter, A. J. *Macromolecules* 32(7) (1999) 2110-2119
- Qiu, J. and Matyjaszewski, K. *Macromolecules* 30(19) (1997) 5643-5648
- Jankova, K. and Hvilsted, S. *Macromolecules* 36(5) (2003) 1753-1758
- Hvilsted, S., Borkar, S., Siesler, H. W., and Jankova, K. *ACS Symposium Series 854, Advances in Controlled/Living Radical Polymerization* (2003) 236-249
- Haddleton, D. M., Kukulj, D., Duncalf, D. J., Heming, A. M., and Shooter, A. J. *Macromolecules* 31(16) (1998) 5201-5205
- Perrier, S., Jackson, S. G., Haddleton, D. M., Ameduri, B., and Boutevin, B. *Macromolecules* 36(24) (2003) 9042-9049
- Jankova, K., Chen, X. Y., Kops, J., and Batsberg, W. *Macromolecules* 31(2) (1998) 538-541



**Thomas Steen Hansen**

Phone: +45 4525 6807  
 Fax: +45 4525 2161  
 E-mail: tsh@polymers.dk  
 WWW: http://www.dtu.dk/Centre/DPC  
 Supervisor: Ole Hassager

Ph.D. Study  
 Started: October 2004  
 To be completed: September 2007

**Testing and Fabrication of All Polymer Micropump**

**Abstract**

The main objective of the project is to fabricate and test microfluidic pumps produced in polymers. Currently the main field of research is the AC electroosmotic micropump, which has the advantage of a simple structure, no movable parts and low requirements to the applied potential. The AC electroosmotic micropump has been constructed using conductive polymers (CP) with a channel system consisting of polyurethane. Before the pump could be realised a number of new processing methods had to be developed. This has let to new knowledge about blending of CP with non conductive polymers and new fabrication methods for patterning of CP. Testing of the all polymer micropump revealed that it exhibited a pumping characteristic similar to pumps made with noble metals.

**Introduction**

The ability to control chemical processes on the micrometer scale has many interesting perspectives and is a field in fast expansion. One of the main issues when dealing with microsystems is the pumping of fluid. Several techniques have been used for this purpose and one of the most interesting is the electroosmotic pump. A special case of this pump is the asymmetric AC electroosmotic pump (ACEO) first suggested by Ajdari [1]. The pump consists of an array of asymmetric electrodes in a channel with an AC potential between

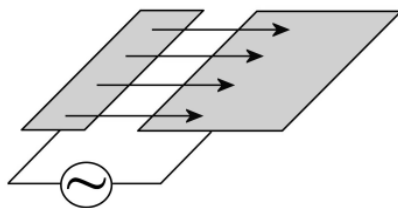


**Figure 1:** The principle of an ACEO pump. The asymmetric shape of the electrodes creates an asymmetric electric field, which induces a non-zero horizontal force to the ions in the fluid. The friction between the ions and the fluid creates a pumping effect from the small to the large electrode.

the electrodes. This is presented in figure 1. The advantages of the pump are the uncomplicated construction, no moveable parts and low potential (1-5 V) requirements. The ACEO pump has been described both experimentally [2-7] and theoretically [1], [2], [8] [9], but no numerical simulations of the system have

been performed. As a mean to optimise the geometry numerical simulations of the ACEO pump were therefore conducted.

**Theory**

The three governing equations when simulating the ACEO pump are Poisson's equation (1), the mass transfer equation (2) and the incompressible Navier-Stokes equation (3).

The electric regime is described by Poisson's equation, and simplifying the system to a monovalent salt yields equation (1) where  $\phi$  is the potential,  $\rho$  is the space charge density and  $\epsilon$  is the dielectric constant of the fluid,  $F$  is Faradays constant,  $c^+$  and  $c^-$  are the concentration of the positive and negative ions.

$$\nabla\phi = -\frac{\rho}{\epsilon} = -\frac{F(c^+ - c^-)}{\epsilon} \tag{1}$$

The flux of the charged ions is found by using the mass transfer equation (2), where  $D$  is the diffusion coefficient,  $\mathbf{v}$  is the flowfield with the components  $v_x$  and  $v_y$ ,  $z$  is the charge of the ion and  $u$  is mobility [10].

$$\frac{\partial c_i}{\partial t} + \mathbf{v} \cdot \nabla c_i = D_i \nabla^2 c_i + z_i u_i \nabla \cdot (c_i \nabla \phi) \tag{2}$$

The fluid mechanical part of the system is evaluated by the incompressible Navier-Stokes equation (3a) and (3b), where  $\rho_{\text{dens}}$  is the density of the fluid,  $\mu$  is the viscosity and  $p$  is the pressure. The last term in eq. (3a) is the force caused by the moving ions.

$$\rho_{dens} \left( \frac{\partial \mathbf{v}}{\partial t} + \mathbf{v} \cdot \nabla \mathbf{v} \right) = -\nabla p + \eta \nabla^2 c_i + \sum z_i F c_i \nabla \phi \quad (3a)$$

$$\nabla \cdot \mathbf{v} = 0 \quad (3b)$$

Using equation (1), (2), and (3) it has been possible to perform numerical simulations of ACEO pump and optimise the geometry to its maximum performance.

### Numerical simulation

The numerical simulations revealed that especially the height of the channel is important for the pumping properties. The propulsion of the fluid occurs at the walls near the surface of the electrodes and in contrary to normal systems the pump is most efficient at low diameters. The maximum pressure delivered by the pump is approximately inversely proportional to the squared height of the channel. Another interesting perspective revealed by the numerical simulations was the pumps ability to pump in both directions. The

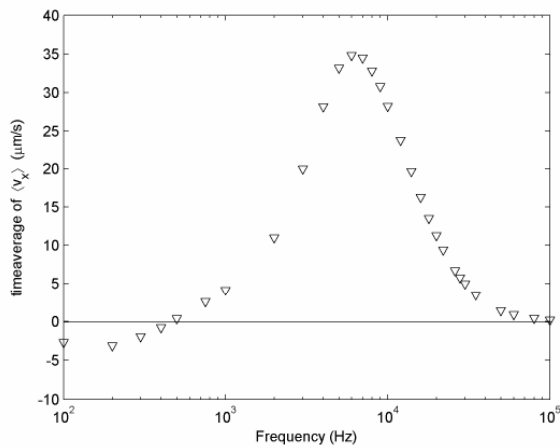


**Figure 2:** A simulated frequency sweep of the micropump. The pump is capable of pumping in the reverse direction at low frequencies.

pumping direction can be reversed by lowering the frequency of the AC potential, which enhances the positive prospects of the ACEO pump. The result of a simulation series is presented in figure 2. In the linear regime below 0.025 volts it has been possible to confirm analytical analysis made in the literature.

These have however not been conducted on the nonlinear regime above 0.025 volts and the numerical simulations in the 'high' potential is therefore used to examine the properties of this system. The studies shown complicated correlations between the maximum velocity in both directions and the potential applied, which have not been shown earlier. The reason for the reverse pumping effect is to be found in the phase shift between the potential and the charge at the surface. At the optimal frequency the charge is shifted 45° from the potential. At low potential the large and small electrode have the same phase shift, but at higher potentials the phase shifts begin to differ. This means that the small

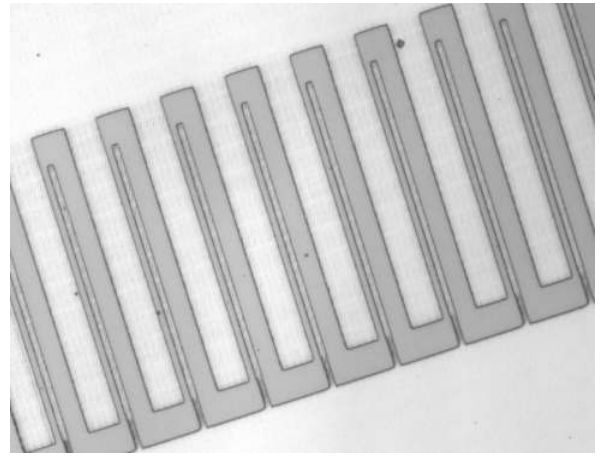


**Figure 3:** A picture of the micropump seen from above. The pump consists of gold (bright) on glass (dark). The small electrodes have a size of 4  $\mu\text{m}$  and the large electrodes have a size of 20  $\mu\text{m}$ .

electrode has the optimal phase shift at low frequencies, and the large electrode has the optimal phase shift at higher frequencies. At low frequencies the small electrode is therefore governing causing the flow to be reversed, whereas at higher frequencies the large electrode takes over and changes the flow direction.

The numerical simulations were followed up with experimental work and pumps were produced using classical lithographic methods for microsystems. A picture of a pump is presented in figure 3. The electrodes are gold layers on glass. The produced pumps have been tested and showed a good pumping effect and the expected ability to pump in both directions. One of the problems with the current design and fabrication method is that the electrode array is damaged at high potentials (above 2-3 V). This problem could be solved by choosing another material than gold for the electrodes, because gold does not have good adhesive properties with glass.

### Conductive polymers

Recent research has shown that it is possible to produce highly conducting polymer films of poly(3,4-ethylenedioxythiophene) (PEDOT) on large areas [11] and with a high stability [12]. This has led to an increasing interest in making all-polymer micropump based on PEDOT. One of the major problems in utilising the reported films is the often poor adhesion of the conducting polymers to glass and non-conducting polymer substrates. Aqueous environment, as required for microfluidic applications, pose particular problems: The adhesion may be so weak that the PEDOT layer sometimes delaminates from the substrate upon immersion in water. A commercial product is available from AGFA (Agfa-Gevaert group, Mortsel Belgium) [13], which can be applied to various substrates by spin coating. However, the surface conductivity of films resulting from this product is significantly lower than films produced by in situ polymerisation. The method developed permits facile application of a PEDOT layer onto most non-conductive polymer substrates and is also demonstrated to be applicable to other conducting polymers.

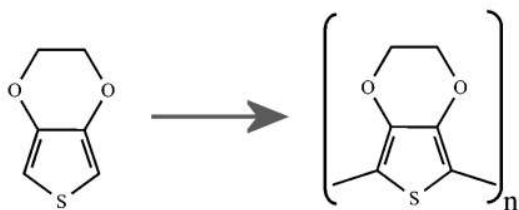


**Figure 4:** The polymerization of 3,4-ethylenedioxythiophene yields the conductive polymer PEDOT.

Winther-Jensen et al. [14] has shown that PEDOT can be anchored to silicon using plasma treatment which permits micro structuring by classical lithographic and lift-off techniques. Furthermore, it has been shown that PEDOT and polypyrrole can be polymerised in polyurethane foam [15] [16] by vapour phase polymerisation resulting in conductivities of  $10^{-3}$ - $10^{-1}$  S/cm. The method developed during this PhD project does not require any vacuum techniques and still yields high conductivity. The conducting polymer is washed into a non-conducting polymer substrate and integrated into the top layer of the substrate structure. The resulting hybrid material acquires some of the mechanical properties of the substrate, while still remaining as conductive as a pristine layer of PEDOT.

We have demonstrated the integration of PEDOT into poly(methyl methacrylate) (PMMA), polycarbonate (PC), cyclic olefin copolymer (COC), poly(ethylene terephthalate) (PET) and polystyrene (PS) with the best results observed on PMMA, PC, or COC. The investigation of the integration of conducting polymers into non-conducting polymer substrates is focussed on the PEDOT on PMMA system, but many of the properties can most likely be extended to other combinations of conducting polymers and substrates.

PEDOT polymer coatings were fabricated using in situ polymerization of EDOT with Fe(III) tosylate as oxidation agent [17,18] and with pyridine as inhibitor [19]. This yields a highly conducting polymer coating with conductivity between 500 S/cm and 1000 S/cm. After polymerisation the polymer layer contains a large amount of residual and spent oxidant from the oxidation. The salt can be removed by washing, usually using water or alcohol, resulting in shrinkage of the polymer structure to 5% of its original thickness [20, 21]. Aben et al. [20] demonstrated trapping of tetraethoxysilane (TEOS) in the shrunken conducting polymer layer by using a TEOS containing washing solution. Later, it has also been shown that a number of conducting polymers can be loaded with macromolecules and other polymers during the washing step [21].

In the present research, the ability to load the conducting polymer is used to integrate it into the surface of a non-conducting polymer substrate. A layer of the conducting polymer is polymerised onto a non-conductive polymer, followed by washing with a solvent that partially dissolves the substrate. The top part of the substrate is washed into the conducting

polymer layer during the shrinkage, and due to entanglement of the polymer chains the conducting polymer layer is effectively integrated into the substrate. Furthermore mechanical and chemical properties of the conducting polymer/substrate surface resemble the substrate surface. This is an advantage because the mechanical strength of conducting polymers can be quite poor. In order to integrate the conducting polymer into a substrate it is required that a solvent exists which is capable of dissolving both the substrate and the residual salt. PEDT on PMMA samples were produced as described previously [12], with surface resistances of 50-100  $\Omega$ /sq, and an optical transmission in the visible range (400-700 nm) of 50-70 %. The integrated PEDT in PMMA samples were coated by Microposit S1813 photoresist using spin coating at 2000 rpm for 30 seconds, and prebaked at 85° C for 20 minutes in a convection oven. The samples were exposed in a mask aligner (365 nm illumination) at a dose of 200 mJ/cm<sup>2</sup> and developed in 15% MF-351 developer for 60 seconds. The samples were then etched in the RIE for 3 minutes at 300 watts and 50 mTorr O<sub>2</sub>. The remaining photoresist was removed by immersing the sample in ethanol for a few minutes. All fabrication steps took place in a class 10 clean room (Clear, Risø National Laboratory). The depth of the integrated PEDOT layer was examined by gradual removal of the surface layer while monitoring its optical and electrical properties. An integrated PEDOT/PMMA sample was made by the production method presented above with a spinning velocity of 500 rpm, which would result in a PEDOT layer with a thickness of 235 nm if washed in water. The sample was placed in a Plasmatherm 740 Reactive Ion Etcher (RIE) (Unaxis, St. Petersburg, FL) and partially covered with a glass microscope slide leaving 1/5 of the sample uncovered. The sample was then etched with 50 sccm O<sub>2</sub> at 50 mbar and a power of 150 watts at 13.56 MHz for 5 seconds. The glass slide was moved to leave 2/5 of the sample uncovered, which was etched again. This procedure was repeated 4 times in all resulting in five different parts which in total had been etched 20, 15, 10, 5 and 0 seconds, respectively. The etching depth of each part was measured by profilometry and is presented in Table 1. The edges between the steps were not as well defined as if the regions had been defined by photolithography. The accuracy of the step heights is approximately  $\pm$  10 nm.

Assuming that all parts of the PEDOT layer contributes equally to the conductance, it is possible to calculate how the PEDOT is distributed in the PMMA. The surface resistance of each layer was measured using the four point probe described above, and based on comparison with the undiluted thickness from the B series, we can estimate the degree to which PEDOT is diluted by the substrate polymer. The amount of PEDOT in the remaining layers was also determined from visible light absorption at 700 nm using Lambert-Beer's law. Based on the conductivity and absorption measurements the amount of PEDOT in the PMMA was determined as a function of etch depth – see table 1. It

should be noted that the ion bombardment participating in the etching process could potentially cause selective implanting of different atoms. However, the degree of implantation of the two purely organic molecular species EDOT and MMA is not expected to differ significantly.

There is a fairly good correlation between the distributions determined by resistivity and absorption (Table 1), showing that the top layer of the substrate contains approximately 30-40% PEDOT. The examination also reveals that the PEDOT is present at substantial depths in the PMMA substrate, with 25-30% of the conducting polymer at depths greater than 500 nm, although the pure PEDOT layer is only 235 nm thick. The integration of the PEDOT into the PMMA

quite remarkable that the charged hydrophilic polymer PEDOT can be integrated with the very hydrophobic polymer COC. This indicates that more than ordinary blending plays a significant role in the integration of conductive polymers. All of the integrated samples showed conductivity of the same order of magnitude as pure PEDOT.

#### Patterning conductive polymers

A test series of conducting lines of decreasing width was constructed in PEDT to test the resolution of the lithographic techniques applied to the PEDT/PMMA samples. The electrodes had a length of 500  $\mu\text{m}$  and widths of 20, 15, 12, 10, 6, 4, and 2  $\mu\text{m}$ , respectively. Each of the conducting lines was connected at their ends

**Table 1:** Results from the  $\text{O}_2$  etching of the PEDOT/BA sample. The PEDOT content was determined using both surface resistivity and optical absorption (700 nm). The result shows that the top 500 nm of the PMMA sample consist of app. 30-40 % PEDOT

Etching time (s)	Depth (nm)	Step size (nm)	Surface resistance ( $\Omega/\text{sq}$ )	PEDOT remaining based on conductance	Percent PEDOT in layer based on conductance	Absorbance at 700 nm	PEDOT remaining based on absorbance	Percent PEDOT in layer based on absorbance
0	0	-	75.07	100%	40%	0.365	100%	32%
5	150	150	100.47	75%	33%	0.291	79%	28%
10	290	140	136.50	55%	30%	0.230	63%	36%
15	400	110	184.20	41%	39%	0.168	46%	36%
20	500	100	309.10	24%	-	0.112	31%	-

substrate matrix must be considered the main reason for the superior mechanical properties of the conductive layer compared to a surface adlayer.

The method for PEDOT integration was tested with other polymer substrates and for polypyrrole on PMMA. The polypyrrole was polymerised using vapour phase polymerisation as reported in [18] on a PMMA substrate and washed in the same manner as described above. The film was absorbed into the PMMA substrate, and showed much better mechanical properties than a polypyrrole adlayer on PMMA washed with water. Furthermore, several other kinds of substrates were tested. The results of the examination are presented in Table 3. The integration of PEDOT was most successful on PMMA, PC and COC, whereas no integration was obtained in cross-linked PDMS. This is accordance with our understanding of the integration process. Since PDMS is cross linked, and therefore insoluble, transport of polymer material from the substrate into the likewise insoluble PEDOT phase is prohibited. The integration of PEDOT into PET was quite poor because of the poor solubility of PET in the applied solvents. Integration was, however, demonstrated using chloroform, but the resulting surface layer was milky in appearance. It is

to two large 15 x 50 mm squares of conducting polymer, functioning as electrical contact pads. Four-point probe measurement of the resistance of the lines as function of the nominal line width was performed by applying two of the four probes to each of the large contacting squares. The result of the resolution test showed that electrodes down to 4  $\mu\text{m}$  in width could easily be constructed, whereas electrodes of 2  $\mu\text{m}$  width showed a relative large decrease in conductance. Interpolation of the conductance measurements showed an edge effect of approximately 500 nm, i.e. the outermost 500 nm along the edge of each line had a markedly lower conductance than the rest of the line. The edge effects probably originate from the exposure in the mask aligner: The substrate consists of extruded PMMA that has been spin coated and heated three times [22] before being exposed. It is therefore difficult to achieve a completely planar surface, which may lead to a small separation between the mask and the substrate, and an associated exposure of edge regions of the masked areas. The outcome of the resolution test was that 4  $\mu\text{m}$  structures with high conductivity can be fabricated with fairly good precision and the smallest features were therefore chosen to be 4  $\mu\text{m}$ .

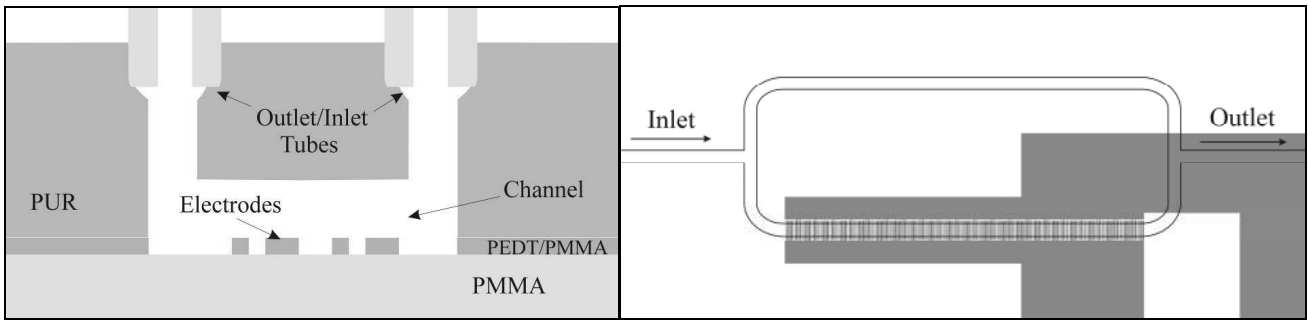


**Figure 6:** left: A schematic cross-section of the pump structure perpendicular to the electrode lines. Right: an image of the assembled pump seen from above. The inlet and outlet channels are used for purging the system, but are sealed when pumping. The fluid velocity is measured on the channel on the opposite site of the arrays.

The surface resistance of the PEDT after patterning was found to be 70-90  $\Omega/\text{sq}$ . The RIE removed approximately 600 nm of PEDT/PMMA as measured by profilometry. The surface resistance in the etched areas was higher than 211 M  $\Omega/\text{sq}$  (detection limit). An image of the final PEDT pattern is shown in figure 5.

The channel part of the pump was constructed in a flexible thermoplastic PUR, which in many ways has properties resembling PDMS. PDMS has been used in many microfluidic applications because of ease of fabrication, flexibility, and high transparency [23]. The PUR chosen for our work shares the same properties, but in addition PUR is a thermoplastic polymer, that may be injection moulded, embossed, or extruded. This is a major advantage over PDMS, that cannot be processed with ordinary mass production equipment due to its cross-linking. Furthermore, PMMA and polyurethane are partially mixable [24, 25, 26]. This makes it possible to bond the PMMA to PUR by heating the substrates to near the glass transition temperature. PUR is slightly hydrophilic showing a contact angle to water of 81°-82°. This implies that no further treatment is required for bonding or surface wetting. In contrast, the surface of PDMS must be oxidised both for bonding and for reducing the contact angle of 108°-109° to below 90° [27, 28, 29]. Furthermore, PDMS loses its hydrophilicity after a period of time in air, giving PDMS-based devices a limited shelf-life. None of these problems occur with PUR. PUR can be heat-bonded to a range of polymers, such as PMMA, polycarbonate and polystyrene but not to glass or silicon.

The channel system consists of a loop with a total length of 30 mm and with an entrance and exit channel (figure 6 right). The height of the channel is 25  $\mu\text{m}$  and the width 200  $\mu\text{m}$ . The pressure drop over the contour length of the loop is approximately  $4 \cdot 10^4 \text{ Pa}/v_{\text{ave}}$ , where  $v_{\text{ave}}$  is the average velocity measured in m/s. This yields a pressure drop of 4 Pa at an average velocity of 100  $\mu\text{m}/\text{s}$ , setting a lower limit on the required pressure generation of the pump. Each segment of the electrode array consists of a narrow electrode of width 4  $\mu\text{m}$ , a gap of 4  $\mu\text{m}$ , a wide electrode of width 20  $\mu\text{m}$  and a large gap of 16  $\mu\text{m}$ , giving a total segment width of 44  $\mu\text{m}$ . This is repeated 200 times with a resulting array length of 8800  $\mu\text{m}$ . The ratio between the electrodes and the gaps is based on numerical optimisation of the

geometry presented in a previous publication [19]. The length of the electrodes is 500  $\mu\text{m}$  and the fluid channel of width 200  $\mu\text{m}$  does therefore only cover a part of the electrodes.

### Testing the pump

The pump was tested using a  $10^{-4}$  M KCl solution with 2 ppm (by weight) microspheres in suspension. The channel system was flushed with pumping fluid between each test. Confocal laser scanning microscopy was employed for visualising the motion of the fluorescent spheres. The particle motion was recorded in the loop lane without pumping electrodes to avoid confounding local motion patterns in the vicinity of the electrodes. The microscope system was capable of scanning an area of approximately 500  $\mu\text{m} \times 500 \mu\text{m}$  at 10 Hz, yielding a suitable image quality for particle tracking analysis. The spheres were tracked using a dedicated particle image velocimetry program running under MatLab (Mathworks, Natick, Massachusetts, US). Particle velocities were measured at a range of driving potentials for three different frequencies, 10 kHz, 20 kHz, and 40 kHz. The results of the analysis are presented in figure 7. Positive velocities are defined as fluid (particle) motion from the wide towards the

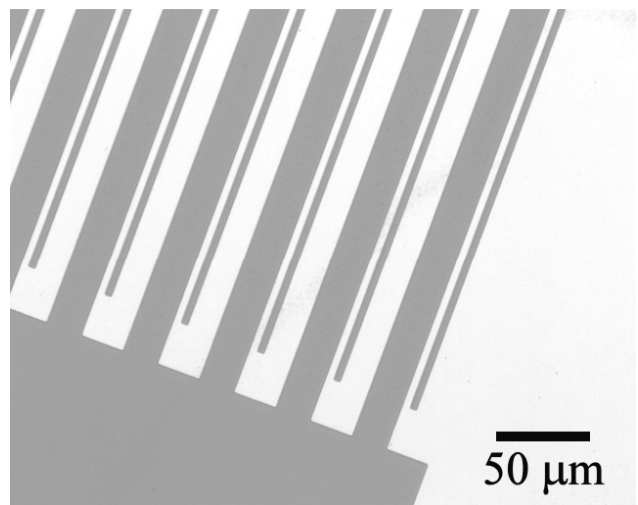


**Figure 5:** An all polymer micropump, consisting of a PEDOT array on PMMA. The thickness of the PEDOT layer is 160 nm and the width of the electrodes is 8  $\mu\text{m}$  and 40  $\mu\text{m}$ .

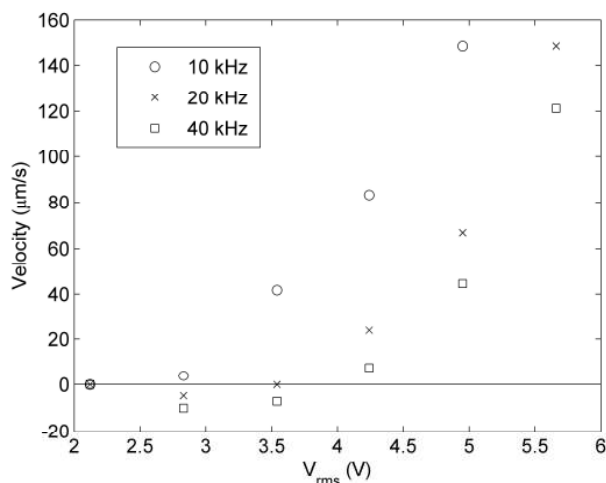


**Figure 7:** The velocity in the loop against the potential at 3 different frequencies. The reverse pumping is not significant at the measured frequencies and potential.

narrow electrode within an electrode segment (opposite to the definition used in some other publications). The properties of the pump such as velocity and pumping direction correspond with those described in the literature. The pump is capable of pumping in both directions, although at the highest velocities in the positive direction with the tested parameters. The pump requires a few seconds before reaching a constant velocity. This is most likely due to elasticity or bubbles in the channel system needing some time to adjust to the changed pressure/flow field.

The limits of driving potential and frequency were also examined. The limits were similar to those observed by Studer et al. for a corresponding electrode system made from platinum/titanium on glass, except for our system having a slightly higher susceptibility to electrode damage for voltages above 5 V at frequencies below 10 kHz. This is also the reason why the point at 10 kHz and 5.6 V<sub>rms</sub> is not included in figure 7. Two types of damage behaviour were observed. In the first type, the electrodes turn dark blue. This is a well known phenomenon when PEDT is reduced and the positive charge carriers are eliminated. This causes a decrease in conductivity and therefore in pumping efficiency, but the conductivity can be restored by re-oxidising the electrodes. This phenomenon was observed for low frequencies and intermediate potentials. The second type of damage is removal of the PEDT electrode material. The removal is probably caused by the same phenomenon that damages the platinum electrodes used by other authors. This behaviour was observed at high potentials and intermediate frequencies. Another problem that arises from the use of conductive polymers as electrode material is the release of ions from the PEDT. The conductive polymer consists of a positive charged PEDOT backbone and negatively charged tosylate ions. Although integrated into the PMMA it cannot be guaranteed that the tosylate does not migrate out of the polymer or that other anions migrate into the PEDOT. Both damage to the electrodes and ion migration can be avoided if the electrodes are coated

with an insulating encapsulating layer. This was explored using either 100 nm thick PMMA or 200 nm thick cyclic olefin copolymer (Topas 8007, Ticona, Frankfurt, Germany). The damage to the electrodes is reduced, but so is the pumping efficiency. None of the coated pumps were capable of pumping at a velocity higher than 40 µm/s. The pumps were however very stable and the PMMA covered pump were capable of pumping at 20 µm/s for 40 minutes at 5.6 V<sub>rms</sub> and a frequency 15 kHz without a decrease in velocity and without visible electrode damage

## References

- 1 A. Ajdari, *Physical Review E*, 2000, **61**, 45;
- 2 A. B. D. Brown, C. G. Smith and A. R. Rennie, *Physical Review E*, 2000, **63**, 16305
- 3 N.G. Green, A. Ramos, A. González, H. Morgan, A. Castellanos, *Physical Review E*, 2000, **61**, 4011
- 4 N.G. Green, A. Ramos, A. González, H. Morgan, A. Castellanos, *Physical Review E*, 2002, **66**, 26305
- 5 M. Mpholo, C. G. Smith and A. B. D. Brown, *Sensors and actuators B*, 2003, **93**, 262
- 6 V. Studer, A. Pépin, T. Chen, A. Ajdari, *The Analyst*, 2004, **129**, 944;
- 7 S. Debset, C.J Hayden, C. Dalton, J.C.T Eijkel, A. Manz, *Lab on a Chip*, 2004, **4**, 396;
- 8 N.G. Green, A. Ramos, A. González, H. Morgan, A. Castellanos, *Physical Review E*, 2000, **61**, 4019
- 9 N. A. Mortensen, L. Belmon, L. H. Olesen. And H. Bruus, *Not published yet*;
- 10 E. yeager, J.O. Bockris. B. E. Conway And S. Sarangapani, *Comprehensive treatise of electrochemistry* 6, 1983, 1<sup>st</sup> ed., Plenum Press;
- 11 Winther-Jensen B, West K, *Macromolecules* 2004; 37; 4538-4543
- 12 Winther-Jensen B, West K, *Reactive & Functional Pol.*, 2006; 66; 479-483
- 13 Tehrani P et al, *Smart Mater. Struct.*; 2005; 14 N21-N25
- 14 Winther-Jensen B, Normman K, Kingshott P, West K, *Plasma Proc & Pol* 2005; 2; 319-327
- 15 Shenoy SL, Kaya I, Erkey C, Weiss RA, *Synthetic metals* 2001; 123; 509-514
- 16 Fu Y, Weiss RA, *Polymer engineering and science* 1998; 38; 857-862
- 17 Fu Y, Weiss RA, Gan, PP, Bessette MD, *Polym. Engrn. & Sci.* 1998; 38; 857-862
- 18 Winther-Jensen B, Chen J, West K, Wallace G, *Macromolecules* 2004; 37; 5930-5935
- 19 Winther-Jensen B, Breiby DW, West K, *Synthetic Metals* 2005; 152; 1-4
- 20 Aben GVA, Somers MJM, Hanssen PHC, Schrooten LM, *SID 98 DIGEST 1998*, P-21; 528-531
- 21 Winther-Jensen B, Chen J, West K, Wallace G, *Polymer* 2005; 46; 4664-4669
- 22 Hansen T S, West K, Hassager O, Larsen N B, *Synt. Metals*, 2006 (in press: doi:10.1016/j.synthmet.2006.08.009)
- 23 Mcdonald J C et al, *Electrophoresis*, 2000, 21, 27-40
- 24 Poomalai P, Siddaramaiah, *J. Macromole. science – pure and appl. chem.*, 2005, 10, 1399-1407
- 25 Kumara H, Siddaramaiah, *Polymer*, 2005, 46, 7140-7155
- 26 Desal S, Thakore IM, Brennan A, Devi S, *J. Applied Polymer Science* 2002, 83, 1576-1585
- 27 Bhattacharya S, Datta A, Berg J M, Gangopadhyay S, *J Microelectromechanical systems*, 2005, 14, 590-597
- 28 Morra M et al, *J colloid and Interface Science*, 1990, 137, 11-24
- 29 Hillborg H, Gedde UV, *Polymer*, 1998, 39, 1991-1998



**Peter Dybdahl Hede**  
Phone: +45 4525 2853  
Fax: +45 4525 2258  
E-mail: PtHd@novozymes.com  
WWW: <http://www.kt.dtu.dk>  
Supervisors: Anker Degn Jensen  
Poul Bach, Novozymes A/S

Ph.D. Study  
Started: September 2005  
To be Completed: August 2008

## Scale-Up of Fluid Bed Coating Systems

### Abstract

Fluid bed granulation is a vital operation in the pharmaceutical, enzyme and food/feed industry and fluid beds are used extensively to form liquid formulations into solid products. Although widely used, fluid bed operations are still not fully understood or described. This means that industrial fluid bed operations and optimisation are still highly dependent on empirical approaches. Especially up-scaling of fluid bed systems is a challenging task with decisions to be made at many levels. This Ph.D. project aims at the fundamental understanding of the fluid bed granulation process in an industrial context having successful scale-up as its primary focus.

### Introduction

Particle processing in fluidised beds is a key operation to many types of industries including the food and pharmaceutical industries. In the production of solid enzyme products, fluid beds are used to produce enzyme granules with the proper product properties by spraying the enzyme concentrate through nozzles onto the agitated fluidised bed often consisting of inactive filler cores. In that sense agglomeration is an unwanted phenomenon but in other applications, agglomeration is indeed desired. In either case, control of agglomeration is essential.

Proper product quality is highly dependent on the precise control and optimisation of the process. As there is more than forty parameters involved in the fluid bed coating process, and as many of these parameters interact, fluid bed optimisation is an extremely difficult exercise. The situation is further complicated by the fact that during fluid bed processing many different processes occur simultaneously including wetting, drying, chance of agglomeration, attrition and more. As, in addition, particle trajectories inside fluid beds are chaotic, modelling and simulation of the coating process with commercial products is not an easy task. Thus, the present situation with fluid bed processes and products is still highly dependent on experimental results although this is tedious, time consuming and thereby expensive.

Often, optimisation of a fluid bed process is done in small- or medium-scale and then transferred to the large production-scale. This requires detailed knowledge of

not just process and formulation properties but also knowledge of scaling principles and parameters; e.g. which parameters should be kept constant during scale-up and which parameters may be varied. Currently, scaling is still more of an art rather than science being a mix of physics, mathematics, experience, common sense and qualified guesses as reviewed by Hede (2006b). This is not a satisfactory situation - neither from an academic nor from an industrial point of view.

### Specific Objectives

It is the objectives of the Ph.D. project to achieve a fundamental quantitative understanding at particle level of what is going on inside the fluid bed during processing. Further, it is the objective to be able to propose and test new principles for successful scale-up of the fluid bed coating process from pilot plant-scale into large-scale.

### Experimental

In a number of scaling studies, coating operations in three different top-spray fluid bed scales were conducted in order to try to match the particle size fractions as well as the tendency of agglomeration across scale. The three fluid bed scales was as follows: Small-scale - A modified GEA Aeromatic-Fielder Strea-1 top-spray fluidised bed with a stainless steel fluidising chamber of 12 L allowing a particle bed load of 500 g to be fluidised, a medium-scale standard Niro-Aeromatic Multiprocessor type MP-1 with a stainless steel fluidising chamber of 16 L allowing a particle bed load

of 4000 g to be fluidised (thereby being eight times larger in capacity in respect to the Strea-1 set-up), a large-scale GEA Aeromatic-Fielder MP-2/3 with a vessel volume of 60 L allowing a particle bed load of 24000 g to be fluidised (thereby being six times larger in capacity in respect to the MP-1 and 48 times in respect to the Strea-1 set-up).

### Scaling parameters and conditions

Two parameters were tested as possible scaling parameters being the *relative droplet size* and the *drying force*.

Based on the results by Mehta (1988), Rambali et al. (2003) scaled up a fluidised granulation process from small-scale to medium- and large-scale by looking at the effect of the particle bed moisture contents during and at the end of the spraying process and the effect of droplet size on the granule size. The fluidisation flow rate was kept constant in all their experiments in order to have a constant airflow and to have approximately similar breaking forces on the granules. The droplet size was controlled in terms of a relative droplet size (Rd) according to the ratio of the spray rate  $\dot{m}_{\text{spray}}$  divided by the airflow through the nozzle  $\dot{m}_{\text{nozzle air}}$  squared according to:

$$Rd = \frac{\dot{m}_{\text{spray}}}{(\dot{m}_{\text{nozzle air}})^2} \quad (\text{Eq. 1})$$

In the scaling experiments by Rambali et al. (2003) it was seen that the effect of the change in relative droplet size was different for each fluid bed scale, but that the granulation process was successful by scaling up to the large-scale bed from small-scale, considering only the relative droplet size.

Results by Hede (2005) clearly indicate that the drying force may be closely related to the tendency of agglomeration during fluid bed coating. The drying force is not a Newtonian force known from mechanics but rather an indication of the vapour capacity in humid air expressed in pressure units. The drying force combines the bed temperature and the bed moisture contents during steady state coating conditions in one parameter according to the following equation:

$$\text{Drying Force} = P_{\text{sat}}|_{T_{\text{bed}}, 100\%rH} - P_{\text{actual}} \quad (\text{Eq. 2})$$

where  $P_{\text{sat}}$  is the saturated pressure at the dry bulb temperature and  $P_{\text{actual}}$  is the actual vapour pressure of the fluidisation air at the bed temperature and the bed relative humidity conditions.  $P_{\text{actual}}$  is given as:

$$P_{\text{actual}} = \frac{\text{Bed } rH\%}{100 \text{ } rH\%} \cdot P_{\text{sat}}|_{T_{\text{bed}}} \quad (\text{Eq. 3})$$

In order to test the scalability in terms of the drying force, different levels of the bed temperature were

chosen and fixed. The humidity of the inlet air could not be controlled in any of the three fluid bed set-ups but they were all recorded and no significant variation in room relative humidity was observed. Equation 2 and 3 indicate furthermore, that the drying force is less sensitive to the relative humidity than to the bed temperature. Thus, it was possible to maintain the drying force at almost distinct levels without being able to precisely control the humidity of the inlet air.

### Materials

Two types of core materials were used for the coating experiments – slightly porous sodium sulphate cores (Santa Marta - void fraction around 20.7 % determined with Micromeritics Autopore II intrusion/extrusion mercury porosimetry) pre-sieved in the size range of 250 – 350  $\mu\text{m}$  and non-porous glass ballotini (Potters Industries) pre-sieved in the size range of 250 – 350  $\mu\text{m}$ . The sodium sulphate cores have sphericities in the range of 0.86 whereas the glass ballotini cores are almost perfect spheres. Microscope pictures of both core materials may be seen in figure 1.

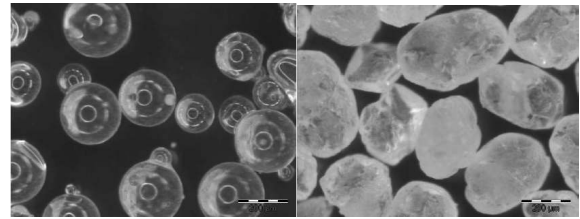


**Figure 1.** Materials used in the coating experiments. Left) Uncoated glass ballotini cores. Right) Uncoated sodium sulphate cores.

Both types of core materials were coated with aqueous solutions of crushed sodium sulphate in an amount of 15 w/w% using 1 w/w% Dextrin (CAS no. 9004-53-9 - Bulk density  $\sim 0.8 \text{ g/cm}^3$ ). Demineralised water was used as solvent. Triphenylmethane colour (Sicovit Patent blue - CAS no. 3536-49-0) was added as well as colouring agent for all experiments in amounts of 0.1 w/w% in order to study the level of droplet penetration and the coating layer structure of the final coated granules.

### Scaling procedure

In the effort to fix as many parameters as possible across scale, the three different fluid bed set-ups were carefully build up as similar as possible. All three fluid beds were top-sprayed fluid beds each having a single two-fluid nozzle. In all three cases, an outlet nozzle diameter of 1.2 mm was chosen. Likewise was the coating liquid feed in each case led from the external heated reservoir at a constant heating temperature of 60  $^{\circ}\text{C}$  to the nozzle through an adjustable electrical peristaltic tube pump. A sketch of the general set-up in each of the three fluid bed systems may be seen from figure 2.

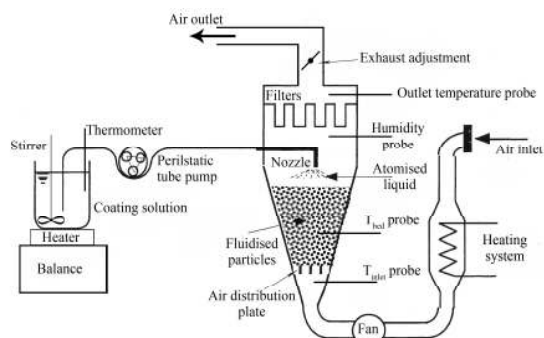


**Figure 2.** Formal sketch of the general top-spray set-up used for all three fluid bed scales.

The fluidisation velocity in m/s was kept constant at 3.3 m/s at a height in the fluidisation chamber just above the bottom plate throughout all experiments and across scale in order to try to maintain a similar granule collision velocity as well as a similar level of attrition across scale. All three types of fluid beds have a conical fluidisation chamber shape but the wall angles, bottom plate and other length dimensions are not in any way dimensionally consistent going from small- to medium- and large-scale. A fluidisation velocity just above the bottom plate at 3.3 m/s correspond in  $\text{m}^3/\text{hr}$  to 93  $\text{m}^3/\text{hr}$  in the Strea-1 set-up, 270  $\text{m}^3/\text{hr}$  in the MP-1 and 680  $\text{m}^3/\text{hr}$  in the MP-2/3 set-up depending on the exact inlet temperature.

In the present studies, the relative droplet size was kept constant during scale-up as the nozzle pressure was kept constant at two distinct levels (1 bar or 3 bar) in each scale and the liquid feed rate to the nozzle controlled and fixed at the tube pump in order to maintain a constant relative droplet size across scale. Even though the nozzle diameter of 1.2 mm was identical and the nozzle pressure identical in all three scales, the airflow in g/min and liquid feed flow in g/min were not identical as the flow of nozzle air naturally is larger, the larger the fluid bed scale.

Initial experiments had to be conducted in order to determine the airflow through the nozzle for different nozzle pressures without connecting the liquid feed. This was done by connecting a simple household gas-meter to the nozzle outlet and then measure the airflow rate versus the nozzle pressure. The relative droplet parameter was kept constant across scale as follows: Knowing the airflow rate through the given nozzle at a given nozzle pressure, the value of the relative droplet size from the small-scale fluid bed was kept constant during scaling by calculating the liquid feed rate in g/min necessary to achieve an identical relative droplet size in the medium- and large-scale. The tube pump was thereby adjusted and fixed at this value throughout the coating experiment. With given choice of drying force value and the choice of bed temperature, only the inlet temperature was changed in each experiment in order to match the drying force and relative droplet size values across scale.

Prior to coating, the core bed load was heated until the relative humidity inside the fluidisation chamber was constant, typically ranging from 5 RH% to 7 RH% depending on weather conditions. In each coating operation the aim was to coat until the bed load had increased 20 w/w%. This was done in order to make sure that a reasonable coating layer (thickness  $\sim 5 - 10 \mu\text{m}$ ) had developed on the core particles. After coating, the bed load was kept fluidised at identical fluidisation velocity and temperature conditions in order to dry the coated granules. This was done until the relative humidity inside the chamber was identical to the conditions prior to coating. The coated bed load was afterwards weighed in order to make sure that the bed load had gained in weight about 20 w/w%. For all the experiments the batch weight gain was in the range of 18.7 w/w% – 19.5 w/w% indicating little loss of core material as well as little loss of coating solution due to spray drying.

### Results: Matching the agglomeration percentages and particle size fractions across scale

In order to test the application of the drying force and relative droplet size as scaling parameters, a campaign of 18 different fluid bed coating experiments (6 in each scale) was set up. An overview of the different experiments may be seen from table 1.

**Table 1:** Schematic overview of selected results from the six scaling experiments (\* indicates that the core material was glass ballotini in that scaling experiment).

Scaling exp.	Relative droplet size (in $\text{min}/\text{g}$ )	Drying force (in kPa)	Agglomeration tendencies	P-value from $\chi^2$ test
A	$3.5 \cdot 10^{-3}$	12	All within 2 x Std. dev. ( $\sim 1\%$ )	0.07
B*	$3.5 \cdot 10^{-3}$	12	All within 2 x Std. dev. ( $\sim 0.5\%$ )	0.59
C	$24.5 \cdot 10^{-3}$	12	Outside 2 x Std. dev. (36 – 49 %)	0.02
D	$3.5 \cdot 10^{-3}$	8.5	All within 2 x Std. dev. ( $\sim 1\%$ )	0.14
E	$3.5 \cdot 10^{-3}$	6	Outside 2 x Std. dev. (7 - 33 %)	$\approx 0$
F*	$24.5 \cdot 10^{-3}$	12	All within 2 x Std. dev. ( $\sim 45\%$ )	0.48

For each batch an agglomeration percentage was determined and a  $\chi^2$  test was performed on the particle size fractions within that scaling experiment. A p-value above 0.05 from such a test indicates that on a 95% confidence interval the particle size fractions are similar. In terms of the agglomeration percentage, it was seen from repeated sieve analysis that the standard deviation was 0.82 % thereby indicating as a common rule of thumb that different batches having agglomeration percentages in the range of  $\pm 1.64\%$  are not statistically different.

There are many interesting things to extract from the results in table 1. Going horizontally in table 1 within each scaling experiment, the drying force as well as the relative droplet size is maintained whereas either one or

both of these parameters are changed going in the vertical direction. Comparing scaling experiment A, D and E, in which only the relative droplet size has been kept constant, it becomes evident that there is a relation between the drying force and the agglomeration tendency, but that the relation is not in any way linear. E.g. has the drying force been reduced from around 12 in experiment A to around 8.5 in experiment D whereas the agglomeration percentages are not statistically significant different. When further reducing the drying force to around 6, the agglomeration tendency increases significantly.

These tendencies are qualitatively all in accordance with expectations as it is reasonable to expect higher agglomeration tendency with decreasing drying force. With decreasing drying force the coating droplets will dry slower leaving the coating layer wet for a longer time on the cores surfaces, again increasing the chance of liquid bridge building between particles resulting in solid bridge bonding formation upon drying and thereby permanent agglomeration.

The influence of the relative droplet size on the agglomeration tendency may be observed from the comparison of scaling experiments A and C. Going from experiment A to C, the relative droplet size is roughly increased seven times whereas the agglomeration tendency is increased more than thirty-five times. This tendency is qualitatively in accordance with expectations. With the increased relative droplet size, the actual droplet size is increased as well, although not as much as seven times. With increased droplet diameter under similar drying force conditions, the larger droplets will remain wet for a longer time thereby increasing the chance of liquid bridge building between particles and thereby increased chance of agglomeration.

Comparing the agglomeration tendencies within each scale in experiment A, D and E as well as in experiment A and C indicates that process control in terms of either drying force alone or relative droplet size alone may not seem as a successful choice as the agglomeration tendency within each scale cannot be maintained in terms of fixing either of these parameters alone. Next is to determine whether or not a combination of the relative droplet size and the drying force may be applied for successful up-scaling.

A quick horizontal overview of the agglomeration tendencies from the six scaling experiments, and the corresponding p-values from the  $\chi^2$  tests, indicate that successful scaling is achieved in scaling experiment A, B, D and F all having agglomeration percentages far inside the  $\pm 1.64\%$  range within each scaling experiment and furthermore, all have p-values above 0.05. This means that not only are the cut-off values corresponding to the agglomeration percentages matched across three scales but in addition, the different particle size fractions are identical on a 95% confidence level. This may also be visualised in a Rosin-Rammler-Bennet-Sperling-plot as it may be seen from figure 3

showing the particle size fractions from scaling experiment A

Graph: ...g AICHE\Peters temp\Modifications equal\Small-scale.rdf (ala.atg)

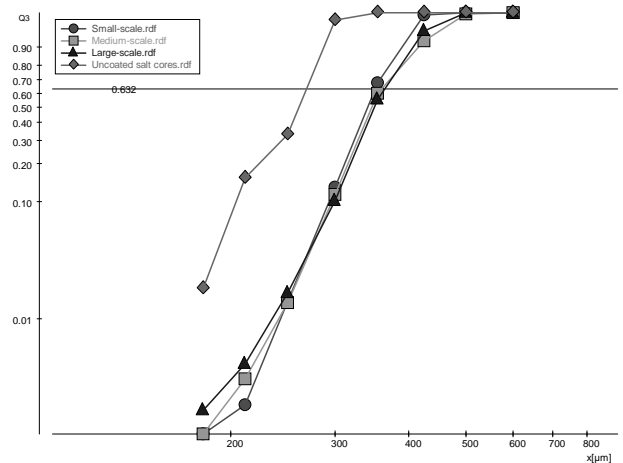


**Figure 3.** RRSB-plot (Rosin-Rammler-Bennet-Sperling) of particle size fractions from scaling experiment A.

Interestingly, the best results are found with the glass ballotini core experiments in scaling experiment B and F. Here the tendency of agglomeration is closely reproduced across scale and the p-values are far above 0.05 indicating high reproducibility of the particle size fractions. This is in accordance with expectations as the glass ballotini cores in many ways may be seen as the ideal core material. Besides being almost perfectly spherical, glass ballotini cores are furthermore non-porous meaning that issues such as droplet penetration, dewatering of droplet solvent and more is not likely to interfere with the tendency of agglomeration in the same complex manner as it may be the case with sodium sulphate cores. The comparison of scaling experiment A with B and experiment C with F indicate however that the agglomeration tendency is fairly similar on an overall level whether the core material is sodium sulphate cores or glass ballotini cores. The somewhat smaller agglomeration tendencies in the medium- and large-scale experiments in experiment C compared to experiment F could indicate that possible droplet penetration into the sodium sulphate cores could result in decreased tendency of agglomeration in accordance with other experiments by Hede (2005).

Two scaling experiments C and E are statistically unsuccessful as the agglomeration percentages are beyond the  $\pm 1.64\%$  range. Likewise are the p-values from the  $\chi^2$  tests below the 0.05 limit although scaling experiment C is not far away with a p-value of 0.02. In both cases the agglomeration tendency is largest in the small-scale indicating that, with identical process and formulation conditions, the small-scale fluid bed is more prone to agglomeration. The reasons for this could be

the fact that the temperature is less uniform within the bed the smaller the scale, as the heat loss in respect to the particle bed load is much higher the smaller the scale.

The scaling experiments C and E are characterised by having a combination of a high relative droplet size and high drying force and a combination of a low drying force and low relative droplet size respectively which means that the experiments could be in the extreme ends of the plausible range of the drying force and relative droplet size parameters. This could explain why these two scaling experiments are not successful while the others are.

### SEM studies of coating layer morphology

The effect of the relative droplet size and thereby the actual average droplet size on morphology was further studied by comparison of SEM pictures from scaling experiment B and F in which only the relative droplet size was changed in the medium-scale glass ballotini core experiments. As observed from figure 4, the effect of increasing the relative droplet size seven times, which corresponds to an increase in actual average droplet size around five times from roughly 8  $\mu\text{m}$  to 41  $\mu\text{m}$  estimated with the use of a standard equation for two-fluid nozzles adapted from Masters (1972), is unambiguous.



**Figure 4.** Effect of relative and actual average droplet size on coating layer morphology. Left) Coated glass ballotini core from scaling experiment B. Right) Coated glass ballotini core from scaling experiment F.

Although both granules in figure 4 have relatively smooth coating surfaces, droplet footprints may be observed in both cases. As no droplet penetration was possible into the non-porous glass ballotini cores, the effect of droplet size on morphology is easily detected in figure 4. Corresponding to the increase in droplet size going from the left to the right in figure 4, the radii of the footprints are significantly larger on the right photo. Although the large droplets in the right photo have spread to some extent on the ballotini surface they have not had sufficient time to merge homogeneously together before complete drying. The result of fewer but larger droplets impacted on the core surface is clearly observed in form of craters that make the coating layer appear as a lunar landscape. Such uneven coating may very well result in poor mechanical properties with

possible chance of chipping off flakes of the coating layer upon granule impact. This is yet to be tested.

### Conclusion

On an overall level, the successful up-scaling of top-spray fluid bed coated particles by 48 times in weight from the small-scale over medium-scale to the large-scale fluid bed is a significant achievement. Not just the tendency of agglomeration was repeated but also the nine particle size fraction classes within each batch were reproduced across scale. Although two of the six scaling experiments were statistically unsuccessful, and clearly illustrates the limitations of the drying force and relative droplet size as universal scaling parameters, the scaling results presented in this paper are most promising in terms of maintaining particle size fractions across scale during top-spray fluid bed coating. The best results were achieved with non-porous highly spherical glass ballotini cores but also statistically sound scale-up results were achieved with commercial sodium sulphate cores being potato-shaped and slightly porous.

The results presented in this paper suggest that two parameters are kept constant during scale-up: A drying force parameter combining bed temperature with humidity conditions inside the fluidisation chamber during steady state coating conditions, and a relative droplet size parameter relating the liquid nozzle feed rate to the nozzle airflow. The present scale-up experiments thereby focus on nozzle conditions as well as temperature and humidity conditions during coating – both properties known to be of major importance regarding agglomeration tendency and coating layer properties. The paper further propose that nozzle conditions are fixed throughout the coating process and that conditions inside the fluidisation chamber are adjusted only in terms of the inlet air temperature.

Studies of coated granules in SEM and by visual microscopy showed similar coating morphology across scale when the drying force and the relative droplet size were kept constant. This gives reasons to believe that the mechanical properties are well reproduced across scale as well.

Scale-up in terms of combined drying force and relative droplet size is a new scale-up proposal and involves focus on the particle-level scale as well as on the unit-operation scale. The principles presented in this paper provide simple engineering principles for successful scale-up and may be seen as an important first step towards the quantitative scale-up of top-spray fluid bed system.

### Acknowledgements

This Ph.D. project is partly funded by Novozymes A/S.

The Author is a member of the Novozymes Bioprocess Academy as well as the MP<sub>2</sub>T Graduate School in Chemical Engineering

## References

1. Hede, P.D.: *Fluid bed coating and granulation*, Master Thesis, Department of Chemical Engineering, CHEC Research Centre, Technical University of Denmark, pp. 1 – 227, **2005**.
2. Hede, P.D.: *Towards Mathesis Universalis: Modern aspects of modelling batch fluid bed agglomeration and coating systems – a review*, Department of Chemical Engineering, CHEC Research Centre, Technical University of Denmark, pp. 1 - 100, **2006**.
3. Masters, K.: *Spray Drying – An Introduction to Principles, Operational Practice and Applications*, Leonard Hill Books, London, **1972**.
4. Mehta, A.M.: *Scale-up considerations in the fluid-bed process for controlled-release products*, Pharmaceutical Technology, No. 12, pp. 46-52, **1988**.
5. Rambali, B., Baert, L. and Massart, D.L.: *Scaling up of the fluidized bed granulation process*, International Journal of Pharmaceutics, No. 252, 197-206, **2003**.

## List of Publications

1. Hede, P.D., Bach, P. and Jensen, A.D.: *Small-scale top-spray fluid bed coating: Granule impact strength, agglomeration tendency and coating layer morphology*, Powder Technology (Under final review).
2. Hede, P.D., Bach, P. and Jensen, A.D.: *Top-spray fluid bed coating: Scale-up in terms of relative droplet size and drying force*, Powder Technology (In preparation).
3. Hede, P.D.: *Towards Mathesis Universalis: Modern aspects of modelling batch fluid bed agglomeration and coating systems – a review*, Department of Chemical Engineering, CHEC Research Centre, Technical University of Denmark, pp. 1 - 100, **2006**.
4. Hede, P.D.: *Fluid Bed Particle Processing*, ISBN 87-7681-153-0, Ventus Publishing, pp. 1 - 80, **2006**.
5. Hede, P.D.: *Modelling Batch Systems Using Population Balances – A Thorough Introduction and Review*, ISBN 87-7681-180-8, Ventus Publishing, pp. 1 - 58, **2006**.
6. Hede, P.D.: *Advanced granulation theory at particle level*, ISBN 87-7681-153-0, Ventus Publishing, pp. 1 - 62, **2006**.
7. Hede, P.D.: *Introduction to hydrodynamic modelling and granular dynamics*, ISBN 87-7681-172-7, Ventus Publishing, pp. 1 - 42, **2006**.
8. Hede, P.D. and Beier, S.P.: *Kemi*, ISBN 87-7681-079-8, Ventus Publishing, pp. 1 - 189, **2006**.

## Conference contributions

1. Hede, P.D., Bach, P. and Jensen, A.D.: *Small-scale top-spray fluid bed coating: Influence of selected process and formulation parameters on granule impact strength, agglomeration tendency and coating layer morphology*, Presented at 5<sup>th</sup> World Congress on Particle Technology (WCPT5), Orlando, FL, April **2006**.
2. Hede, P.D., Bach, P. and Jensen, A.D.: *Agglomeration and Coating in Fluidised Bed*, Presented at DK<sub>2</sub> – Dansk Kemiingeniør-konference, DTU, May/June **2006**.
3. Hede, P.D., Bach, P. and Jensen, A.D.: *Top-spray fluid bed coating: Scale-up in terms of relative droplet size and drying force*, Presented at the 2006 AIChE Annual Meeting, San Francisco, CA, November **2006**.
4. Hede, P.D., Bach, P. and Jensen, A.D.: *Experimental validation of macro- and micro-level scaling laws in small- and medium-scale top-spray fluidised bed coaters*, To be presented at ECI2007 – 12<sup>th</sup> International Conference on Fluidization (abstract accepted), Vancouver, B.C., May **2007**.
5. Hede, P.D., Andersen, S.M., Madsen, K., Michelsen, M.L., Bach, P. and Jensen, A.D.: *Testing solution approaches of one-dimensional population balances of batch fluid bed agglomeration and coating*, To be presented at PARTEC2007 – International Conference on Particle Technology, Nuremberg, Germany, March **2007**.



## Michael Lykke Heiredal

Phone: +45 4525 4828  
Fax: +45 4525 2258  
E-mail: mlh@kt.dtu.dk  
WWW: <http://www.kt.dtu.dk>  
Supervisors: Anker Degn Jensen  
Flemming Frandsen  
Joakim R. Thøgersen, Haldor Topsøe A/S

### Industrial Ph.D. Study

Started: September 2006  
To be completed: August 2009

## Particle Dynamics in Monolith Catalysts

### Abstract

Emission of nitrogen oxides from pulverized coal combustion is a major environmental problem today. The most used methods for reduction of nitrogen oxides in the flue gas from coal fired power stations is Selective Catalytic Reduction (SCR) of nitrogen oxides with ammonia as reducing agent. A major problem with using the SCR process is the risk of plugging and erosion/attrition of the monolith catalysts because of fly ash and particles in the flue gas. The objective of this Ph.D. project is to develop a model that in combination with Computational Fluid Dynamics can simulate the degree of plugging in monolith catalysts with flue gas containing high dust load. The model should be a function of particle properties, gas velocities, angle of incidence to the monolith, and geometry of the catalyst and character of the surface.

### Introduction

The formation of nitrogen oxides ( $\text{NO}_x$ ) during combustion processes takes place partly because of reaction between oxygen and nitrogen in the combustion air and partly because of reaction between oxygen in the air and nitrogen in the fuel. The formation of  $\text{NO}_x$  is an unwanted reaction because it contributes to acidifying the rain water and also is unhealthy for human beings.

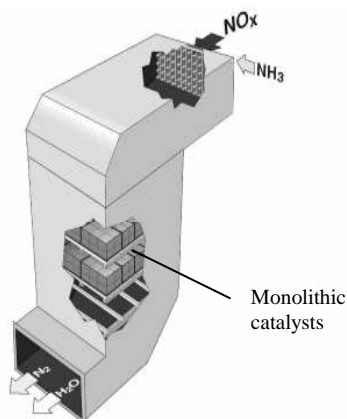
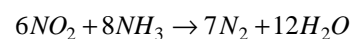
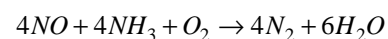


**Figure 1:** Illustration of a high dust SCR reactor with monolithic catalysts.

The most used methods for reducing  $\text{NO}_x$  in the flue gas from coal fired power stations is Selective Catalytic

Reduction (SCR) of  $\text{NO}_x$  where ammonia ( $\text{NH}_3$ ) is used as reduction agent. Figure 1 shows an illustration of a high dust SCR reactor with monolithic catalysts. The global reactions for the process are:



The products are free nitrogen ( $\text{N}_2$ ) and water ( $\text{H}_2\text{O}$ ) which are harmless for the environment.

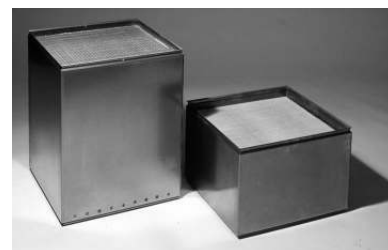


**Figure 2:** Picture of Haldor Topsøe DeNOx SCR Catalyst.

Industrial catalysts in general consist of vanadium and wolfram ( $\text{V}_2\text{O}_5/\text{WO}_3$ ) dispersed on a titanium oxide ( $\text{TiO}_2$ ) carrier. Figure 2 shows a picture of a Haldor Topsøe DeNOx catalyst. The high dust zone in the stationary power stations is usual preferred for placing

the SCR reactor. The operating temperature in the high dust zone is in the range from 300 to 400 °C and the pressure is atmospheric which is ideal for the catalytic activity. The content of NO<sub>x</sub> in the flue gas is typical about 300 to 700 ppm and NO<sub>x</sub> can thereby be reduced by up to 80 to 90% over the SCR catalyst with an ammonia slip of around a few ppm.

A major problem with using the SCR process under high dust conditions is the risk of plugging and erosion/attrition of the monolith catalysts because of fly ash and particles in the flue gas. The content of fly ash formed by the combustion processes is usually about 5-20 g/Nm<sup>3</sup> [1]. Monolithic catalysts are generally designed as a collection of catalytic channels where the flue gas flows parallel to the wall to minimise the risk of plugging. Despite of regular soot blowing it is observed that a major part of the channels in the catalysts have been deactivated due to plugging. The plugging can be minimised by using larger channel diameters but a consequence of that is that the catalyst volume has to be larger to obtain the same conversion which makes the reactor more expensive. One of the main design criteria is that they should be able to operate under heavy dust load and be compact to reduce cost and at the same time function effectively without plugging.

### Objective

To meet these design criteria it is necessary with a fundamental study of the particle dynamics in monolith catalysts to understand the mechanism that can transport fly ash and particles to the surface of the catalyst. The transport can depending on the size of the particles be due to thermophoresis [6], Brownian diffusion [7], particle inertia, aerodynamic forces [2], buoyancy or turbulent diffusion [8]. The objective of this Ph.D. project is to develop a model that in combination with Computational Fluid Dynamics (CFD) can simulate the degree of plugging in monolith catalysts with flue gas containing high dust load. The model should be a function of particle properties, gas velocities, angle of incidence to the monolith, geometry of the catalyst and character of the surface.

### Conclusion

Today there exist a lot of models in the literature for transport of particles and aerosol in duct flow including deposition of these. It is also possible to use CFD to simulate transport and deposition of particles and aerosols in turbulent gas flow [3,4]. There also exists CFD models that can simulate the performance of the SCR reactor down stream in coal fired power stations regarding pressure loss, temperature and mixing of chemical species [5]. But none of these models take deposition and plugging into account in the channels of the monolithic catalysts.

### Future work

Experimental work during this Ph.D. project will be done both at Haldor Topsøe and at Department of

Chemical Engineering at DTU. Experiments at Haldor Topsøe will be carried out with a plugging pilot with the objective of investigating fly ash deposition in monolith catalysts as a function of different fly ash types, particle concentration in the gas flow, the linear gas velocity and angle of incidence to the monolith. At DTU detailed experiments with deposition of aerosols in a single channel will be carried out and based on the experimental results numerical models for the degree of deposition and plugging will be developed. Different numerical software tools e.g. Fluent and Comsol Multiphysics will be used in this Ph.D. project.

### References

1. E. Raask, Minerals Impurities in Coal Combustion. Behavior, Problems and Remedial Measures, Taylor & Francis, 1 edition, U.K., 1985.
2. P.G. Saffman, Journal of Fluid Mechanics, 22 (2) (1965) 385-400.
3. C.M. Winkler, S.L. Rani & S.P. Vanka, Powder Technology, 170 (2006) 12-25.
4. R. Maniero & P. Canu, Chemical engineering Science 61 (2006) 7626-7635.
5. K. Rogers, M. Albrecht & M. Varner. Babcock & Wilcox, Technical Paper (2000).
6. C. Tsai, J. Lin, S.G. Aggarwal & D. Chen, Aerosol Science and Technology, 38 (2004) 131-139.
7. J.M. Frey, P. Schmitz, J. Dufreche & I.G. Pinheiro, Transport in Porous Media, 37 (1999) 25-54.
8. A. Kitamoto & Y. Takashima, Bulletin of the Tokyo Institute of Technology, No. 127 (1975).



**Guilin Hu**

Phone: +45 4525 2831  
 Fax: +45 4588 2258  
 E-mail: gh@kt.dtu.dk  
 WWW: http://www.chec.kt.dtu.dk

Supervisors: Prof. Kim Dam-Johansen  
 Assoc. Prof. Stig Wedel

Ph.D. Study  
 Started: February 2004.  
 To be completed: January 2007

**SO<sub>2</sub> Emission from Cement Production**

**Abstract**

SO<sub>2</sub> emission from cement production by the dry process is often a problem for cement manufacturers. Oxidation of pyrite contained in the raw materials, usually different types of limestone, clay and shale, in the cyclone preheater used in the dry process is the main source of SO<sub>2</sub> formation. The emission level of SO<sub>2</sub> is determined by the formation of SO<sub>2</sub> by the oxidation of pyrite in the raw materials and the subsequent absorption of the formed SO<sub>2</sub> on the limestone particles.

The oxidation of pyrite is significantly influenced by reaction conditions such as temperature, oxygen concentration and particle size, and may take place by direct oxidation or by a two-step process (first thermal decomposition of the pyrite and then subsequent oxidation of the formed pyrrhotite) depending on reaction conditions. In the cyclone preheater, the pyrite is directly oxidized in the first stage cyclone (the one on the top), but may be oxidized by the two-step process in the second stage cyclone.

The sulfation of limestone in the cyclone preheater is the direct sulfation. The direct sulfation of limestone involves nucleation and crystal grain growth of the solid product (anhydrite), and is usually under mixed control by both chemical reaction and solid-state diffusion. The direct sulfation of limestone can be enhanced by increasing solid-state diffusion by the addition of additives such as various alkali metal salts and CaCl<sub>2</sub>.

**Introduction**

Today, the dry process is the dominant process technology used for cement production due to its superior energy efficiency. In this process, raw materials are first milled to the required particle size and mixed to form raw meal (homogenised mixture of raw material powders). The raw meal is then preheated in a cyclone preheater through direct heat exchange with the hot flue gas from the rotary kiln and/or the calciner. After preheating, the raw meal passes first through the calciner, where limestone in the raw meal is calcined. The calcined raw meal goes then into the rotary kiln, where the calcined raw meal is burned at high temperatures to form cement clinker. The formed clinker is then cooled down and milled to produce final cement products.

Figure 1 illustrates an in-line dry kiln system with a preheater consisting of 5 cyclones (the upper 4 cyclones are used for preheating).

In each stage of the cyclone preheater, the raw meal particles are suspended in the up-going and hot flue gas in the riser in concurrent flow and heated up. The solid phase is then separated in the cyclone and enters the

stage underneath. The flow in the preheater is concurrent in each cyclone, but count current in general. The raw meal is typically heated up from about 350 K to about 1073 K before it enters the calciner. The flue gas is cooled down from about 1173 K to about 573 K.

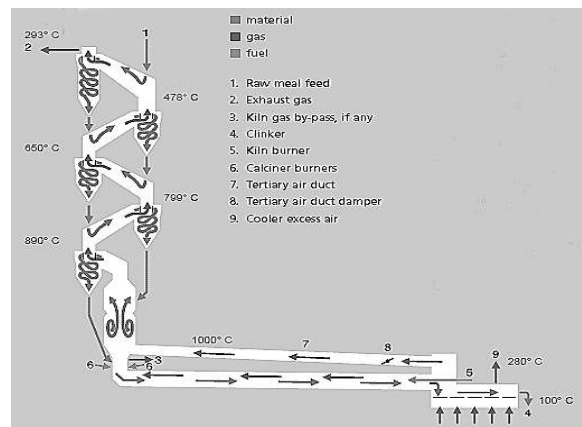


**Figure 1:** Illustration of a 5 stage cyclone preheater.

Cement production uses different types of limestone, clay and shale as raw materials. These raw materials are all minerals, and contain often a few percent of pyrite ( $\text{FeS}_2$ ). During the preheating process in the cyclone preheater the sulfur contained in the pyrite is partly oxidized to  $\text{SO}_2$  by the hot and oxygen-containing flue gas from the rotary kiln and/or the calciner. Part of the formed  $\text{SO}_2$  is absorbed on the limestone particles in the raw meal. The rest is released into atmosphere with the flue gas, and is the main source of  $\text{SO}_2$  emission from cement production. The emission level of  $\text{SO}_2$  from different plants can vary from a few hundred ppm to several thousand ppm depending on the pyrite content in the used raw materials. It is desired that this emission is reduced as much as possible in the benefit of better environment.

### Specific Objectives

In this project, a comprehensive literature survey is performed concerning the oxidation of pyrite at elevated temperatures; the sulfation reaction between limestone and  $\text{SO}_2$  are studied in laboratory scale reactors with and without addition of additives. The main purpose is to get better understanding of the mechanisms and kinetics of the oxidation of pyrite and the sulfation of limestone in a cyclone preheater-like environment.

### Oxidation of Pyrite

The oxidation of pyrite in an oxygen-containing atmosphere is complicated. Three different situations can occur depending on the reaction conditions [1, 2, 3, 4, 5] as illustrated in Figure 2:

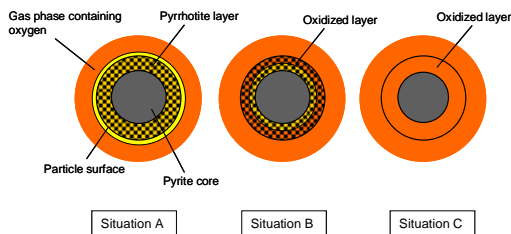
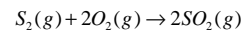
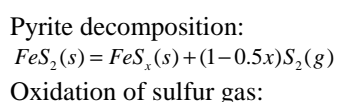
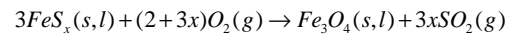
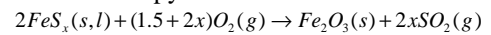


**Figure 2:** Illustration of pyrite transformation in an oxygen-containing atmosphere.

In situation A, the oxidation of pyrite takes place by a two-step process. The pyrite undergoes first thermal decomposition to form pyrrhotite (iron sulfides of lower sulfur content,  $\text{FeS}_x$ ,  $1 \leq x \leq \text{ca. } 1.2$ ) and sulfur gas. The formed pyrrhotite is then oxidized subsequently after the decomposition process is completed. This situation can occur when the oxidation of the sulfur gas outside the particle is able to consume all oxygen during its diffusion to the particle surface. This is normally the case when the reaction temperature is high and/or the oxygen concentration is low. The whole process can be represented by the following overall reactions:



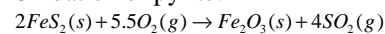
Oxidation of pyrrhotite:



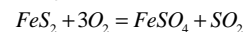
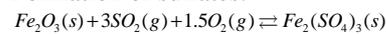
In situation B, the pyrite is also oxidized by the two-step process as in situation A. The oxidation of the formed pyrrhotite takes place now alongside the gas phase oxidation of sulfur gas before the completion of the decomposition of the pyrite. This situation can occur when the reaction temperature is not very high and the oxygen concentration is relatively high. The overall reactions are the same as in situation A.

In situation C, oxygen is in direct contact with the pyrite core. The pyrite is now oxidized directly. This situation can occur when the reaction temperature is low (often lower than about 800K) and the oxygen concentration is high. During the direct oxidation, small amounts of iron sulfates may be formed. This will result in a denser product layer since the molar volumes of iron sulfates are much higher than those of iron oxides. This dense layer will restrict the inward diffusion of the oxygen and the outward diffusion of the sulfur gas, and then influence the overall oxidation process. The whole process can be represented by the following overall reactions:

Oxidation of pyrite:



Formation of sulfates:



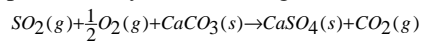
Which kind of situation occurs in practice will depend on the relative rates of the transport of oxygen to and into the particle and the thermal decomposition of pyrite under given conditions (the oxidation of sulfur gas can be assumed to be infinitely fast). The two-step process will take place if the rate of the oxygen transport through the gas film and the product layer toward the interface of the unreacted pyrite core is slower than what is needed for the oxidation of the sulfur gas generated by the decomposition of the pyrite. In this case, the oxygen will be consumed before it reaches the interface of the unreacted pyrite core. Direct oxidation of pyrite will take place if the rate of oxygen transport through the gas film and the product layer is faster than that needed for the oxidation of the released sulfur gas. In this case, the oxygen is able to reach the interface of the unreacted pyrite core.

Recent investigation [6] shows that in a cyclone preheater-like environment, the oxidation of pyrite contained in shale is strongly influenced by temperature, oxygen concentration and flow condition, and becomes significant at a temperature that is higher than around 623K. The formation of  $\text{SO}_2$  is observed to be reduced significantly with the increase of the oxygen concentrations at temperatures lower than about 673K, probably due to the formation of sulfates. The pyrite is most likely directly oxidized (as in situation C) in the

first stage cyclone as the temperature in this stage is normally much lower than 800K. In the second stage, the oxidation of the pyrite may take place by the two-step process as the temperature in this stage is often higher than 800K. Oxidation by the two-step process is more likely to occur with smaller particles in the raw meal due to the faster heating-up with small particles than with large particles.

### Absorption of SO<sub>2</sub> on Limestone

Limestone (CaCO<sub>3</sub>) is one of the most important and basic ingredients for Portland cement production. Limestone is fortunately also a sorbent of SO<sub>2</sub>. In the cyclone preheater, calcination of the limestone does not take place because of the relatively higher CO<sub>2</sub> partial pressure in the flue gas. The sulfation reaction is therefore the so-called “direct sulfation reaction”, which can be represented by the following overall reaction:



Experimental results show that the direct sulfation of limestone involves nucleation and growth of crystal grains of the solid product (anhydrite) [7], which is illustrated in Figures 3-5. Figure 3 shows the unreacted surface of limestone (Faxe Bryozo). Figure 4 shows the formation of nuclei/crystal grains of anhydrite at a relatively low conversion. Figure 5 shows the limestone surface that is covered by crystal grains of anhydrite at a much higher conversion. The nucleation and growth are orientated—the nucleation/growth of the solid product crystals only take place at certain lattice sides of calcite where lattice sizes of anhydrite and calcite closely match each other and grow at certain directions because of the direct lattice connection between anhydrite and calcite.

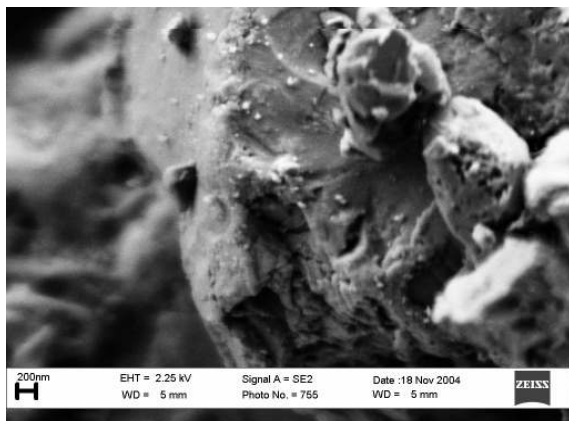


**Figure 3:** SEM image of unreacted surface of Faxe Bryozo

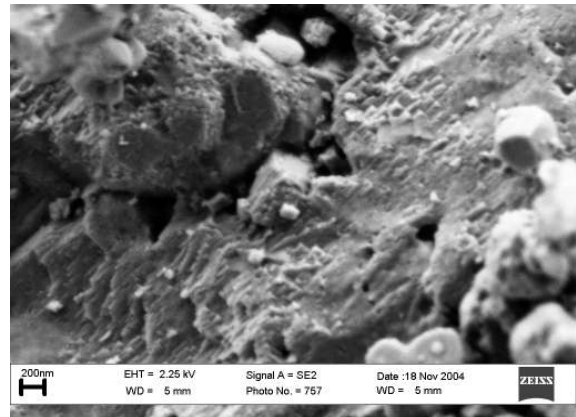


**Figure 4:** SEM image of Faxe Bryozo surface sulfated at 873 K for 10 min. ( $x \approx 0.5\%$ ) showing the emission of crystal grains of the solid product—anhydrite

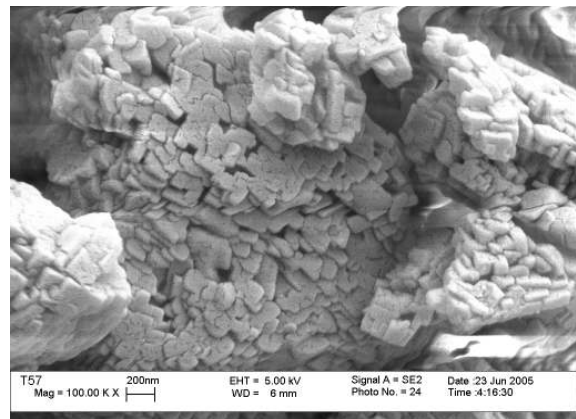


**Figure 5:** SEM image of Faxe Bryozo surface sulfated at 973 K for 10 min. ( $x \approx 4.5\%$ ) showing well shaped and orthorhombic anhydrite crystals covering the limestone surface

The entire sulfation process can be divided into two stages. The first stage extends from the start of the sulfation reaction to the initial nucleation of the formed solid product, since for the nucleation process to proceed, the sulfate concentration at the surface first has to reach a critical level for the formation of stable nuclei. The second stage involves further sulfation, nucleation and growth of the formed nuclei. A thin layer, possibly a solid solution of the formed product anions in the parent structure of calcite, may exist at the surface of the unreacted core. This thin layer acts as a kind of parent layer for both the nucleation and the subsequent growth. The surface of the parent layer is the gas–solid reactant interface as well as the reaction front for the sulfation reaction. The formed sulfate ions ( $SO_4^{2-}$ ) diffuse in solid–state through/across the parent layer to the root of the product crystal grains and feed the growth process. Carbonate ions ( $CO_3^{2-}$ ) diffuse in solid–state to the gas–solid reactant interface to participate in the reaction. Figure 6 is an illustration of the process occurring in the second stage.

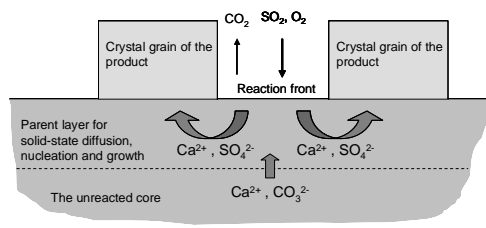


**Figure 6:** Schematic illustration of the sulfation process

The whole sulfation process consists of 5 sequential steps, i.e. gas phase diffusion, pore diffusion, chemical reaction at the gas–solid reactant interface, solid–state diffusion and nucleation and growth. At lower conversions, the sulfation process is most likely under mixed control by solid–state diffusion and chemical reaction, which explains most of the kinetic behaviors of the direct sulfation of limestone.

The direct sulfation of limestone can be significantly enhanced by increasing solid–state diffusivity by the addition of additives such as alkali metal salts,  $\text{CaCl}_2$  and HCl [8].

Alkali metal salts enhance the sulfation process by increasing solid–state diffusivity in both the solid reactant (calcite) and the solid product (anhydrite). The increase of solid–state diffusivity in the solid reactant results in the formation of fewer but larger nuclei/crystals of the solid product, while the significant increase of solid–state diffusivity in the solid product crystals causes the product crystals to lose their normal orthorhombic form and coalesce easily. A progressive covering of the surface of limestone particles/grains by the coalesced product crystals takes place during the sulfation process. Figure 7 shows the SEM image of NaCl-doped and sulfated limestone surface as a representative example for alkali metal salts.

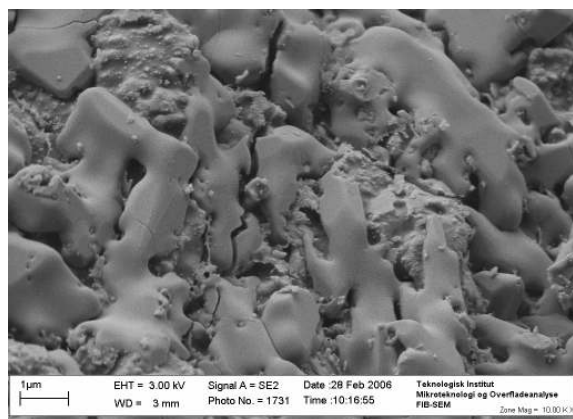


**Figure 7:** SEM image of NaCl-doped Faxo Bryozo particles sulfated at 873 K for 10 minutes (conversion = 4.4 %)

$\text{CaCl}_2$  enhances the sulfation process by increasing only solid–state diffusivity in the solid reactant (calcite).

Increase of solid–state diffusivity solely in the solid reactant results in the formation of relatively large, individual and well shaped anhydrite crystals as show in Figure 8.

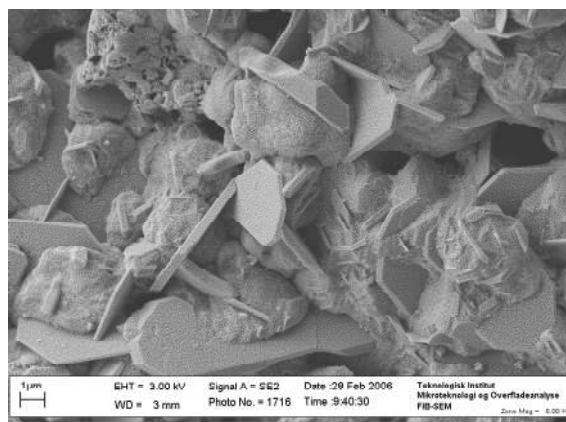


**Figure 8:** SEM image of Faxo Bryozo particles doped with  $\text{CaCl}_2$  and sulfated at 823 K for 30 minutes

The direct sulfation of limestone can be significantly enhanced by HCl in the gas phase. The enhancement is related to the formation of  $\text{CaCl}_2$  by the chlorination reaction of limestone and the formation of a melt-like product layer. The formation of the melt-like product layer is directly related to HCl in the gas phase.

### **SO<sub>2</sub> Emission from the Cyclone Preheater**

In a cyclone preheater-like environment, the sulfation of limestone is very slow at a temperature lower than about 823K. This means that the absorption of the  $\text{SO}_2$  formed by the oxidation of pyrite is ineffective in the first two stage cyclones, particularly in the first stage cyclone. The emission of  $\text{SO}_2$  from the cyclone preheater is thus a result of the combination of the fast oxidation of the pyrite contained in the raw meal and the relatively slow absorption of the formed  $\text{SO}_2$  on the limestone particles in the raw meal in the first two stage cyclones. The  $\text{SO}_2$  emission from the cyclone preheater may be reduced by, for example, the addition of alkali metal salts in the raw meal to enhance the absorption of  $\text{SO}_2$  on limestone particles in the first two stage cyclones.

### **Conclusion**

In the cyclone preheater, the pyrite contained in the raw materials is probably oxidized directly in the first stage cyclones, but by the two-step process in the second stage cyclone.

The direct sulfation of limestone involves nucleation and crystal grain growth of the solid product (anhydrite) and is usually controlled by both chemical reaction and solid–state diffusion.

The emission of  $\text{SO}_2$  from cement production is mainly caused by the fast oxidation of pyrite contained in the raw materials and the relatively slow sulfation of the limestone particles in the first two stage cyclones of the cyclone preheater because of the relatively low

temperatures in these two stage cyclones. The emission of SO<sub>2</sub> from the cyclone preheater may be reduced by addition of additives which can enhance the sulfation process by increasing solid-state diffusivity.

### **Acknowledgements**

This work is part of the CHEC (Combustion and Harmful Emission Control) Research Center funded a.o. by the Technical University of Denmark, the Danish Technical Research Council, the European Union, the Nordic Energy Research, Dong Energy A/S, Vattenfall A.B., F L Smidth A/S, and Public Service Obligation funds from Energinet.dk and the Danish Energy Research program, and is financially supported by the Technical University of Denmark and FLSmidth A/S.

### **References**

- [1] Jorgensen, F. R. A. and Moyle, F. J.; *Journal of Thermal Analysis*, 25 (1982) 473-485.
- [2] Dunn, J. G. and De, G. C. and O'Connor, B. H.; *Thermochimica Acta*, 145 (1989) 115-130.
- [3] Dunn J. G. and De, G. C.; *Thermochimica Acta*, 155 (1989) 135-149.
- [4] Hong, Y. and Fegley, B.; *Ber. Bunsenges. Phys. Chem. Vol. 101, No.12, 1997*, pp1870-1881.
- [5] Hu, G.; Dam-Johansen, K.; Wedel, S. and Hansen, J. P.; *Progress in Energy and Combustion Science*, 32 (2006) 295-314.
- [6] Hansen, Jens-Peter.; Ph. D. thesis in the Department of Chemical Engineering, Technical University of Denmark, August 2003.
- [7] Hu, G.; Dam-Johansen, K.; Wedel, S. and Hansen, J. P.; *Direct sulfation of limestone (paper submitted to AIChE J, 2006)*
- [8] Hu, G.; Dam-Johansen, K.; Wedel, S. and Hansen, J. P.; *Mechanisms of the enhancement of the direct sulfation of limestone by alkali metal salts, calcium chloride and hydrogen chloride (paper submitted to AIChE J, 2006)*





### Ling Hua

Phone: +45 45 25 28 61  
Fax: +45 45 93 29 06  
E-mail: lih@kt.dtu.dk  
WWW: <http://www.kt.dtu.dk>  
<http://www.novozymes.com>  
Supervisors: Anne Meyer  
John Villadsen  
Mogens Wümpelmann, Novozymes A/S

Ph.D. Study  
Started: September 2005  
To be completed: August 2008

## Upgrading of Microbial Biomass for Recovery of Valuable Products

### Abstract

Lipoteichoic acid (LTA), a cell wall component of most gram-positive bacteria, has been reported to induce various inflammatory mediators and to play a key role in gram-positive-microbe-mediated septic shock.  $\beta$ -1,3-Glucan, a major component of yeast cell wall, has also attracted attention due to bioactive and medicinal properties. The purpose of this project is to explore a mild and environment-friendly approach for the recovery of LTA and  $\beta$ -1,3-glucan from industrial biomass waste. In the meanwhile, it is necessary to establish relevant analytical methods to characterize the product structure and biological properties. Further work may be required to modify the product properties by using specific enzymes.

### Introduction

Lipoteichoic acid (LTA) is a cell wall component found in most gram-positive bacteria. It is an amphiphilic, negatively charged glycolipid. LTA has become increasingly considered to be an important pathogen-associated molecular pattern capable of stimulating innate immunity and responsible for gram-positive bacterial sepsis [1]. Although LTA was discovered 36 years ago [2], there is yet no standard procedure for the preparation of this biopolymer. Traditional methods adopted from lipopolysaccharide purification are based on extraction of bacteria with hot or cold aqueous phenol [3]. When adequately purified, phenol-extracted LTA turned out to be essentially inactive in inducing cytokine release as a measure of immunostimulatory activity. It was found that LTA was degraded and the residues, especially D-alanine substituents, were lost after the phenol extraction [4]. Recently Morath *et al.* isolated LTA from *Staphylococcus aureus* by butanol extraction, in which the D-alanine substituents of the polyglycerophosphate (Gro-P) backbone were preserved [4]. The highly purified LTA could efficiently stimulate monocytes via TLR2 to produce TNF- $\alpha$  [5].

$\beta$ -1,3-Glucan is another interesting biopolymer which has a wide variety of uses in the chemical, food and pharmaceutical industries. In the last decades, it has been described to show many benefits for the health of humans and animals such as immune-stimulating, anti-inflammatory, cholesterol-lowering, radioprotective, and wound-healing [6]. One important source of  $\beta$ -1,3-

glucan is the cell wall of yeasts, particularly of the baker's and brewer's yeast *Saccharomyces cerevisiae* [7]. A large number of different methods were reported for the isolation of yeast  $\beta$ -1,3-glucan [7]. Most of them use hot alkali, acids or a combination of both, which may lead to a strong degradation of the glucose chain. Therefore, there has been a need for a mild isolation process, in which the native structure of  $\beta$ -1,3-glucan is maintained, while the undesirable components like protein, lipids and other polysaccharides are removed.

Novozymes has a significant interest in investigating structure-function relationships with regard to immune modulating properties of LTA and  $\beta$ -1,3-glucan eventually in conjunction with other cell constituents.

### Specific Objectives

The first objective of this project is to design an up-scalable, environment-friendly down stream process for the recovery and purification of LTA and yeast  $\beta$ -1,3-glucan.

The second objective is to establish a simple and reliable analytical method to quantify the content of LTA and yeast  $\beta$ -1,3-glucan, which is crucial for the evaluation of each recovery step.

The third objective is to determine the chemical structure of recovered LTA and yeast  $\beta$ -1,3-glucan, and to characterize their properties by applying relevant analytical methods.

The last objective is to modify the product structure by applying pre-selected enzymes, and to investigate the structure-function relationship.

The whole approach to the project rests on the following hypotheses:

1) That microbial cells left over from industrial production of enzymes and other products harbor components that may find use as specific biomedical substances, food supplements or as (functional) food ingredients.

2) That enzymes may aid in releasing the valuable compounds or in removing undesired substances from the microbial cells for the valorization of the microbial cell substances.

### LTA and $\beta$ -1,3-Glucan Structures

Many LTAs are macroamphiphiles with their glycolipid anchored in the membrane and their poly(Gro-P) chain extending into the wall [3]. The glycolipid is Glc( $\beta$ 1-6)Glc( $\beta$ 1-3)(gentiobiosyl)diacyl-Gro in staphylococci, bacilli, and streptococci (Figure 1A). The chain length of poly(Gro-P) varies in LTA isolated from different bacteria (Figure 1B). Figure 1C shows the side chain substituents of LTA. Therefore, the microheterogeneity of LTAs is the result of several variables: (1) fatty acid composition, (2) kind and extent of glycosyl substitution, (3) length of hydrophilic chain, and (4) degree of D-alanylation [1].

In *S. cerevisiae* cells, the  $\beta$ -1,3-glucan chains, with a degree of polymerization of ~1,500 glucose units/chain, have a coiled spring-like structure that confers elasticity and tensile strength to the cell wall [7]. In cell wall extracts,  $\beta$ -1,3-glucan is found as a branched polymer with  $\beta$ -1,6 interchain links (Figure 2).  $\beta$ -1,3-Glucan is covalently linked to the other wall components: its nonreducing ends are cross-linked to the reducing ends of chitin chains through a  $\beta$ -1,4 link;  $\beta$ -1,6- and  $\beta$ -1,3-glucan chains are attached by a still-uncharacterized link. Some O-mannosylated cell wall proteins are attached to  $\beta$ -1,3-glucan via an alkali-sensitive bond.

### Methodology

The approach for this study can be briefly described as the following:

1) Search literature sources for the existing purification procedures and the analytical methods;

2) Recover LTA and  $\beta$ -1,3-glucan by adjusting the existing process;

3) Build up the analytical methods, and analyze the obtained products qualitatively and quantitatively;

4) Recover LTA and  $\beta$ -1,3-glucan with an enzyme-assisted extraction process;

5) Optimize the purification process in order to achieve high purity and high efficiency;

6) Introduce pre-screened enzymes to modify the product structure;

7) Analyze the properties of the enzymatically modified products.

### Acknowledgments

The PhD project is financed by Novozymes Bioprocess Academy, the Graduate School MP<sub>2</sub>T in Chemical Engineering, and the Technical University of Denmark.

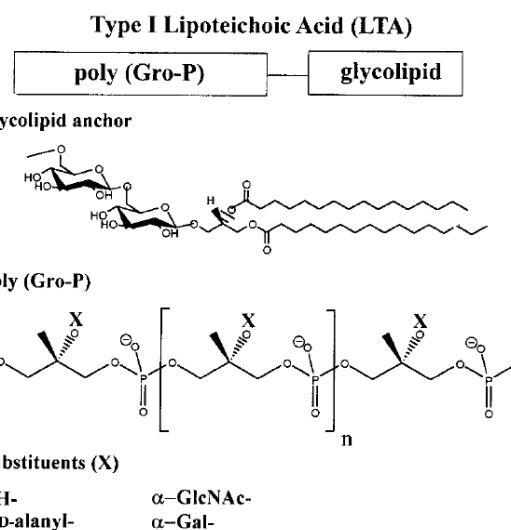


**Figure 1.** Type I LTA. (A) Glycolipid anchor, (B) poly(Gro-P), and (C) substituents (X) [1].

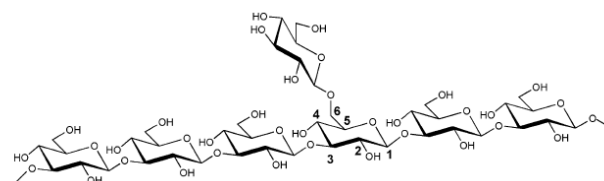


**Figure 2.** Chemical structure of 1,3- $\beta$ -D-glucan with 1,6-linked branches of glucopyranosyl units [6].

### References

1. F.C. Neuhaus, J. Baddiley, *Microbiol. Mol. Biol. Rev.* 67 (4) (2003) 686–723.
2. A.J. Wicken, K.W. Knox, *J. Gen. Microbiol.* 60 (1970) 293–301.
3. W. Fischer, H. U. Koch, R. Haas, *Eur. J. Biochem.* 133 (1983) 523–530.
4. S. Morath, A. Geyer, T. Hartung, *J. Exp. Med.* 193 (3) (2001) 393–397.
5. E. Ellingsen, et al., *Med. Sci. Monit.* 8 (5) (2002) BR149-BR156.
6. S. Freimund, M. Sauter, O. Käppeli, H. Dutler, *Carbohydr. Polym.* 54 (2003) 159–171.
7. F.M. Klis, P. Mol, K. Hellingwerf, S. Brul, *FEMS Microbiol. Rev.* 26 (2002) 239–256.



## Jakob Kjøbsted Huusom

Phone: +45 4525 2801  
Fax: +45 4525 2906  
E-mail: jkh@kt.dtu.dk  
WWW: <http://www.dtu.dk/Centre/DPC>  
Supervisors: Sten Bay Jørgensen  
Niels Kjølstad Poulsen (IMM)

### Ph.D. Study

Started: February 2005  
To be completed: January 2008

## Identification for Control – Under Control

### Abstract

Optimizing process operation through model based control strategies requires ideally a control oriented identification of the plant model. Identification for control should be performed under the conditions the process is operated at i.e. under closed loop control. Identification in closed loop implies an iterative procedure where the closed loop performance is optimized. Estimation of a process model from closed loop data needs to take the correlation between the process input and the external noise signal into account.

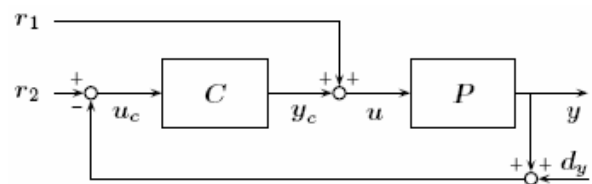
### Introduction

The increasing competition on the global market has rendered optimizing process operation a necessity for new as well as existing production in the chemical industry. Advanced control strategies based on models for a specific process plays an important role in this respect. In particular implementation of model predictive controllers (MPC) in recent years, have contributed to increase competition capabilities of the product supply chain. Control oriented process modelling is part of the frame work on application oriented modelling. System identification is an area that has received much attention but within identification for control there is still a need for development of systematic methods. Identification for control implies experiments where the collected data for identification are retrieved from a process operated under control i.e. in closed loop.

The benefits and challenges in closed loop identification has been motivated several times in the literature where a key point is, that it is the performance of the closed loop that is object for the optimization [4,7]. Since then several research groups have worked on development of suitable systematic methods for handling an iterative procedure of closed loop experiments, model parameter estimation, and enhanced control design. Most existing theory is derived for linear time invariant system and extension is not straight forward. This project is devoted to further development of optimization methods for processes through control oriented system identification.

### Closed loop identification

A stable feedback connection  $T(P,C)$ , consisting of the possible unstable system  $P$  and the controller  $C$ , will due to the controller reject disturbances and track set points. The performance of the loop can be evaluated through some norm of a performance cost function  $J(P,C)$ . In order to excite the system to reveal the dynamics, two external perturbations signals can be introduced to the system. The closed loop system with external probing signals is shown on the figure.



The signal  $r_1$  introduces a deviation from the optimal control input to the system which will act as a known disturbance on the plant input. The second signal  $r_2$  acts as a known perturbation in the reference signal and can therefore be used to move the process around to span a desired region of the output space.

### Methodology

Closed loop identification is an iterative procedure due to the influence of the control. The identified plant model is used to design a new controller in order to enhance the performance of the loop. If the performance specifications are not met repeated iterations will have

to be performed according to the following scheme until the performance is satisfactory.

- Closed loop experiment
- Estimation of a plant model,  $P_i$
- Implement controller  $C_{i+1}$  based on  $P_i$
- Evaluation of closed loop performance,  $\|J(P, C_{i+1})\|$

Identification in closed loop through the iterative scheme involves some inherent problems and design challenges that needs to be addressed in order to ensure convergence of the procedure [1]. It must be required that the performance of the control loop is equal to or better than the performance of the loop for the previous iteration.

#### Estimation

Three main approaches to model estimation from closed loop data emerge, each with a number of advantages and disadvantages [6].

- Direct identification
- Indirect identification
- Joint input/output identification

In direct identification  $\{u, y\}$  are used to estimated the process model as in open loop identification. The basic principle of not having inputs that are correlated with noise are violated by this method. A consistent estimate is only produced by this method if the data are informative and the estimate contains the true model structure. That is really the case in practice. This can imply that a very high model order have to be chosen in order to avoid bias. The advantages of the direct estimation is that it is simple and applicable regardless whether the controller are know and its complexity.

In the indirect identification a model is estimated using  $\{r, y\}$  which prevent the problem with correlations. Given this estimate of the closed loop an estimate for the process is deduced using knowledge of the controller. This method will work if the controller is known. It also requires a linear control without input saturation and anti wind up, otherwise these effects can be transferred to the estimate of  $P$ .

The joint input/output identification estimates the transfer from the excitation signals  $r_i$  to both  $u$  and  $y$ . The system model is then equal the ratio between the two transfer functions. The joint input/output method can be utilized even for a system containing an unknown nonlinear controller.

#### Approaches to closed loop optimization

In order to ensure a robust control design based on an estimated model, it is necessary to estimate both a nominal model and its uncertainty set. In the thesis by de Callafon, [1], this is done by fractional identification through the dual-Youla parameterization and robust

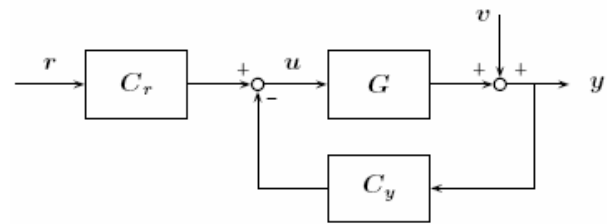
control design is based on  $\mu$ -synthesis. Through an iterative procedure, the closed loop performance is optimized in a robust sense.

A more simple approach is to replace the robust infinity norms in the identification and control design with the 2-norm to facilitate the calculations. That could lead to a least squares identification problem and a frequency weighted LQG-control design [8]. This design does not have the same robust stability or performance properties as the infinity norm design. Given an identified model and the parameter confidence regions, stability and performance can be ensured for all systems within the confidence region. This approach will improve robustness properties but only for parametric uncertainty. If the identified model structure is wrong, stability can not be guaranteed.

In the following section a data driven method will be presented which does not depend on a identified model of the system.

#### Iterative Feedback Tuning

This method of iterative performance enhancement does not include an estimate of the process model. The basic idea is to formulate a cost function and use an optimization algorithm to minimize this cost function with respect to the controller parameters. Evaluations of the partial derivatives of the cost function with respect to the controller parameters,  $\rho$ , are based on measurements taken form the closed loop system. The algorithm was first presented in [5] and have since been extended and tested in a number of papers. See [2] and [3] for an extensive overview of the development of the method and for references to applications.



Given a description of a closed loop system as depicted on the figure above, where the two degree of freedom controller,  $C = \{C_r, C_y\}$ , is implemented on the discrete linear time invariant system  $G$ , the transfer functions are given as:

$$y = \frac{C_r G}{1 + C_y G} r + \frac{1}{1 + C_y G} v = T r + S v \quad (1a)$$

$$u = \frac{C_r}{1 + C_y G} r - \frac{C_y}{1 + C_y G} v = S C_r r - S C_y v \quad (1b)$$

where  $r$  is the reference value for the measurements  $y$ ,  $u$  is the actuator variable and  $v$  is a noise signal for the system which is presented in deviation variables.  $S$  and

$T$  are the sensitivity and the complementary sensitivity function respectively. Given a desired reference model for the closed loop  $T_d$ , the desired response from the loop is given as  $y_d = T_d r$ . The performance criterion can then be formulated as a typical quadratic cost function,  $F(\rho)$ , with penalty on deviations from the desired output and the control effort. The deviation of the outputs is given as

$$\tilde{y} = y - y_d$$

The optimal set of parameters will then require that the partial derivative of the cost function with respect to the controller parameters is zero and these represent the global minimum given the admissible parameter space. This optimal solution to the minimization problem can be obtained through an iterative gradient based search algorithm in case where the cost function is convex.

$$\begin{aligned} \rho_{i+1} &= \rho_i - \gamma_i R_i^{-1} \frac{\partial F(\rho_i)}{\partial \rho} \\ &= \rho_i - \gamma_i R_i^{-1} J(\rho_i) \end{aligned} \quad (2)$$

where  $R_i$  is a positive definite matrix and  $J$  is the Jacobian. The  $i$ 'th step is then given by  $h_i = -\gamma_i R_i^{-1} J(\rho_i)$ . In case  $R = I$  the algorithm steps in the steepest decent direction. In case  $R = H(\rho)$  or an approximation to the Hessian, the Newton or Gauss-Newton algorithm appears.  $\gamma_i$  determine the step length and the choice of  $R$  and  $\gamma$  will thus affect the convergence properties of the method [5]. The determination of  $\gamma_i$  can be evaluated using a line search method.

The key contribution in Iterative Feedback Tuning is that it supplies an unbiased estimate of the cost function gradient without estimating a plant model, given that the noise  $v$  is a zero mean, weakly stationary random signal [3]. Using an estimate of the Jacobian in equation (2) instead of the analytical Jacobian as a stochastic approximation, the method will still make the algorithm converge to a local minimizer, provided that the estimate is unbiased. Given the cost function

$$F(\rho) = \frac{1}{2N} E \left[ \sum_{t=1}^N \tilde{y}_t(\rho)^2 + \lambda \sum_{t=1}^N u_t(\rho)^2 \right] \quad (3)$$

where the minimization criterion is

$$0 = J(\rho) = \frac{1}{N} E \left[ \sum_{t=1}^N \tilde{y}_t(\rho) \frac{\partial \tilde{y}_t}{\partial \rho} + \lambda \sum_{t=1}^N u_t(\rho) \frac{\partial u_t}{\partial \rho} \right] \quad (4)$$

it is seen that estimates of the gradients of deviation of the output and the control are needed in order to produce an estimate of the Jacobian. Since  $y_d$  is not a function of the controller parameters the gradient of the output is used instead of the deviation from the desired

output. The partial derivatives of the in- and output with respect to the controller parameters can be evaluated based on equation (1).

$$\frac{\partial y}{\partial \rho} = \frac{1}{C_r(\rho)} \frac{\partial C_r}{\partial \rho} T(\rho) r - \frac{1}{C_r(\rho)} \frac{\partial C_y}{\partial \rho} T(\rho) y \quad (5a)$$

$$\frac{\partial u}{\partial \rho} = \frac{\partial C_r}{\partial \rho} S(\rho) r - \frac{\partial C_y}{\partial \rho} S(\rho) y \quad (5b)$$

Estimates of these two gradients can be produced given data from three separate closed loop experiments on the system. The three experiments can be designed as follows:

1.  $r^1 = r$  i.e. the reference in the first experiment is the same as for normal operation of the process.
2.  $r^2 = y^1$  i.e. the reference in the second experiment is the output from the first experiment
3.  $r^3 = r$  i.e. the reference in the third experiment is the same as for normal operation of the process just as in the first experiment.

these experiments gives the following in- and outputs

$$\begin{aligned} \text{Ex. no 1: } & y^1 = T(\rho)r + S(\rho)v^1 \\ & u^1 = S(\rho) (C_r(\rho)r - C_y(\rho)v^1) \\ \text{Ex. no 2: } & y^2 = T(\rho)y^1 + S(\rho)v^2 \\ & u^2 = S(\rho) (C_r(\rho)y^1 - C_y(\rho)v^2) \\ \text{Ex. no 3: } & y^3 = T(\rho)r + S(\rho)v^3 \\ & u^3 = S(\rho) (C_r(\rho)r - C_y(\rho)v^3) \end{aligned}$$

The sequence of input/output data from these experiments  $\{y^i; u^i\}$  where  $i$  is 1,2 or 3 will be utilized as

$$\tilde{y} = y^1 - y^d \quad (6a)$$

$$u = u^1 \quad (6b)$$

$$\frac{\partial \hat{y}}{\partial \rho} = \frac{1}{C_r(\rho)} \left( \frac{\partial C_r}{\partial \rho} y^3 - \frac{\partial C_y}{\partial \rho} y^2 \right) \quad (6c)$$

$$\frac{\partial \hat{u}}{\partial \rho} = \frac{1}{C_r(\rho)} \left( \frac{\partial C_r}{\partial \rho} u^3 - \frac{\partial C_y}{\partial \rho} u^2 \right) \quad (6d)$$

It can be seen from equation (6a) and (6b) that the first experiments gives the measurement of the deviation from the desired output and the input which are needed in the estimate of  $J(\rho)$ . The estimate of the gradients of the input and output can be written as

$$\frac{\partial \hat{y}}{\partial \rho} = \frac{\partial y}{\partial \rho} + \frac{S(\rho)}{C_r(\rho)} \left( \frac{\partial C_r}{\partial \rho} v^3 - \frac{\partial C_y}{\partial \rho} v^2 \right) \quad (7)$$

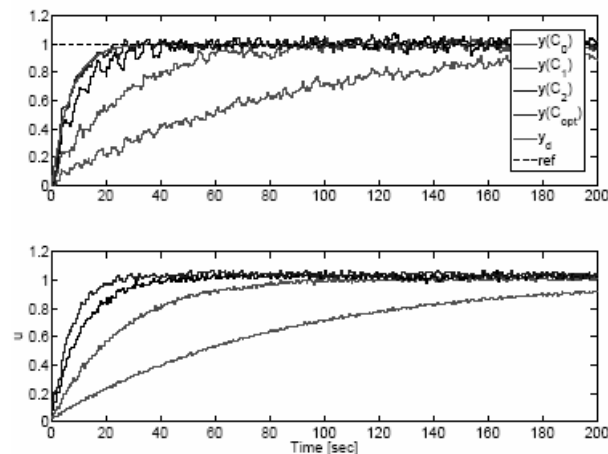
$$\frac{\partial \hat{u}}{\partial \rho} = \frac{\partial u}{\partial \rho} - \frac{S(\rho)C_y(\rho)}{C_r(\rho)} \left( \frac{\partial C_r}{\partial \rho} v^3 - \frac{\partial C_y}{\partial \rho} v^2 \right) \quad (8)$$

From this result it can be seen that the noise signal  $v^1$  plays an active part in the optimization of the controller

parameters while only the noise terms from the second and third experiment act as nuisance.

### Simulation Example

The figure and table shows the result of optimizing the setting time for a second order process with Iterative Feedback Tuning. Responses are shown for the initial, the two first iterations and for the optimal set of parameter for a PID controller with a first order derivative filter. The loop is implemented with PI action on the reference and full PID action in the feedback. The red curve  $y_d$  shows the desired response.



Iter.	$K_c$	$\tau_I$	$\tau_D$	$\alpha$	Cost
Initial	0.0250	2.0000	1.0000	0.1000	0.0757
No 1	0.0379	0.9314	0.9976	0.0916	0.0131
No 2	0.0522	0.5525	0.9921	0.0905	0.0015
Opt.	0.0705	0.4874	4.9580	0.1184	0.0003

### Conclusion

Identification for control is a strategy of iterative performance enhancement where data are collected from the closed loop system. Several approaches exist for deriving the plant model from closed loop data and for the methods of consecutive identification and control design steps.

Iterative feedback tuning is a purely data driven approach to loop performance enhancement. In a short example it has been shown that the closed loop performance can be improved in very few iterations for a settling time problem.

### Perspectives

In the future the Iterative Feedback Tuning method will be investigated with respect to obtain more informative experiments and tested for more complex controllers.

### References

- [1] Raymond Arnaud de Callafon. *Feedback Oriented identification for Enhanced and Robust Control - a fractional approach applied to a wafer stage*. PhD thesis, Technical University of Delft, The Netherlands, October 1998.
- [2] Michel Gevers. A decade of progress in iterative process control design: from theory to practice. *Journal of process control*, **12**(4):519--531, 2002.
- [3] Håkan Hjalmarsson. Iterative feedback tuning - an overview. *International journal of adaptive control and signal processing*, **16**:373--395, 2002.
- [4] Håkan Hjalmarsson, Michel Gevers, Franky De Bruyne, and Juliette Leblond. Identification for control: Closing the loop gives more accurate controllers. *IEEE Proceedings of the 33rd Conference on Decision and Control*, 4150--4455, 1994.
- [5] Håkan Hjalmarsson, Svante Gunnarsson, and Michel Gevers. A convergent iterative restricted complexity control design scheme. In *Proceedings of the 33rd IEEE Conference on Decision and Control*, volume 2, 1735--1740, 1994.
- [6] Lennart Ljung. *System identification - Theory for the user*. Prentice hall, 2 edition, 1999.
- [7] Ruud J. P. Schrama. Accurate identification for control: The necessity of an iterative scheme. *IEEE Transactions on automatic control*, **37**(7):991--994, 1992.
- [8] Zhuquan Zang, Robert R. Bitmead, and Michel Gevers. Iterative weighted least-squares identification and weighted LQG control design. *Automatica*, **31**(11):1577--1594, 1995.



## Jacob Skibsted Jensen

Phone: +45 4525 2943  
Fax: +45 4525 2258  
E-mail: jsk@kt.dtu.dk  
WWW: <http://www.kt.dtu.dk>  
Supervisors: Anne S. Meyer, BioProcess Engineering  
Max Egebo, FOSS A/S

### Industrial PhD Study

Started: February 2005  
To be completed: January 2008

## Prediction of Wine Quality from Phenolic Profiles of Grapes

### Abstract

Assessment of the phenolic content of red grapes is an important prerequisite for understanding how grape phenolics impact wine quality. In the search for a rapid and robust extraction method for grapes we have investigated the influence of selected factors on extraction efficiency of phenolics from eight different red wine grape cultivars. By applying optimized extraction conditions we found that it was possible to extract an average of 93.5 % total phenolics and 98.9 % of the anthocyanins from the grapes with only five minutes of solvent contact time. The future work will focus on investigating the relation between grape and wine phenolics and applying infrared spectroscopy for rapid measurement of the phenolics.

### Introduction

Phenolics in red wine are closely related to wine characteristics, especially wine color and astringency. The color and astringency of a red wine play an important role of wine quality and depends on the concentration and profiles of the phenolics in the wine [1]. The phenolics in wine originate mainly from the grapes, but also to a smaller degree the oak used in the wine production.

The two most abundant groups of phenolics found in grapes are anthocyanins and flavanols (figure 1). Anthocyanins are almost exclusively found in the outer layers of the grape skin and are under acidic conditions highly colored compounds, which are responsible for most of the color in young red wines [2]. Flavanols are mainly found in the skins and seeds of the grapes and are important for both the astringency and the color stability of wines [2, 3].

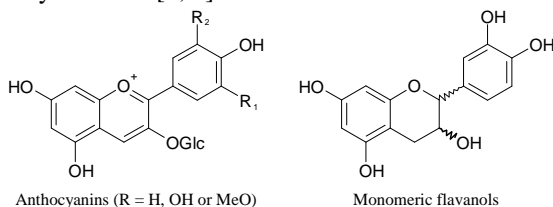


**Figure 1** - Structure of anthocyanins and monomeric flavanols.

Due to various physico-chemical phenomena and chemical reactions that occur during wine production [4], and the significant influence of various factors on

these reactions, the relationship between the grape's phenolic profiles and the phenolic profiles and quality of wines is not straight forward. Nevertheless, a main hypothesis in our ongoing work on grape and wine phenols is that the phenolics present in the grapes have a significant influence on the quality of the finished wine and that it may be possible to predict the wine quality from analysis of the phenolics in the grapes

The overall aim of the PhD study is to unravel the relation between grape and wine phenolics to be able to predict red wine quality from the phenolic profiles of grapes.

### Specific Objectives

A first requirement for quantification of grape polyphenols is to find an optimal procedure for extracting the polyphenols from grapes. The first objective is to investigate how different extraction conditions affect the extraction efficiency and robustness on different grape cultivars. This has been investigated using statistically designed experiments and used to find the optimal extraction conditions for future experiments.

A second objective is to determine the relation between grape and wine phenolics. For this purpose parallel extraction studies on different grape cultivars will be compared with wine extractions by applying controlled fermentation conditions.

The last objective is to investigate rapid measurement of grape and wine phenolics with near and mid infrared spectroscopy.

## Results and Discussion

The first requirement of a robust and efficient protocol for the extraction of grape phenolics has been investigated for selected parameters in solvent extractions on grape homogenates. The experiment was conducted as a full factorial design and the responses were fitted to a linear model accounting for main and interaction effects [5] The response levels  $y_i$  for all  $i$  observations were estimated in a linear model of the factor levels ( $x_1$ ,  $x_2$  and  $x_3$ ) accounting for main and interaction effects (equation 1).

$$y_i = \beta_0 + \beta_1 x_1 + \beta_2 x_2 + \beta_3 x_3 + \beta_{12} x_1 x_2 + \beta_{13} x_1 x_3 + \beta_{23} x_2 x_3 + \varepsilon_i \quad (1)$$

It was found, that extraction temperature (20 to 60 °C), aqueous solvent levels of ethanol (0 to 50 % v/v) and hydrochloric acid (0 to 0.1 M) had a high significant impact on the extraction efficiency of total grape phenolics (table 1).

**Table 1** - Impact of selected extraction parameters on the mean extraction degree of total phenolics across eight cultivars.

Term	Total phenolics (model fit: $R^2 = 0.99$ )		
	Prob > F	$\beta$ estimate	Std Error
Intercept	<.0001	66.49	0.36
EtOH	<.0001	18.75	0.48
HCl	<.0001	6.69	0.39
Temp	<.0001	6.63	0.48
EtOH*HCl	0.446	-0.37	0.48
EtOH*Temp	0.425	0.48	0.58
HCl*Temp	0.367	0.45	0.48

These findings were used to design an optimal extraction protocol. Using 50 % v/v acidified aqueous ethanol (0.1 M HCl) and a 1:1 ratio of solvent to grape, we found that it was possible to extract an average of 93.5 % total phenols and 98.9 % of the anthocyanins from the grapes with only five minutes of solvent contact time at 40 °C. The protocol allows high extraction of grape phenolics with an acceptable standard deviation across different cultivars (table 2).

**Table 2** - Fast extraction of grape phenolics.

	Mean extraction degree	Relative standard deviation
Anthocyanins	98.9 %	4.6 %
Total phenolics	93.5 %	5.6 %

The optimal extraction conditions will be applied in the ongoing experiments trying to unravel the relation between grape and wine phenolics.

## Conclusions and future work

In the search for a tool to predict wine quality from grape phenolics a fast solvent extraction protocol for grape homogenates has been developed. The future work will be focused on investigating the relation between grape and wine phenolics and measuring grape and wine phenolics with infrared spectroscopy.

## Acknowledgements

The Danish ministry of Science and Technology are acknowledged for their financial support for the project.

## References

1. S. Preys, G. Mazerolles, P. Courcoux, A. Samson, U. Fischer, A. Hanafi, D. Bertrand and V. Cheynier. *Anal. Chim. Acta* 563 (2006) 126-136.
2. J.A. Kennedy, M.A. Matthews and A.L. Waterhouse. *Phytochemistry* 55 (2000) 77-85.
3. D.O. Adams. *Am. J. Enol. Vitic.* 57 (2006) 249-256.
4. K.L. Sacchi, L.F. Bisson and D.O. Adams. *Am. J. Enol. Vitic.* 56 (2005) 197-206.
5. D.C. Montgomery. *Design and Analysis of Experiments*. John Wileys & Sons, New York, NY. 2001.



**Kent Johansen**

Phone: +45 4525 2876  
 Fax: +45 4525 2258  
 E-mail: kej@kt.dtu.dk  
 WWW: http://www.ivc-sep.dtu.dk  
 Supervisors: Alexander A. Shapiro  
 Erling H. Stenby

Ph.D. Study  
 Started: September 2004  
 To be completed: July 2007

**Statistical Methods for History Matching**

**Abstract**

A precise description of the physical properties of an oil reservoir can facilitate the operation of the oil field. Traditionally, the parameters determining the nature of the reservoir are determined by laboratory measurements of core samples and by history matching of the initial production data. In history matching measured production data is fitted by running full reservoir simulations. This process is very time consuming even when the simulations are carried out on powerful computers. Therefore, an alternative method to perform the history matching or parts of this is desired. This project deals with the application of statistical methods to carry out history matching and reservoir characterization.

**Introduction**

History matching is an important part of the characterization of an oil or gas reservoir. It is a process where production data from the initial stage of reservoir development is used to determine reservoir parameters and to predict the production in advance. The particular parameters measured at the production site are the injection rate, the oil production rate, the watercut, the gas-oil ratio, the bottom-hole pressures and others, as functions of time. History matching involves determination of permeability, porosity, relative permeabilities etc. Traditionally, full scale simulations on computers are carried out until the simulated production history matches the production history from the actual field sufficiently well. The method suffers from the fact that full scale simulations are computationally hard and time consuming. Also, the method demands an element of human intervention when parameters are adjusted which again makes the task of history matching a slow process. It is the aim of this project to develop a method which can facilitate the history matching of oil reservoirs.

**Specific Objectives**

The specific objective of the project is the development of a viable method which can facilitate the process of history matching. The method should honor the recorded production history from the field as well as honoring possible geological knowledge from e.g. test drillings or seismic surveys.

**Discussion**

History matching may be regarded as an optimization problem where an error function measuring the misfit between simulated and observed production data is minimized. This is done by modifying the properties of the reservoir model on the grid block scale. The error function may take the form

$$E = \sum_{i=1}^{N_T} \left( \frac{p_i^{Sim} - p_i^{Obs}}{p_i^{max}} \right)^2 + (WCUT_i^{Sim} - WCUT_i^{Obs})^2 \quad (1)$$

where  $p_i$  is pressure at time  $i$  and  $WCUT_i$  is the corresponding watercut. The terms in equation (1) may be weighted by individual weights if specific parts of the history are expected to be more important than others.

In a general formulation the history matching problem may be formulated as the following optimization problem:

$$\mathbf{K}^* = \underset{\mathbf{K}}{\text{Argmin}}[E(\mathbf{K})] \quad (2)$$

where the matrix  $\mathbf{K}$  represents the absolute permeability in every grid block of the reservoir model. Even for a small reservoir model the dimension of  $\mathbf{K}$  is in the order of magnitude of  $\mathbf{R}^{100} \times \mathbf{R}^{100}$  and can be significantly larger. If additional properties such as porosity or water saturation are included in the history

matching these must be included in the formulation too. Solution of the problem is computationally hard and no unique solution exists since many different permeability fields may honor the measured production data.

### Mathematical statement of the problem

The governing equations for the two-phase immiscible problem studied in this paper are derived by considering the conservation of mass for the water and oil components. Neglecting diffusion/dispersion effects, the equations are:

$$\frac{\partial}{\partial t}[\phi \rho_w S_w] - \nabla \cdot \left[ \rho_w \frac{\mathbf{k} k_{rw}}{\mu_w} (\nabla P - \rho_w g \nabla Z) \right] + Q_w = 0 \quad (3)$$

$$\frac{\partial}{\partial t}[\phi \rho_o S_o] - \nabla \cdot \left[ \rho_o \frac{\mathbf{k} k_{ro}}{\mu_o} (\nabla P - \rho_o g \nabla Z) \right] + Q_o = 0$$

in which  $\mathbf{k}$  is the permeability tensor,  $k_{rj}$  is the relative permeability of phase  $j$ ,  $\mu_j$  is the viscosity of phase  $j$  and  $Z$  is the depth of the reservoir (downwards positive), and  $g$  is the gravitational acceleration.  $Q_w$  and  $Q_o$  represent sources/sinks due to wells. Darcy's law is used to represent phase velocities.

The system of equations is solved together with a number of constraints acting at the wells as boundary conditions. In the case considered later it is assumed that external boundaries of the reservoir act as impermeable barriers, i.e. no-flow conditions are imposed on external boundaries. Injection wells are constrained to inject at a specified rate and production wells are constrained to a constant bottomhole pressure.

The measurable values are the pressures in the injection wells and the ratio of water in the production (watercut) as functions of time. They are measured during a period  $0 < t < T$ . On the basis of this data, the permeability field  $\mathbf{k}$  should be inferred. In the examples considered here we consider a setup with 2D flow and gravity is neglected. The reservoir is assumed to be isotropic and the permeability tensor is reduced to be a single permeability coefficient which differs from one gridblock to another. The flow occurs in a simple system of wells consisting of three injection wells and one production well, corresponding to a symmetry element of a fixed nine spot well pattern. Generalization onto more complex cases is straightforward.

Spatial and temporal discretization of the governing flow equations gives:

$$\mathbf{T}^{n+1} \mathbf{u}^{n+1} - \mathbf{D}(\mathbf{u}^{n+1} - \mathbf{u}^n) - \mathbf{Q} = \mathbf{R}^{n+1} \quad (4)$$

where  $\mathbf{u} = [p_1 S_1 \dots p_N S_N]$  is the vector of unknowns which in the fully implicit formulation consists of gridblock pressures and (water) saturations and possibly well pressures depending on the constraints imposed on the system. Matrices  $\mathbf{T}$  and  $\mathbf{D}$  are dependent on the discretization scheme, which in our case is a first order fully implicit finite difference

scheme.

In the fully implicit formulation the accumulation term can be expressed as:

$$\mathbf{D}(\mathbf{u}^{n+1} - \mathbf{u}^n) = \frac{\mathbf{V}}{\Delta t} (\phi \rho \mathbf{S} |_{t+\Delta t} - \phi \rho \mathbf{S} |_t) \quad (5)$$

where  $\mathbf{V}$  contains the gridblock volumes and  $\Delta t$  is the time step given as  $t^{n+1} - t^n$ .  $\mathbf{S}$  is a vector with the gridblock water and oil saturations.

### Adjoint Formulation

We are now setting up the basis to calculate the sensitivity of a scalar function  $\beta$  with respect to a reservoir property  $\mathbf{m}$ , e.g. absolute permeabilities at gridblocks. The function  $\beta$  will be treated as a function of  $\mathbf{u}$ , and  $\mathbf{m}$ , i.e.

$$\beta = \beta(\mathbf{u}^1, \dots, \mathbf{u}^L, \mathbf{m}) \quad (6)$$

where  $\mathbf{u}^i$  is the solution of the discretized model equations at the  $i$ th time step and  $L$  is the last time step where the sensitivity is desired.  $\mathbf{m}$  is an arbitrary physical parameter, e.g. a permeability field. The adjoint formulation is based on the formation of an adjointed system of equations in which the discretized model equations (4) are acting as constraints. Adjoining the discretized equations to  $\beta$  yields:

$$J = \beta + \sum_{n=0}^L (\lambda^{n+1})^T \mathbf{R}^{n+1} \quad (7)$$

where  $\lambda^{n+1}$  is the vector of adjoint variables, or alternatively, a vector of Lagrange multipliers for the model constraint at time step  $n+1$ .

Since the constraints are driven to zero by the nonlinear solver in the simulator the following equation holds ([1], [2]):

$$\nabla_{\mathbf{m}} J = \nabla_{\mathbf{m}} \beta \quad (8)$$

The size of the adjoint vector is similar to the size of  $\mathbf{u}$ , i.e. it has the length  $2N + N_{inj}$  where  $N$  is the number of gridblocks and  $N_{inj}$  is the number of injectors. Here it is assumed that producers are pressure constrained and injectors are rate constrained. In the following derivation the variable  $\mathbf{m}$  is assumed to represent the permeability field and the notation  $\mathbf{k}$  will be used in stead of  $\mathbf{m}$ .

The total differential of the adjointed system of equations (7) is calculated:

$$dJ = d\beta + \sum_{n=0}^L [(\lambda^{n+1})^T (\nabla_{\mathbf{u}^{n+1}} (\mathbf{R}^{n+1})^T)^T d\mathbf{u}^{n+1} + (\nabla_{\mathbf{k}} (\mathbf{R}^{n+1})^T)^T d\mathbf{k}] + \sum_{n=0}^L (\lambda^{n+1})^T (\nabla_{\mathbf{u}^n} (\mathbf{R}^{n+1})^T)^T d\mathbf{u}^n \quad (9)$$

Changing the sum to start from index 1 gives:

$$dJ = d\beta + \sum_{n=1}^L [((\lambda^n)^T (\nabla_{\mathbf{u}^n} (\mathbf{R}^n)^T)^T + (\lambda^{n+1})^T (\nabla_{\mathbf{u}^n} (\mathbf{R}^{n+1})^T)^T) d\mathbf{u}^n + (\lambda^n)^T (\nabla_{\mathbf{k}} (\mathbf{R}^n)^T)^T d\mathbf{k}] + BT \quad (10)$$

where

$$BT = (\lambda^{L+1})^T [(\nabla_{\mathbf{u}^{L+1}} (\mathbf{R}^{L+1})^T)^T d\mathbf{u}^{L+1} + (\nabla_{\mathbf{k}} (\mathbf{R}^{L+1})^T)^T d\mathbf{k}] + (\lambda^1)^T (\nabla_{\mathbf{u}^0} (\mathbf{R}^1)^T)^T d\mathbf{u}^0 \quad (11)$$

The initial conditions are invariant which implies that  $d\mathbf{u}^0 = 0$ . If  $\lambda^{L+1}$  is chosen to be 0 the  $BT$  term is obviously zero. This will serve as the end condition for the adjoint problem.

Lets us now take the total differential of the scalar parameter  $\beta$ :

$$d\beta = \sum_{n=1}^L [(\nabla_{\mathbf{u}^n} \beta)^T d\mathbf{u}^n] + (\nabla_{\mathbf{k}} \beta)^T d\mathbf{k} \quad (12)$$

Equation (10) is combined with equation (12):

$$dJ = \sum_{n=1}^L [(\nabla_{\mathbf{u}^n} \beta)^T + (\lambda^n)^T (\nabla_{\mathbf{u}^n} (\mathbf{R}^n)^T)^T + (\lambda^{n+1})^T (\nabla_{\mathbf{u}^n} (\mathbf{R}^{n+1})^T)^T] d\mathbf{u}^n + (\lambda^n)^T (\nabla_{\mathbf{k}} (\mathbf{R}^n)^T)^T d\mathbf{k} + (\nabla_{\mathbf{k}} \beta)^T d\mathbf{k} \quad (13)$$

The essential operation in the adjoint approach is to simplify the total differential in equation (13) by forcing the terms multiplying the  $d\mathbf{u}$  terms to vanish. This is done by equating the proper terms to zero, i.e.:

$$(\nabla_{\mathbf{u}^n} \beta)^T + (\lambda^n)^T (\nabla_{\mathbf{u}^n} (\mathbf{R}^n)^T)^T + (\lambda^{n+1})^T (\nabla_{\mathbf{u}^n} (\mathbf{R}^{n+1})^T)^T = 0 \quad (14)$$

Transposing equation (14) gives:

$$(\nabla_{\mathbf{u}^n} (\mathbf{R}^n)^T)^T \lambda^n = -(\nabla_{\mathbf{u}^n} (\mathbf{R}^{n+1})^T)^T \lambda^{n+1} - (\nabla_{\mathbf{u}^n} \beta)^T \quad (15)$$

which is the system of adjoint equations. If  $\lambda^n$  is consistent with the adjoint equation (15) the sensitivity of  $\beta$  with respect to the parameter vector  $\mathbf{k}$  can be calculated from equation (13) which reduces to:

$$dJ = \sum_{n=1}^L [(\lambda^n)^T (\nabla_{\mathbf{k}} (\mathbf{R}^n)^T)^T d\mathbf{k}] + (\nabla_{\mathbf{k}} \beta)^T d\mathbf{k} \quad (16)$$

The sensitivity is therefore given as (remember equation (8)):

$$\frac{dJ}{d\mathbf{k}} = \nabla_{\mathbf{k}} \beta = \sum_{n=1}^L [(\lambda^n)^T (\nabla_{\mathbf{k}} (\mathbf{R}^n)^T)] + (\nabla_{\mathbf{k}} \beta) \quad (17)$$

Let us now dwell a little on the structure of the adjoint system (15). The equation is linear in the Lagrange multipliers (or equivalently the adjoint variables). The multipliers may be determined by stepping backwards in time starting from  $t = t_L$ . The condition  $\lambda^{L+1} = 0$  is used to initialize the system. The matrix  $(\nabla_{\mathbf{u}^n} (\mathbf{R}^n)^T)$  multiplying the Lagrange multiplier  $\lambda^n$  can be identified as the transposed Jacobian of the discretized model equations. The Jacobian is formed during the forward simulation to be used in the nonlinear solver (which is the Newton method) and is therefore known. The other matrix

occurring in equation (15) multiplying  $\lambda^{n+1}$  is a block diagonal matrix related to the accumulation term in the model equations. The scalar function  $\beta$  is chosen by the user. In general reservoir engineering applications  $\beta$  may be the bottom hole pressure at injectors or the watercut or other measurable quantities. If several sensitivities are required, e.g. for bottom hole pressures at multiple injectors, an adjoint equation system has to be formulated for each pressure. However, it is important to recognize that only the righthand sides of equation (15) change when  $\beta$  is changed. This means

that only one factorization of the left hand side matrix is required which reduces the computational work significantly. If  $\beta$  does not depend explicitly on  $\mathbf{k}$  the derivative  $\nabla_{\mathbf{k}} \beta$  in the sensitivity equation (17) disappears. The implemented adjoint based gradient calculation has been verified by comparison with numerical results obtained from perturbing the gridblock permeabilities. A good agreement has been observed with errors occurring around the second digit.

Only one reservoir simulation and one solution of the adjoint system are needed to calculate the sensitivity regardless of the number of grid blocks. This is the main

advantage of the adjoint based method since the number of grid blocks is usually very high in realistic reservoir simulations. Figure 1 shows an example of a sensitivity calculation for a quarter nine spot well configuration.

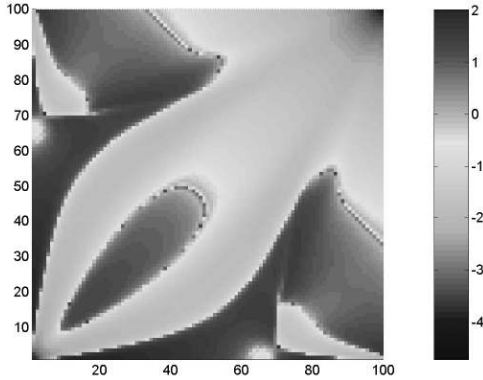


**Figure 1:** Example of a sensitivity field calculated by the adjoint approach. The figure shows the sensitivity of bottom hole pressure with respect to permeability for an injector in the grid block positioned at (1,1) at a particular time in a quarter nine spot configuration. A scaling has been used to enhance visual quality.

### Regularization

The problem of history matching oil production is usually very ill-posed because of the sparsity of the measured production data compared to the huge number of unknowns that are being determined by history matching. To deal with the underdetermined system one can either introduce a suitable parameterization of the system to reduce the number of unknowns. This can be done by constraining the permeability by geostatistical means, e.g. gradual deformation [3] or probability perturbation [4]. Another approach is to regularize the system. The latter approach is used in the present work.

In order to regularize the problem the sum-of-squares objective function (1) is augmented with a term which penalizes deviations from the initial guess. The initial guess is denoted as  $\mathbf{k}^{prior}$ . Regularization increases the number of equations with the number of grid blocks which means that the problem goes from being underdetermined to being overdetermined. The problem is no longer as ill-posed and a standard optimization method can readily be used to find the optimal permeability distribution. The initial guess (or prior) significantly influences the final results. Thus, it should be based on the additional information available about the reservoir, e.g. from geological or seismic data. The regularized objective function takes the form:

$$E = \frac{1}{2} \sum_{i=1}^{N_{obs}} w_i (d_i^{obs} - d_i^{sim})^2 + \frac{\sigma^2}{2} \sum_{j=1}^{N_{blk}} (k_j^{prior} - k_j)^2$$

Where  $d$  denotes measured or simulated production

data. The parameter  $\sigma$  controls the degree of regularization and is commonly denoted as the regularization parameter. It is difficult to come up with a suitable value for the regularization parameter based on a priori knowledge and therefore some sort of trial and error investigations must be expected to be necessary before a reliable result is obtained. The regularization punishes deviations from an initial realization of permeability which we will refer to as the *prior*. Information regarding the statistics of the permeability distribution or samples of permeability may be input to the optimization problem through the prior.

### Optimizer

In this particular work the Levenberg-Marquardt method has been chosen for the optimization. This method is specially designed to deal with nonlinear least squares problems and is thus suitable for the history matching purpose. The method is generally recognized for being robust as well as efficient in a wide range of optimization problems.

### Results

A synthetic heterogeneous reservoir is used to test the gradient based optimization method. The reference field is generated by sequential Gaussian simulation and is shown in Figure 2 and is discretized into a 50 by 50 grid, i.e. we will have 2500 unknown permeabilities to adjust in the history matching. The matching will be based on measurements of bottom hole pressures in the three injectors and measurements of the fraction of water (i.e. watercut) at the producing well. The measurements are acquired at 8 times during the first 200 days of production.

Figure 3 shows the prior permeability field used in the regularization of the objective function. The prior has been constrained to the reference permeabilities at the four well locations. This is justified since it is expectable that core samples from the drilling operations are available.

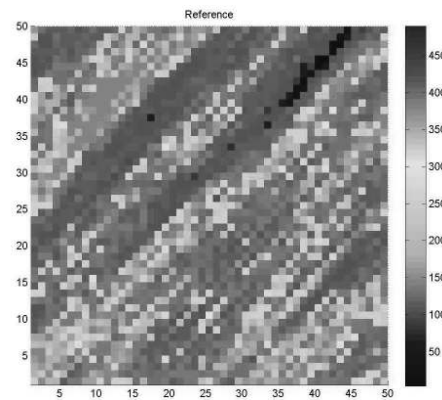


**Figure 2:** Synthetic reference permeability field. The field is operated as a quarter nine spot configuration with the producer in the upper right corner of the reservoir.

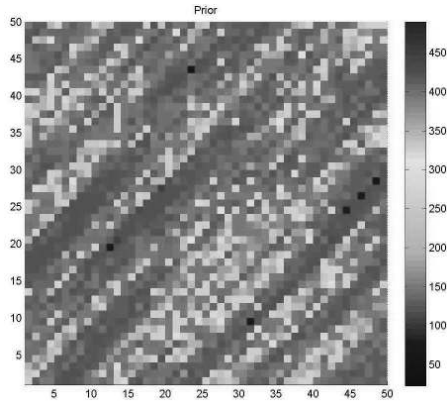


**Figure 3:** The prior permeability field. The field is conditioned to the known permeabilities at the four wells and the same second order statistics as the reference.

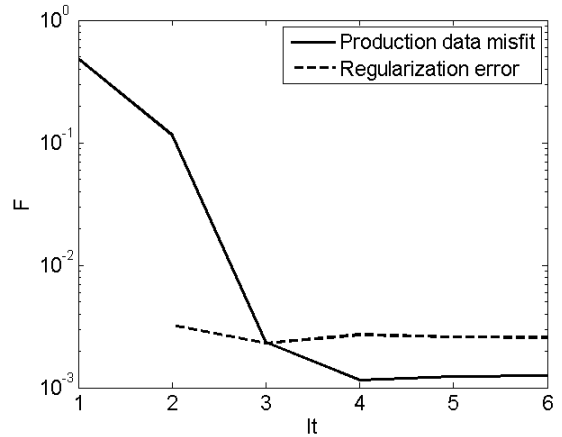


**Figure 6:** Evolution of the objective function during optimization. The solid line represents the production data mismatch term and the dashed line represents the regularization term in the objective function.

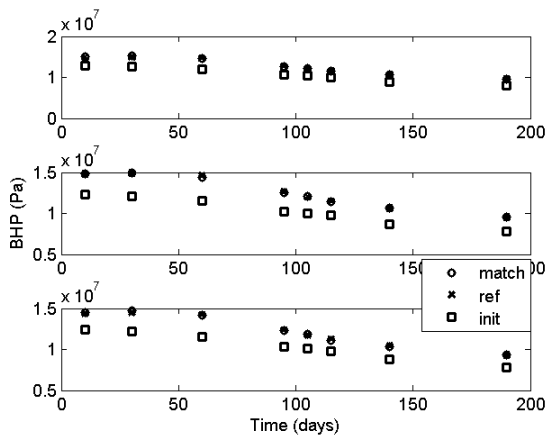


**Figure 4:** Reference, initial and matched bottom hole pressures.

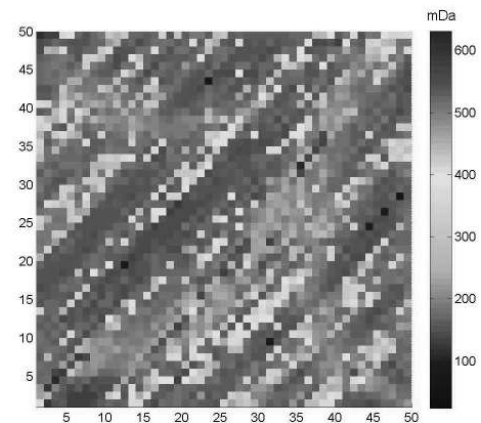


**Figure 7:** Resulting field after history matching.

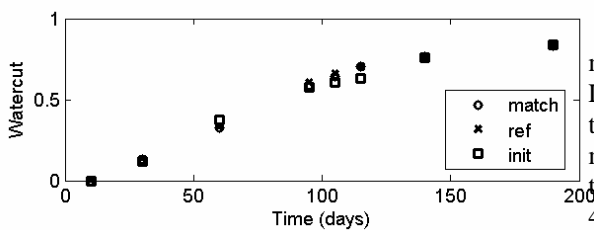


**Figure 5:** Reference, initial and matched watercut.

Figures 4 and 5 show the reference, initial, and matched pressures and watercut, respectively. The Levenberg-Marquardt method is capable of adjusting the permeability field to achieve a significantly better match than the initial model provides. The evolution of the objective function is shown on Figure 6. After only 4 iterations the match is achieved. A general observation based on several other cases is that improvement of the production mismatch ceases when the regularization term becomes comparable or larger than the production mismatch term. This circumstance can be dealt with by applying a dynamic update of the regularization parameter where the regularization impact is decreased as the match becomes better. A simple implementation of a dynamic update has been carried out but will not be discussed any further here. Figure 7 shows the resulting permeability field. If this field is compared to the prior it is evident that the optimization has increased the permeability on the diagonal. This has been done in order to restore the higher connectivity in the North-East direction which is seen in the reference. It should be noted that the

resulting field is still consistent with the heterogeneity seen in the reference. In other words, the optimization has not deteriorated the geologic consistency in the permeability field. The gradient based history matching technique has proven to be efficient in cases with Gaussian fields as shown above. Coupled with a dynamic update of the regularization parameter the method is relatively robust. However, the end result is very dependant on the prior used in the regularization term.

### Conclusion

The use of geostatistical parameterizations in history matching is a powerful way of integrating various data types into a reservoir model. However, such methods are known to have slow convergence and are thus intractable in realistic cases if the number of core samples or other geologic information is low. Here we have focused on the use of classical optimization theory in a history matching context. Regularization has played an important part in this approach since the regularization not only makes the problem less ill-posed but also provides a convenient way of integrating prior knowledge into the reservoir model. The Levenberg-Marquardt method has been used to adjust the reservoir model. This approach is only possible due to the efficiency of the adjoint based gradient calculation which enables us to calculate the sensitivity of production data with respect to grid block permeabilities efficiently. The method has been tested on a 2D synthetic heterogeneous reservoir. Within 4-5 iterations in the Levenberg-Marquardt method a 2500 gridblock model was matched to historic pressure and watercut data. The resulting reservoir model was still consistent with the second order statistics of the reference permeability distribution.

### Future Perspectives

Future work will be invested in development of a more hybridized approach where geostatistical information plays a more direct role. Especially, handling of higher order statistics will be investigated. Higher order statistics play an important role in the description of more complex geologic scenarios like channelized reservoirs. Merging the gradient techniques with methods based on categorical variables is also a challenge which has a large practical applicability.

### Acknowledgements

The project is part of the Molecular Products and Product Technology (MP2T) in the graduate school in chemical engineering. The industrial cooperater is Dansk Olie og Naturgas A/S.

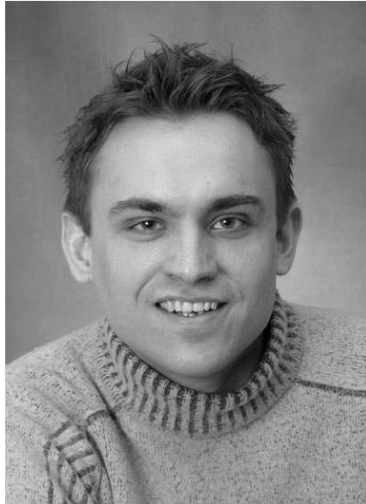
### List of Publications

K. Johansen, A. A. Shapiro, E. H. Stenby, 'Stochastic and Deterministic History matching techniques', IEA-EOR symposium on Reservoir Management through Monitoring, 2006, France.

K. Johansen, A. A. Shapiro, E. H. Stenby, 'Gradient Based History Matching Utilizing Gradual Deformation', Society of Petroleum Engineers, 2007, *working title, in preparation.*

### References

- [1] Wu, Z., Reynolds, A. & Oliver, D. (1998), 'Conditioning geostatistical models to two-phase production data', *Society of Petroleum Engineers (SPE No. 49003)*, 205–216.
- [2] Li, R., Reynolds, A. & Oliver, D. (2001), 'History mathing of three-phase flow production data', *Society of Petroleum Engineers (SPE No. 66351)*
- [3] Hu, L. Y. (2000), 'Gradual deformation and iterative calibration of Gaussian-related stochastic models', *Mathematical Geology* **32**(1), 87–108.
- [4] Caers, J. (2002), 'Geostatistical history matching under training-image based geological model constraints', *Journal of Petroleum Science and Engineering (SPE No. 77429)*.



**Morten Rode Kristensen**  
Phone: +45 4525 2876  
Fax: +45 4525 2258  
E-mail: mrk@kt.dtu.dk  
WWW: <http://ivc-sep.kt.dtu.dk/staff/MRK/mrk.htm>  
Supervisors: Per G. Thomsen, IMM  
Michael L. Michelsen, KT  
Erling H. Stenby, KT

Ph.D. Study  
Started: August 2004  
To be completed: August 2007

## Numerical Simulation of In-Situ Combustion

### Abstract

Numerical simulation of fluid flow in petroleum reservoirs has been an active area of research for several decades. Increasingly large models are being solved on powerful computers, but simulation capacity still limits the size and complexity of models needed to describe advanced recovery processes. This is especially true for simulation of the *in-situ combustion* enhanced oil recovery process, which rely on air injection into the reservoir. Simulating in-situ combustion is a challenging multi-scale problem. The purpose of this project is the development of accurate, efficient and reliable models and algorithms for performance prediction in in-situ combustion processes.

### Introduction

In-situ combustion (ISC), also known as high pressure air injection or fire-flooding, is receiving strong renewed interest in the petroleum industry because the easy to produce oil reserves are declining. This thermal process can be effective in improving recovery of existing reservoirs as well as unlocking the vast reserves of heavy oil in the world in an environmentally sound manner. ISC is the process of injecting air into an oil reservoir to oxidize a small fraction of the hydrocarbons present. A schematic is shown in Figure 1. The slow moving combustion front is propagated by a continuous flow of air. Figure 1 gives a schematic representation of characteristic temperature and saturation zones in ISC. Starting from the injection well the burned zone is the volume already swept by the combustion zone. In the combustion zone injected oxygen reacts with residual hydrocarbons generating carbon oxides and water, and producing heat. Hydrocarbons contacted by the leading edge of the high temperature zone undergo thermal cracking and vaporization. Mobilized light components are transported downstream where they mix with the original crude. The heavy residue, which is normally referred to as coke, is deposited on the core matrix and is the main fuel source for the combustion. Downstream of the vaporization zone is the steam plateau which is formed from water of combustion and vaporization of formation water. Further downstream the steam condenses when the temperature drops below the steam saturation temperature, and a hot water bank is formed. The leading edge of this bank is the primary area of oil mobilization where the oil is banked by the hot water.

Thermal conduction allows heat to sweep areas of the reservoir not directly contacted by hot fluid. For heavy oils, the recovery efficiency is substantially improved because of the dramatic reduction of the viscosity of heavy oils with temperature. But, ISC is applicable to lighter oils as well because it also promotes production through flue-gas drive, thermal expansion, steam and water drive, and vaporization of lighter oils. ISC can recover oil economically from a variety of reservoir settings.

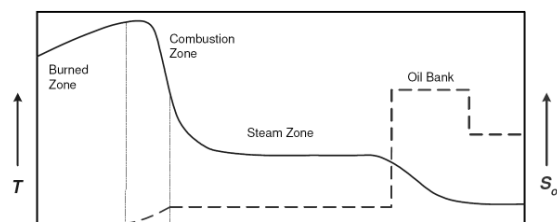


**Figure 1:** Characteristic temperature and saturation profiles in an ISC process.

### A Multi-Scale Process

ISC is one of the most physically complex enhanced oil recovery processes currently in use. Driven by complex chemical reactions the oil mobility is increased with the elevated temperatures and the fluids are displaced by a combination of steam, water and gas drive. The spatial as well as temporal scales in ISC on vary over many orders of magnitude. The bulk of the chemical reactions take place in the narrow reaction zone that may be less than a meter in thickness compared to reservoir scales

of hundreds or thousands of meters. Moreover, combustion reactions often occur in fractions of a second, whereas the temporal scales associated with convective transport may be running to days or years. Accurate prediction of field performance in such a multi-scale process is an immense challenge requiring a hierarchical approach, in which both spatial and temporal resolution is adapted in order to capture the crucial input from all levels of activity.

The overall performance of an ISC process is governed in a complex way by reservoir heterogeneity, well configurations, injection rates and composition, initial oil saturation and distribution and both thermodynamic and chemical properties of the rock and fluids. Reliable prediction of field performance requires a fully integrated approach in which the important contributions from all levels are taken into account.

The spatial scales affecting ISC span from large geological features such as faults of the size of the reservoir to the very small scale at which chemical reactions happen in the combustion zone. Faults, fractures and the placement of wells determine global flow patterns, but local displacement efficiency is governed by small scale heterogeneity in porosity and permeability of the reservoir and by the chemical and thermodynamic behavior of the fluids. Permeability fields are often obtained from high-resolution geocellular models having gridblock sizes on the order of a meter. Reservoir simulations, however, are carried out using gridblocks that are 1–2 orders of magnitude larger due to computational constraints. Upscaling of the permeability or transmissibility field, in which local flow behavior is taken into account, is routinely done. As mentioned above, the bulk of the chemical reactions happen in a narrow combustion zone being less than a meter in thickness compared to standard gridblock sizes of, say, 50 meters. Thus, the spatial scale for chemical reactions is smaller than the smallest scale normally resolved in reservoir simulations. Consequently, the temperature profile on the simulation grid will be too smooth, and important phenomena such as ignition/extinction or quenching may not be predicted correctly.

Relating to temporal scale, a number of different processes may be identified in ISC, each having its own characteristic scale. Most of the existing ISC models include convective mass transfer, convective and conductive heat transfer, kinetically controlled chemical reactions and fluid phases in thermodynamic equilibrium. The phase equilibrium assumption implicitly states that the time scales for the interphase mass transfer processes occurring when phases come to an equilibrium state, are much faster than all other time scales. Of the remaining processes, the chemical reactions are likely to occur on time scales that are again much faster than the scales for mass and heat transport.

Although being multi-scale in nature, the question remains whether all the processes in ISC represent essential physics that needs to be resolved in a simulation. The goal of ISC simulation is to provide

reliable predictions of performance, typically in terms of production, for a given ISC project. The production certainly depends on large scale features such as well placement, but the small scale behavior, spatial as well as temporal, in the combustion zone may be equally important. ISC processes are driven by chemical reactions. Chemical kinetics depends strongly on temperature, thus failing to capture temperature peaks and, in general, smoothing out temperature profiles on too coarse a grid will lead to inaccurate prediction of reaction, which in turn will affect the amount of heat released and combustion gases evolved, ultimately resulting in wrong predictions of oil displacement. Ahead of the combustion front (see Figure 1) the oil is mobilized by a combination of steam, water and gas drive. Lighter oil components will vaporize easily and be transported downstream. The compositional behavior in this region will determine the amount and composition of the oil left behind as fuel for the combustion. Therefore, accurate prediction of phase behavior as well as flow is likely to impact overall performance. Errors at this small scale will feed into overall production calculations, thereby rendering the results unreliable. Hence, the important processes in ISC are indeed multi-scale with strong nonlinear interactions between different scales and efficient computational methods must be developed that handle this multi-scale nature.

#### **Adaptive Framework for ISC Simulation**

The multi-scale challenge may be approached computationally by either attempting to resolve all relevant scales or by making use of appropriate subgrid scale models to represent the small scale processes. The approach taken in this project is to resolve the relevant scales by using adaptive numerical methods.

Adaptivity in space is achieved by using adaptive gridding techniques, in which the computational grid is adapted dynamically to the regions of interest. A dense grid can then be used to resolve the fine scale changes in the combustion zone, whereas a much coarser grid is used in regions away from the combustion zone.

In order to capture the fast dynamics of chemical reactions in the combustion zone, the reaction kinetics must be integrated using time steps that are much smaller than those necessary for capturing the effects of convection and conduction. An intuitive way of approaching this problem numerically is by splitting and fractional time stepping where convective and conductive terms in the equations are separated from reaction terms. Each global time step then consists of a series of substeps, in which the individual terms are integrated separately, the advantage being that small time steps can be applied only to those terms requiring high resolution. The separation of scales in the problem is thereby exploited numerically by adapting the time integration to the individual scales. The cost of using a splitting method is a numerical error introduced, since in each substep only one process is taken into account and the interaction with the other processes neglected.

### Specific Objectives

The overall objective of this project is to develop the computational framework for ISC simulation. We focus in particular on aspects related to temporal integration. The use of operator splitting techniques allows a separation of the algorithmic development into specific components, each tailor-made for integration of different parts of the overall equations. The project is carried out in collaboration with Department of Energy Resources Engineering at Stanford University. The DTU focus in the project is on efficient methods for integration of chemical kinetics and phase behavior and the integration of this component into the splitting framework. The Stanford focus is on adaptive mesh refinement techniques and high-resolution methods for computation of transport.

### Efficient Reaction Integration

In a global time step of the simulation, the operator splitting method breaks down the problem into individual subproblems on each physical process (reaction, convection, conduction, etc.). The ISC equations comprise a set of partial differential algebraic equations (PDAEs) consisting of energy and mass balances and thermodynamic equilibrium constraints. The splitting scheme applied to the ISC equations is a hybrid IMEX and additive splitting scheme. The individual steps in the scheme are illustrated in Figure 2.

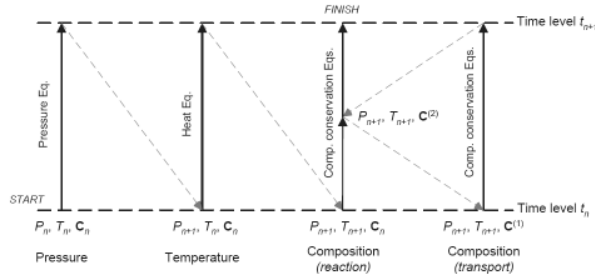


**Figure 2:** Illustration of the IMEX-ADS splitting scheme applied to the ISC equations.

Each global time step consists of five substeps. Initial conditions for each substep are indicated in the figure. In the first two substeps, the pressure and temperature are solved using an IMEX approach for the pressure and heat equations, respectively. Next, reaction and transport are solved using Strang splitting. We will focus here on the reaction substeps, in which chemical reactions are integrated subject to phase equilibrium constraints. In this way, the stiff reaction kinetics can be integrated with implicit methods designed for stiff ODEs, whereas, for example, convective transport can be integrated with high-resolution explicit methods. The solutions to the subproblems are subsequently tied back together to form an approximation to the full equation.

To facilitate the development of tailored solvers for reaction we constructed a kinetic cell model, representing the behavior of chemical kinetics and phase behavior in a closed cell. In the reaction substep

of the splitting scheme, each gridblock in the domain is effectively treated as small kinetic cell as illustrated in Figure 3.

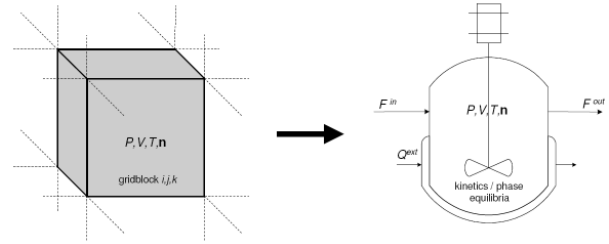


**Figure 3:** Using a splitting scheme for solving the ISC equations, the reaction substep effectively treats each gridblock in the domain as a small chemical reactor.

The active set of equations for the reaction substep can be represented as a set of ODEs describing the dynamics of chemical reactions along with a set of AEs expressing thermodynamic equilibrium in the system:

$$\mathbf{M} \frac{d\mathbf{u}}{dt} = \mathbf{f}(t, \mathbf{u}), \quad \mathbf{u}(t_0) = \mathbf{u}_0, \quad (1)$$

where  $\mathbf{u} \in R^m$  is a vector of state variables depending on  $t$ , and  $\mathbf{f}$  is a vector function mapping  $R \times R^m$  into  $R^m$ .  $\mathbf{M} \in R^m \times R^m$  is a (singular) mass matrix. The right-hand-side functions of (1) may be discontinuous because of phase changes.

The short integration intervals between operator splitting updates and the stiff reaction kinetics are the primary characteristics guiding our choice of integration method. We choose the class of ESDIRK (Explicit Singly Diagonally Implicit Runge-Kutta) methods for integration of reactions. These methods are attractive for a number of reasons. First of all they are one-step methods, which makes them more efficient for short-interval integration, as required in operator splitting, compared to multi-step method such as the widely used BDF methods. Secondly, they can be constructed with strong stability properties needed when integrating stiff problems. Finally, being diagonally implicit, they represent a good compromise between order of accuracy and computational complexity. For the expected accuracy range of interest (2-4 significant correct digits in the solution), low to medium order methods are sufficient. We have derived and implemented a range of ESDIRK methods of varying order and compared them to the widely used off-the-shelf codes for stiff ODEs, LSODE and DASSL, which both are implementations of BDF methods. For the accuracy range of interest, the ESDIRK methods show speed-up factors of 3-5 over LSODE and DASSL.

### Discontinuities Due to Phase Changes

Phase changes in the system cause discontinuities in the right-hand-side functions of Eq. (1). Straightforward integration across these discontinuities may lead to non-physical phase changes, poor convergence and repeated step failures. We have proposed an algorithm for robust detection and location of phase changes by considering

the kinetic cell model as a discrete event problem. The appearance or disappearance of a fluid phase marks the occurrence of a “discrete event”, e.g. a change from a single phase region to a two-phase region, or vice-versa. The time of the phase change can not be determined a priori. The detection of a phase change and subsequent location of the exact time of change are the main components of the proposed discrete event algorithm.

We extended the ESDIRK methods with a discrete event algorithm. In this algorithm phase changes are detected by monitoring sign changes of special event functions. Once a change is detected, the exact time of change is located by locating the zero-crossing of the event function. The proposed algorithm proved robust in detecting and locating phase changes, and lowered the number of convergence and error test failures by more than 50%. The DASSL and LSODE solvers that are not equipped with a phase change algorithm will, in most cases, successfully integrate across the change after repeated step size reductions caused by convergence and error test failures. Overall efficiency gains from using the phase change algorithm when measured over a long integration interval with only one or two phase changes occurring are modest, but the improved robustness near phase boundaries is certainly valuable.

### Interaction of Phase Behavior and Kinetics

A dual purpose of the kinetic cell model, apart from being a tool for algorithmic development, is to apply it for studying the interaction of kinetics and phase behavior in ISC processes. We have implemented the model with two different phase equilibrium representations. One is based on simplified K-value correlations, while the other uses the more rigorous equation of state (EoS) based approach. In the EoS based approach we use the Peng-Robinson equation. We simulate an experiment in which an oil sample is heated in the kinetic cell under air circulation. We use a two component lumping of the oil and an ISC reaction model with 4 reactions accounting for thermal cracking of the oil and oxidation of the oil components along with oxidation of the coke formed in the cracking reaction.

Figure 4 compares the simulation results for the experiment. The K-value approach over-predicts the oil volatility leading to an earlier oil phase disappearance. This simple sensitivity study between a K-value based approach and an EoS based approach to phase equilibrium shows that reaction paths are quite sensitive to phase behavior treatment. Relatively small differences in the prediction of phase changes lead to a large impact on the amount of coke formed and therefore the amount of oxygen consumed. In the reservoir, phase behavior in the downstream region of the combustion front will determine the amount and composition of fuel left behind for combustion. Incorrect prediction of phase behavior in this region is likely to affect the whole ISC process.

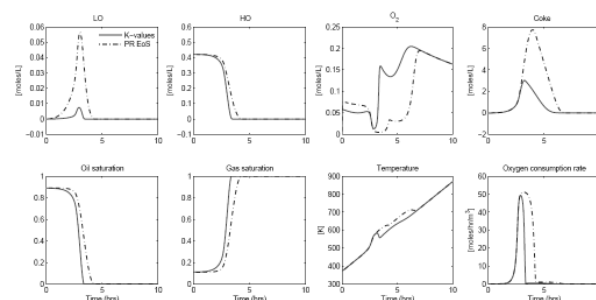


**Figure 4:** Simulation results for a ramped temperature experiment. The concentration of light oil (LO), heavy oil (HO), oxygen and coke is shown along with oil and gas saturations, cell temperature and oxygen consumption rate. Comparison is made between using K-value correlations and the Peng-Robinson EoS for the phase equilibrium description.

### Conclusion

A general framework for simulation of the in-situ combustion enhanced oil recovery process was presented. The fundamental idea in the framework is to localize the computational effort in both time and space by exploiting adaptive numerical methods to the widest possible extent.

The main contributions to the overall framework from this work are:

- Development of tailored ESDIRK methods for integration of chemical kinetics and phase behavior. ESDIRK methods are well suited for stiff kinetics due to their strong stability properties. In particular, when implemented in an operator splitting environment, the ESDIRK methods outperform stiff multi-step methods. Experiments show that the methods lead to speed-up factors of 3-5 compared to multi-step methods.
- A phase change detection algorithm based on discrete event system theory. The algorithm improves the robustness of the integration process when crossing phase boundaries by reducing integration step failures and therefore also computational time.
- Development of a kinetic cell model. The model is a novel and useful tool for analyzing kinetics and phase behavior in ISC processes. It can provide simulation support for laboratory kinetic cell experiments, and be used for studying interactions between kinetics and phase behavior as well as interactions with the reservoir through specialized boundary conditions. It is implemented with both a simplified and a rigorous EoS based phase equilibrium description.



## Thomas Ricco Ølholm Larsen

Phone: +45 4525 2974  
Fax: +45 4588 2161  
E-mail: tol@kt.dtu.dk  
WWW: <http://www.dtu.dk/Centre/DPC>  
Supervisors: Martin E. Vigild  
Tom L. Andersen, Risø

### Ph.D. Study

Started: January 2004  
To be completed: January 2007

## Tribological Properties of Polymer-Matrix Composites when Dry-Sliding Against Steel Counterfaces

### Abstract

Polymer-matrix composites are increasingly used in applications where friction and wear are important parameters. Beside beneficial properties such as a high strength-to-density ratio and chemical resistance, polymers generally also show a relatively low coefficient of friction even when dry-sliding against steel counterfaces. Here, the friction and wear properties of an epoxy resin reinforced by either a glass fiber weave (G/EP) or a carbon/aramid hybrid weave (CA/EP) are reported. Furthermore, experiments with incorporation of micro-scale PTFE and nano-scale CuO particles into both the neat epoxy resin and into the epoxy resin along with the carbon/aramid weave are reported.

### Introduction

Tribology is the science of friction, wear and lubrication of interacting surfaces in relative motion [1]. Polymer-matrix composites (PMCs) are used increasingly for purposes where friction and wear are important parameters [2]. Examples of this are gears, seals, rollers, tank track pads, bearings, brakes and artificial joints. PMCs are often preferred over other materials because of their easy processability, high strength-to-density ratio, chemical resistance and generally low coefficient of friction [3-4]. Furthermore, some PMCs have self-lubricating properties, which make them an excellent choice for systems where addition of lubricants such as oil or grease is inexpedient [5]. The dry-sliding ability of PMCs decreases the need for maintenance and the risk of emergency sliding conditions, which are seen in the case of metals, when lubricating systems fail [6].

Despite of the increasing use of PMCs, the knowledge on their tribological behaviour are largely empirical and have limited predictive capability. Thus, there is a need for a better understanding of how different designs and compositions of PMCs affect their tribological properties [2].

The tribological behaviour of polymeric materials are frequently optimized by reducing adhesion to the counterpart and improving the mechanical properties e.g. hardness, toughness and stiffness. This has traditionally been done by adding solid lubricants, e.g. PTFE (polytetrafluoroethylene) or graphite flakes, different strength giving fibers, e.g. carbon, glass and

aramid fibers [7], or inorganic microscale particles e.g. CuO, SiO<sub>2</sub> and TiO<sub>2</sub> [4].

Results regarding the ability of inorganic nanoscale particles to optimize tribological properties of PMCs have been published recently [8-14]. The mechanism behind this optimization is not entirely understood, however, it seems to be the case that such particles in some cases promote adhesion of a transfer film to the counterface, which reduces wear and often also friction. Furthermore, a unique feature of nanoparticles is their ability to increase toughness and stiffness simultaneously [15], which is a desired property combination according to basic tribological models [16-17].

### Objectives

The aim of this study is partly to produce a PMC with excellent tribological properties when performing in a well-defined test system, and partly to examine new material combinations and thereby contributing with new knowledge in this area. In this study PMCs based on an epoxy resin (EP) are tested. Epoxy resins do generally not exhibit good tribological properties due to the cross linked structure, which inhibits the formation of an efficient transfer film and results in a relatively high degree of brittleness. However, epoxy resins poses other favourable properties such as strong adhesion to many materials, good mechanical and electrical properties, relatively high chemical and thermal resistance [1], and a low price compared to state-of-the art polymers such as PEEK and Polyimide. From this

perspective, it is an attractive goal to obtain an epoxy-based composite with excellent tribological properties by incorporating the right kind of components e.g. fibers and particles. In this yearbook contribution, results regarding the friction and wear behavior of an epoxy resin reinforced with two types of fibrous reinforcement are presented. That is, a plain glass fiber weave (G/EP) and a carbon/aramid hybrid weave (CA/EP), respectively. Tribological tests are performed at nine different combinations of contact pressure ( $p$ ) and sliding velocity ( $v$ ) also referred to as  $pv$  factors. The purpose is to systematically examine the relative performance level of these two materials while going from mild to severe sliding conditions. Additionally, this paper reports preliminary experiments with incorporating micro-scale PTFE particles and nano-scale CuO particles into either the neat epoxy resin or into the resin along with the carbon/aramid weave. Compositions and nomenclature for tested composites are given in table 1.

### Methods

The tribological properties of the produced composites are tested on a custom made Pin-On-Disk (POD) tribotester built at DTU as a part of this project, cf. figure 1. The principle of the Pin-On-Disk method is as follows: a test specimen in the form of a pin is fixated in a lever-arm and loaded perpendicular against a rotating steel disk. The normal load ( $W$ ) is adjusted simply by placing different weights on top of the lever-arm. The latter, which can move freely both in the vertical and horizontal direction, will have a tendency to swing in the same direction as the disk revolves due to friction between the surfaces. However, it is kept in a fixed position by a force transducer which measures the frictional force ( $F_f$ ). The coefficient of friction ( $\mu$ ) is obtained by using Amontons well-known first law of friction i.e.  $\mu = F_f / W$ , and is reported as a time-averaged value based on data points in the steady state regime. The wear rate is obtained simply by measuring the weight loss of the pin after being worn a certain amount of time under steady state conditions. Furthermore, a non-contact thermometer estimates the contact temperature by collecting infrared radiation from the side of the steel disk.

Information about the microstructure of composites, wear mechanisms and the appearance of transfer films on the counterface are examined by different microscopic methods such as optical, SEM, FE-SEM and TEM.

### Theory

Wear can be defined as removal of material from interacting surfaces in relative motion. It has frequently been found experimentally that the volume, or mass, of lost material is proportional to  $W$  and the sliding distance ( $l$ ) respectively. That this should be the case can also be shown theoretically, for instance, from

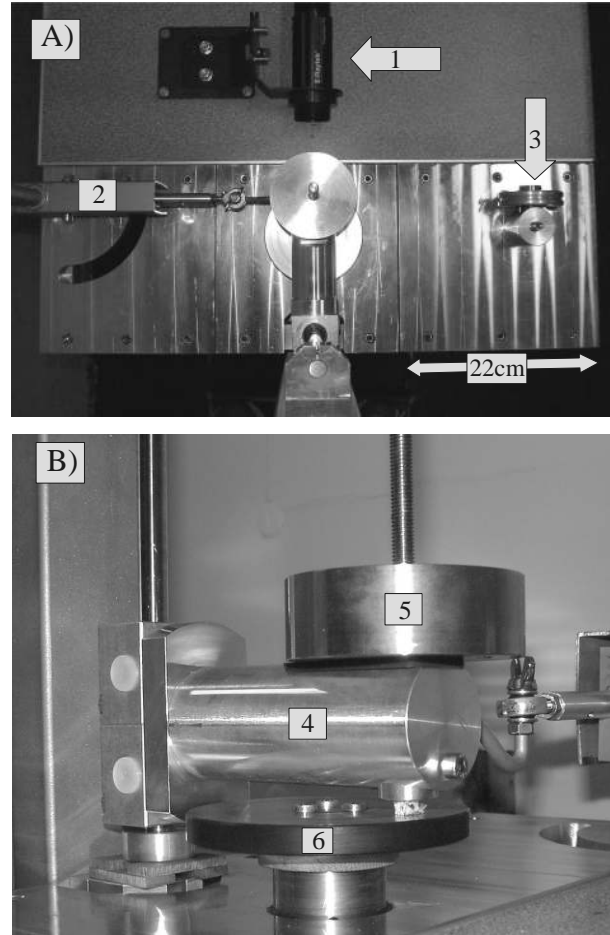


**Figure 1.** A) Top-view of the mechanical parts: 1. Infrared temperature sensor, 2. Force transducer and 3. Pulley for calibration of the force transducer. B) Side-view of a composite pin loaded against the rotating steel disk: 4. Lever-arm, 5. Weight and 6. Steel disk.

simple models for abrasive and adhesive wear, or by assuming that the wear rate is proportional to the rate of energy dissipation in the interface. The specific rate of energy dissipation ( $Q_d$ ) is given by equation 1, and is simply the rate of energy dissipation per unit apparent contact area.

$$Q_d = \mu \cdot pv \quad (1)$$

Based on the relations mentioned above, a depth wear rate ( $w_t$ ) can be derived, cf. equation 2.

$$w_t = \frac{\Delta h}{t} = k^* \cdot pv \quad (2)$$

Where  $\Delta h$  is height reduction of the worn component,  $t$  is time and  $k^*$  is the wear factor. Note, that  $w_t$  is directly proportional to the  $pv$  factor as long as  $k^*$  is a constant. The latter depends on both material properties and system properties. Thus, if the system properties are fixed,  $k^*$  can to some extent be regarded as a material property. The wear factor is often also referred to as the

specific wear rate ( $w_s$ ), which conveniently can be calculated from measured quantities, cf. equation 3.

$$w_s = \frac{\Delta m}{l\rho W} \quad (3)$$

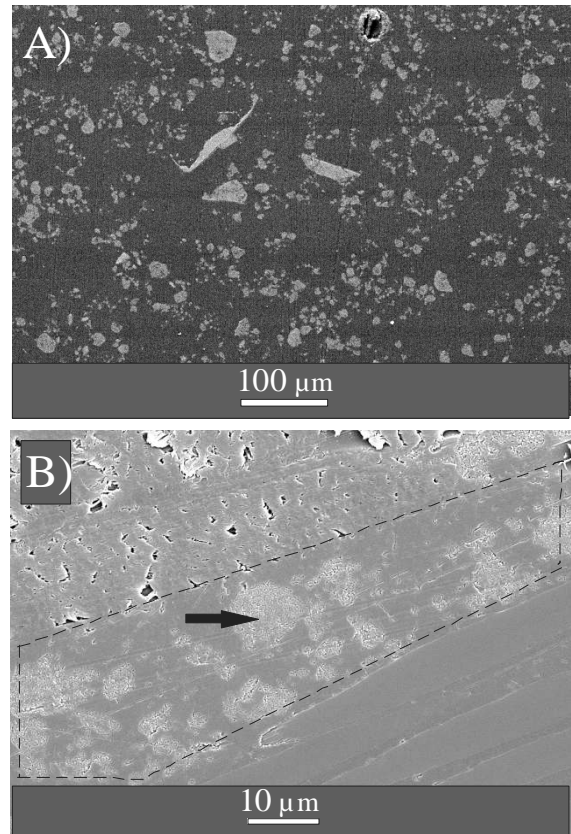
Where  $\Delta m$  is weight loss and  $\rho$  is density of the worn material. Equation 3 does not take temperature increases in the interfacial zone into consideration. However, in agreement with equation 1, the temperature in the interfacial zone will rise with increasing  $pv$  factors and does furthermore depend on the thermal conductivities of the sliding partners, the ambient temperature and on the real area of contact. Generally, equation 2 applies inside a certain range of moderate  $pv$  factors. However, if either  $v$  and/or  $p$  exceed a certain level, a change in wear mechanism might occur due to e.g. thermal softening, decomposition or yielding of the material. The  $pv$  factors where equation 2 breaks down and excessive wear can be observed is referred to as the limiting  $pv$  factor ( $pv_{lim}$ ) which can be regarded as a performance parameter for a given PMC. Thus, for performance improvement it is sought to decrease  $k^*$  and increase  $pv_{lim}$ .

**Table 1.** Nomenclature and compositions of tested composites.

Nomen-clature	Epoxy (vol%)	Weave type / vol%	Particle type / vol%
EP	100	-	-
EP/PTFE	92.5	-	PTFE / 7.5
EP/CuO	99.0	-	Nano-CuO / 1.0
G/EP	56	glass fiber / 44	-
CA/EP	56	Carbon/ aramid / 44	-
CA/EP/PTFE	48	Carbon/ aramid / 47	PTFE / 5.0
CA/EP/CuO	54	Carbon/ aramid / 45	Nano-CuO / 1.0

## Results and discussion

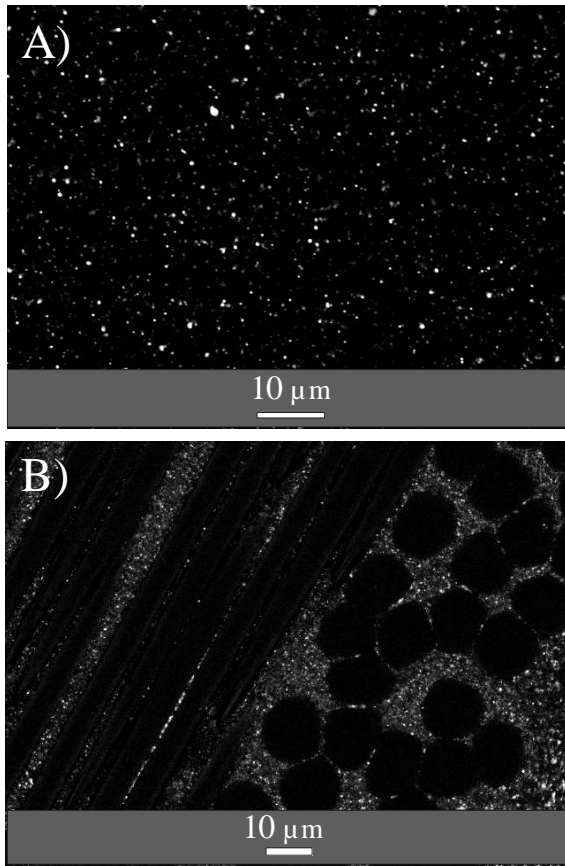
SEM images are given in the following to document the micro-structures of some of the produced and tested composites. It is chosen to show particle containing composites as examples, since a good particle distribution is important for the properties and can be difficult to achieve. Figure 2. shows the micro-structures of A) EP/PTFE and B) CA/EP/PTFE. In the case of EP/PTFE, it is seen that the



**Figure 2.** SEM images showing the composite structures of A) EP/PTFE and B) CA/EP/PTFE. The light gray phase is PTFE and a single particle is marked by an arrow. The area given by the dashed line is a zone of resin where the PTFE particles are located. The lower right corner and the upper left corner of B) show carbon fibers and aramid fibers, respectively, parallel to the surface.

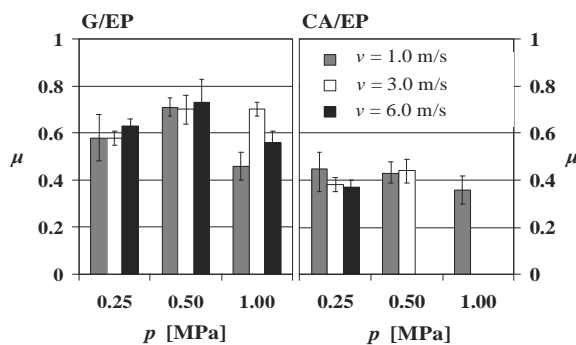
micro-particles are relatively well-distributed in the resin. The image of CA/EP/PTFE shows a zone of resin, marked by the dashed line, containing the PTFE particles. Within this resin zone, the particles are relatively well-distributed. However, it is generally seen that the PTFE particles are only located in resin between, and not within, bundles. Thus, the particles are too large to enter the fiber bundles, which thereby act as filters preventing a more homogeneous particle distribution. This filtering effect is a common problem with micro-scale particles especially in relation to injection techniques such as Resin Transfer Molding (RTM).

Figure 3. shows the micro-structures of A) EP/CuO and B) CA/EP/CuO. The CuO particles seem to be relatively well-dispersed in the epoxy resin. Based on figure 3,A it is not possible to see if the nano-particles are present as primary particles or as small clusters. However, all particles or clusters appear to be sub-micron in size.



**Figure 3.** SEM images showing the composite structures of A) EP/CuO and B) CA/EP/CuO. Nano-CuO particles are seen as bright stars. In B) carbon fibers and aramid fibers, respectively, are seen oriented parallel and normal to the surface.

Image 3,B shows nano-particles distributed in the resin both between and within fiber bundles. Thus, the problem with particle filtering seen for the micro-scale PTFE particles is avoided by going to nano-size.



**Figure 4.** Coefficients of friction  $\mu$  measured at different combinations of  $p$  and  $v$  for G/EP and CA/EP, respectively.

Figure 4. shows measured values of coefficients of friction  $\mu$  for G/EP and CA/EP. The average level of  $\mu$  for CA/EP is 0.41 as opposed to 0.63 for G/EP, which means that a general decrease of approximately 35% is obtained by substituting the glass fiber weave with the

given carbon/aramid weave. This difference in the level of  $\mu$  might be attributed to the following factors. Due to the hardness of glass fibers these are observed to cause a significant roughening of the steel counterface. Furthermore, fragments of glass fibers located in the interfacial zone can act as abrasive particles. Both of these factors might increase the deformation, or plowing, contribution to  $\mu$ . Carbon fibers, on the other hand, might act as a solid lubricant decreasing the interfacial shear force due to the partial graphite structure of these fibers. With respect to abrasiveness, carbon fibers are also found to roughen steel counterfaces under some circumstances but typically not to the same extent as glass fibers. According to Amontons laws of friction,  $\mu$  should be independent of  $p$  and  $v$ . However, in the case of polymeric materials this have often been found not to be the case [17]. The data in figure 4 show some variation in  $\mu$  at different combinations of  $p$  and  $v$ , however, no clear trends are observed. Thus, it might be concluded that despite of a few exceptions,  $\mu$  is fairly constant considering the relatively large range of  $p$ ,  $v$  and contact temperatures.

In figure 5 and 6 measured wear rates  $w_t$  and contact temperatures for G/EP and CA/EP, respectively, are given. By comparing  $w_t$  at the same  $pv$  conditions for the two materials, it is found that the average wear rate is a factor of 22 higher in the case of G/EP compared to CA/EP. According to SEM images (not shown) this significant difference seems to be caused by the following main factors. The aramid fibers inhibit micro-cracking of the resin, which in the case of glass and carbon fibers leads to exposed fiber ends. These exposed, and brittle, fiber ends seem to be fragmented and broken easily relative to the tough aramid fibers, which are worn by a fibrillation mechanism. Furthermore, third body abrasive wear caused by fragmented glass fibers probably also contributes to the high wear rate found for G/EP.

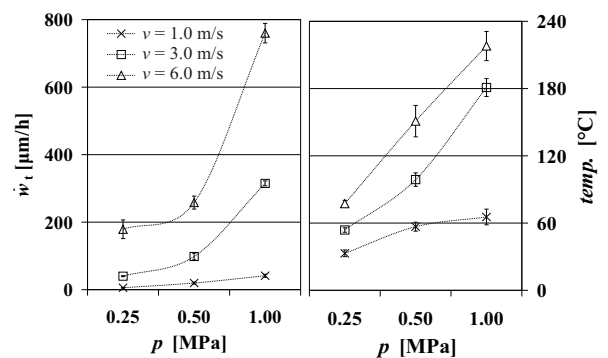


**Figure 5.** Depth wear rates  $w_t$  and contact temperatures measured at different combinations of  $p$  and  $v$  for G/EP.

Furthermore, a gradual increase in both contact temperature and  $w_t$  are observed as a function of  $p$  and  $v$ , respectively, as expected from equation 1 and 2. More specifically, equation 2 predicts a linear relationship between  $w_t$  and the  $pv$  factor with a slope equal to  $w_s$  (or

the wear factor). Actually,  $w_t$  increases more rapidly as a function of  $p$  and  $v$  than predicted by the linear model.

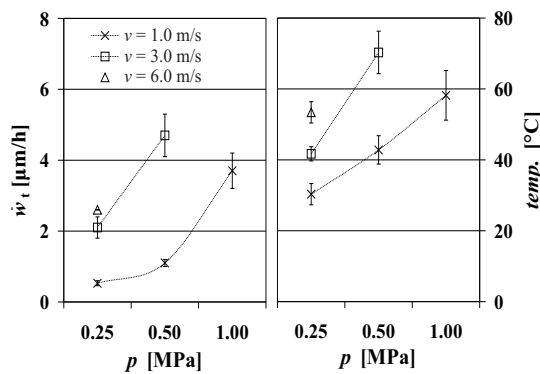


**Figure 6.** Depth wear rates  $w_t$  and contact temperatures measured at different combinations of  $p$  and  $v$  for CA/EP.

As previously mentioned, the wear factor is a function of both material properties and system properties and these are both treated as constants. However, considering that the contact temperature varies from  $33^{\circ}\text{C}$  at the lowest  $p v$  factor to  $218^{\circ}\text{C}$  at the highest  $p v$  factor, it is obvious that the material properties will change in this relatively large temperature range. Certainly, the resin properties will change at the glass transition temperature and at the decomposition temperature.

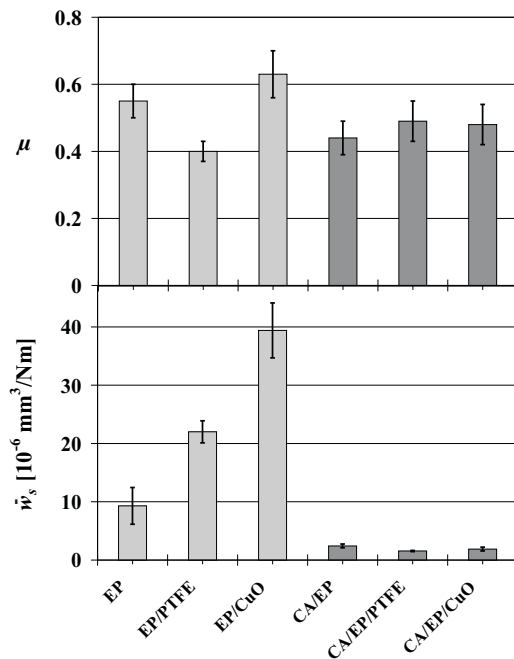


**Figure 7.** Specific wear rates ( $w_s$ ) and coefficients of friction ( $\mu$ ) measured for different materials. Composites without carbon/aramid reinforcement are measured at the  $p v$  condition: 0.25 MPa, 6.0 m/s, whereas composites with carbon/aramid reinforcement are measured at the  $p v$  condition: 0.50 MPa, 3.0 m/s.

Thus, this excessive increase in  $w_t$  as a function of  $p v$  might be related to a gradual deterioration of the resin properties, and thereby also in the composite properties, with increasing contact temperatures. The measured effects on friction and wear of adding PTFE and nano-CuO particles are shown in figure 7. As a general observation, the use of carbon/aramid reinforcement has a large positive impact on the wear behavior but only a minor impact on the frictional behavior. For materials without fiber reinforcement, it is seen that addition of PTFE and especially nano-CuO leads to an increase in wear rate. This behavior is frequently seen when PTFE is incorporated into a stronger polymer resin. The relatively poor strength and adhesive properties of PTFE most likely result in deterioration of mechanical composite properties. However, PTFE shows the intended effect on the frictional behavior. EP/PTFE has a coefficient of friction approximately 30% lower than EP, which consequently also results in a decrease in measured steady state temperature from  $69 \pm 3^{\circ}\text{C}$  to  $50 \pm 6^{\circ}\text{C}$ . Regarding nano-particles, the influence on mechanical properties is less predictable. Both positive and negative effects of adding nano-particles are found in the literature, and the mechanisms behind reported improvements are not entirely understood. In this study, it is hypothesized that the high wear rate for EP/CuO is associated with the large interfacial area between particles and resin, which might result in a strength reduction of the material and thereby in an elevated wear rate. When PTFE and nano-CuO are added along with the carbon/aramid weave, a minor improvement in wear behavior is seen instead of a negative influence. The coefficient of friction is basically unaffected by addition of these particles. Thus, the negative effect of nano-CuO on wear seen for EP/CuO is not found for CA/EP/CuO, and the positive effect of PTFE on friction seen for EP/PTFE is not found for CA/EP/PTFE. This indicates that the friction and wear behavior are largely controlled by the fibers and not the particles. The reason why PTFE has no effect on friction for CA/EP/PTFE might be due to the stiffness of the carbon fibers, which on micro-scale possibly act as a stiff brush. If a PTFE containing third-body (or transfer film) is formed, it is likely to be disrupted or abraded by these stiff fibers.

## Conclusions

An average decrease in friction of approximately 35% is found by substituting a glass fiber weave with a carbon/aramid hybrid weave. This decrease is considered to be due to the lubricating effect of carbon fibers as opposed to the abrasive nature of glass fibers. Besides from a few exceptions, the coefficient of friction is found to be roughly independent of pressure and velocity. The average level of wear rates for G/EP is a factor of 22 higher than for CA/EP. This significant difference is believed to be caused by the negative effect of the brittle and abrasive glass fibers compared to, partly the toughness of aramid fibers, inhibiting micro-scale cracking, and partly the lubricating effect of carbon fibers. Incorporation of micro-scale PTFE

particles and nano-scale CuO particles into either the neat epoxy resin or into the resin along with the carbon/aramid weave is reported. According to SEM images, the micro-structures and particle distributions in the produced composites seem promising. However, additions of nano-CuO into the neat resin results in deterioration in friction and especially wear properties. PTFE particles also cause an increase in wear but a 30% decrease in friction.

When these particles are added along with carbon/aramid reinforcement, a minor improvement in wear and no difference in friction are found. This indicates that the friction and wear properties are largely controlled by the fibers.

### Acknowledgement

The work is financially supported by a grant given in equal parts by the Technical University of Denmark, The Danish Research Training Council and Civilingeniør Frederik Leth Christensens ALMENNYTTIGE FOND. The latter is furthermore gratefully acknowledged by the authors for financing the applied Pin-On-Disk apparatus.

### References

1. Serop Kalpakjian and Steven R. Schmid, *Manufacturing Engineering and Technology*, Prentice Hall, 2001.
2. Friedrich, K. & Reinicke, P, *Mechanics of Composite Materials* 34, 1998.
3. Harsha, A. P. & Tewari, U. S., *Polymer Testing* 21, p. 697–709, 2001
4. Schwarts, C. & Bahadur, S., *Wear* 251, 1532–1540, 2001.
5. Unal, H. & Mimaroglu, A. , *Materials and Design* 24, p. 182–187, 2003.
6. Häger, A. M. & Friedrich, K. , *Wear* 162, 1993.
7. Zhang, Z., Breidt, C., Chang, L. & Friedrich, K., *Tribology International* 37, p. 271–277, 2004.
8. Li, F., Hu, K. a., Li, J. l. & Zhao, B. y., *Wear* 249, p. 877–882, 2002.
9. Sawyer, G. W., Freudenberg, K. D., Bhimaraj, P. & Schadler, L. S., *Wear* 254, 2003.
10. Shi, G., Zhang, M. Q., Rong, M. Z., Wetzel, B. & Friedrich, K., *Wear* 254, 2003.
11. Christian J. Schwarts and Shyam Bahadur, *Wear* 237, p. 261-273, 2000.
12. Jin Lu, Ming Qui Zhang, Min Zhi Rong, Shu Li Yu, Bernd Wetzel and Klaus Friedrich, *Journal of Materials Science* 39, p. 3817-3820, 2004.
13. Ming Qui Zhang, Ming Zhi Rong, Shu Li Yu, Bernd Wetzel and Klaus Friedrich, *Wear* 253, p. 1086-1093, 2002.
14. Min Zhi Rong, Ming Qiu Zhang, Liu Hong, Hanmin Zeng, Bernd Wetzel and Klaus Friedrich, *Industrial Lubrication and Tribology* 53, p. 72-77, 2001.
15. Bernd Wetzel, Frank Hauptert, Klaus Friedrich, Ming Qiu Zhang, and Min Zhi Rong, *Polymer Engineering and Science* 42, 1988.
16. Klaus Friedrich, in: Klaus Friedrich (Eds.), *Friction and Wear of Polymer Composites - Composite Materials Series volume 1*, Elsevier, New York, 1986, p. 233-285.
17. I. M. Hutchings. *Tribology: Friction and Wear of Engineering Materials*, Edward Arnold, 1992.



### **Jens Lolle Laursen**

Phone: +45 4525 6800  
Fax: +45 4588 2161  
E-mail: JLLL@novonordisk.com  
WWW: <http://www.polymers.dk>  
Supervisors: Martin E. Vigild  
Andy Horsewell, IPL, DTU  
Lasse Christoffersen, Novo Nordisk A/S

### **Industrial Ph.D. Study**

Started: December 2005  
To be completed: December 2008

## **Processability and Fracture Mechanical Performance of Tribologically Modified Plastics**

### **Abstract**

The present project deals with the influence of friction-modifying additives on processing and fracture mechanical performance of selected polymeric grades, used in the medico-device industry. The processing and test procedures are chosen to simulate the state and conditions under which the materials are used to the best effect. The project will potentially make possible the safe use of new tribologically superior plastic grades, providing reduced frictional losses in the device mechanisms, without compromising product safety and failure rates.

### **Introduction**

Plastics with friction-reducing additives are to an increasing extent being used as replacement for external lubrication of mechanisms in medico-technical devices. Novo Nordisk A/S (NNAS) is active in research within combinations of new plastics with friction-reducing additives especially developed for the conditions under which the materials operate in injection devices, such as insulin pens. Preliminary results indicate an appreciable reduction in coefficient of friction compared to the best constellations of commercially available grades. The studies, however, also indicate some processing difficulties when injection molding these new plastic grades, such as weak weld lines, poor surface quality and internal zones of reduced coherence. An effort towards the understanding of the underlying phenomena is crucial for the potential application of these new grades and also provides for development of procedures for characterization and benchmarking of future plastics.

### **Specific Objectives**

The primary project objectives are to provide understanding of the mechanisms behind the observed processing difficulties, to make possible quantification of the extent to which these difficulties occur for a given grade and to quantify the reduction in specific mechanical performance induced hereby. Based on these studies, a design guideline will be prepared for use in future in-house formulation of low-friction grades.

### **Tools and Means Overview**

The processing properties of the materials (the “processability”) will be investigated by injection molding and analysis of test specimens with a simplified geometry. A major project task is to develop one or more test geometries, which reflect processing conditions in large-scale industrial production, allows for monitoring of relevant molding parameters in the melt, and makes possible the subsequent analysis of the mechanical and tribological properties of the materials. The latter will be tested according to internal NNAS procedures, simulating field conditions for device use.

Another aspect of the project is to define and test the characterization means for the described failure mechanisms and geometries. The mechanical performance will be investigated through fracture mechanical studies, providing high sensitivity towards inherent material flaws, combined with genuine information on constitutive material behavior.

A third aspect of the project is to describe the correlation between processing parameters and functional properties through models, based on the composition and microstructure of the material, in combination with the physical and chemical context in which they perform. Microstructure and morphology will be analyzed by polarized light-optical microscopy (PLM), scanning electron microscopy – energy dispersive x-ray analysis (SEM-EDX), Fourier transformed infrared spectroscopy (FTIR) and/or modulus/hardness-mapping via micro/nanoindentation.

### Model Materials and Variables

Two generic polymers will be used as basis material (matrix), namely polyoxymethylene (POM) and polypropylene (PP). These have been chosen as representatives for poor and good compatibility with the additives, respectively. The chosen additives include polydimethylsiloxane (PDMS) as an all-liquid state additive (liquid during both material processing and usage phases), polyethylene (PE) as a liquid-solid state additive and polytetrafluoroethylene (PTFE) as an all-solid state additive.

Other variables include grade composition variables, like additive concentration, form and size distribution, processing variables like injection shear rate, temperature gradients and holding pressure, and fracture mechanical test variables like load point displacement rate and material temperature.

### Test Geometry and Injection Molding

The fracture mechanical tests will be based on a single edge notched beam geometry (SENB), taken from square plates of 60 mm edge length. The specimens will be milled to required length and width dimensions. The plate thickness will remain as molded, either 1.5 mm or 6 mm. The former represents a realistic thickness in medico-devices and will thus also be used for microstructure studies; the latter makes possible testing of materials which, under the given conditions, would not comply with the requirements posed by linear elastic fracture mechanics (LEFM) in a 1.5 mm thickness.

The influence of orientation, being that molecular or fiber orientation, will be examined by comparing specimens milled to having their length axis either parallel or perpendicular to the direction of melt flow.

A double inlet system, based on hot runners, with optional gating from both of two opposing side edges, will provide for test specimens with a central weld line, so also this deficiency can be characterized strength-wise.

A straight flow front will be realized by means of two so-called sculptured fan inlets, where three dimensional double curving profiling provides a flow-path independent pressure drop across the gate.

### Fracture Mechanical Testing

To simulate the impact conditions under which the materials are most likely to fail in use, a LEFM procedure will be adopted through the use of the ISO 17281:2002-standard [1], which specifically addresses fracture mechanical characterization at relevantly high displacement (i.e. strain) rates. The standard deals with determination of both the critical strain energy release rate:

$$G_{Ic} \equiv -\partial\Pi/(b\partial a)$$

(b is sample thickness,  $\Pi$  is elastically bound energy and a is crack length) and the critical stress intensity factor:

$$K_{Ic} \equiv \lim_{x_1 \rightarrow 0} \sigma_{22}(x_1)(2\pi x_1)^{1/2}$$

( $\sigma_{ij}$  is the stress tensor in a Cartesian coordinate system  $\{x_1..x_3\}$  with origin at the tip of the crack).

If LEFM contrary to expectation turns out to be insufficient as means for determining onset of unstable crack propagation (ineligible plasticity) a J-integral approach will be adopted instead, based on the ASTM E1820-99-standard [2] and the work by Fasce et al. [3].

The force/displacement data, which forms the basis for calculation of either of the characteristic fracture mechanical properties, will be measured by means of a drop tower impact tester, equipped with a 4.1 MHz PC based data sampling unit. As this apparatus makes possible logging of the full force and displacement time-traces, it also provides means for additional verification of the data analysis method used.

### Results and Discussion

Experiments are still under preparation. Preliminary results are expected December 2006 and first full-scale study spring 2007.

### Conclusions

Based on the presented framework, a thorough analysis of causes for the performance deterioration brought about by the friction-modifying additives will be made possible, as will establishment of procedures for comprehensive benchmarking of new grades and guidelines for the composition hereof.

### Acknowledgements

The author greatly acknowledges the supervisors for their invaluable sparring during both project procurement and early-stage effectuation.

### References

1. ISO 17281:2002, Plastics – Determination of Fracture toughness ( $G_{Ic}$  and  $K_{Ic}$ ) at moderately high loading rates (1m/s)
2. ASTM E1820-99, Standard Test Method for Measurement of Fracture Toughness
3. A. Fasce, V. Pettarin, R. Seltzer, P. Frontini, Evaluation of Impact Fracture Toughness of Polymeric Materials by Means of the J-Integral Approach, Polymer Engineering & Science 43 (5) (2003) 1061
4. W. Brostow, R. Corneliussen, Failure of Plastics, Hanser Publishers, 1986
5. R. Brown, Handbook of Polymer Testing – Physical Methods, Marcel Dekker, 1999
6. V. Pettarin, R. Seltzer, L. Fasce, P. Frontini, K. Leskovics, G.B. Lenkey, T. Czigan, Analysis of Low Temperature Impact Fracture Data of Thermoplastic Polymers, Structural Integrity and Fracture (2004).



### Yi Lin

Phone: +45 4525 2869  
Fax: +45 4588 2258  
E-mail: yil@kt.dtu.dk  
WWW: www.ivc-sep.kt.dtu.dk/staff/YIL/YIL.htm  
Supervisors: Kaj Thomsen

### Ph.D. Study

Started: September 2003  
To be completed: September 2006

## Multi Component Equations of State for Electrolytes at a Wide Temperature Range

### Abstract

Four equations of state have been implemented and evaluated for multi-component electrolyte solutions at different temperatures and atmospheric pressure. The equations contain terms accounting for short-range and long-range interactions in electrolyte solutions. The resulting electrolyte equations of state were tested by determining the optimal ion specific parameters for the multi-component test system consisting of  $\text{H}_2\text{O}$ ,  $\text{Na}^+$ ,  $\text{H}^+$ ,  $\text{Ca}^{2+}$ ,  $\text{Cl}^-$ ,  $\text{OH}^-$ ,  $\text{SO}_4^{2-}$ . The parameters in the equations of state, both temperature dependent and temperature independent, were fitted to experimental data consisting of apparent molar volumes, osmotic coefficients, mean ionic activity coefficients, and solid-liquid equilibrium data at the temperature range of  $-45\text{ }^\circ\text{C} \sim 150\text{ }^\circ\text{C}$ . The ability of the equations of state to reproduce the experimental data is demonstrated. The performance of the equations of state for multi-component systems is compared and analyzed in view of the various short range and long range terms employed.

### Introduction

Electrolyte solutions are encountered in many natural and industrial processes. Since the 1920s, many different engineering models, either empirical or semi-empirical, have been proposed and constructed for calculating the thermodynamic properties of electrolyte solutions for engineering applications.

The electrolyte EOS are established through the residual Helmholtz free energy formalism. It is well known that electrolyte solutions are considerably more difficult to model than solutions with non-electrolytes. Additional Helmholtz free energy terms are therefore needed in electrolyte EOS to describe the electrostatic interactions between ions and between ions and solvents in electrolyte solutions. Several EOS for electrolyte solutions have been published since the attempts of Planche and Renon (1981) [1]. The most notable ones are the equations of Jin and Donohue [2-4], Fürst and Renon [5, 6], Wu and Prausnitz [7], Myers *et al.* [8] and the electrolyte SAFT (the statistical associated fluid theory)

EOS of Galindo and coworkers [9] (1999), Cameretti *et al.* [10], Tan *et al.* [11,12] (2005) and Liu *et al.* [13].

The SLE calculation of multi component electrolyte systems is a fundamental problem in the design and operation of many industrial processes involving electrolytes [14]. Since relatively little work has been conducted for electrolyte EOS on this subject so far, we have examined the possibility of using electrolyte EOS based on ion specific parameters to reproduce experimental SLE phase diagrams at a wide range of temperatures besides the conventional correlation of density, mean ionic activity coefficient and osmotic coefficient. We would like to evaluate different short range terms and long range terms by applying them to a chosen multi component system of aqueous electrolytes in a wide temperature range. The equation parameters are ion specific.

## Expression of the Electrolyte EOS

1) **Myers, Sandler and Wood Electrolyte equation of state<sup>8</sup> (MSW EOS)**. In this work the MSW EOS is used with ion specific parameters rather than the salt specific parameters used by Myers *et al.*<sup>8</sup>. The expression for the total change in Helmholtz free energy to form the electrolyte system is:

$$\begin{aligned} A(T, V, \mathbf{n}) - A^{IGM}(T, V, \mathbf{n}) \\ = \Delta A^{PR} + \Delta A_{ex}^{MSA} + \Delta A_{dis}^{Born} + \Delta A_{chg}^{Born} \end{aligned} \quad (1)$$

The PR EOS with volume translation parameter was used here as the short-range term.

2) **Modified Myers, Sandler and Wood Electrolyte EOS (mMSW EOS)**. The simplified explicit MSA term **Error! Reference source not found.** in MSW EOS is replaced by the simplified implicit MSA term **Error! Reference source not found.** to construct the new modified EOS:

$$\begin{aligned} A(T, V, \mathbf{n}) - A^{IGM}(T, V, \mathbf{n}) \\ = \Delta A^{PR} + \Delta A_{im}^{MSA} + \Delta A_{dis}^{Born} + \Delta A_{chg}^{Born} \end{aligned} \quad (2)$$

### 3) The Electrolyte CPA EOS (eCPA EOS)

The eCPA EOS has the following general form.

$$\begin{aligned} A(T, V, \mathbf{n}) - A^{IGM}(T, V, \mathbf{n}) \\ = \Delta A^{SRK} + \Delta A^{Assoc} + \Delta A_{im}^{MSA} + \Delta A_{dis}^{Born} + \Delta A_{chg}^{Born} \end{aligned} \quad (3)$$

The association term is only used to account for the self-association of water. Ionic association has been neglected here.

### 4) Debye-Hückel SRK electrolyte EOS (SRK+DH EOS)

The expression for SRK+DH EOS is as follows:

$$\begin{aligned} \ln \gamma^{\pm}(T, V, \mathbf{n}) \\ = \ln \gamma^{SRK}(T, V, \mathbf{n}) + \ln \gamma^{sDH}(T, \mathbf{n}) \end{aligned} \quad (4)$$

$\gamma^{\pm}$  is the mole-fraction based activity coefficient of a component in a mixture.  $\ln \gamma^{sDH}$  is the truncated, simplified Debye-Hückel term in (4).  $\ln \gamma^{SRK}$  is the activity coefficient contribution from SRK EOS. Since the Debye-Hückel term makes no contribution to the system volume, the volume is calculated from the SRK EOS alone.

In the above four EOS,  $\mathbf{n}$  is the vector of the number of moles of each component of the mixture. The volume translation parameter  $c$  for ions in MSW and mMSW EOS was set equal to zero for all ions. In the MSW EOS, mMSW EOS and eCPA EOS, the attraction  $a(T)$  and the ion diameter  $\sigma(T)$  is temperature dependent

$$\begin{aligned} a(T) &= a_0 + a_1 \Delta T + a_2 \Delta T^2, \\ \sigma(T) &= \sigma_0 + \sigma_1 \Delta T, \end{aligned} \quad (5)$$

where  $\Delta T = T - 298.15$  K

while the co-volume parameters  $b$  is temperature independent and one binary interaction parameter  $k_{ij}$  for each species pair.

The MSW, mMSW and the eCPA EOS are still referred to as “three-parameter EOS”. The SRK+DH EOS has two ion specific parameters: the temperature dependent attraction parameter  $a(T)$  and the temperature independent co-volume parameter  $b$ . This equation also has one binary interaction parameter  $k_{ij}$  per species pair in SRK term.

The data used for the parameter estimation are all from the IVC-SEP electrolyte databank<sup>[15]</sup>. The combined algorithm alternating between a gradient method (Marquardt method) and a direct search method (Nelder-Mead simplex search method) for non-linear least square minimization have been adopted. The four electrolyte equations of state were tested by determining the optimal multi-temperature model parameters for the multi-component system consisting of water,  $\text{Na}^+$ ,  $\text{H}^+$ ,  $\text{Ca}^{2+}$ ,  $\text{Cl}^-$ ,  $\text{OH}^-$ , and  $\text{SO}_4^{2-}$  ions.

## Results and Discussion

### Multi component Aqueous Electrolyte Solution at a wide temperature range (-30 to 130 °C) and 0.101325 MPa (Binary and Ternary Systems)

It is better to perform the parameter optimization in progressive stages than in a all-in-one-step manner with all experimental data points. It helps the optimization routine to find the optimal parameter set more quickly and smoothly. We followed this methodology to determine the best temperature dependence function for EOS parameters. The parameter regressions were performed in four progressive stages using various amounts and types of data:

- 1) Multi temperature water activity, mean ionic activity coefficient and osmotic coefficient data, short as  $\gamma_{\pm} + \Phi$  data.
- 2) Multi temperature binary and ternary SLE data.
- 3) Multi temperature binary and ternary SLE data, multi temperature water activity, mean ionic activity coefficient data and osmotic coefficient data, short as SLE +  $\gamma_{\pm} + \Phi$ .
- 4) AMV data at 25 °C plus all multi temperature data of 3), short as AMV+SLE +  $\gamma_{\pm} + \Phi$ .

The SRK+DH EOS has no adjustable ion-size parameter  $\sigma$ , therefore only the second order polynomial of  $a(T)$  was implemented for this EOS. Besides, AMV data were not used in the SRK+DH EOS parameter optimization.

The duration of the parameter optimization of mMSW and eCPA EOS is three times longer than that of MSW EOS. This is because of the heavy computational load of implicit MSA term and the association term. Good results were obtained for the three-parameter EOS in stage 4). The mMSW EOS performs not as good as the MSW EOS while the eCPA EOS performs slightly better in stage 4). The final objective function value of eCPA is 8% smaller than MSW EOS while that of

mMSW is 2.4% larger than MSW EOS. Graphical results are also presented. Note the isotherms of mean ionic activity coefficient, osmotic coefficient or ternary SLE data at certain temperatures have been shifted a distance away from their original place along the x or y axes in some figures. The exact values of the distance for each shifted isotherms (denoted as  $a$  here) are indicated in the figures as  $y \pm a$  or  $x \pm a$ , meaning that the constant value  $a$  has been added to or subtracted from the  $y$  or  $x$  values of the isotherms. Otherwise most isotherms will overlap or intersect with each other in the figure, making it impossible to distinguish them from one another.

For SRK+DH EOS, the reproduced mean ionic activity coefficient and osmotic coefficient for most systems are not as accurate as the values reproduced by the three parameter EOS. SRK+DH EOS only partly succeeded in fitting experimental data in stage 3). For some difficult systems such as the osmotic coefficient of  $\text{Na}_2\text{SO}_4$ ,  $\text{CaSO}_4$  and mean ionic activity coefficient of  $\text{CaCl}_2$ ,  $\text{CaSO}_4$  and  $\text{NaOH}$ , the reproduced results are largely deviated. SRK+DH EOS is only able to capture the trend of the curvature of these difficult systems. The solubility of binary systems is better reproduced than the mean ionic activity coefficient or osmotic coefficient. The multi temperature ternary SLE data are the most difficult data sets to reproduce. Only the two ternary systems  $\text{NaCl}+\text{HCl}$ ,  $\text{NaCl}+\text{NaOH}$  systems, could be fitted reasonably well. The largely deviated isotherms calculated with the SRK+DH EOS are therefore not plotted in the figures with the graphical results of other EOS.

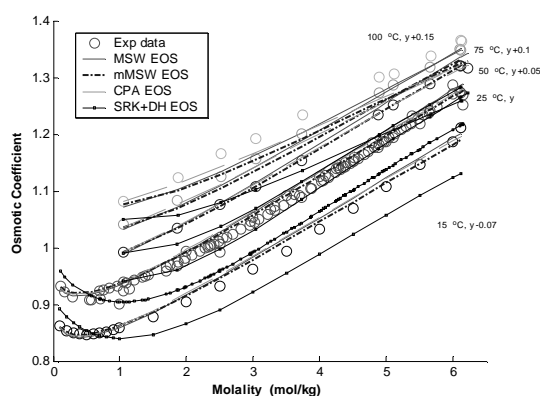


**Figure 1.** Osmotic coefficient of aqueous NaCl at different temperatures. A constant is added to some data at different temperatures to separate them from each other.

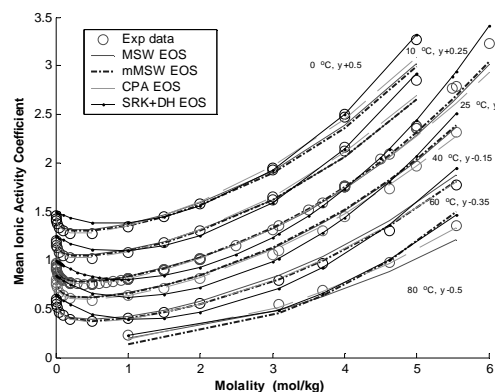


**Figure 2.** Mean ionic activity coefficient of aqueous HCl at different temperatures. A constant is added to some data at different temperatures to separate them from each other.

The solubility diagrams of binary systems are very well reproduced except at high or low temperature. For calcium chloride aqueous solution, the predicted results at temperature over  $125\text{ °C}$  or below  $-50\text{ °C}$ , the deviations of the three parameter EOS start to increase. The fitting results of binary systems of  $\text{CaSO}_4$  and  $\text{Ca}(\text{OH})_2$  are acceptable. For  $\text{Na}_2\text{SO}_4$  and  $\text{CaCl}_2$  systems, we only partly succeeded in fitting certain branch with SRK+DH EOS.

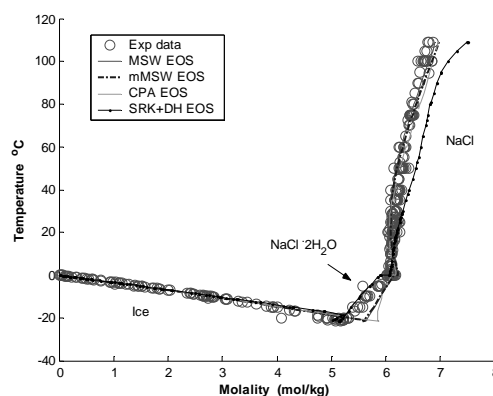


**Figure 3.** Solubility phase diagram of aqueous NaCl system.

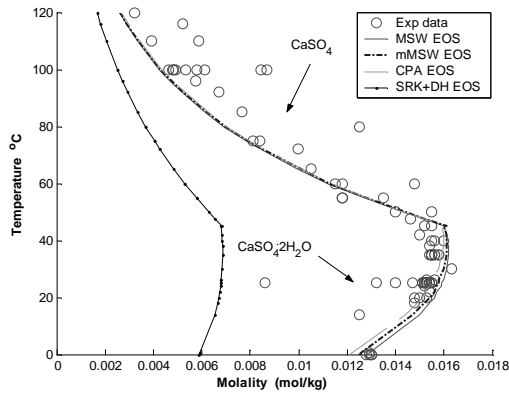


**Figure 4.** Solubility phase diagram of aqueous CaSO<sub>4</sub> system.

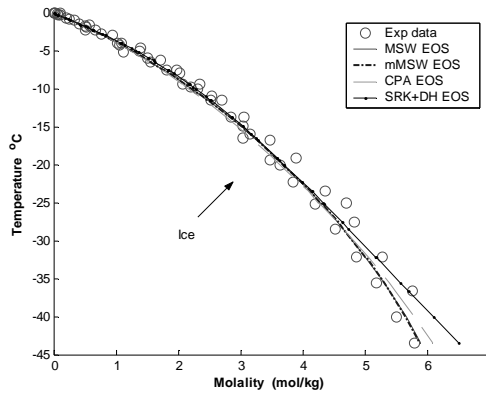


**Figure 5.** Solubility phase diagram of aqueous HCl system.

We failed to reproduce most ternary SLE systems with the SRK+DH EOS, but we reproduced most ternary SLE system with the three-parameter EOS at moderate temperatures. Within the temperature interval [-20, 100] °C, the saturation curves for ice, ice and salt mixture, salt with crystal water or pure salt are all very well represented. This suggests that the temperature dependence function is still not very adaptive at too high or too low temperature. It is still necessary to find better temperature dependence function for attraction parameter and ion-size parameter.

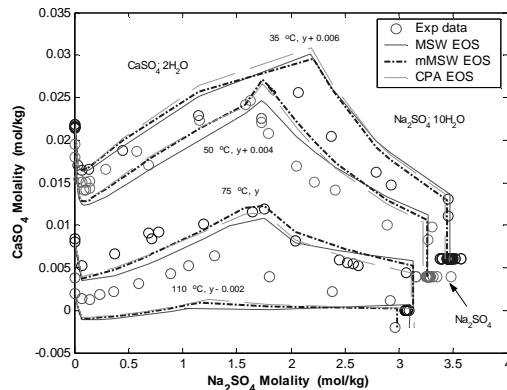


**Figure 6.** Phase diagram of the ternary aqueous

system Na<sub>2</sub>SO<sub>4</sub> and CaSO<sub>4</sub> system at high temperature. A constant is added to some data at different temperatures to separate them from each other.

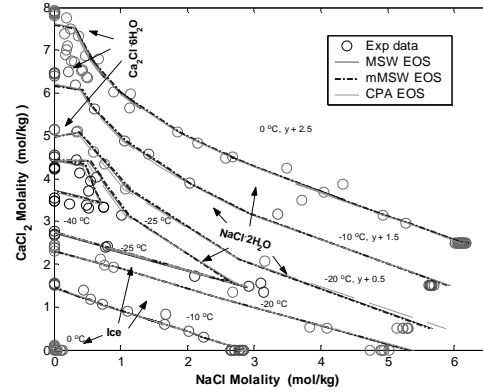


**Figure 7.** Phase diagram of the ternary aqueous system NaCl and CaCl<sub>2</sub> from -25 °C to 0 °C. A constant is added to some data at different temperatures to separate them from each other.

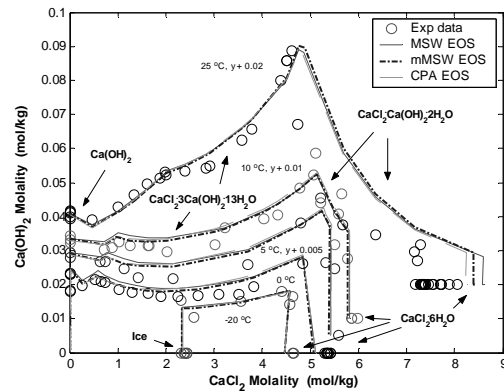


**Figure 8.** The predicted phase diagram of the ternary aqueous system CaCl<sub>2</sub> and Ca(OH)<sub>2</sub> from -20 °C to 25 °C at 0.101325 MPa. A constant is added to some data at different temperatures to separate them from each other.

### Conclusion

From all of the presented results above, it can be seen that there is no big difference between the complete and

the simplified MSA terms in our study. As regard to the short range term of PR EOS and CPA EOS, it seems CPA EOS provides slightly better results in aqueous systems. For the future mixed solvent systems containing associating compounds, CPA EOS is believed to be more advantageous. By using the simplified explicit MSA terms in MSW EOS, we obtained similar results to using the simplified implicit MSA term. In future work, eCPA EOS can be used with the simplified explicit MSA term to enhance computational speed and reduce the complexity of the EOS. Blum also proposed a new and more theoretical based mixing rule for simplified explicit MSA term, which significantly reduced the error between of the simplified explicit MSA term and the complete MSW term. This new mixing rule is worthwhile to be implemented. Association term should be studied to see whether it helps to improve the goodness of fit of EOS in the high concentration range where ion complex start to form. The SRK+DH EOS should be further improved in its temperature dependence function to improve its correlation results of multi temperature multi component SLE data.

## References

1. H. Planche, H. Renon. Mean Spherical Approximation applied to a simple but non-primitive model of interaction for electrolyte solutions and polar substances. *J Phys Chem.* 5 (1981) 3924-3929.
2. G. Jin, M.D. Donohue. An equation of state for electrolyte solutions. 1. Aqueous systems containing strong electrolytes. *Ind Eng Chem Res.* 27(1988) 1073-1084.
3. G. Jin, M.D. Donohue. An equation of state for electrolyte solutions. 2. Single volatile weak electrolytes in water. *Ind Eng Chem Res.* 27(1988) 1737-1743.
4. G. Jin, M.D. Donohue. An Equation of State for Electrolyte Solutions. 3. Aqueous Solutions Containing Multiple Salts. *Ind Eng Chem Res.* (30)1991 240-248.
5. W. Fürst, H. Renon. Representation of Excess Properties of Electrolyte Solutions Using a New Equation of State. *AIChE J.* 39(1993) 335-343.
6. J.Y. Zuo, D. Zhang, W. Fürst. Predicting LLE in Mixed-Solvent Electrolyte Systems by an Electrolyte EOS. *AIChE J.* 46(2000) 2318-2328.
7. Wu J, Prausnitz JM. Phase Equilibrium for systems Containing Hydrocarbons, Water and Salt: An Extended Peng-Robinson Equation of State. *Ind Eng Chem Res.* 37(1998) 1634-1643.
8. J.A. Myers, S.I. Sandler, R.H. Wood. An Equation of State for Electrolyte Solutions Covering Wide Range of Temperature, Pressure and Composition. *Ind Eng Chem Res.* 41(2002) 3282-3297.
9. A. Galindo, A. Gil-Villegas, G. Jackson, A.N. Burgess. SAFT-VRE: Phase Behavior of Electrolyte Solutions with the Statistical Associating Fluid Theory for Potentials of Variable Range. *J Phys Chem B.* 103(1999) 10272-10281.
10. L.F. Cameretti, G. Sadowski, J.M. Mollerup. Modeling of aqueous electrolyte solutions with perturbed-chain statistical associated fluid theory. *Ind Eng Chem Res.* 44 (9) (2005) 3355-3362
11. S.P. Tan, H. Adidharma, M. Radosz. Statistical Associating Fluid Theory Coupled with Restricted Primitive Model To Represent Aqueous Strong Electrolytes. *Ind Eng Chem Res.* 44 (2005) 4442-4452.
12. X.Y. Ji, S.P. Tan, H. Adidharma, M. Radosz. Statistical Associating Fluid Theory Coupled with Restricted Primitive Model to Represent Aqueous Strong Electrolytes: Multiple-Salt Solutions. *Ind Eng Chem Res.* 44(19) (2005) 7584 - 7590.
13. Liu Z, Wang W, Li Y. An equation of state for electrolyte solutions by a combination of low-density expansion of nonprimitive mean spherical approximation and statistical associating fluid theory. *Fluid Phase Equilib.* 227 (2005) 147-156.
14. Chen CC. Representation of solid-liquid equilibrium of aqueous electrolyte systems with the electrolyte NRTL model. *Fluid Phase Equilib.* (27)(1986): 457-474.
15. <http://www.ivc-sep.kt.dtu.dk/databank/>





**Piotr Tomasz Mitkowski**

Phone: +45 4525 2910  
Fax: +45 4525 2906  
E-mail: ptm@kt.dtu.dk  
WWW: <http://www.capec.kt.dtu.dk>  
Supervisors: Rafiqul Gani  
Gunnar Jonsson

**Ph.D. Study**

Started: February 2005  
To be completed: February 2008

## **Computer Aided Design of Hybrid Processes Consisting of Reactor and Membrane-Based Separation Unit**

### **Abstract**

In fine chemical and biochemical industry multi-step reactions usually progress in aqueous-organic solutions or in organic solvents. On-site removal of desired product enhances the process directly. In addition to that removal of undesired products would inhibit side reaction which in turn would increase process selectivity. It is quite common to find products that may be heat-sensitive which preclude the conventional thermal separation processes. In order to make the process economically feasible, one alternative is to increase the product yield by combining the reactor with a membrane separation unit or with better solvents, or both. Currently, reactors and membrane separation units are usually combined to operate as a hybrid process through an experiment-based trial and error approach which is acceptable in terms of reliability but it is time consuming and expensive. Through model-based computer-aided techniques, it is possible to select better solvents and identify feasible membrane-based separation processes which when combined with the reactor would increase process productivity. A systematic modelling framework for designing of hybrid reactors-separator systems is presented and its application is highlighted through a case study.

### **Introduction**

In pharmaceutical, fine chemicals and biochemical manufacturing reactions are most often carried out in a batch or semi batch reactor followed by multiple separations and cleaning steps. Irrespective of whether these reactions are equilibrium or kinetically controlled, on-site removal of products usually enhance the yield and lead to reduced process times. In the case of undesired side reactions, the removal of product(s) could also improve process performance. When solvents are used, it can either be recycled or substituted with another more appropriate solvent. For all these reasons, it is beneficial to couple the reactor with a separation unit.

One option to remove products from reactions (for example, when the product is heat sensitive and/or the separation technique requires operation at temperature below the degradation temperature) is to introduce membrane-based separation process. Membrane imparts selectivity to specific components based on either the difference in size or the chemical potential of the molecules. Also, membrane-based separation techniques enjoy advantages such as low operational costs, high selectivity, modular design and lower environmental impact.

Membrane-based separation techniques like pervaporation and nanofiltration have been extensively studied [1-3]. Pervaporation has been used in the production of MIBK (methylisobutylketone) [4] and MTBE (methyl tert-butyl ether) [5]. Nanofiltration is emerging as an option in separation of molecules with  $M_w$  ranging from 500 – 2000 from dilute solutions. Now the membranes which are resistant to degradation by organic solvent are also commercially available. These membranes are fairly reasonable option when the separation is based on size.

Coupling of reactor and separation unit is called hybrid process since the two processes influence the performance of each other and the optimisation of the design must take into account this interdependency. Lipnizki et al. [6] highlighted two types (R1 and R2) of hybrid processes consisting of reactor and membrane-based separation based on the type of molecule to be separated. Type R1 is an example where product is removed from recycle loop around the reactor when type R2 removes by-product. These hybrid processes are presented in Fig. 1a and 1b where the separation unit is physically set apart. It is also possible to integrate the membrane separation process within the reactor unit which is usually referred as the membrane reactor (Fig.

1c); however in such case it is impossible to set separation at different condition (T, P) on the “feed side” than those present in reaction medium.

Currently, reactor and membrane separation unit are combined through an experiment-based trial and error approach, which is time consuming and expensive. The main focus of this work is to give a computer aided framework for design/analyse of hybrid process systems.

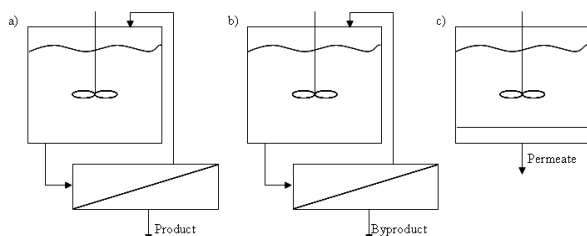


Fig. 1 Hybrid process layouts, a) type R1, b) type R2, c) internal membrane unit

### Model-based design methodology of hybrid systems

Design of hybrid process system consisting of reactor and membrane-based separation units is usually carried out through trial-and-error approaches involving also experiments. Even though they are acceptable in terms of reliability, they are time consuming and expensive while the solution is ad-hoc by nature. Based on a model-based framework for systematic analysis, it is possible to design hybrid process systems to find improved process design alternatives in terms of process output parameters such as reaction yield, selectivity, processing time and environmentally friendly solvents.

A model-based framework for systematic investigation of hybrid process systems is presented in Fig. 2, where the workflow for every step is indicated by the grey-boxes, while the needed models by rounded white-boxes and data are indicated through the white-boxes. Based on the knowledge of reactant properties like size of molecules, temperature of degradation, partial pressure etc, reaction kinetics and conditions of reaction are defined (step 1a). In the sub-step (step 1b), influence of solvent on reaction as well as on the process design is considered. A short list of chemicals which could be the potential solvents is generated based on the method of solvent selection given by Gani et al. [7] and their performance is evaluated in the hybrid process. This method includes use of computer-aided molecular design tool ICAS-ProCAMD [7]. The properties of solvent which play the biggest role in specific reaction are reactivity of solvent, miscibility with products, polarity, melting and boiling point, vapour pressure, selectivity and Environmental Health and Safety (EHS) properties. Influence of solvent on membrane-based separation method also needs to be considered due to its effect on membrane stability and fluxes. The process output depends on process parameters such as product purity, reaction yield and process time. The objective of the step 2 is to specify these process parameters in order to determine the values of process variables such as temperature,

permeability, membrane area etc. which will give the desired process output. Step 3 combines all collected knowledge with membrane separation models to identify the feasible membrane-based separation techniques. The membrane parameters like diffusivity, solubility etc. (for dense membrane) and porosity, pore size etc. (for porous membrane) used in membrane model should represent the available membranes. In the last step (step 4), various process scenarios are chosen and tested with given operational limits defined in terms of process yield, reaction time and membrane unit variables. If these constraints are satisfied, a feasible design is obtained; otherwise, decisions from earlier steps will need to be reviewed. This methodology consists of an efficient and systematic generate and test approach, which is able to save time and resources by avoiding duplication of work and efficient decomposition of the problem into integrated sub-problems (as highlighted in Fig. 2).

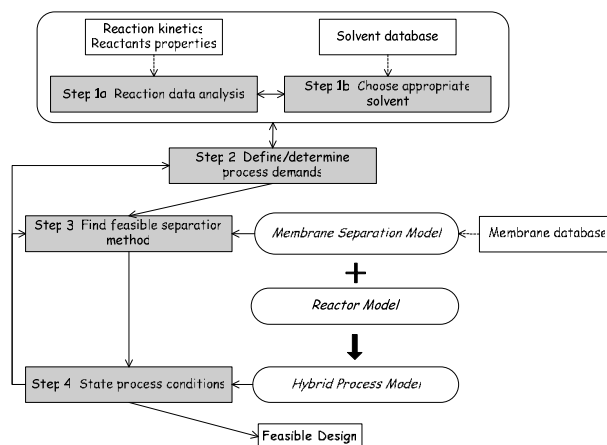


Fig. 2 Methodology of design/analyze hybrid process system

### Process scenarios

Step 4 of given methodology requires analysis of different process scenarios in order to satisfy process constraints defined in step 2. Various process scenarios could be differentiated into three groups of operation: (1) batch reactor, (2) semi-batch and continuous reactor, and (3) hybrid process. (1) *Batch operations* use fixed initial amounts of components, which also include amount of enzyme/catalyst. Results obtained through simulations of these operations can be also used to verify the kinetic model by comparing with experimental data and when needed, parameter optimization can be executed. (2) *Semi-batch operations* are done for different rates of components/feed addition or as well as for process outlets. Two cases appear to be worthy to look in more details: (2.1) solvent addition in order to increase conversion of limiting component by changing the component concentration and (2.2) addition of substrate(s) of reaction(s) in which main product is obtained (based on the law of mass action) in order to increase yield and selectivity. However for *continuous operations* different residence times are tested. (3) *Hybrid process operations* consider

continuous or semi-batch operation of system consisting reactor and membrane separation unit, where permanent product(s) addition as well as removal is present. At this stage of design, constant properties of membrane are assumed. However, for membrane separation processes it is unusual to maintain constant membrane properties which usually results in decline of components fluxes. In such cases a fixed decrease of component fluxes could be considered to indicate their effect on the system. In some cases when one of the reactions is slower the product removal could be applied in the point when the yield of the slowest reaction is high enough. This entails sequence of operations to overcome ‘bottle neck’ of the process.

All those scenarios discussed above have to be investigated qualitatively and quantitatively in order to explore and propose the best possible process scenario or at least the feasible operational window where the optimal design may exists.

### Generic model for the hybrid reactor-membrane process

The process scenarios described above need a generic model for the hybrid reactor-membrane process from which problem specific models can be generated and tested. General balance equations ((1)-(2)) for hybrid reactor-membrane process are derived based on scheme given on Fig. 3.

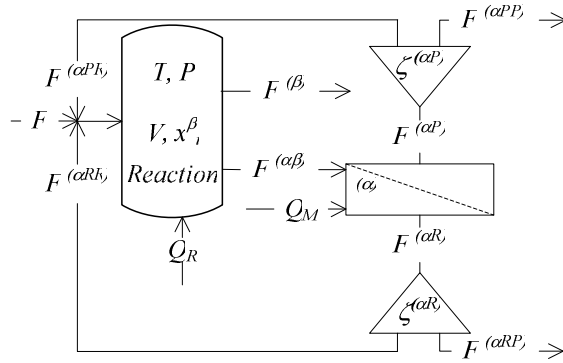


Fig. 3 The general scheme of hybrid process

The differential equations are the states of the system at discrete time points and algebraic equations are the constitutive and control equations. This generic hybrid process model contains process ((1)-(4)) and property sub-models ((5)-(7)) for both reactor and separation units. These equations are derived from mass and energy balances, which form a DAE system of equations.

$$\left[ \frac{\partial n_i}{\partial t} \right] = [F_i] + [F_i^{(\alpha PR)}] + [F_i^{(\alpha RR)}] - [F_i^{(\beta)}] - [F_i^{(\alpha PP)}] - [F_i^{(\alpha RP)}] + \left[ \sum_{k=1}^{NKR} V_{i,k}^{\beta} r_k^{\beta} \right] \quad (1)$$

$$\left[ \frac{\partial H}{\partial t} \right] = [Fh^{(F)}] + [F^{(\alpha PR)}h^{(\alpha P)}] + [F^{(\alpha RR)}h^{(\alpha R)}] - [F^{(\beta)}h^{(\beta)}] - [F^{(\alpha PP)}h^{(\alpha P)}] - [F^{(\alpha RP)}h^{(\alpha R)}] + \left[ \sum_{k=1}^{NKR} r_k^{\beta} \Delta H_k^R \right] + [Q_R] + [Q_M] \quad (2)$$

$$F_i^{(\alpha P)} = F_i^{(\alpha P)}(J_i, A_m, F_i^{(\alpha \beta)}, \zeta^{(\alpha P)}, T_M^{(\alpha P)}, P_M^{(\alpha P)}) \quad (3)$$

$$F_i^{(\alpha R)} = F_i^{(\alpha R)}(J_i, A_m, F_i^{(\alpha \beta)}, \zeta^{(\alpha R)}, T_M^{(\alpha R)}, P_M^{(\alpha R)}) \quad (4)$$

$$h^{(j)} = h^{(j)}(T, P, x_i^{(j)}) \quad (5)$$

$$r_k^{\beta} = r_k^{\beta}(T, V, k_p^{\beta}) \quad (6)$$

$$J_i = J_i(T, P, x_i^{(\alpha \beta)}) \quad (7)$$

Where  $A_m$  – membrane area,  $x_i$  – molar fraction in liquid phase,  $z_i$  – molar fraction in fresh feed,  $F$  – molar flow,  $F_i$  – component molar flow,  $J_i$  – component flux through the membrane,  $k_p$  – reaction rate constant,  $P$  – pressure,  $r$  – reaction rate,  $t$  – reaction time,  $T$  – temperature,  $V$  – reactor volume,  $v_{i,k}$  – stoichiometric coefficient, subscripts:  $i$  – components,  $M$  – membrane,  $R$  – reactor,  $r$  – retentate, superscript:  $\alpha$  – membrane unit,  $\beta$  – liquid phase,  $\alpha PP$  – permeate leaving system,  $\alpha RP$  – retentate leaving system,  $\alpha PR$  – recycled permeate,  $\alpha RR$  – recycled retentate.

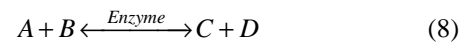
For hybrid process design, the objective is to combine *Flow out* and *Recycle* terms (Eq.1) into a single term representing the effluent from the hybrid system, which depends on membrane related variables ( $A$ ,  $J_i$  or  $F^{(\alpha \beta)}$ ), directly into reactor model. Advantage of such a reformulated model is simplicity to investigate the performance of the hybrid system. Moreover, this operation reduces number of variables and the degrees of freedom. Using this generic model and the specific details of any problem, the specific hybrid reactor-membrane process can be generated and tested.

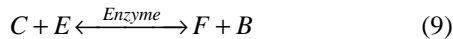
### Case study: Enzymatic esterification

Application of the model-based framework is illustrated through an enzymatic esterification reaction. Data used in this study were published by Egger et. al. [8]. Objective of this study is to analyze esterification process in order to propose feasible process set-up with highest possible process yield.

#### Step 1a: Reaction data collection

Enzymatic esterification is carried out in two reactions where phospholipase-A<sub>2</sub> is used as enzyme. First one is hydrolysis (Eq.(8)) of phosphatidylcholine (1) to lysophosphatidylcholine and second esterification (Eq.(9)) of lysophosphatidylcholine to phosphatidylcholine (2). However, hydrolysis is faster than esterification, which makes second reaction limit the overall process yield. The net enzymatic esterification reaction can be represented schematically as:





Where:  $A$  – phosphatidylcholine (1),  $B$  – water,  $C$  – lysophosphatidylcholine,  $D$  – palmitic acid,  $E$  – oleic acid,  $F$  – phosphatidylcholine (2).

Although, this kind of reaction has been studied at temperatures equal to or higher than 50°C, all data used in this work has been obtained at ambient conditions. No heat effect was reported. Egger ET. al. [8] reported equilibrium yields in various water activity conditions and substrate concentrations, which has been correlated and verified here to generate the kinetic model. All reactants except water are heat sensitive. Molecules  $A$  and  $C$  have  $M_w$  734 and 495 while  $M_w$  of  $D$  and  $F$  are 282 and 760 respectively.

#### Step 1b: Solvent selection

Reactions required solvent to reduce viscosity of reaction medium and to keep low water content but still sufficient amount required for enzyme stability. Based on information obtained from literature [8] toluene was chosen as the first solvent. Other likely solvents generated with ICAS-ProCAMD include, n-hexane, n-heptane, isopropylacetate 2-dimethylhexane, n-nonane, 2-methylnonane and many more.

#### Step 2: Process demands

Esterification reaction, which is kinetically controlled, has a low product yield. The objective is to increase the process productivity by removing the water. Moreover, reaction requires an inert organic solvent and minimum water content (related to enzyme activity).

#### Step 3: Separation method selection

Pervaporation (PV) is chosen as the membrane-based separation technique because of the possibility of introducing hydrophilic membranes that would allow only water to permeate. Sirkar and Winston Ho [10] reported a cross-linked polyvinyl alcohol membrane in PV to dehydrate organic mixtures, even with very small water concentration.

#### Step 4: Process conditions and feasible design

Two operations have been studied: batch and hybrid of type R2 (Fig.1b). Batch operations were selected since small production is considered. All set-ups are investigated under assumptions that: reactor is well mixed, reaction occurs only in the reactor volume in the liquid phase. With respect to membrane separation, water flux in PV is constant and fluxes for all other components present in the system are neglected. From the generic hybrid model (Eq. (1)), the problem specific hybrid process model is generated (Eq.(10)).

$$\frac{dn_i}{dt} = -J_i A_m + V \sum_{k=1}^{NKR} v_{i,k} r_k \quad (10)$$

The accumulation in the membrane process is neglected because change of state variables along the length and time (steady state) are assumed constant. Reaction kinetics is described by reversible Michaelis-Menten kinetics. Process yield is defined as ratio of moles of

desired product (phosphatidylcholine (2)) to initial of limiting reactant (phosphatidylcholine (1)), ( $Yield = N_P/N_{A0}$ ). Whole DAE model of hybrid system contain 7 ordinary differential equations, 13 algebraic equations with 73 variables and it is solved in the ICAS-MoT [9] modelling environment, which is a computer aided modelling tool with option of model translation analysis and solution. With the generated problem specific hybrid process model, five scenarios have been investigated in terms of process yield and superiority of the hybrid process over batch reaction is obtained. All simulations have been performed with the same initial conditions with respect to reactor:  $C_{A0} = 10\text{mM}$ ,  $C_{B0} = 36.5\text{mM}$ ,  $C_{E0} = 800\text{mM}$  and  $V = 1\text{dm}^3$ . Performance of hybrid system is strongly dependent on the membrane area ( $A_m$ ) and component fluxes ( $J_i$ ). For reactor coupled with pervaporation unit (RCPV), four cases with different values of factor  $J_B A_m$  ( $J_B$  – water flux) have been studied. For process carried out in 20h yield is improved from 0.25 (batch) to 0.57 (RCPV3) by removing water from the system using a reasonable design for a PV-unit ( $J_B = 0.5\text{mmol}/(\text{m}^2\text{h})$ ,  $A_m = 2.56\text{m}^2$ ). However, possibility of reducing time into 10h were found for  $A_m = 5.12\text{m}^2$ . Values for the different design variables for the five scenarios are given in Table 1 while the yield-time behaviour is shown in Fig. 3.

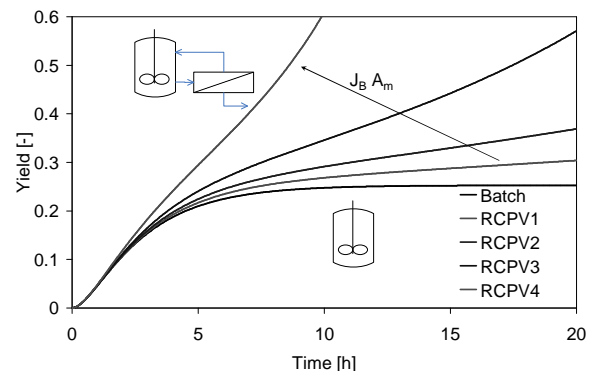


**Fig. 3** Comparison of hybrid process systems with batch in terms of process yield

**Table 1** Process parameters and process yields

	Batch	RCPV1	RCPV2	RCPV3	RCPV4
$J_B A_m$ [mmol/h]	-	0.32	0.64	1.28	2.56
$t$ [h]	20.00	20.00	20.00	20.00	9.91
Yield [-]	0.25	0.30	0.37	0.57	0.60

Two different membranes polyvinyl alcohol and cellulose acetate membranes with various solvents have been investigated under assumption that solvent does not change kinetic parameters and fluxes of other components can be neglected. To make easy comparison between membranes the same membrane area was used in all simulations. Data used for pervaporation unit was found in literature and result are summarised in Table 2.

For further experimental studies semi-batch reactor coupled with pervaporation is recommended. However, at first impact of isopropyl-acetate and hexane on reaction should at first be verified experimentally. If experiments would represent no change in kinetics, the recommended solvent is isopropyl-acetate with assisted cross-linked polyvinyl alcohol membranes.

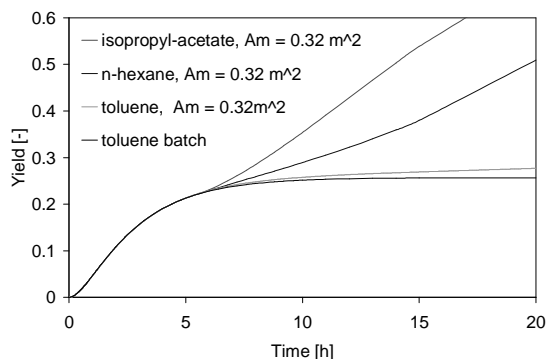


**Fig. 4** Comparison of hybrid process systems with various membranes and solvents

**Table 2** Various membranes versus different solvents

Possible membranes	Solvents	Yield [-]	t [h]
Poly(vinyl alcohol) [11]	isopropyl-acetate	0.6	17
Poly(vinyl alcohol) [10]	toluene	0.26	20
Cellulose acetate [12]	n-hexane	0.5	20

## Conclusions

A model-based framework for systematic investigation of hybrid systems consisting of well mixed reactor and membrane-based separation unit has been presented along with the application to the enzymatic esterification case study. The work-flow and the corresponding data-flow for the methods and computer aided tools needed by the model-based framework have been developed. Problem specific hybrid process models are generated from generic model and used for specific reaction systems. From this work, it is clear that hybrid processes consisting of reactor and membrane unit could show their advantages where difficulties exist to incorporate other separation methods and gives significant increase in process yield by overcoming limitations of kinetically controlled reactions and also by reducing the process time. That work present also great impact of solvent for membrane separation unit. It is considerably important that experimental trials needed to verify the hybrid process are reserved for the final step, thereby saving time and resources.

## Acknowledgment

Author is pleased to acknowledge the PRISM the Marie Curie Research Training Network, European Community's Sixth Framework Program.

## References

1. J.A. Whu, B.C. Baltzis, K.K. Sirkar, Modelling of nanofiltration – assisted organic synthesis, *Journal of Membrane Science*, 163, (1999), 319-331.
2. F. C. Ferreira, S.Han, A.Boam, S.Zhang, A.G.Livingstone, Membrane aromatic recovery system (MARS): lab bench to industrial pilot scale, *Desalination*, 148, (2002), 267-273.
3. J.T.Scarpello, D.Nair, L.M. Freitas dos Santos, L.S.White, A.G. Livingstone, The separation of homogeneous organometallic catalysts using solvent resistant nanofiltration, *Journal of Membrane Science*, 203, (2002), 71-85.
4. C. Staudt-Bickel, R.N.Lichtenthaler, Integration of pervaporation of the removal of water in production process of methylisobutylketone, *Journal of Membrane Science*, 111, (1996), 135-141.
5. M. Matouq, T. Tagawa, S. Gotp, Combined process for production of methyl tert-butyl ether from tert-butyl alcohol and methanol, *Jurnal of Chemical Engineering of Japan*, 27, (1994), 302-306.
6. F. Lipnizki, R.W. Field, P-K. Ten, Pervaporation-based hybrid process: a review of process design, applications and economics, *Journal of Membrane Science*, 155, (1999), 183-210.
7. R. Gani, C. Jim'ene-Gonz'alez, D.J.C. Constable, Method for selection of solvents for promotion of organic reactions, *Computers and Chemical Engineering*, 29, (2005), 1661-1676.
8. D. Egger, E. Wehtje, P. Adlercreutz, Characterization and optimisation of phospholipase A2 catalyzed synthesis of phosphatidylcholine, *Biochimica et Biophysica Acta*, 1343,(1997),76-84
9. M.Sales-Cruz, R. Gani, 2003, *Computer-Aided Chemical Engineering*, vol. 16: Dynamic Model Development, Eds. S.P. Asprey and S. Macchietto, Elsevier, Amsterdam.
10. K.K.Sirkar, W.S.Winston Ho, *Membrane Handbook*, Van Nostrand reinhold, 1992
11. M.T. Sanz, J. Gmehling, Esterification of acetic acid with isopropanol coupled with pervaporation. Part I: Kinetics and pervaporation studies, *Chemical Engineering Journal* 123 (2006) 1–8
12. I.J. Kang, P.H. Pfromm, M.E. Rezac, Real time measurement and control of thermodynamic water activities for enzymatic catalysis in hexane, *Journal of Biotechnology*, 119, (2005), 147-154





## **Ricardo Morales Rodríguez**

Phone: +45 4525 2911  
Fax: +45 4525 2906  
E-mail: [rmr@kt.dtu.dk](mailto:rmr@kt.dtu.dk)  
WWW: <http://www.capec.kt.dtu.dk/>  
Supervisor: Rafiqul Gani

Ph.D. Study  
Started: February 2006  
To be completed: January 2009

## **Computer-Aided Multiscale Modelling for Chemical Process Engineering**

### **Abstract**

Usually, chemical processes are modeled through monoscale approaches, which, while not adequate, they satisfy a useful role in product-process design. Therefore, use of a multi-dimension and multi-scale model-based approach is desirable in product process development. A computed-aided framework for model generation, analysis, solution and implementation will allow the development and application of the desired model-based approach for product-centric process design/analysis. This goal can be achieved through the combination of a system for model development (ModDev), and a system for model analysis and solution (MoT); also, it should be possible to have a connection with any other external software or process simulators through COM-Objects or CAPE-OPEN Link.

### **Introduction**

The development of special materials and/or chemical products as well as a broad variety of scientific and engineering problems, requires models covering a wide spectrum of partial and temporal scales. Traditionally, chemical processes have been modeled through monoscale approaches, which, while not adequate, nevertheless satisfy a useful role in product-process design. Product-centric process design integrates aspects of product evaluation into the process design problem. In this case, use of multi-dimension and multi-scale model-based approach is beneficial in product-process development which basically consists of dividing a complex problem into a family of subproblems that exist at different scales and that can be organized along various scales depending on the system and on the intended use of the model [1].

A flexible computed-aided framework for model generation, analysis, solution and implementation will allow the development and application of the desired model-based approach for product-centric process design/analysis. This can be achieved through the integration of a model generation system (ModDev), and a modelling tool (MoT) for model translation, analysis and solution. The combination of ModDev, MoT and ICAS (Integrated Computer Aided System) or any other simulators or external software (through COM-Objects) will permit that different models and/or process configurations to be simulated very easily and quickly, reducing time and human resources for model

development and solution with almost zero programming effort, and thereby, producing customized simulators for a particular process.

### **Specific Objectives**

The objective of this project is to develop a new Computer-Aided Modelling Framework, and through it, the synergy between ModDev and MoT; together with new modelling features such as multiscale modelling and models needed for specific product-centric process design that are usually not found in commercial simulators (for example, fuel cells, thin-film evaporators) allowing the development of customized simulators with models generated through ModDev-MoT and using it in other computational tools such as simulation engines (Icassim and Dynsim available in ICAS software), external software (i.e. excel) or external simulators through COM-Objects or/and CAPE-OPEN link.

### **Computer-Aided Modelling Framework**

Nowadays, computer-aided process modelling frameworks have become an important tool in the development and solution of process and product engineering problems.

Computer-Aided Process Modelling Frameworks can be classified in general as: generic modelling languages and domain-oriented modelling languages. Process Modelling Languages (PML) could be classified as part of domain-oriented modelling

languages [2]. PML should be provided with multiscale modelling approach to enhance the accuracy in the behaviour of some model-processes involving multiscale phenomena. Multiscale is an essential prerequisite for making full use of advances in scientific understanding within engineering applications of practical interest. As It is pointed out by [3], Chemical engineers are turning to multiscale modelling to extend traditional modelling approaches into new application areas and to achieve higher levels of details and accuracy. The challenges and opportunities for multiscale modelling for chemical process are open and taken into account in this project.

Integrated Computer Aided System (ICAS) is a computer-aided tool for modelling, simulation (including property prediction), synthesis/design, control and analysis into a single integrated system [4], developed by CAPEC at DTU. ModDev and MoT are modelling tools that can be found in ICAS software; both of them are aimed and classified as computer-aided modelling frameworks. But, *why do we need to use ModDev and MoT together as a new modelling framework?* Because through their interaction, model equations for a specific equipment, process or operation would be developed by ModDev; and then translated, analyzed and solved through MoT with almost zero programming effort, and thereby, producing customized simulators for a particular process.

In addition, after the model equations have been successfully derived/generated, the user has the option to generate a COM-object of the model for transfer and use in external software (e.g. excel, see figure 1). On the other hand, the connection of these COM-Objects with other external software such as commercial simulators can be done through the CAPE-OPEN link (see figure 1).

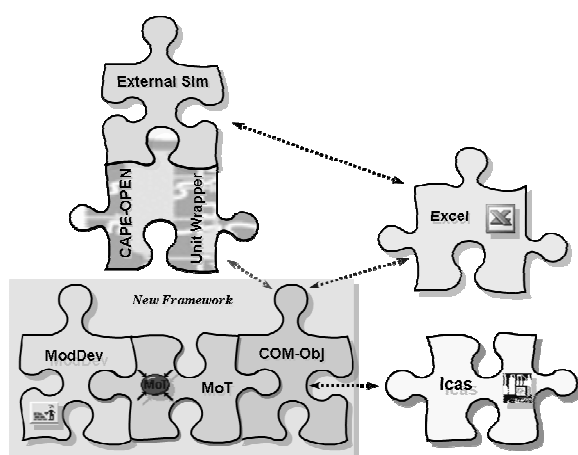


**Fig. 1.** Computer-Aided Modelling Framework

Also, the generated MoT-COM is able to interact with the ICAS environment, thereby providing models

for new unit operations that can be used with available models for other unit operations. Some of the external simulators can also be used under Microsoft Excel together with MoT-COM. Thereby providing greater availability of models and true interoperability of software tools in process-product design.

### Acknowledgement

The author acknowledges the financial support of the Technical University of Denmark.

### References

1. E. Németh, R. Lakner, K. M. Hangos and I. T. Cameron, ESCAPE-15, Spain, May 2005.
2. L. von Wedel, W. Marquardt and R. Gani, Computer-aided Chem. Eng., vol. 11 (2002) 89.
3. G.D. Ingram, I.T. Cameron and K.M. Hangos, Chem. Eng. Sci., No. 59 (2004) 2171.
4. R. Gani, G. Hytoft, C. Jaksland and A. K. Jensen, Comput. Chem. Eng., No. 10 (1997) 1135.



### **Martin Nordvig Mortensen**

Phone: +45 4525 6819  
Fax: +45 4588 2161  
E-mail: mnm@kt.dtu.dk  
WWW: <http://www.polymers.dk>  
Supervisors: Søren Hvilsted  
Jens Glastrup, the Danish National  
Museum

#### **Ph.D. Study**

Started: June 2005  
To be completed: May 2008

## **Stabilisation of Polyethylene Glycol in Archaeological Wood**

### **Abstract**

Damaged PEG was detected in a sample from the Skuldelev Viking ships in Roskilde using Matrix Assisted Laser Desorption Ionisation-Time of Flight Mass Spectrometry (MALDI-TOF MS), this could suggest that PEG degradation has taken place. Accelerated ageing of tetraethylene glycol showed that formic acid is a product of PEG degradation. Formic acid was detected in samples from the Skuldelev ships using a gas chromatographic technique, which is a possible indication of PEG degradation. However, it remains to be determined if the formic acid found in the sample originates solely from PEG and not from the wood components, a carbon isotope analysis is being set up to reveal this.

### **Introduction**

Waterlogged wooden archaeological objects are normally impregnated with polyethylene glycol (PEG) after salvage. This is done to prevent the wood from cracking and shrinking when dried. PEG has proven useful for this purpose many times, a few examples include the Vasa (SE), the Hjortspring boat (DK), the Batavia (AU), the Skuldelev ships (DK) and the Bremen cog (D), which are all PEG treated wooden shipwrecks on exhibition today. During re-conservation of the Hjortspring boat, indications that PEG had degraded in the wood were observed [1]. This caused concern that PEG degradation could be taking place in other objects that have received a similar impregnation. If this turns out to be the case, many important objects around the world are affected.

It is well known that PEG itself degrades at elevated temperatures in the presence of air [2-5]. Several investigations of the degradation mechanism have been conducted some of the more successful use nuclear magnetic resonance (NMR) for detection [6-8]. However, these experiments were conducted at very high temperatures. To assume that the mechanisms identified in those experiments, extends to room temperature without problems, would be optimistic.

There is agreement though that degradation of PEG leads to shortening of the polymer chain.

In lack of precedence the ultimate consequences of PEG degradation in the wood are hard to predict. Some speculate that PEG will start to seep out of the wood if the molecular weight gets low enough, since such PEG is a hygroscopic liquid. Other ideas are based on sorption isotherms of different PEG types [9]. If the air humidity fluctuates around 60% relative humidity for example, the amount of water that is moved in and out of the material is larger for low molecular PEG types than for high molecular ones. As a result the objects would become increasingly responsive to climate fluctuations, as PEG degrades.

The work that has been done so far includes characterisation of the PEG impregnation in the Vasa and the Skuldelev Viking ships [10]. Besides showing the amounts and distribution in the wood of the different PEG types used for impregnation, it was also the aim to assess the state of this PEG. In most samples no obviously degraded PEG was observed with the techniques used, except for a few samples from the Skuldelev ships. In these samples mass spectrometry indicated the presence of damaged PEG. Accelerated

ageing of the PEG model molecule tetraethylene glycol has been studied using Gas Chromatography Mass Spectrometry (GC-MS) [11]. One of the results obtained from these experiments showed that formic acid is a product of tetraethylene glycol degradation. With this information it is clear that there must be formic acid in the timbers if PEG degradation takes place. For this reason a series of formic acid measurements using Solid Phase Micro Extraction (SPME) GC-MS were conducted on a range of PEG treated wooden archaeological objects including the Vasa and the Skuldelev ships. This showed that the objects contain formic acid [12].

### Specific Objectives

It is the aim to characterize PEG and possible PEG degradation products in the Vasa and in other PEG treated artefacts using appropriate analytical techniques. Based on this information a method that can show if PEG degrades or not, should be devised. If degradation is taking place then ways of inhibiting the process should be investigated.

### Results and Discussion

Matrix Assisted Laser Desorption Ionization Time of Flight Mass Spectrometry (MALDI-TOF MS) has been used in the characterization of PEG from the Skuldelev Viking ships. One such spectrum is shown in figure 1, it is dominated by ions corresponding to PEG ( $[\text{PEG}]\text{Na}^+$ ). The Skuldelev ships were impregnated with PEG 4000 only which is observed as a symmetrical distribution around  $m/z$  4000. However, PEG with a lower molecular weight ( $m/z < 2000$ ) and highly unsymmetrical molecular weight distribution is observed too. Size Exclusion Chromatography is in agreement with the MALDI-TOF result (data not shown). It suggests that approximately half of the PEG that is in the sample consists of low molecular PEG ( $M_w < 2000$ ), the other half being PEG 4000. The low molecular fraction could be interpreted as a product of degradation (of PEG 4000), but there could also be other explanations for this fraction. In principal there are three possibilities: either the low molecular fraction was present in the PEG starting material that was used in the impregnation process, it could also have formed during the impregnation process, and it could have formed during the period where the ship has been on exhibition in the museum.

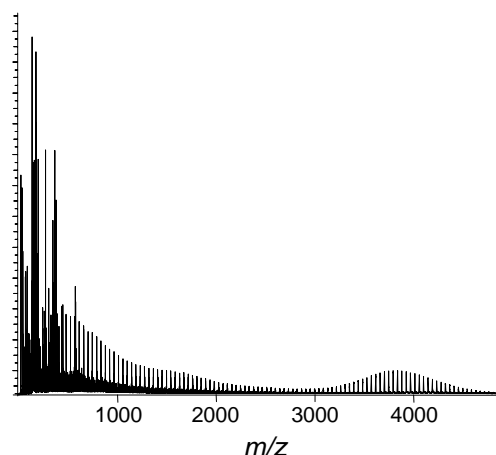


**Figure 1.** MALDI-TOF mass spectrum of PEG extracted from the keelson of the Skuldelev 2 Viking ship. The sample corresponds to the outer 4 mm of the wood.

None of the PEG starting material has been saved, so comparison to see if the low molecular fraction was present from the beginning is not an option. Thus MALDI-TOF MS does not rule out PEG degradation but it does not confirm it very well either.

PEG degradation leads to formic acid. We have been able to measure the formic acid content of samples from the Skuldelev ships, most of them contain just below 1 % (wt.) formic acid [12]. This result is in agreement with PEG degradation taking place, but it does not prove it either. In order to use formic acid as an indication of PEG degradation it must be taken into account, that there could be other sources to this formic acid. It is not unlikely that the formic acid, at least some of it, originates from the wood components. Thus it is necessary to find a way of telling if the formic acid comes from wood or from PEG. Such a method is currently being developed using radiocarbon analyses. The basic idea is illustrated in figure 2.

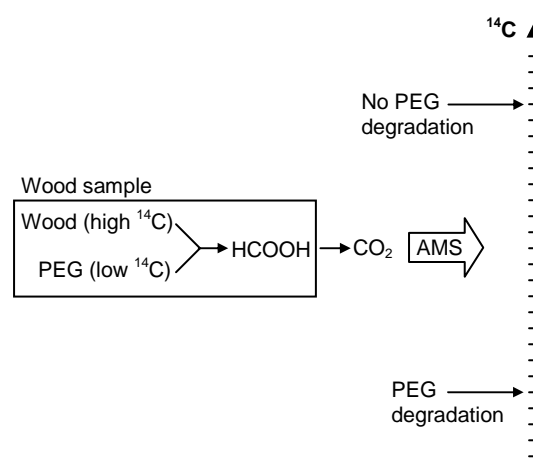


**Figure 2.** The radiocarbon strategy. A wood sample (box) contains wood, PEG and formic acid. The sources to formic acid can be either wood or PEG that have

different  $^{14}\text{C}$  contents. The formic acid is isolated and oxidised to  $\text{CO}_2$ . The  $^{14}\text{C}$  content is measured by AMS and the origin of the formic acid can be determined.

$^{14}\text{C}$  is a radioactive isotope that decays with time, the archaeological wood in question here though, still contains plenty of  $^{14}\text{C}$  for analysis. PEG is a petrochemical and therefore  $^{14}\text{C}$  depleted. We intend to take advantage of this difference to determine the origin of the formic acid. If the formic acid in the object is a product of either wood or PEG then the  $^{14}\text{C}$  content of this formic acid will be either high or low respectively (the box in figure 2.). Experimentally formic acid is isolated by ion exchange chromatography followed by vacuum distillation, it is then oxidized selectively to  $\text{CO}_2$  using a reaction with mercury(II)chloride. The  $\text{CO}_2$  is trapped on a vacuum line and the  $^{14}\text{C}$  content measured by Accelerator Mass Spectrometry (AMS). The  $^{14}\text{C}$  content of the  $\text{CO}_2$  isolated reflects the  $^{14}\text{C}$  content of the formic acid and since we know the  $^{14}\text{C}$  content of both the wood and the PEG, the origin of the formic acid can be revealed. The experimental procedures are currently being tested.

### Conclusions

Damaged PEG was detected in a sample from the Skuldelev Viking ships by MALDI-TOF MS. This is a possible indication that PEG degradation may have been taking place.

Formic acid is a product of PEG degradation and it was detected in PEG treated archaeological wood. This could indicate that PEG degradation has taken place but it is necessary to make sure that the formic acid does in fact originate from PEG. It is the intention to determine this by carbon isotope analyses.

### Acknowledgements

This project is funded by the National Maritime Museums of Sweden research project "Save the VASA" sponsored by The Bank of Sweden Tercentenary Foundation, The Swedish National Heritage Board, The Swedish Foundation for Strategic Research (SSF), The Swedish Research Council for Environment, Agricultural Sciences and Spatial Planning (FORMAS), and The Swedish Agency for Innovation Systems (Vinnova). The Danish Ministry of Culture and the Danish National Museum are also kindly acknowledged for funding.

### References

1. T. Padfield, J. Winsløw, W. B. Pedersen, J. Glastrup, in: K. Grimstad (Ed.) 9th Triennial Meeting Dresden, German Democratic Republic 26-31 August 1990, ICOM Committee for Conservation, Los Angeles, (1990) 243-245.

2. J. Glastrup, *Polym. Degrad. Stabil.*, 52 (1996) 217-222.
3. A. D. Dale, M. B. Evans, *J. Chromatogr.*, 552 (1991) 161-167.
4. L. Costa, A. M. Gad, G. Camino, G. G. Cameron, M. Y. Qureshi, *Macromolecules*, 25 (1992) 5512-5518.
5. S. Morlat, J.-L. Gardette, *Polymer*, 42 (2001) 6071-6079.
6. L. Yang, F. Heatley, T. G. Blease, R. I. G. Thompson, *Eur. Polym. J.*, 32 (1996) 535-547.
7. O. A. Mkhathresh, F. Heatley, *Macromol. Chem. Phys.*, 203 (2002) 2273-2280.
8. O. A. Mkhathresh, F. Heatley, *Polymer International*, 53 (2004) 1336-1342.
9. Clariant, product catalog, polyalkylene/polyethylene glycols, 26-27.
10. M. N. Mortensen, H. Egsgaard, S. Hvilsted, Y. Shashoua, J. Glastrup, *Journal of Archaeological Science*, in press (2006).
11. M. N. Mortensen, *Graduate Schools Yearbook*, (2005), 139-141.
12. J. Glastrup, Y. Shashoua, H. Egsgaard, M. N. Mortensen, *Holzforschung*, 60,3 (2006) 259-264.





## **Hanne Hostrup Nielsen**

Phone: +45 4525 2838  
Fax: +45 4588 2258  
E-mail: hhn@kt.dtu.dk  
WWW: <http://www.chec.kt.dtu.dk>  
Supervisors: Peter Glarborg  
Stefan Mayer, MAN Diesel A/S  
Sønnik Clausen, Forskningscenter RISØ

### **Industrial Ph.D. Study**

Started: March 2006  
To be completed: February 2009

## **In-Situ Investigations of the Combustion in Large, Two-Stroke, Diesel Engines**

### **Abstract**

Due to restrictions on the emission levels from marine engines, MAN Diesel, the worlds largest producer of large, two-stroke, Diesel engines are conducting thorough research in areas connected with combustion optimization and emission reduction. An important tool in the combustion investigations is numerical analysis of the various combustion phases, but a lack of reliable experimental data provides an obstacle in validation and optimization of the developed code. For years, various optical analysis methods have been applied for investigations of the combustion in smaller engines, but due to the more restricted access, extremely sooting combustion and very high pressures, similar investigations have not been undertaken at larger engines under realistic combustion conditions. This project considers optical in-situ investigations on a large, two-stroke Diesel engine, located at the Test Centre at MAN Diesel A/S in Copenhagen. The aim of the investigations is to provide experimental data for the combustion under realistic running conditions, by means for example of high speed recordings of combustion images, and to use these data for validation and optimization of an existing CFD-code.

### **Introduction**

Large, marine engines are responsible for approximately 2 % of the total world fuel consumption, and many of these engines are two-stroke Diesel engines. Strong restrictions are expected to be imposed on the industry, thereby forcing the leading engine manufactures to focus further on emission reduction and engine performance optimization in general.

The costs of performing physical tests on large engines are very large, which makes numerical analysis (CFD-calculations) a natural choice. Obviously, some tests are necessary for validation of the numerical codes, and the developments in optical methods within the areas of measurements of complex flows make these a natural choice. These methods have been used for several years in smaller engines, though the transient character of the combustion, and the large and fast variations in pressure and temperature have provided several challenges in the design of both optical accesses and experimental equipment.

Unfortunately, the results obtained on smaller engines cannot be scaled up to the conditions present in the larger engines. This is mainly due to large difference in both length and time scale of the engine processes and the use of different types of fuel.

The aim of the present Industrial Ph.D.- project is to develop an optical access to the 8 MW, 4 cylinder Test Diesel engine located in the Test Center at MAN Diesel A/S in Copenhagen, and through this to provide experimental data for validation and optimization of the in-house developed numerical models.

As opposed to many of the investigations undertaken so far, this project focuses on in-situ measurements, thereby enabling validations of more local character, like local 'hot spots', flame formation and - spread. Further, it is expected to be able to perform recordings at a frequency that allows for analysis of cycle-to-cycle variations.

### **Optical investigations in engines**

The predominant method for optical investigations of the combustion in engines is by use of a special designed laboratory 1-cylinder engine constructed with an entire wall of a transparent material. Due to the very large heat- and pressure stresses in the larger engines, this approach is impossible. Alternatively, an endoscope can be used for looking into a more limited space of the engine. This approach also opens up for the possibility of using all ready existing openings in the engine, but naturally also limits the total accessible volume of the combustion chamber. The latter problem can though

partially be solved by the wide range of industrial endoscopes available today, allowing for various directions and angles of view.

For investigations of the actual combustion, various imaging techniques are often applied, as the rapid and massive soot formation ensures lots of light. Thereby, it is possible to investigate factors like ignition and flame spread. For imaging of for example fuel spray and evaporation, a very strong light source will need to be incorporated, thereby typically inducing the need for another access point. This is especially troublesome at large, full size engines running under realistic conditions, as the space at the cylinder cover typically is very limited.

A very common method for determination of local temperatures in engines is the use of the Two-Color Method, which merely includes recording the combustion emissivity, originating from the hot soot particles, at two different wavelengths and calculating the temperature at the soot particle surfaces from Planck's Radiation Law. This method though implies that the soot particles are in thermal equilibrium with the surrounding gas phase at all times. Further, an assumption of the connection between the soot particles emissivity and the emitted light wavelength must be used. Finally, the temperatures determined this way are often determined based on the total emissivity of a soot cloud, thereby also inducing approximations on the soot cloud size and soot concentration [1].

Alternatively, IR or UV emission investigations could give more precise information on both temperatures and combustion components distribution. At the moment though, no, or only very few reference data are available for this purpose at the relevant temperatures and pressures, and will thus need to be provided beforehand.

#### **Numerical investigations undertaken at MAN Diesel**

At MAN Diesel, numerical methods have been used for investigating and improving fuel spray directions, combustion chamber geometries etc. for the last 15 years. This has lately been done by use of a CFD-program, KIVA, which is especially suitable for engine calculations. The calculations performed now are based on fairly simple models for turbulence,  $\text{NO}_x$ - and soot formation, but have still been able to produce relatively good predictions compared to experimental global investigations on parameters like gas phase temperatures and pollutant formations. The local variations are though still un-resolved, and are naturally very dependent on more local measurements of temperatures, flow velocities, swirl and gas phase concentrations.

#### **The experimental setup**

The optical access to the 4T50ME-X test engine at MAN Diesel in Copenhagen is presently under development. Focus has so far been on determining the optical point of access, along with the actual design of the access. It has been chosen to use an existing

entrance, the starting air valve, which then is to be modified into a hollow dummy valve, with room for an endoscope, cooling pipes, and instrumentation inside. Finally, the endoscope will be shielded from the combustion chamber by a sapphire window.

A major obstacle has been the mounting of the sapphire window into the end of the starting air valve. Even though sapphire is chosen for its high resistance to heat, pressure and most chemicals, it is also a very brittle material, which causes trouble when it is to be mounted strong enough to withstand pressures varying between 7 and almost 180 bars twice every second.

In co-operation with a German company, Klein & Becker, and largely inspired by earlier work from a similar research area [2], a special mounting method has been developed. This includes a high temperature force fitting/soldering technique, performed under vacuum, and with a soldering material that reacts actively with the sapphire.

The mounting technique has been tested on a dummy fuel nozzle, equipped with a miniature sapphire window, a thermo couple, and an optical fibre. These tests have proven both the functionality of the window mounting method, along with a way of solving the troubles with sooting and deposition of residues from the lubricating oil on the sapphire window. The latter has been shown to be reduced drastically by only inserting the dummy after having run the engine warm along with turning of the lubricating system when testing.

Further, the window mounting technique allows for a rather exposed surface of the sapphire window, at which temperature measurements show that the initially accumulated soot begins to burn off when the inside of the sapphire window reaches approx. 350-400 °C.

#### **Future work**

Having developed and tested the technique for mounting the sapphire window securely in a dummy fuel nozzle, the next step will be the final design of the larger, optical access, the starting air valve. With this, and an endoscope with an angle of view pointing in the direction of the spray, it should be possible to record images of the combustion in the engine under realistic conditions.

Further, high temperature IR and UV emission investigations of typical combustion gases at a special designed high temperature gas cell at the Risø Laboratories will reveal the potential for applying these methods for spectroscopic investigations of the combustion.

#### **References**

1. H. Zhao, N. Ladommatos, Prog. Energy Sci. 24 (1998) 221-255
2. H. Philipp, E. Winklhofer, US Patent No. 2002/0134138 A1, Pub. Sep. 26, 2002



## Jens Kromann Nielsen

Phone: +45 4525 6809  
Fax: +45 4588 2161  
E-mail: jkn@kt.dtu.dk  
WWW: <http://www.student.dtu.dk/~s973715/dpc/>  
Supervisors: Ole Hassager, DTU  
Kristoffer Almdal, Risø  
Kell Mortensen, Risø

### Ph.D. Study

Started: February 2004  
To be completed: January 2007

## Rheology, Structural Studies, and Synthesis

### Abstract

The elongational flow dynamics of polymer melts reveals much about the structural information of the individual behavior chains in the melt. Current well established constitutive models for polymer flows are in good agreement with shear flow experiments, but recent experiments on linear and branched polymers [1-2], performed at DTU, cannot be explained by any of the available models. An essential part of the project is to measure the elongational rheology of polymers with well-known molecular structure and set up corrections to current models to get better agreement between theory and experiments.

### Background: Measuring Extensional Viscosity for Polymer Melts

In many polymer-processing operations the polymer molecules experience a significant amount of orientation and chain stretching. These effects can sometimes be of benefit to the product, for example in a polymer fiber, when alignment of the molecules in the axial direction gives favorable characteristics for the finished product. On the other hand, the effect sometimes gives undesirable effects for the product, for example thermal form instability that may result in warpage of the product. Chain stretching and orientation also has a significant effect on the processing of the final product. Processing is often limited by sample breaks that are induced by the rheology of the polymer. Thus, knowledge of the chain orientation and stretch is of interest for not only scientists who are interested in polymer dynamics, but also for product engineers.

The conventional way of measuring the rheology of a given material is by using a shear rheometer. This method is good at inducing chain orientation in the sample, and a large amount of data in this area has insured very reliable models of chain orientation and its effect on rheology. However, because of the rotational nature of the shear flow, the chains are given a chance to relax before a significant amount of chain stretching is observed. Hence, shear rheology is not usable for probing chain stretch. The consequence of this lack of data is poor modes available for estimating the effects of chain stretching on the rheology and as a result, poor

model predictions of processes at high deformation rates.

Still, there have been attempts on creating measuring apparatuses for generating the necessary flow for chain stretching. The most common instrument is the Meissner rheometer where ideal extensional flow is achieved by stretching a sample between four conveyer belts and estimating rheological relevant properties by relevant forces and deformation rates. The problem with this approach is however, that only the overall deformation rate can be set. As the stretching of the filament becomes unstable very fast, local instabilities cannot be controlled and filament breakup usually occurs before the chains become fully extended. This problem is even more severe as the instabilities evolve very fast when the chains become extended. Another technique used for the measurement is the "Filament Stretching Rheometer" (FSR). In this approach, the sample is simply placed between two parallel discs, the discs are separated at a given rate, and the forces are measured on one of the discs.

As the flow in the beginning of the experiment defines where the instability takes place, the diameter of the filament at this place is measured during the entire experiment, using a laser micrometer, ensuring an exact measure of the deformation at all times. In addition, regulating the separation of the two discs can control this deformation. Until today, the FSR has only been used at room temperature. The reason is that high temperature gradients in the setup, measurement of the

deformation is difficult in an oven and the polymer melts does not stick very well to the end plates.

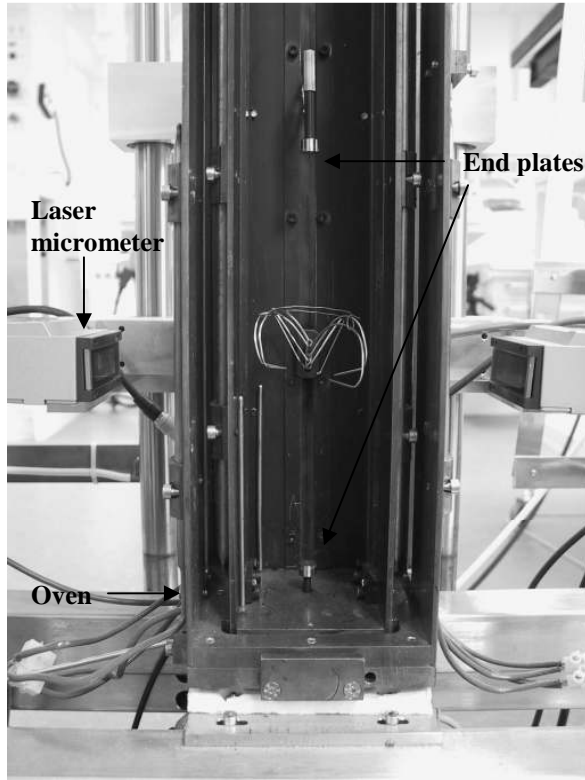


**Figure 1:** Close up of the Filament Stretching Rheometer

At the Danish Polymer Center Ph.d. Anders Bach constructed a filament stretching rheometer, in 2000-2003, which is capable of measuring extensional viscosity at high temperatures. Using several temperature controls solves the problem regarding temperature gradients. To further reduce temperature gradients inside the oven, the oven is build in copper, which is a good heat conductor, and all copper surfaces facing inside the oven are painted black to increase the radiant heat emission.

Another major problem in doing filament-stretching experiments is getting the filament to stick to the end plates. By choosing polymers melts, and take care in applying the end plates, we have overcome this limitation. However, we note that some polymer systems might not be measurable in the filament stretching rheometer without either gluing the sample to the end plates or use of some kind of mechanical grips.

#### “Master curve” approach

Another problem in doing experiments on polymer melts is controlling the deformation rate. To obtain usable data, the rate must be constant during the entire transient experiment.

We started using a “master curve” approach proposed by Orr and Sridhar (1999) [3], which relate the distance between the end plates and the radius of the filament.

We consider an axisymetrical filament between two parallel plates separated with distance  $L(t)$ . The filament has a plane of symmetry parallel to the two end plates and the radius of the filament is here  $R(t)$ . The desired mid radius, or set point of the system  $R_{ideal}(t)$  is given by:

$$R_{ideal}(t) = R_0 \exp\left(-\frac{\dot{\epsilon}t}{2}\right) \quad (1)$$

Where  $R_0$  is the initial mid radius. The radius in the middle of the filament defines Hencky strain  $\epsilon(t)$  at a given time in the experiment

$$\epsilon(t) = -2 \ln\left(\frac{R(t)}{R_0}\right) \quad (2)$$

We see that in an ideal experiment  $\epsilon = \dot{\epsilon}t$ . If the filament deforms as an ideal cylinder the extensional flow would demand the separation length between the end plates to be:

$$L(t) = L_0 \exp(\dot{\epsilon}t) \quad (3)$$

$L_0$  is the separation between the endplates a  $t=0$ . To relate the connection between  $L$  and  $R$ , we define a function  $f$  such that

$$E = \ln\left(\frac{L(t)}{L_0}\right) = f\left(-2 \ln\frac{R(t)}{R_0}\right) \quad (4)$$

The function  $f$  is a  $n$ 'th order polynomial and is called the “Master curve”.  $E$  is a measure of the end separation.

In the Master curve-approach, successive stretching experiments are performed with different polynomial functions for  $f$ . After each experiment,  $\ln(L(t)/L_0)$  is plotted against  $-2\ln(R(t)/R_0)$  and a 10'th order polynomial is fitted to this. The plate separation in the next experiment is then performed according to the newly found function of  $f$ .

Using this approach the development in radius converges towards the desired profile, as defined in equation (1), and four experiments is usually required before a satisfactory development is obtained. In figure 2, we show how the radius converges towards the desired exponential decay.

#### Control approach

When working with stretching of melts one experiment usually takes 2-3 hours including temperature

stabilization and sample preparation, so we have devolved a new technique to relate the plate separation with the diameter of the melt.

We approach the problem of plate separation as a closed loop-control problem, where the endplates must be adjusted during the experiment to ensure that the radius at the middle of the filament decreases in an exponential way, as defined in equation (2).

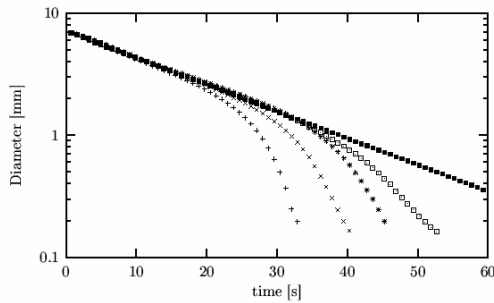


**Figure 2:** Measured radius as function of time in experiments with desired rate of  $0.1 \text{ s}^{-1}$ . Data (+), (x), (\*) and (□) show convergence in the “master curve approach”. (■) is obtained using the controller.

The controller was compared to the “master curve”-approach by performing stretching experiments on a duo disperse polystyrene melt.

The “master curve” approach was tested first, and the results are plotted in figure 2. The plot clearly shows poor convergence in the measured radius, and after 4 iterations, the radius only has an acceptable exponential decay until  $\epsilon=3.5$ . In the plot we also show an experiment performed using the controller, which here includes proportional and integral terms, PI. This time the radius is exponentially decaying throughout the experiment and no further experiments are required. We further observe that the difference between desired and achieved radius is never more than  $\pm 1\%$ .

Measurements done on the rheometer have been compared with measurements done on a Meissner type rheometer (Rhematics polymer Melt Elongational rheometer RME [4]). In figure 3 we plot experiments done on a low-density polyethylene; experiments are performed at strain rates  $1 \text{ s}^{-1}$  and  $0.01 \text{ s}^{-1}$ . The plot has been non-dimensionalized by plotting the transient Trouton ratio as function of Hencky strain. The Trouton ratio is the transient extensional viscosity normalized

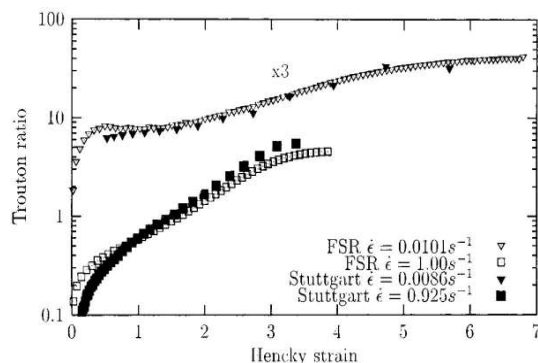


**Figure 3:** Comparison between DTU-FSR and Stuttgart measurements. Non-dimensional viscosity, Trouton ratio, vs. strain for LDPE.

with the zero shear viscosity and

## Results

The control mechanism in filament stretching, combined with the design of the oven has made it possible to measure up to very high extensions. In other extensional rheometers without the control mechanism the melt usually ruptures at strains above 3, especially if the melts is not very strain hardening. Monodisperse polystyrene is an example of such a polymer, and this is why Anders Bach was the first to measure the extensional viscosity to such a high extension that the stress became constant. This steady state was known to exist for polymer solutions, but was until 2003 considered to be experimentally out of reach for melts.

Later, during my phd-study, the steady state viscosity was determined for a commercial polydisperse low density polyethylene, LDPE, which is a branched polymer. But the startup behavior of the linear PS and the branched LDPE was significantly different. Figure 4 shows the startup viscosity for the linear PS-melt, and figure 5 the startup stress for the LDPE, where

$$\sigma_{zz} - \sigma_{rr} = \eta^+ \dot{\epsilon}$$

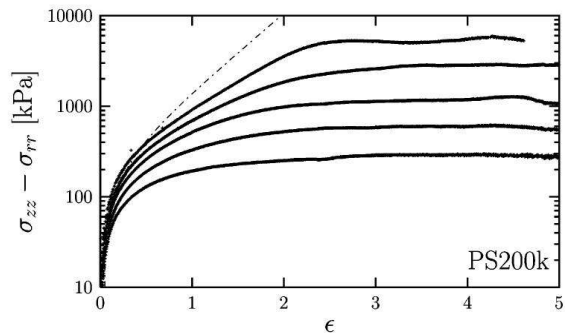


**Figure 4:** Startup stress of a monodisperse PS200K melt for four different elongational rates

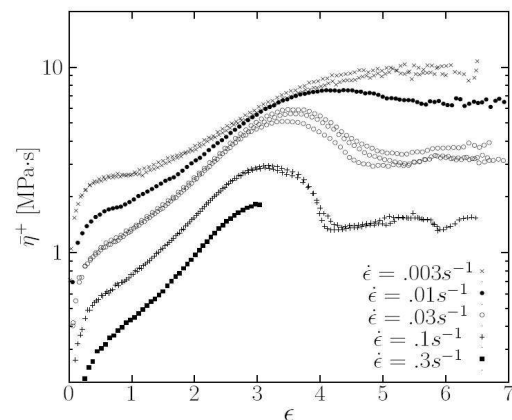


**Figure 5:** Startup viscosity of a polydisperse LDPE melt for five different elongational rates

We see that the startup viscosity for the monodisperse PS increases homogenously vs. Hencky strain and finally reaches a steady state. The startup viscosity for the LDPE however increases with Hencky strain, and

for high elongational rates, goes through a maximum and finally reaches steady state. We believe that this qualitatively different behavior is due to the fact that the side chains of the branched LDPE collapse into a tube along the axis of the backbone, as shown in figure 6.

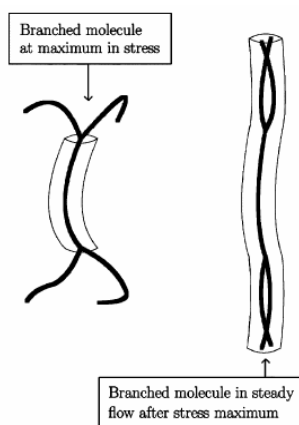


**Figure 6:** Interpretation of reduction in stress in terms of Pom-Pom picture. At the maximum in stress, the arms contribute to the tension in the backbone. At steady state, the molecule becomes effectively a linear polymer without arms

## Nonlinear Branch-Point Dynamics of Multiarm Polystyrene

### Introduction <sup>[6]</sup>

The specific structure of commercial LDPE is not known and the polymer is not suited for model working, because of its polydispersity and structural uncertainty. Well-defined branched polymer melts have proven valuable as model materials useful to gain insight into the complex physics of long chain branched (LCB) polymer melts. In one model architecture, often denoted pom-pom polymer, two branch points are connected by a polymer backbone denoted by the cross-bar. A number of arms emanate from the branch points. We refer to the pom-pom as  $A_n-C-C-A_n$  and to the asymmetric star as  $A_n-C$ . Note that all blocks in the polymers consist of homopolymers. Figure 7 shows a schematic drawing of a pom-pom polystyrene molecule with three arms.

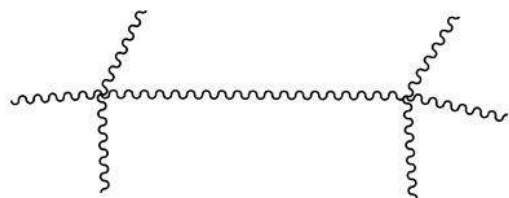


**Figure 7.** Schematic drawing of a pom-pom molecule with three branches linked to the cross-bar. The chemical formula for the polymer is  $(St_m)_n-(St_k)-(St_k)-(St_m)_n$  where St is styrene, n is the number of arms, m is the number of monomers in the arms, and k is half the number of monomers in the cross-bar. We simplify the nomenclature so that the arm is  $A=St_m$  and cross-bar is  $C=St_k$ . The pom-pom is referred to as  $A_n-C-C-A_n$  and the asymmetric star as  $A_n-C$ .

Knauss and Huang [5] developed a method for preparation of  $A_n-C-C-A_n$  polystyrenes by anionic polymerization. The number of arms is not a fixed value but rather a distribution with an average value given by the stoichiometry. To be able to compare with H-polymer theory, we have synthesized an  $A_n-C-C-A_n$  with about two entanglements in each arm. With this length of the arms the final step in the pom-pom synthesis, the reaction between two asymmetric stars appeared to be a difficult task. However, we used an alternative coupler 2,2-dimethyl-1,3-ditosylenepropene (DMDSP), that did enable a high yield of the desired  $A_n-C-C-A_n$  pom-pom polystyrene. Important for the success of the pom-pom synthesis was also the determination of the rate constant for the anionic polymerization in the presence of THF, whereby the optimal time for addition of the coupler could be computed. In the elongational flow rheology we use a filament stretching rheometer modified with a thermostat for polymer melts. While elongational rheometers normally require large quantities of the polymer, this instrument operates with samples of about 0.1-0.2 g for a single measurement.

### Experimental Section

**Materials.** Styrene (from Aldrich with purity larger than 99%) was first filtered through a column of aluminum oxide (Aldrich) to remove stabilizer and water. The styrene was vacuumdistilled twice from dibutylmagnesium immediately before use. Living styryl anion was generated in the solvent, cyclohexane (Fisher Scientific, HPLC grade with purity larger than 99.8%), by adding styrene and *sec*-butyllithium (Aldrich, 1.6 M in hexane). Following reflux under argon the cyclohexane was distilled into the reactor. Tetrahydrofuran (THF) (purity larger than 99.5%) from Fisher Scientific was purified by passage through aluminum oxide before it was refluxed under argon in the presence of sodium (Aldrich, 30-35 wt % dispersion in paraffin). 4-(Chlorodimethylsilyl) styrene (CDMSS) was synthesized as reported in ref [5] from *p*-chlorostyrene (Aldrich, purity larger than 97%) and dichlorodimethylsilane (Aldrich) in a Grignard reaction and purified by vacuum distillation prior to use.

**Coupling and Kinetics Experiments.** Linear styryl anions were polymerized in a solvent consisting of 97 wt % cyclohexane and 3 wt % THF to a length of about 50 kg/mol at 8 °C. The stoichiometric amount of the bifunctional coupler, dichlorodimethylsilane, was then titrated into the reaction mixture over approximately 60 min, at which point the mixture changed color from yellow to colorless, indicating that all anions had reacted. A similar experiment was performed with an alternative bifunctional coupler, DMDSP. The coupling reaction is shown in Figure 8. The coupling reaction with DMDSP was considerably slower than using dichlorodimethylsilane, and the change in color from yellow to colorless took about 24 h. To compare the two coupling agents both polymers were analyzed by size exclusion chromatography (SEC), as shown in Figure 9.

We observed that the styryl anions in the 97% cyclohexane/3% THF solvent even at reduced temperature were less stable than in a 100% cyclohexane solution at room temperature and in fact deactivate after about 3 h, leaving almost no chemically active “asymmetric star” molecules. To estimate the optimal time and temperature for introduction of the DMDSP coupler further, two model experiments were conducted. Anionic polymerization of linear polystyrene was performed in a Argon atmosphere in a solvent with a 97% cyclohexane/3% THF. In the two experiments we initiated styrene with *sec*-butyllithium at 3 and 8 °C, respectively. During the polymerization a series of exactly 1.00 mL samples were transferred from the reaction mixture to vials containing a toluene/methanol mixture, where methanol acts as a terminating agent for the polymerization. The conversion was determined by measuring the polymer mass concentration (proportional to the integrated differential refractive index (DRI) signal) in these samples. The amounts of chemicals used in the two experiments along with the temperatures used are listed in Table 1.

	temp (°C)	[BuLi] (mol/L)	vol of styrene (mL)	vol of cyclo- hexane (mL)	vol of THF (mL)
expt 1	3	$0.92 \times 10^{-3}$	11.21	201.40	6.20
expt 2	8	$1.76 \times 10^{-3}$	27.97	251.00	7.20

Table 1: Experimental Conditions for Determination of Rate Constants for Anionic Polymerization

### Synthesis of the Asymmetric Star

All polymerizations were performed in a round-bottom flask with five necks, thermostated in a water bath. The anionic polymerizations were done in an argon atmosphere under a slight overpressure of 0.2 bar. The first step was to synthesize the linear polystyrene for the arms of the stars. Styrene was dissolved, 5-10 wt %, in cyclohexane, and a stoichiometric amount of *sec*-butyllithium was added using a gastight syringe. This mixture was left overnight at room temperature under stirring. In the second step, the temperature was lowered to 8 °C, and purified THF was added by cannula to reach 3 wt % THF. The stoichiometric amount of CDMSS was then added using a gastight syringe, all at once, and the coupling reaction was left for 1-2 h. In the third step more styrene monomer was added to make the long arm in the asymmetric star. To terminate the living anion in the “asymmetric star” formation, degassed methanol was added after a reaction time of about 100 min. This reaction time is estimated from an independent kinetics investigation. The dissolved polymer solutions was then precipitated in 2-propanol and washed with HPLC-grade methanol before being filtered. The reaction mixture was fractionated to remove low molecular weight byproducts. We used toluene/methanol as solvent/nonsolvent pair for fractional precipitation of the highest molar mass polystyrene component.

### Synthesis of the Pom-Pom

The synthesis of the pom-pom followed the same protocol as for the asymmetric star, except instead of terminating with methanol a fourth step was added after the 100 min. In this step, two-thirds of the stoichiometric amount of DMDSP was added and the reaction was left overnight. Then more bifunctional coupler was added slowly until the yellow color from the styryl anion disappeared. The expected coupling scheme is shown in Figure 8.

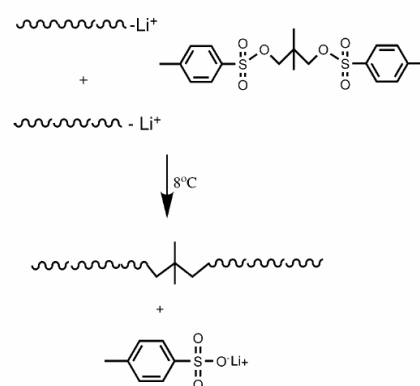


Figure 8: Bifunctional coupling using 2,2-dimethyl-1,3-ditosylenepropane (DMDSP)

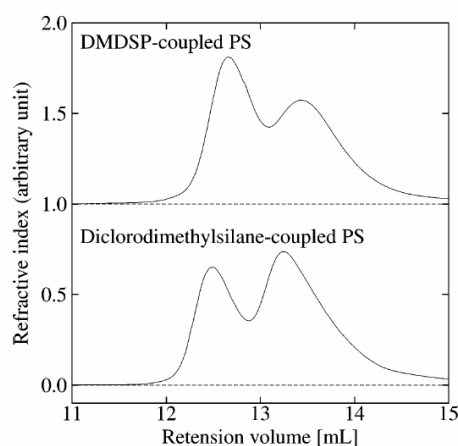
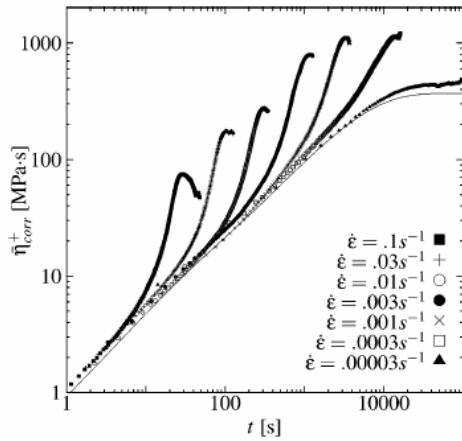


Figure 9: Comparison of SEC output for model linear polystyrene obtained from coupling styryl anions with DMDSP and dichlorodimethylsilane, respectively.

## Results

### Elongational results.

Figures 10 and 11 show the measured corrected transient elongational viscosity  $\eta^+(t)$  for the pom-pom and asymmetric star molecule along with predictions from LVE at 130°C. The elongational viscosity measurements rates were performed at 130°C, except for the two lowest elongational rates for the pom-pom molecule. They were measured at 150 °C, and then subsequent time-temperature superposition shifted to 130 °C. In both plots there is agreement between measurements and LVE predictions up to a certain level



**Figure 10.** Transient elongation viscosities  $\eta^+$  of the pom-pom melt at 130 °C, as a function of the time,  $t$ . The line is the linear viscoelastic prediction of the transient elongational viscosity.  $\eta^+$  was measured at seven different elongational rates (shifted to 130 °C) of 0.1, 0.03, 0.01, 0.003, 0.001, 0.0003, and 0.00003  $s^{-1}$

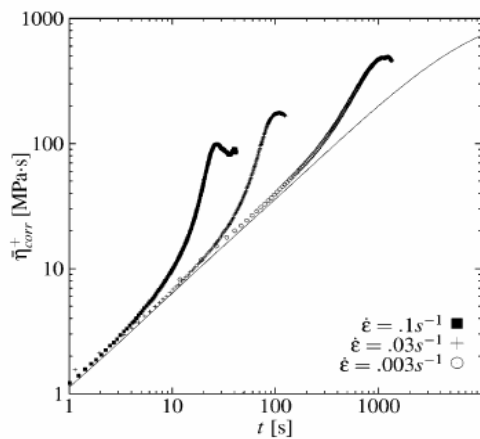


**Figure 11.** Transient elongation viscosities  $\eta^+$  of the “asymmetric star” melt at 130 °C, as a function of the time,  $t$ . The line is the linear viscoelastic prediction of the transient elongational viscosity.  $\eta^+$  was measured at three different elongational of 0.1, 0.03, and 0.003  $s^{-1}$ .

of strain. It is seen that the transient elongational viscosity rises above LVE at intermediate strains. Note that the transient elongational viscosity for the pom-pom melt exhibits a maximum as a function of time for the elongational rate of 0.1  $s^{-1}$ . Such a maximum has been observed previously in branched polymer melts (low-density polyethylene) but to our knowledge not in a well-characterized material. Generally all data points in Figures 10 and 11 have been reproduced within a 15% scattering.

1. Bach, A.; Almdal, K.; Rasmussen, H. K.; Hassager, O. *Macromolecules* (2003), **36**, 5174.
2. Rasmussen, H. R.; Nielsen, J. K., et. al. Viscosity overshoot in the start-up of uni-axial elongation of LDPE melts. *J. Rheology*, (2005), **49**, 369-381
3. Orr, N. V., and T. Sridhar, *J. Non-Newtonian Fluid Mech.* (1999), **82**, 203–232
4. Bastian, H., “Non-linear viscoelasticity of linear and long-chain-branched polymer melts in shear and extensional flows,” Ph.D. thesis, Institut für Kunststofftechnologie der Universität Stuttgart, (2001)
5. Knauss and Huang. *Macromolecules* (2002), **35**, 2055-2062
6. Nielsen, J. K., Rasmussen H., Denberg M, Almdal K. and Hassager, O., “Nonlinear Branch-Point Dynamics of Multiarm Polystyrene”, *Macromolecules*, in press, 2006.



## Rudi Pankratz Nielsen

Phone: +45 2210 2522  
Fax: +45 3645 2516  
E-mail: [rpn@scf-technologies.com](mailto:rpn@scf-technologies.com)  
WWW: <http://www.scf-technologies.com>  
Supervisors: Kaj Thomsen & Nicolas von Solms  
Erik G. Søgaaard, Aalborg University  
Tommy Larsen, SCF Technologies A/S

### Industrial Ph.D. Study

Started: May 2006  
To be completed: April 2009

## Analysis of the Physical Chemistry of the CatLiq™ Process

### Abstract

With increased focus on CO<sub>2</sub> emissions from fossil fuels the interest in biofuels has increased in the last decade. The CatLiq™ process is a method for catalytic conversion of biomass to biofuel such as biodiesel. It is intended to optimize the process to achieve a standard conforming bio-crude oil product, but also modeling of the process is a main focus. To model the process both thermodynamics as well as experimental work is required to achieve a thorough understanding of the process and effect of parameters.

### Introduction

In recent years the focus on biofuels, fuel made from renewable sources of organic material, such as biomass, have increased significantly. A testimony to this is the number of publications made regarding biodiesel for which annual number of publications has increased by a factor 20 from 1993 to 2003 [1]. According to Koonin [2] 2 % of the fuel used for transport today is produced from biomass, while the remaining 98 % are still fossil fuels. The CO<sub>2</sub> emissions from conventional energy sources have been increasing steadily for years as shown in figure 1.

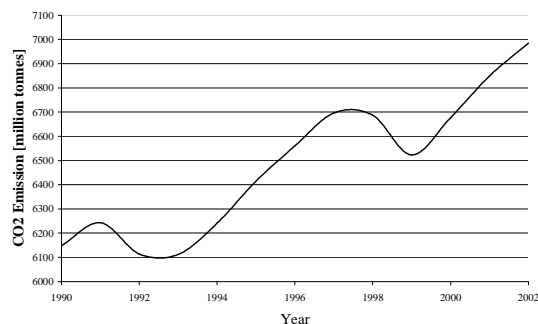


**Fig. 1.** Global emission of CO<sub>2</sub> from 1990 to 2002 (data from [3]).

The total emission in 2002 was 6984 million tonnes, which is an increase of 14 % over a 10 year period from 1992 to 2002 [3]. It must of course be taken into

account that these figures are overall emissions and thus not restricted to emissions from transport fuels.

The most notable methods for biomass conversion are hydrothermal upgrading, supercritical water gasification and transesterification [1][4]. Another method for biomass conversion is the CatLiq™ technology, which is a catalytic conversion of biomass in water at near-critical conditions.

The CatLiq™ technology is a technology for catalytic conversion of aqueous biomass to transport fuels. The process runs at near-critical conditions in water with heterogeneous and homogeneous catalysts. The general principle of the process is illustrated in figure 2.

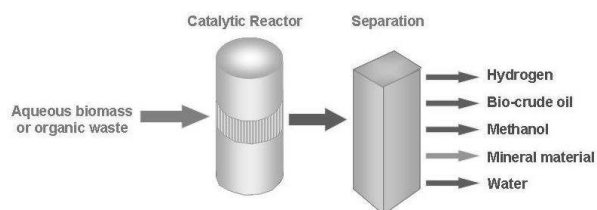


**Fig. 2.** Principle of the CatLiq™ process.

Several catalysts, both heterogeneous and homogeneous, are present in the reactor to ensure proper conversion. Zirconium oxide is currently being used as the heterogeneous catalyst while the homogeneous catalysts are primarily potassium carbonate and trace metals in the feedstock.

The feedstock for this process is intended to be almost any biomass that can be pumped, but the CatLiq™ process is particularly well suited for difficult-

to-treat wet feedstock like sewage sludge, liquid manure or fermentation residues.

Products from the process include a gas phase consisting of hydrogen and methane, a bio-crude oil product and water soluble fuel components such as methanol and ethanol.

### **Specific Objectives, Results and Discussion**

In the study of the CatLiq™ process several aspects will be investigated. These are primarily thermodynamics, experimental investigation of the process and characterization of the oil product.

The process must be adequately understood with regards to thermodynamics. This will allow better description of the process and will particularly be useful in the separation step. This work will deal with equations of state and determining which would be suitable for describing the environment inside the reactor at operating conditions. As there is no given composition of the feedstock used for the CatLiq™ process such equation of state will have to be modified to some degree to accommodate the complex composition of the feedstock. To separate the end products it is necessary to be able to describe phase behaviour of the mixture that the end product consists of. As this mixture will contain a multitude of different components, a number of components must be selected as key components for the thermodynamic modelling of the system to simplify the system. IVC-SEP at DTU will play a major role in this part of the study, due to their extended expertise with thermodynamics.

A major part of the work will be experimental investigations conducted at Aalborg University Esbjerg. For this a laboratory scale system is being built that will allow several modes of operation such as batch and flow type processes. The system will be operating in the range 300-360°C and 225-275 bar i.e. near-critical conditions for water. The principle of the system will be two reactors in series with one functioning as a holding tank while heating the biomass and the other being the catalytic reactor for the conversion process. Due to the demands pumping at operating temperature puts on the pump the biomass will be at room temperature while being pumped and subsequently heated to process temperature. To facilitate sampling and in case of recirculation in the system a heat exchanger will be incorporated to lower the temperature after the catalytic reactor. The design phase of the equipment is done in close relation with SCF-Technologies due to their experience with plant design. By means of statistical methods the effect of key variables, such as pressure, temperature, composition of feedstock and residence time in the reactor, on the end product will be investigated. The statistical models will be based on tests with various compositions of the feedstock and will thereby allow for determining the relationships between the previously mentioned factors. As the normal feedstock for the CatLiq™ process contains a vast amount of different components and in varying concentrations i.e. the feedstock composition is not

necessarily the same for each batch, it is of interest to identify key components. These can be salt compounds, cellulose and other compounds which, based on experiments, can be defined as key components e.g. fats and/or licnine.

The primary end product, i.e. the bio-crude oil, which is a mixture containing oil compounds, must be optimized and characterized. This is needed since oil product must conform to the criteria given for bio-fuels and bio-crude oils to allow for sale of it. These criteria must be set for an acceptable end product before optimization of the process can commence. The criteria for the oil are to be determined from European Standards which gives the accepted values of for instance iodine, methanol and sulfur content as well as carbon residue and cetan and acid values. Without such criteria and methods for characterizing the oil and comparing results to the criteria the process can only be optimized with regards to the economy of the process conditions which is also needed but a fully optimized process must also be optimized with regards to the quality of the end product.

### **Conclusions**

The CatLiq™ process will be investigated to optimize the fuel products and allow better control of the process with regards to which products are being formed.

### **Acknowledgements**

The author would like to acknowledge the Danish Ministry of Science, Technology and Innovation for funding this industrial Ph.D. project.

### **References**

1. M. Mittelbach, C. Remschmidt, Biodiesel - The Comprehensive Handbook. Martin Mittelbach, Graz, Austria, 2003, p. 4.
2. S.E. Koonin, Getting Serious About Biofuels. Science (311) (2006) 435.
3. G. Marland et. al., Global, Regional, and National CO<sub>2</sub> Emissions, Trends: A Compendium of Data on Global Change. Carbon Dioxide Information Analysis Center, Oak Ridge National Laboratory, U.S. Department of Energy, Oak Ridge, Tenn., U.S.A., 2006
4. E.v. Thujil et. al., An overview of biofuel technologies, markets and policies in Europe, ECN report ECN-C-03-008, 2003.



### **Ben Niu**

Phone: +45 4525 2895  
Fax: +45 4525 2258  
E-mail: beni@kt.dtu.dk  
WWW: <http://www.ivc-sep.kt.dtu.dk>  
Supervisors: Alexander Shapiro  
Erling H. Stenby

### **Ph.D. Study**

Started: September 2006  
To be completed: September 2009

## **Carbon Dioxide Injection in the Carbonate Reservoir**

### **Abstract**

Carbon dioxide injection is a widely used EOR (Enhanced Oil Recovery) method. During the injection of carbon dioxide into reservoir at the MMP (Minimum Miscible Pressure), it will become miscible with original oil. The compositional simulation including the reaction between carbon dioxide and carbonate matrix will also be investigated. The asphaltene precipitation induced by the carbon dioxide injection will serve as another potential direction.

### **Introduction**

Today's largest global challenges are climate changes and security of energy supply. With its efficient power plants located near the coast and the North Sea Denmark has a unique position to enable the development of methods to combine the utilization of CO<sub>2</sub> with enhanced oil recovery (EOR). This project is a part of the main project, "Enhanced Oil Recovery through CO<sub>2</sub> utilization" which is to ensure the build-up of knowledge within EOR in Denmark.

During laboratory and field studies, several problems become significantly important. The determination of MMP has direct relationship with the efficiency and success of EOR project. And asphaltene precipitation, as it happens in most gas injection program, will cause huge damage to the reservoir formation and economic loss to the oil company. The reaction between carbon dioxide and carbonate matrix will change the porosity and permeability of rock matrix, and further influence the injectivity, and finally limit the longevity of the whole project.

The aim of this project is to investigate problems induced by carbon dioxide injection. The current research is focused on literature search of relevant topics.

### **Process description**

The injection of CO<sub>2</sub> into a petroleum reservoir will result in either a miscible or immiscible displacement. If under the prevailing reservoir temperature and pressure, the injected gas is miscible with the reservoir fluid in all

proportions, this type of displacement is called first – contact miscible (FCM)<sup>1</sup>. If the injected gas is enriched enough to be completely miscible with reservoir fluid at the front, this kind of displacement is referred as multicontact miscible flood (MCM)<sup>1</sup>. The last type of displacement is in which phases at the gas-oil front can not be miscible. Because the first two kinds of displacement finally achieve similar high recovery efficiency, the MMP has become an important optimization parameter in CO<sub>2</sub> injection.

### **MMP**

The concept of MMP is defined for two-phase gas injection. The mechanism for the two-phase case, although complex, is well-studied and satisfactorily described. However, fluid systems in real reservoirs are generally more than two phase. Water is almost ubiquitous in reservoirs. Although it is often taken as an inert phase which does not interact with oil and gas compositionally, the assumption does not hold for CO<sub>2</sub> due to its relatively high solubility. Even the solubility can be neglected, how the water flow will influence MMP or how we interpret the meaning of two-phase MMP for three-phase system is still unclear. A more complicating factor is that CO<sub>2</sub> injection can form more than two liquid hydrocarbon phases even not counting possible asphaltene precipitation. MMP for multi-phase systems is therefore a challenge for CO<sub>2</sub> injection.

### **Reaction between CO<sub>2</sub> and reservoir rock**

For a carbonate system the kinetically controlled reactions is<sup>3</sup>:



The reaction can change the porosity and permeability at the same time. The change is complex due to its dependence on rock type and the injection scheme. Both increase and decrease in injectivity can be caused after the first slug of CO<sub>2</sub> in WAG<sup>4</sup>.

### **Asphaltene precipitation**

Gas injection into reservoir oil can induce asphaltene precipitation even for oil with low asphaltene concentration, which results in formation damage and huge economic loss. The mechanism of asphaltene precipitation is not well understood. There is no predictive model and even experimental data are often subject to large uncertainties. However, the problem must be addressed in CO<sub>2</sub> injection to avoid potential production problems.

### **Future Work**

Future research will be focused on MMP and chemical reaction in carbonate reservoir. Numerical simulation will be performed to give a preliminary analysis. Based on analysis, more detailed plan for modeling and experimental work will be made. The influence of asphaltene precipitation on gas injection will also be studied. The emphasis will be on whether there will be significant influence. Other potential problems regarding phase equilibrium and multiphase flow during CO<sub>2</sub> injection will also be investigated.

### **References**

1. S. Haynes Jr. and R.B. Alston, SPE/DOE 20190 presented at SPE/DOE Seventh Symposium on Enhanced Oil Recovery, Tulsa, Oklahoma, 1990
2. J. Bon, H.K. Sarma and A.M. Theophilos, SPE 97536 presented at the SPE international Improved Oil Recovery Conference in Asia Pacific, Kuala Lumpur, Malaysia, 2005
3. O. Izgec, B. Demiral, H. Bertin and S. Akin, SPE 100809 presented at the SPE Annual Technical Conference and Exhibition, San Antonio, Texas, USA, 2006
4. R.K. Svec and R.B. Grigg, SPE 71496 presented at the SPE Annual Technical Conference and Exhibition, New Orleans, Louisiana, USA, 2001
5. R.K. Srivastava, S.S. Huang and Mingzhe Dong, SPE 37468 presented at the SPE Production Operations Symposium, Oklahoma City, Oklahoma, USA, 1997



### Stefan Møller Olsen

Phone: +45 4525 2842  
Fax: +45 4525 2258  
E-mail: sto@kt.dtu.dk  
WWW: <http://www.kt.dtu.dk>  
Supervisors: Søren Kiil  
Kim Dam-Johansen  
Lars Thorslund Pedersen, Hempel A/S  
Merete Hoegh Laursen, Hempel A/S

Industrial Ph.D. Study  
Started: November 2005  
To be completed: October 2008

## Controlled Release of Environmentally Friendly Antifouling Agents from Marine Coatings

### Abstract

The lifetime of commonly applied antifouling agents in the marine environment is fairly long, which make them prone to bioaccumulation. It is therefore of interest to replace them with agents of shorter residence times. To achieve the effect of instable compounds on the surface of an antifouling coating, such compound must be produced in-situ. The production can come about by means of enzymatic conversion of substrate present in the coating, or in the marine environment in general. Alternately the enzymes themselves can be the compound intended for fouling inhibition. In this paper the concept of one enzymatic antifouling solution applying production of hydrogen peroxide is presented. The generation of a flux of hydrogen peroxide for preliminary testing of antifouling potency is described.

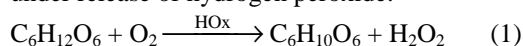
### Introduction

Biofouling on man-made structures pose a problem for a variety of industrial constructions. On ship hulls, increased fuel consumption, due to higher drag resistance is the major obstacle, but promotion of corrosion, and the potential of introducing foreign species to new habitats via the ship hulls are also of major concern. Fouling has been fought for thousands of years, and the means, with which antifouling has been undertaken, have been plentiful and diverse [1]. Recently environmental considerations forced paint manufacturers to discard the more toxic of the compounds utilized. Organotin has been eliminated, cuprous oxide being its primary substitute. Metallic biocides are prone to bioaccumulation, and are therefore of interest to replace by even more environmentally friendly solutions. In the near future, antifouling coatings based on controlled release of short-lived antifouling agents are likely to be introduced. The controlled release mechanisms can come about by means of enzymes. The purpose of this project is to develop a marine coating based on the controlled release of environmentally friendly antifouling agents.

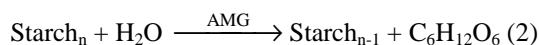
### Specific objectives

The major focus of this project will be on the production of the short-lived antifouling compound by means of enzymatic conversion of substrates added to the paint.

Hydrogen peroxide is intended as antifouling agent. It has a short life-time in seawater, and is therefore of little harm to non-target marine organisms. The production of hydrogen peroxide in a coating can be done by enzymes found in the marine environment [2]. Hexose oxidase (HOx) is known to oxidize hexose sugars (e.g. glucose) under release of hydrogen peroxide.



The very water soluble glucose is expected to leach from a coating rapidly following immersion of a ship. Therefore, glucose should also be produced in-situ. Glucose can be delivered by another enzyme system. Amyloglycosidase is known to cut of glucose-residues from the ends of starch molecules.



To achieve the goal of an efficient environmentally friendly antifouling coating, by the production of hydrogen peroxide, the following topics are to be investigated.

- Release rate of hydrogen peroxide necessary for potent antifouling.
- Modification of enzyme properties to provide miscibility and stability in paint.
- Optimization of paint formulation to achieve controlled polishing behavior of the antifouling coating.

- Mathematical modeling of the coating in service.

The feasibility of the concept is to a large degree dependent on the release-rate of hydrogen peroxide capable of efficient inhibition of fouling. Generally when the potency of antifouling agents is evaluated, the bulk concentration showing effect on the fouling organism is estimated [3]. Such number is difficult to translate into the needed amount of substrate in a coating. It is therefore of great importance to be able to generate and control a flux of hydrogen peroxide under conditions controllable in a laboratory and natural to fouling organisms. A system capable of generating a flux by diffusion has been designed.

## Results and Discussion

To test the ability of the system to continuously release hydrogen peroxide from a surface, the accumulation of hydrogen peroxide in the bulk solution was been measured. Figure 1 shows the concentration of hydrogen peroxide measured as a function of time under two different conditions.

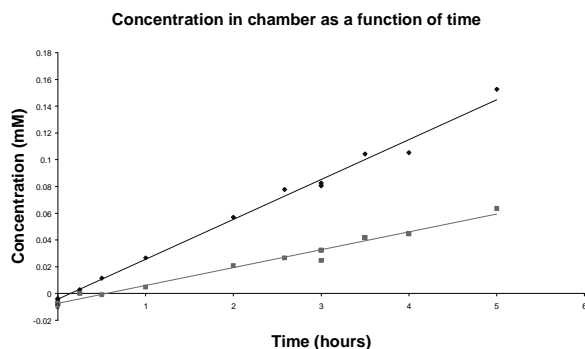


**Figure 1.** The accumulation of  $H_2O_2$  in flux set-up.

The slopes in figure 2 can be translated into fluxes. For the pink line, the flux generated is  $45 \mu\text{g}/(\text{cm}^2\text{d})$  and for the blue line, the slope translates into  $166 \mu\text{g}/(\text{cm}^2\text{d})$ . Release rates of interest is in the order of  $10 \mu\text{g}/(\text{cm}^2\text{d})$  evaluated on the maximal starch content of a film with the lowest acceptable operational time.

## Conclusion and future work

The set-up is capable of generating a stable flux, in the region of interest. The release-rate is easily manipulated. It is the goal within the near future to be able to evaluate the settling on the flux-generating surfaces, in a laboratory assay. This requires stable conditions for test animals as well as optimal settling conditions (temp, light, nutrients etc.).

## References

1. D. M. Yebra, S. Kiil, K. Dam-Johansen, Progress in Organic Coatings 50 (2003) 75-104
2. C. H. Poulsen, K. M. Kragh, United States Patent Application Publication, US2002/0106361A1
3. S. Ikuta, S. Ichikawa, Y. Wakao, K. Nishimura, T. Yasunaga, the American Society of Mechanical Engineers (1988).



**Anne Kathrine Kattenhøj Overgaard**

Phone: +45 4525 6817  
Fax: +45 4588 2161  
E-mail: ako@polymers.dk  
WWW: http://www.polymers.dk  
Supervisors: Søren Hvilsted  
Jakob Vange, Coloplast Research  
Hanne Everland, Coloplast Research

Ph.D. Study  
Started: September 2004  
To be completed: August 2007

## Coupling of Active Components to Synthetic Polymers

### Abstract

Materials for medical devices should provide more than just structure. Some synthetic polymers are ideal materials for tissue repair because of their high biocompatibility and the possibility of tailoring their properties. Active components can be coupled to the synthetic polymers to obtain materials that support cell ingrowth. This coupling could take place via the very mild and highly efficient 'click' coupling of azides and alkynes. Due to solubility incompatibilities of the two materials it might be necessary to employ a heterobifunctional linker.

### Introduction

Future materials for medical devices should be more than just materials that provide structure. The materials should be intelligent and take an active part in the process, e.g. by absorbing smell or by initiating cell growth.

In the case of tissue damage the normal biological healing process has been impaired and the application of a scaffold as a kind of artificial support is necessary to help the healing process. The principle of a scaffold-assisted healing process is demonstrated on a burn wound in Figure 1.

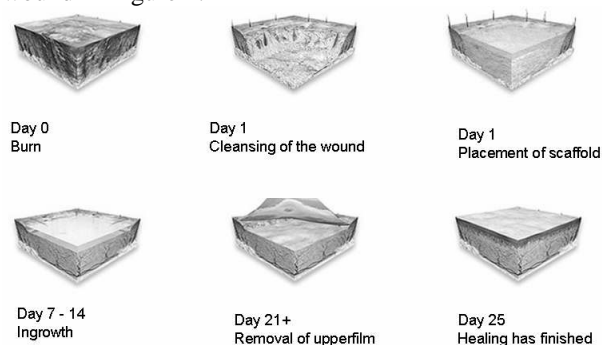


**Figure 1** Principle of the wound healing process when a scaffold is applied.

A burn wound has irrevocably destroyed the skin. On day 1 the damaged tissue is removed and a scaffold is placed in the wound. The scaffold is porous and with interconnectivity, so during the first three weeks ingrowth of cells should take place. After this the upperfilm can be removed. The healing process should be finished after approximately one month and over the

same period of time the scaffold material should be degraded and have disappeared so that only new skin remain.

For a material to be utilized in such a wound-healing scaffold it has to comply with certain requirements. The ideal material for tissue repair should be biocompatible, biodegradable and easy to process [1,2,3]. The material must mimic the extra cellular matrix (ECM), it has to uphold structure, i.e. maintain the mechanical properties to provide a suitable environment for the new tissue [4], it should promote cell adhesion and growth and degrade as new tissue forms.

The most important requirement for a tissue repair material is the biocompatibility. The material should possess the right surface chemistry to promote cell attachment; it should support cell ingrowth and at the same time it should not provoke any unwanted tissue response [5].

Several different materials may be used in a scaffold for tissue repair and among these natural as well as synthetic polymers should be considered.

The advantages of using natural compounds in a tissue repair scaffold are the excellent biocompatibility and the ability of the material to interact favorably with cells, the cell recognition [6]. However, the differing batch compositions and the poor mechanical performance of the natural polymers might provide a problem; if these materials should be employed as the only material in a scaffold for wound healing [7].

As an alternative to the natural polymers, the synthetic polymers have certain advantages: They can, in principle, be tailored to give a wider range of properties and a more uniform composition than natural

compounds. Furthermore, synthetic polymers are known for high processability, and porous materials with well-controlled microstructure can be made available. The key advantages include the ability to tailor mechanical properties and degradation kinetics to suit various applications. Most synthetic polymers are degraded via chemical hydrolysis and therefore insensitive to enzymatic processes, so that their degradation will not vary from patient to patient. Moreover, it should be possible to design synthetic polymers with chemical functional groups that can induce tissue ingrowth [8].

### Specific Objectives

The ideal material for a medical device would, however, presumably, consist of as well natural compounds as synthetic polymers. The material would exploit the excellent cell growth promoting properties of the natural compound in combination with the superior mechanical properties of the synthetic polymer.

The current project is mainly experimental. Focus is on obtaining an ideal material to be used in a wound healing scaffold or alternative medical devices. Mixes of natural compounds and synthetic polymers have previously been applied in medical scaffolds [9]. It is, however, believed that superior materials can be obtained if the compounds are chemically bonded to each other. The synthetic polymers will be able to uphold the structure of the scaffold as cell ingrowth and proliferation take place, and the natural compounds will promote these cell actions. By chemically bonding the materials the positive effects of both is ensured for a longer period of time.

The chemical bonding of the materials could be achieved through the well known 1,3-dipolar cycloaddition of an azide with an alkyne group to form a 1,4-triazole. This reaction has been known since the early 1960's where Huisgen and coworkers carried out a monumental work in this area.

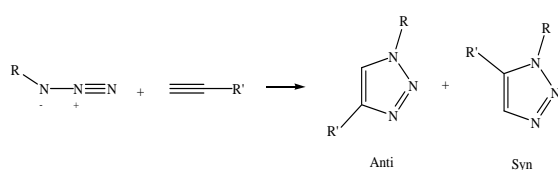


**Figure 2** The general Huisgen reaction – 1,3-dipolar cycloaddition resulting in two products [10].

The reaction to form a triazole by the conventional Huisgen 1,3-dipolar cycloaddition at elevated temperature gives rise to two different products: an anti- and a syn-triazole. The formation of two products can be prevented by running the same reaction in the presence of a Cu(I) catalyst at room temperature. This reaction can take place in organic solvent as well as in water; it gives rise to only one product: the anti product (1,4-triazole), and the reaction takes place with approximately 100 % conversion. Because of the very mild conditions, the high yield and the stereospecificity this reaction has been termed a 'click' reaction by K.B. Sharpless *et al.* [11]. The advantage of this reaction is the formation of a stable bond under mild reaction conditions. The mechanism for the 'click' reaction can be seen in Figure 3, which also explains why the reaction only takes place with terminal alkynes.

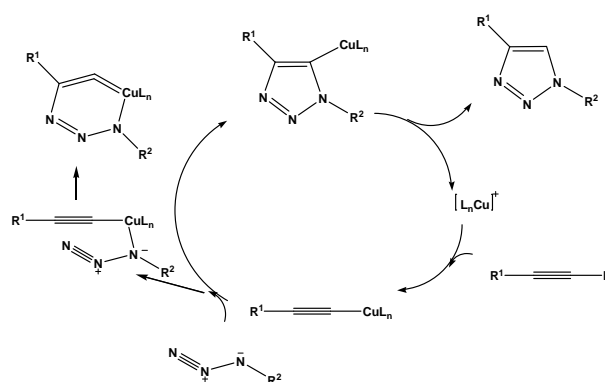


**Figure 3** Reaction mechanism for the click reaction. The Cu(I)-catalyst can only coordinate to a terminal alkyne [12].

The aim of the project is to obtain materials consisting of natural components coupled to synthetic polymers via the 1,4-triazole. This is obtained by functionalizing the natural compound and the synthetic polymer with either an alkyne or an azide and then couple the materials by the 'click' reaction.

### Results and Discussion

The natural components, which are to be used in this project, contain several hydroxy groups, which have similar chemical properties. So far it has been desirable, if not crucial, that the functionalization with either azide or alkyne only takes place at one specific position in the molecule. It has been very important to carry out stereoselective reactions, primarily due to characterization reasons. Reactions have been carried out on a model compound, N-Acetyl-D-Glucosamine, to find the optimal conditions to employ on the natural component.

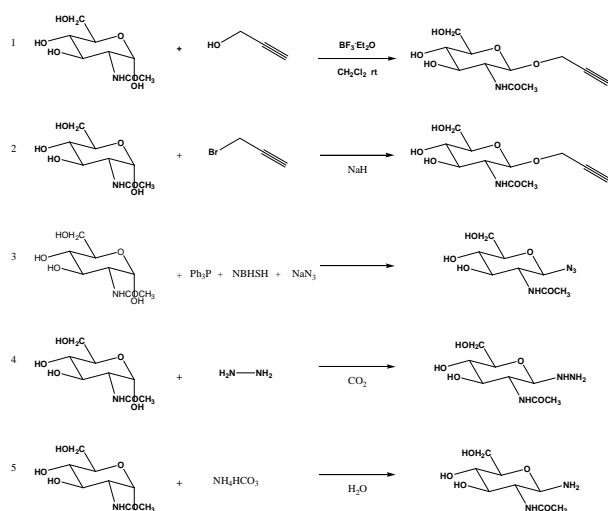


**Figure 4** Reactions carried out on the model compound N-Acetyl-D-Glucosamine.

The attempted reactions can be seen in Figure 4. Problems were experienced in most of the reactions due to the solubility of the model compound. As the natural component the model compound is only soluble in water and consequently the major part of the attempted reactions, which are typically taking place in organic solvents, have proved unsuccessful. Reaction number 5, the amination of the anomeric center of N-Acetyl-D-Glucosamine with ammonium bicarbonate, is taking place in water and has thus proved successful. The reaction product has been characterized by  $^1\text{H-NMR}$  and the resulting spectrum can be seen in Figure 6. Comparison of this spectrum with the  $^1\text{H-NMR}$  of N-Acetyl-D-glucosamine in Figure 5 clearly supports, that a reaction has taken place.

In Figure 5 the proton from the anomeric center is to be found at  $\delta$  5.10 ppm and the coupling constant is small ( $\sim 3$  Hz) indicating that the proton is equatorial. Furthermore there are no peaks, from the compound, in the spectrum between  $\delta$  4.00 ppm and 5.00 ppm. The peak at  $\sim\delta$  4.70 ppm is from the NMR solvent  $\text{D}_2\text{O}$ . In the spectrum of the reaction product (Figure 6) the proton from the anomeric center has moved to  $\delta$  4.05 ppm and the coupling constant is now  $\sim 8$  Hz indicating that the anomeric proton now is in the axial position. Furthermore the coupling pattern of the glucosidic protons in the area between  $\delta$  3 and 4 ppm has changed, confirming that a reaction has taken place on the anomeric center.

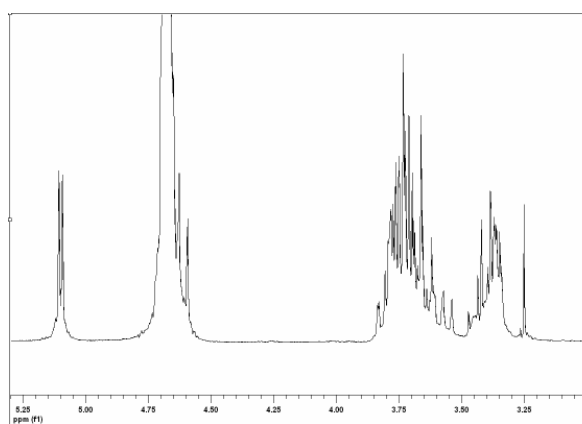


**Figure 5**  $^1\text{H-NMR}$  spectrum of the model compound N-Acetyl-D-Glucosamine.

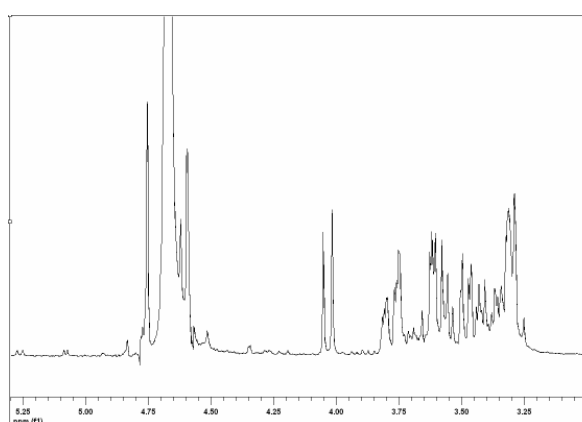


**Figure 6**  $^1\text{H-NMR}$  spectrum of N-Acetyl-D-Glucosamine after reaction with  $\text{NH}_4\text{CO}_3$ .

Although one manipulation on the anomeric center of a model compound has proved successful, focus has moved onto functionalizing along the chain of the natural polymer. Having the functional group present on several positions in the natural component will greatly enhance the possibility of coupling a synthetic polymer onto the material and thereby obtaining the desired compounds.

In addition polymerizations employing different initiators have been carried out to obtain synthetic polymers, which can be coupled to the natural component.

The coupling of the natural component to the synthetic polymer should take place via the 'click' reaction between an azide and a terminal alkyne. The product will be a 1,4-triazole with two substituents. It is not known whether it will have an effect on the material properties from which compound the azide and the alkyne stems. Therefore it is very important to keep every option open and functionalize as well the natural component as the synthetic polymer with either of the functionalities and subsequently investigate if the origin of the functional group has any influence on the properties of the final product.

Solubility issues might have an influence on the possibility of combining the two materials. The natural compound is only soluble in water, while the synthetic

polymer can only be dissolved in organic solvents. Different methods of combining the materials should therefore be employed. Possibilities of casting a film with the functional groups present on the surface and subsequent 'clicking' of the other material onto this could be a possibility. Alternatively a heterobifunctional linker material, which is soluble in both solvents, can be employed to improve the possibility of combining the compounds. This linker could be used as a macroinitiator in the synthesis of the synthetic polymer and subsequently 'clicked' onto the functionalized natural component. Work has been carried out on synthesizing such a linker material and perhaps it will be necessary to incorporate this.

Characterization of the synthesized materials will take place by Size Exclusion Chromatography (SEC), Nuclear Magnetic Resonance (NMR) techniques, Differential Scanning Calorimetry (DSC) and Infrared Spectroscopy (IR). Furthermore X-Ray Photoelectron Spectroscopy (XPS) could be employed to determine the surface composition of a casted film and Organic Elemental Analysis (OEA) might be an alternative characterization method, which is independent of the solubility properties of the synthesized materials.

### Conclusions

Stereoselective reactions on the anomeric center of the natural compound have so far been a crucial point in the project. It has been possible to manipulate only the anomeric center of a model compound, and experiences from reactions on the model compound could be carried on to manipulate the anomeric center of the natural component. To improve the possibility of 'clicking' the two materials together, focus has, however, moved onto functionalizing along the polymer chain. Polymerization reactions have been and will be carried out with different initiators. Furthermore work has been carried out on synthesizing a heterobifunctional linker material, which can be used to conquer problems that might arise in the combination of the two materials due to solubility differences.

In addition to this an investigation of the material property dependency of the alkyne and azide origin will be carried out. Characterization of the synthesized materials is an essential point in the project and different methods (SEC; NMR; DSC; IR and perhaps XPS and OEA) will be employed to verify that the reactions have taken place.

### Acknowledgements

The author greatly acknowledges Coloplast A/S, the Technical University of Denmark and The Danish Research Training Council for the financial support to this project, which is part of The Graduate School of Polymer Science.

### References

1. B.E. Chaignaud, R. Langer, J.P. Vacanti, in: A. Atala, D. Mooney, R. Langer, J.P. Vacanti, (Eds.),

- Synthetic Biodegradable Polymer Scaffolds, Birkhäuser, Boston, 1997, Chapter 1.
2. L.G. Cima, J.P. Vacanti, C. Vacanti, D. Ingber, D. Mooney, R. Langer, J. Biomech. Eng. 113 (1991), 143-151
3. C.M. Agrawal, R.B. Ray, J. Biomed. Mater. Res. 55 (2001) 141-150
4. M.A. Slivka, N.C. Leatherbury, K. Kieswetter, G.G. Niederauer, Tissue Engineering 7 (2001), 767-780
5. S. Yang, K.-F. Leong, Z. Du, C.-K. Chua, Tissue Engineering 7 (2001) 679-689
6. M.C. Peters, D.J. Mooney, Materials Science Forum 250 (1997) 15-42
7. V. Maquet, R. Jerome, Materials Science Forum (1997) 43-52
8. P.A. Gunatillake, R. Adhikari, European Cells and Materials 5 (2003) 1-16
9. F.A. Maspero, K. Ruffieux, WO2004056405, 2004
10. R. Huisgen, in: A. Padwa (Ed), 1,3-Dipolar Cycloaddition Chemistry, Wiley, New York, 1984, p 1
11. H.C. Kolb, M.G. Finn, K.B. Sharpless, Angew. Chem. Int. Ed. 40 (2001) 2004-2021
12. V.V. Rostovtsev, L.G. Green, V.V. Fokin, K.B. Sharpless, Angew. Chem. Int. Ed. 41 (2002) 2596



## Brian Richard Pauw

Phone: +45 4525 6864  
Fax: +45 4588 2161  
e-mail: brian@stack.nl  
www: <http://www.dtu.dk/Centre/DPC>  
Supervisors: Martin E. Vigild  
Kell Mortensen, Risø Forskningscenter  
Enno A. Klop, Teijin Twaron, Netherlands

### Ph.D. Study

Started: October 2006  
To be completed: September 2009

## On the Microstructure of High-Performance Polymer Materials

### Abstract

This research aims to provide an uncompromising and authoritative methodology to the determination of the nanostructure of high-performance polymer materials. Much of this research is based upon methods derived in the era before computational power was readily available, and thus aims to concatenate the most valid relationships and update them where required. This methodology will be utilized to characterize high-performance aramid yarns, whilst varying many environmental conditions.

### Introduction

High performance polymers, such as the aramid yarn used for example in bulletproof vests, competition sails and as asbestos replacement, are by definition unparalleled in their physical characteristics. These yarns, as the main focus of this research, have been investigated in detail since their appearance in the marketplace approximately 30 years ago. The crystal structure of the polymer material has been characterized, as well as a great number of physical properties such as tensile strength and phase diagrams. However, only a few attempts have been made with respect to the determination of the microstructure of the yarn, i.e. structural elements with sizes bigger than what can be observed by crystallography, but smaller than the optical limit. Especially the micropore structure, with structural elements (micropores) in the range of 1-100 nanometers, is a lesser known area [1].

The main technique to investigate such microscale structures, is Small-Angle X-ray Scattering (SAXS). This is the only technique that can determine such structural elements (henceforth referred to as *contrasting objects* when associated with SAXS) without destructive sample preparation, and above all, results in average parameters, valid over the entire irradiated area [2]. These values are much more representative for the entire yarn, when compared to the other techniques of the microscopic kind, for microscopic techniques can only scrutinize small cross-sections of material at once. Naturally, techniques such as Transmission Electron Microscopy (TEM) and Scanning Probe Microscopy (SPM) will nevertheless be employed to provide visual cues to data measured with techniques such as SAXS. Furthermore Wide-Angle X-

ray Scattering (WAXS) and Positron Annihilation Lifetime Spectroscopy (PALS) can be used to provide additional data [3, 4].

Whilst in the past the nanostructure of carbon and cellulose yarns was well researched, the analysis of the measurements was limited for the sake of computability at that time [5, 6, 7]. Then, the used fitting functions required simplification, and therefore were limited in their validity. Often enough, linearisation was required for the determination of individual constants. Such were the Debye and Porod relationships, from which several micro-structural parameters could be determined [2, 8]. These could be expressed in linearly related terms, allowing for graphical analysis. For such linearisations to succeed, severe assumptions had to be made. These standard analysis methods of that time thus describe dilute systems of randomly-oriented, monodisperse contrasting objects (Guinier methods), or at the very least assume a random orientation of the contrasting objects (Porod and Debye relationships) [2, 8].

Current-day computing technologies allow for fitting of much more elaborate functions than possible at the time the original Porod and Debye relationships were generated. However, not many examples can be given of application of such expanded Porod or Debye functions to systems of oriented contrasting objects, such as found in aramid yarns, indicating a standstill of methodology advancement in that area.

Many features make the aramid yarns an uncommon subject for study by SAXS (which main application lies in determining the size of contrasting objects in solution, usually randomly oriented). The first feature is the orientation of the contrasting objects with respect to the fiber axis [3]. Not a perfect orientation,

but more of an orientation distribution. This feature dominates the scattering pattern, transforming it from a pattern with radial symmetry to a pattern with only (double) mirror symmetry (c.f. Figure 1).

Another uncommon feature is the large polydispersity of the sample, which may or may not be coupled to the orientation distribution. For example, pores of smaller sizes may have more freedom of orientation than larger pores. For a better understanding of this, a more thorough knowledge of the yarn spinning process itself and its effects on the microstructure is of great importance.

A third feature is that the contrasting objects are not expected to be perfectly cylindrical or cigar-shaped. Given the crystalline nature of the aramid material, the individual fibrils will most likely influence the shape of the contrasting objects significantly.

It is the combination of these features, amongst others, that demand a thorough re-evaluation of the standard methods

### Specific objectives

This research focuses on nano-scale structural elements, and attempts to bring a clear and authoritative view to the conflicting opinions in this area [10, 11]. Furthermore, valuable relationships are to be determined between the microstructural properties and the physical characteristics of the yarn. Also, the effect of external forces acting on the yarn is to be investigated.

Whereas previous research focused on the averaging of the obtained oriented data, and subsequent analysis on the thus obtained 1-dimensional plots, this research purports to introduce data fitting of entire 2D SAXS plots to the general research community.

### Collaborations

Teijin Twaron, manufacturer of the high-performance materials and co-contributor to the project, will collaborate extensively with this project. Amongst others, they will provide the phenomenological parameters measured at their own research lab, crucial for making the structure-property relationships. Furthermore, the company will supply custom yarns to the project.

Knowledge on the DTU and Risø side, will be combined with the knowledge on the Teijin Twaron side, resulting in unparalleled science.

For introduction of 2D fits to the research community, a collaboration has been initiated with Karsten Joensen of JJ-Xray. The free Matlab program developed as a result of this collaboration shall include a GUI-like approach to 2D data fitting.

### Results and Discussion

Initial results on the 2D data fitting of oriented structures look promising. Fitting results are not shown here as the project is in its initial stages, but an example of the 2D data is shown in Figure 1. The short

dimension of the cylinder-shaped contrasting objects causes the main scattered lobes (vertical)

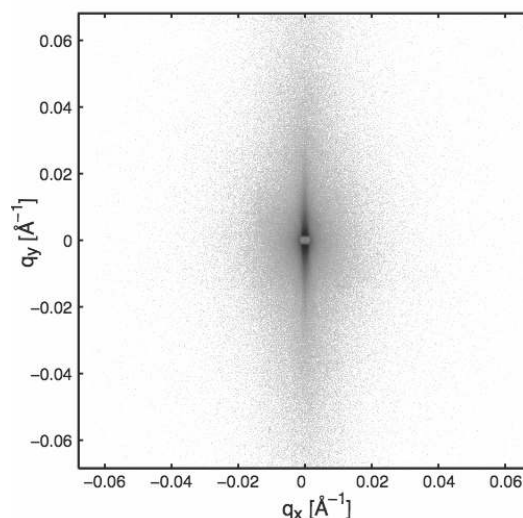


**Figure 1:** logarithmic scattered X-ray intensity of a Twaron® (aramid) yarn. The filament axes are aligned horizontally with respect to the shown figure.

### Conclusions

The knowledge of SAS, the main applied technique for this project, is likely to be sufficient for making a complete, lasting and authoritative analysis of the microstructure of high-performance yarns. The consolidated knowledge on such systems from the years of knowledge available on the topic will be implemented in a freely available program, in order to assist the expedient advancement of science.

### Acknowledgments

The author would like to express his sincere gratitude to Jens Wenzel Andreasen, for his selfless assistance and contributions to this project.

### References

- [1] J. Aerts, *J. App. Cryst.* 24 (1991) 709-711
- [2] P. Debye and A. M. Bueche, *J. App. Phys.* 20 (1949) 518-525
- [3] Y. Cohen and E. L. Thomas, *Macromolecules* 21 (1988) 433-435
- [4] P. Winberg, M. Eldrup, and F. H. J. Maurer, *Polymer* 45 (2004) 8253-8264.
- [5] W. Ruland, *J. Pol. Sci. C*, 28 (1969) 143-151
- [6] W. Ruland, *J. App. Cryst.*, 3 (1970) 525-532
- [7] W. Ruland, *J. App. Cryst.*, 4 (1971) 70-73
- [8] G. Porod, *Kolloid Zeitschrift* 124 (1951) 83-114
- [9] B. Chu and B. S. Hsiao 101 (2001) 1727-1761
- [10] S. Ran, X. Zong, D. Fang, B. S. Hsiao, B. Chu, P. M. Cunniff, and R. A. Phillips, *J. Mat. Sci.* 36 (2001) 3071-3077
- [11] S. Ran, D. Fang, X. Zong, B. S. Hsiao, B. Chu, and P. M. Cunniff, *Polymer* 42 (2001) 1601-1612



**Kim Hougaard Pedersen**

Phone: +45 4525 2890  
Fax: +45 4588 2258  
E-mail: kvp@kt.dtu.dk  
WWW: <http://www.chec.kt.dtu.dk>  
Supervisors: Anker Degn Jensen  
Kim Dam-Johansen

Ph.D. Study  
Started: September 2004  
To be completed: October 2007

## Application of Fly Ash from Solid Fuel Combustion in Concrete

### Abstract

Fly ash, a by-product from pulverized coal combustion, is utilized in the concrete manufacture where it serves as partial replacement of Portland cement. The residual carbon in fly ash is known to interfere with the chemicals added to the concrete to enhance air entrainment. The degree of interference is not only related with the amount of residual carbon, but also the properties of this carbon. The main objective of this project is to obtain knowledge of how the combustion conditions of pulverized coal is related with the amount and properties of the residual carbon in fly ash with emphasis on its utilization in concrete. Part of the work will focus on improvement fly ash quality by post treatment methods and development of standardized method to quantify the interactions between fly ash and air-entraining chemicals.

### Introduction

About 24 % of the electricity produced worldwide (2002) is generated in coal fired power plants. As a consequence, large amounts of fly ash are produced. The demand for environmentally clean and cost effective power generation has increased the motivation of fly ash recycling.

The pozzolanic property of fly ash, i.e. its capability to react with water and calcium hydroxide to form compounds with cementitious properties at ambient temperature, makes it useful in the concrete industry, where it serves as partial replacement of cement and give rise to increased strength of concrete [1]. However, the fly ash has been reported to interfere with air entrainment in concrete, which is important to obtain high resistance toward freezing and thawing conditions [2]. Special surfactants, called air-entraining admixtures (AEAs), control this air entrainment by stabilizing the air as small bubbles in the concrete paste. They adsorb strongly to the air-water interface, but fly ash present in the concrete paste are capable of adsorbing the AEAs as well. Hereby less AEAs are available to support the air bubbles and the entrained air is lowered. Increasing the dosage of the AEAs may compensate for the adsorption loss, but normal variations in ash properties lead to large and unacceptable variations in the entrained air [3].

Even though modern coal fired power plants have high burnout efficiencies, significant amounts of carbon still exist in the fly ash after combustion. This residual carbon and not the mineral matter of fly ash is responsible for the adsorption of AEAs [3]. A large part of the carbon surface is non-polar compared with the polar surface of the mineral matter. This provides active adsorption sites for the hydrophobic part of the surfactants, thus the carbon competes with the sites at the air/water interface [4] as illustrated in Figure 1.

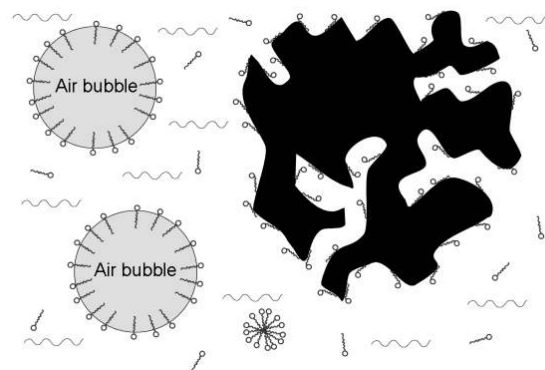


**Figure 1:** Adsorption sites for AEAs at air/water interface and at carbon surface [4]. The small circles of the AEAs correspond to the polar end and the tail corresponds to the hydrophobic end.

The problem with decreased air entrainment in fly ash concrete has worldwide lead to regulations for its application in concrete taking the presence of carbon in fly ash into account. These regulations are based on a maximum limit of the amount of carbon in fly ash, e.g. according to the Danish Standard DS/EN 450 the carbon content in fly ash are not allowed to exceed 5 wt%. However, in recent years the carbon content of a fly ash has been found insufficient as a criterion for its application in concrete and problems with air entrainment have been observed with fly ashes having levels of carbon below the limits [3]. These observations have lead to further studies of the interactions between AEA adsorption and properties of carbon in fly ash; factors such as accessible surface area and surface chemistry of the residual carbon are believed to affect the AEA adsorption as well [4].

The combustion conditions under which the fly ash has been produced influences the properties of the residual carbon. The worldwide introduction of improved burner technologies in order to reduce NO<sub>x</sub>-emissions has lead to problems with achieving a correct amount of air entrainment in fly ash concrete [5]. These burner technologies work with hot fuel rich zones in order to combust under reducing conditions and these conditions are believed to create fly ash being poor in quality for concrete utilization.

The AEA adsorption capacity of a fly ash is usually determined by the foam index (FI) test, which is a simple laboratory titration procedure involving the use of commercial AEAs and visual observation of foam stability. These parameters reduces the comparability of the test, i.e. commercially available AEAs vary in chemical nature and criterion on foam stability is operator individual. Therefore, it is of interest to develop a reproducible method, which is able to determine the fly ash quality with respect to air entrainment in concrete [6].

### Specific Objectives

The aim of this project is to obtain further knowledge of how the combustion conditions of pulverized coal influences the fly ash quality for concrete utilization with emphasis on the air entrainment in concrete. Part of the work will focus on improvement of fly ash quality by post treatment methods. Furthermore, steps will be taken toward the development of a reproducible test method to replace the foam index test.

### Method Development

The new method developed to determine fly ash quality is based on surface tension measurements instead of foam stability observations. Moreover, a standard surfactant (sodium dodecyl benzene sulfonate, SDDBS), which can be prepared in known concentrations, is used as a model for a commercial AEA. The surface tension is measured on a suspension of cement and fly ash particles and the procedure only slightly differs from the foam index test, i.e. in the foam index test the AEAs are added continuously until stable foam is obtained on top

of the suspension, whereas in the new method the surfactants are added in one step. After 5-30 minutes of mixing, the aqueous phase is separated from the particles followed by surface tension measurements using the maximum bubble pressure method; a capillary is introduced into the solution and bubbles are grown on the tip. The pressure difference required in the bubble formation is proportional to the dynamic surface tension of the solution [7]. The lifetime of the bubbles have an impact on the measured surface tension, e.g. increasing bubble lifetime lowers the measured surface tension due to the surfactants will have more time to diffuse to the bubble surface.

First part of the method development included determination of initial SDDBS concentration and applied bubble lifetime, and the optimal conditions are based on the experimental data presented in Figure 2 and 3.

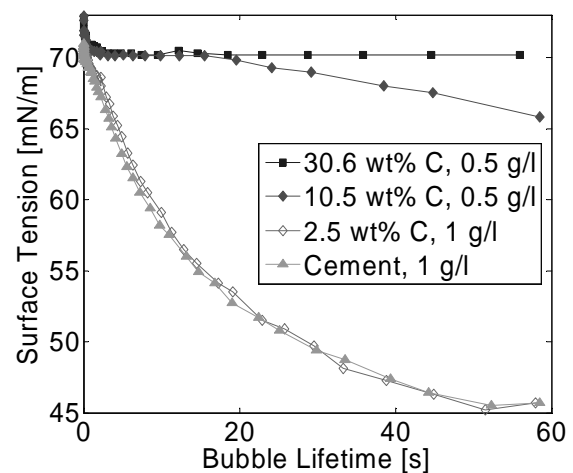


**Figure 2:** Dynamic Surface tension compared with bubble lifetime at starting concentrations 0.5 and 1 g/l SDDBS

The consequence of having a low initial concentration of SDDBS is revealed in Figure 2, where only a minor difference in the measured dynamic surface tension can be detected in a wide span of bubble lifetime between two high carbon ashes. It appears as if both ashes have adsorbed most of the added surfactant, making it difficult to measure any difference in their adsorption capacity. On the other hand, a high initial concentration of SDDBS leads to similar dynamic surface tension measurements of both cement and a low carbon ash, indicating that the amount of surfactant adsorbed by the fly ash is low compared to the remaining SDDBS in the solution. The critical micelle concentration (CMC) of SDDBS may explain this observation. Normal surfactant behavior is observed below CMC, i.e. surfactants are found as monomers and the concentration relates to the surface tension [8]. Above CMC the hydrophobic part of the surfactant interacts with other surfactants leading to micelle formation, where only the hydrophilic part is in contact with the aqueous phase. The micelles are not surface active and hence will not contribute to changes in surface tension.

Addition of a 0.6 g/l SDBS solution appears to give a detectable difference between both low and high carbon ashes as shown in Figure 3.

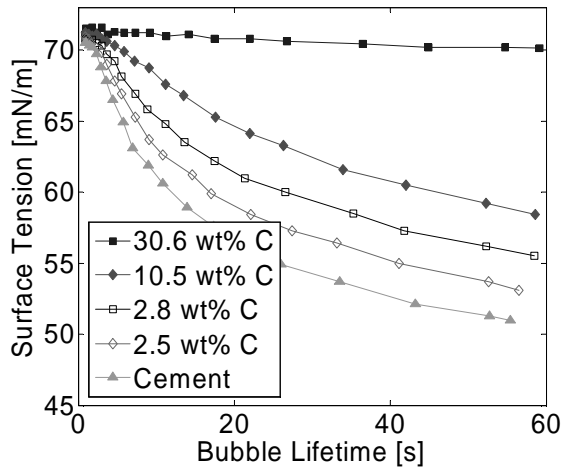


**Figure 3:** Dynamic surface tension compared with bubble lifetime at initial SDBS-concentration on 0.6 g/l.

It is evident, how utilization of a short bubble lifetime leads to similar surface tension results. Equilibrium between surfactants in the solution and at the surface are not obtained due to a short surface age and the surface tension of the pure solvent is measured, being water in this case (72.3 mN/m at 23 °C). At high bubble lifetime, the surfactants move toward equilibrium and the surface tension is lowered. Hence, any variation in surface tension between the samples can be detected. On the other hand, the difference in surface tension between the samples appears not to increase further when a bubble lifetime above 20 seconds is applied, making it a reasonable choice in further measurements. Moreover, testing time will be significantly extended with higher bubble lifetime because the results are based on the average of several measurements.

Other parameters that influence the test method have been investigated in the present study. Both the mixing time of the surfactant, cement and fly ash suspension and variation in temperatures were found to have a significant impact on the reported surface tension values. The transport of surfactants from the aqueous phase into the interior of the residual carbon particles is diffusion controlled [4] and thus, the surfactant concentration decreases with longer mixing time. No endpoint was found even after 30 minutes, and it was decided to proceed with 10 minutes in incubation time corresponding to the usually time expenditure of the foam index test. The surface tension of the filtrate was found to decrease with rising temperature, which leads to implementation of isothermal conditions.

Figure 4 presents surface tension measurements on filtrate from cement/fly ash samples compared with their respective foam index values. The results display a good correlation between the two methods.

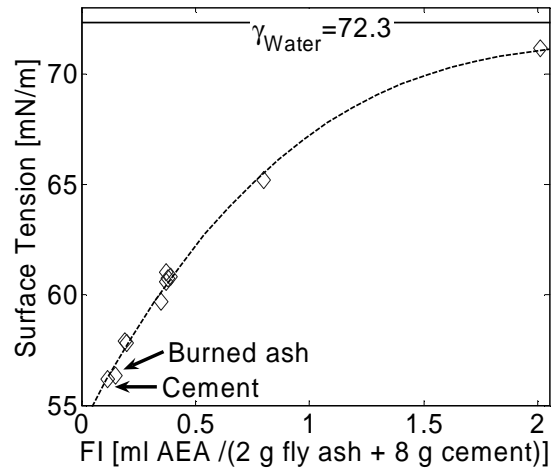


**Figure 4:** Surface tension of filtrate compared foam index. The temperature of the filtrate was between 22.7-22.9 °C. 0.6 g/l SDBS in initial concentration and 10 minutes in incubation time.

Increasing foam index of a fly ash corresponds to higher adsorptivity of surfactants and thereby a greater interference with air entrainment in concrete. In the surface tension method, the concentration of surfactants in the aqueous phase is reduced by the adsorption, leading to higher surface tensions. The correlation appears to be linear within lower adsorption capacities of fly ashes. At higher adsorption capacities, the test meets its limit under the applied conditions. Surface tension values can not exceed the surface tension of the pure liquid. Thus, ashes with high adsorption capacities will result in filtrates with low surfactant concentrations and show surface tensions close to pure water, making it difficult to detect any variance in their adsorption capacities. Measurements on activated carbon (foam index > 14 ml/2 g C) confirm this behavior. The surface tension was measured to 71.9 mN/m, indicating that the surfactant may have been exhausted from the supernatant fluid completely. To include these high adsorption ashes in the detectable region involves higher initial concentration of SDBS. However, as Figure 2 shows, the difference between ashes with lower adsorption capacities will be more difficult to detect.

#### Combustion Conditions and Fly Ash Quality

Fly ash has been produced from combustion of pulverized coal under various combustion conditions in an entrained flow reactor (EFR) sketched in Figure 5.

The main part of the EFR is an electrically heated ceramic reactor, where the combustion of the fuel takes place. The coal and part of the combustion air is introduced from the top and into the reactor through a water-cooled feed probe. The remaining air is pre-heated before it is mixed with the coal/air mixture. A particle sampling probe is mounted in the bottom of the reactor. The fly ash particles are sampled from the flue gas stream by isokinetic gas sampling and collected on a filter further downstream. The parameters adjusted in

the combustion experiments are the total excess air ( $\lambda_{total}$ ) and the ratio between feed and total air ( $\lambda_{feed}/\lambda_{total}$ ). The collected fly ashes are analyzed for carbon content (determined by weight loss, LOI) and foam index.

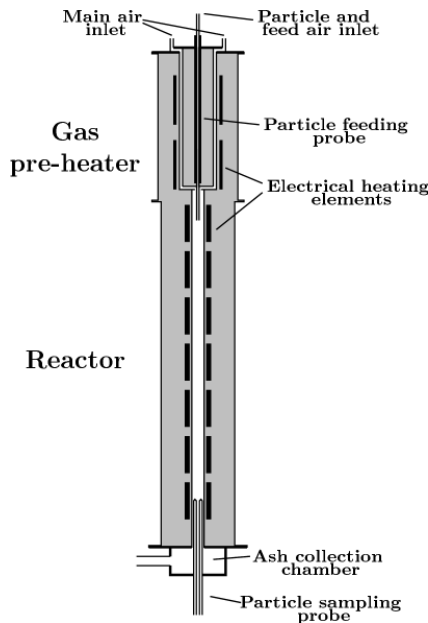


**Figure 5:** Sketch of EFR. The ceramic reactor is 2 m long and 8 cm in diameter. Conditions used in the EFR: coal feed rate: 0.34-0.46 kg/h, temperature: 1350 °C, feed air: 6-17 NI/min, total air: 58 NI/min, gas mean residence time: 1.7 s

Figure 6 shows the residual carbon content of the collected fly ashes produced at different feed/total air ratios and total excess air.

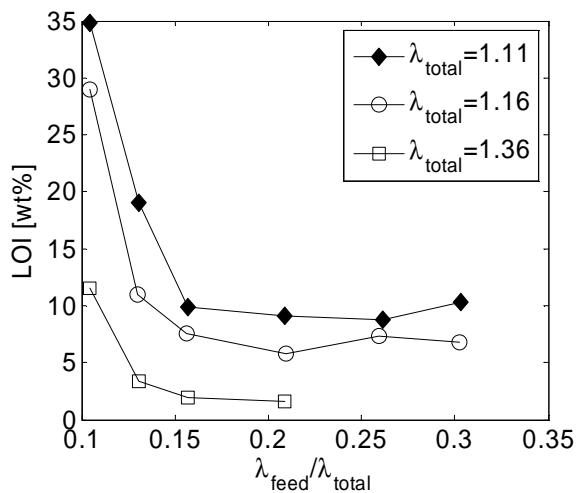


**Figure 6:** Carbon content (LOI) in fly ashes compared with the feed/total air ratio at different total excess air.

The carbon content of the fly ashes are found to decrease with increasing feed/total air ratio and excess air. The feed/total air ratio is observed to have major impact on the carbon content at lower ratios, but not at ratios above app. 0.16, where the fly ashes are produced

with constant carbon content. The initial decline in carbon content with the ratio are presumably due to an improved mixing between coal and air caused by increasing jet velocity at higher feed/total air ratio. This leads to increased oxygen concentrations in the early stage of combustion and thereby a higher conversion of the coal particles. A further rise in feed air reduces the temperature and concentration of coal particles in the air flow, which can result in a delayed ignition [9] and this may explain the constant carbon content found in ashes produced at higher feed/total air ratios. The increase in total excess air raises the oxygen concentrations in the reactor and gives rise to decreased carbon content in the produced ashes as well.

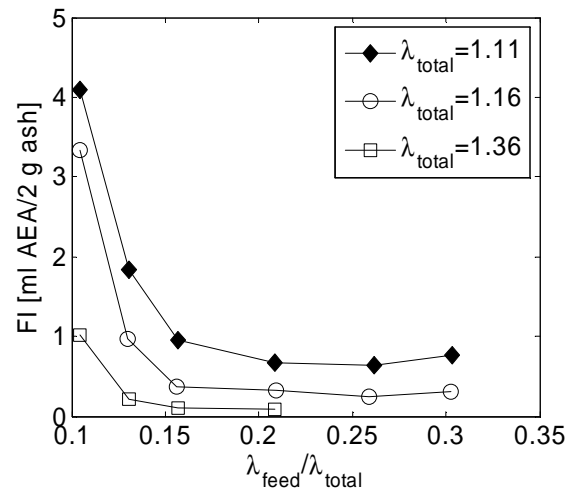


**Figure 7:** Foam index of fly ashes compared with the feed/total air ratio at different total excess air. The foam index test is performed on two grams of fly ash and the results are reported as ml AEA per two gram of fly ash.

The determined foam index values of the coal ashes (Figure 7) are from a visual comparison observed to follow the tendency of the carbon content; increasing excess and feed/total air ratio results in ashes with lower foam index values and low feed/total air ratios do highly affect the foam index, which on the other hand stays constant at higher ratios. The high foam index found among ashes with elevated carbon content are in agreement with results from others [3], that the residual carbon accounts for the adsorption of AEAs in concrete mixtures.

In order to uncover whether the difference in foam index between the ashes is solely caused by a change in carbon content, or if it may be due to a variation in the AEA adsorption properties of the residual carbon as well, the foam index is normalized to the carbon content of the fly ash, also known as the specific foam index. The results are presented in Figure 8, where the AEA adsorption capacity of the residual carbon (spec. FI) is found to decrease with the feed/total air ratio. Moreover, higher specific foam indexes are found at the lowest overall excess air ( $\lambda=1.11$ ). Thus, the variations in AEA adsorption of the produced ashes are apparently caused

by changes in both carbon content and AEA adsorption capacity of the residual carbon.

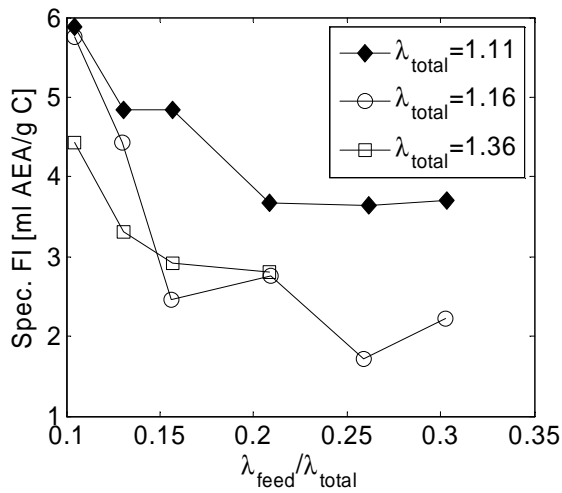


**Figure 8:** Specific foam index of fly ashes compared with the feed/total air ratio at different total excess air. The specific foam index corresponds to AEA adsorption capacity of the residual carbon.

It is found that more fuel rich conditions (lower excess air or feed/total air ratio) do not only lead to an increased carbon content and thereby a raise in foam index of the produced ashes, but the carbon is also capable to adsorb higher amounts of AEAs, making the consequences of increased carbon content worse.

The present observations support what others have discussed about the mechanism of the AEA adsorption [5]. It has been suggested [5] that a stable film of oxides is formed on the surface of carbon during conversion in an oxidizing environment. The increased polarity of the carbon surface creates less adsorption sites for the hydrophobic part of the AEA and thus, less AEA is adsorbed by carbon as illustrated in Figure 9.

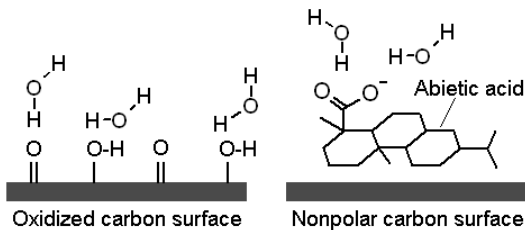


**Figure 8:** The hydrophobic part of a surfactant molecule (in this case abietic acid) interacts by dispersion forces, with the non-polar carbon surface (right). On the other hand, at the polar carbon surface (left), water molecules interact with the surface oxides by hydrogen bonding. The dispersion forces from the surfactant are not strong enough to displace water and hence, the surfactant is not adsorbed by the carbon.

Opposite to this, fuel-rich combustion conditions will drive off surface oxides, leading to a less polar surface. These fuel rich conditions are usually found near the burner in low- $\text{NO}_x$  environment, where they reduce the formation of  $\text{NO}_x$  but lead to lower fly ash quality. It is noted that variations in AEA adsorption of the residual

carbon may be due to its surface area and particle size as well and this will be subject for further investigation.

A linear relationship was found between  $\text{NO}_x$  emission and the feed/total air ratio. The foam index of the produced ashes compared with measured  $\text{NO}_x$  emissions are presented in Figure 9. The foam index is within each series of constant total excess air series found to decrease with the  $\text{NO}_x$  emission

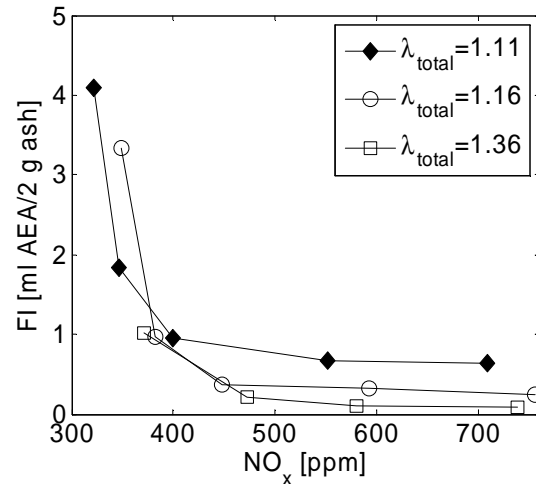


**Figure 9:** Foam index of the produced fly ashes and  $\text{NO}_x$  emissions at different total excess air.

until it reaches a constant level at app. 450 ppm  $\text{NO}_x$ . Therefore, increased fly ash quality in the EFR is achieved when operating at enhanced oxidizing conditions (expressed as higher  $\text{NO}_x$  emissions), but only until a certain level. It appears as if there exist optimal conditions in the EFR where both low foam index of the fly ashes and low  $\text{NO}_x$  emissions are achieved. From a practical point of view this is interesting, i.e. will the same apply at full-scale utilities?

## Conclusion

The commonly employed foam index test, which determines the fly ash quality for concrete utilization, has been compared with a new method based on surface tension measurements and there appears to be a good relationship between the two methods. The new method takes away the individual operator criterion of foam stability, making the test easier to standardize. Moreover, the test can be based on using a pure surfactant instead of an air-entraining agent, where commercial products show variation in chemical nature and concentrations.

Pilot scale experiments on an EFR have shown how low- $\text{NO}_x$  combustion of pulverized coal generates fly ash with higher carbon content, increased foam index and increased AEA adsorption of the residual carbon, all making the fly ash less suitable as concrete additive. The results indicate that optimal conditions exist between the foam index of the produced fly ashes and  $\text{NO}_x$  emissions on the present setup. Work will continue on the EFR involving other types of fuel and temperatures.

## References

1. K. Wesche, Fly Ash in Concrete: Properties and Performance, Spoon, London, 1991, p. 5.
2. Y-M. Gao, H-S. Shim, R.H. Hurt, E.M. Suuberg, N.Y.C. Yang, Energy & Fuels 11 (1997) 457-462.
3. E. Freeman, Y-M. Gao, R. Hurt, E. Suuberg, Fuel 76(8) (1997) 761-765.
4. L. Hachmann, A. Burnett, Y-M. Gao, R.H. Hurt, E.M. Suuberg, Proceedings of the Combustion Institute 28 (1998) 2965-2971.
5. Y. Gao, I. Külaots, X Chen, E.M. Suuberg, R.H. Hurt, J.M. Veranth, Proceedings of the Combustion Institute 29 (2002) 475-483.
6. O.E. Manz, Fuel 78 (1999) 133-136.
7. L. Schulze, K. Lohmann, Tenside Surfactants Detergents 36 (6) (1999) 384-386.
8. D. J. Shaw (Ed.), Introduction to Colloid and Surface Chemistry, 4<sup>th</sup> Edition, Butterworth-Heinemann, Cornwall, 2000.
9. X. Jun, X. Sun, S. Hu, D. Yu Fuel Processing Technology 68 (2) (2000) 139-151.

## List of publications

1. K. H. Pedersen, S.I Andersen, A.D. Jensen, K. Dam-Johansen, Replacement of the foam index test with surface tension measurements (submitted).
2. K. H. Pedersen, A.D. Jensen, M.S Skjøth-Rasmussen, K. Dam-Johansen, A review of the interference of carbon containing fly ash with air entrainment in concrete (submitted).



### Nanna Petersen

Phone: +45 4525 2861  
Fax: +45 4593 2906  
E-mail: nap@kt.dtu.dk  
WWW: <http://www.kt.dtu.dk>  
Supervisors: Krist V. Gernaey  
Anna Eliasson Lantz, BioCentrum  
Stuart Stocks, Novozymes

### Ph.D. Study

Started: October 2006  
To be completed: October 2009

## Data-Driven Modeling for Monitoring and Control of *Streptomyces* Cultivations

### Abstract

One of the main challenges of modeling and controlling industrial cultivations is the lack of on-line measurements of important variables such as the biomass and product concentration. On-line spectroscopic measurements can be utilized to provide information about these important variables. The aim of this project is to examine the different methods for modeling the spectral data, estimate reliable models and implement the models in a monitoring and control scheme on a *Streptomyces* cultivation.

### Introduction

Sensory information is indispensable for monitoring and optimization of fermentation processes, where reliable first engineering principles models are very time consuming to develop. Several promising on-line sensory methods are emerging such as Multi-Wavelength Fluorescence (MWF) and Near-Infrared spectroscopy (NIR). The recent Process Analytical Technology (PAT) initiative of the FDA has greatly encouraged the introduction of advanced on-line sensors in manufacturing.

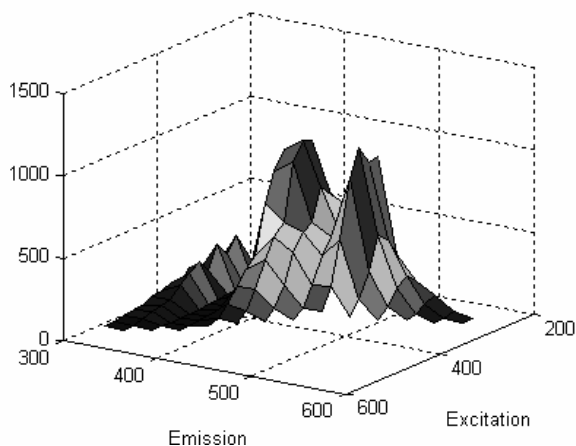


**Figure 1.** Multi-wavelength fluorescence spectrum.

Fluorescence measurements can be used to monitor fermentation processes by exploiting the fluorescence of

different organic and biologically relevant compounds [1-3].

Examples of such fluorophores are tryptophan, phenylalanine, tyrosine, different vitamins i.e. pyridoxine and folic acid as well as NADH and NADPH. As these compounds can be associated with different process variables such as the biomass concentration it is possible to use these measurements for monitoring a given cultivation. In *Multi-wavelength* fluorescence several excitation/emission combinations are measured, thus resulting in a 2-dimensional data set for each measurement point (figure 1). Thus it is possible to measure several fluorophores simultaneously.

Near-infrared spectroscopy is widely used in many industries for quality control at different stages of the production process. More recently it has also been used for monitoring of fermentation processes [4]. A given molecule will absorb light in the IR region only if there is a shift in the polarity of the molecule. C-H, N-H, O-H and S-H all have a high dipole moment and thus the stretching and bending vibrations of these bonds may contribute to the NIR spectra. These bonds are common constituents of biological matter and thus the NIR spectroscopy may be used for monitoring the development of a fermentation process. The spectral information can be acquired in two different modes: transmission or reflectance. The transmission mode is most often used in low density fermentations in which case the measurements are taken according to:

$$A = \log(1/T)$$

Where  $A$  is the absorbance and  $T$  is the transmission. The reflectance mode may be more suitable in high cell

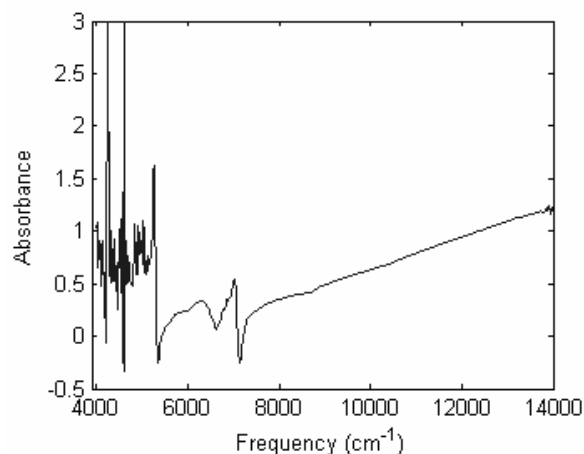


**Figure 2.** Near-infrared spectrum from cultivation.

density fermentations or in fermentations where the biomass has a complex structure e.g. fermentation broths with filamentous organisms. In the reflectance mode the absorbance is measured according to the equation:

$$A = \log(1/R)$$

Where  $A$  is the absorbance and  $R$  is the reflectance. An example of a NIR spectrum is shown in figure 2.

The raw NIR and MWF spectra are difficult to interpret directly. In the NIR spectra several substances may contribute to the absorption at one wavelength and a single substance may absorb light at different wavelengths. Furthermore, the concentration of different substances may be highly correlated during a fermentation process. Finally, the data sets are very large which makes it difficult to simply visualize the data as well as to interpret them. Therefore, multivariate data analysis techniques are employed in the analysis of these spectral data.

Partial Least Squares Regression (PLSR) can be considered the industry standard for the analysis of multivariate data. It is a supervised learning method which can be used to find correlations between output variables (e.g. biomass and substrate concentration) and a set of input variables (spectral data). PLSR is able to handle correlations in the data by reducing the dimensionality of the data. The data are projected to a subspace spanned by vectors determined to maximize the variance of the input data as well as the correlation with the output variables. Multi-way PLSR or traditional PLSR may be used for the analysis of the 3-dimensional MWF data depending on the unfolding of the data.

### Specific Objectives

A first project objective is to establish a data set consisting of a number of batch fermentations with *Streptomyces coelicolor* – a filamentous bacterium producing useful secondary metabolites such as

antibiotics – as model organism, and using advanced on-line sensors (NIR, MWF) for data collection in addition to standard on-line measurements. As such, establishing this data set is already a challenge, since the application of spectroscopic methods such as NIR in cultivations with filamentous organisms is far from straightforward. The fermentation data set can then serve as a basis for finding and evaluating correlations between sensor data and the course of the submerged bioprocess. A second project objective is to provide a comparison of the performance of several data-driven modeling methods – linear versus non-linear, single model versus multiple local models – on this fermentation data set. In one part of this modeling work, data-driven modeling/chemometrics will be applied to the multivariate sensor data for prediction of relevant process variables. In another part of the modeling, these methods will also be employed for developing process monitoring applications (e.g. detection of sensor and actuator faults). For process monitoring, it will specifically be investigated how availability of advanced on-line measurements can contribute to our ability of identifying erroneous process behavior. A third project objective is to actively use the on-line process variable information obtained from the advanced on-line sensor data in feedback control loops. Once feedback control using advanced on-line sensors is established, the project focus will shift towards fermentation process optimization.

### Acknowledgements

This Ph.D. project is part of the Innovative BioProcess Technology research consortium, and is financed by Novozymes A/S and the Danish Research Council for Technology and Production Sciences.

### References

1. A. E. Humphrey. The potential of on-line fluometric measurements for the monitoring and control of fermentation systems. *Aust. J. Biotechnol* 9 (6) (1988) 141-147.
2. G. Lidén. In situ fluorescence measurements – clarifying the blurring picture? *Pure Appl. Chem* 65 (1993) 1927-1932.
3. M.B. Haack, A. Eliasson, L. Olsson. On-line cell mass monitoring of *Saccharomyces cerevisiae* cultivations by multi-wavelength fluorescence. *J. Biotechnol.* 114 (2004) 199-208.
4. M. Scarff, S. A. Arnold, L. M. Harvey, B. McNeil. Near Infrared Spectroscopy for Bioprocess Monitoring and Control: Current Status and Future Trends. *Critical Reviews in Biotechnology* 26 (2006) 17-39.



**Trine Lütken Petersen**  
Phone: +45 4525 2708  
Fax: +45 4588 4148  
E-mail: tlp@biocentrum.dtu.dk  
WWW: http://www.biocentrum.dtu.dk  
Supervisors: John Villadsen  
Timothy Hobley  
Jesper Brask, Novozymes

Ph.D. Study  
Started: April 2004  
To be completed: April 2007

## Avoiding Proteolysis in Fermentation Broths through Removal of Proteases using High Gradient Magnetic Fishing (HGMF)

### Abstract

A novel method for removing proteases from fermentation broths during the fermentation has been investigated. Contrary to commonly used techniques for avoiding degradation of interesting extracellular peptide products during fermentation, this novel technique, High Gradient Magnetic Fishing, has been found to be an easy and efficient technique that does not disturb the growth of the microorganisms in the fermentation.

### Introduction

Proteolysis in fermentation broths is a common phenomenon that leads to degradation of interesting extracellular peptide products. The proteolysis is due to the production of unwanted proteases during the fermentation. To avoid the damage done by proteases many strategies have been implemented, such as avoiding protease formation through genetic manipulation or inactivating the proteases in the fermentation broth during fermentation. None of these strategies are however without problems. The production of mutants with reduced expression of extracellular proteases requires the knock out of many genes and can be problematic. Expressing the wanted protein in organisms without extracellular protease production, can be a problematic and tedious solution and in certain industries the use of GMOs is not possible. Inactivating the proteases by adding protease inhibitors to the fermentation has certain disadvantages since inhibitors that are peptide based are not stable in fermentation broths for very long and are expensive. Many chemical based inhibitors are on the other hand poisonous and therefore useless within certain industries.

A new and very straight forward idea is to remove the proteases directly from the fermentation broth during the fermentation using High Gradient Magnetic Fishing. The expected advantages of using this new technique to avoid the proteolysis, are that the fermentation would not be disturbed during the process, the product not damaged, the technique should be easy and efficient, the magnetic adsorbents used for the purpose can be expected to be re-usable and their

approval for making products for the food industry straightforward.

### The concept

The concept behind this project is that it is possible to bind proteases via their active sites to *magnetic* supports by using affinity ligands To be able to bind a wide range of proteases and thereby hopefully most of the proteases present in a fermentation broth. Bacitracin, a general inhibitor of proteases, has been chosen as the ligand on the magnetic supports (Figure 1).

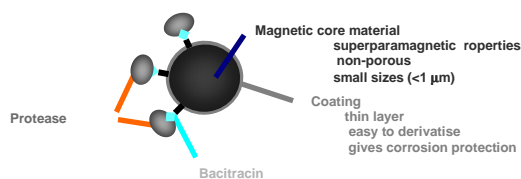


**Figure 1:** Schematic representation of a protease bound to bacitracin on a magnetic adsorbent. The adsorbent core is non porous and superparamagnetic (no remnant magnetism when removed from a magnetic field). Thus the supports can be captured or released from a magnetic filter when the field is turned on or off. The small support size increases the surface area to volume ratio giving high capacity.

By adding magnetic beads with a bacitracin ligand to a fermentation broth during the fermentation, the proteases present in the broth are adsorbed specifically to the beads and by the use of a magnetic field, the magnetic beads with bound proteases can be removed

from the bioreactor, thereby stabilizing the products generated during the fermentation (Figure 2).

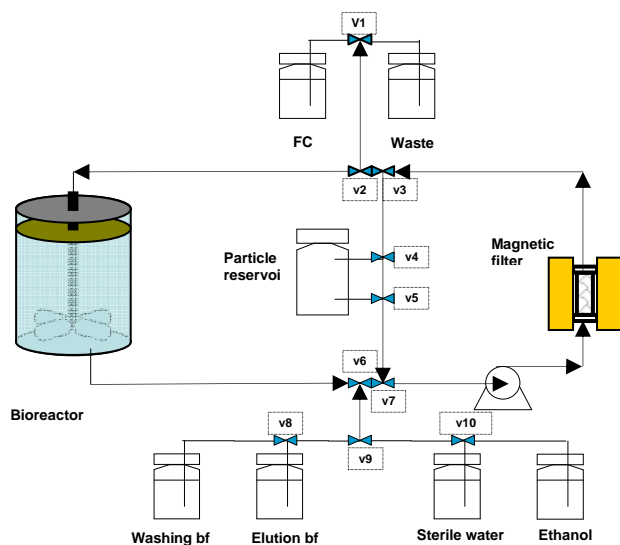


**Figure 2:** Schematic for process of stabilising a fermentation product using High Gradient Magnetic Fishing. The process involves the bioreactor and a valve system that connects a magnetic filter to the different solutions needed for the High Gradient Magnetic Fishing.

### Results and discussion

Magnetic supports derivatised with bacitracin have been constructed and the adsorption isotherm showed high specific binding of a protease, Savinase with a dissociation constant of  $1.8 \cdot 10^3$  U/L [0.79  $\mu$ M] and a maximum capacity of  $3.6 \cdot 10^3$  U/g [158 mg/g].

Magnetic particles that are reusable are highly desirable for the process of protease removal because of the potential large-scale application of this process. Testing the reusability of the manufactured particles has been carried out by completing repeated binding/elution cycles (Figure 3). The result of this testing showed no loss in binding and elution characteristics after 4 cycles.

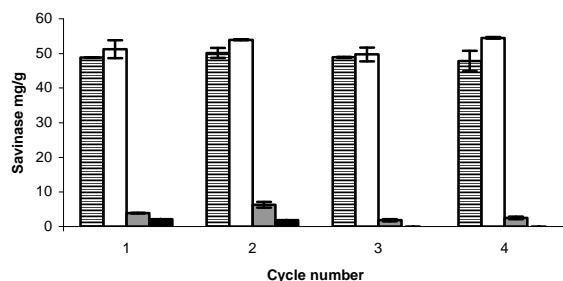


**Figure 3:** Reusability of magnetic particles. The striped bars show the amount of Savinase bound to the particles while the white, grey and black bar show, respectively, three sequential elutions of Savinase for each binding cycle.

The first test of the concept of removal of proteases from a cultivation of *Bacillus licheniformis* was carried out in shake flask cultivations. The protease activity in the fermentation broth clearly dropped when the High Gradient Magnetic Fishing was carried out (Figure 4). The protease activity was reduced by 60% due to the removal of proteases from the fermentation broth.

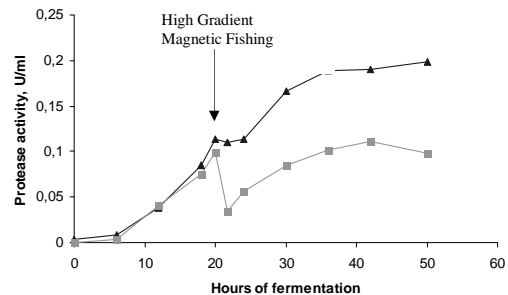


**Figure 4:** Plot of the protease activity in a shake flask fermentation in which the proteases were removed using High Gradient Magnetic Fishing (■) and in a reference shake flask (▲). The protease activity is plotted as a function of the fermentation time.

Proving the product stabilising effect of removing proteases from fermentation broths, was done by following the degradation of a common protein, bovine serum albumin, as a consequence of the formation of proteases during two fermentations. The shake flask where proteases were removed using HGMF and the reference shake flask are shown in Figure 5. BSA was added to both shake flasks after 19 hours of fermentation, just before HGMF removal of the proteases.

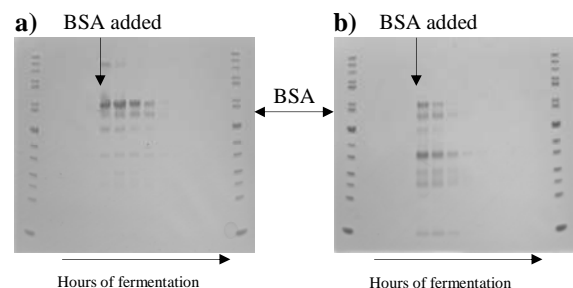


**Figure 5:** SDS-PAGE gels showing BSA degradation during the fermentation in the shake flask where the proteases were removed using High Gradient Magnetic Fishing (a) and in a reference shake flask (b).

Figure 5 shows that the BSA is degraded into many small peptides when proteases are present in the fermentation broth, as seen in 5b. However, when the proteases are removed during the fermentation using HGMF, the degradation of BSA is reduced, as seen in 5a. Observations of the cells using microscopy and measurements of the growth indicated that the process using magnetic beads had not harmed the *Bacillus*.

### Acknowledgements

Novozymes Bioprocess Academy is acknowledged for funding the project



### **Jamal El Bashir Ali Rashed**

Phone: +45 4525 2811  
Fax: +45 4525 2906  
E-mail: Jar@kt.dtu.dk  
WWW: <http://www.capec.dtu.dk>  
Supervisor: Rafiqul Gani

Ph.D. Study  
Started: January 2006  
To be completed: December 2008

## **Model-Based Retrofit Design and Analysis of Petrochemical Processes**

### **Abstract**

Driving force based models are developed for different separation and reaction processes for application in model based retrofit design and analysis of petrochemical processes. The design and analysis employs the reverse design approach and generates improved retrofit (design) alternatives. According to the reverse approach, the design variables that match the specified process targets for each unit operation in the process are determined by solving a new class of unit operation models based on the driving-force that “drives” the operation. The reverse approach has been developed and tested for vapor-liquid, liquid-liquid, solid-liquid based separation processes and reaction operations.

### **Introduction**

Competition in the petrochemical market has increased during the past decades. Therefore, to be still competitive, many existing production processes require constant improvements through retrofitting while new processes need to satisfy stricter regulations with concerns to pollution and process safety, thereby making the petrochemical processes more sustainable.

Processing alternatives such as replacing a distillation operation by a membrane based separation will be investigated. Also, a solvent – based separation may be replaced by reactive distillation, or, a reaction producing undesirable by – products may be replaced by another providing better product yield (through, for example, better catalysts). That is, use of a better solvent or catalyst to improve the process and reduce the environmental impact would be investigated. All this knowledge will be used by the design algorithm to generate feasible retrofit process alternatives that will produce the same product from the same raw material but under significantly better conditions. Operational, economic, and environmental indicators will be used to generate better alternatives.

Based on a set of indicators, estimates for the desired design (process) target will be established. The reverse approach will be used to identify the final design details. Here, the design variables that match the design targets for each unit operation in the process will be determined by solving a new class of unit operation models based on the driving-force that “drives” the operation. First, the driving force needed to convert a given feed stream to the desired product streams, is

calculated. Next, the variables (design) through which the calculated driving-force can be matched, are determined. Since from the model the design variables are calculated for specified values of input and output, instead of the opposite, the same reverse approach is used for this design technique.

### **Specific Objectives**

The main objectives of this project can be summarized as follows. The first objective is to analyze a class of current petrochemical processes and to identify their weak points from a point of view of operability, environmental impact, flexibility and energy efficiency. The second objective is to develop a systematic methodology that can generate new and significantly better alternatives, and to identify from them, the optimal design. The third objective is to verify and validate the optimal design through further model – based analysis.

### **Illustrative Example**

A case study involving a process for styrene production is illustrated in this work. In the first stage, the flowsheet of a process, based on steady state mass and energy balances of a reference process operating state (base case) is simulated. The second step is to analysis the process to identify their weak points from a point of view of operability, environmental impact, flexibility and energy efficiency.

The separation of the desired styrene product from the light ends, heavy ends, benzene and toluene is relatively easy, being accomplished by conventional

sequential distillations. Separation by distillation of the styrene (S) from the unreacted ethylbenzene (EB), however, presents a considerably more difficult problem due primarily to their close similarity in volatility. First of all, the boiling points of ethylbenzene and styrene, 136.15° C. at 1 atm and 146.0° C. at 1 atm, respectively, are so close. That separation by fractional distillation is difficult. In the reference design of the process, this EB/SM separation has been accomplished by distillation under vacuum conditions in large, sophisticated, and expensive distillation columns requiring a large number of theoretical plates to achieve the desired separation. Due to the high energy consumption for this separation, other alternatives that will increase operating efficiency and reduce energy consumption need to be investigated.

The most promising technologies for replacement of distillation include: membranes, extraction, absorption, and hybrid systems, which combine technologies, often combining distillation to reduce energy usage.

### Alternative 1: Extractive Distillation

Ethylbenzene cannot be easily removed from styrene by distillation because of the closeness of their boiling points. Ethylbenzene can be readily separated from styrene by means of extractive distillation using certain nitrogenous organic compounds as solvents. Through a search of database, three possible solvents have been found, Nitrobenzene, 2,6-dinitrotoluene and Adiponitrile. Vapor – liquid equilibrium data has been generated for these systems through the use of the UNIFAC model for liquid phase, and the ideal gas model for the vapor phase. Reverse approach has been used to identify the design parameters for extractive distillation. The driving force diagram (solvent-free) is shown in Fig. 1.

From the solvent free driving force in Fig. 2, it is possible to select a solvent fraction of 0.8 to obtain a solvent free maximum driving force above 0.25. From the mass balance calculations and the solvent fraction it is possible to determine that an inlet of 343 kgmol/h of 2,6-dinitrotoluene is needed in the first column. The 2,6-dinitrotoluene is mixed with styrene and ethylbenzene mixture. The first column is recovering near pure product of ethylbenzene at the top. The bottom product of the first column is sent to the second column to perform Styrene/2,6-dinitrotoluene separation.

**Table 1.** Design parameters of the columns in the ethylbenzene/styrene separation

Column	EB extraction	Styrene/2,6-dinitrotoluene
Number of plates	40	10
Feed plate location	25	8
Purity of light key	99.5	99.5

From the styrene/2,6-dinitrotoluene solvent driving force diagram in Fig. 3, the design parameters for the column are calculated using the reverse approach and given in Table 1.

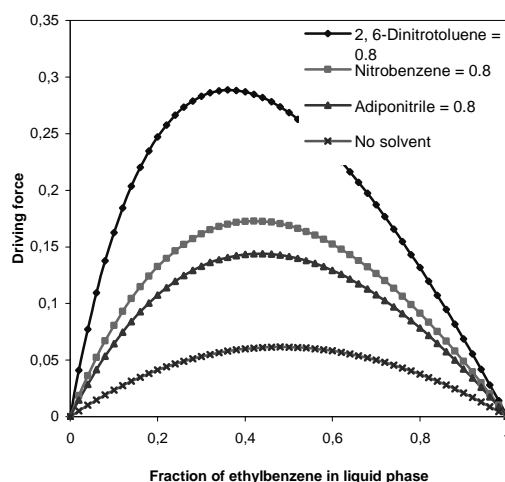


**Figure 1.** Solvent free driving force diagrams for styrene/ethylbenzene with the Nitrobenzene, 2,6-dinitrotoluene and Adiponitrile

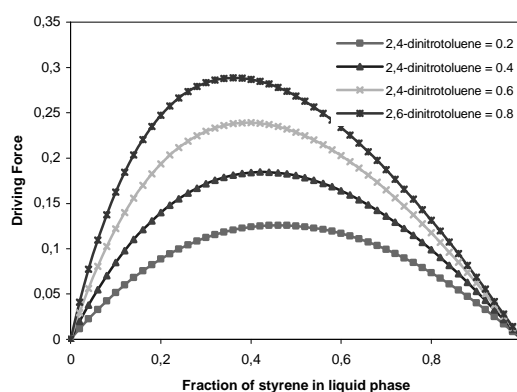


**Figure 2.** Solvent free driving force of the Styrene/Ethylbenzene with the 2,6-dinitrotoluene

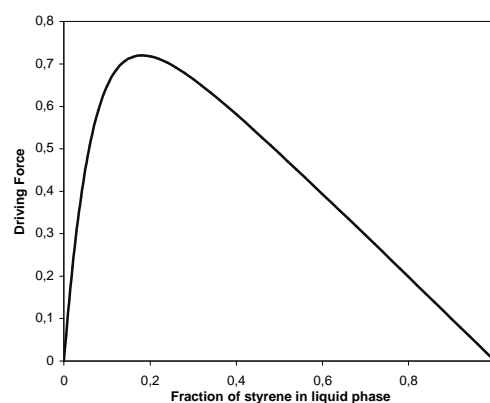


**Figure 3.** Styrene/2,6-dinitrotoluene driving force at 1 atm

The generated alternative flowsheet for the styrene process has been simulated in Pro/II with the design parameters determined by means of driving force based method. The results are given in Table 2. The results show that, using extractive distillation as alternative to

distillation column in styrene to separate styrene and ethylbenzene show good potential for energy saving. That is, replacing a distillation by extractive distillation will save energy. By using extractive distillation as alternative to distillation the energy saving is 76.50%.

**Table 2.** Comparison of results (using a distillation and extractive distillation to separate styrene and ethylbenzene)

Column	Distillation (base case)	Alternative 1 Extractive Distillation	
		Column I	Column II
Number of plates	115	40	10
Feed plate location	36	23	8
Reboiler Duty (MM J/hr)	$3.736 \times 10^5$	$6.972 \times 10^4$	$1.98 \times 10^4$
Purity of Styrene	99.90%	/	99.5%

Other alternatives based on liquid liquid extraction, absorption and membrane separation are currently being investigated. The reverse approach will be used to identify the final design details for all these alternatives.

### Conclusions

The benefit of employing the reverse approach is that by solving for the constitutive variables directly from the balance equations of the process model, it is possible to define the design (retrofit) targets. Matching the target through a generate and test procedure then becomes relatively easy to achieve. Results from the case study indicates good potential for energy saving by replacing a distillation by extractive distillation as alternative for separate ethylbenzene from styrene in the styrene process.

### Acknowledgements

The author greatly acknowledges Libyan petroleum institute for supporting this project.

### References

1. L. d'Anterrosches. Process flow Sheet Generation and Design through a Group Contribution Approach. PhD Thesis, Technical University of Denmark, 2005.
2. C. Jakslund. Separation Process Design and Synthesis Based on Thermodynamic Insights. PhD thesis, Technical University of Denmark, 1996.
3. E. Bek-Pedersen. Synthesis and Design of Distillation based Separation Schemes. PhD thesis, Technical University of Denmark, 2003.





## Christian Lund Rasmussen

Phone: +45 4525 2964  
Fax: +45 4525 2258  
E-mail: CLR@kt.dtu.dk  
WWW: <http://www.student.dtu.dk/~s973578>  
Supervisor: Peter Glarborg

### Ph.D. Study

Started: February 2004  
To be completed: April 2007

## Direct Partial Oxidation of Natural Gas to Liquid Chemicals

### Abstract

Direct partial oxidation of natural gas to liquid chemicals has a strong potential to improve natural gas recovery from remote resources. The project focuses on the direct homogeneous conversion of natural gas to methanol and, in particular, the search for optimal reaction conditions to provide high yields of the desired product. The work involves a fundamental experimental and kinetic modeling study of hydrocarbon combustion chemistry under various conditions.

### Introduction

Natural gas is one of the World's most important resources for energy production as well as chemical feedstock. The direct partial oxidation of natural gas to liquid chemicals; preferably methanol, is known as the gas-to-liquid (GTL) process, where natural gas is converted to a readily transportable state in a simple one-step-process under fuel-rich, high pressure and relatively low temperature conditions. The GTL process exhibits a significant commercial potential by enabling an increased utilization of the abundant natural gas reserves that are allocated in remote areas of the Planet. The partial oxidation of natural gas has been extensively explored over several decades, but past efforts to obtain competitive yields of methanol have been unsuccessful due to a lack of understanding of the complicated free radical mechanisms that governs the process. Consequently, it is necessary to study the chemistry on an elementary level before a process optimization can be attempted. This can be achieved by the use of detailed chemical kinetic modeling and well-defined experimental measurements.

### From Fundamental Understanding to Process Optimization

The available studies in the field have demonstrated that low temperatures and high pressure in the range of 600-800 K and 50-100 bars respectively, along with a high methane/oxygen ratio ( $\text{CH}_4/\text{O}_2$ ) in the feed (range 10-30), are key parameters to obtain high selectivity's of methanol ( $\text{CH}_3\text{OH}$ ). Investigations at these conditions impose some difficulties as they require methane concentrations in the range of 90-95% resulting in a

significant heat release during the conversion. This makes it almost impossible to conduct a well-defined experimental investigation. As a consequence, this project initially abandons the focus on the optimal conditions in favor of a search for the fundamental mechanisms that govern natural gas oxidation at an extended range of process conditions. When a satisfactory disclosure of the kinetic scheme is completed, these results will eventually be utilized for a determination of the optimal process conditions using a numerical global optimization routine that has been developed by C.L. Rasmussen.

### Detailed Chemical Kinetic Modeling

Conversion of hydrocarbon fuels in combustion processes is the result of a complex chain of fast radical reactions that propagate towards the terminal combustion products through subsequent formation and consumption of reactive radical species; e.g. atomic hydrogen (H), oxygen (O), hydroxyl (OH), hydrogenperoxyl ( $\text{HO}_2$ ), and methyl ( $\text{CH}_3$ ). It is fairly easy to convert measurements of the fuel conversion to empirical rate expressions. However, empirical models are very sensitive to model extrapolation outside the validated range of conditions, including changes in the reactor design, which is a common problem during e.g. industrial scale-up.

Detailed chemical kinetic models (DCKM) are in contrast to empirical models. They are comprehensive models that approach chemical mechanisms on an elementary reaction level. Consequently, DCKMs do not include empirical constants. DCKMs are typically developed in connection to the optimization of a

specific process, but the mechanistic description of the chemistry makes them independent of the process and allows model extrapolation to reaction conditions outside the range of experimental verification with an expected accurate response.

The task of describing the interactions between hundreds of very fast radical reactions is greatly simplified by dividing the system into subsystems that can be analyzed individually. Chemical kinetic reaction mechanisms are connected in a strictly hierarchical structure where the mechanisms of complex molecules include submechanisms of more simple components. Hence, oxidation of CO in moist air includes the kinetics of the H<sub>2</sub>/O<sub>2</sub>-system. The resulting CO/H<sub>2</sub>/O<sub>2</sub>-mechanism is a subsystem of the kinetics of methane oxidation, and so forth.

In this project, a DCKM has been developed to provide accurate predictions of the oxidation chemistry of C<sub>1-2</sub> fuels in the presence or absence of NO<sub>x</sub> and, to some extent, SO<sub>2</sub>/H<sub>2</sub>S. The designated operational range of the model includes pressures from atmospheric to about 100 bars and temperatures from roughly 500 to 1100 K. At the present time, the model includes more than a thousand reversible elementary reactions, of which about half of them are used to describe the pure hydrocarbon oxidation chemistry. The model is designed to run with the CHEMKIN<sup>®</sup> software.

#### Oxidation of Methane at High Pressure

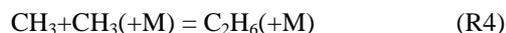
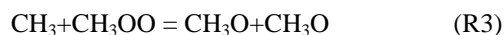
In order to illustrate the level of details used by the developed DCKM, this section provides an outline of the most important reaction pathways when methane (CH<sub>4</sub>) is oxidized at high pressure. An overview of the reaction network is initially presented in Fig. 1.

The reaction sequence is initiation by H-abstraction from CH<sub>4</sub>, which is facilitated by hydroxyl radicals (OH). (' = ' represents a reversible reaction, i.e. →/←)



The pool of methyl radicals (CH<sub>3</sub>) has three primary drains with their individual contributions being highly

dependent on the reaction conditions:



M represents an arbitrary collision partner, which is proportional to the pressure.

The contribution to the CH<sub>3</sub> removal from the self-recombination reaction (R4) to ethane (C<sub>2</sub>H<sub>6</sub>) is low except at fuel-rich conditions (ϕ > 1). In addition, higher temperatures and low absolute concentrations of O<sub>2</sub> favor this pathway. Reaction (R2) is the predominant pathway to methylperoxy radicals (CH<sub>3</sub>OO), which means that the carbon flux through (R3) is constrained by the flux through (R2). The thermal stability of CH<sub>3</sub>OO is poor, but high pressure combined with relatively low temperatures promote the formation and make CH<sub>3</sub>OO a key intermediate product.

A fraction of the CH<sub>3</sub>OO radicals is intermediately converted to methyl peroxide (CH<sub>3</sub>OOH) through H-addition from hydrogen peroxy radicals (HO<sub>2</sub>) or hydrogen peroxide (H<sub>2</sub>O<sub>2</sub>) instead of being directly converted to methoxy radicals (CH<sub>3</sub>O) via reaction (R3).

The intermediate formation of CH<sub>3</sub>OOH only constitutes a minor detour of the hydrocarbon flux since CH<sub>3</sub>OOH subsequently decomposes to CH<sub>3</sub>O. The reaction sequence is outlined in (R5)-(R7).



Excess O<sub>2</sub> combined with low temperatures and high pressure promote formation of peroxides and peroxy radicals, and a significant carbon flux is expected to pass through CH<sub>3</sub>OOH under oxidizing conditions (ϕ <

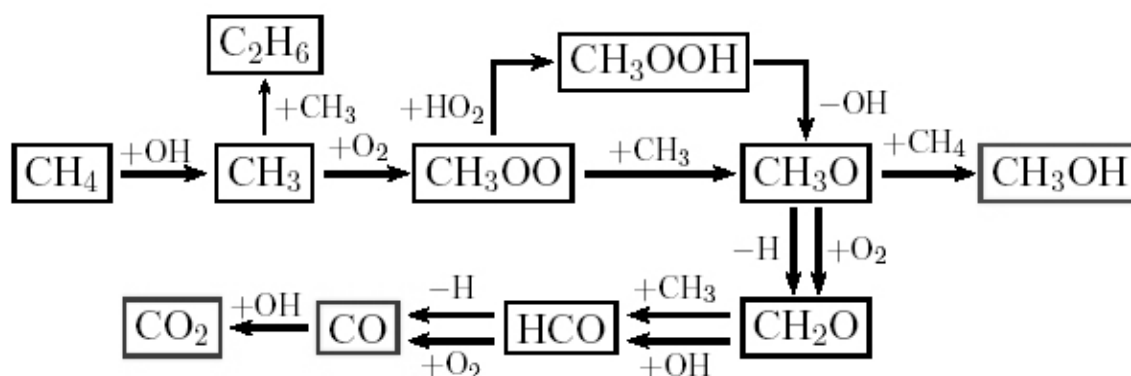
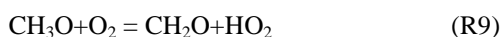
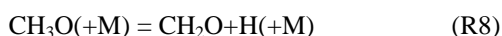


**Figure 1:** Primary reaction pathway when methane is oxidized at high pressure. Framed species are methane (CH<sub>4</sub>), methyl radical (CH<sub>3</sub>), ethane (C<sub>2</sub>H<sub>6</sub>), methylperoxy radical (CH<sub>3</sub>OO), methylperoxide (CH<sub>3</sub>OOH), methoxy radical (CH<sub>3</sub>O), methanol (CH<sub>3</sub>OH), formaldehyde (CH<sub>2</sub>O), formyl (HCO), carbonmonoxide (CO), and carbondioxide (CO<sub>2</sub>). Other species are important reactants (+) or products (-). The attractive product is methanol, while the deep oxidation products CO and CO<sub>2</sub> are unwanted.

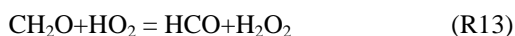
1). Reducing conditions combined with a low absolute concentration of O<sub>2</sub> favor CH<sub>3</sub> as the primary reactant with CH<sub>3</sub>OO via (R3), while by-passing CH<sub>3</sub>OOH. The formation of CH<sub>3</sub>OOH is largely determined by the key ratio (R3)/(R5+R6). A decreasing ratio is equivalent to an increasing net-production of OH radicals via intermediate formation and decomposition of CH<sub>3</sub>OOH. OH facilitates a number of the key elementary steps including the initial conversion of CH<sub>4</sub>.

CH<sub>3</sub>O is typically converted to formaldehyde (CH<sub>2</sub>O); either through decomposition (R8) or reaction with O<sub>2</sub> (R9). However, it may also be converted to methanol (CH<sub>3</sub>OH) by H-addition from CH<sub>4</sub>.



Reaction (R9) and (R10) require high absolute concentrations of O<sub>2</sub> and CH<sub>4</sub> respectively. If CH<sub>3</sub>O collides with any other compounds, conversion will proceed according to (R8). This explains why a high CH<sub>4</sub>/O<sub>2</sub> ratio favors methanol formation, as previously stated, while the opposite has an adverse effect and increases production of CO and CO<sub>2</sub>. Based on experiences from the literature 10 < CH<sub>4</sub>/O<sub>2</sub> < 30 is recommended in order to obtain high methanol yields, while a reasonable conversion of CH<sub>4</sub> is still obtained.

Oxidation of CH<sub>2</sub>O to formyl radicals (HCO) can be operated by a number of radical species depending on the reaction conditions. The most important reactions are shown in (R11)-(R14).



Reaction (R11) and (R12) are only important at reducing conditions, while (R13), and especially reaction (R14), predominate at oxidizing conditions.

HCO is converted to CO either by decomposition or by H-abstraction performed by O<sub>2</sub> via reaction (R15) and (R16) respectively. The ratio (R15)/(R16) changes from > 1 to << 1 as the reaction conditions change from reducing towards oxidizing conditions.



CO is converted to CO<sub>2</sub> through reaction with OH through intermediate formation of HOCO, as shown in (R17). This conversion is limited under reducing conditions.



### High Pressure Flow Reactor

In order to validate the performance of the developed DCKM, well-defined experimental data are required. However, relevant data are rarely encountered in the literature at pressures above 10 bars. For this reason, a novel laboratory-scale high pressure laminar flow reactor setup has been developed to enable well-defined investigations of most homogeneous combustion systems involving gaseous reactants of the elements H, O, C, N and S at pressures from 10 to 100 bars and temperatures up to 925 K [1,2]. A schematic overview of the system is provided in Fig. 2. The reaction takes place in a tubular flow reactor made of quartz to minimize surface reactions (i.d. 8 mm, o.d. 10 mm, lgt. 1545 mm). The reactor is enclosed in a stainless steel tube (i.d. 22 mm, o.d. 38 mm) that acts as a pressure shell. A pressure control system automatically delivers N<sub>2</sub> to the shell-side of the reactor to obtain a pressure similar to that inside the quartz tube, thus avoiding devastating pressure gradients across the fragile quartz glass. The steel tube is placed in an oven with three individually controlled electrical heating elements that produce an isothermal reaction zone of approx. 50 cm. Reactant gases are premixed before entering the reactor. Product analysis is conducted by on-line GC-TCD/FID and conventional IR- and chemiluminescence based gas analyzers. The system enables measurements of concentration profiles as a function of the reactor temperature including the products O<sub>2</sub>, N<sub>2</sub>, CO, CO<sub>2</sub>, most hydrocarbons (<C<sub>5-6</sub>), several oxygenated hydrocarbons, some nitrated hydrocarbons, NO<sub>x</sub>, SO<sub>2</sub> and H<sub>2</sub>S.

Even though the system is designed for homogeneous gas phase oxidation of light hydrocarbons at conditions relevant to this project, a secondary objective is the versatile application of the setup with respect to other homogeneous systems, e.g. sulfur chemistry. This is strongly encouraged by the fact that well-defined experimental results in the literature at high pressures are extremely rare for most homogeneous systems.

### Presentation of Selected Results

Since the commissioning of the high pressure flow reactor setup in the Autumn of 2004, a number of experimental campaigns have been completed in connection to the project. These include investigations of CO/H<sub>2</sub>/O<sub>2</sub>/NO<sub>x</sub>, CH<sub>4</sub>/O<sub>2</sub>, CH<sub>4</sub>/C<sub>2</sub>H<sub>6</sub>/O<sub>2</sub>, C<sub>2</sub>H<sub>6</sub>/O<sub>2</sub>, CH<sub>4</sub>/O<sub>2</sub>/NO<sub>x</sub>, and CH<sub>4</sub>/O<sub>2</sub>/H<sub>2</sub>S at high pressure and reaction stoichiometries varying from highly reducing to oxidizing conditions. Selected results from this work are presented in Fig. 3-6. Points represent measured concentrations of important stable species as a function of the reactor temperature, while lines denote corresponding model predictions.

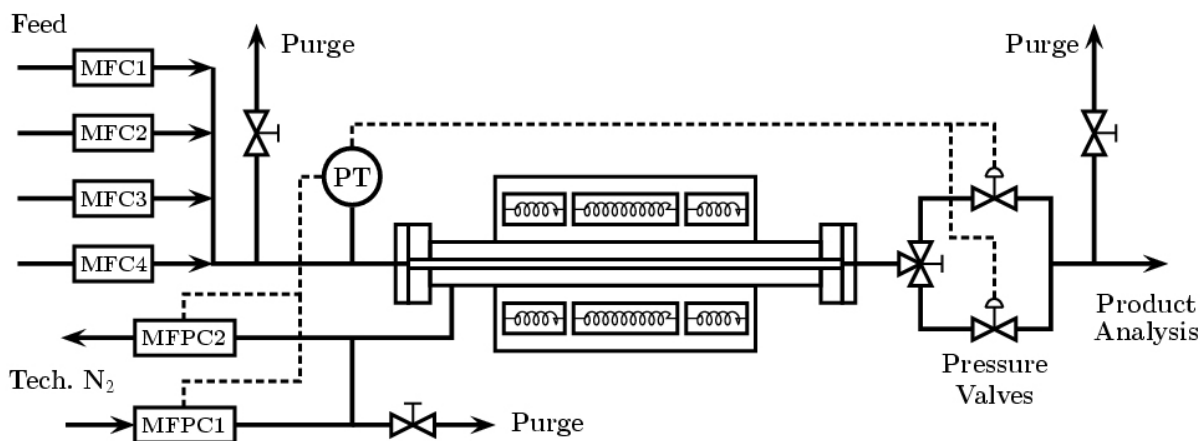


**Figure 2:** Schematic overview of the high pressure flow reactor system [1]. Reactant gases are premixed from up to four different digital mass flow controllers (MFC) before the reactor inlet.  $N_2$  is supplied to the pressure shell through two thermal mass flow pressure controllers (MFPC). The steel shell with the tubular quartz reactor inside is positioned in an electrically heated oven with three heating elements. Reduction of the pressure to atmospheric level is obtained in the downstream section through one of two pneumatic pressure valves. A pressure transducer (PT) provides the signal for the acting pressure control loops. The simplified control loops are indicated with dashed lines.

The results will not be further analyzed. Instead, the attention should be drawn to the satisfactory agreement between the experimental and numerical data. This indicates that the governing reaction mechanisms are well-described by the model.

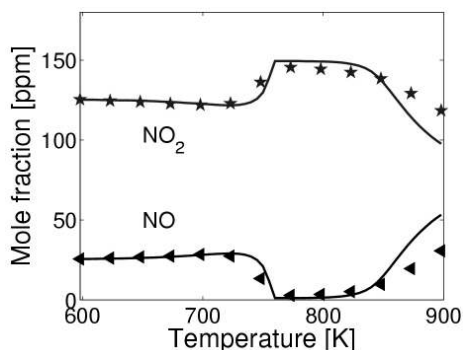
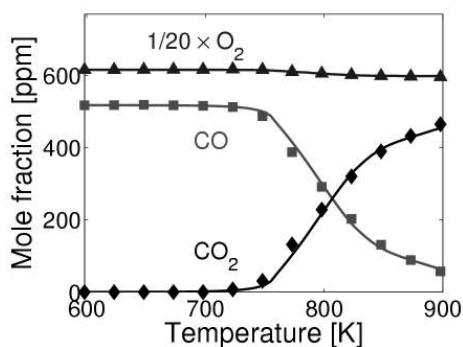


**Figure 3:** Conversion of  $CO/H_2/O_2/NO_x$  at 50 bar and strongly oxidizing conditions ( $\phi = 0.06$ ) [1]. Reactants are diluted with  $N_2$ .

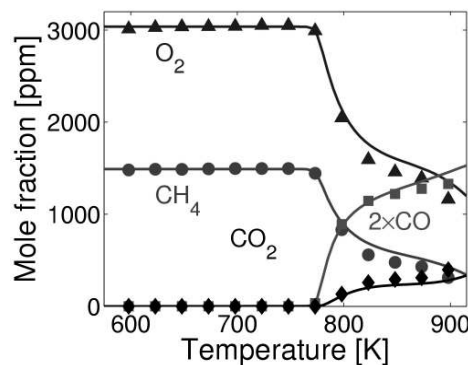


**Figure 4:** Conversion of  $CH_4/O_2$  at 90 bar and stoichiometric conditions ( $\phi = 0.98$ ). Reactants are diluted with  $N_2$ .

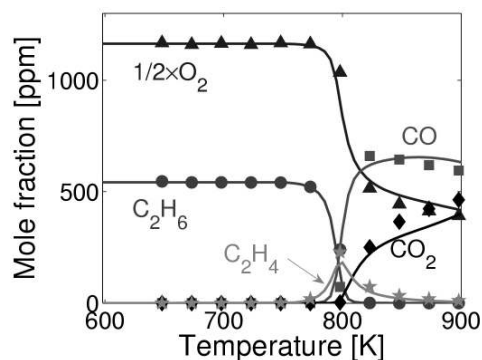


**Figure 5:** Conversion of  $C_2H_6/O_2$  at 50 bar and weakly oxidizing conditions ( $\phi = 0.82$ ) [3]. Reactants are diluted with  $N_2$ .

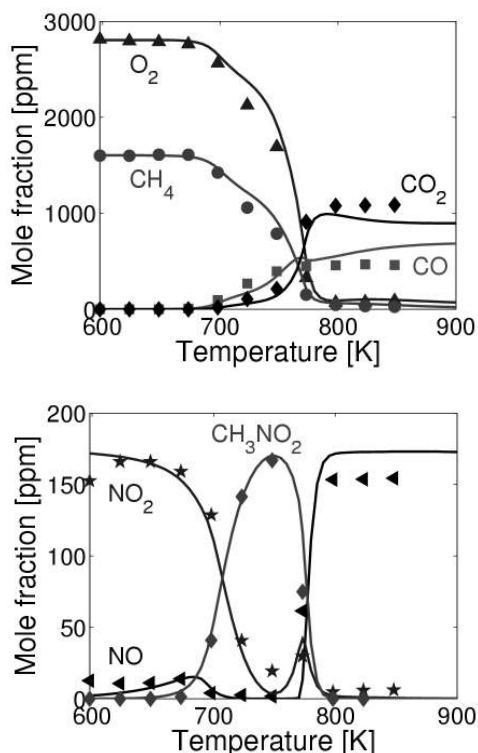


**Figure 6:** Conversion of  $\text{CH}_4/\text{O}_2/\text{NO}_x$  at 100 bar and weakly reducing conditions ( $\phi = 1.09$ ). Reactants are diluted with  $\text{N}_2$ . Top: The initiation temperature of the  $\text{CH}_4/\text{O}_2$  conversion is decreased due to the presence of  $\text{NO}_x$  (compare with Fig. 4). Bottom: Intermediate formation of nitromethane ( $\text{CH}_3\text{NO}_2$ ) is characteristic at high pressure [4].

### Global Process Optimization

Figure 3-6 show that the DCKM indeed is able to predict the fundamental mechanisms of hydrocarbon combustion at high pressure. Soon, this knowledge will be utilized to determine optimal process conditions that provide high yields of methanol. A numerical global optimization routine will be applied for this task.

The routine uses interval analysis [5] to narrow down the global minimizer of an objective function within a finite region of the independent variables. The intervals become multidimensional if more than one independent variable appears in the objective function. All possible combinations of independent variables within a multidimensional interval result in function values that lie within an upper and a lower bound. When the lower bound of a function value span exceeds the upper bound from another interval, it is evident that the former interval does not contain the global minimizer, in which case it is safe to discard this interval from further analysis. By continuously performing this comparison while the intervals are refined according to the listed criteria below, more and more intervals can be discarded until a single narrow interval remains that contains the global minimizer. The principle is illustrated in Fig. 7.

- Split an interval in two. Recalculate the function value span and compare with other intervals.
- Scrap intervals that contain monotonically behaving function values, i.e.  $0 \notin f'(x)$ .
- When  $0 \notin f''(x)$ , run a Newton iteration within the specific interval to find the local minimizer, i.e.  $f'(x) = 0$ .

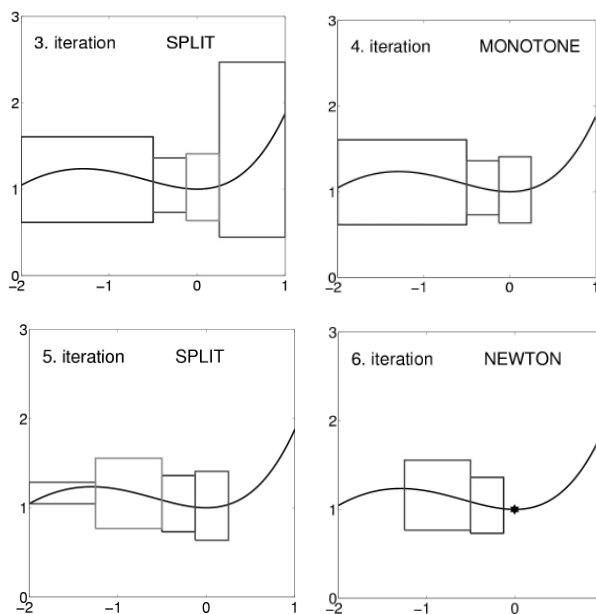


**Figure 7:** 2D-illustration of the global optimization routine based on the objective function  $f(x) = e^x - \sin(x)$  for  $X_0 = [-2, 1]$ . The widths of the squares represent intervals of  $x$  (the independent variable), while their heights indicate the corresponding function value span. The global minimizer in the example is ascertained after 11 iterations.

### Conclusions

Direct partial oxidation of natural gas to methanol at homogeneous, high pressure, and relatively low temperatures conditions, is an attractive industrial process with a significant potential to improve the utilization of the World's natural gas resources. An important obstacle in the development of this process is the lack of understanding of the complex free radical mechanisms that govern the hydrocarbon conversion.

The project has successfully elucidated a number of fundamental mechanisms related to hydrocarbon combustion. These mechanisms are described in a comprehensive detailed chemical kinetic model and validated against experimental results conducted at well-defined conditions in a novel laboratory-scale high pressure flow reactor setup. This improved understanding of fundamental combustion mechanisms will soon be utilized to determine optimal process conditions for methanol production using a global optimization routine developed by the author.

### Acknowledgments

This work is part of the CHEC (Combustion and Harmful Emission Control) Research Center funded a.o. by the Technical University of Denmark, the Danish Technical Research Council, the European Union, the Nordic Energy Research, Dong Energy A/S, Vattenfall A.B., F L Smidth A/S, and Public Service Obligation funds from **Energinet.dk** and the Danish Energy Research program. This particular project is financed by the Danish Technical Research Council and the Technical University of Denmark.

### References

1. C.L. Rasmussen, J. Hansen, P. Marshall, P. Glarborg, Experimental Measurements and Kinetic Modeling of CO/H<sub>2</sub>/O<sub>2</sub>/NO<sub>x</sub> Conversion at High Pressure, to be submitted, 2006.
2. C.L. Rasmussen, A.E. Rasmussen, J. Hansen, P. Glarborg, 045-12 High Pressure Flow Reactor – Operations Manual, Technical Report R0604, CHEC, Dept. of Chemical Engineering (KT), DTU, 2006.
3. J.G. Jakobsen, Direct Conversion of Natural Gas to Liquid Fuels, M.Sc. Thesis, Dept. of Chemical Engineering (KT), DTU, 2006.
4. C.L. Rasmussen, P. Glarborg, Direct Partial Oxidation of Natural Gas to Liquid Chemicals, Poster P10, Dansk Kemiingeniør Konference, DTU, Kgs. Lyngby, May-Jun., 2006.
5. O. Caprani, K. Madsen, H.B. Nielsen, Introduction to Interval Analysis, Report, Dept. of Informatics and Mathematical Modeling (IMM), DTU, 2002.

### List of Publications

1. C.L. Rasmussen, P. Glarborg, Dansk Kemi 85(12), 30-32, 2004.
2. C.L. Rasmussen, P. Glarborg, Dansk Kemi 86(2), 30-33, 2005.
3. C.L. Rasmussen, Direct Partial Oxidation of Natural Gas to Liquid Chemicals [web page], www.student.dtu.dk/~s973578, Feb. 2006.
4. C.L. Rasmussen, A.E. Rasmussen, P. Glarborg; The Sensitizing Effect of NO<sub>x</sub> on CH<sub>4</sub> Oxidation at High Pressure. - Experimental and Modeling Investigation, Proceedings of the 1<sup>st</sup> Baltic Combustion Meeting, The Polish Section of the Combustion Institute, Warszawa, 125-128, Nov. 2005.
5. C.L. Rasmussen, P. Glarborg, Direct Partial Oxidation of Natural Gas to Liquid Chemicals, Poster P10, Dansk Kemiingeniør Konference, DTU, Kgs. Lyngby, May-Jun., 2006.
6. C.L. Rasmussen, P. Glarborg, P. Marshall, Mechanisms of Radical Removal by SO<sub>2</sub>, accepted for publication, Proc. Combust. Inst., 31, 2006.
7. C.L. Rasmussen, J. Hansen, P. Marshall, P. Glarborg, Experimental Measurements and Kinetic Modeling of CO/H<sub>2</sub>/O<sub>2</sub>/NO<sub>x</sub> Conversion at High Pressure, to be submitted, 2006.

8. C.L. Rasmussen, A.E. Rasmussen, J. Hansen, P. Glarborg, 045-12 High Pressure Flow Reactor – Operations Manual, Technical Report R0604, CHEC, Dept. of Chemical Engineering (KT), DTU, 2006.
9. C.L. Rasmussen, J. Hansen, P. Glarborg, Teoretiske og praktiske undersøgelser af homogen gasfasekemi ved højt tryk, accepted for publication, Dansk Kemi 87(12), 2006.

**Lisa Rosgaard**

Phone: +45 4446 0623  
Fax: +45 4442 8600  
E-mail: S040053@student.dtu.dk  
WWW: <http://www.kt.dtu.dk>  
Supervisors: Anne S. Meyer  
Sven Pedersen, Novozymes

**Ph.D. Study**

Started: May 2004  
To be completed: April 2007

## Enzymatic Hydrolysis of Lignocellulose

**Abstract**

Cellulases play an important role in the biomass to ethanol process. Currently research is being invested in elucidating how to make the process feasible in relation to the pretreatment process, the enzymatic hydrolysis, substrate loading and the factors influence the optimum enzyme system. One of the aims of this project is to evaluate enzyme mixtures from fungi to potentially boost the activity of a known cellulase product. Furthermore the effect of fed-batch loading of pretreated lignocellulose in relation to enzymatic hydrolysis is being investigated.

**Introduction**

Starch and sucrose stocks are well-established raw materials for industrial ethanol manufacture that provide alcohol for alcoholic beverages, various technical purposes as well as fuel ethanol for blending with gasoline [1, 2]. For many years attention has been focused on also utilizing lignocellulosic biomass, e.g. straw, softwood, hardwood chips, and corn stover for industrial production of ethanol for fuel purposes [3, 4].

Significant research efforts have been invested in evaluating and understanding the enzymatic hydrolysis of lignocellulosic substrates by cellulases produced by the fungus *Trichoderma reesei* [1-3]. Commercial products of various *T. reesei* isolates have long been available for cereal foods, brewing, and fruit and vegetable processing and have also been widely evaluated and applied in relation to bioethanol production processes [4-5]. Because of the high levels of cellulases produced by *T. reesei* strains, these seem to be a well-suited starting point for obtaining improved cellulose hydrolysis via boosting of certain cellulase activities, rather than by complete replacement with a novel system from another cellulolytic fungus. We speculated that enzymes from these fungal strains might enhance the cellulolytic effect of Celluclast if the two enzyme systems were mixed to test the hypothesis that boosting of a widely used *T. reesei* cellulase product by addition of enzymes from other fungi might be a fruitful avenue for obtaining improved cellulose hydrolysis.

**Specific objectives**

The objectives of the Ph. D. study are to make the enzymatic hydrolysis of barley and wheat straw more

effective in relation to optimising the enzyme mixture applied, and the enzyme and substrate loading with respect to glucose yield and change in viscosity during hydrolysis.

**Results**

To assess the potential cellulolytic boosting effect of the novel fungal cellulase systems, a low dosage, corresponding to 10 wt % of the total enzyme protein load, of each of the fungal fermentation broths was supplemented to an enzyme mixture comprising Celluclast and NS 188 (8 FPU and 13 CBU per gram TS, respectively). To evaluate the effect of the pH and temperature on the enzymatic reaction, the hydrolytic efficacy of each of six selected fungal broths was examined in a surface response experimental template comprising a pH range from 3.5 to 6.5 and a temperature range from 35 to 65 °C. There were no statistically significant main or interactive effects of the reaction parameters on any of the fungal broths. The cellulose conversion was, however, significantly increased by addition of the fermentation broth samples compared to the yields obtained with the benchmark Celluclast + NS 188 dosage (BM) (Figure 1). Notably, at pH 5 and 50 °C five of the six broth samples, i.e., all except the *C. thermophilum* sample, gave glucose yields (and cellulose conversion) that were equivalent to or higher than those obtained with twice the benchmark loading of Celluclast supplemented with NS 188 (Figure 1, black stars).

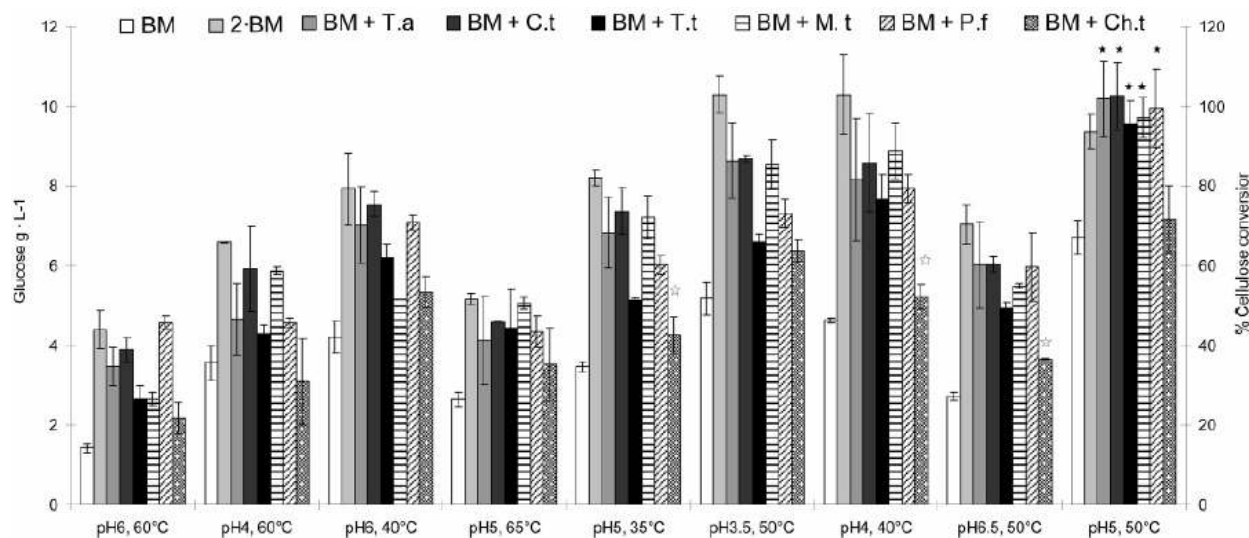


**Figure 1.** Diagram displaying the glucose release and extent of cellulose conversion of 6 h enzymatic hydrolyses of steam-pretreated barley straw at 2% TS by weight. The benchmark dosage (BM) was 2.3 mg Celluclast and 1 mg NS 188 per gram reaction (~8 FPU and 13 CBU, respectively, per g TS); 2-BM was twice the Celluclast benchmark dosage (~16 FPU and 13 CBU, respectively, per gram TS). Abbreviated names for fungal producers are the same as those in Table 1. The fungal enzyme extracts were added to the same final protein concentration of 0.0348 mg.

A few isolated sets of results, e.g., the low glucose yields (cellulose conversion) obtained for the treatments at pH 6, 40 °C with BM + *M. thermophila* and BM + *C. thermophilum* and with the BM + *C. thermophilum* after the treatments at pH 5, 35 °C; pH 4, 40 °C, and pH 6.5, 50 °C (Figure 1, white stars), indicated that the *C. thermophilum* broth was apparently the least efficient and the most sensitive to pH changes among the broth preparations. However, within the experimental conditions evaluated, none of the other fungal broths stood out as performing significantly better or worse than the others (Figure 1). The findings that supplementation with 10% of the total enzyme protein gave glucose yields equivalent to twice the benchmark dosage of Celluclast + NS 188 indicated the significant cellulolytic boosting potential of the five best broths.

The fermentation broths were also applied to a pure, more crystalline cellulose substrate, Avicel, and examined under different reaction conditions using the surface response design. To supplement the glucose quantification, the amount of reducing ends was also quantified. If oligomers larger than cellobiose would be produced upon addition of the fermentation broths, it was expected that the levels of reducing ends would be higher than the neat glucose levels analyzed by HPAEC.

The results showed no main effects or significant interacting effects of pH or temperature with addition of either fermentation broths to Avicel. The highest effect on glucose release was found at the center point reaction (pH 5, 50 °C). However, the amount of reducing ends determined by addition of DNS reagent showed a significant increase in reducing ends ( $\text{mol}\cdot\text{L}^{-1}$ ) when any of the fermentation broths were added compared to the effect of Celluclast and NS 188 alone (Figure 2, white bars).

This effect did not correlate to the theoretical amount of reducing ends as calculated from the glucose concentration determined by HPAEC (Figure 2, compare white bars with dark gray bars) nor to the sum of reducing ends theoretically present in the samples arising from glucose and cellobiose (Figure 2, compare white bars with light gray bars). These results suggest the presence of more active endoglucanases or a skewed ratio of endoglucanase and cellobiohydrolases in the crude fermentation broths compared to the well described cellulase spectrum present in Celluclast. These results therefore emphasize that the nature of the substrate has a significant impact on the observed effects of cellulolytic enzyme mixtures.

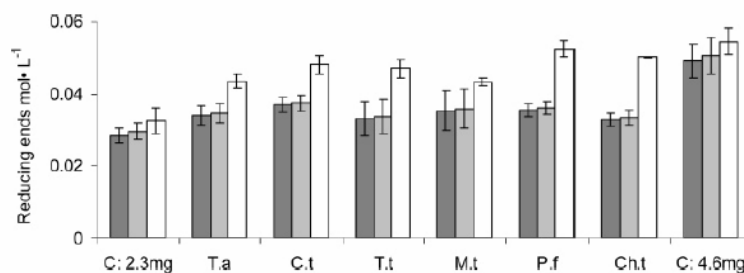


**Figure 2.** Diagram displaying the amount of reducing ends ( $\text{mol}\cdot\text{L}^{-1}$ ) produced from hydrolysis of Avicel determined by addition of DNS (white bars), equivalents of reducing ends ( $\text{mol}\cdot\text{L}^{-1}$ ) calculated from glucose and cellobiose (light gray bars) determined by HPAEC, and equivalents of reducing ends ( $\text{mol}\cdot\text{L}^{-1}$ ) calculated from the concentration of glucose determined by HPAEC (dark gray bars). Abbreviated names used for fungal enzyme producers are the same as those as in Figure 1. The calculated moles of reducing ends correspond to data from the center points shown in Figure 1.

### Conclusions and future work

The results showed that it is possible to increase the cellulytic activity of Celluclast supplemented with  $\beta$ -glucosidase (NS 188) by addition of crude fermentation broths from various fungal sources. Although the fungal sources were classified as thermophilic, there were no effects or shifts in the temperature optimum with the fermentation broths applied compared to that asserted by Celluclast + NS 188 alone. Since addition of the fermentation broth did not result in an increase in glucose production when applied to Avicel but did increase the amount of reducing ends produced, it is concluded that the experimental fungal broths contained endoglucanase activity(ies) that were more active on pure cellulose than those present in the *T. reesei* Celluclast preparation

In many cases, the lignocellulosic residues must undergo pretreatment to partly remove lignin and hemicellulose to make the cellulose accessible to enzymatic hydrolysis [6]. The pretreatment procedure often generates degradation products from hemicellulose sugars and lignin which are inhibitory to both yeast and enzymes [7] and might influence the enzymatic mixture necessary for efficient hydrolysis. The pretreatment also renders the resulting cellulose residue highly water retaining. When it is considered that current starch based processes are conducted at substrate loadings as high as 33-37 w/w % DM [8, 9], the requirement for high substrate dry matter loadings pose a particularly competitive challenge for the enzymatic conversion of lignocellulosic substrates. A way to increase the solids loading for the enzymatic hydrolysis might be to add multiple batches of substrate to overcome the extremely high initial viscosity which hinders blending and slows hydrolysis.

### Acknowledgment

This research was partially financed by the European Commission Framework V, contract no. NNE5/2001/685 (The Babilafuente Bioethanol Project).

### References

1. Stenberg, K, Bollok, M, Reczey, K, Galbe, M. *Biotechnol. Bioeng.* 68 (2000) 204-210.
2. Tengborg, C, Galbe, M, Zacchi, G. *Biotechnol. Prog.* 17 (2001) 110-117.
3. Palonen, H, Tjerneld, F, Zacchi, G, Tenkanen, M. J. *Biotechnol.* 107 (2004) 65-72.
4. Ryu, D. Y, Mandels, M. *Enzyme Microb. Technol.* 2 (1980) 91-102.
5. Nieves, R. A, Ehrman, C. I, Adney, W. S, Elander, R. T, Himmel, M. E. *World J. Microbiol. Biotechnol.* 14 (1998) 301-304.
6. Vinzant, T. B, Adney, W. S, Decker, S. R, Baker, J. O, Kinter, M. T, Sherman, N. E, Fox, J. W, Himmel, M. E *Appl. Biochem. Biotechnol.* 91/93 (2001) 99-107.
7. Palmqvist, E, Hahn-Hägerdal. *Bioresource Tech.* 74 (2000) 17- 24.

8. Thomas, K. C, Ingledew, W. M. *Jour. Industrial Microb.* 10 (1992) 61- 68.
9. Devantier, R, Pedersen, S, Olsson, L. *Biotechnol. Prod. Process Eng.* 68 (2005) 622- 629.

### List of publications.

Rosgaard, L, Andric, P, Johansen, K. D, Pedersen, S, Meyer, A. S. *Submitted to Applied Biochemistry and Biotechnology*

Rosgaard, L, Pedersen, S, Cherry, J. R, Harris, P, Meyer, A. S. *Biotech. Prog.* 22 (2006) 493- 498.





### Kavitha Chelakara Satyanarayana

Phone: +45 4525 2981  
Fax: +45 4525 2906  
E-mail: kac@kt.dtu.dk  
WWW: <http://www.capec.kt.dtu.dk>  
Supervisors: Jens Abildskov  
Rafiqul Gani, CAPEC

Ph.D. Study  
Started: June 2006  
To be completed: May 2009

## Molecular Modelling of Polymers Using Grid Technology

### Abstract

Establishing structure property relationship for polymer molecules is the main objective of this work, which involves of Cheminformatics and Computational chemistry. But as this work involves a handling of massive computations that are highly time and computer resource consuming, Grid technology is used to over come this problem. On the whole this work is basically on designing property prediction models for polymers using the combination of Cheminformatics, Computational chemistry and grid technology.

### Introduction

Increasing consumer demands for new and better chemical products based on specific properties, is driving the chemical, material and pharmaceutical industries to search for new chemicals and investigate whether they meet the specific demands of the end users. It is no longer feasible to depend on old methodologies which involve production and experimental testing of thousands of alternative chemicals for the specified properties, as they are time consuming, tedious and capital intensive. Emerging technologies involve the use of computer aided molecular design (CAMD) techniques that can partially replace the same. ProCAMD (a tool for computer aided molecular design) and ProPred (a tool for property prediction) are some of the established software that is finding an increasing use in the industry.

Using ProCAMD, it is relatively easy to generate and test the structures of relatively simple molecules (such as solvents and refrigerants) that match a set of desirable target properties, while, using ProPred it is possible to predict the properties of an organic molecule defined by its molecular structure. While these software are able to handle a wide range of organic chemicals, in order to extend the CAMD technique to structured chemicals like polymers, new property models are required. The objective of this work is to develop new property models for polymer properties based on analysis of the polymer structure and using the grid technology to reduce the model development time and effort.

### Specific Objectives

Generating structure property relationship for polymers is a challenging task from several decades. Different methods and approaches were made by several people till date, like additive group contribution method developed by van Krevelen [2], connectivity indices based property prediction methods for polymers by Bicerano [3], etc. These models were limited to few groups or parameters. Hence high accuracy cannot be expected. This evokes the necessity of using Marrero Gani group contribution method [1], which has a larger range of groups, classified under first-order, second-order and third-order groups, and may be used to generate a new polymer property prediction models.

Marrero and Gani (MG) group contribution method is described in the equation below:

$$f(X) = \sum_i N_i C_i + w \sum_j M_j D_j + z \sum_k O_k E_k \quad (1)$$

Where  $C_i$  is the contribution of the first-order group of type- $i$  that occurs  $N_i$  times,  $D_j$  is the contribution of the second-order group of type- $j$  that occurs  $M_j$  times and  $E_k$  is the contribution of the third-order group of type- $k$  that has  $O_k$  occurrences in a compound. In the first level of estimation, the constants  $w$  and  $z$  are assigned zero values because only first-order groups are employed. In the second level, the constant  $w$  and  $z$  are assigned unity and zero values respectively because only first- and second-order groups are involved while in the third level, both  $w$  and  $z$  is set to unity values. The left-hand

side of Eq. (1) is a simple function of  $f(X)$  of the target property X. The selection of this function has been based on the following criteria:

- The function has to achieve additivity in the contributions  $C_i$ ,  $D_j$  and  $E_k$ .
- It has to exhibit the best possible fit of the experimental data.
- It should provide good extrapolating capability and therefore, a wide range of applicability [1].

The inductive learning [4] method is the root of this work, where the experimental data set is collected, a model is derived from the data set and the properties are predicted.

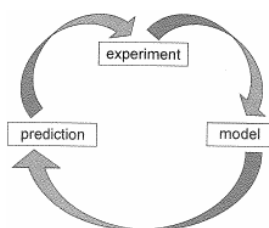


**Fig. 1** Inductive learning

Experimental data set of properties is collected. Using MG group contribution method, a model is generated, and property parameters for MG groups are estimated.

Since, the experimental data for polymers are limited and it may not be possible to estimate property parameters for all MG groups, connectivity index based property models are also developed simultaneously, so that contributions of missing groups can be predicted.

Application of Grid technology:

Grid computing, an emerging computing model that provides the ability to perform higher throughput computing by taking advantage of many networked computers to model a virtual computer architecture that is able to distribute process execution across a parallel infrastructure [5].

Property model and parameter estimation can be generated in parallel for different properties using Grid computing. This not only reduces the time of generating the models by using the freely available computer resources.

### Acknowledgements

The Ph.D. study is completely sponsored by NABIIT.

### References

1. J. Marrero, R. Gani, Fluid Phase Equilibria 183-184 (2001) 183-208.
2. D. W. van Krevelen, Properties of Polymers, Elsevier –third edition 1990.

3. Jozef Bicerano, Prediction of Polymer properties, Marcel Dekker, Inc.- third edition, revised and expanded 2002.
4. J. Gasteiger, T. Engel, Cheminformatics, Wiley-VCH, 2003, p 2-3.
5. [http://en.wikipedia.org/wiki/Grid\\_computing](http://en.wikipedia.org/wiki/Grid_computing)



**Daniel Schäpper**  
Phone: +45 4525 2960  
Fax: +45 4593 2906  
E-mail: dsc@kt.dtu.dk  
WWW: <http://www.kt.dtu.dk>  
Supervisors: Krist V. Gernaey  
Anna Eliasson Lantz, BioCentrum  
Stuart Stocks, Novozymes A/S

Ph.D. Study  
Started: May 2006  
To be completed: April 2009

## Continuous Culture Microbioreactors

### Abstract

The current microbioreactors mostly operate as fed-batch or continuous culture with *E. coli* as culture strain. This projects aims to design a microbioreactor running continuous cultures of *S. cerevisiae* in a reactor volume of approximately 100  $\mu$ L. The most important culture parameters can be measured online allowing for a high information-per-experiment ratio. Industrial relevance will be proven through comparisons of continuous culture microbioreactor experimental data with bench-scale experiments performed at BioCentrum-DTU.

### Introduction

Biotechnology plays an increasingly important role in production processes in the food, the chemical and the pharmaceutical industry. Well-known examples of biotech-based products that have an important function in the life of many people are enzymes used in laundry detergents, pharmaceuticals such as insulin, etc.

However, starting up a new biotechnological production is usually preceded by a tremendous research effort in which for example the productivity of different candidate production strains is compared (=screening). Usually, such screening is done in shake flask cultures. In a later stage of production process development, experiments done in bench scale reactors are performed to investigate the influence of process conditions on productivity.

Experiments done in shake flasks (typically with a volume of 100 mL to 1 L) are easy to set up. However, shake flask cultures only allow batch experiments, and the information gained per experiment is limited: typically only end-point measurements of for example the product quality are performed. If additional measurements are needed, manual sampling is required, which additionally disturbs the culture. Compared to shake flasks, bench scale reactors (typically with a volume of 1 to 10 L) have the advantage that they allow online measurements. Moreover, bench scale reactors are flexible since they can be operated in batch or fed-batch, but also as a continuous culture. However, the work effort needed to prepare, operate and subsequently clean bench scale reactors is vast.

Summarizing, biotechnological process development is expensive, for example because both traditional cultivation methods work with substantial volumes that

in turn then require preparation of the appropriate amount of expensive nutrient media.

### Motivation

Microbioreactors (MBRs) offer the possibility to circumvent many of the above-mentioned problems:

- The production cost of the MBRs is low, since they can be produced from polymers.
- The working volumes are very small (in the  $\mu$ L/mL range), keeping costs for culture media low.
- Online measurements are possible for the most important culture parameters (optical density (OD), dissolved oxygen (DO), pH).
- Batch, fed-batch and continuous culture conditions can be created in MBRs.
- The reactors are disposable after use and thus require no cleaning effort at all.
- Scaling out MBRs to systems with many parallel reactors allows for high-throughput screening, thus yielding a massive gain in information per experiment with continuously small working volumes.

The above advantages result in more-information-per-experiment (online measurements), financial savings (small volumes, less labor intensive) and the possibility to develop production schemes on the resource-saving micro-scale before scaling up a process.

### Objectives

Currently, MBRs described in the literature are operated either as fed-batch or as continuous cultures, most often with *E. coli* as the culture strain. This project aims at the development of a continuous culture MBR that can perform experiments with yeast (*S. cerevisiae*).

Compared to a batch experiment, the continuous culture has the advantage that steady-state conditions can be achieved. Additionally, it should be possible to induce step changes in the dilution rate, forcing the culture from one steady-state to the other with continuous measurement of the important culture parameters, thus leading to dynamic information on the behavior of the culture under well-controlled experimental conditions.

The planned working volume is in the range of 100  $\mu$ L, which is smaller than most of the current reactors running continuous cultures.

In the first part of the project, a reactor with the above features is to be designed and fabricated, and a complete measurement & control setup is to be installed. The second step will then be to prove the industrial relevance through comparisons of experimental MBR results with larger-scale data from the literature and from *S. cerevisiae* cultivations performed at BioCentrum-DTU.

Naturally, MBR construction also poses some challenges. Proper mixing for example is very essential for good cultivation results, since substrate gradients in the culture might otherwise lead to a varying (location dependent) metabolic state of the culture. In the projected volume range turbulent flow is difficult to achieve due to the small Reynolds numbers. On the other hand the volume is too large to be able to rely on diffusion alone. Therefore one of the challenges in the project is to find a mixing regime which efficiently reduces diffusion distances.

Another challenge is the mechanical integration of the various sensors, a mixing apparatus and the aeration system into the small volume in such a fashion that the device is easy to manufacture.

### Microbioreactor Technology

The current reactor is designed to have a working volume of 100  $\mu$ L which is sufficiently large to allow enough space for the sensors and actuators, but still small enough to considerably reduce the amount of media needed.

Contrary to conventional reactors which are mostly aerated by means of bubbles, microbioreactors are designed to work bubble-free. Aeration is done through a semi-permeable silicone membrane which allows both the incoming transport of oxygen and the outgoing transport of CO<sub>2</sub>.

PH and DO are both measured with fluorescent sensor spots which change both the amplitude and the phase of the emitted light with a change in the sensitive parameter. A lock-in amplifier measures the phase difference and thus quantifies the measured parameter.

Optical density is continuously measured both in the reactor itself and in the outflow channel. Light from a LED is guided into the reactor with optical fibers, sent through the substrate and then guided to a photo detector (**Figure 1**).

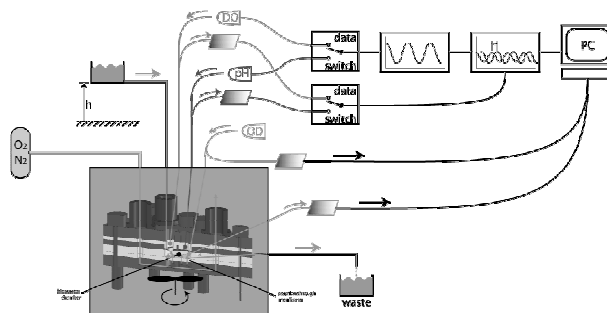


**Figure 1:** Schematic of a MBR setup

The flow rate is currently adjusted by the height of an elevated media reservoir but can also be controlled by e.g. peristaltic pumps or syringe drives. Both continuous and step changes in flow rate are possible which allows for various changes in dilution rates.

The reactor is currently fabricated out of the polymers poly(methylmethacrylate) (PMMA) and poly(dimethylsiloxane) (PDMS), which both are cheap materials. Additionally, no clean room fabrication steps are necessary which allows for cheaper manufacturing. Indeed, it means that the final product can be mass-produced, sterilized and pre-packaged similar to syringes.

### Work Done

In the first six months of the project a MBR design considering various aspects (e.g. geometric design, mixing, flow, sensor placement) was developed and fabricated. A new, simpler membrane fabrication methodology was developed and investigated (fabrication parameters  $\leftrightarrow$  resulting membrane thickness), again aiming at reducing MBR manufacturing cost. Additionally, the mechanical setup for the three optical measurements was designed and fabricated.

### Next Steps

The very next steps are concerned with setting up the measurement & control system (e.g. using LabView control and data acquisition) in such a fashion that the system can autonomously run a cultivation following pre-set parameters. Once this setup is complete, cultivations shall be run which first prove the principal functionality of the system and then demonstrate the industrial relevance through comparisons with larger scale data.

In a next step other measurement principles shall be investigated which might increase the amount of information per experiment.

### Acknowledgements

The Novozymes Bioprocess Academy is acknowledged for the financial support of this project.

Also, I would like to thank all my supervisors during these first 6 months for their continuing support.



**Ravendra Singh**  
Phone: +45 4525 2911  
Fax: +45 4593 2906  
E-mail: rs@kt.dtu.dk  
WWW: <http://www.capec.kt.dtu.dk/people/phd>  
Supervisors: Rafiqul Gani  
Krist V. Gernaey

Ph.D. Study  
Started: September 2006  
To be completed: August 2009

## Model-Based Computer Aided Framework for Design of Process Monitoring and Analysis Systems

### Abstract

In the manufacturing industry, for example the pharmaceutical industry, obtaining a consistent end-product quality is often mandatory. To obtain the desired properties in the end-product a well designed monitoring and analysis system is required, as well as a thorough understanding of the process. This project focuses on developing a model-based framework which will provide the guidelines for the design of the monitoring and analysis system as an add-on to traditional chemical process design methods. The model-based framework will provide a novel approach to analyze the process, to identify the critical points and process variables and to select the appropriate monitoring and control system for the process.

### Introduction

The ability to diagnose whether or not a manufacturing process is functioning properly is essential in today's high tech industry [1]. Even more important is the ability to actively use the diagnosis results to adjust the process until the desired product quality is obtained. Clearly, a deep understanding of the process will be helpful in both the diagnosis of current process state and – if needed – its subsequent adjustment.

The FDA (U.S. Food and Drug administration) have recently taken a new initiative called PAT (process analytical technology), which was defined as, “a system for the analysis and control of manufacturing processes based on timely measurements of critical quality parameters and performance attributes of raw materials and in-process materials” [2]. The primary aim of the PAT initiative is to increase the available knowledge and understanding of the manufacturing process in order to improve the ability to drive the manufacturing process to the desired operating state with the help of a properly designed process monitoring, analysis and control system

The *design of a process monitoring and analysis system* is a step-wise procedure consisting of the selection of critical process variables, followed by the proper selection and placement of suitable monitoring and analysis equipment to keep track on these critical process variables, and finally also including the coupling of the monitoring and analysis system to a control system to ensure that critical process variables

can be controlled. The design of a process monitoring and analysis system is thus an important add-on to traditional process design methods, and is as such a way to already ensure in the process design phase that the process will be able to achieve the desired product quality. In this project, design of a process monitoring and analysis system will be achieved by means of a *model-based Computer Aided Framework* which will allow identifying the critical points and variables in the process, and will subsequently assist in selecting a suitable monitoring and control system.

A typical manufacturing process is complex: It involves many variables like pressure, temperature, concentration, composition of ingredients, nature (e.g. size, shape etc.) of ingredients etc. The values of these process variables may change in each and every point of the process flow and will also change as a function of time. The end-product quality will depend on a sub-set of these process variables – the critical variables – which need to be monitored and controlled throughout the process in order to obtain the desired end-product quality. It is thus very important to make a proper selection of the variables that should be monitored, of the appropriate process steps in which these variables should be monitored, of the appropriate tools by which these variables can be monitored and of the appropriate manipulated variables by which these variables can be controlled efficiently. In other words, a *well designed monitoring, analysis and control system* is required for

each production line in order to consistently achieve product quality requirements.

### Specific objectives

The main objective of the project is to develop a model-based framework for supporting the design, implementation and verification of PAT systems. The model-based framework should be able to perform the following tasks:

- Analyze the manufacturing process in order to identify the critical process variables
- Identify the variables that need to be measured and the variables that will need to be manipulated to achieve the desired product quality.
- Select the proper methods for obtaining the measured data
- Connect the measured variables with the manipulated variables (sensor-actuator pairing)

combined with an industrial survey and data collection, while the necessary process operational models can be built through the modeling tool MOT.

Models are required to relate the critical process variables to end-product quality, to study the sensitivity of the end-product quality to variations in the process variables (manipulated, input flow stream, design, controlled etc.), to investigate the influence of selecting specific measurement and monitoring tools, and to investigate the performance of proposed control structures.

The model-based framework enhances the process understanding, helps in the measurement of critical attributes and process analysis and provides the basis for developing the process control strategy. A well understood process is essential to implement the monitoring and control system efficiently [3]. The process can be considered well understood if the deviation between the desired and achieved quality is minimal which can be achieved through a well configured model-based framework.

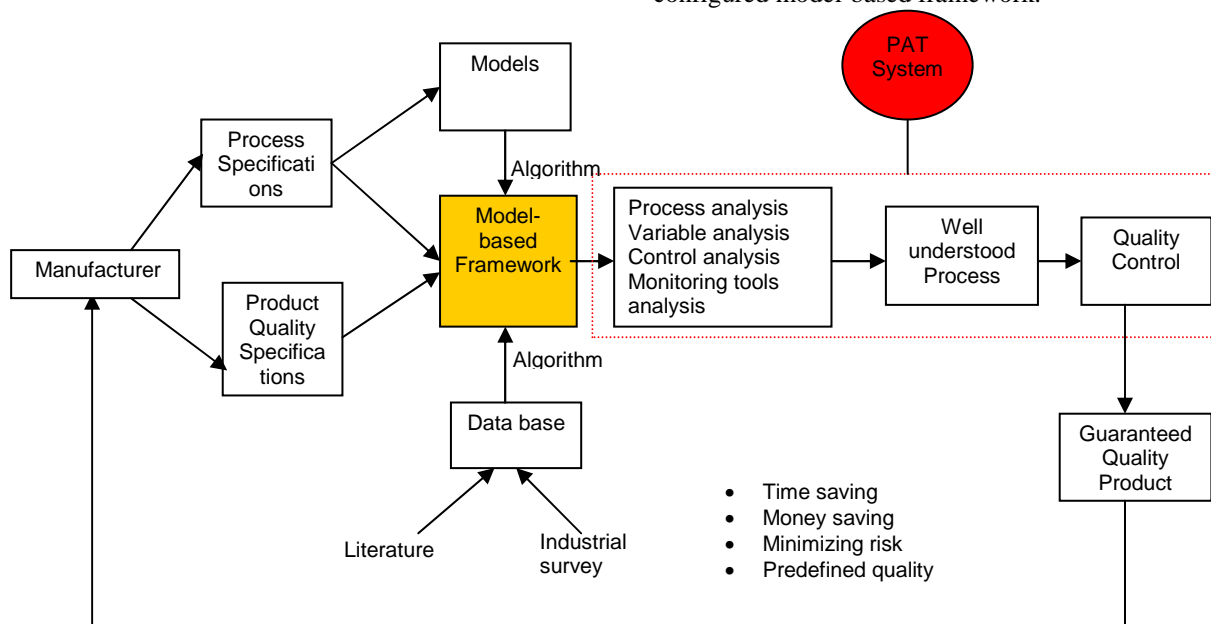


Figure 1

### Discussion

The proposed model-based framework will be a powerful tool which will help to understand the process better and will provide the guidelines for PAT system design. The proposed framework needs to generate the guidelines either through searching a knowledge base or through a calculation algorithm combined with simulation models. In other words, the models connecting the critical process variables should be incorporated in the framework.

As shown in figure 1 the process specifications and the desired product quality have to be specified by the manufacturer and then the analysis regarding process, variables, monitoring systems and control systems can be achieved through the developed framework. An extended *knowledge base and a model library are the critical supporting tools of the framework*. The knowledge base can be built by searching the literature

### Acknowledgement

The author acknowledges the financial support of the Technical University of Denmark.

### References

1. S. Wold, J. Cheney, N. Kettaneh, C. McCready, The chemometric analysis of point and dynamic data in pharmaceutical and biotech production (PAT) — some objectives and approaches, *Chemometrics and Intelligent Laboratory Systems* 84 (2006) 159–163.
2. CDER, Office of Pharmaceutical Sciences, “Process and Analytical Technologies Initiative”, <http://www.fda.gov/cder/OPS/PAT.htm>.
3. U.S. Food and Drug Administration, “Draft guidance”, <http://www.fda.gov/Cder/guidance/5815dft.htm>



### Jakob Sloth

Phone: +45 4525 2923  
Fax: +45 4525 2258  
E-mail: jsl@kt.dtu.dk  
WWW: <http://www.chec.kt.dtu.dk>  
Supervisors: Søren Kiil  
Anker D. Jensen  
Poul Bach, Novozymes A/S

Ph.D. Study  
Started: September 2004  
To be completed: August 2007

## Formation of Enzyme Containing Particles by Spray Drying

### Abstract

The droplet drying process which takes place inside a spray dryer is investigated using both a modeling based and an experimental approach. The modeling is carried out to quantify the phenomena controlling the drying kinetics and to achieve a fundamental understanding of morphology formation. Experiments are conducted to support the theoretical approach and validate developed models. The knowledge obtained by the investigations is used to meet product requirements such as mechanically stable particles and a narrow particle size distribution when spray drying enzyme containing slurries. Further, during drying the enzymes partially deactivate due to the high temperatures prevailing in the spray dryer. This deactivation is investigated and suggestions for process optimization are made.

### Introduction

Spray drying is of one several methods used in industry for conversion of a solution or slurry into a dried powder product. Spray drying is a flexible process which allows production of powders with many different properties such as a special particle size, particle morphology and residual solvent content. Many industrial enzymes are subject to spray drying because product handling is easier and enzyme stability is better than in liquid formulations.

In production of enzyme granules it is crucial that the formed particles have a low porosity to provide mechanical stability. Further, the particles must have a narrow size distribution to prevent segregation in the final detergent product. These particle properties must be obtained while avoiding thermal enzyme deactivation due to the high temperatures which exist in the spray dryer.

Though spray drying is used in numerous industrial applications, fundamental understanding of drying kinetics, morphology formation and enzyme deactivation remains limited.

### Spray Drying and Single Droplet Drying

In spray drying a slurry or solution is fed to the drying chamber where it is atomized (figure 1). The formed droplets are mixed with a hot gas and the contact between the droplets and the gas causes the solvent of the droplets to evaporate, leaving dried particles. These particles may subsequently be separated from the gas stream, using a cyclone or a particle filter [1]. Droplets

drying in a spray dryer undergo different periods with different rates of evaporation and droplet temperatures. Changes in droplet mass and temperature during the course of drying is shown on figure 2.

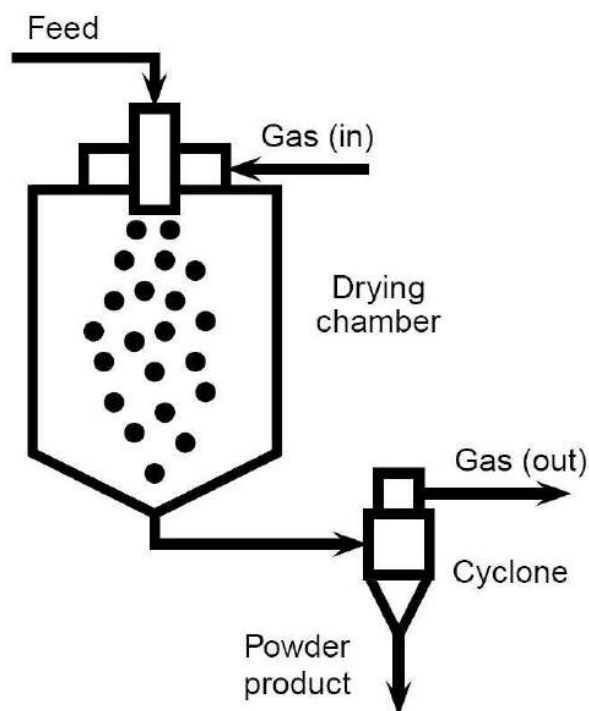
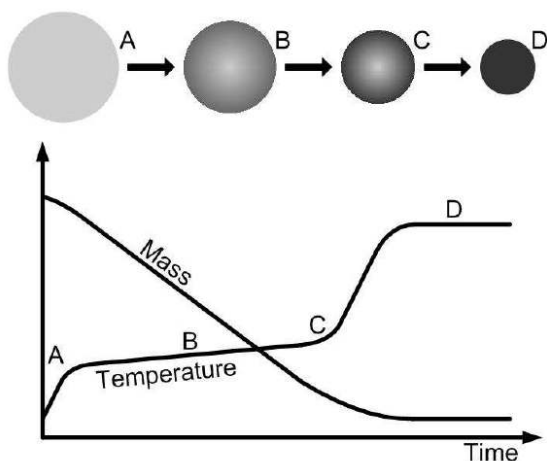
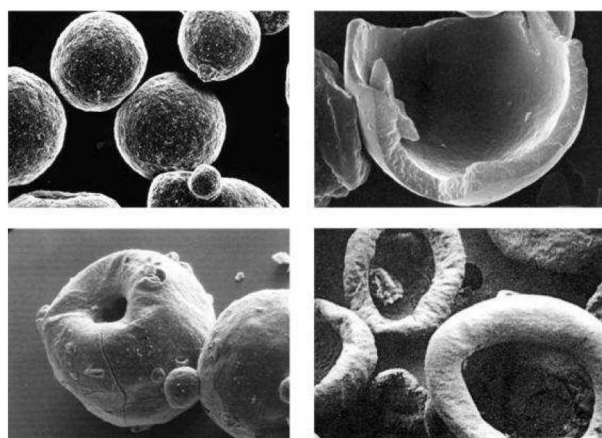


Figure 1: Spray Dryer



**Figure 2:** Mass and temperature change during the course of drying for a droplet in a spray dryer. The formation of a solid dense particle is shown - darker colour indicates higher concentration.



**Figure 3:** Examples of different morphologies of spray dried particles [3].

After atomization the droplet experiences initial heating followed by a period where the evaporation is fast because the solvent is readily available at the droplet surface.

As drying progresses the droplet shrinks and the concentration of solute at the droplet surface increases. The concentration is a significant resistance to evaporation and the rate of mass change decreases. This gives rise to considerable droplet heating [2].

The droplet drying process is complex and several different morphologies may form depending on drying conditions and the nature of the droplet (figure 3).

### Specific Objectives

In this PhD project the effect of formulation on the drying kinetics and morphology formation of enzyme-containing granules during spray drying is investigated and modeled. This knowledge is subsequently used in the design of improved granules (i.e. stable particles with uniform size distribution). The results must be applicable to industrial scale process equipment.

Also, the thermal enzyme deactivation during drying is investigated experimentally and the deactivation reaction is modeled, providing quantitative results for the degree of deactivation. Model simulations are used to optimize process parameters.

### Methods

The project consists of two parts - an experimental and a theoretical part. In the experimental part the drying kinetics and morphology formation of drying droplets is investigated using a spray dryer pilot plant located at the Department of Chemical Engineering. The results are compared to experiments conducted with a commercial spray dryer at the Novozymes test facilities in Bagsværd, Copenhagen.

The experimental investigations are supplemented by theoretical modeling studies. A model for the droplet drying process is set up as the various phenomena controlling the process are quantified and the most important ones identified in order to achieve a fundamental understanding of drying kinetics. Further, computational fluid dynamic (CFD) simulations are conducted for the Novozymes spray dryer to map differences between this commercial unit and the pilot plant.

The kinetics of the enzyme thermal deactivation reaction are determined from experiments using a differential scanning calorimeter (DSC) at the Novozymes laboratories. The experimental data is used to find parameters in a first order reaction kinetics model which includes an Arrhenius type expression for the reaction constant. Also, the water content of the samples influence the rate of deactivation, necessitating quantification of the reaction order of water in the deactivation reaction.

Below the different parts of the project are elaborated and current status of the work is given.

### Experimental Work

The experimental apparatus (figure 4) named the Droplet Dryer used for drying kinetics and morphology investigations consists of two parts - an atomizer and a drying tower. The atomizer (called the JetCutter) is located at the top of the drying tower and generates droplets with a size of approximately 275  $\mu\text{m}$  at about 0.4 g/s.

The droplets dry as they fall freely down the 6 m tall ( $\varnothing 200$  mm) drying tower in a cocurrent air stream. The temperature of the air stream may be set in the interval of [25 – 250°C] and the velocity in the interval [0.1 - 1.0m/s]. In the bottom of the tower the dry particles are collected in a steel bucket while the drying air is exhausted to the ventilation.

The drying tower is equipped with sampling ports at 12 different levels. Through these sampling ports the droplets may be collected in a small aluminum foil cup containing a small amount of paraffin oil. When the drying droplets hit the paraffin oil they immediately sink to the bottom of the oil because of a difference in density. This means that evaporation from the droplets

is stopped. The samples collected are subsequently subject to Karl Fischer titration by which the droplet water content is found. Sampling at different levels in the tower allows for a drying profile to be determined because the droplet water fraction as a function of distance traveled in the tower is known.

The slurry from which the droplets are formed consists of primary particles, solvent and usually a third component. The primary particles are insoluble particles (e.g. rice starch, Al<sub>2</sub>O<sub>3</sub> or TiO<sub>2</sub>) in the size range [0.1 - 10µm]. The solvent is always water while the third component may be inorganic salts, binders (dextrins) or viscosity enhancing compounds (e.g. carboxy methylcellulose).

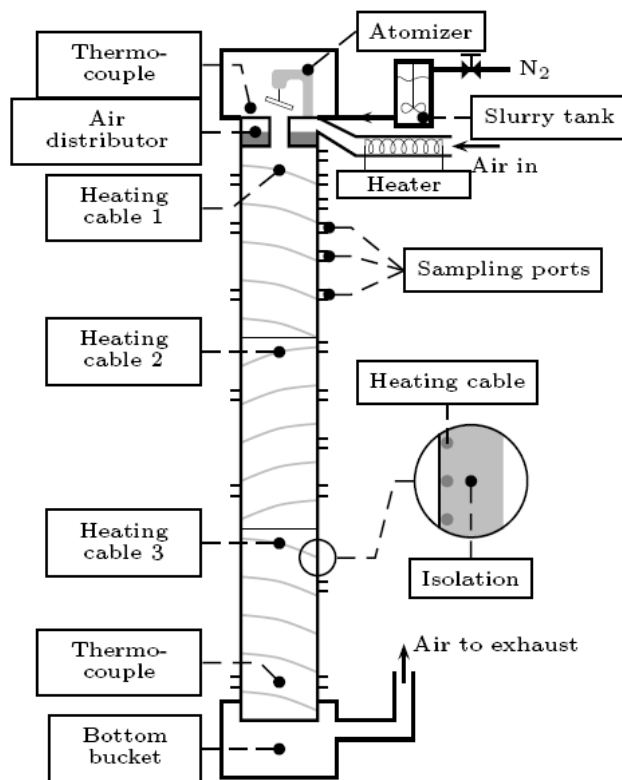


**Figure 4:** The Droplet Dryer – experimental apparatus for investigations of droplet drying kinetics and morphology formation

### Experimental Results

As described above the drying kinetics are determined as the percentage water evaporated as a function of the distance traveled by the droplets. An example for a result for the drying kinetics is given in figure 5. The slurry used contained water, 43.95%wt rice starch and 0.99%wt carboxymethylcellulose. The drying temperature was 150°C.

Also, the particles collected at the bottom of setup are investigated using scanning electron microscopy (SEM). The experiments have shown that process parameters such as drying air temperature may determine the final particle morphology. The example in figure 6 shows a rice starch containing slurry dried at 150, 200 and 250°C[4]. Also, small changes in slurry

ingredients may have large influence on the morphology formation. Particles dried at 150°C consisting of rice starch and 0, 0.51, 3.24 and 6.45 %wt maltodextrin are shown in figure 7.

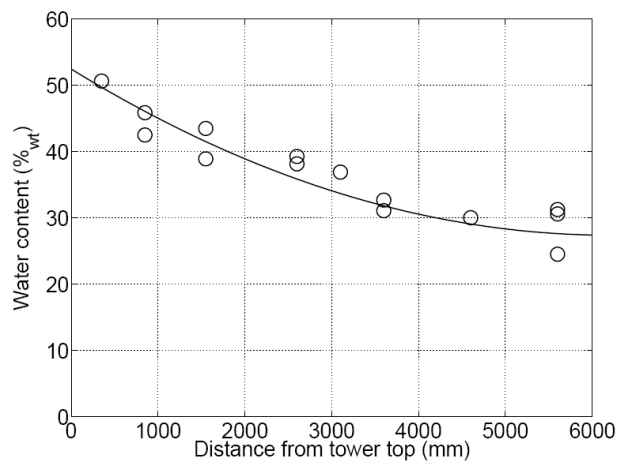


**Figure 5:** Kinetics for drying a slurry containing water, 43.95%wt rice starch and 0.99%wt carboxy methylcellulose. A trend line is inserted.

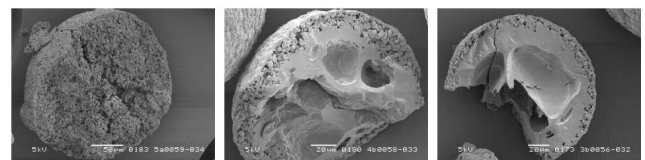


**Figure 6:** SEM pictures showing morphology of particles dried on the Droplet Dryer. Left: Drying temperature 150°C. Center: Drying temperature 200°C. Right: Drying temperature 250°C. The particle diameter is approximately 250 µm.

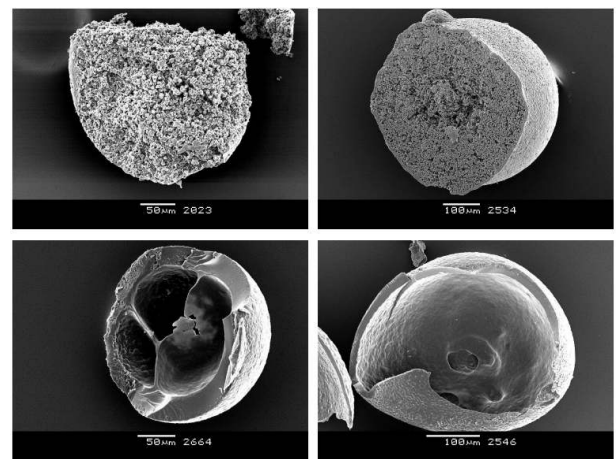


**Figure 7:** SEM pictures showing the influence of slurry content on the morphology formation. Rice starch slurries with maltodextrin have been dried – the amount of rice starch is constant while the maltodextrin content increases from one picture to the next. The particle diameter is approximately 250 µm.

### Modeling results

The results from the Droplet Dryer are to be compared to experimental results from a commercial spray dryer located at the Novozymes test facilities in Bagsværd, Copenhagen. To achieve a fundamental understanding of the drying process inside the commercial spray dryer CFD-simulations are conducted using the Fluent<sup>®</sup> software.

Figure 8 shows a simulation of the air flow field inside the spray dryer. The air enters the so called air distributor at the top of the dryer. It is then forced down the funnel part of the distributor into the drying chamber. Inside the drying chamber the air moves rather chaotically before exiting in the bottom of the dryer.

Analogous simulation results for the temperature and humidity distributions show only small variations of these variables inside the drying chamber. This result was to be expected because mixing in cocurrent spray dryers usually is good [1].

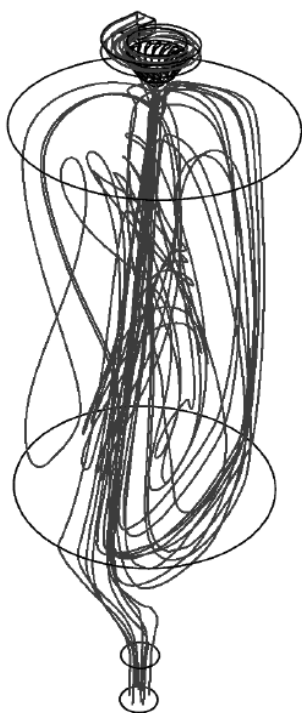


**Figure 8:** CFD-simulations of the air flow field inside the Novozymes spray dryer.

### Further Work – Enzyme Deactivation Kinetics

Setting up a model capable of simulating the deactivation of enzyme during spray drying requires calculations of the deactivation rate. Determining the deactivation rate is based on a combination of experiments and reaction kinetics modeling. Concerning the experiments the performance and general applicability of the final model is highly dependent on the following

1. The deactivation rate must be measured transiently to ensure fast and accurate data collection.
2. Based on the experimental data a model for the reaction kinetics must be developed.

3. The sample sizes must be small so that different enzymes and enzyme formulations can be tested at low cost, i.e. the method may be used for formulation screening. Also, to keep costs low the method should demand very few man hours per experiment.

Based on the requirements above Differential Scanning Calorimetry (DSC) has been chosen.

The DSC experiment will be used for setting up a model for the deactivation rate. The deactivation rate will be a function of the water content and temperature inside the drying enzyme containing droplet. Thus, this model is readily coupled to a model for the drying kinetics which calculates the water content and temperature of a drying droplet.

The combined model may be used for simulating the deactivation at different process conditions such as drying air humidity or temperature and initial droplet size and water content. Based on these simulations suggestions for process optimization are made.

### Acknowledgments

This project is funded by the Novozymes Bioprocess Academy.

### References

1. K. Masters, *Spray Drying Handbook*, 5th ed., Longman Scientific and Technical, 1991.
2. S. Nestic & J. Vodnik, *Kinetics of Droplet Evaporation*, *Chem. Eng. Sci.*, 46, 1991, pp. 527-537.
3. D. E. Walton & C. J. Mumford, *Spray Dried Products - Characterization of Particle Morphology*, *Trans IChemE*, 77, 1999, pp. 21-38.
4. K. Jørgensen, PhD-thesis, Department of Chemical Engineering, Technical University of Denmark, 2005.



**Vipasha Soni**

Phone: +45 4525 2910  
 Fax: +45 4593 2906  
 E-mail: vso@kt.dtu.dk  
 WWW: http://www.capec.kt.dtu.dk/  
 Supervisors: Rafiqul Gani  
 Gunnar Jonsson  
 Jens Abildskov

Ph.D. Study  
 Started: November 2004  
 To be completed: October 2007

**Model and Analysis of Vacuum Membrane Distillation for the Recovery of Volatile Aroma Compounds from Black Currant Juice**

**Abstract**

A vacuum membrane distillation (VMD) model has been developed and validated with experimental data. The model employs an extended transport model for the VMD process and is able to predict the effects of concentration and temperature polarization on the overall process performance. The VMD model has been validated with experimental data collected from the recovery of aroma compounds from black currant.

**Introduction**

Fruit juice technology involves a purification operation where the solid content of the juice is increased from 10–12% up to 65–75% by weight in order to reduce liquid volume, which not only lowers the costs in terms of storage, packaging and transportation, but also assists in preventing microbial spoilage of the juice concentrate. Lately, membrane distillation, reverse osmosis and pervaporation have been considered as alternatives to the conventional techniques for the purification step in fruit juice industries. Lower operating temperatures and reduced vapor spaces (as compared to conventional distillation), lower operating pressures (as compared to other pressure driven membrane separations), reduced chemical interactions between membrane and process solutions and less demanding membrane mechanical property requirements are some of the benefits of membrane distillation over other more popular separation processes.

pore size and the system operating conditions the VMD membrane may impart some selectivity based on individual Knudsen diffusing species, but the largest degree of the separation is realized as a result of the vapor-liquid equilibrium conditions at the membrane solution interface [5]. The schematic diagram of the process is shown in Fig.1 along with the vapor liquid interface.

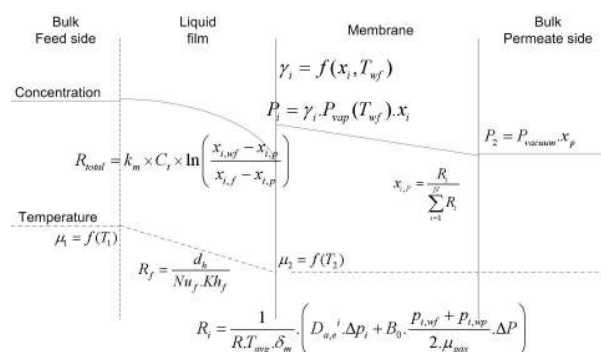


**Figure 1.** Schematic diagram of VMD process

**Vacuum Membrane Distillation**

The driving force in a membrane distillation unit is partial pressure difference and this is created by applying a vacuum on the permeate side in the case of vacuum membrane distillation (VMD) unit.

In practice, the feed solution is brought into contact with one side of the microporous membrane, and a vacuum is maintained on the other side to create a driving force for trans-membrane flux. This microporous membrane acts only as a support for a vapor-liquid interface. Depending on the membrane

The concentration and temperature conditions at the interface, at which the separation process is taking place, are affected by heat and mass transfer rates within the liquid phase. So, the process flux and selectivity are determined also by the heat and mass transfer resistances, in addition to Knudsen diffusion through the membrane [1]. Knudsen model together with temperature and concentration polarization models have been used in order to reproduce theoretical fluxes and then compared to experimental fluxes.

## Modeling

The VMD model is developed for the membrane module, where boundaries of the system are defined. In vacuum membrane distillation, a simultaneous heat and mass transfer occurs and an enthalpy flux exists across the hydrophobic membrane from the feed to the permeate.

*Assumptions:*

- In VMD systems molecular diffusion resistance can be omitted due to extremely small pore sizes.
- Due to vacuum on the permeate side, corresponding boundary layer resistance may be omitted.
- There are no temperature gradients in the membrane.

A total mass and energy balance is established over the length of the membrane module from  $z=0$  to  $z=L$  (see Fig. 2).

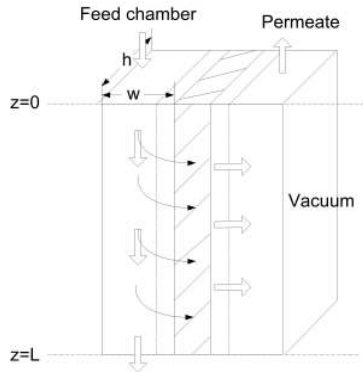


**Figure 2:** Membrane module giving system boundaries

The overall mass balance is given as:

$$\frac{du_i}{dz} = -\frac{J(z)}{h.n_c}, \text{ where } i=f, p \quad (1)$$

Where,  $u_i(z=z_0)=u_{i,0}$  (2)

Since there is no change in temperature on the permeate side, the model for a temperature profile is derived only for the feed side:

$$\frac{dT_f}{dz} = \frac{1}{V_f} \left( \frac{-q_{process} \cdot w}{\hat{C}_p} + J(z) \cdot w \cdot T_f \right) \quad (3)$$

With initial condition as:  $T_{bf}(z=z_0)=T_{bf,0}$  (4)

*Constitutive Equations:*

At the pores of the feed side of the membrane surface, liquid feed vaporizes and the vapors and liquid are assumed to be in equilibrium with each other. This assumption of vapor liquid equilibrium (VLE) can then be used to determine the partial pressures of components on the feed side. The partial pressure of the non ideal binary mixture can then be given as:

$$P_{i,wf} = P_i^{sat}(T_{wf}) \cdot \gamma_i(T_{wf}, x_{if}) \cdot x_{if} \quad (5)$$

For the permeate side the partial pressures can be calculated as a function of the vacuum pressure and the molar fractions on the permeate side as:

$$P_{i,wp} = P_{vac} \cdot x_{i,wp} \quad (6)$$

Mass transfer in vacuum membrane module can be divided in three regions of concentration profiles; in the liquid film on the feed side, the membrane and the vapor film on the vacuum side (Fig. 1). Mass transfer across the boundary layers or concentration polarization may play an important role in the performance of a VMD system. Such mass transfer through the liquid phase can be adequately described by the film theory model [5].

$$R_{total} = k_m \times C_i \times \ln \left( \frac{x_{i,wf} - x_{i,p}}{x_{i,f} - x_{i,p}} \right) \quad (7)$$

where  $R_{total}$  is the total molar flux through the membrane, which is the sum of individual fluxes of all components in the system,  $k_m$  is the mass transfer coefficient, which can be calculated from Sherwood number as:

$$k_m = \frac{D_{AB} \cdot Sh}{dh} \quad (8)$$

The Sherwoods correlations are then used to calculate the Sherwood number, and the correlation can take three different forms depending on whether the flow is laminar, transitional or turbulent [7]:

$$Sh = f(Re, Sc, dh, L, \mu) \quad (9)$$

$Re < 2100$  Laminar regime

$$Sh = 1.86 \left( Re \cdot Sc \cdot \frac{dh}{L} \right)^{0.33} \left( \frac{\mu_{bf}}{\mu_{wf}} \right)^{0.14} \quad (10)$$

$2100 < Re < 10000$  Transitional regime

$$Sh = 0.116 \left( Re^{2/3} - 125 \right) \cdot Sc^{0.33} \cdot \left( 1 + \left( \frac{dh}{L} \right)^{2/3} \right) \left( \frac{\mu_{bf}}{\mu_{wf}} \right)^{0.14} \quad (11)$$

Where,

$$Re = \frac{u_f \cdot \rho \cdot dh}{\mu} \quad (12)$$

$$Sc = \frac{\nu}{D_{AB}} \quad (13)$$

$dh$  is the hydraulic radius and can be defined as:

$$dh = \frac{2 \cdot w \cdot h}{w + h} \quad (14)$$

Under the operating conditions of interest, Knudsen-viscous diffusion is the prevailing mechanism for mass transfer through the membrane. The water molar flux,  $R_w$ , as well as the molar flux of the generic aroma  $R_i$  can be represented through the following relationships [5]:

$$R_i = \frac{1}{R \cdot T_{avg} \cdot \delta_m} \left( D_{a,e}^i \cdot \Delta p_i + B_0 \cdot \frac{P_{i,wf} + P_{i,wp}}{2 \cdot \mu_{gas}} \cdot \Delta P \right) \quad (15)$$

The values of the constants in the flux equation can be calculated as:

$$K_0 = \frac{2\epsilon r}{3\tau} \quad (16)$$

$$B_0 = \frac{\varepsilon r^2}{8\tau} \quad (17)$$

and

$$D_{a,e}^i = K_0 \sqrt{\frac{8RT_{avg}}{\pi M_i}} \quad (18)$$

Where,

$$\tau = \frac{1}{\varepsilon} \quad (19)$$

$$r = \frac{\text{pore size}}{2} \quad (20)$$

As there is no resistance to mass transfer beyond the membrane the molar fraction of components remain the same as on the permeate side membrane surface and bulk permeate. Molar fraction of component  $i$ , on the permeate side can be calculated as:

$$x_{i,p} = \frac{R_i}{\sum_{i=1}^N R_i} \quad (21)$$

The total heat consumption in the process is:

$$q_{process} = q_{abs} + q_{vap} + q_{des} \quad (22)$$

where heat of absorption and heat of desorption are numerically same with opposite signs, so they cancel out each other. So the only heat consumption is heat of vaporization. Heat flux is then given as:

$$Q_{process} = R_{total} \cdot q_{process} \quad (23)$$

The heat transfer from bulk of the feed to the permeate side of the membrane can be described by simple heat transfer equations:

$$Q_{process} = h_{film} (T_{feed} - T_{wf}) \quad (24)$$

where  $h_{film}$  can be calculated from Nusselt's Equations:

$$h_{film} = \frac{u_f \cdot Nu}{dh} \quad (25)$$

Nusselt's number again depends on the flow regime (divided into three regions):

$$Nu = f(Re, Pr, dh, L, \mu) \quad (26)$$

$Re < 2100$  Laminar regime

$$Nu = -1.86 \left( Re \cdot Pr \cdot \frac{dh}{L} \right)^{0.33} \left( \frac{\mu_{bf}}{\mu_{wf}} \right)^{0.14} \quad (27)$$

$2100 < Re < 10000$  Transitional regime

$$Nu = -0.116 \left( Re^{2/3} - 125 \right) \cdot Pr^{0.33} \quad (28)$$

$$\left( 1 + \left( \frac{dh}{L} \right)^{2/3} \right) \left( \frac{\mu_{bf}}{\mu_{wf}} \right)^{0.14}$$

$Re > 10000$  Turbulent regime

$$Nu = -0.023 \cdot Re^{0.8} \cdot Pr^{0.33} \left( \frac{\mu_{bf}}{\mu_{wf}} \right)^{0.14} \quad (29)$$

Where,

$$Re = \frac{u_f \cdot \rho \cdot dh}{\mu} \quad (30)$$

$$Pr = \frac{\mu Cp}{\lambda} \quad (31)$$

and heat transfer coefficient for the membrane can be calculated as:

$$h_m = k_{memb} / \delta_m \quad (32)$$

where,  $k_{memb}$  and  $\delta_m$  are thermal conductivity and thickness of the membrane.

In the VMD model derived above there are a number of pure component properties that need to be evaluated as a function of changing temperature along the length of membrane module. Some of these properties were retrieved from the ICAS database (ICAS-DB) [3] and for the more exotic aroma compounds for which the properties were not available in the databases searched, a tool for property prediction Pro-Pred (ICAS) [6] was used to generate them. The properties were then fitted to the following expressions:

$$\text{Density} \left[ \frac{\text{kmol}}{\text{m}^3} \right]: \rho = \frac{A}{B \left( 1 + \left( 1 - \frac{T}{C} \right)^D \right)} \quad (33)$$

$$\text{Viscosity} \left[ \frac{\text{kg}}{\text{m.s}} \right]: \mu = \exp \left( A + \frac{B}{T} + C \cdot \ln(T) + D \cdot T^E \right) \quad (34)$$

$$\text{Specific heat} \left[ \frac{\text{J}}{\text{kmol.K}} \right]: Cp = A + \quad (35)$$

$$B \cdot T + C \cdot T^2 + D \cdot T^3 + E \cdot T^4$$

$$\text{Thermal conductivity} \left[ \frac{\text{J}}{\text{m.s.K}} \right]: k_m = A + B \cdot T + \quad (36)$$

$$C \cdot T^2 + D \cdot T^3 + E \cdot T^4$$

$$\text{Gas Viscosity} \left[ \frac{\text{kg}}{\text{m.s}} \right]: \mu_g = A \cdot T \frac{B}{1 + C/T + D/T^2} \quad (37)$$

$$\text{Heat of Vaporization} \left[ \frac{\text{J}}{\text{kmol}} \right]: \quad (38)$$

$$H_{vap} = A \cdot (1 - Tr)^{B+C \cdot Tr + D \cdot Tr^2}$$

The degree of separation are given by concentration factors which are defined as the ratio of molar fractions of aroma compounds in permeate to that in the feed:

$$CF = \frac{x_p}{x_f} \quad (39)$$

The model was implemented through a computer aided modeling toolbox, ICAS-MoT [2], which also provides options for simulation. The model is a Differential Algebraic Equation (DAE) system, containing 3 ordinary differential equations (ODEs) and 62 algebraic equations and has 122 variables.

### Model Validation

Simulations for the recovery of aroma compounds from Black currant juice using the VMD model was made under different conditions of operation. The unique aroma profile of black currant juice comprises more than 60 constituents but in this work, the twelve most characteristic aroma compounds have been used to

validate the VMD model. The individual aroma components differ according to their molecular structure, which in turn defines the solubility, the boiling point, and the volatility of each type of compound [4]. In general, the aroma components are present in different concentrations and combinations, where the concentrations of individual aroma substances in common fruit juices usually range from less than 1 to 20 ppm. The aroma profile of Black currant juice comprise of specific profiles of terpenoids, aliphatic esters, carbonyl compounds and alcohols that make up the characteristic black currant aroma of the juice. The twelve aroma compounds, representing various chemical groups, used in this study are ethyl butanoate, iso amyl acetate, 3-methyl-1-butanol, cis-3-hexene-1-ol, ethyl hexanoate, benzaldehyde, linalool, octanal, 1,8 cineole, furfural, eugenol and diacetyl. The model requires calculation of properties of all components of the system. This was done by using group contribution method by employing computer aided property tool box Pro-Pred (ICAS). A sensitivity analysis was made on all the properties and it was noted that except for infinite dilution activity coefficients and saturation pressures of pure component the other properties do not have any significant effect on the concentration factors (see Fig. 3 and 4).

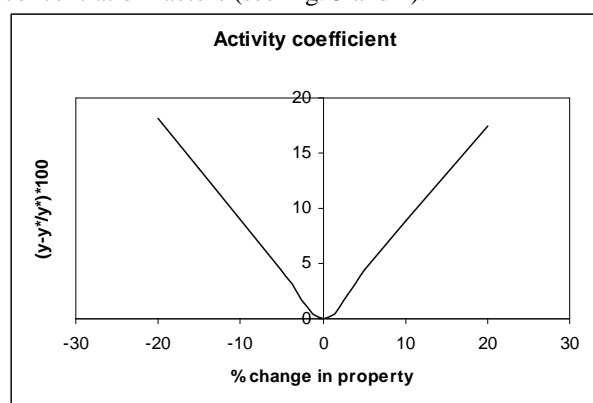


**Figure 3:** Sensitivity analysis of activity coefficient

This can be explained from the fact that the aroma compounds in the mixture are present in such small quantities that after applying the ideal mixing rule and calculating the mixture properties, the contribution of aroma part of the property is very small. However, activity coefficients and vapor pressures are used directly to calculate the partial pressures on each side of the membrane which is the driving force to the process and have a large impact on the separation. So, care has to be taken while choosing the property models for these properties. In this study the infinite dilution activity coefficients for most of aroma compounds have been taken from experimental data, while most of vapor pressures are predicted.

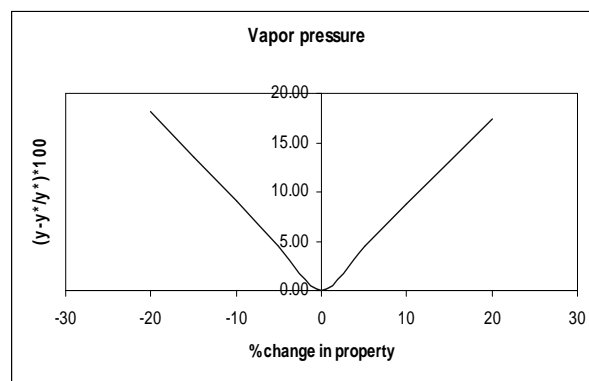


**Figure 4:** Sensitivity analysis of vapor pressure

The membrane used in the experiments was Polytetrafluoroethane (PTFE). The properties of the membrane and specifications of the membrane module are given in Table 1.

**Table 1:** Membrane specifications

Membrane Specification	Value
Pore size, $[\mu\text{m}]$	0.2
Porosity, $\mathcal{E}$ [-]	0.75
Width, $w$ , [cm]	3.8
Height, $h$ , [cm]	1
Length, $L$ , [cm]	9.75
Number of channels, $n_c$	1

The developed VMD model predicts the permeate concentration of the aroma compounds given the feed composition, operating temperature and vacuum pressure. The feed concentration of the aroma compounds have been fixed at 1 ppm for the simulations (which is in accordance with the available experimental data). The concentration of aroma compounds in feed is so low that it was assumed that the presence of one aroma compound does not affect the transport of another. This assumption ultimately leads to the simplification of the system under study resulting in taking the system as twelve binary systems of each aroma compound with water rather than a multicomponent system. The results are shown in Fig. 5, where the molar fractions of aroma compounds in permeate from the model is compared versus those obtained from experiments [4] at three different feed flow rates (300, 400 and 500 l/h). The values show a maximum deviation of 15% which is considered good in this case as the molar fractions are of order of 1ppm.

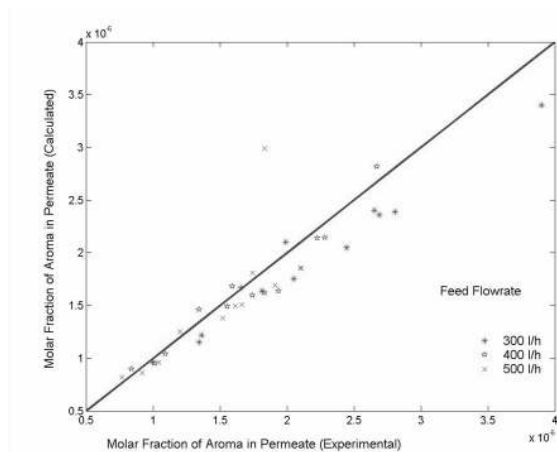


**Figure 5:** Comparison of molar fractions in permeate from model and experiments at 30°C and 300, 400 and 500 l/h.

### Results Analysis

After the validation of the model, three aroma compounds, for which the infinite dilution activity coefficients were known as a function of temperature, were selected and simulations were made at different process conditions to see the behavior of the process variables on the separation factors. Calculations were made for ethyl butanoate, benzaldehyde and eugenol for the temperature ranging from 30°C to 50°C and flow rates from 300 l/h to 500 l/h. The plots are shown in Fig 6(a) – 6(c).

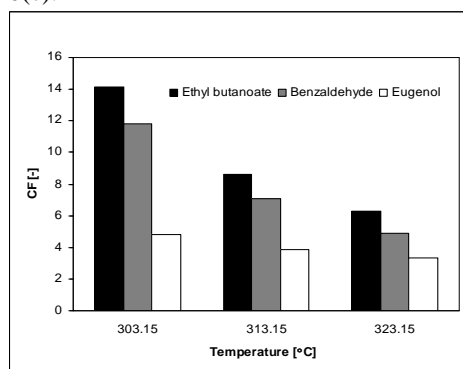


**Figure 6(a):** Comparison of CF of aroma compounds at 300l/h and T=30, 40, 50°C

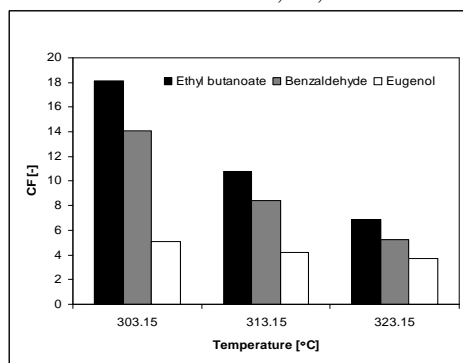


**Figure 6(b):** Comparison of CF of aroma compounds at 400l/h and T=30, 40, 50°C

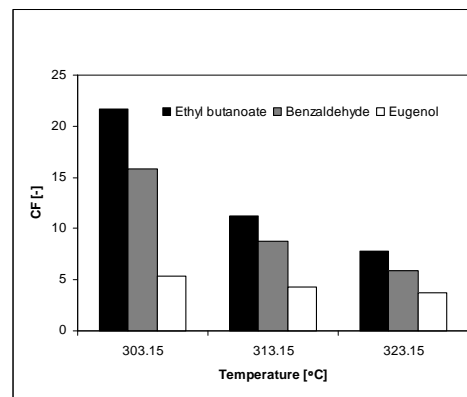


**Figure 6(c):** Comparison of CF of aroma compounds at 500l/h and T=30, 40, 50°C

It can be seen from the histograms that with the increase in temperature of the feed from 30°C to 50°C the concentration factors of aroma compounds decreased. With increasing the flow rate the concentration factors showed some increase but the change was not much. The change is much more when the temperature is changed and the reason for this is that the infinite dilution activity coefficients and vapor pressures of the aroma compounds change significantly with change in temperature but not with the flow rates. The sensitivity analysis made on all properties also showed that the concentration factors of aroma compounds is very sensitive to activity coefficient and vapor pressures as compared to any other property. With a change of 20°C in temperature the percentage change in the activity coefficients for ethyl butanoate, benzaldehyde and eugenol is 13.5%, 11.86% and 23.86% respectively. While for the change in flow rate from 300-500 l/h this change was only around 0.01% for each compound. It was observed that even though all aroma compounds show a common trend, they change with a different degree with change in the process variables (see Fig. 6(a) – 6(c)). This mainly depends on the different selectivities of different compounds.

With the increase in temperature the permeate flux increases which decreases the concentration of individual aroma compounds at the membrane surface due to concentration polarization, which ultimately leads to the drop in the concentration factors. Fig. 7 illustrates this effect on the concentrations of aroma compounds at the membrane surface with temperature. The concentration factor drop is 59.01%, 55.53% and 29.73% for benzaldehyde, ethyl butanoate and eugenol respectively. This can be explained by noting the change in the molar fraction drop of these compounds at the membrane surface of the feed side of the membrane, which is 51.01%, 32.96% and 24.85% for benzaldehyde, ethyl butanoate and eugenol respectively.

### Conclusions

A VMD model together with the corresponding property models capable of predicting the behavior of the VMD process under different operating conditions has been presented in this paper. Experimental results

for recovery of aroma compounds from black currant juice were used to validate the model. A comparison of the experimental and simulated values for the molar fractions of aroma compounds in the permeate stream exhibited a maximum of 15% relative error. So, it can be concluded that the model represents reasonably well, the physical behavior of the process.

A model based analysis of the process made for three selected aroma compounds explained the experimentally observed trends with respect to the change in temperature and flow rate of the feed mixture. With the increase in temperature of the feed from 30° C to 50° C the concentration factors of aroma compounds decreased, while not much effect with respect to the change of the flow rate could be observed. The model was able to predict the effects of concentration and temperature polarization well.

The VMD model given above, in general, is an integration of process model explaining the underlying physics and of property models for both the compounds and polymer used. It is flexible in terms of process variables and the polymer used which can be adjusted to design the VMD process when the desired separation criteria is predefined.

### References

- [1] Bandini S. and Sarti G.G., Heat and Mass Transport Resistances in Vacuum Membrane Distillation Per Drop, *AIChE Journal*, 45 (1999), 7, 1422-1433.
- [2] Sales-Cruz. A.M., and Gani R., Development of a computer aided modeling system for bio and chemical process and product design, Ph.D. thesis, CAPEC, Technical University of Denmark (2006)
- [3] Integrated Computer Aided System (ICAS) Version 8.0. developed by Computer Aided Process-Product Engineering Center (CAPEC) at Technical university of Denmark.
- [4] Jørgensen R.B., Meyer A.S., Varming C. and Jonsson G., Recovery of volatile aroma compounds from black currant juice by vacuum membrane distillation, *Journal of Food Engineering*, 64(2004), 23-31.
- [5] M. Khayet, P Godino, J.I. Mengual, Nature of flow on sweeping gas membrane distillation, *J. Membr. Sci.* 170 (2000) 243.
- [6] Marrero J. and Gani R., Group contribution based estimation of pure component properties, *Fluid Phase Equilibria*, 183 (2001), 183-208.
- [7] Mulder M., *Basic Principles of Membrane Technology*, Kluwer Academic Publishers, 1996.

### Acknowledgements

The author would like to acknowledge DANISCO for funding the project.

### List of publication

1. V. Soni; J. Abildskov; G. Jonsson; R. Gani, A hierarchal approach based on reverse design algorithm for simultaneous design and analysis of product and processes, ESCAPE 16, Garmisch Partenkirchen Germany.
2. V. Soni, J. Abildskov, G. E. Jonsson, R. Gani, Model and Analysis of Vacuum Membrane Distillation for the Recovery of Volatile Aroma Compounds from Black Currant Juice, Submitted to *J. Memb. Science*



**Piotr Szewczykowski**

Phone: +45 4525 6814  
 Fax: +45 4588 2161  
 E-mail: pps@kt.dtu.dk  
 WWW: http://www.polymers.dk  
 Supervisors: Martin E. Vigild  
 Sokol Ndoni, Risø  
 Rolf H. Berg, Risø

Ph.D. Study  
 Started: February 2005  
 To be completed: February 2008

**Nano-Porous Materials Based on Block Copolymer Self-Assembly and Their Possible Membrane Application**

**Abstract**

Block copolymers are very interesting materials from both a science and an application point of view thanks to their amazing self-assembly properties. It is possible to control the morphology of self-organized structure on the nano-scale level by choosing the proper ratio (volume fraction) of one block to another. Synthesized diblock copolymer has to be cross-linked and etched to obtain final nano-porous material. Many different techniques allow for the characterization of the structure of the nano-porous materials. Here the obtained morphologies are used as membranes and the materials are investigated for gas permeability (nitrogen).

**Introduction**

Self-organization in block copolymers is very interesting in relation to active nanostructuring. [1] The interplay between block immiscibility and connectivity generates a rich variety of nanophase-separated mesoscopic morphologies. Different morphologies can be obtained by controlling molecular weight and composition of block copolymers. "Living" anionic polymerization offers a readily feasible preparation of copolymers in a wide range of molar masses and chemical structures. [2,3]

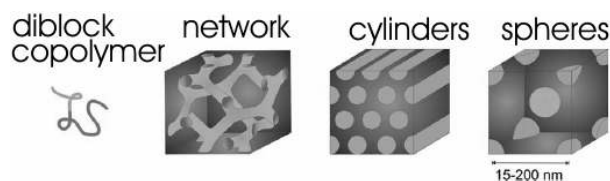


**Fig. 1** Illustration of the individual (green-blue) diblock copolymer and the structures, which are formed upon self-organisation: gyroid (network), cylindrical and spherical morphology of the (green) minority block.

The main force which causes microphase separation is chemical incompatibility between different blocks. In the simplest case of diblock copolymers (Fig.1) there is only the issue of compatibility between A and B blocks. By multiplying

Flory-Huggins interaction parameter  $\chi_{AB}$  (segment-segment interaction energy) and degree of polymerization  $N$  we obtain degree of segregation  $\chi_{AB}N$ . On the phase diagram for AB diblock copolymer we can observe changes of copolymer morphology depending on composition  $f$  for fixed  $\chi_{AB}N$ , where  $f_A = N_A/N$  (Fig. 2). [4, 5]

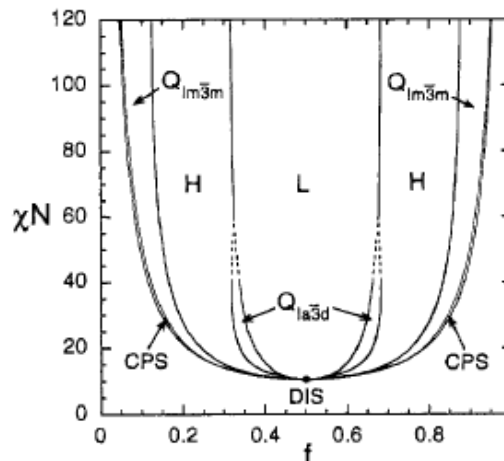


**Fig. 2** Phase diagram for linear AB diblock copolymers showing equilibrium morphologies: lamellar (L), hexagonal cylinders (H), gyroid  $1a3d$  cubic ( $Q_{1a3d}$ ), bcc spheres ( $Q_{1m3m}$ ), close packed spheres (CPS) and disordered (DIS). [6]

After removal of the minority block from the copolymer one can obtain nanoporous material with

predictable morphology and narrow pore size distribution. Depending on morphology and possible alignment of internal structure the nanoporous materials can find very interesting applications like-high-surface area support for catalyst, templates for the synthesis of nanoobjects and for confined crystallization, membranes for selective transport. [7-11]

### Nanoporous materials preparation

Preparation of nanoporous materials from diblock copolymers consists of four steps:

1. Synthesis – block copolymers are synthesized by anionic polymerization.
2. Alignment – this step refers mainly to cylindrical, hexagonal morphology. After solvent casting (SC) polymer, the cylinders of minority blocks will be randomly oriented. Orientation of cylinders in one direction by using external forces like shearing (SHR) could be interesting from application point of view.
3. Cross-linking – this step is necessary in case of polymers which glass transition is below room temperature. The cross-linking is necessary to reinforce the matrix domain to a sufficient mechanical strength for the morphology to withstand the increased internal stress resulting from the selective removal of the minority component. Dicumyl peroxide (DCP) is used as a crosslinker.
4. Etching – to obtain final nanoporous material, the minority block has to be removed. Tertbutylammonium fluoride (TBAF) solution in THF is used as etching compound. TBAF is a source of fluorine anions, which are able to cleave silicon – oxygen bonds in polydimethylsiloxane chain.

### Materials characterization

Mainly two different diblock copolymers were investigated: polyisoprene-*b*-polydimethylsiloxane (PI-PDMS) showing hexagonal structure (HEX) with PI weight fraction  $w_{PI}=0.74$ , overall molecular weight of  $M=14\,200\text{ g/mol}$ , polydispersity index of  $PDI=1.1$  and 1,2-polybutadiene-*b*-polydimethylsiloxane (PB-PDMS) showing hexagonal structure with PB weight fraction  $w_{PB}=0.69$ , overall molecular weight of  $M=12\,900\text{ g/mol}$ , polydispersity index of  $PDI=1.14$ . Another PD-PDMS sample was made showing gyroid structure (GYR) with PB weight fraction  $w_{PB}=0.593$ , overall molecular weight of  $M=10\,680\text{ g/mol}$ , polydispersity index of  $PDI=1.04$ .

Both polymers and both structures (HEX and GYR) were successfully investigated by electron microscopy techniques: scanning electron microscopy (SEM) (Fig.3), transmission electron microscopy (TEM) and small angle x-ray scattering technique (SAXS) (Fig.4). Furthermore the internal surface area, pore diameter and pore size distribution for PB-PDMS was investigated with nitrogen adsorption technique. (Table 1)

**Table 1** Summarization of materials investigated with different characterization methods.

MATERIAL	BLOCK COPOLYMERS		
	PI-PDMS	PB-PDMS	
STRUCTURE	HEX	HEX	GYR
ALIGNMENT	SHR	SHR	-
CHARACTERISATION	SEM TEM SAXS		
	SANS	N <sub>2</sub> adsorption	
APPLICATION		MEMBRANES	

By using above techniques of characterization we are able to measure pore diameter, distance between centers of the pores (for HEX), internal surface and spacing between primary symmetry planes. Data is presented in Table 2.

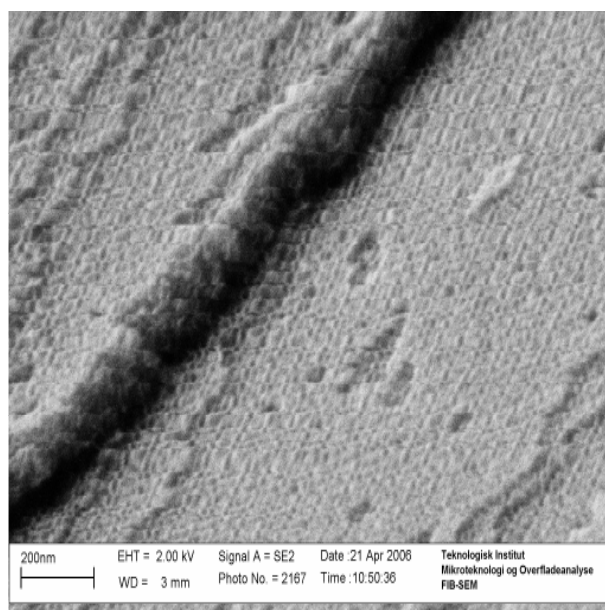


**Fig. 3** SEM picture showing gyroid structure of PB-PDMS.

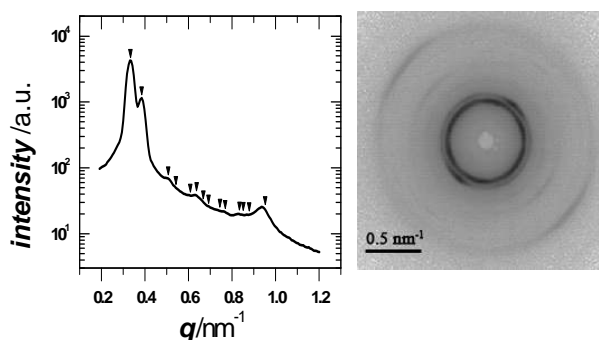


**Fig. 4** 1D data (to the left) showing plot of SAXS intensity vs. scattering vector  $q$  from PB-PDMS sample. The position of characteristic peaks are marked for gyroid structure. 2D data (to the right) of the SAXS.

**Table 2** Pore diameter, distance between centers of the pores, internal surface and spacing between primary symmetry planes for investigated materials.

		PI-PDMS	PB-PDMS		
		HEX	HEX		GYR
		SHR	SC	SHR	SC
Pore diameter [nm]	SEM		9±2	8±1	12±2
	TEM	7.6±1	8±1	8±1	
	N <sub>2</sub> ads		12±3	13±3	15±4
Distance between centers of the pores [nm]	SEM		12±2	23±2	
	TEM		15±1		
Internal surface [m <sup>2</sup> /g]	N <sub>2</sub> ads		85	70	278
Spacing between primary symmetry planes [nm]	SEM		18±3	14±3	50±4
	TEM	13.3±1	15±2		26±1
	SAXS	14.04	19.5	19.3	17±1

### Different structures and their potential application as a membrane

The gyroid structure is most interesting as a membrane. The advantage of the gyroid structure is that it is a cubic isotropic structure, so we do not have to orient it to get permeation from one surface of a membrane to another [12]. Here, discs of crosslinked and etched 1,2-polybutadiene-*b*-polydimethylsiloxane are investigated as a membrane.

The cylindrical, hexagonal morphology can also be potentially used as a membrane. However, in this case the minority block cylinders should be oriented perpendicular to the membrane main surface by using for example electrical field.

### Membrane preparation

The block copolymer (PB-PDMS) was dissolved together with a crosslinker (DCP) in tetrahydrofuran (THF). The solution was prepared in 30 mm diameter Petri Dish and left overnight to let the solvent evaporate. The mass of dissolved polymer was calculated to ensure different polymer thickness after solvent evaporation: 0.2; 0.3 and 0.5mm. Petri dishes were placed in a metal cylinder, which was filled with nitrogen. Closed and sealed metal cylinder was placed in oven (filled with argon) for 2 hours at 140°C. After 2 hours the cylinder was rapidly cooled down by placing in an ice bath. Cross-linked polymer was removed from Petri dish and placed in TBAF for 36 hours to etch the minority block of copolymer. After 36 hours etched samples were placed in THF and alternately in these mixtures:

- 80% THF/20% MeOH
- 60% THF/40% MeOH
- 40% THF/60% MeOH
- 20% THF/80% MeOH
- 100% MeOH

This procedure was used to avoid cracks due to rapid THF evaporation (TBAF is a THF solution). Samples were left overnight to let MeOH evaporate. Round knives were used to cut 9 and 14mm diameter discs (Fig.5) of crosslinked and etched material. This sequence of preparation steps is called *Technique 1*. Two other sequences were used. (Table 3)

**Table 3** Three sequences of steps for membrane preparation

Technique 1	Technique 2	Technique 3
x-linking	x-linking	x-linking I
etching	cutting	cutting
cleaning	etching	x-linking II
cutting	cleaning	etching
		cleaning

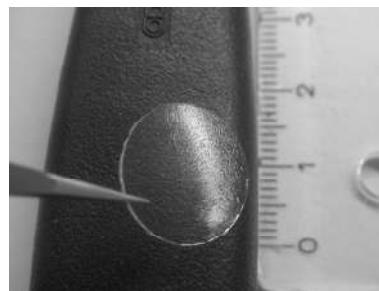


**Fig. 5** 14mm diameter disc cut from crosslinked and etched PB-PDMS

Prepared discs were investigated to check gas permeability (nitrogen) at different pressures. A simple setup for gas permeability consists of: 1. Gas container; 2. Manometer; 3. Membrane device; 4. Bubble flow meter.

Bubble flow meter enables to measure time needed to fill given volume by gas after going through the membrane at given pressure. From this the gas volume flux can be calculated.

Experimental data was compared to calculated theoretical data. Theoretical nitrogen fluxes were calculated from Knudsen flow equation. Knudsen flow occurs when a mean free path of gas molecules is larger or close to the membrane pore size diameter (Fig.6). [12].

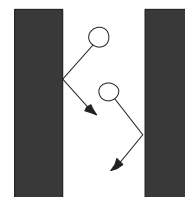


**Fig. 6** Schematic drawing depicting Knudsen flow

Flux of gas in Knudsen flow is given by:

$$J = \frac{\pi \cdot n \cdot r^2 \cdot D_k \cdot \Delta P}{R \cdot T \cdot \tau \cdot l}$$

Where:

$J$	- volume flux
$n \cdot \pi \cdot r^2 = \varepsilon$	- porosity
$D_k$	- Knudsen diffusion coefficient
$\Delta P$	- pressure difference
$R$	- gas constant
$T$	- temperature
$\tau$	- pore tortuosity
$l$	-membrane thickness

The tortuosity factor was calculated as a function of the porosity from [13]:

$$\tau = \frac{(2 - \varepsilon)^2}{\varepsilon}$$

Figure 7 represents the experimental and theoretical results of nitrogen flux for 0.79cm<sup>2</sup> membrane, 0.405mm thickness prepared from PB-PDMS crosslinked with 1% DCP for 2h at 140°C according to Technique 2. The theoretical calculations of fluxes for gyroid structure should be improved.

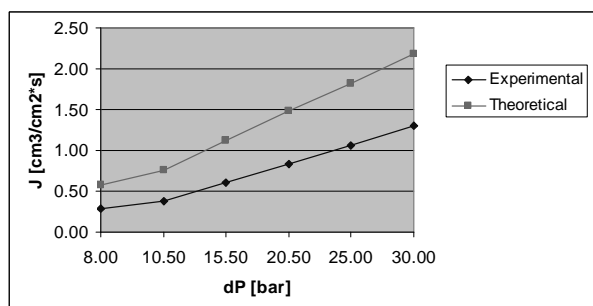


**Fig. 7** Experimental and theoretical data for nitrogen flux through nanoporous PB-PDMS disc at different pressures

## Conclusions and future plans

We managed to prepare nanoporous materials from diblock copolymers with well define structural dimension. The PB-PDMS with gyroid structure was used to prepare membranes and showed experimental fluxes of nitrogen in the range of theoretical predictions. However, the calculated values are not satisfactorily predicting experimental data and the modeling of the flow should be improved. Future work will aim at studying the flow of liquids through the membranes.

## References

1. M. S. Hansen, M. E. Vigild, R. H. Berg, S. Ndoni, *Polymer Bulletin* 51, (2004) 403-409
2. S. Ndoni, M. E. Vigild, R. H. Berg, *J. Am. Chem. Soc.* 125 (2003) 13366-13367
3. S. Ndoni, C. M. Papadakis, F. S. Bates, K. Almdal, *Rev. Sci. Instrum.* 66 (1995) 1090-1095
4. F. S. Bates, G. H. Fredrickson, *Physics Today* 52 (2) (1999) 32-38
5. N. Hadjichristidis, S. Pispas, G.A. Floudas "Block Copolymers-Synthetic Strategies, Physical Properties, and Applications" A John Wiley & Sons, New York, USA, 2003
6. M.W. Matsen, F.S. Bates *Macromolecules* 29 (4) (1996) 1091-1098
7. K. A. Cavicchi, A. S. Zalusky, M. A. Hillmyer, T. P. Lodge *Macromolecular Rapid Communications* 25 (2004) 704-709
8. J. Rzayew, M. A. Hillmyer *Macromolecules* 38 (2005) 3-5
9. Huiming Mao, Marc A. Hillmyer *Macromolecules* 38 (9) (2005) 4038-4039
10. Huiming Mao, Pedro L. Arrechea, Travis S. Bailey, Bret J. S. Johnson, M.A. Hillmyer *Faraday Discussions of the Chemical Society* 128 (2005) 149-162
11. Johanna H. Wolf, Marc A. Hillmyer *Langmuir* 19 (2003) 6553-6560
12. M. A. Hillmyer *Block Copolymers II Advances in Polymer Science* 190 (2005) 137-181
13. M. Mulder, *Basic Principles of Membrane Technology*, Kluwer Academic Publishers, Dordrecht, The Netherlands, 2003, p.227
14. S. B. Iversen, V. K. Bhatia, K. Dam-Johansen and G. Jonsson *Journal of Membrane Science* 130 (1997) 205-217



## Anders Daugaard Thomsen

Phone: +45 4525 6819  
Fax: +45 4588 2161  
E-mail: adt@kt.dtu.dk  
WWW: <http://www.dtu.dk/Centre/DPC>  
Supervisor: Søren Hvilsted

### Ph.D. Study

Started: March 2006  
To be completed: February 2009

## Micro-Sensor Based on Click Chemistry

### Abstract

During the last couple of years micro-sensors have received increased attention and the fabrication of micro devices shows a great promise for future applications. During recent years click chemistry, a novel functionalization technique has been introduced in macromolecular chemistry and this method has proven very efficient for functionalization of polymers. Preliminary work on the functionalization of polymers with carboxylic acids by click chemistry is presented here, while the ultimate target of this project is to use this method for direct linkage of sensor/detector molecules to the polymer backbone by a similar approach.

### Introduction

Functional (block-/co)polymers can be synthesized by a number of methods e.g. using functional mono-mers, by combination of preformed polymers or by postfunctionalization of a backbone. Regarding the linkage of sensor molecules to a polymer, the post-functionalization approach would be the better approach, though this is very dependent on the efficiency of the coupling reaction. In 2001 Sharpless et al.[1] introduced the concept click chemistry as a term for “perfect”, high yielding reactions for pharmaceutical applications. Of these reactions especially the Cu(I) catalyzed 1,3-dipolar cycloaddition of azides and alkynes[2,3] have shown promising use in macromolecular chemistry.

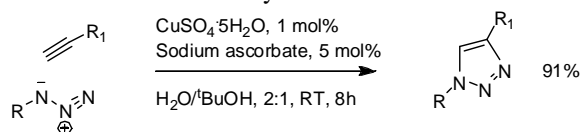


**Figure 1.** Cu(I) catalyzed 1,3-cycloaddition of azide and alkyne click reaction.

Linear polymers have been functionalized with Dendrons[4] and poly(ethylene glycol)s[5], and even simultaneous orthogonal ester and click reactions on polymer backbones have been performed[6], clearly highlighting the potential of click chemistry.

### Specific Objectives

This project is targeted towards the synthesis of functional (block-/co-)polymers and subsequent post-functionalization by click chemistry. This approach should then be used for micro-sensor fabrication and possibly for area specific bonding. Specifically the

project is currently oriented towards carboxylic acid polymers for applications in microfluidic systems.

### Synthesis Strategy

The applicability of click chemistry for polymer functionalization has been investigated with the synthesis of carboxylic acid polymers. These are difficult to produce by traditional polymerization techniques, and are believed to have an application in electro osmotic micropumps.

Poly(4-hydroxystyrene) (PHS) was chosen as backbone since it is easily alkyne functionalized through a Williamson ether synthesis. In addition azide derivatives are readily available from their respective bromides or alcohols through tosylation.

### Results and Discussion

The alkyne synthesis was performed using a Williamson ether synthesis as shown in Figure 2.

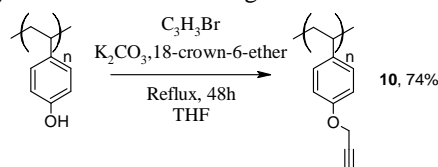


**Figure 2.** PHS-alkyne synthesis.

In parallel four different carboxylic acid derivatives were synthesized from the corresponding bromides by reaction with sodium azide as shown in Figure 3 for 4-(azidomethyl)benzoic acid (**1**) and equivalently for 6-azidohexanoic acid (**2**), 5-(6-azidohexoxy)iso-phthalic acid (**3**) and 2-(6-azidohexyl)malonic acid (**4**).

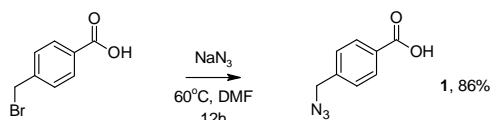


**Figure 3.** Synthesis of aromatic azide **1**.

Subsequently the alkyne polymer and the different azides were applied in click reactions to give the functional polymers as shown in Figure 4.

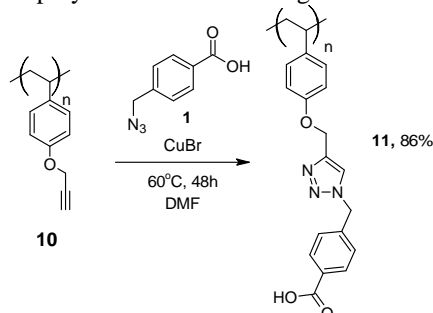


**Figure 4.** Homopolymer Functionalization of polymer alkyne **10** with the aromatic azide, **1**.

In addition to these carboxylic acid homopolymers a random copolymer of PHS-*co*-PMMA and a blockcopolymer of PHS-*b*-PS have also been synthesized. An overview of the different polymers is shown in Table 1 together with the glass transition temperatures ( $T_g$ ) for all the products.

#### Thermal Properties

Thermal analysis by Differential Scanning Calorimeter (DSC) has shown a clear correlation between the  $T_g$  and functional group modifications and grafting of the polymer backbone. Especially when comparing aromatic and aliphatic side chains a clear tendency toward high and low  $T_g$ 's becomes apparent, which is very important for the properties of the polymer. The influence from the number of groups on this effect is currently under investigation.

#### Conclusions

An alkyne-functionalized PHS showed excellent reactivity through click reactions with four different azides, and provided fully substituted polymers. The applicability of the approach has been illustrated through functionalizations of a random co-polymer, PHS-*co*-PMMA, as well as a block copolymer, PHS-*b*-PS.

Thermal investigations have shown a direct correlation to the changes in functionalities on the backbone.

The presented method has developed novel unprecedented polymers with a high carboxylic acid loading otherwise very difficult to prepare. Through these results the initial steps towards specifically functionalized polymers with e.g. sensor or detector molecules have been taken.

Presently the effect of a lower degree of substitution on the backbone and application of these polymers in micro fluidic devices are being investigated.

**Table 1.** Polymer click combinations, and  $T_g$ .

Alkyne	Azide	Product $T_g$ (°C)
 <b>10</b>	 <b>1</b>	98
	 <b>2</b>	54
	 <b>3</b>	118
	 <b>4</b>	60
 <b>15</b>	 <b>3</b>	90
	 <b>4</b>	65
 <b>18</b>	 <b>3</b>	100
	 <b>4</b>	104

#### Acknowledgements

DTU and the Danish Research Council for Technology and Production Sciences (framework programme "Design and Processing of Polymers for Microfluidic Applications", grant 26-04-0074).

#### References

- H.C. Kolb, M.G. Finn, K.B. Sharpless, *Angew. Chem. Int. Ed.* 40 (2001) 2004-2021.
- C.W. Tornøe, C. Christensen, M.J. Meldal, *J. Org. Chem.* 67 (2002) 3057-3064.
- V.V. Rostovtsev, L.G. Green, V.V. Fokin, K.B. Sharpless, *Angew. Chem. Int. Ed.* 41(2002) 2596-2599.
- B. Helms, J.L. Mynar, C.J. Hawker, J.M.J. Fréchet, *J. Am. Chem. Soc.* 126 (2004) 15020-15021.
- B. Parrish, R.B. Breitenkamp, T.J. Emrick, *J. Am. Chem. Soc.* 127 (2005) 7404-7410.
- M. Malkoch, R.J. Thibault, E. Drockenmuller, M. Messerschmidt, B. Voit, T.P. Russell, C.J. Hawker, *J. Am. Chem. Soc.* 127 (2005) 14942-14949.

#### List of Publications

- A. D. Thomsen, E. Malmström, S. Hvilsted, Oral Presentation, Nordic Polymer Days, Copenhagen, DK, May 2006.
- S. Hvilsted, E. Malmström, A. D. Thomsen, *Macro* 2006, Rio de Janeiro, BR, July 2006.
- A. D. Thomsen, E. Malmström, S. Hvilsted, *J. Pol.Sci. Part A. Pol. Chem.*,44(2006) 6360-6377.

**Amra Tihic**

Phone: +45 4525 2863  
Fax: +45 4525 2800  
E-mail: amt@kt.dtu.dk  
WWW: <http://www.ivc-sep.dtu.dk>  
Supervisors: Georgios M. Kontogeorgis  
Nicolas von Solms  
Michael L. Michelsen

**Ph.D. Study**

Started: May 2005  
To be completed: June 2008

## Advanced Thermodynamic Tools for Computer-Aided Product Design

**Abstract**

The simplified perturbed-chain statistical associating fluid theory (PC-SAFT) is applied to phase equilibria of binary systems that include a variety of non-associating compounds. Pure-component parameters of compounds that are not available in the literature are estimated by correlating vapor-pressure and liquid-density data. 450 new PC-SAFT parameters are estimated and tested for different families of non-associating compounds (polynuclear aromatics, sulfides, cyclo- and fluorinated- hydrocarbons, etc.). The overall behaviour of simplified PC-SAFT to successfully predict vapor-liquid equilibria for non-associating systems has been good. In a few cases, a small binary interaction parameter  $k_{ij}$  is needed for the satisfactory correlation of the experimental data.

**Introduction**

The prediction or correlation of the thermodynamic properties and phase equilibria with equations of state remains an important goal in chemical and related industries.

In the early 1980's the theory of Wertheim emerged from statistical thermodynamics. This method has been implemented into a new generation of engineering Equations of State (EoS) called Statistical Associating Fluid Theory (SAFT). Numerous modifications and improvements of different versions of SAFT have been proposed and applied. Three comprehensive reviews of the development and applications of the various types of SAFT are available for further information [1-2].

Simplified PC-SAFT [3-4] is as a non-cubic, segment-based equation of state designed specifically to deal with systems containing polymers and associating fluids and has been successfully applied to a number of complex systems over wide ranges of conditions. The model development of the PC-SAFT EoS is described in detail by Gross and Sadowski [3], while the main equations of the simplified PC-SAFT are given by von Solms *et al.* [4].

Our work aims in developing a theoretically based engineering tool that can be used for complex mixtures of importance to polymer and pharmaceutical industries. Common characteristics of all of these applications are complexity of molecules involved, the presence of various types of intermolecular forces (polarity,

hydrogen bonding, etc.) and the frequent coexistence of many phases at equilibrium e.g. vapour-liquid-liquid or solid-liquid-liquid. The thermodynamic model to be developed is a group-contribution version of the simplified PC-SAFT [4] equation of state where the parameters of the model are estimated via group contributions which are based on the so-called "conjugation principle" [5].

**Specific Objectives**

Most SAFT-type models require three parameters for each pure non-associating compound: the segment number ( $m$ ), the interaction energy ( $\epsilon/k$  in K), and the hard-core segment radius ( $\sigma$  in Å) that are typically estimated from vapour pressure and liquid density data over extended temperature ranges. This has been possible for small complex compounds for which such data are readily available. However for more complex compounds such as polymers, pharmaceuticals and pesticides extensive vapour pressures and liquid densities are not available and in many cases they can not be even measured. As mentioned, this limits the applicability of the models.

The suggested solution to this problem is to develop a group contribution scheme for estimating the parameters of these equations of state from low molecular weight compounds for which data is available

and then extrapolate to complex molecules. However, to be able to do this, it is necessary to have a very extensive PC-SAFT parameter table for numerous compounds so that in a subsequent step, a group contribution scheme for parameter estimated can be developed.

## Results and discussion

The following section firstly summarizes the main equations of simplified PC-SAFT. Secondly, presents a few modeling results for vapor-liquid equilibria of binary systems obtained with the simplified PC-SAFT as well as show some calculations of infinite activities for a few asymmetric systems.

The reduced Helmholtz energy for mixtures of associating molecules is given as follows:

$$\tilde{a} = \frac{A}{kTN} = \tilde{a}^{id} + \tilde{a}^{hc} + \tilde{a}^{disp} + \tilde{a}^{assoc} \quad (1)$$

where the first term is the ideal gas contribution, the second term is the contribution of the hard-sphere chain reference systems, the third term is the dispersion contribution arising from the square-well attractive potential, and the last term is the contribution due to association. The expressions for the contributions from the ideal gas and dispersion are identical to those of Gross and Sadowski [3]. The contribution to the hard-chain term is made up of two contributions: the hard-sphere term and the chain term,  $\tilde{a}^{hc} = \tilde{m}\tilde{a}^{hs} - \sum_i x_i(m_i - 1) \ln g_{ii}^{hs}(d_{ii}^+)$  (2)

where  $x_i$  is the mole fraction of component  $i$  and  $\tilde{m}$  is a mean segment length defined as  $\tilde{m} = \sum_i x_i m_i$  and the

hard-sphere term is given by

$$\tilde{a}^{hs} = \frac{4\eta - 3\eta^2}{(1-\eta)^2} \quad (3)$$

The radial distribution function at contact is

$$g^{hs}(d^+) = \frac{1-\eta/2}{(1-\eta)^3} \quad (4)$$

The volume fractions  $\eta = \pi\rho\tilde{m}d^3/6$  are based on an average diameter given as following:

$$d = \left( \frac{\sum_i x_i m_i d_i^3}{\sum_i x_i m_i} \right)^{1/3} \quad (5)$$

where the individual  $d_i$  are temperature-dependent segment diameters

$$d_i = \sigma_i \left[ 1 - 0.12 \exp \left( -3 \frac{\epsilon_i}{kT} \right) \right] \quad (6)$$

Thus, it is assumed that all the segments in the mixture have a mean diameter  $d$ , which gives a mixture volume fraction identical to that of the actual mixture.

In our recently published paper [6], beside the complete PC-SAFT table with around 200 newly estimated parameters for different families of non-associating compounds, phase equilibrium calculations

for ethers, aromatic compounds, nitroalkanes, fluorinated compounds, siloxanes, and plasticizers in order to investigate the reliability of those newly estimated parameters are presented. Some of these results are shown as the following.

The introductory phase of the project has focused on the parameters' behaviour when used by simplified PC-SAFT for mixture phase behaviour.

The linear relationship of simplified PC-SAFT parameters can be employed for various compounds as shown in Figure 1 where the group's segment number,  $m$ , is plotted as function of molecular weight [3]. A very similar trend has been observed for other SAFT-family models. The success of this extrapolation further underlines the sound physical basis of the equation of state.

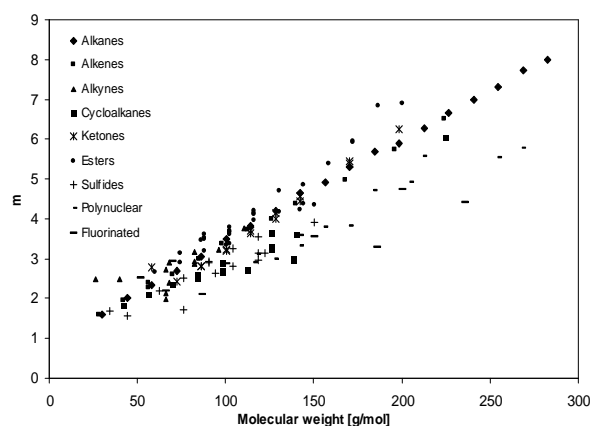


**Figure 1.** The segment number,  $m$ , versus molecular weight for different families of compounds.

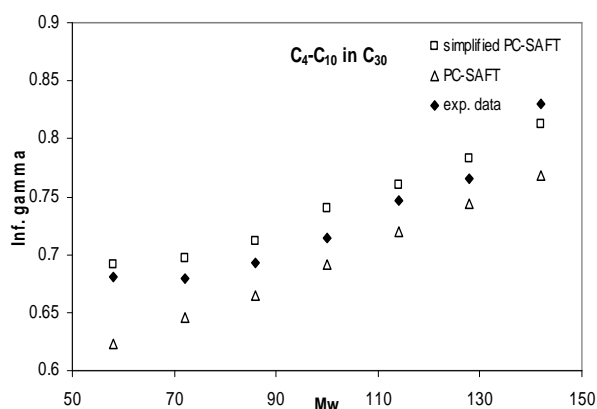
Furthermore, we have tested the ability of the model to describe the activity of a long-chain molecule using our new parameters for heavy alkanes, because if simplified PC-SAFT describes  $\gamma_2^\infty$  successfully, then the model can be perform liquid-liquid equilibria calculations in polymer mixtures as well. Infinite dilution activity coefficient calculations ( $\gamma_2^\infty$ ) have been performed in mixtures of heavy hydrocarbons ( $C_{12}$ - $C_{36}$ ). Additionally, some results of infinite dilution activity coefficient calculations ( $\gamma_1^\infty$ ) of light alkanes ( $C_4$ - $C_{10}$ ) in heavy ones  $C_{36}$  as shown in Figure 2. All those calculations have been performed with the  $k_{ij}$  equal to zero.

Table 1 shows an improved performance of simplified PC-SAFT to predict activity coefficients at infinite dilution in the majority of the studied systems when using newly estimated parameters for heavy alkanes. "old" estimated parameters from a previous published paper [7]

**Table 1.** Average percent deviations (% AAD) between experimental data and predicted ( $k_{ij}=0$ ) activity coefficients at infinite dilution with simplified PC-SAFT using new and old estimated pure compound parameters for heavy alkanes.

% AAD	Simplified PC-SAFT new	Simplified PC-SAFT old
$C_{12}-C_{36}$ in $C_6$	10	16
$C_{18}-C_{36}$ in $C_7$	8	15
$C_4-C_{10}$ in $C_{30}$	2	5
$C_4-C_{10}$ in $C_{36}$	3	6

\*Cx indicate an alkane with x carbon atoms.



**Figure 2.** Experimental and predicted activity coefficients at infinite dilution for light alkanes in  $n-C_{30}$  as function of the molecular weight of the heavy alkane.

The results in Figure 2 show that for this particular system, the model overestimates the experimental data in almost all cases. As expected, the deviation of simplified PC-SAFT from original PC-SAFT is more obvious when the molecular weight of the heavy alkanes increases, in other words, when the size-difference between the two components is greater.

Binary vapor-liquid predictions for propane with a series of linear heavy alkanes are presented in Table 2, where the obtained average deviation for vapour pressure is only 1.5%.

**Table 2.** VLE predictions with simplified PC-SAFT for propane-n-alkane systems

n-alkane	x	Temp. range [K]	AAD P <sup>1</sup> [%]
Eicosane	0.2448	293-350	2.67
	0.3445	304-357	2.40
Tetratriacontane	0.0112	320-366	0.13
	0.3969	336-427	1.21
Hexacontane	0.2405	365-419	1.74
	0.3902	368-413	1.00

<sup>1</sup>AAD P = average deviation in vapour pressure

Besides the previous mentioned results, the solubility of carbon dioxide in butane is studied by the simplified PC-SAFT using the same positive value of

the interaction parameter  $k_{ij}$  as this type of mixtures is important in supercritical extraction and in enhanced oil recovery. Figure 3 shows the binary phase diagram for the system when treating carbon dioxide without incorporating quadropolar interactions can still yield satisfactory results using  $k_{ij}=0.075$ .

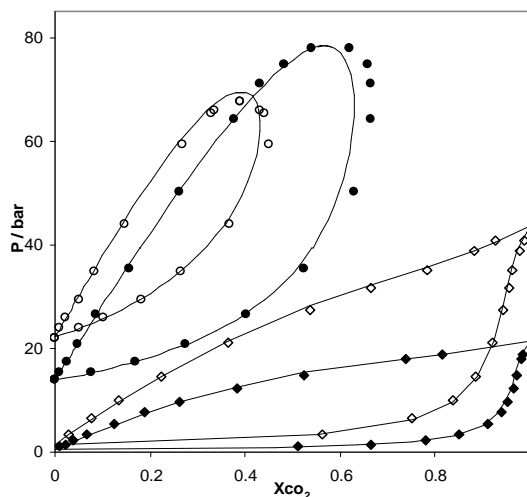


**Figure 3.** Vapor-liquid equilibrium for butane-carbon dioxide mixtures at four temperatures (120, 95, 10 and -45°C). Lines are correlations with simplified PC-SAFT ( $k_{ij}=0.075$ ).

## Conclusions

The prediction or correlation of thermodynamic properties and phase equilibria with a good thermodynamic tool still remains a very important goal in chemical and related industries. During the past few years, modern equations of state such as the modified PC-SAFT developed at IVC-SEP, has been proved to be very successful in modeling many kinds of equilibria in binary as well as ternary complex systems with good accuracy.

In this work, we have estimated the three pure compound PC-SAFT parameters for additional 450 non-associating compounds and tested the simplified PC-SAFT equation of state to model VLE and LLE in systems containing a range of non-associating compounds.

Our basic conclusion is that simplified PC-SAFT is quite successful in predicting and correlating vapour-liquid and liquid-liquid equilibrium behaviour in a variety of different types of binary system when using newly estimated PC-SAFT parameters. The obtained results furthermore justify the capability of simplified PC-SAFT in describing many different types of systems. In a few cases, where predictions are not accurate, a small value of the binary interaction parameter is required to satisfactorily correlate experimental data.

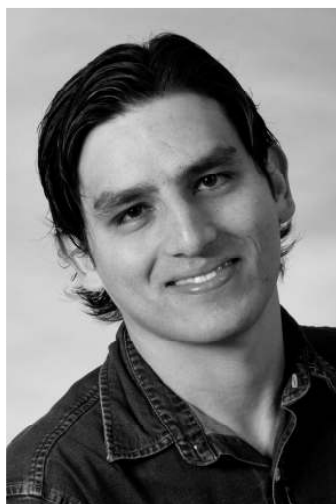
### **Acknowledgments**

The author and the supervisors wish to thank the Danish Technical Research Council (STVF) for financial support of this work as part of a grant entitled "Advanced Thermodynamic Tools for Computer-Aided Product Design".

The author wishes furthermore to thank Georgios Kontogeorgis, Michael Michelsen and Nicolas von Solms for their supervision, as well as Dr. Leonidas Constantinou for having contributed significantly in the presented work.

### **References**

1. E.A. Müller, K.E. Gubbins, *Ind. Eng. Chem. Res.* 40 (2001) 2193
2. I.G. Economou, *Ind. Eng. Chem. Res.* 41 (2002) 953
3. J. Gross, and G. Sadowski, *Ind. Eng. Chem. Res.* 40 (2001) 1244
4. N. von Solms, M.L. Michelsen, and G.M. Kontogeorgis, *Ind. Eng. Chem. Res.* 42 (2003) 1098
5. L. Constantinou, R. Gani, *AIChE J.*, 40 (1994) 1697
6. A. Tihic, G.M. Kontogeorgis, N. von Solms, M.L. Michelsen, *Fluid Phase Equilibria*, 248 (2006) 29
7. I.A. Kouskoumvekaki, N. von Solms, T. Lundvig, M.L. Michelsen, G.M. Kontogeorgis, *Ind. Eng. Chem. Res.* 43 (2004) 2830



### Hugo Edson González Villalba

Phone: +45 4525 2912  
Fax: +45 4588 2258  
E-mail: heg@kt.dtu.dk  
WWW: <http://www.capec.kt.dtu.dk/People/phds>  
Supervisors: Rafiqul Gani  
Jens Abildskov

Ph.D. Study  
Started: October 2005  
To be completed: September 2008

## Development of Group Contribution<sup>Plus</sup> Models for Properties of Organic Chemical Systems

### Abstract

In product and process design involving chemical and pharmaceutical industries, it is necessary to have available, reliable and predictive property models supported by a large and reliable thermophysical data bank. This project focuses on developing new and better group contribution models for pure components and mixtures involving high-value chemicals and mixtures. Two study cases will be highlighted to show the performance of GC-plus models.

### Introduction

In computer-aided model-based methods and tools for synthesis and design of the product-process, the applicability of the product-process model and its reliability is governed by the property models within the total model. In addition to reliability of the property models, another important need in product-process synthesis and design is that the models need to be predictive and fairly simple and easy to use. Group contribution (GC) based property models satisfy most of the above requirements and are therefore, routinely used in product-process synthesis and design. There are however some limitations, for example, they are not very reliable for complex chemicals or systems of complex chemicals; group parameters may not be available; not enough experimental data is available to develop a large set of group parameters; reliability is often dependent on how the chemical structure is represented by the groups. These limitations make the synthesis and design of high-value chemical products such as drugs, pesticides, structured polymers, etc., difficult with model-based methods since the necessary reliable property models are not available.

### Specific Objectives

The objective of the PhD-project is to develop a new class of group contribution plus models, which addresses the limitations of the current GC-models so that industrially important chemical product-process synthesis and design problems can be solved through reliable and efficient model-based approaches. The "GC-plus" indicates that the developed models will use

hybrid models that will combine the simplicity and the predictive nature of GC-models with the additional molecular structure based contributions that are needed to improve the property estimations and to significantly extend the application range.

### Case Study 1.

#### *Normal boiling point for cis-trans compounds*

Many biological, medical, pharmaceutical, agricultural and food products and their processes involve stereoisomers. Their chemical, medicinal, organoleptic and biological properties can differ significantly. Knowing how their thermodynamic properties differ is necessary to model such systems. Predictive GC models fail to take into account 3D features that are intrinsic of the cis-trans isomers. The main reason is the 2D nature of GC methods, which mostly satisfy the needs of typical chemical engineering problems where it is sufficient to work with suppressed hydrogen graphs.

Based on Marrero-Gani (MG) GC model for estimation of the normal boiling point (NBP) a model able to predict the NBP differences between cis-trans isomers with reasonable accuracy has been developed.

The work includes the: 1) Generation of a new database for cis/trans isomers including atom interactions, steric properties and intermolecular forces (generated through atomic level calculations) related with specific properties of interest; 2) Derivation of a new term that takes into account 3D structural parameters and 3) Implementation of this term into a GC-plus method.

### Use of MM2 force field.

The MM2 method based on molecular mechanics considers atoms as spheres and bonds as springs. So, the method takes into account molecular features such as the ability of bonds to stretch, bend or twist. The force field also takes into account the possibility of non-bonded interactions such as repulsion and attraction forces. Therefore, the energy associated to the force field can be described by

$$\text{Energy} = \text{stretching} + \text{bending} + \text{torsion} + \text{non-bonded} \quad (1)$$

So, basically we have five contributions to the intrinsic energy of the molecule: Stretch energy, bend energy, torsion energy, van der Waals forces, and electrostatic forces. Table 1 summarizes the physical meaning of each property.

**Table 1.** The force field interactions and their meaning

INTERACTION	MEANING
Bond Stretching	Bond stretching between directly bonded atoms
Angle Bending	Angle bending between atoms that are geminal to each other
Torsional Energy	Torsional angle rotation between atoms that are vicinal each other
Repulsion/Attraction (van der Waals) forces	Repulsion between atoms that are too close to each other and attraction at long range from dispersion forces
Interaction Energy	Interaction from charges, dipoles, quadrupoles (electrostatic interactions)

A correlation based analysis has been performed in order to choose the best interactions for developing the GC-plus model. Using MM2 from CHEM3D<sup>®</sup> the following interactions were selected: torsion, bend, Van der Waals and non- Van der Waals.

The proposed model for the estimation of normal boiling point using these properties is the following:

$$\exp\left(\frac{T_b}{T_{b0}}\right) = \exp\left(\frac{T_b}{T_{b0}}\right)_{\text{Marrero-Gani}} + \sum_{i=1}^n a_i N_i^A w_b + b \cdot w_b + c \cdot \text{bend}_i + d \cdot \text{torsion}_i$$

$w_b = \alpha W + \text{non-}\alpha W$

$a..d$ : parameters

$i$ : compound- $i$

$A$ : Atom- $A$

$N_i^A$ : Atoms-of-type- $A$ -in-molecule- $i$

Here  $\exp(T_b/t_{b0})_{\text{Marrero/Gani}}$  denotes the estimate with the Marrero/Gani<sup>[1]</sup> model.

Using the GC-plus model the results have been evaluated in terms of two perspectives: a quantitative analysis that refers to the minimization of the error related with the NBP values predicted and the comparison with the experimental data. A qualitative analysis that focuses on the prediction of the right trend on the differences between cis and trans isomers, this is, if the real cis NBP of the compound “x” is bigger than the trans one, the prediction must follow the same trend.

The former behavior is one feature that is most difficult to overcome between cis/trans isomers. The numerical differences between the molecular descriptors can be used to improve the Marrero-Gani (MG) method and make it predict the correct trend. The databank that we use includes: the CAPEC database, external free-databases, and data from members of the CAPEC industrial consortium.

### Results and discussion.

The quantitative results have been evaluated using the sum of squares error (SSE) based on the estimated values and the correspondent experimental data. The SSE for the selected database using MG is 8181.75 and using MG-plus is 7172.53.

The qualitative analysis involves a selection of pairs of cis-trans isomers, since the comparison must be done between pairs of isomers. For this reason the database used for comparison purposes decreases in number. The results are expressed in terms of % of “right trend” on the predictions. The result is that 58.33% of the estimations exhibit the right trend on the qualitative analysis.

It is clear that the GC-plus model improves the predictive power of previous GC models for cis-trans isomers. A collection of much more data is necessary in order to increase the accuracy of the estimations. Also as have been pointed out, a further refinement on the model to deal with the qualitative approach is necessary. The next step must be in the sense of collect more data, improve the model, and extend the range of properties predicted using GC-plus models.

### Case Study 2.

#### UNIFAC-CI Group Contribution plus model.

Regarding GC-plus models for mixtures; *Le Bert- Gani -Abildskov*<sup>[2]</sup> had proposed the use of CI (connectivity indices) –as molecular descriptors- to overcome the lack of GIP’s on the UNIFAC group contribution method for VLE. The basic idea behind this work is to derive a relation between the group interaction parameters with the CI and atom constitution of the groups describing the molecules under study. In this way, with a database of CI and the number of atoms, the uncertainty between group interaction parameters GIP’s and the derived relation is what we call atom interaction parameters (AIP’s).

Once a work system is defined; for example, VLE involving compounds with C,O atoms and their groups

information (in terms of CI and number of atoms ) and the AIP's fitted, it is possible to: 1) Generate values for missing GIP's on the UNIFAC matrix 2) Reestimate (if its necessary) one or some GIP's 3) Create a group and estimate its GIP's.

*Le Bert- Gani-Abildskov* have already the AIP's for the VLE system involving C,O atoms. It must be pointed out that as the CI uses hydrogen suppressed graphs, the presence of hydrogen atoms are implicit. In this work, nitrogen related compounds have been added to the system under study.

Relation between group- and atom-interaction parameters. The atom-atom interactions are taken at 4 different levels:

Level 1: interaction between 0<sup>th</sup> and 0<sup>th</sup> order valence connectivity indices.

Level 2: interaction between 0<sup>th</sup> and 1<sup>st</sup> order valence connectivity indices.

Level 3: interaction between 1<sup>st</sup> and 1<sup>st</sup> order valence connectivity indices.

Level 4: interaction between 0<sup>th</sup> and 2<sup>nd</sup> order valence connectivity indices.

For two groups noted k and l, where k has a lower group index than l, the following two relations apply:

$$\begin{aligned}
 a_{kl} = & \underbrace{b_{C-C} (A_{kl}^{CC})_0 + b_{C-O} (A_{kl}^{CO})_0 + b_{C-N} (A_{kl}^{CN})_0 + \dots}_{0^{\text{th}}\text{-order interactions}} \\
 & + \underbrace{c_{C-C} (A_{kl}^{CC})_1 + c_{C-O} (A_{kl}^{CO})_1 + c_{C-N} (A_{kl}^{CN})_1 + \dots}_{1^{\text{st}}\text{-order interactions}} \\
 & + \underbrace{d_{C-C} (A_{kl}^{CC})_2 + d_{C-O} (A_{kl}^{CO})_2 + d_{C-N} (A_{kl}^{CN})_2 + \dots}_{2^{\text{nd}}\text{-order interactions}} \\
 & + \underbrace{e_{C-C} (A_{kl}^{CC})_3 + e_{C-O} (A_{kl}^{CO})_3 + e_{C-N} (A_{kl}^{CN})_3 + \dots}_{3^{\text{rd}}\text{-order interactions}}
 \end{aligned} \quad (3)$$

And:

$$\begin{aligned}
 a_{lk} = & \underbrace{\overline{b_{C-C}} (A_{kl}^{CC})_0 + \overline{b_{C-O}} (A_{kl}^{CO})_0 + \overline{b_{C-N}} (A_{kl}^{CN})_0 + \dots}_{0^{\text{th}}\text{-order interactions}} \\
 & + \underbrace{\overline{c_{C-C}} (A_{kl}^{CC})_1 + \overline{c_{C-O}} (A_{kl}^{CO})_1 + \overline{c_{C-N}} (A_{kl}^{CN})_1 + \dots}_{1^{\text{st}}\text{-order interactions}} \\
 & + \underbrace{\overline{d_{C-C}} (A_{kl}^{CC})_2 + \overline{d_{C-O}} (A_{kl}^{CO})_2 + \overline{d_{C-N}} (A_{kl}^{CN})_2 + \dots}_{2^{\text{nd}}\text{-order interactions}} \\
 & + \underbrace{\overline{e_{C-C}} (A_{kl}^{CC})_3 + \overline{e_{C-O}} (A_{kl}^{CO})_3 + \overline{e_{C-N}} (A_{kl}^{CN})_3 + \dots}_{3^{\text{rd}}\text{-order interactions}}
 \end{aligned} \quad (4)$$

Where:

$b_{X-Y}, c_{X-Y}, d_{X-Y}, e_{X-Y}, \overline{b_{X-Y}}, \overline{c_{X-Y}}, \overline{d_{X-Y}}, \overline{e_{X-Y}}$  are the interaction parameters between atoms of type X

and atoms of type Y ( $A_{kl}^{XY}$ )<sub>m</sub> are the coefficients to be used with the corresponding atom-interactions, i.e. at the order m, between atoms of type X and atoms of type Y, in the interaction between group k and group l, and which are defined by the following equations for each order:

$$(A_{kl}^{XY})_0 = \frac{n_X^{(k) \vee} \chi_{(l)}^0 - n_Y^{(l) \vee} \chi_{(k)}^0}{\vee \chi_{(l)}^0 \vee \chi_{(k)}^0} \quad (5)$$

and so on for the higher order coefficients.

Where  $n_X^{(k)}$  is the number of atoms of type X in the group k and  $\vee \chi_{(k)}^m$  is the m-th order valence connectivity index for the group k.

At this moment the following UNIFAC groups have been covered: CH<sub>2</sub>, C=C, ACH, ACCH<sub>2</sub>, OH, CH<sub>3</sub>OH, H<sub>2</sub>O, ACOH, CH<sub>2</sub>CO, COH, CCOO, HCOO, CH<sub>2</sub>O, CH<sub>2</sub>O, CNH<sub>2</sub>, (C)<sub>2</sub>NH, (C)<sub>3</sub>N, ACNH<sub>2</sub>, CCN, and CNO<sub>2</sub>. Instead fitting 460 GIP's that represent the mixtures using the above groups, a set of 72 AIP's need to be regressed for the UNIFAC-CI method.

**Parameter optimization.** The database for the regression step includes 32 binary measurement series (462 values) for VLE systems involving C,O,N atoms and 227 binary measurement series (3946 values) for VLE systems involving C,O atoms. The parameter estimation of this work is exclusively based on isothermal data and checked for thermodynamic consistency (Van Ness<sup>[3]</sup>). The optimization algorithm used for the data fitting was the Levenberg-Marquardt<sup>[4][5]</sup> technique, which is a local optimization method. It is therefore strongly dependent on the initial guesses for the parameters. The proposed objective function is the following:

$$S = \frac{1}{N} \sum_{i=1}^N \left( \frac{P_{\text{exp}} - P_{\text{calc}}}{P_{\text{exp}}} \right)^2 + w_{\text{reg}} \sum_j (AIP_j - AIP_j^{\text{IG}})^2 \quad (6)$$

where N is the number of experimental data points, AIP<sub>j</sub> is the current value of the atom-interaction parameter j, AIP<sub>j</sub><sup>IG</sup> its corresponding initial guess, and w<sub>reg</sub> a weighting value used to increase or decrease the influence of regularization in the optimization.

## Results and Discussion

The plots on figure 1 present the comparison between the deviation from experimental data with the original UNIFAC method and UNIFAC-CI. The deviation

plotted in these figures is the average absolute relative deviation (AARD %) for the data set as is define on equation 7.

$$AARD(\%) = \frac{1}{N} \sum_{i=1}^N \left| \frac{P_{exp} - P_{calc}}{P_{exp}} \right| \times 100 \quad (7)$$

From the plots it is clear that UNIFAC-CI exhibit a reasonable good range of deviation from the experimental using the AIP's to calculate GIP's in comparison with the range of deviation of the original UNIFAC method.

For the plots on figure 1 it is shown a comparison between original UNIFAC and UNIFAC-CI according to the AARD % for each data set. The data regression was performed with different regularization options. It

can be seen that after using a regularization parameters of  $reg=1.0e2$  or above, the correlation error can be decreased.

The regularization scheme that shows the least error is the one corresponding to  $reg=1.0E2$  since the average AARD % is 4.4266. However as we can see from the plots, the differences between regularization options are not so big.

From plots of fig. 1, one can see that the deviation from the experimental data using the atom-interaction parameters to calculate group-interaction parameters is very comparable to the deviation of the original UNIFAC method. The deviations are even better in most cases, especially for the systems that are poorly represented with original UNIFAC method.

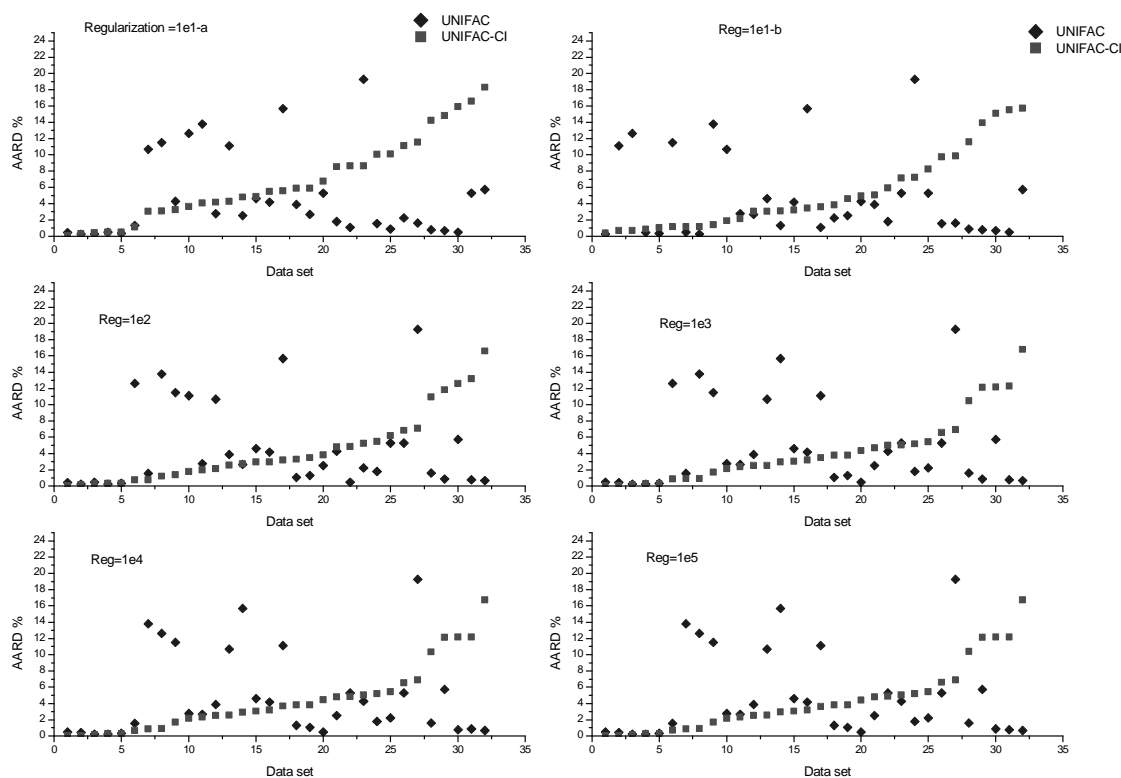


**Figure 1.** AARD % for both original UNIFAC and UNIFAC-CI among regularization schemes. The lowest value for AARD % corresponds to  $reg = 1.0E2$ .

## Conclusions

GC-plus models have been developed and tested for the improvement on property estimations for pure compounds and mixtures. In addition, the models have been compared with well known conventional GC models of the method and found to give good results. The next logical step is the further refinement of the method to improve the accuracy of the models, the extension to other properties and the implementation of the method as a computer aided tool into ICAS<sup>[6]</sup> (Integrated Computer Aided System) from CAPEC.

For the NBP GC-plus model, it is necessary to create a larger database in order to increase the reliability of the calculations.

For the UNIFAC-CI model, further work includes the extension to atoms other than C,O,N, for example chlorine. This is quite dependent on the amount of available data. Also, the extensions of this method to models for LLE and SLE are being considered.

### **Acknowledgements**

Funding for Hugo E. Gonzalez Villalba through the National Council of Science and Technology (CONACyT) from Mexico is gratefully acknowledged.

### **References**

1. Marrero, J.; Gani, R. A Group Contribution Based Estimation of Pure Component Properties. *Fluid Phase Equilibria*. 2001, 183, 183.
2. Le Bert B., Gani R., Abildskov J., Prediction of Missing UNIFAC Group Interaction Parameters through Connectivity Indices, *AIChE J.* (submitted) 2006.
3. Van Ness, H.C. Thermodynamics in the treatment of (vapor + liquid) equilibria. *J. Chem. Thermodynamics*. 1995, 27, 113-134.
4. Levenberg, K. A Method for the Solution of Certain Problems in Least Squares. *Quart. Appl. Math.* 1944, 2, 164-168.
5. Marquardt, D. An Algorithm for Least-Squares Estimation of Nonlinear Parameters. *SIAM J. Appl. Math.* 1963, 11, 431-441.
6. ICAS, KT-CAPEC, DTU, Lyngby, Denmark.



**Yanwei Wang**

Phone: +45 4525 6809  
Fax: +45 4588 2161  
E-mail: wyw@kt.dtu.dk  
WWW: <http://www.kt.dtu.dk>  
Supervisors: Ole Hassager  
Flemming Yssing Hansen  
Guenther Peters

Ph.D. Study  
Started: August 2005  
To be completed: August 2008

## Molecular Modeling of Polymer Properties

### Abstract

A variety of molecular modeling techniques have been applied into the study of polymer properties. Such techniques include Equilibrium and Non-Equilibrium Molecular Dynamics (EMD, NEMD), Brownian Dynamics (BD), Dissipative Particle Dynamics (DPD) and a variety of Monte Carlo (MC) algorithm, and many others. In this article, we attempt to summarize our understanding on those techniques in the study of polymer structure, dynamics and rheological properties.

### Introduction

Molecular modeling is a collective term that refers to theoretical methods and computational techniques to model or mimic the behavior of molecules. Those techniques are becoming more and more valuable in polymer science for the exploration of the rich properties of polymer systems. In the past two years, we investigated a variety of molecular simulation methods including EMD [1, 8, 10], NEMD [11], BD [6, 9], DPD [7] and MC in our study of polymer properties, and we attempt to summarize our understanding on the capability/applicability of those techniques here. This survey is organized into three main parts concerning polymer structure, dynamics and rheological properties respectively, and we mainly concentrate on our own simulation results.

### Explore the Structure Properties

A complete description of a polymer molecule typically requires a wide range of length scales. Intra-molecular correlations and local packing of chains in bulk exhibit features on the length scale of bond lengths and atomic radii, i.e. a few Å. The Kuhn length of a typical synthetic flexible polymer coil is on the order of 1 nm and can be considerably large for stiff polymers, such as DNA. The radius of gyration of a entire chain in the amorphous bulk scales as  $N^{1/2}$  with the chain length  $N$  and is on the order of 10 nm for typical molecular weights; the smallest dimension of micro-phases (lamellae, cylinders, spheres) in micro-phase separated block copolymer systems is also on the order of 10 nm, while crystallite size in semi-crystalline polymers and

domain size in immiscible polymer blends may well be on the order of  $\mu\text{m}$ . [2]

Due to the wide spectrum of length scales involved, coarse-graining is often necessary in the study of polymer properties. A common way of getting rid of all the chemical details on the monomer level is to adapt the Gaussian chain approximation, i.e. assuming polymers can be described by random walks in space. Such an assumption is often valid for long flexible polymers in bulk melt state or being dissolved in a theta solvent. In a good solvent, long range excluded volume interaction becomes important, and polymer swells, in which case a self-avoiding walk can be crucial. When the chain is placed in a poor solvent, polymer collapses, due to the fact that it is thermodynamically favorable for chain segments stay close [3]. In dynamic simulations like MD, DPD and BD, polymer molecules are often represented by a bead-spring model, and an apparent difference among those different simulation methods is that the interaction force law is different.

Besides the multi-length scale problem, the time spectrum associated with the complicated dynamic behavior of polymer chains is also widely spread, which will be discussed in detail in the section for polymer dynamics. For such reasons, Monte Carlo methods are often of an advantage in obtaining structure properties of polymers provided that we are only interested in the structure properties. If we adapt the Gaussian chain approximation, polymers with arbitrary architecture can be studied by constructing random walks in space, resulting in a variety of useful structure properties of the complex molecule (Figure 1). Such methodology has been incorporated in our recent model developed for

obtaining elution curves for size exclusion chromatography (SEC) of complex mixed polymer samples. Besides, properties such as zero-shear bulk viscosity and the steady state recoverable compliance can be calculated from size calculations according to the Rouse theory [4].

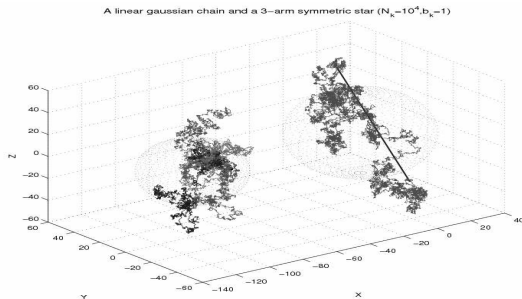


**Figure 1:** Gaussian chain model for polymers. Plotted are 3D structures of a 3-arm symmetric star polymer (left) and a linear polymer (right) with the same number of chain segments. The spheres shown by dots having the center at the center of mass and radii equal to the radius of gyration of each polymer.

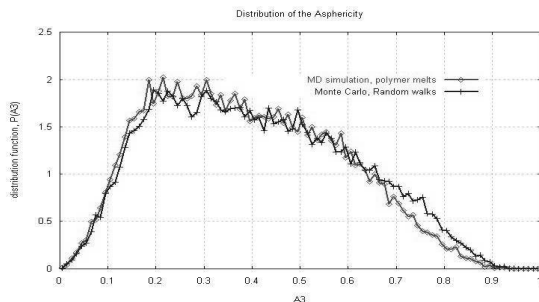


**Figure 2:** distribution of chain asphericity calculated from MD simulation of polymer melts (square symbol) and random walks (cross symbol). The system includes 32 chains with 100 beads on each chain interacting through the so called “Kremer-Grest Model. [1] Chain asphericity is a quantity describing how the chain conformation deviates from spherical symmetry with the value equal to 0 for a sphere and 1 for a rod [5].

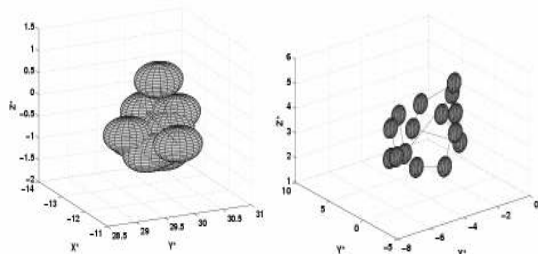


**Figure 3:** snapshots of chain conformation in a BD simulation. The chain is composed by 15 beads. The left figure represents the collapsed state when a polymer chain is placed in a poor solvent, and the right figure represents a theta solvent condition where the chain conformation is Gaussian.

However, often we are not only interested in the structure properties of polymers, but also the dynamics

properties. Since dynamic information is not involved in usual Monte Carlo simulations, dynamic simulations such as MD, BD and DPD have to be used. In such cases, structure properties can also be easily calculated as a byproduct of the dynamic simulation. In Figure 2~4, some results concerning structure properties of polymer chains are presented, and those results are obtained from our MD, BD and DPD simulations respectively.

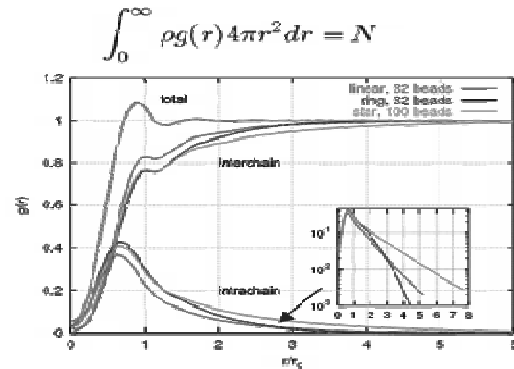


**Figure 4:** radial distribution function calculated from DPD simulations. Radial distribution function described how the chain segments are packed locally. Plotted are the total, inter-chain and intra-chain radial distribution functions for three melt systems: linear polymer of 32 beads, ring polymer of 32 beads and star polymer of 100 beads. Due to the soft repulsive potential used in DPD simulations, chain crossing cannot be avoided. In melt state, polymer chains are highly overlapping.

### Explore the Dynamic Properties

As we mentioned briefly in the previous section, compared to the multi-length scale problem, the range of time scales characterizing the dynamic properties of polymers is even broader. While localized vibration modes of chains have periods on the order of 10 fs, conformation transitions of individual bonds over torsional energy barriers in the melt state exhibit waiting times in excess of 10 ps. Longer and longer sequences of segments along the backbones need longer and longer correlation time to rearrange. The longest relaxation time, required for a chain to diffuse over its own size and thus forget its previous conformation, is critical to the Viscoelastic response of polymer melts in flow. This time scales as  $N^2$  for low molecular weight melts in the Rouse regime and as  $N^{3,4}$  above a critical molecular weight for chain entanglements, i.e. in the reptation regime. For a  $C_{800}$  polyethylene melt at 450 K this time is on the order of 3  $\mu$ s, while it can easily exceed the millisecond time scale for the molecular weight encountered in typical processing operations. The time scales for morphology developed through nucleation and growth or spinodal decomposition processes typically exceed 1 s, while the characteristic times for volume and enthalpy relaxation in a glassy polymer at temperature just 20  $^{\circ}$ C below the glass transition temperature are on the order of years. [2] Atomistic MD simulation, on the other hand, typically tracks the

evolution of model systems of length scale about 10 nm for time scales up to a few decades of ns. While the length scale can be increased significantly by use of domain decomposition strategies on parallel computers, there is little one can do about the time scales.

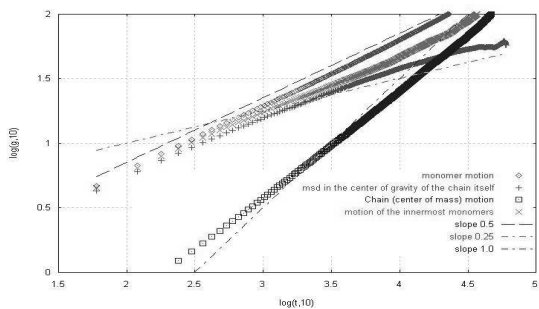


**Figure 5:** Motion of a polymer chain in melt state (32 chains with 100 beads on each chain). Mean-square displacement of chain segment motion (red), innermost segment motion(magenta), mean square displacement of chain segments relative to center of gravity of the chain itself (green) and mean square displacement of the center of mass(blue). The Rouse time, at which chain segment will follow the motion of the center of mass, was not reached in the simulation.[1].

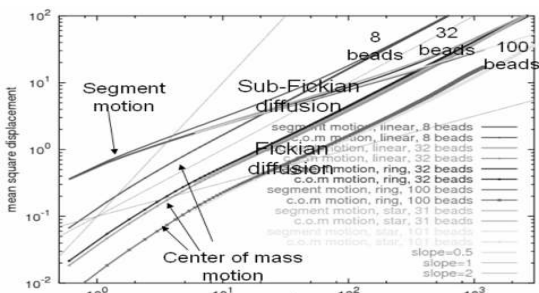


**Figure 6:** polymer dynamics in DPD simulations. Both the segment motion and the center of mass motion are shown. We studied polymer chains with different architecture (linear, ring and star) and with different number of beads. The simulation results show Rouse dynamics, and the simulated diffusion behavior depends more on the number of beads along than chain rather than the chain architecture. This is in consistent with the Rouse model, and could be caused by the exclusion of chain uncrossibility.

Nevertheless, techniques such as MD, DPD and BD have been shown to be useful in the study of diffusion behavior of polymers (Figure 5~7). For polymer melts, entanglement dynamics can be probed with long chains interacting through the Kremer-Grest potential model [8]. For unentangled polymer melts, Rouse dynamics can be studied by both MD and DPD simulations. Due to soft repulsive interaction potential used in DPD simulation, entanglement dynamics due to chain uncrossibility can not be probed. For polymer solutions, both DPD and BD simulations have been shown to be useful. In DPD simulations, solvent molecules are explicitly included, while in BD simulations, solvent effects are implicitly included through excluded volume

interaction, local drag, random force and hydrodynamic interaction. DPD simulations have an advantage in dealing with confinement effect and flow under complex geometries. However, the Schmidt number ( $Sc$ ) in DPD simulations has been shown to be far less than the value for real physical fluids [7]. On this aspect, BD simulations with hydrodynamic interactions may possess a sounder physical basis, since momentum transport in real fluids is much faster than mass diffusion (i.e.  $Sc \gg 1$ ).

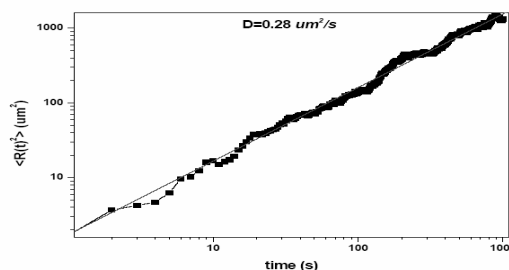


**Figure 7:** Mean square center of mass displacement of a 21  $\mu m$  DNA molecule represented by a 10 beads bead spring model. Hydrodynamic interaction is included by the RPY tensor, friction force and Brownian force satisfies the dissipation-fluctuation theorem. With BD simulation, large time scale dynamic behavior can be probed.[9].

### Explore the Rheological Properties

In Equilibrium dynamic simulations, such as equilibrium MD, DPD, stress autocorrelation function can be computed, which allows us to obtain quantities such as viscosity, storage and loss module through the Green-Kubo formula, which is the same type of formula used to obtain diffusion coefficient through computing velocity autocorrelation function. However, since stress autocorrelation function is a system property, in principle, we should run a series of simulations to get better statistics. This is quite time consuming since each individual simulation is already computationally expensive. For one single simulation, the statistics can be improved by taking averages over different time origins [10], but still the results can be very noisy (Figure 8), which makes it difficult to get useful information such viscosity and module. An alternative way to obtain viscosity information may be to use the Stokes-Einstein relation from diffusion coefficient and thermal temperature. This idea is similar to the recent experimental micro-rheology approach.

On the other hand, non-equilibrium simulations, such as NEMD [11], Non-equilibrium DPD and BD simulations with external flow field [12], may be more efficient in obtaining rheological properties (Figure 9), and a distinct advantage over equilibrium dynamic simulation techniques is that Non-equilibrium simulation doesn't require either long or large simulations.

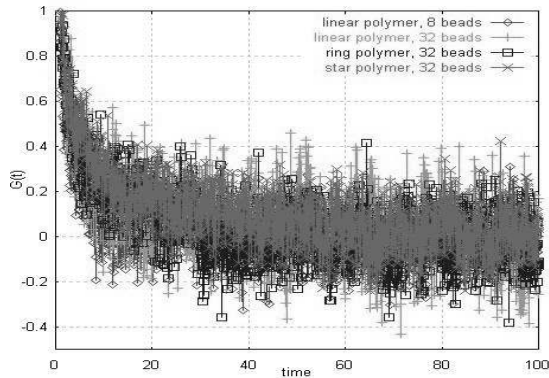


**Figure 8:** stress relaxation curve calculated from equilibrium DPD simulations. Plotted are simulation results for 4 melt systems: linear chains with 8 and 32 beads, 32-bead star and ring. According to the Rouse theory, 8-bead and 32-bead linear polymer systems should have the shortest and longest stress relaxation time respectively. However, such features can not be verified clearly due to noisy nature in the results.

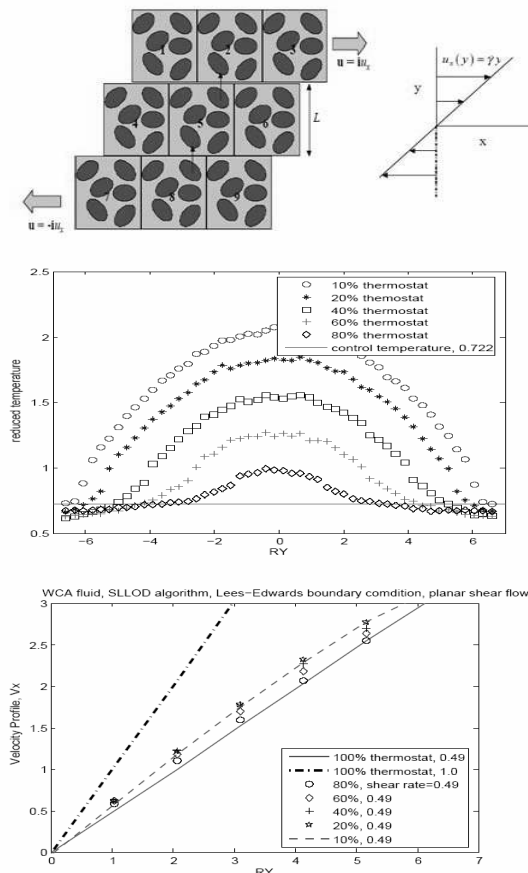


**Figure 9:** NEMD of WCA fluid, the shear flow is set up by the SLLOD algorithm with Lees-Edwards boundary condition. The simulation results show how the temperature profile affects the shear profile. For liquid, the viscosity decreases with increasing temperature. Such a study can be extended to polymer systems.

However, in recent years, NEMD simulations have been questioned for having a far too large deformation rate, i.e. the Deborah number is too large compared to

real rheological experiments and practical processing conditions. For BD simulations with external flow field, the simulated Deborah number can be comparable to practical flow situations.

### Summary

We illustrated the capability of molecular modeling techniques in probing the structure, dynamics and rheological properties of polymer systems. Several examples are shown based on our own study of different molecular modeling techniques.

### References

1. Yanwei Wang, MD Simulation of Polymer Melts, master thesis, DTU, June, 2005.
2. D.N. Theodorou, SIMU Programme Newsletter, Issue 1 (2000), 19-40.
3. M. Doi, Introduction to Polymer Physics, Clarenton Press, Oxford, 1996.
4. M. Doi, S.F. Edwards, the Theory of Polymer Dynamics, Oxford University Press, Oxford, 1986.
5. J. Rudnick, G. Gaspari, J. Phys. A: Math Gen. 19, 191, 1986.
6. D.L. Ermak, J.A. McCammon, J. Chem. Phys. 69 (4) (1978), 1352-1360.
7. R.D. Groot, P.B. Warren, J. Chem. Phys. 107 (11) (1997) 4423-4435.
8. K. Kremer, G.S. Grest, J. Chem. Phys. 92 (8) (1990)
9. Xueyu Zhu, Brownian Dynamics Simulation of Polymer Behaviors in Microfluidic Systems, master thesis, DTU, July, 2005.
10. F.Y. Hansen, G. Peters, Molecular Dynamics Simulations, from Theory to Practice, text book for DTU course 26250.
11. D.J. Evans, G.P. Morriss, Statistical Mechanics of Non-equilibrium Liquids, Academic Press, London, 1990.
12. R.M. Jendrejack, D.C. Schwartz, J.J. de Pablo and M.D. Graham, J. Chem. Phys., 120 (5) (2004), 2513-2529.

**Ayten Yilmaz**

Phone: +45 4525 2920  
Fax: +45 4588 2258  
E-mail: ayt@kt.dtu.dk  
WWW: www.kt.dtu.dk  
Supervisors: Peter Glarborg  
Hans Livbjerg  
Per G. Kristensen, DGC

**Ph.D. Study**

Started: August 2005  
To be completed: September 2008

## Particle Formation during Natural Gas Combustion at Domestic Appliances

**Abstract**

Epidemiological associations between illness and nitrogen dioxide may be the consequence of confounding by fine particle numbers. Like many other phenomena in nature, the presence of carbon nano-forms in blue combustion flames went virtually unrecognized because it was essentially unexpected. Observation of carbon nano-forms in relatively efficient burning, mostly blue combustion flames suggests that the proliferation of so-called clean-burning gaseous fuel sources, particularly methane-series gases ( $C_nH_{2(n+1)}$ ;  $n=1,2,3\dots$ etc) may, in fact, make a significant contribution of carbon nanocrystal forms to both the indoor and outdoor air environment. In this PhD study, particle formation from gas cookers are investigated.

**Introduction**

The contribution of the home environment and other life style factors in the pathogenesis of allergic disease has attracted much attention, particularly the role of indoor pollution from gas cooking appliances via nitrogen dioxide ( $NO_2$ ) and carbon-monoxide (CO) emissions. In particular, natural gas is recognized as one of the most important cooking fuels for domestic gas burners in developed countries (1).

A recent hypothesis (2) is that the epidemiological associations between illness and nitrogen dioxide may be the consequence of confounding by particle numbers. When particles are measured as mass the greatest contribution comes from the largest particles, but the greatest number of particles by far are the submicron ones. These ultrafine particles are generated, as is  $NO$ , by the combustion process, and therefore the two pollutants (ultrafine particles and  $NO_2$ ) are likely to correlate closely.

There are several studies available in literature reporting the effects of cook-top burner design and operation factors (such as cap material, cap size, port shape, port size, port spacing, central secondary aeration, flame inserts, load height, load height to flame length ratio, thermal input, etc ) on the gaseous emissions ( $NO_x$ , CO and hydrocarbon emissions) from the natural gas fired cook-top burners (3, 4, 5). However these studies do not provide any correlations for particulate matter or soot emissions. Gas composition is particularly a vital parameter affecting

burner performance. It is known that using the same gas stove to burn natural gas with various heating values other than the intended fuel is inappropriate and hazardous due to the possible occurrence of incomplete combustion (i.e. a increase of CO emissions and/or soot formation) lift-off, flashback and inadequate heat input.

It was communicated that like many other phenomena in nature, the presence of carbon nanotubes in blue combustion flames went virtually unrecognized because it was essentially unexpected (6). Observations of carbon nanotubes and related nano-forms in relatively efficient burning, mostly blue combustion flames such as propane and natural gas suggests that the proliferation of so-called clean- burning gaseous fuel sources, particularly methane-series gases ( $C_nH_{2(n+1)}$ ;  $n=1,2,3\dots$ etc) may, in fact, make a significant contribution of carbon nanocrystal forms to both the indoor and outdoor air environment. Murr et al (7) reported aggregated multiwall carbon nanotubes with diameters ranging from 3 to 30 nm and related carbon nanocrystal forms ranging in size from 0.4 to 2  $\mu m$  (average diameter) in the combustion streams for methane/air, natural gas/air, and propane gas/air flames from domestic (kitchen) stoves.

**Specific Objectives**

In this PhD study, particle formation during natural gas combustion at domestic appliances will be investigated. The work involves determination of particle size distribution and chemical composition of the particles

together with the total amount of particles formed. Once the particles have been identified, mechanism of formation of the particles will be studied and a model for particle formation during gas combustion will be developed. Depending on the nature of the particles, the project may focus on the precursor chemistry (formation and conversion of PAH prior to soot inception; formation of SO<sub>3</sub> as the limiting step in sulfuric acid formation) or on nucleation and particle growth. The heat transfer characteristics of the flame may also be part of the study.

## Results and Discussions

Preliminary experiments were carried out using the gas cooker in its normal procedure - natural gas supplied from the city line and air supplied from the surroundings. There were no pots placed above the cooker. Samples were collected at ~10cm above the burner using a gas ejector probe developed for particle analysis in a research program instigated to study fine particles (8). Particle concentrations are measured with a Model 3775 Condensation Particle Counter (CPC). Particles are classified with a Model 3080 Electrostatic Classifier with a Model 3081 LDMA (Long Differential Mobility Analyzer), and/or a Model 3085 NDMA (Nano Differential Mobility Analyzer).

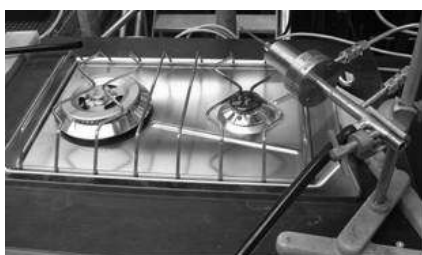


**Figure 1:** Gas cooker and the ejector probe

Since particle concentrations in the ambient air were changing over time and there was no experimental control over the gas quality, the repeatability of experiments was not likely. It has been observed that the –supposed to be blue flame – was sometimes becoming a colour between yellow to orange. This change in the flame could be due to any impurities coming with the gas or just the changes in air flow around the burner.

Despite changing conditions in each experiment, CPC and SMPS measurements show that particle concentrations increase and size distributions change right after turning on the burner. However the elevated particle concentrations do not go beyond sharp peaks observed once in a while, which could indicate a release of high amount of fine particles at some instant during gas combustion. Because of the changing conditions in each experiment, it is not possible to report a trend for the size and frequency of these peaks. Before correlating these peaks directly to the gas combustion, controlled experiments are required.

For this reason, a well-controlled experimental set-up is prepared. Domestic gas cookers usually apply partial-premixed flame. A reactor, made of steel, is built

keeping this configuration.

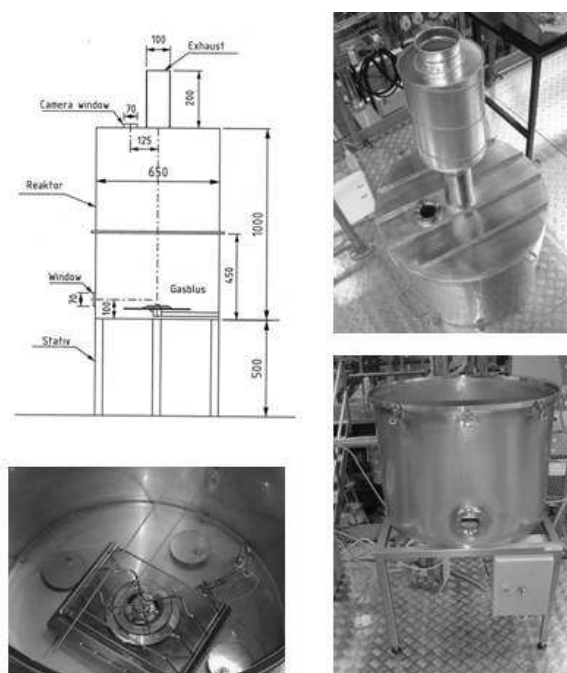


**Figure 2:** The reactor-technical drawing and the two compartments.

The reactor is composed of two compartments, as presented in Figure 2: 1. The lower compartment where the burner is placed at the bottom with the required gas connections and four ports through which particle free combustion air is supplied to the reactor. The ignition and flow control panel of the burner is kept outside the reactor, leaving the primary air supply nozzle inside the reactor. The reactor bottom allows using different gas rings after the required arrangement of primary air supply nozzle distance. 2. The upper compartment provides extra volume and sampling ports. A silencer is installed at the reactor outlet for preventing noise during experiments.

In order to assure flame stability, flow velocity through the reactor is kept below 10cm/s (9). The excess air ratio of the system is kept above 10. Sampling ports are placed along the reactor to allow sampling at different locations above the flame. The glass windows placed at both compartments allows observation and video recording of the flame through the experiments.

Experimental procedure can be summarized as measurement of total particle concentration, gas concentrations and temperatures along the reactor before, during and after combustion. The gas concentrations of interest are oxygen, carbon monoxide, carbon dioxide, nitric oxide and nitrogen oxides. Particle measurements are to be carried out at the reactor outlet when the reactor reaches steady state.

During the test period of the reactor, a black deposit is collected on the central part of the burner. This deposit is shown in Figure 3. At the initial stage of the deposit formation, the shape of the deposit is observed to be triangular – which indicates that it could be related to the second flame zone where the gas nozzles are not continuous but located in equally distanced three regions. The deposit is suspected to be soot. A thermal gravimetry method is applied, results of which are presented in Figure 4. Thermal Gravimetric Analysis (TGA) is an analytical technique that measures the weight loss (or weight gain) of a material as a function of temperature. The sample weight loss started around 350°C and the sample totally disappeared around 575°C.



**Figure 3:** Black deposit collected on the burner

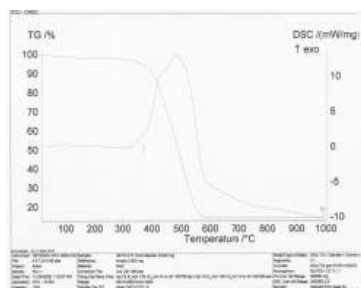


**Figure 4:** Results of thermal gravimetry method applied to the black deposit collected on the burner.

As soot formation is often related to primary air, the primary air supply opening was increased from 2,3mm to 2,5 mm. The effect of this change in the primary air flow-rate is not calculated, instead the effect is tested directly. The latter did not have any effect on either deposit formation or the flame structure visually.

In order to determine the reason of deposit formation, a simple test is carried out: The reactor is operated for 8 hours without placing the upper compartment. Particle free air was supplied from the reactor bottom, and temperatures and gas concentration were measured through the sampling ports. At the end of 8 hours, there was no deposit. This experiment is repeated under the same conditions, the only difference being that the upper compartment is placed. After 8 hours of operation, the deposit is observed. Thus it is concluded that the deposit formation has its source in the conditions appearing during combustion in the closed environment.

### Future Work

Experiments are being carried out in order to point out the differences in temperature and gas concentrations above the flame, between the open and closed operation of the reactor. Temperature and concentration profiles along the reactor are being studied for different air and gas flow-rates, for both cases where the upper compartment is in place and displaced.

Once the temperature and gas concentration profiles in the reactor are determined experimentally, reactor will be used for particle investigations at different experimental conditions, i.e varying the gas and air flow-rate. Currently experiments are being carried out using natural gas from the city line. In the future, experiments will be carried out using pure methane, a mixture of methane and H<sub>2</sub>S or a gas mixture simulating natural gas. This is aimed to enable us with observing the affects of different components on particle formation.

A CFD model will be prepared to simulate the conditions inside the reactor. This model will be validated by experimentally determined temperature and gas concentration profiles in the reactor. This will allow us to visualize the conditions inside the reactor, in other words to foresee the possible improvements required in order to simulate the conditions in a real kitchen environment.

As there is no mixing in the reactor, temperatures and concentrations vary in both horizontal and vertical axes.

With the present construction of the reactor, only one type of measurement (particle concentration, gas concentration or temperature) can be carried out at a single sampling point at one time. Thus if one needs to know the temperature and gas concentrations at the same sampling point where particles are sampled, there is a need for a reference which provides a value for the latter under the same experimental conditions which were performed previously. In order to overcome this complexity, a second line of sampling ports will be opened at the opposite site of the available sampling ports. This will allow us to perform temperature or gas measurements at the same point.

In addition to all above, it is worth to mention about the type of particles formed. During the test period, particle concentrations were measured at the reactor outlet. A study will be carried out to identify the nature of these particles, namely their chemical composition.

### Acknowledgements

This PhD study is co-funded by The Graduate School in Chemical Engineering, DTU: Molecular Products and Product Technology MP2T, Danish Research Training Council - FUR under the Ministry of Science, Technology & Development and DGC (Dansk Gas - teknisk Center).

## References

1. Chauhan, A.J., *Clinical and Experimental Allergy*, (29) (1999) 1009–1013.
2. Seaton, A., Dennekamp, M., *Thorax* (58) (2003) 1012-1015.
3. Junus, R., Stubington, J. F., Sergeant, G. D., *International Journal of Environmental Studies* (45) (1994) 101-121.
4. Stubington, J.F., Beashel, G., Murphy, T., Junus, R , Ashman, P.J., Sergeant, G.D., *Journal of Institute of Energy* (67) (1994) 143-155.
5. Shaddix, C. R., Harrington, J.R., Smyth, K.C., *Combustion and Flame* (99) (1994) 723-732.
6. Bang, J.J., Guerrero, P.A., Lopez, D.A., Murr, L.E., Esquivel, E.V. *Journal of Nanoscience and Nanotechnology* (4.7) (2004) 716- 718.
7. Murr, L.E., Bang, J.J., Esquivel, E.V., Guerrero, P.A., Lopez, D.A. *Journal of Nanoparticle Research* (6) (2004) 241–251.
8. Johannessen, J.T., Pratsinis, S.E., Livbjerg,H., *Chemical Engineering Science*, 55(1), (2000) 177-191.
9. Matthews, T. G., Thompson, C. V., Wilson, D. L., Hawthorne, A. R., *Environment International*, (15),(1989) 545-550.